U. S. Department of Energy
1000 Independence Avenue, S.W.
Washington, D.C. 20585

Fiscal Year 2023: First Quarter

Progress Reports:

Advanced Battery Materials Research (BMR) Program & Battery Consortia

Released May 2023
for the period of October – December 2022

Approved by

Tien Q. Duong
Manager, Advanced Battery Materials Research Program & Battery500 Consortium
Batteries & Electrification R&D
Office of Energy Efficiency and Renewable Energy – Vehicle Technologies Office
U.S. Department of Energy

ACKNOWLEDGMENTS

This report has been edited by the following team members:

- **T. A. Zachry,** Energy & Environmental Resources Group
- **Patricia H. Smith,** Naval Sea Systems Command – Carderock Division

TABLE OF CONTENTS

Battery Consortia

TABLE OF FIGURES

TABLE OF TABLES

A MESSAGE FROM THE MANAGERS: ADVANCED BATTERY MATERIALS RESEARCH AND BATTERY CONSORTIA

This quarter, we introduce three new consortium projects to the Advanced Battery Materials Research (BMR) Program. The Cathode-Electrolyte Interphase (CEI) Consortium project is led by J. Xiao of Pacific Northwest National Laboratory (PNNL) and focuses on studying lithium-ion battery cathode materials and their interfaces in liquid electrolytes. The CEI Consortium involves 10 national laboratories: PNNL, Argonne (ANL), Brookhaven (BNL), Idaho (INL), Lawrence Berkeley (LBNL), Lawrence Livermore (LLNL), Oak Ridge (ORNL), National Renewable Energy Laboratory (NREL), Sandia National Laboratories, and SLAC National Accelerator Laboratory. G. Ceder, LBNL, leads the Cation Disordered Rocksalt (DRX+) Materials Consortium. This project aims to develop high-energy, high-rate Ni- and Co-free DRX materials based on manganese as a cost-effective, earth-abundant, and safe redox-active element. The DRX+ Consortium includes investigators from LBNL, ANL, ORNL, and SLAC National Acceleratory Laboratory. The Earth-Abundant Cathode Active Materials (EaCAM) Consortium, led by J. Croy (ANL), is also working to design and enable novel electrodes that utilize zero cobalt. The EaCAM team includes scientists from ANL, NREL, ORNL, LBNL, and PNNL. The projects began this quarter and will report their progress starting next quarter.

A few notable achievements from BMR investigators during the October 1, 2022, through December 31, 2022, quarter are summarized below:

- Y. Cui's group at Stanford University investigated the effect of halogen (I, Br, Cl) on $Li_{10}B_{10}S_{20-x}X_{2x}$ solid electrolyte conductivity. Comparisons were made against the baseline material ($Li_{10}B_{10}S_{20}$). The iodine-doped material with the composition $Li_{10}B_{10}S_{19}I_2$ had the highest ionic conductivity at 1.02 mS/cm.
- J. Ye's team at LLNL demonstrated full-cell lithium iron phosphate batteries with a 30 wt% Li-La-Zr-O/ polyurethane composite electrolyte. Cells displayed a capacity of 117 mAh/g over 200 cycles when cycled at 25°C and 1C rate.
- A. Westover's team compared ORNL evaporated lithium to rolled lithium on copper foil. The data showed that the commercially rolled lithium outperformed the evaporated lithium metal. They further highlighted that a key reason all of the lithium sources fail is due to parasitic side reactions, which are somewhat limited by a thicker surface layer.
- E. Wachsman's team at University of Maryland (UMD) successfully coated $LiNi_{0.6}Mn_{0.2}Co_{0.2}$ with Li_4SiO_4 and Li_5AlO_4 interlayers. The coatings reduced the interfacial resistance between the cathode and the electrolyte by a factor of 5 to 10.
- C. Johnson's group at ANL successfully developed two-layered oxide cathodes with improved cycling stability for Na-ion batteries. Full concentration gradient O3-type $NaNi_{0.8}Co_{0.1}Mn_{0.1}O_2$ displayed an 80% capacity retention for 300 cycles. P2-type Fe/Mn layered oxide materials had a 73% retention after 300 cycles.

A few notable achievements from the Battery500 Team this quarter include:

- The State University of New York, Binghamton, team led by S. Whittingham compared the reactivities of different commercial $LiNi_{0.8}Mn_{0.1}Co_{0.1}$ cathode materials and found the critical role of particle size, morphology, distribution, and surface or bulk modification in suppressing undesired side reactions and structural degradation of the material.
- C. Wang's team at UMD identified a new ester-based electrolyte that can achieve a high lithium cycling efficiency of 99.7%. Through molecular design, the anodic stability has been extended to > 5 V with no sacrifice to the anode.

- P. Liu's team at University of California, San Diego, synthesized a new sulfurized polyacrylonitrile (SPAN) cathode that has a higher sulfur loading (60 wt%) than regular SPAN (39-43 wt%) material. It is theorized that the new material, named CS SPAN, is able to host extra sulfur by forming N-S bonds. Cells utilizing CS SPAN and a localized high-concentration electrolyte delivered capacities over 900 mAh/g at 0.2C after 50 cycles. This represents a 200 mAh/g improvement over conventional SPAN material.

For more information about these and other BMR projects, we encourage you to attend the Vehicle Technologies Annual Merit Review. This year, the event will be held virtually on June 12-15, 2023. To register, please visit https://www.energy.gov/eere/vehicles/vehicle-technologies-annual-merit-review. Our next quarterly report is anticipated in July 2023.

On behalf of the Vehicle Technologies Office Team,

Tien Q. Duong

Tien Q. Duong
Manager, Advanced Battery Materials Research Program & Battery500 Consortium
Batteries & Electrification R&D
Office of Energy Efficiency and Renewable Energy
U.S. Department of Energy

Simon T. Thompson

Simon T. Thompson, Ph.D.
Manager, Battery Technology Development
Vehicle Technologies Office
Office of Energy Efficiency and Renewable Energy
U.S. Department of Energy

TASK 1 – Solid-State Electrolytes

Team Lead: Andrew Westover, Oak Ridge National Laboratory

Summary

The U. S. Department of Energy (DOE) has made a clear goal of realizing next-generation batteries with an energy density greater than 500 Wh/kg, that can cycle for more than 300 cycles, and that can demonstrate high-rate capabilities. To achieve this step-change in battery performance, a significant change in the battery chemistry and cell design is needed. This task focuses on developing solid-state electrolytes (SSEs) that enable Li-metal anodes and high-energy cathodes to achieve just such a step change. This task includes 23 projects centered in DOE national laboratories, companies, and universities across the United States. These projects span the gamut of different materials for SSEs, interfacial design strategies to enable Li-metal anodes, and high-energy cathodes. Together, they can significantly impact the successful realization of the DOE battery performance targets.

In summary, the projects focus on research and development of a range of solid electrolytes (SEs), including:

- sulfur ceramics and glasses (1.1 – 1.5, 1.18, 1.19, 1.22, 1.23),
- oxide and halide ceramics (1.6-1.8, 1.20),
- polymers (1.9 – 1.10, 1.21),
- composites (1.11 – 1.14),
- multiple electrolytes / full cells (1.15 – 1.16), and
- Li-metal – SSE interface (1.17).

These projects encompass common research themes essential to achieving high-energy solid-state batteries (SSBs), including:

- engineering high ionic conductivity > 1 mS/cm,
- developing electrolytes that are stable with various high-energy cathodes, including layered oxide cathodes, high-voltage spinels, and conversion cathodes such as sulfur and FeF_3,
- developing electrolytes or interfaces that are stable with lithium metal,
- developing thin SEs 20-µm to 100-µm thick, and
- understanding the mechanics of SSBs.

Highlights

The highlights for this quarter are as follows:

- J. Connell's group at Argonne National Laboratory (ANL) used thermogravimetric analysis to measure the weight gain of argyrodite powders with various atomic layer deposition (ALD) coatings when exposed to O_2. They found that 1-100 ALD layers of Al_2O_3 effectively mitigates the reaction of the electrolyte with air.
- G. Xu's ANL team showed that O-doped argyrodite electrolytes of the composition of $Li_{5.5}PS_{4.4}O_{0.1}Br_{1.5}$ have improved critical current densities (CCDs) up to 1.4 mA/cm^2 compared to the undoped argyrodite at 0.9 mA/cm^2.
- Y. Cui's group at Stanford University compared the effect of iodine doping into the $Li_{10}B_{10}S_{20-x}X_{2x}$ SE, finding that the composition $Li_{10}B_{10}S_{19}I_2$ had the highest ionic conductivity at 1.02 mS/cm.

- J. Nanda's SLAC Stanford Battery Research Center and Oak Ridge National Laboratory (ORNL) team developed thin-film sulfide SE separators with < 5% binder content with room-temperature ionic conductivities up to 0.25 mS/cm and thicknesses less than 50-µm thick.
- D. Lu's group at Pacific Northwest National Laboratory successfully developed small pouch cells using a S-C cathode, an argyrodite SE, and a Li-In anode. They did this using a separator that was approximately 100-µm thick.
- J. Ye's team at Lawrence Livermore National Laboratory demonstrated full-cell lithium iron phosphate batteries with a Li-La-Zr-O (LLZO) / poly (ethylene oxide) (PEO) composite electrolyte with a capacity of about 100 mAh/g over 200 cycles.
- Z. Chen and T. Li's ANL group demonstrated that their newest antiperovskite electrolyte compositions reached a room-temperature ionic conductivity of 0.1 mS/cm. They also demonstrated the use of a high-precision leakage current measurement system.
- R. Sacci's team at ORNL successfully synthesized Li_3YCl_6, both by a mechanochemical synthesis and from an ammonium-assisted, solution-based method. The best conductivity was achieved with the ammonium-assisted method at 0.65 mS/cm.
- N. Balsara's team at University of California, Berkeley (UCB) measured the limiting current poly(pentyl malonate) electrolytes; they found that for a salt concentration of 0.04, the electrolytes had a limiting current more than twice that of PEO-based electrolytes.
- Z. Bao and Y. Cui's Stanford University group showed that Stanford's salt-philic solvent-phobic (SP^2) electrolyte increased the amount of fluorine in the solid electrolyte interphase formed with liquid electrolytes, which is a key reason for its improved performance.
- S. Tepavcevic's ANL group investigated the effect of mixed salt additives to PEO electrolytes including lithium bis(trifluoromethanesulfonyl)imide (LiTFSI), lithium bis(fluorosulfonyl)imide (LiFSI), and $LiNO_3$. They found the highest CCD and Coulombic efficiency (CE) for cells with an LiFSI salt in the PEO electrolyte.
- X. C. Chen's team at ORNL explored several new ethylene carbonate (EC) based single ion conducting (SIC) electrolytes. They found that the electrolyte labeled 60VEC-SIC formed a solid film that had an ionic conductivity of 6×10^{-7} S/cm at 20°C.
- B. McCloskey's UCB group started synthesizing LLZO – poly(ethylene glycol) – poly(lithium bistrifluorosulfonylimide methacrylate) (LLZO-PEG-PMTFSI) composite electrolytes. The best conductivity was found with a 40 wt% LLZO in a 3:1 PMTFSI-PEG polymer electrolyte.
- E. Hu's Brookhaven National Laboratory team demonstrated the use of Celgard® as a template and reinforcement to a polypropylene electrolyte that enabled the formation of a 20-µm-thick membrane. This membrane had a limiting current and CCD near 2.4 mA/cm^2 at 50°C.
- H. Kim's team at UCB developed their active buffer layer (ABL) for Li-metal anodes, successfully casting ABL about 10-µm thick. They developed a model of the soft, clay-like LiCl-GaF_3 SE. The model demonstrated that the plastic deformation was enabled by formation of $GaCl_3$ clusters that are weakly bound together by Van Der Waals forces. They also focused on developing succinonitrile (SN) – lithium salt mixtures, finding that the SN-LiTFSI mixture had a voltage stability of about 4.8 V versus Li/Li^+ and an ionic conductivity of 3.5 mS/cm. They further explored solution processing of Li-P-S-Cl (LPSCl) – poly(phenylene oxide) glass-polymer composites. They found that both the dispersion method and solution precipitation method decrease the ionic conductivity of the LPSCl; however, it still reaches a conductivity of > 0.1 mS/cm.
- A. Burrell's National Renewable Energy Laboratory team developed an improved high-pressure testing cell for SSBs capable of applying between 5-100 MPa during cycling. The team also demonstrated use of $LiCoO_2$ – LPSCl – In batteries with a capacity of 100 mAh/g active material with only 1.6 MPa of pressure.

- A. Westover's team compared ORNL evaporated lithium to a rolled lithium on copper foil. The data showed that the commercially rolled lithium outperformed the evaporated lithium metal. They further highlighted that the key reason all of the lithium sources fail is due to parasitic side reactions that are somewhat limited by a thicker surface layer.
- D. Wang's Pennsylvania State University team demonstrated that both an additive and their new SSE improve ionic conductivity in sulfur cathode composites.
- T. Yersak's General Motors group found that hot pressing of FeS_2-$Li_7P_3S_{11-x}O_x$-C composites had significantly better performance than cold-pressed cathode composites. This is related to the improved processibility of the glassy $Li_7P_3S_{11-x}O_x$ SSE.
- E. Wachsman's team at University of Maryland (UMD) successfully coated $LiNi_{0.6}Mn_{0.2}Co_{0.2}$ (NMC-622) with higher-Li-content Li_4SiO_4 and Li_5AlO_4 coatings. These coatings reduce interfacial resistance between co-sintered LLZO and NMC cathodes by 5 to 10 times, compared to uncoated NMC.
- L. Madsen's team at Virginia Polytechnic Institute and State University showed full-cell data for batteries using molecular ionic composite SE. They identified that the limiting current for this electrolyte is 0.3 mA/cm^2 at room temperature.
- S. Martin's Iowa State University team focused this quarter on developing a high-quality preform needed for drawing an ultrathin ion-conducting sulfide glass.
- C. Wang's UMD team compared the use of small (5 µm) and large (10 µm) $LiNi_{0.8}Mn_{0.1}Co_{0.1}O_2$ (NMC-811) cathode. In all cases, the cathodes with smaller NMC particles outperformed the batteries with larger NMC in cycle stability, CE, and overall cell resistance. They also developed a model that includes the surface energies, with initial data suggesting that some lithiophobicity in SE defects can help prevent lithium penetration.

Task 1.1 – Multifunctional Gradient Coatings for Scalable, High-Energy-Density Sulfide-Based Solid-State Batteries
(Justin Connell, Argonne National Laboratory)

Project Objective. This task seeks to develop scalable approaches to synthesize gradient-coated sulfide solid-state-electrolyte (SSE) particles to improve their air/moisture tolerance and provide chemical compatibility with Li-metal anodes and high-voltage oxide cathodes. The compositional gradient is targeted to provide the additional advantage of lower interfacial impedance due to mitigation of detrimental, spontaneously formed space-charge layers and/or elemental interdiffusion at the sulfide SSE-oxide cathode interface.

Impact. Development of coated SSE materials that provide stable, low-impedance interfaces with both anode and cathode will enable high-energy-density, all-solid-state full cells with improved cyclability at high rates relative to benchmarked, uncoated materials. Coating the SSE directly will also remove the need for separate anode and cathode coatings, significantly reducing the cost and complexity associated with materials processing while maintaining compatibility with roll-to-roll manufacturing.

Approach. The team will leverage a surface science-based, integrated experimental-theoretical approach to synthesize gradient-coated SSE powders, to characterize the structure, composition, and intrinsic stability of coated SSEs in contact with reactive electrodes, and to directly correlate this understanding with their electrochemical performance. Gradient coatings will be developed using atomic layer deposition (ALD) and/or physical mixing methodologies viable at the kg/ton scale, ensuring technical and commercial relevance of the final, optimized coating process. Well-characterized, model surfaces will be used to understand the electronic structure and chemical stability of the gradient coatings as a function of gradient composition and thickness to understand the effect of space-charge layers and chemical reactions on interface resistance. They will accelerate development and optimization of the gradient coatings for improved performance in full cells by establishing a tight feedback loop between materials synthesis and experimental/computational characterization of interfacial (electro)chemistry.

Out-Year Goals. The out-year goals are to demonstrate high-energy-density, low-impedance full cells assembled from fully optimized, gradient-coated SSE powders, high-energy-density cathodes, and Li-metal anodes. The team will also significantly improve the ability to manipulate the formation of space-charge layers at sulfide SSE-oxide cathode interfaces based on mechanistic understanding of the extent to which they can be mitigated to reduce overall cell impedance.

Collaborations. This project funds work within multiple divisions and directorates at Argonne National Laboratory and includes in-kind contributions from Solid Power.

Milestones

1. Identification of multiple gradient coating chemistries that deliver > 50% reduction in weight gain during humidified air exposure. (Q1, FY 2023; Completed)

2. Assembly and assessment of Li||Li symmetric cells with coated argyrodite SSEs. (Q2, FY 2023; In progress)

3. Computational assessment of stability of coated lithium argyrodite SSEs against electrodes. (Q3, FY 2023; In progress)

4. Small format full-cell assembly demonstration and baseline SSE|cathode interfacial impedance assessment. (Q4, FY 2023; In progress)

Progress Report

Sulfide-based SSEs with an argyrodite-type cubic structure and $Li_{7-y}PS_{6-y}X_y$ (LPSX; X = Cl, Br, I) composition have high ionic conductivities (> 1 mS/cm), wide band gaps, and favorable mechanical and processing properties, making them particularly promising candidate materials for all-solid-state batteries. The team's experimental and theoretical approach in previous quarters focused on nanoscale coatings from ALD on LPSCl powders; these coatings specifically build on all these advantages and enable investigations of interfacial properties critical to operation of these SSEs. Experimental studies this quarter addressed the reactivity of uncoated and coated argyrodite particles in the presence of a (humidified) oxygen environment. Specifically, three chemistries of ALD coatings (that is, Al_2O_3, ZnO, and ZnS) on LPSCl were prepared, and the impact of these coatings on the LPSCl stability toward pure oxygen and humified oxygen was investigated.

The team began their investigation with argyrodite powders coated with ALD Al_2O_3, as they extensively investigated this chemistry during the first year of this program. They leveraged the power of thermogravimetric analysis to better understand the impact of the ALD Al_2O_3 coatings on LPSCl when these electrolytes were subjected to oxidizing conditions. Specifically, they probed the mass change of the powders under a flow of dry and humidified O_2, as argyrodites are notoriously unstable under humid and oxidizing conditions.[1-2] The mass gain was collected on a thermogravimetric analyzer (TA Instruments) under a flow of O_2 as well as under a flow of O_2 bubbled through deionized H_2O. Mass gains for argyrodites under oxidizing and humid conditions can be correlated with the decomposition of the electrolyte into H_2S, lithium sulfates, etc. in combination with H_2O adsorption. The argyrodite powders coated with ALD Al_2O_3 showed significantly lower weight gain under dry and humidified O_2 exposure compared to the uncoated LPSCl (Figure 1). Specifically, argyrodite powders coated with 10 cycles of ALD Al_2O_3 exhibited negligible (≤ 1%) weight changes following 240 minutes of dry O_2 exposure, and only a ~ 17% weight gain following 240 minutes of humid O_2 exposure. This compares to ~ 19% and ~ 100% weight gains for the uncoated argyrodite exposed to dry and humidified O_2, respectively. It is remarkable that even one ALD Al_2O_3 cycle can significantly suppress weight gain under these conditions, particularly during humidified O_2 exposure.

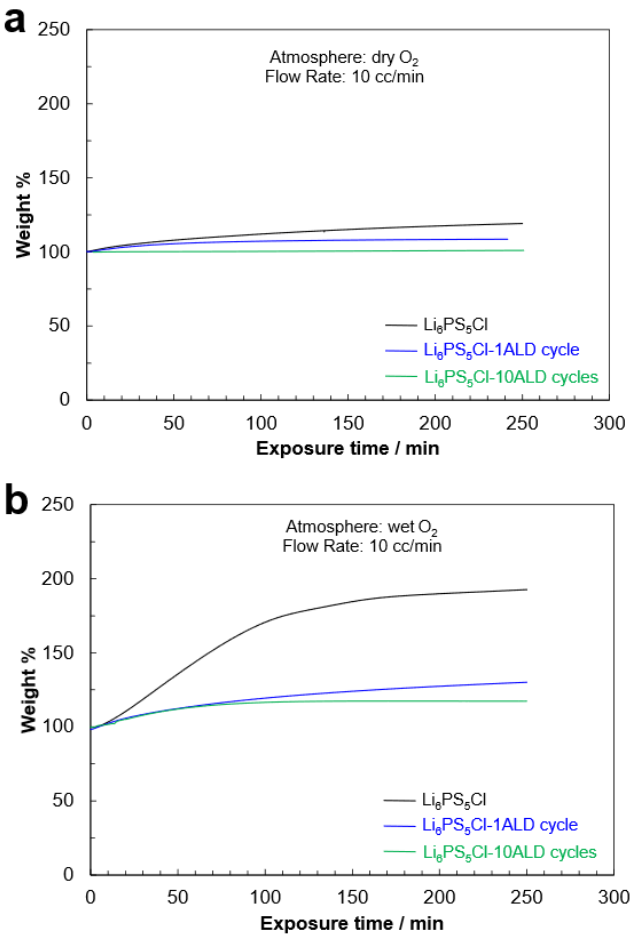

Figure 1. Weight gain of uncoated Li_6PS_5Cl powders and Li_6PS_5Cl powders after 1 and 10 ALD Al_2O_3 cycles during exposure to (a) pure O_2 and (b) humidified O_2.

To gain a more holistic understanding of the impact of the ALD coatings on argyrodites under humid and oxidizing conditions, the team compared their results for ALD Al_2O_3 coatings to their recently developed process to grow ZnO and ZnS coatings on LPSCl. These new chemistries were grown onto LPSCl by first depositing a thin Al_2O_3 seed layer (with one ALD Al_2O_3 cycle) followed by 10 ALD ZnO or ZnS cycles. The ALD Al_2O_3 seed layers were used because the team discovered that the ALD ZnO and ZnS do not readily nucleate on the argyrodite surface. The argyrodite powders coated with both ALD ZnO and ZnS showed significantly improved stability under humidified O_2 exposure compared to the

uncoated LPSCl (Figure 2), achieving > 50% reduction in weight gain relative to uncoated material after ~ 80 minutes. This metric is particularly important for development of SSE coatings that are compatible with realistic processing environments, as the SSE may be in contact with ambient conditions for approximately 60-80 minutes (for example, in a dry room).[3] While the ZnS and ZnO coatings appear to affect the reaction kinetics between LPSCl and humidified O_2, the ALD Al_2O_3 coatings appear to be most effective for protecting the argyrodite powders against decomposition reactions. This conclusion is corroborated by calculated reaction energies for ZnO and Al_2O_3 with LPSCl and water. Al_2O_3 is less reactive (reaction energy of -0.05 eV/atom) toward LPSCl than ZnO, which reacts to form Li_2S, Li_3PO_4, ZnS, and LiCl with energy of -0.38 eV/atom. However, the reaction of ZnO with water to form hydroxides is not favorable, with an energy of ca. 0 eV/atom.

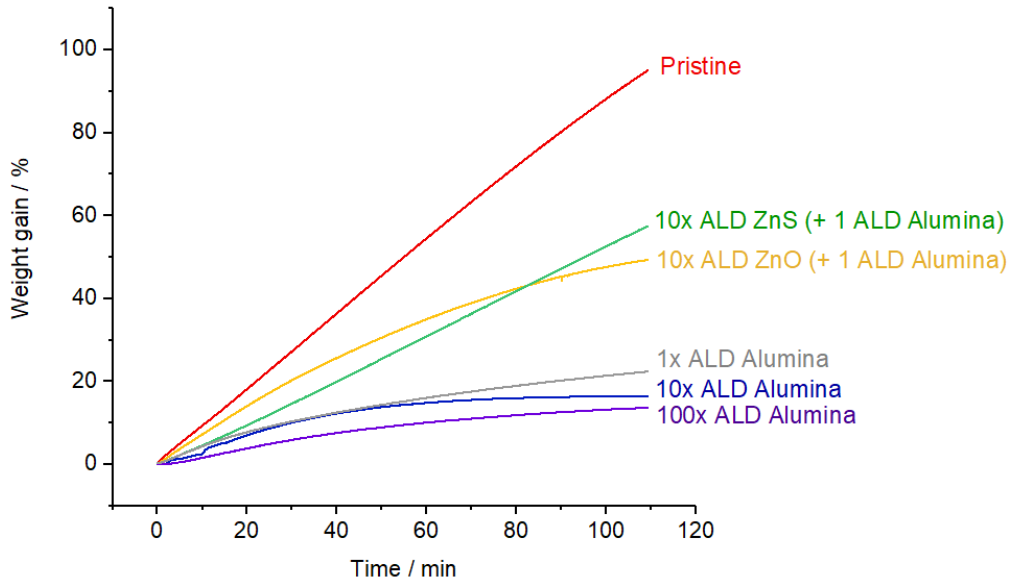

Figure 2. Weight gain of uncoated Li_6PS_5Cl powders and Li_6PS_5Cl powders after 1, 10, and 100 ALD Al_2O_3 cycles, 10 ALD ZnS cycles, and 10 ALD ZnS cycles during exposure to humidified O_2.

To date, the team has demonstrated that precise control of the thickness of ALD coatings on Li_6PS_5Cl powders provides significant benefits to the chemical stability of these materials. Specifically, ALD coatings improve the stability of argyrodites under both humid and oxidizing conditions, a benefit that has now been demonstrated for three distinct coating chemistries, suggesting there is likely a broad spectrum of coatings that can realize similar benefits to sulfide SSE stability against environmental conditions. They have further demonstrated that these coatings significantly stabilize LPSCl to reactivity against lithium metal, and density functional theory calculations suggest favorable ionic and electronic transport properties through interfacial layers formed on coated materials that may facilitate Li-ion migration across the interface and improve interfacial contact. With these achievements in mind, they plan to evaluate the electrochemical performance of coated LPSCl materials in Li||Li symmetric cells and compare this against the performance of uncoated materials to determine the extent to which the many chemical benefits of these ALD coatings translate to improved electrochemical performance.

References

[1] Nikodimos, Y., C-J. Huang, B. W. Taklu, W-N. Su, and B. J. Hwang. "Chemical Stability of Sulfide Solid-State Electrolytes: Stability toward Humid Air and Compatibility with Solvents and Binders." *Energy & Environmental Science* 15, No. 3 (2022): 991–1033. https://doi.org/10.1039/D1EE03032A.

[2] Banik, A., Y. Liu, S. Ohno, Y. Rudel, A. Jiménez-Solano, A. Gloskovskii, N. M. Vargas-Barbosa, Y. Mo, and W. G. Zeier. "Can Substitutions Affect the Oxidative Stability of Lithium Argyrodite Solid Electrolytes?" *ACS Applied Energy Materials* 5, No. 2 (2022): 2045-2053.

[3] Presentation: Vehicle Technologies Office Solid-State Review Meeting; Berkeley, California (August 17–18, 2022).

Patents/Publications/Presentations

The project has no patents, publications, or presentations to report this quarter.

Task 1.2 – Sulfide Electrolytes for High-Energy, All-Solid-State, Lithium-Sulfur Batteries (Guiliang Xu, Argonne National Laboratory)

Project Objective. The project objective is to develop ultrathin (< 30 μm) sulfide solid-state electrolytes (SSEs) with high room-temperature ionic conductivity (> 0.01 S/cm) and high chemical/mechanical/electrochemical stability, and further integrate them with lithium metal and high-loading Se-doped sulfur cathodes through rational interface engineering to develop all-solid-state Li-S batteries (ASSLSBs) with high energy density and long cycle life.

Impact. The project is related to development and mass production of high-performance sulfide SSEs for high-energy all-solid-state Li-S pouch cells. The project's success in meeting or exceeding U. S. Department of Energy targets can promote practical implementation of Li-S batteries in electric vehicles, electric aviation, and grid energy storage, and hence significantly reduce oil dependence and emissions of carbon dioxide. It can also mitigate the domestic supply challenge on critical raw battery materials (for example, nickel and cobalt).

Approach. The thickness and chemical/interfacial stability of sulfide SSEs are the critical challenges for energy density, cycle life, and mass production of all-solid-state Li-S pouch cells. The team will combine innovative material design, electrode architecture fabrication, and advanced diagnostics tools to address these challenges. Specifically, the approaches include: (1) improving air stability and ionic conductivity of sulfides through synthetic control and cation/anion doping, (2) fabricating flexible thick SeS cathode supported thin sulfide electrolytes to ensure intimate contact and increase energy density, (3) stabilizing Li-metal/sulfide electrolytes interface via interlayer and additives design to increase critical current density (CCD) of lithium stripping/plating, (4) advanced Li-S pouch-cell design, and (5) multiscale advanced diagnostic such as *in situ* X-ray diffraction (XRD), X-ray absorption spectroscopy, X-ray imaging, and focused ion beam – scanning electron microscopy (SEM) to understand and overcome the degradation pathways.

Out-Year Goals. The out-year goals are to scale up the optimal sulfide SSEs to develop Ah-level all-solid-state Li-S pouch cells that can reach a cell energy density of > 500 Wh/kg with 80% capacity retention for > 300 cycles at a current density of > 1 mA/cm^2.

Collaborations. The team is closely collaborating with top scientists at University of Chicago (X. Huang) and at Advanced Photon Source (C. Sun, W. Xu, D. Zhang, and J. Deng) and Center for Nanoscale Materials (Y. Liu and M. Chan) of Argonne National Laboratory for *in situ* diagnostics on the synthesis and aging mechanism of the proposed sulfide SSEs.

Milestones

1. Synthesizing $Li_{1-x}PS_{5-x-y}O_yBr_{1+x}$ with an ionic conductivity of > 1 mS/cm. (Q1, FY 2023; In progress)
2. Completing test and understanding on moisture stability of $Li_{1-x}PS_{5-x-y}O_yBr_{1+x}$. (Q2, FY 2023; In progress)
3. Optimizing structure of sulfur cathode and composite cathode to achieve > 1000 mAh/g and stable cycle life in solid-state Li-S cells. (Q3, FY 2023; In progress)
4. Fabricating thin (thickness: 25-100 μm) sulfide electrolytes membrane. (Q4, FY 2023; In progress)

Progress Report

Last fiscal year, the team used *in situ* synchrotron XRD to probe the solid-state synthesis of $Li_{1-x}PS_{5-x-y}O_yBr_{1+x}$ and evaluated the effects of temperature, dopants, holding time, and cooling process on the crystal and local structures of final products. This quarter, the team has synthesized $Li_{6-x}PS_{5-x-y}O_yBr_{1+x}$ according to the guideline from *in situ* XRD results and evaluated their crystal structures, morphologies, ionic conductivity, and CCD of Li/Li stripping/plating.

Figure 3a shows the XRD pattern of $Li_{5.5}PS_{4.5}Br_{1.5}$ synthesized at 500°C for 12 hours with natural cooling, which is mostly in accordance with the standard XRD pattern of Li_6PS_5Br. Nevertheless, XRD peaks belonging to LiBr impurity can be also seen. When introducing oxygen dopants into $Li_{5.5}PS_{4.5}Br_{1.5}$, the LiBr impurity was decreased, and no impurity peaks belonging to Li_2O can be found in the $Li_{5.5}PS_{4.4}O_{0.1}Br_{1.5}$@500°C, indicating that oxygen has been successfully doped into the lattice (Figure 3b). However, when calcinated at a higher temperature of 600°C, the amount of LiBr impurity was significantly increased (Figure 3c). The results highlight the importance of temperature control.

The team further characterized their morphologies by SEM. As shown in Figure 3d, the synthesized $Li_{5.5}PS_{4.5}Br_{1.5}$ shows secondary aggregates that are further comprised of primary particles of hundreds of nanometers. After introducing oxygen, the size of primary particles became larger (Figure 3e-f), which can impact their ionic conductivity.

They have further used electrochemical impedance spectroscopy to measure the room-temperature ionic conductivity of these three electrolytes. The pressure used to fabricate the pellets (10 mm diameter) was 400 Mpa, and the corresponding thickness was ~ 800 µm. During testing, the stack pressure was controlled at 20 Mpa. The ionic conductivity of $Li_{5.5}PS_{4.5}Br_{1.5}$, $Li_{5.5}PS_{4.4}O_{0.1}Br_{1.5}$@500°C, and $Li_{5.5}PS_{4.4}O_{0.1}Br_{1.5}$@600°C was 0.45 mS/cm, 0.40 mS/cm, and 0.32 mS/cm (See Figure 4a; the latter is not shown). The difference could come from both LiBr impurity and particle size. They have used the same process to measure the ionic conductivity of commercial Li_6PS_5Cl material from Ampcera. As shown in Figure 4b, the ionic conductivity of commercial Li_6PS_5Cl was measured to be 0.4 mS/cm, which is similar to the team's materials.

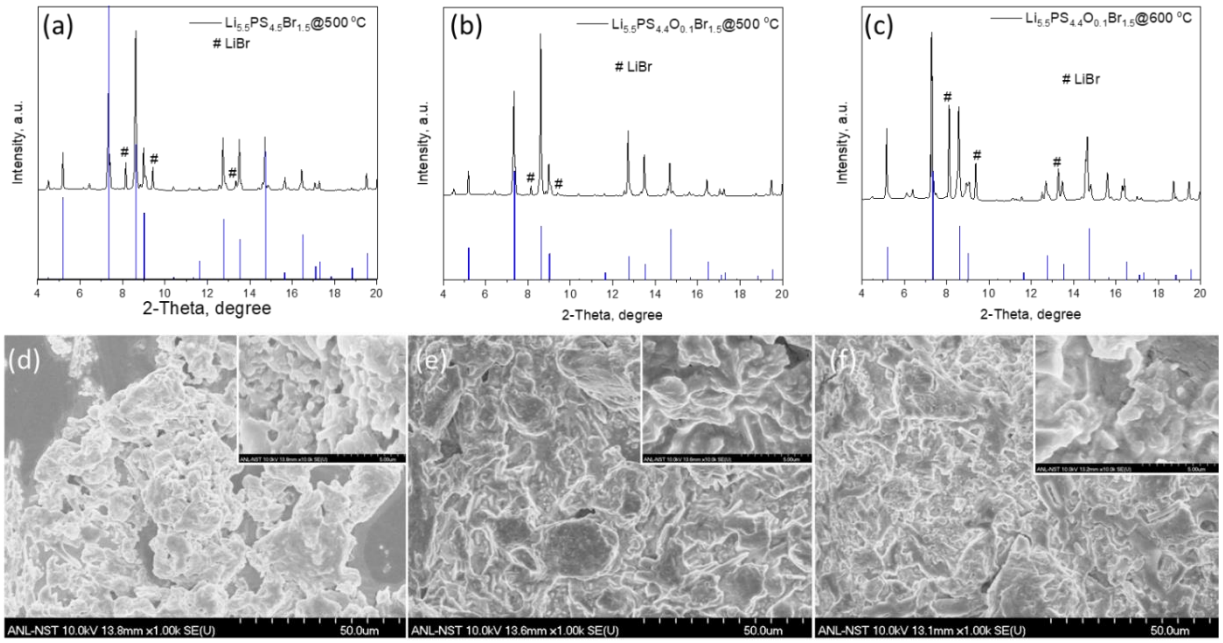

Figure 3. Synchrotron X-ray diffraction patterns of (a) $Li_{5.5}PS_{4.5}Br_{1.5}$ synthesized at 500°C for 12 hours, and $Li_{5.5}PS_{4.4}O_{0.1}Br_{1.5}$ synthesized at (b) 500°C for 12 hours and at (c) 600°C for 12 hours. Scanning electron microscopy (SEM) images of (d) $Li_{5.5}PS_{4.5}Br_{1.5}$ synthesized at 500°C for 12 hours and of $Li_{5.5}PS_{4.4}O_{0.1}Br_{1.5}$ synthesized at (e) 500°C for 12 hours and at (f) 600°C for 12 hours; insets show corresponding high-magnification SEM images.

The team has further compared the lithium stripping/plating behavior of $Li_{5.5}PS_{4.5}Br_{1.5}$ and commercial Li_6PS_5Cl that has similar ionic conductivity. The cells were tested at continuously increased current densities for 1 hour per stripping or plating process with a stack pressure of 20 MPa. As shown in Figure 4c-d, commercial Li_6PS_5Cl shows slightly higher critical current density of 1.4 mA/cm^2 than that of $Li_{5.5}PS_{4.5}Br_{1.5}$ (1.0 mA/cm^2).

The optimization of the solid-state synthesis of $Li_{6-x}PS_{5-x-y}O_yBr_{1+x}$ is time consuming. The team has not investigated the effect of quenching process, ball milling time/speed, or ratio of Br/O dopants. Next quarter, they will continue to optimize these processes to increase ionic conductivity/CCD. They will use *in situ* XRD to evaluate moisture stability under different humidities. Meanwhile, they will use commercial Li_6PS_5Cl material as their starting material to study the structure/composition's effect of sulfur cathodes. In the future, they will combine their best solid electrolytes and sulfur cathode to achieve high sulfur utilization and long cycle life in ASSLSBs.

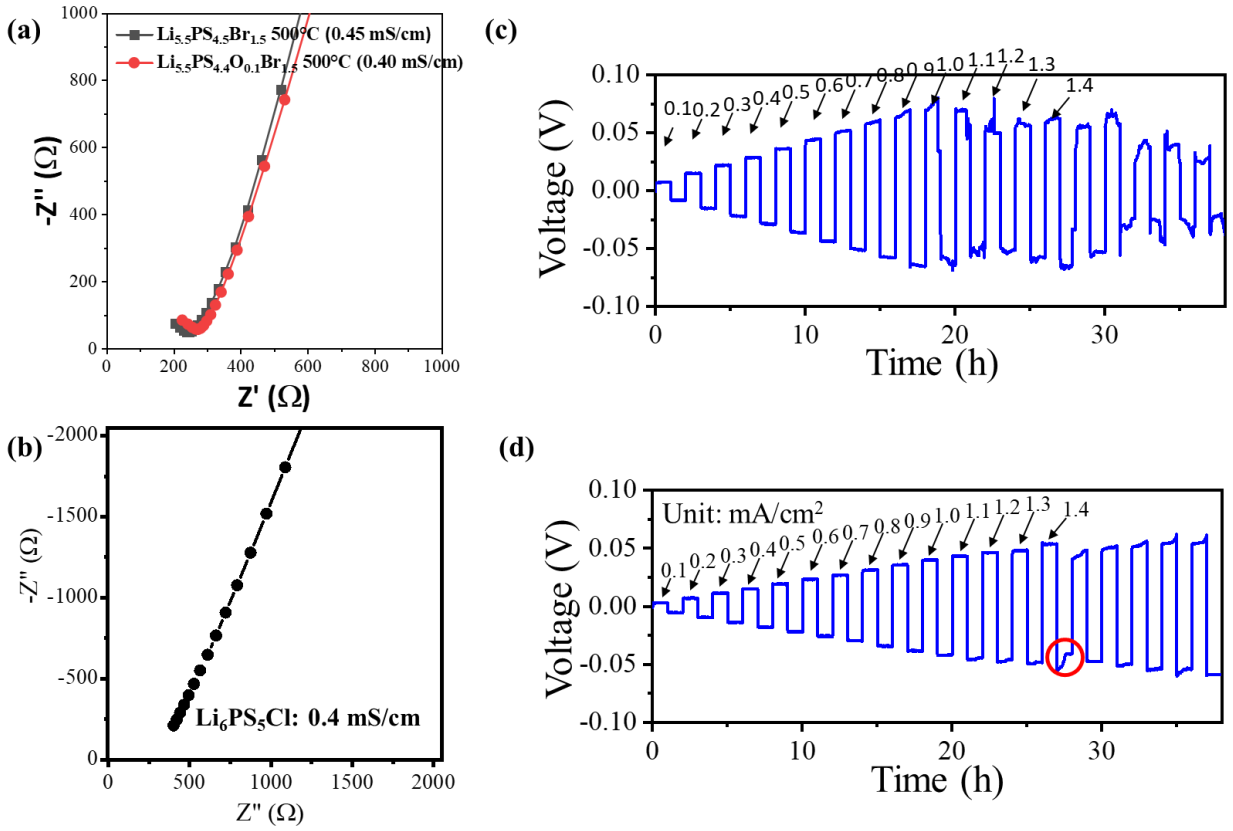

Figure 4. (a) Room-temperature ionic conductivity measurement of $Li_{5.5}PS_{4.5}Br_{1.5}$ synthesized at 500°C for 12 hours and of $Li_{5.5}PS_{4.4}O_{0.1}Br_{1.5}$ synthesized at 500°C for 12 hours. (b) Room-temperature ionic conductivity measurement of commercial Li_6PS_5Cl from Ampcera (10 µm). (c-d) Lithium stripping/plating behavior of symmetrical cells using solid electrolytes of $Li_{5.5}PS_{4.5}Br_{1.5}$ synthesized at 500°C for 12 hours (c) and commercial Li_6PS_5Cl (d). The current densities were increased gradually from 0.1 mA/cm^2 to 1.4 mA/cm^2.

Patents/Publications/Presentations

The project has no patents, publications, or presentations to report this quarter.

Task 1.3 – Thioborate Solid-State Electrolytes for Practical All-Solid-State Batteries (Yi Cui, Stanford University)

Project Objective. This project aims to develop novel lithium thioborates (Li-B-S, LBS) as a new class of solid-state electrolytes (SSEs) to realize high-performance all-solid-state batteries (ASSBs), with a particular focus on addressing the technical challenges in electrolyte synthesis, cell integration, failure diagnostics, and scale-up. The approach will be technologically transformative to the current solutions for ASSB development. For the final deliverables, ASSBs with the ability to reach an energy density of 500 Wh/kg and maintain 80% capacity for at least 300 cycles will be demonstrated.

Impact. The project approaches provide new directions toward developing high-conductivity and electrochemically stable sulfur-based electrolytes for ASSBs. Such high-performance electrolytes can enable the practical realization of ASSBs with a high energy density and improved safety.

Approach. The long-term project has a multistep approach toward integration of LBS with high-voltage cathodes, with steps 1-3 as the focus for this year:

1. Fabricate undoped LBS powders using an all-solid-state synthesis method to achieve high ionic conductivity, low electronic conductivity, and a wide operational voltage window.
2. Integrate LBS SSEs into symmetric Li/LBS/Li cells and into full batteries using high-voltage cathodes including lithium Ni-Mn-Co (NMC) oxide.
3. Study atomic, particle, and cell-scale Li-metal-SSE interface development and dendrite growth mechanisms in SSEs using advanced characterization tools. Use knowledge to better develop SSEs and modify interfaces for stable cycling in full cells.
4. Fabricate doped LBS powders and develop particle/surface modifications to increase ionic conductivity as well as stability in full batteries and in air for glovebox-free synthesis.
5. Use density functional theory to guide development of new doped LBS materials and to explore interactions at solid-solid interfaces.

Out-Year Goals. In the following year, the team will develop solid-state reaction methods to synthesize undoped LBS powders and construct Li/LBS/Li symmetric cells to test the electrochemical performance of synthesized LBS. Meanwhile, the team will utilize advanced characterization tools [for example, cryogenic electron microscopy (cryo-EM), X-ray computed tomography (CT), etc.] to resolve the nanostructure of Li/LBS interphase and investigate the electrochemical stability between LBS and lithium metal.

Collaborations. The Y. Cui group is collaborating with W. Chueh's group (advanced characterization) and E. Reed's group (crystal structure computation) at Stanford University as well as with Y. Liu (advanced characterization) at SLAC National Accelerator Laboratory.

Milestones

1. Develop solid-state reaction methods to synthesize halide-doped LBS powders. (Q1, FY 2023; Completed)
2. Construct Li/LBS/Li symmetric cells for electrochemical characterizations. (Q2, FY 2023; In progress)
3. Construct NMC/LBS/Li full cells with undoped LBS for electrochemical characterizations. (Q3, FY 2023; In progress)
4. Resolve the nanostructure of Li/LBS interphase using advanced characterizations (for example, cryo-EM and CT). Achieve ionic conductivity of LBS SSE of 3.0 × 10-3 S cm-1. (Q4, FY 2023; In progress)

Progress Report

This quarter, the team aimed to develop a procedure for fabricating halide-doped LBS SSEs. The motivation for this research objective is that halide dopants have been shown to result in ionic conductivity above 1.0 mS cm^{-1} in lithium thiophosphate SSEs. Using a fully solid-state synthesis, they made halide-doped LBS powders and tested the ionic conductivity of doped LBS with the stoichiometry of $Li_{10}B_{10}S_{20-x}X_{2x}$ (maintaining the charge balance). They found that LiI increased the ionic conductivity of the SSE, while LiCl and LiBr reduced the ionic conductivity (Figure 5a). Continuing with LiI doping, they tested four stoichiometries of LiI-doped LBS: $Li_{10}B_{10}S_{19.5}I$ (LBS-I), $Li_{10}B_{10}S_{19}I_2$ (LBS-I_2), $Li_{10}B_{10}S_{18}I_4$ (LBS-I_4), and $Li_{10}B_{10}S_{17}I_6$ (LBS-I_6). LBS-I_2 had the highest ionic conductivity, followed by LBS-I_4, LBS-I, and LBS-I_6 (Figure 5b.). As such, LBS-I_2 had the highest ionic conductivity of all doped and undoped LBS compounds (Figure 5c).

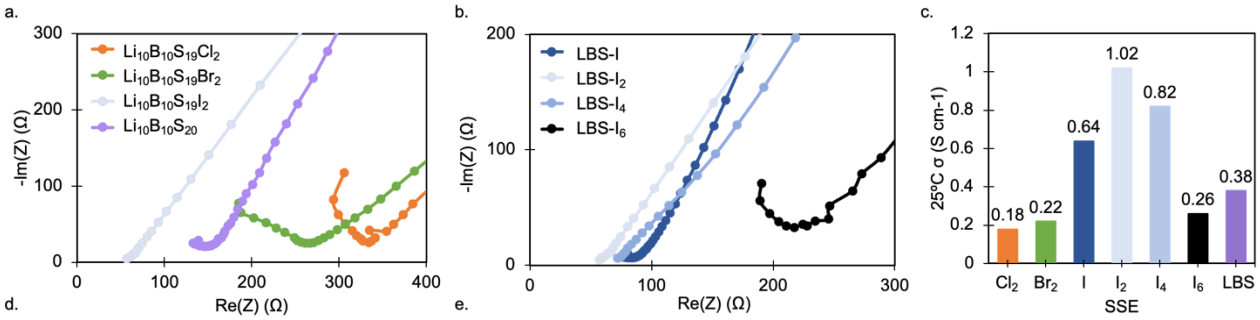

Figure 5. Halide-doped lithium thioborate electrochemical evaluation. (a) Electrochemical impedance spectroscopy (EIS) of SS-$Li_{10}B_{10}S_{19}X_2$-SS (X = Cl, Br, and I) and SS-$Li_{10}B_{10}S_{20}$-SS cells at 360 MPa, room temperature. (b) EIS of SS-$Li_{10}B_{10}S_{20-y}I_y$-SS cells (y = 1, 2, 4, and 6) at 360 MPa, room temperature. (c) Ionic conductivity of each lithium thioborate at 360 MPa, room temperature.

The team performed Fourier-transformed infrared spectroscopy on LBS-I, undoped LBS, and LiI to observe the purity of their materials as well as the extent of LiI incorporation into the LBS (Figure 6). The spectra of LBS and LBS-I are similar, with few notable differences and no additional peaks in the LBS-I spectrum, suggesting no new bonding states from the addition of iodine. The bonding energy of the LBS crystals in the B-S vibrational range is little changed between LBS and LBS-I, suggesting that the structure of the BS_4^- tetrahedron are unchanged between the SSEs. In the LBS-I spectrum, small peaks appear near the LiI regions of the spectrum (1550-1650 cm^{-1} and 3100-3600 cm^{-1}). The LiI peaks in the LBS-I are shifted markedly from 1590 cm^{-1} and 3380 cm^{-1} in LiI to 1616 cm^{-1} and 3410 cm^{-1} in LBS-I, and the peaks are highly broadened relative to the pristine LiI. This shift to higher wavenumber signifies a shift to higher-energy bonding states (shorter wavelength) and reduced free motion of the Li-I bond, suggesting increased confinement of the LiI between crystals.

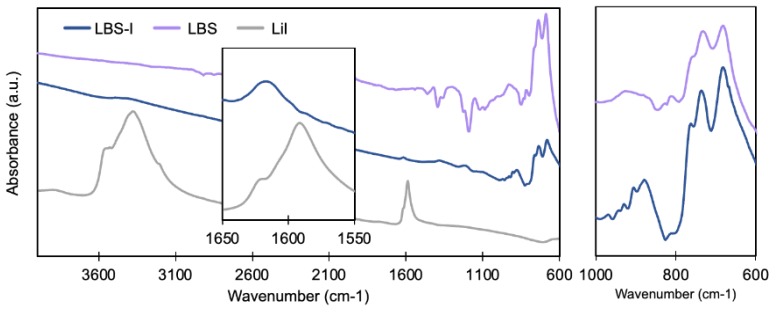

Figure 6. Fourier-transformed infrared spectroscopy of LBS-I, undoped LBS, and LiI. Inset: LiI peak near 1600 cm^{-1}. Right: B-S peaks from the BS_4 tetrahedra.

In the next several quarters, the team plans to further analyze and optimize the LiI-doped LBS and to incorporate these SSEs into batteries with Li-metal anodes and high-energy-density cathodes.

Patents/Publications/Presentations

The project has no patents, publications, or presentations to report this quarter.

Task 1.4 – Substituted Argyrodite Solid Electrolytes and High-Capacity Conversion Cathodes for All-Solid-State Batteries

(Jagjit Nanda, SLAC Stanford Battery Research Center; Guang Yang, Oak Ridge National Laboratory)

Project Objective. The project aims at synthesis and fabrication of Li-ion conducting argyrodite solid electrolytes (SEs) with nominal composition Li_6PS_5X (LPSX), where X = chlorine and/or bromine. The team will combine alternating current (AC) impedance with complementary *in situ* spectroscopy and microscopy to identify buried interfacial side-reaction products and quantify the voltage losses associated with these side reactions. Specifically, they plan to investigate the interfacial reaction between various Li_6PS_5X SE and Li-ion cathodes belonging to different structural families [transition-metal-based sulfides and fluorides (for example, FeS_2 and FeF_2) and high-voltage layered oxides (for example, $LiNi_{0.8}Mn_{0.1}Co_{0.1}O_2$)]. New dopants such as niobium and partial substitution of sulfur with oxygen will be explored to improve stability of argyrodite SEs against lithium metal and high-voltage cathodes.

Impact. The proposed work addresses key technical barriers to achieve Li-metal solid-state batteries (SSBs) with energy densities of > 450 Wh/kg and 1,000 Wh/L, which are critical for next-generation electric vehicles. Integrating new sulfide SEs prepared through scalable, low-cost solvent-mediated routes with high capacity, earth abundant conversion cathodes (for example, sulfur, FeF_3, and FeS_2) will lower SSB cost to $80/kWh and eliminate use of critical materials such as cobalt and nickel.

Approach. Scalable solution-based processing routes will be developed to produce freestanding sulfide/binder solid-state separators with thicknesses < 50 µm and area specific resistance (ASR) < 50 $\Omega\,cm^2$. These ultrathin separators will be integrated with Li-metal anodes and high areal capacity conversion cathodes (for example, sulfur, FeS_2, and FeF_3) to demonstrate lab-scale prototype SSBs. As a cross-cut activity, various *in situ* and *ex situ* passivation methods will be combined with enabling characterization techniques to facilitate Li^+ transport across electrode/SE interfaces.

Out-Year Goals. Optimize SSB performance by (1) identifying solvents and binders compatible with SSE; (2) optimizing binder type and loading to produce free-standing films < 100 µm thick with ionic conductivity ~ 1 mS/cm at room temperature; (3) evaluating the ionic conductivity using electrochemical impedance spectroscopy; (4) using interfacial coatings to stabilize the cathode as needed; use various AC / direct current electroanalytical methods to identify degradation mechanisms during cycling. Targets: produce a free-standing thin-film sulfide SSE with thickness < 100 µm and critical current density > 500 $\mu A/cm^2$; and integrate thin-film SSE with a cathode and thin lithium anode to cycle at reduced pressure.

Collaborations. D. Hallinan and his group are funded collaborators to develop the binder system for sulfide SEs and evaluate compatibility with cathode and Li-metal. P. Jena from Virginia Commonwealth University will be an unfunded collaborator on density functional theory modeling of bulk Li-ion transport and *ab initio* molecular dynamics at SE interfaces.

Milestones

1. Use scalable slurry casting procedures to produce freestanding, dense SE separators. (Q1, FY 2023; Completed)

2. Evaluate structural stability of baseline Li_6PS_5Cl (LPSCl) in various aprotic solvents and binders. Produce LPSX (X = Cl, Br, I) SEs using solvent-mediated routes with ionic conductivity ≥ 1×10^{-3} S/cm^{-1} at room temperature. (Q2, FY 2023; In progress)

3. Compare structure and Li^+ conductivity of thin separators (< 100 µm) and thick pellets (0.5-1 mm). (Q3, FY 2023; In progress)

4. Fabricate and test Li|Li symmetric cell and Li|cathode SSBs containing LPSX free-standing film separators. (Q4, FY 2023; In progress)

Progress Report

This quarter, activities focused on developing a means of fabricating standalone thin sulfide separators.

Most laboratory-based research efforts focus on pelletizing sulfide SEs. Pressing pellets is disadvantageous for two primary reasons: (1) the pressures required to form a pellet approach prohibitive levels when scaled up from laboratory size (~ 1" in diameter), and (2) due to their poor mechanical properties, pellets have a finite lower bound on their thickness that limits their cell-based energy densities. Fabricating a thin free-standing sulfide SSE separator necessitates careful selection of the processing solvents, binders, and dispersants, as well as the combination of them, to form a stable, homogeneous slurry. Further, tape-casting substrates play an essential role in determining the dimensional integrity of the standalone separator on film release. The team explores the effects of poly(isobutylene) (PIB), a non-polar binder, content at 1 wt%, 2 wt%, and 5 wt% on the properties of PIB-LPSCl composite separators. Toluene was chosen as the processing solvent. The slurry was first mixed by a low-energy roller mill to obtain a homogeneous paste-like dispersion, followed by tape casting on a Mylar film using a doctor blade. The as-cast film was then densified through a calendering process. Figure 7 shows the as-fabricated film has a thickness of ~ 66 µm.

Figure 7. Photograph of a thin, freestanding sulfide solid-state electrolyte separator measured by thickness gauge.

Film quality appeared to increase with increasing binder content. The cold press can further promote ionic conductivity (up to one order of magnitude) and lower the contact resistance, as shown in Figure 8 and Figure 9. As such, the ASR of the cold-pressed standalone LPSCl film could be reduced to 25 Ω cm^2, reduced by 80% benchmarked to the as-released film without cold pressing. Therefore, the post-casting processing, such as cold pressing is essential for the ion transport properties of the free-standing sulfide separators.

The relaxation of the polymer binder may affect the ion percolation through the free-standing LPSCl thin film under different compressive stress values. While the pressure-dependent ion transport properties have been well explored for cold-pressed sulfide SEs,[1] study of the free-standing sulfide SE separator is lacking. Conductivity as a function of stack pressure is shown in Figure 10a. The pressure-dependent ionic transport can be elucidated by impedance spectroscopy at various stacking pressure values. 0 wt%, 1 wt%, 2 wt%, and 5 wt% PIB-LPSCl were pressed at 20 MPa for 5 minutes. At the end of 5 minutes, conductivity was recorded, and the pressure was released. After approximately 5 minutes, 10 MPa stack pressure was applied, and conductivity was again recorded. This process was repeated with a stack pressure of 5 MPa. Finally, the conductivity was recorded at approximately 0.5 MPa. The approximate time between measurements was 10 minutes. Interestingly, the ionic conductivity of 5 wt% PIB-LPSCl showed a stronger dependence on stack pressure than the samples containing less binder. Such a phenomenon can be explained as follows. The PIB binder tends to distribute between the LPSCl particles due to the mutual exclusion between the two objects. As the PIB-LPSCl pellet

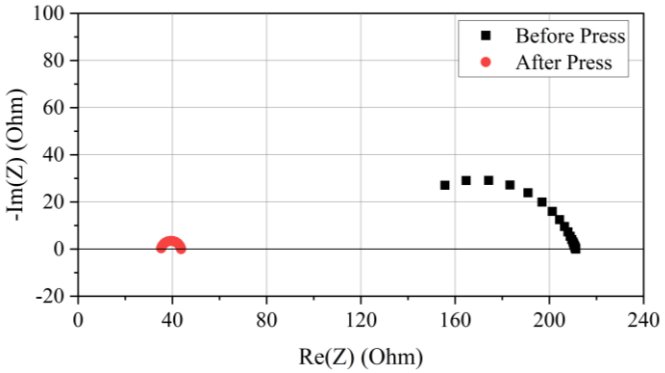

Figure 8. Nyquist plots showing decreased interfacial resistance after cold pressing of a C@Al|5 wt% PIB-LPSCl|C@Al cell.

was compressed, sulfide SE particles formed intimate contact with one another to make Li^+ percolation pathways. Consequently, PIB chains located between particles were deformed from their equilibrium conformations to accommodate the SE particles. As the compressive force was relieved, intramolecular repulsions drove the SE particles apart to allow for the deformed chains to minimize their free energy (that is, maximize conformational entropy). This sulfide SE particle separation resulted in a loss of interparticle contact. Thus, ion conduction pathways were reduced, and conductivity decreased.

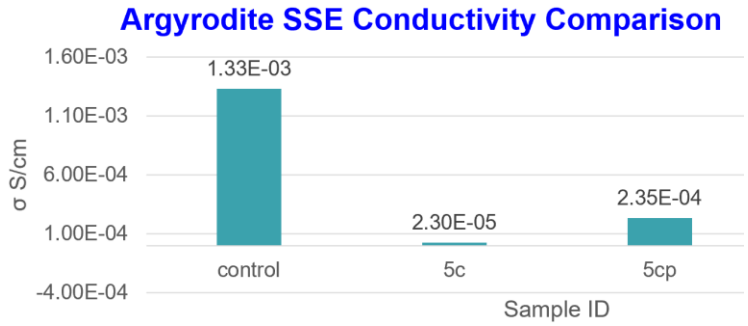

Figure 9. Comparison of the ionic conductivity of various LPSCl separators at room temperature. The control sample is a cold-pressed pellet with a thickness of 490 µm. Sample 5c stands for calendered LPSCl thin film separator with 5 wt% PIB binder (average thickness = 64 µm). Sample 5cp stands for 5 wt% PIB LPSCl thin film separator after cold pressing (average thickness = 48 µm).

The results of the temperature-dependent ionic conductivity data and fits corroborate these findings. The activation energy of each sample was found by fitting experimental data to the Vogel-Tammann-Fulcher (VTF) equation. The VTF equation is given in equation (1), where σ_0 is a prefactor, T is temperature, T_0 is the Vogel temperature, and B_R is the quantity E_a/R. E_a is the activation energy of the material, and R is the gas constant.[2]

$$\boldsymbol{\sigma(T) = \sigma_0\, e^{\left(\frac{-B_R}{T-T_0}\right)}} \qquad \mathbf{(1)}$$

For polymer electrolytes, T_0 is known to represent the ideal glass transition temperature, that is, the temperature at which configurational entropy is zero.[3] For inorganic SEs, T_0 currently bears no physical meaning.[4] T_0 was fixed at a value of 800 K, such that the E_a found for neat LPSCl was near 0.34 eV, a value previously found by Arrhenius-type fitting methods.[5-6] The raw data is plotted with the fit results in Figure 10b. The fit parameters, extracted activation energies, and R^2 values are given in Table 1. In addition to the samples containing toluene-treated LPSCl (0-5 wt% PIB-LPSCl), untreated LPSCl (neat LPSCl) was also tested as a control. According to the fit values, E_a of 0 wt%, 1 wt%, and 2 wt% PIB-LPSCl was not significantly different from that of the neat LPSCl. However, E_a of 5 wt% PIB-LPSCl was significantly greater than the other samples.

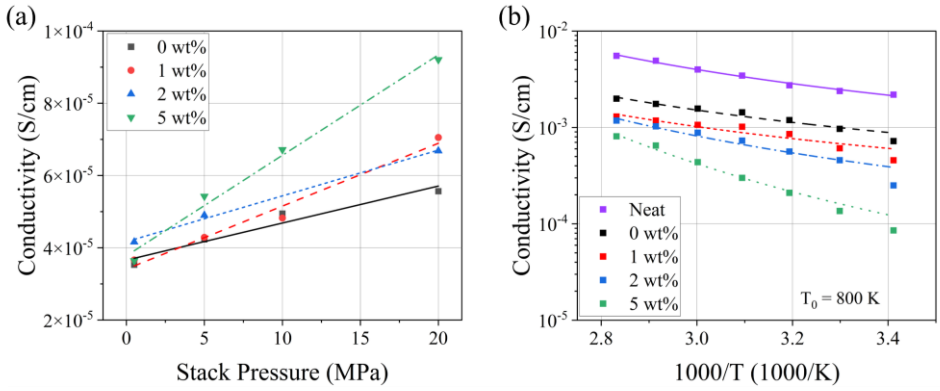

Figure 10. (a) Conductivity as a function of stack pressure. (b) Conductivity as a function of temperature.

Table 1. Results of fitting conductivity data to equation (1). σ_0 is a prefactor, T is temperature, T_0 is the Vogel temperature, and B_R is the quantity E_a/R. E_a is the activation energy of the material, and R is the gas constant.

PIB Content (wt%)	σ_0 (S/cm)	B_R (K)	T_0 (K)	E_a (eV)	E_a (kJ/mol)	R^2
Neat LPSCl	1.47E-06	3688.91	800	0.32 ± 0.03	30.7 ± 3.2	0.991
0	1.52E-06	3223.17	800	0.28 ± 0.07	26.8 ± 6.5	0.956
1	1.26E-06	3124.84	800	0.27 ± 0.10	26.0 ± 10.1	0.895
2	6.28E-08	4420.22	800	0.38 ± 0.08	36.8 ± 7.8	0.950
5	5.99E-11	7356.93	800	0.64 ± 0.10	61.3 ± 9.8	0.984

To sum up, this quarter the team successfully developed a tape-casting method to fabricate flexible, standalone argyrodite sulfide (LPSCl) thin-film separators of low binder loadings (≤ 5 wt%). Two factors contribute to a lower ASR of the thin-film SSEs benchmarked to the cold-pressed powder palette SSE counterparts: 1-2 orders reduced thickness, and comparable ionic conductivity at room temperature after the uniaxial pressing process. The ionic conductivity of the standalone sulfide separators is highly dependent on the polymer binder loading, stack pressure, and temperature. The increase of the binder loading promotes the dimensional stability of the standalone film and increases the film ionic conductivity dependency on the stack pressure, with a concomitant increase in the activation energy. Therefore, careful control of the binder loading and composite processing is essential for standalone sulfide film separator fabrications.

References

[1] Doux, J-M., Y. Yang, D. H. Tan, H. Nguyen, E. A. Wu, X. Wang, A. Banerjee, and Y. S. Meng. "Pressure Effects on Sulfide Electrolytes for All Solid-State Batteries." *Journal of Materials Chemistry A* 8, No. 10 (2020): 5049–5055.

[2] Diederichsen, K. M., H. G. Buss, and B. D. McCloskey. "The Compensation Effect in the Vogel–Tammann–Fulcher (VTF) Equation for Polymer-Based Electrolytes." *Macromolecules* 50, No. 10 (2017): 3831–3840.

[3] Chung, S. H., K. Such, W. Wieczorek, and J. R. Stevens. "An Analysis of Ionic Conductivity in Polymer Electrolytes." *Journal of Polymer Science Part B: Polymer Physics* 32, No. 16 (1994): 2733–2741.

[4] Reddy, M. V., C. M. Julien, A. Mauger, and K. Zaghib. "Sulfide and Oxide Inorganic Solid Electrolytes for All-Solid-State Li Batteries: A Review." *Nanomaterials* 10, No. 8 (2020): 1606.

[5] Wang, S., Y. Zhang, X. Zhang, T. Liu, Y-H. Lin, Y. Shen, L. Li, and C-W. Nan. "High-Conductivity Argyrodite Li_6PS_5Cl Solid Electrolytes Prepared via Optimized Sintering Processes for All-Solid-State Lithium–Sulfur Batteries." *ACS Applied Materials & Interfaces* 10, No. 49 (2018): 42279–42285.

[6] Wang, S., X. Zhang, S. Liu, C. Xin, C. Xue, F. Richter, L. Li, L. Fan, Y. Lin, Y. Shen, J. Janek, and C-W. Nan. "High-Conductivity Free-Standing Li_6PS_5Cl/poly(vinylidene difluoride) Composite Solid Electrolyte Membranes for Lithium-Ion Batteries." *Journal of Materiomics* 6, No. 1 (2020): 70–76.

Patents/Publications/Presentations

Patent

- Invention disclosure (Oak Ridge National Laboratory Invention Disclosure ID# : 202305281).

Presentation

- Second Annual Polymer Research Symposium, American Chemical Society Polymer and Polymer Materials Science and Engineering, Florida A&M University – Florida State University, Tallahassee, Florida (February 18, 2023): "Thin Film Sulfide Solid Electrolyte Composites"; A. Mills, G. Yang, W. Y. Tsai, X. Chen, R. Sacci, B. Armstrong, D. T. Hallinan, and J. Nanda. Invited.

Task 1.5 – Stable Solid-State Electrolyte and Interface for High-Energy, All-Solid-State, Lithium-Sulfur Battery
(Dongping Lu, Pacific Northwest National Laboratory)

Project Objective. The project objective is to address material and interfacial barriers of sulfide-based solid-state electrolyte (S-SSE) for deep cycling of Li-metal anode in all-solid-state lithium batteries (ASSLBs). All proposed work will be focused on development of highly conductive sulfide Li^+ conductors with extremely low lithium / solid-state electrolyte (SSE) interfacial resistance and ultrathin multifunctional interlayers to enable deep and stable lithium cycling. The solid electrolytes (SEs) and interlayer assembly achieved in the project will be tested at practical conditions and validated in realistic Li-S pouch cells.

Impact. ASSLBs have the potential to achieve higher energy and power densities, extending the range of electric vehicles (EVs) and reducing charging time simultaneously. The success of the project would advance the research and deployment of superionic SEs and protective Li-compatible interlayers to support the U. S. Department of Energy Vehicle Technologies Office target of developing next-generation ASSLBs for EVs, accelerating market acceptance of long-range EVs required by the EV Everywhere Grand Challenge.

Approach. The project proposes the following approach: (1) to develop Li-compatible superionic S-SSEs and effective coating approaches, (2) to stabilize Li/SSE interface by employing a multifunctional interlayer, (3) to enable robust Li^+/e^- mixed conduction network for a high-loading sulfur cathode, (4) to develop dry processing for SSE film, cathode, and interlayer fabrication, and (5) to advance the mechanism study of the sulfur cathode, lithium anode, and interfaces by multiscale characterization and multiscale modeling.

Out-Year Goals. This project has the following out-year goals:

- Development of Li-metal-compatible S-SSEs with Li/SSE interfacial resistance $< 5\ \Omega\ cm^2$ and room-temperature Li^+ conductivity > 5 mS/cm.
- Operation of lithium anode at critical current density > 1 mA/cm^2, and lithium cycling for at least 400 cycles.
- Ultrathin multifunctional interlayer to enable deep lithium cycling > 4 mAh/cm^2 to couple high areal-capacity cathode.
- Dry processing of an SSE/interlayer assembly with an overall ionic conductivity > 1 mS/cm.
- Validation of the S-SSE, high-areal capacity cathode, and bilayer assembly in a realistic Li-S pouch cell.

Collaborations. This project engages in collaboration with the following: D. Y. Qu (University of Wisconsin, Madison), Z. K. Liu (Pennsylvania State University), C. M. Wang and J. Bao (Pacific Northwest National Laboratory), H. Du (Ampcera Inc.), and Z. Liu (Thermo Fisher Scientific).

Milestones

1. Down-select optimal materials for the Li-metal interlayer fabrication to enable lithium stripping/plating at > 2 mAh/cm^2 for at least 100 cycles demonstrated in Li/SSE/Cu or Li-S full cells. (Q1, FY 2023; Completed)
2. Mechanism understanding of lithium nucleation and growth in the presence of lithium interlayer through experimental and modeling tools. (Q2, FY 2023; On track)
3. Identify compatible binder and processing method for the C-M composite, demonstrate ultra-thin C-M interlayer, and demonstrate deep lithium stripping/plating at 4 mAh/cm^2. (Q3, FY 2023; On track)
4. Optimize external pressure and C-M interlayer to enable deep and stable lithium cycling (4 mAh/cm^2, > 100 cycles). (Q4, FY 2023; On track)

Progress Report

The LiI as a potential gradient for Li-metal anode interlayer was systematically investigated. To understand the effects of LiI on the lithium plating/stripping, Li/SSE/Cu (where SSE= $Li_7P_2S_8Br_{1-x}I_x$, x = 0, 0.5, 1) cells were assembled and tested with an areal capacity of 2 mAh cm^{-2} (corresponding to ~ 10 µm of lithium). At a current density of 0.2 mA cm^{-2}, the lithium plating in the $Li/Li_7P_2S_8Br/Cu$ cell begins at a large overpotential of -18.5 mV, indicating a large lithium nucleation barrier initially, and then the voltage decreases to -7.7 mV and remains constant (not shown here). The second cycle plating starts with an overpotential of -11.8 mV, which is smaller than that of the initial plating, probably due to the lithium residual serving as nucleation sites. In contrast, the $Li/Li_7P_2S_8Br_{0.5}I_{0.5}/Cu$ cell, where LiI exists in the SSE, does not show such high overpotential for the first and second plating, indicating a much smaller energy barrier for lithium nucleation, which may be due to the favorable SSE/Li interface with presence of the LiI. With the increase in LiI content, even smaller

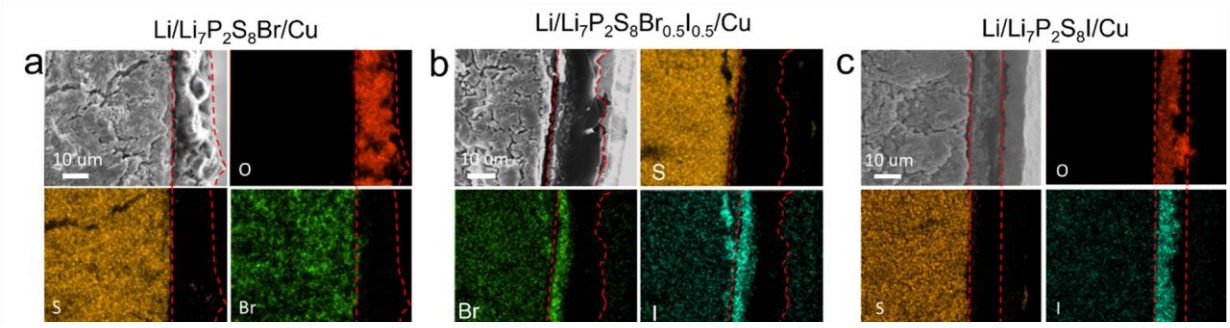

Figure 11. $Li/Li_7P_2S_8Br_{1-x}I_x/Cu$ cross-sectional scanning electron microscopy images and corresponding elemental mappings of the $Li/Li_7P_2S_8Br_{1-x}I_x/Cu$ cells after lithium plating: (a) $Li/Li_7P_2S_8Br/Cu$, (b) $Li/Li_7P_2S_8Br_{0.5}I_{0.5}/Cu$, and (c) $Li/Li_7P_2S_8I/Cu$.

overpotential (that is, -4 mV) and easier lithium plating were observed in the $Li/Li_7P_2S_8I/Cu$ cell. These results suggest that the higher the LiI content, the lower the overpotential for lithium nucleation and plating. To track the LiI evolution during lithium plating/stripping, cells after the first plating were cross-sectioned and subjected to scanning electron microscopy (SEM) and energy dispersive X-ray spectroscopy characterizations (Figure 11). Oxygen signal was detected on the surface of deposited lithium, which is due to the short exposure of samples to the ambient environment when loading samples and could be used as an indicator of metallic lithium. Figure 11a presents the cross-sectional SEM of the plated lithium on the surface of $Li_7P_2S_8Br$. The plated lithium metal is slightly loose, suggesting void formation and corresponding to the high polarization of lithium plating. Much denser lithium plating is observed for $Li_7P_2S_8Br_{0.5}I_{0.5}/Li$ and $Li_7P_2S_8I/Li$, which agrees well with the lower lithium plating polarization. Interestingly, the migration and accumulation of iodine from the SSE to the lithium surface is clearly observed at both interfaces of $Li_7P_2S_8Br_{0.5}I_{0.5}/Li$ and $Li_7P_2S_8I/Li$. Surprisingly, bromine does not migrate in the $Li/Li_7P_2S_8Br/Cu$ cell, but its migration toward lithium is detected in the $Li_7P_2S_8Br_{0.5}I_{0.5}/Li$ cell. These results suggest that I^- not only has higher diffusivity than Br^-, but also spurs the diffusion of Br^-. Accompanying iodine migration to lithium metal, more LiI-rich solid electrolyte interphase is expected to be formed on the interfaces of $Li_7P_2S_8Br_{0.5}I_{0.5}/Li$ and $Li_7P_2S_8I/Li$ during lithium plating. Further understanding of how the iodine element migrates during lithium plating is still being gained through experimental and theoretical study. During the subsequent lithium stripping, the iodine is released and reaccumulated at the SSE/Cu interface (data not shown here), which will promote subsequent lithium plating/stripping. Both electrochemical and morphological characterizations demonstrate that LiI can be enriched and released reversibly, functioning as an artificial interlayer to facilitate dense lithium plating/stripping.

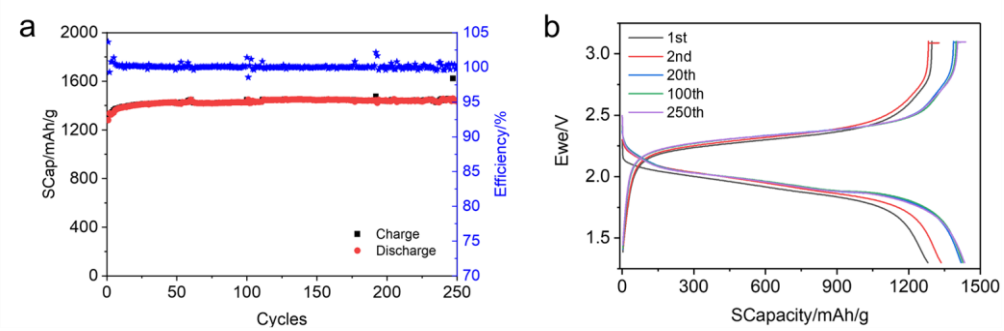

Figure 12. (a) Cycling performance and (b) voltage profiles of the cell S/$Li_7P_2S_8Br_{0.5}$ $I_{0.5}$ /Li under 0.1 C (1 C = 1600 mA g^{-1}) at 2 mAh cm^{-2} and 20°C. Capacities are represented in terms of the mass of the active sulfur. Testing was conducted under a pressure of ~ 30 Mpa.

To validate the applicability of LiI-based interface for long-term cycling of the metallic lithium anode, the SSE $Li_7P_2S_8Br_{0.5}$ $I_{0.5}$ was used to fabricate all-solid-state S/$Li_7P_2S_8Br_{0.5}I_{0.5}$/Li full cells, where sulfur was used as cathode and the metallic lithium was used as the anode directly without any surface treatment or use of additional interlayers. Figure 12a-b presents the cycling performance and voltage profiles of the S/$Li_7P_2S_8Br_{0.5}I_{0.5}$/Li under 0.1 C (1 C = 1600 mA g_{sulfur}^{-1}) at 20°C. At an areal capacity of ~ 2 mAh cm^{-2}, a high reversible capacity of 1440 mAh g_{sulfur}^{-1} was achieved after a gradual activation process. The Li-S solid cell demonstrates stable cycling for 250 cycles without capacity decay or short circuiting, which is among the best cycling performance for all-solid-state sulfur batteries with metallic lithium as the anode. This further validates the extraordinary robustness of the Li/SSE interface benefiting from the LiI-rich interface.

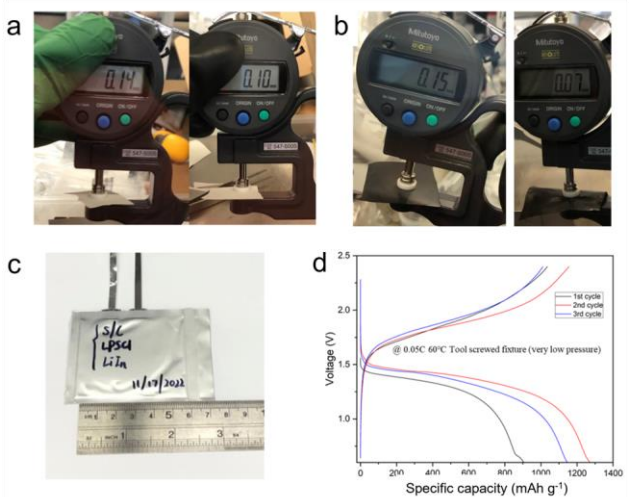

Figure 13. Photo image and thickness measurement of the processed (a) dry solid-state electrolyte film and (b) dry sulfur cathode. (c) Photo image of all-solid-state pouch cell and typical charge/discharge curves at 60°C. Capacities are based on the mass of sulfur. (d) Charge/discharge curves of the first three cycles of the all-solid-state sulfur pouch cell.

For scalable processing of the SSE membrane and solid-state cathode, a dry process method was developed. Please note the argyrodite Li_6PS_5Cl (LPSCl) SSE was used as an example SE for the processing demonstration. The SSE film was fabricated by using dry SSE powders and 0.75 wt% polytetrafluoroethylene (PTFE) at an elevated temperature. As shown in Figure 13, the thickness of the finished SSE film can be controlled between 100~140 μm. The sulfur cathodes consisting of sulfur, carbon, and LPSCl with a weight ratio of 2:1:3 were also fabricated through the dry process using 1.0 wt% of PTFE. The thickness of the sulfur cathode film can be controlled between 70~150 μm. The all-film solid-state pouch cells were assembled by stacking the processed sulfur cathode, SSE membrane, and LiIn anode, and pressing at 20 MPa for 4 minutes (Figure 13). The pouch cell was tested at 60°C by clamping the cell with a fixture. Figure 13d shows charge/discharge curves of the first three cycles of the all-solid-state sulfur pouch cell. In the initial discharge, the cell delivers a specific capacity of 904 mAh g^{-1}, which increases to 1207 mAh g^{-1} and 1129 mAh g^{-1} in the subsequent second and third cycles, respectively. Research to improve processability, cathode mass loading, and sulfur utilization rate is in progress.

Patents/Publications/Presentations

The project has no patents, publications, or presentations to report this quarter.

Task 1.6 – Three-Dimensional Printing of All-Solid-State Lithium Batteries (Jianchao Ye, Lawrence Livermore National Laboratory)

Project Objectives. The project has two primary objectives: (1) down select three-dimensional (3D) printing and post-processing approaches for solid-state electrolyte (SSE) / cathode integration, and (2) understand battery failure mechanisms via *ex situ* and *in situ* characterization.

Impact. The adoption of a thin separator layer, thick cathode structure, and metallic lithium anode will lead to electric vehicle batteries with > 350 Wh/kg energy density for increased mileage per charge. The higher ionic conductivity with suppression of lithium dendrite growth will allow high critical current densities for fast charging applications. The improved electrode/electrolyte contact will increase battery cycle life for long-term service.

Approach. The technical approaches include advanced manufacturing based on 3D printing and related techniques, *ex situ* / *in situ* characterizations, and battery testing. Direct-ink writing 3D-printing techniques will be employed to fabricate thin-film SSEs (< 100 μm), gradient SSEs, and 3D interfaces for battery performance evaluation. Three approaches, including sintering-free, hybrid, and co-sintering, will be investigated. The knowledge obtained from these approaches is transferable and complementary to each technique.

Out-Year Goals. The long-term vision of the team is to 3D-print all components of the all-solid-state lithium battery (ASSLB) to facilitate the scale-up of ASSLB manufacturing. In this project, the team will tackle the issues emerging from integrating solid electrolyte with electrodes. The project goal is to demonstrate a successful 3D-printing approach to integrate SSE into electrodes and show reasonable capacity retention (that is, > 80%) after 300 cycles at current density ≥ 1 mA/cm^2.

Collaborations. The team will work closely with a computational partner (Task 3.10 led by B. Wood) to better understand battery failure mechanisms and design new battery architectures and chemistries for performance improvement. The team is collaborating with S. Kim and G. Cheng from University of Illinois, Chicago, on composite polymer electrolyte (CPE) development.

Milestones

1. Demonstrate that SSE has > 10^{-4} S/cm conductivity and that full battery can charge/discharge with > 80% capacity. (Q1 FY 2023; Completed)
2. Determine the relationship of ionic conductivity and mechanical properties with $Li_{6.4}La_3Zr_{1.4}Ta_{0.6}O_{12}$ (LLZTO) content in CPEs. (Q2, FY 2023; In progress)
3. Improve conductivity and stability of catholytes against cathode. (Q3, FY 2023; In progress)
4. Improve performance of co-sintered electrolyte/cathode bilayer. (Q4, FY 2023; In progress)

Progress Report

The team has achieved the ionic conductivity goal of 10^{-4} S/cm for development of a thin SSE component to be integrated with printed electrodes. This goal was fulfilled by two approaches: laser sintering of LLZTO films, and CPEs. In the first approach, laser sintering started from an ultraviolet (UV)-cured poly(ethylene glycol) (PEG) / LLZTO film, which was then thermally treated to remove PEG binder. The obtained porous LLZTO film was sintered by CO_2 laser scanning at elevated temperature.[1] Laser sintering led to accelerated densification, anisotropic shrinkage, and generated highly dense LLZTO films with a wave-like surface profile. The ionic conductivity reaches 0.26 mS/cm, as shown in Figure 14a. The film can be used as a stiff Li^+ conducting separator for the solid-state battery assembly. In the second approach, the two CPE systems based on PEG [poly(ethylene glycol) diacrylate / poly(ethylene glycol) methyl ether acrylate / poly(ethylene oxide)] and zPU (zwitterionic polyurethane), both with LLZTO and lithium bis(trifluoromethanesulfonyl)imide (LiTFSI) added, showed different ion conducting behaviors. With the increase of LLZTO content up to 7 wt%, PEG CPEs exhibited an increase of ionic conductivity up to 2.01×10^{-4} S/cm in the recipe with ITX as the photoinitiator. The conductivity increase is accompanied by a decrease of the Young's modulus (Figure 14b), which suggests that LLZTO nanoparticles reduce the crystallinity of the polymer matrix. Adding a thermal initiator, benzoyl peroxide (BPO), however, led to a decrease of conductivity to 6.6×10^{-5} S/cm. A recently discovered color change of the PEG/LLZTO suspension after adding BPO suggests a reaction between LLZTO and BPO that might be related to the conductivity difference. The conductivity of the PEG/LLZTO CPEs dropped with further increase of LLZTO content, either because PEG chains may be anchored between adjacent particles, or Li^+ ions cannot effectively cross the PEG/LLZTO interface. In contrast, the zPU CPE with high LiTFSI content may have better interfacial properties for Li^+ transport and thus showed continuously improved ionic conductivity. Based on these findings, the team will evaluate the three SSE options for future 3D battery integration and testing: (1) UV-cured PEG/LLZTO with ≤ 7 wt% LLZTO content; (2) zPU/LLZTO; and (3) laser-sintered LLZTO films.

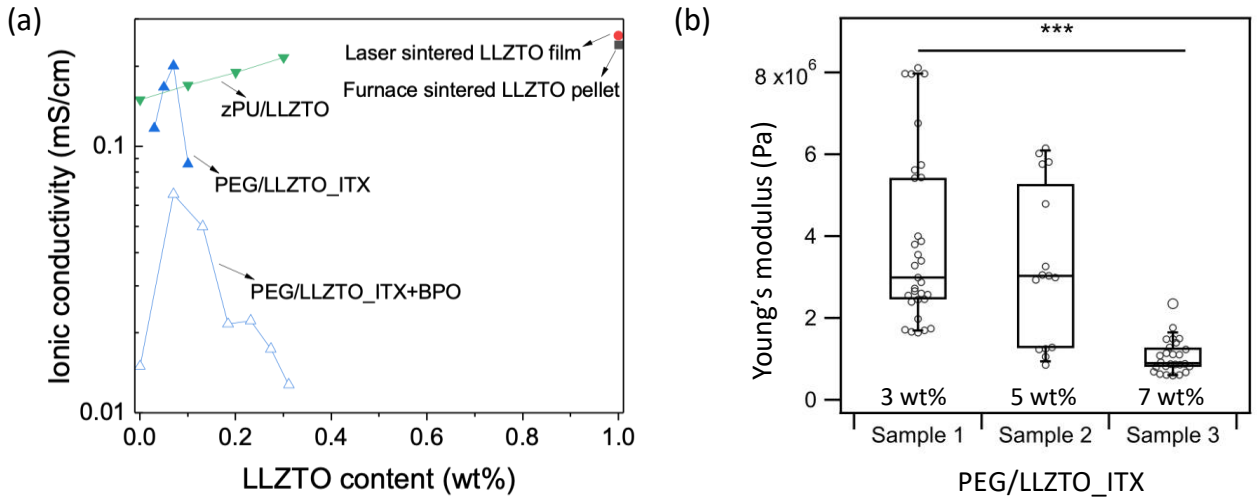

Figure 14. (a) Summary of the conductivities of various solid-state electrolytes developed in this project. (b) The Young's modulus of the composite polymer electrolyte from the PEG/LLZTO_ITX ink recipes, measured using atomic force microscopy in an Ar-filled glovebox. The significant difference was shown by p-value with * for p < 0.001.**

Currently, the Li-F-P (LFP) / lithium cell made of PEG/LLZTO_ITX+BPO CPE possesses a 1st-cycle charging capacity of 163 mAh/g at a 0.8C-rate at 60°C (Figure 15a). However, discharge capacity is only 100 mAh/g, and cycling stability is poor. The CPE used here has relatively low conductivity (2×10^{-5} S/cm at room temperature). By adopting CPEs with higher ionic conductivities, the team expects an increase of the reversible capacity. The drop in the capacity is also reflected in the increase of the interfacial resistance (Figure 15b). The battery performance of the PEG/LLZTO-ITX CPEs with higher ionic conductivities will be investigated.

In contrast, the zPU/LLZTO CPE-based LFP/Li cells show high Coulombic efficiency, even in the first few cycles. The first charge/discharge capacity at 1C-rate and room temperature of the 30 wt% LLZTO cell is ~ 130mAh/g, roughly 80% of theoretical capacity. The value decreases to ~ 117 mAh/g after 9 cycles and becomes very stable in the following 200 cycles. The performance is 13.6% higher than the cells using zPU electrolyte without LLZTO additives. The voltage profiles interestingly show two-plateau behavior, which is not typically observed in LFP cells. The mechanisms of capacity decay in the first 10 cycles, and the two-plateau behavior will be investigated in future studies.

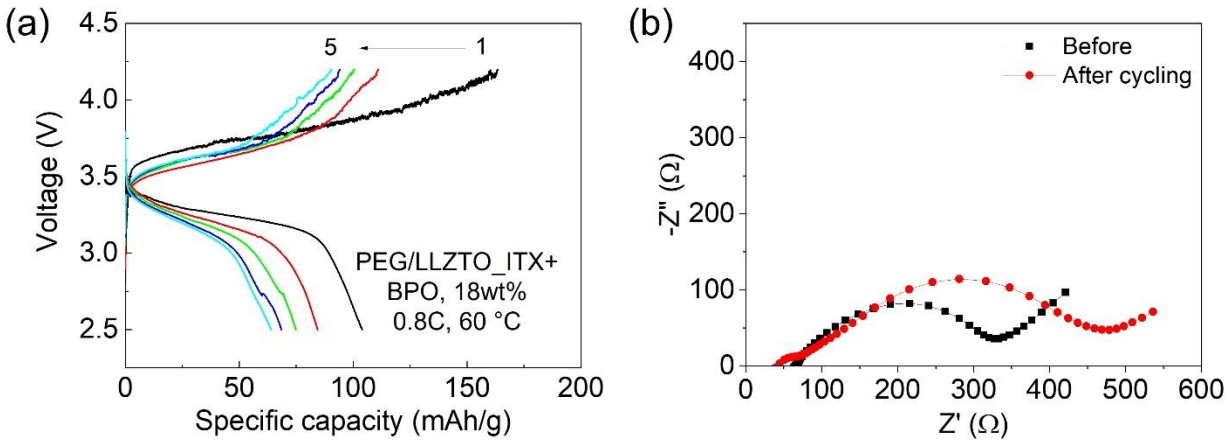

Figure 15. (a) LFP/SSE/Li battery performance in the first 5 cycles at 0.8C-rate, 60°C. Here, solid-state electrolyte is made of a UV and thermally cured PEG/LLZTO/LiTFSI composite polymer electrolyte. PEG is a mixture of PEGDA, PEGMEA, and PEO600K with ratio of 1:8:1 by weight. (b) Electrochemical impedance spectroscopy of the cell before and after 25 cycles.

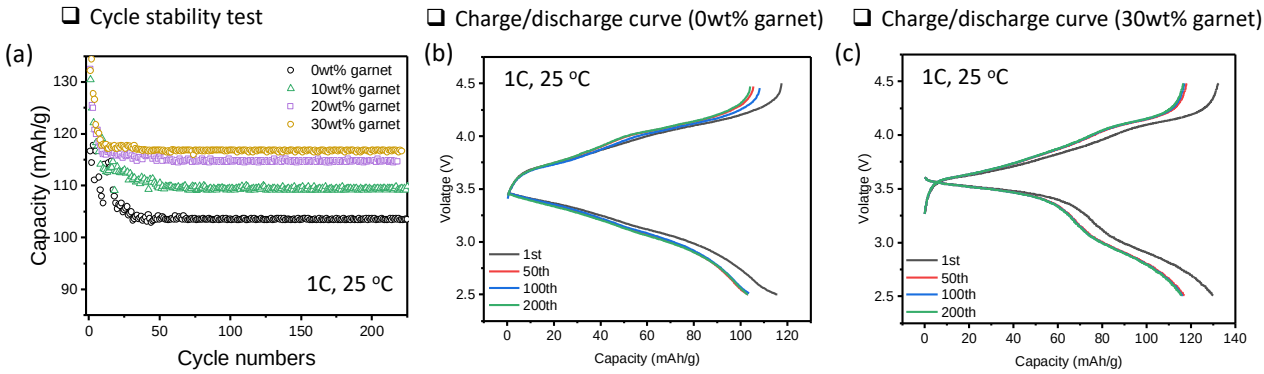

Figure 16. LFP/(zPU/LLZTO/LiTFSI)/Li battery performance at 1C-rate and room temperature. (a) Cycling stability comparison of cells using zPU-based composite polymer electrolyte (CPEs) with varying LLZTO contents. (b) Voltage profiles at selected number of cycles for the LFP/Li cell with zPU electrolyte with no LLZTO addition. (c) Voltage profiles at selected number of cycles for the LFP/Li cell with zPU/LLZTO-30 wt% CPE.

Reference

[1] E. Ramos, et al. "CO_2 Laser Sintering of Garnet-Type Solid-State Electrolytes." *ACS Energy Letters* 7 (2022): 3392–3400.

Patents/Publications/Presentations

The project has no patents, publications, or presentations to report this quarter.

Task 1.7 – Development of All-Solid-State Battery Using Anti-Perovskite Electrolytes (Zonghai Chen and Tao Li, Argonne National Laboratory)

Project Objective. The objective of this project is to develop an optimized anti-perovskite electrolyte with a stabilized interface for scalable fabrication of liquid-free solid-state batteries.

Impact. The project will lead to impact on several areas: (1) establishing a structure-property relationship of anti-perovskite electrolytes, (2) understanding and quantifying the interaction between the electrolytes and the environment, (3) understanding and mitigating the failure of all-solid-state batteries (ASSBs) at the solid-solid interface, and (4) developing a scalable process for fabrication of ASSBs.

Approach. The project approach is multifold: (1) *chemistry design*: multiple doping at anion sites will be pursued to improve structural stability, ionic conductivity, and environmental compatibility; (2) *interfacial design*: surface coating will be deployed to improve the chemical and mechanical stability of the solid/solid interface; and (3) *process development*: a scalable fabrication process based on melt-infiltration or dry lamination will be developed for fabrication of ASSBs.

Out-Year Goals. The project has the following out-year goals:

- Developing high-performance anti-perovskite electrolytes.
- Accessing the air stability and proton mobility of anti-perovskite electrolytes.
- Stabilizing the solid/solid interface through interfacial engineering.
- Prototyping liquid-free cells using anti-perovskite electrolytes.

Collaborations. This project collaborates with Y. Z. Liu and W. Q. Xu (Argonne National Laboratory), X. H. Xiao (Brookhaven National Laboratory), and H. Meng (University of Arkansas).

Milestones

1. Benchmarking of Li/electrolyte interface. (Q1, FY 2023; Completed)
2. Microscopic study of lithium plating behavior. (Q2, FY 2023; In progress)
3. Development of artificial Li/electrolyte interface. (Q3, FY 2023)
4. Validation of impact of artificial Li/electrolyte interface. (Q4, FY 2023)

Progress Report

In previous quarters, the team was able to synthesize phase pure anti-perovskite electrolytes using a simple solid-state reaction at a relatively low processing temperature (~ 300°C). It is also well recognized that one of the bottlenecks of anti-perovskite electrolytes is their relatively low Li-ion conductivity. The team observed that the Li-ion conductivity could be improved by partially replacing chlorine with bromine. However, the Li-ion conductivity is quite low (~ 10^{-5} S/cm). Searching for an alternative electrolyte formula and alternative approach to fabricate electrolyte pellets is needed to further improve the Li-ion conductivity of anti-perovskite electrolytes. Figure 17 shows the measured Li-ion conductivity of the latest electrolyte formula. The electrolyte pellets were fabricated using a warm press (~ 250 MPa at ~ 250°C). The latest formula (AP-5 and AP-6) demonstrated a Li-ion conductivity of ~ 0.1 mS/cm at 25°C, and ~ 1 mS/cm at 75°C.

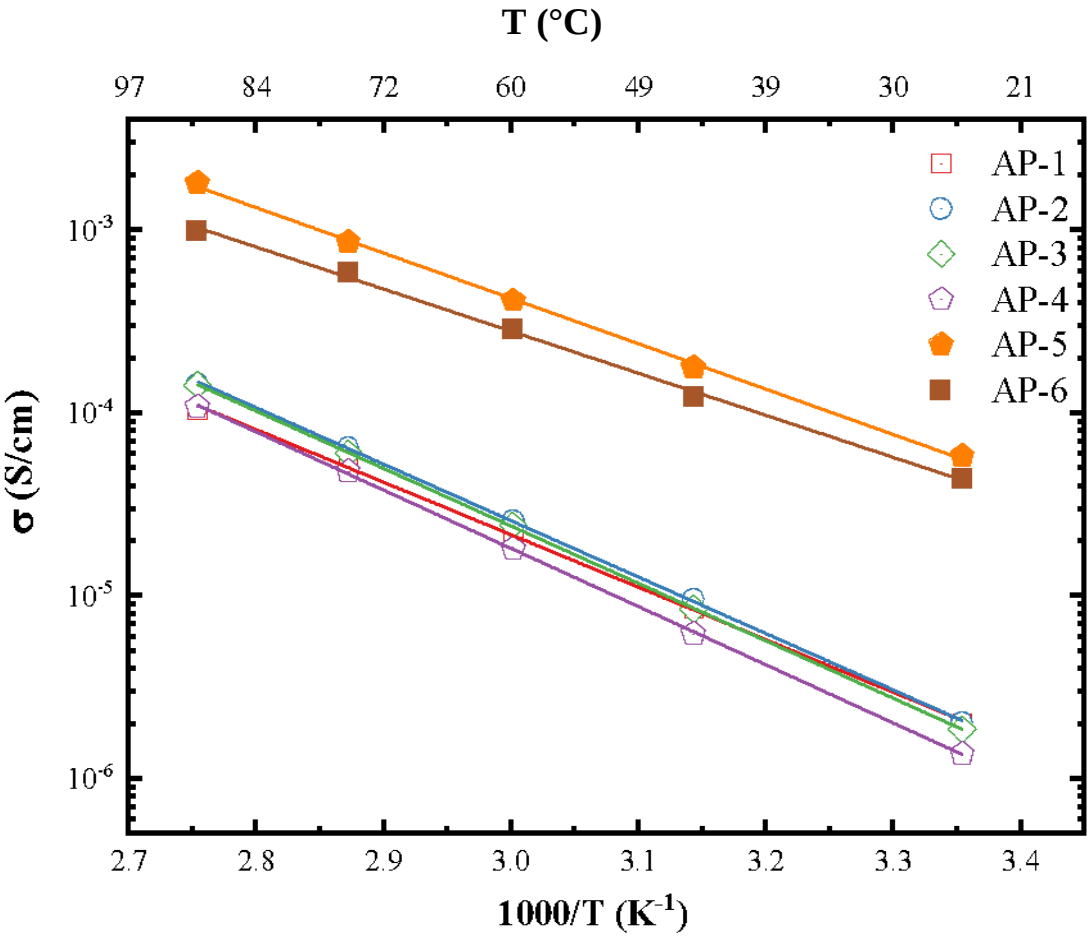

Figure 17. Temperature-dependent Li-ion conductivity measured for different electrolyte formulations. AP-5 has the best Li-ion conductivity.

Figure 18 shows the voltage profile of a symmetrical Li||AP-5||Li cell during repeating lithium stripping/plating cycling. The cell was tested using a constant current of 0.1 mA/cm^2. A normal square wave was observed on the voltage response through the test. Figure 18 also shows a slow increase of the voltage polarization with the cycling time. The slow increase in voltage polarization might imply a change of the morphology of lithium surface or a slow reaction between the metallic lithium and the electrolyte. Further investigation will be conducted to illustrate the potential reaction occurring at the lithium/electrolyte interface.

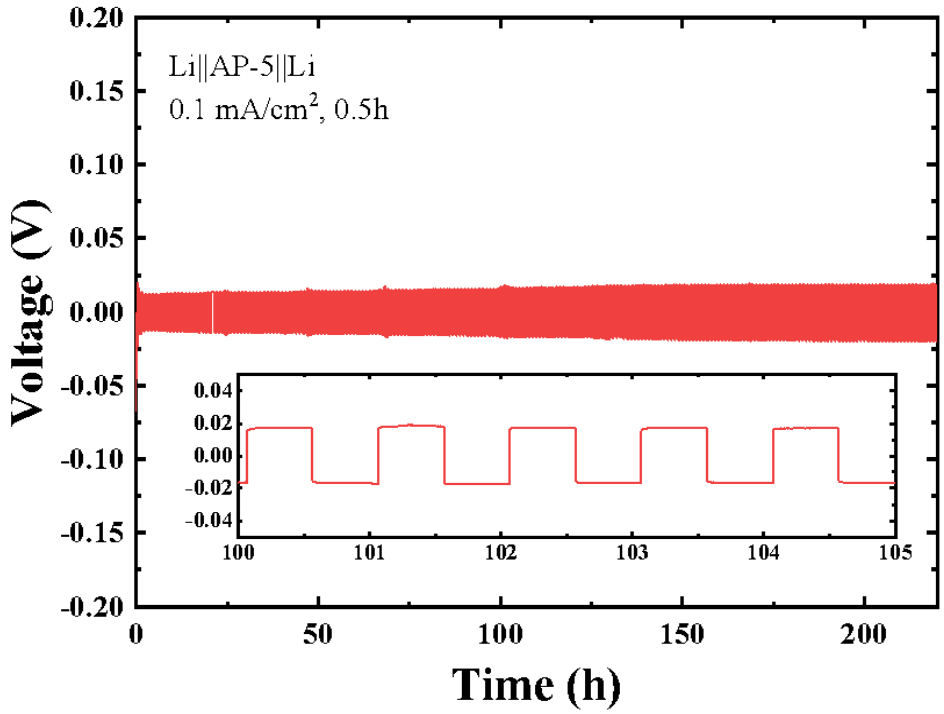

Figure 18. Voltage profile for a continuous cycling of a symmetrical cell using AP-5 as the electrolyte.

High-precision leakage current (HpLC) measurement (Figure 19a for a picture of home-built system) is an advanced electrochemical tool to quantitatively measure the rate of electron transfer reactions at heterogeneous interfaces, such as the cathode electrolyte interface and solid electrolyte interface. To study the intrinsic anodic stability of the electrolyte, a dummy Al||AP-5||Li was assembled and tested using the home-built HpLC system. Figure 19b shows a set of typical data collected at 3.2 V versus Li^+/Li. In this exercise, the cell was constant-voltage charged at 3.2 V for 20 hours, and the current passing through the cell was recorded as a function of the holding time. It can be seen from Figure 19b that the current decayed exponentially. Considering no active cathode material was incorporated, the measured current was purely associated with the side reaction occurring at the Al/electrolyte interface: mostly parasitic reactions to passivate the Al/electrolyte interface. The collected data were then fitted with an exponential function (as shown in Figure 19b) to extract its steady leakage current as an indicator of the rate of the parasitic reactions. Figure 19c shows the dependence of the steady leakage current on the working potential. It can be clearly seen that the steady leakage current peaked at about 3.9 V versus Li^+/Li, after which the steady leakage current was stabilized at about 0.5 nA/cm^{-2}. This peaking behavior signals that the undergoing reaction is a self-regulated passivation reaction. More advanced characterization is needed to confirm the nature of the undergoing reaction.

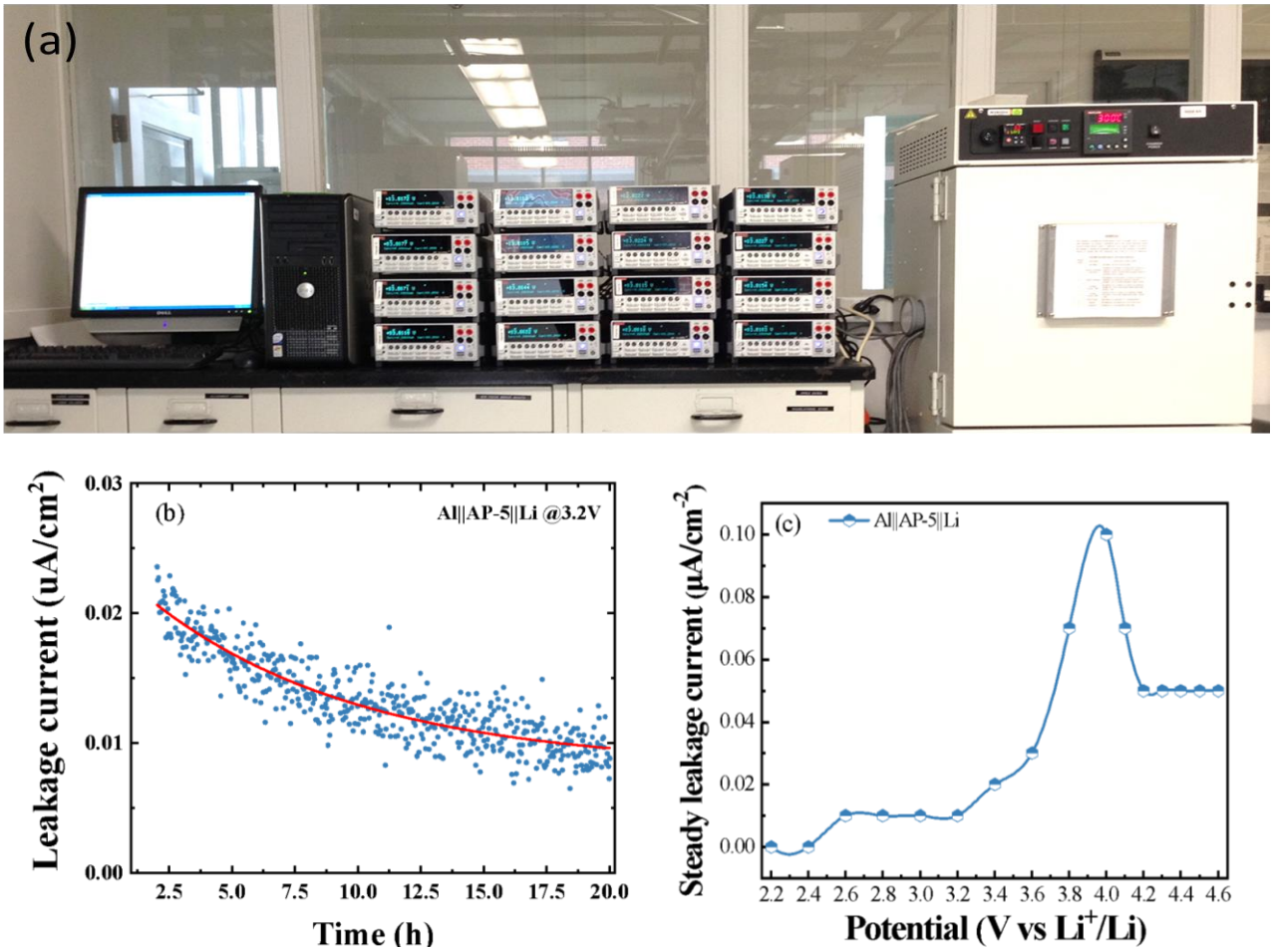

Figure 19. (a) Picture of a home-built high-precision leakage current (HpLC) measurement system for interfacial electrochemical study. (b) A typical set of raw data collected at 3.2 V showing the principle of HpLC measurement. (c) Potential dependent steady leakage current measured on an Al||AP-5||Li cell showing some electrochemical reactivity within the potential window 3.6-4.2 V.

Patents/Publications/Presentations

The project has no patents, publications, or presentations to report this quarter.

Task 1.8 – Lithium Halide-Based Superionic Solid Electrolytes and High-Voltage Cathode Interface (Robert Sacci, Oak Ridge National Laboratory [Jagjit Nanda, SLAC])

Project Objective. The project aims to develop a low-temperature solution-based synthesis strategy for high ionic conducting halide-based solid electrolyte (SE) and to enable approaches to develop a scalable process for integrating halide-based SE within a porous high-voltage Li-ion cathode matrix. Years 1 and 2 aim at developing low-cost, solution-based synthesis routes to produce a halide class of superionic conductor belonging to Li_3MX_6 (where M = Sc, Y, La, Er, In, and X = Cl, Br, I) along with enabling electrochemical and structural characterization. Parallel efforts in years 2 and 3 target developing synthesis and processing methods where the high-voltage stable halide-based SEs can be readily infiltrated within the porous cathode structures such as $LiNi_{0.6}MN_{0.2}Co_{0.2}O_2$ (NMC-622), high-voltage Mn-Ni spinel ($LiMn_{1.5}Ni_{0.5}O_4$), and recent fluorinated Mn-rich disordered rock salt cathodes. Years 3 and 4 focus on designing and fabricating thin halide SE separators with a thickness of 50 µm or lower and optimizing the cathode microstructure. Finally, years 4 and 5 will target developing approaches for anode-free lithium plating and stripping on alloyed or engineered copper current collectors at relatively higher current densities aimed at improving the volumetric energy density of solid-state batteries (SSBs) with a high loading cathode and thin halide SE separator.

Impact. The proposed tasks and metrics aim at addressing the long-term Vehicle Technologies Office goal for developing SSBs at ambient temperature with energy density in the range of 500 Wh/Kg and 1000 Wh/L for electric drive vehicles. Advances in scalable processing of superionic SEs, stabilizing electrode-electrolyte interfaces, and promoting long cycle life are all needed to meet the energy density and cost targets for next-generation batteries for electric vehicles.

Approach. The project employs a multifaceted approach: (1) conduct solution-based synthesis of the metal halide superionic conductor as the platform to enable robust cathode electrolyte interface processing for SSBs, (2) infiltrate pore structures using solution-based processing that deposits high-conductivity SEs within cathode pores, and (3) facilitate lithium transport and improve stability using cation doping (divalent to introduce lithium vacancies, and lanthanum to prevent indium redox).

Out-Year Goals. Demonstrate single-layer, pouch-cell SSB containing a thin halide SE separator coupled with high-voltage cathodes with 70% capacity retention over 300 cycles at 2 mA/cm^2 in an anode-free SSB configuration that can attain 1000 Wh/L in prototype cells.

Collaborations. Y. Yao and team at University of Houston (UH) are funded collaborators for halide-based SSB fabrication, testing, and interfacial studies. The project also involves unfunded collaboration with SLAC National Accelerator Laboratory for X-ray absorption spectroscopy and synchrotron X-ray diffraction of SEs.

Milestones

1. Demonstrate synthesis of doped Li_3InCl_6 for improved stability and conductivity. (Q1, FY 2023)
2. Compare conductivity between different casting methodologies. (Q2, FY 2023)
3. Obtain free-standing SE and SE/cathode composite films < 100-µm-thick. (Q3, FY 2023)
4. Demonstrate 50 cycles of SE/NMC-type cathode composites and Li-P-S coated anodes. (Q4, FY2023)

Progress Report

The team expanded the synthesis of lithium halide-based electrolytes to include Li_3YCl_6. The purpose of changing the multivalent metal site is to increase the operating voltage window. By replacing In^{3+} with Y^{3+}, the voltage window is expected to increase upward of 0.5 V toward the anode. They attempted to replace $InCl_3$ with YCl_3, dissolving it in water along with LiCl and synthesizing it through dehydration similar to Li_3InCl_6. This pathway failed to result in pure Li_3YCl_6. Instead, the product was a mixture of YOCl and LiCl, with little Li_3YCl_6. They followed this reaction using neutron diffraction, which is shown in Figure 20.

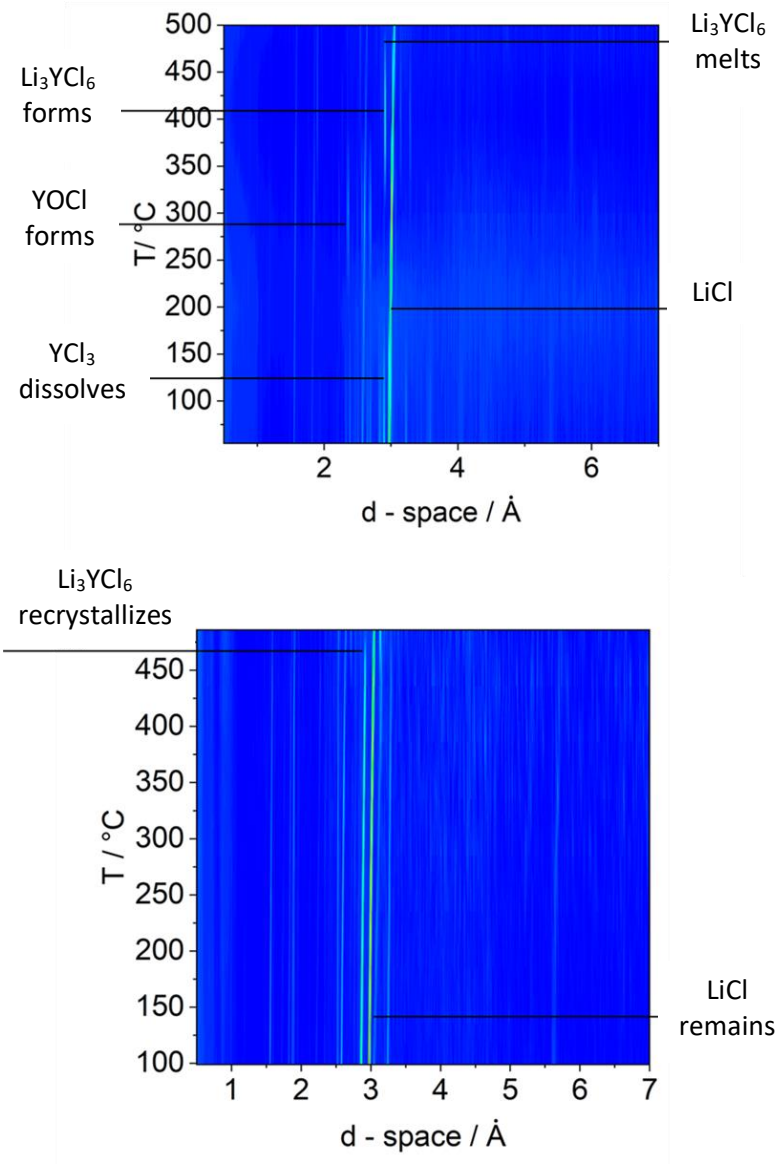

Figure 20. *In situ* neutron diffraction contour plots of the direct water synthesis pathway: (top) heating from room temperature to 500°C, and (bottom) cooling from 500°C to room temperature.

In Figure 20, the precursors were dissolved in water and dried under vacuum at 80°C. Here, YCl_3 vanishes when the dried pellet is heated to 200°C, and Li_3YCl_6 begins to form around 300°C. The impurity phase YOCl is also observed around 300°C, which is in line with reports in the literature, which show that YOCl can be

synthesized from $YCl_3 \cdot 6H_2O$ by heating the precursor to 350°C for 4 hours in the air.[1] Surprisingly, the sample melts at 500°C, leaving behind unreacted LiCl. On cooling, the Li_3YCl_6 reforms around 475°C, resulting in a large LiCl impurity. This result is likely due to the significant consumption of the YCl_3 precursor in the formation of YOCl impurities during heating.

Given the strong coordination between H_2O and Y^{3+}, the team attempted to shift the equilibrium toward the $[YCl_6]^{3-}$ complex by adding excess NH_4Cl. NH_4Cl increases the concentration of chloride ions and undergoes clean sublimation at ~375°C. Figure 21 shows the *in situ* neutron scattering data that seem to confirm their hypothesis. Here, the mixture of YCl_3, LiCl, and NH_4Cl quickly forms the desired Li_3YCl_6 product ~ 200°C. The comparison of the two synthetic routes clearly shows that NH_4Cl is required to protect the YCl_3 precursor from hydrolysis during heating.

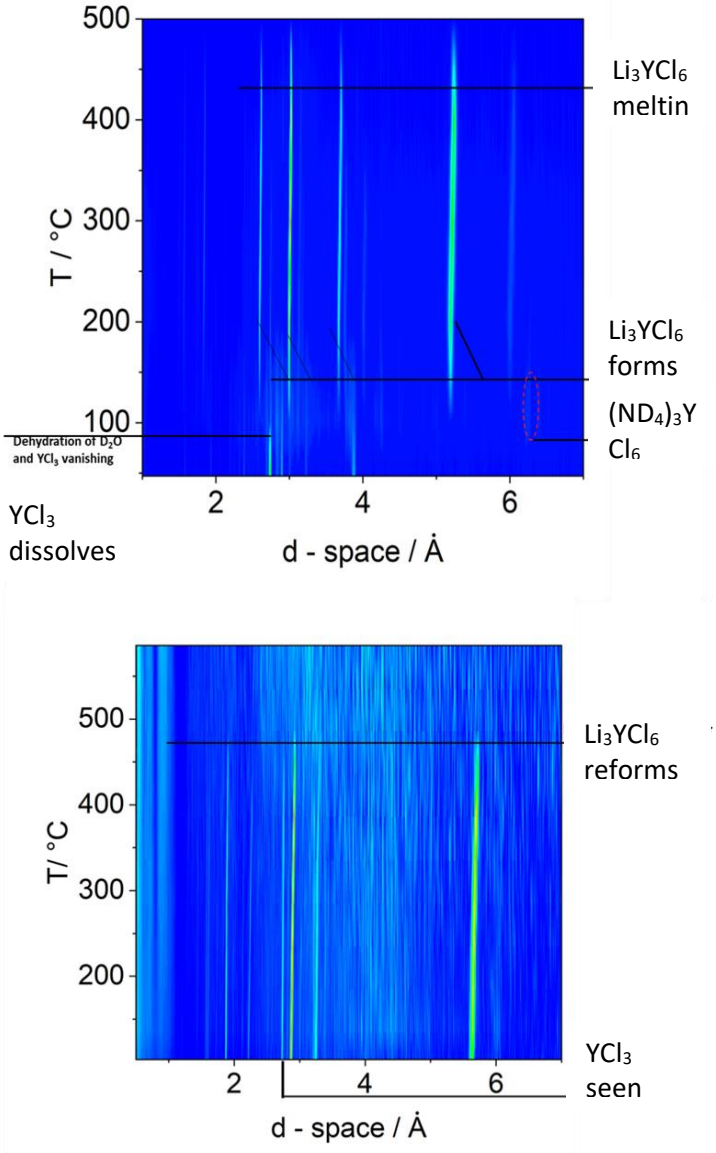

Figure 21. *In situ* neutron diffraction contour plots of the ammonium-assisted synthesis pathway: (top) heating from room temperature to 500°C, and (bottom) cooling from 500°C to room temperature. The top panel depicts the presence of YCl_3 precursors along with the early formation of $(ND_4Cl)_3[YCl_6]$ intermediate at ~ 100°C.

The team also synthesized the Li_3YCl_6 from a purely mechanochemical method. Here, they ground anhydrous YCl_3 and LiCl together for 16 hours in a planetary mill. From here, they divided the batch between amorphized (unannealed) and crystalline (annealed). The annealed sample was pelletized and heated at 500°C (ramp rate 5°C/min) for 5 hours under argon flow in a glovebox.

They compared the conductivity of the three pure products [that is, ammonium assisted (AA), mechanochemical (MC), and mechanochemical annealed (MCA)] in Figure 22. The AA product showed the greatest room temperature conductivity of the three samples at 0.65 mS/cm, with MC and MCA being 0.37 mS/cm and 0.13 mS/cm, respectively. The Li^+ transport activation energy as derived from Equation (1):

$$\sigma_{ionic} = \sigma_0 exp\left(-\frac{E_a}{k_B T}\right) \qquad \text{Equation (1)}$$

where σ_0, k_B, and T are the temperature-independent Arrhenius scalar, the Boltzmann constant, and the absolute temperature, respectively. The activation energy for the total conductivity for both mechanochemical products was 0.35 eV, while that of the AA product was 0.39 eV. The MCA product conductivity is lower than that of the MC sample and is likely driven by annealing-induced ordering within the sample. This is in line with previous reports regarding the effect of annealing time on the mechanochemically derived Li_3YCl_6 where it was observed that the conductivity decreased as the milled sample was annealed for longer periods of time ranging from 1 minute to 1 hour.[2] This was attributed to the large amount of cation site disorder induced during milling and the subsequent reordering caused by annealing.

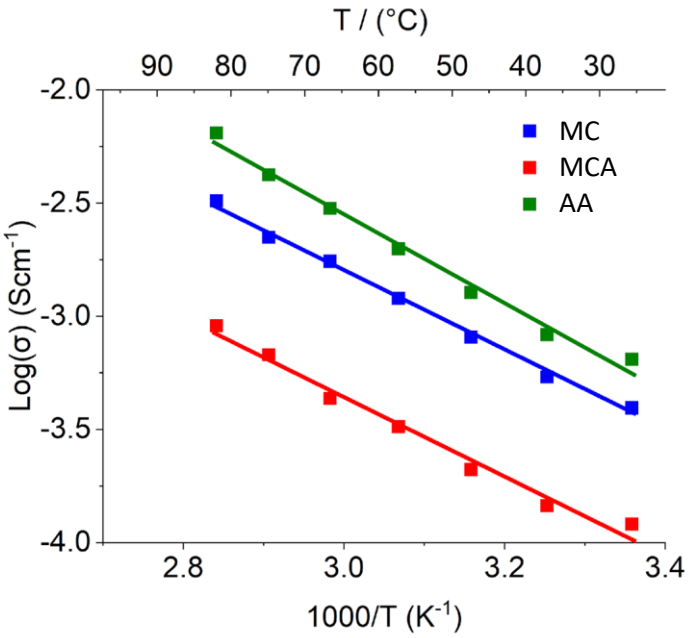

Figure 22. Arrhenius plot comparison for the Li_3YCl_6 MC, MCA, and AA samples.

Recent work has shown that electrochemical performance can be affected by the choice of a synthesis route for sulfide and halide SEs.[3] To understand this relationship for Li_3YCl_6, $LiNi_{0.8}Mn_{0.1}Co_{0.1}O_2$ (NMC-811)/ Li_3YCl_6/Li-In cells were constructed for the MC, MCA, and AA samples. A Li-In anode was used in place of lithium metal because Li_3YCl_6 has been shown to be unstable against lithium metal.[4] The alloy was formed by lithiating indium foil on the 1st charge cycle of each cell. Figure 23 presents the initial charge-discharge capacities for each cell at 66 µA/cm^2, in which the Li_3YCl_6-MCA cell has a much higher initial charge capacity, 188 mAh/g, compared to just 148 mAh/g for the Li_3YCl_6-MC, but the initial loss between the 1st charge and discharge is also substantially higher for the Li_3YCl_6-MCA cell, ~ 29% compared to just 0.7% capacity fade for the Li_3YCl_6-M cell. These cells were cycled at ~ 6 MPa; Y. Yao at UH is cycling these cells in parallel at greater stack pressures to understand the effect of contact loss during cycling.

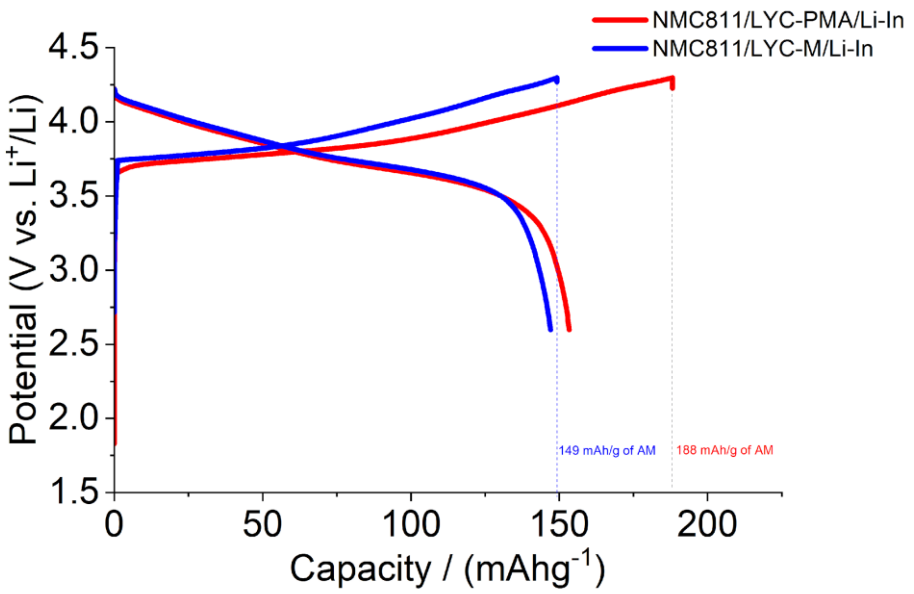

Figure 23. Initial charge-discharge comparison for NMC-811/Li_3YCl_6/Li-In cells.

References

[1] Todd, P. K., M. J. McDermott, C. L. Rom, A. A. Corrao, J. J. Denney, S. S. Dwaraknath, P. G. Khalifah, K. A. Persson, and J. R. Neilson. "Selectivity in Yttrium Manganese Oxide Synthesis via Local Chemical Potentials in Hyperdimensional Phase Space." *Journal of the American Chemistry Society* 143, No. 37 (2021): 15185–15194. https://doi.org/10.1021/jacs.1c06229.

[2] Schlem, R., S. Muy, N. Prinz, A. Banik, Y. Shao-Horn, M. Zobel, and W. G. Zeier. "Mechanochemical Synthesis: A Tool to Tune Cation Site Disorder and Ionic Transport Properties of Li 3 MCl 6 (M = Y, Er) Superionic Conductors." *Advanced Energy Materials* 10, No. 6 (2020): 1903719. https://doi.org/10.1002/aenm.201903719.

[3] Koç, T., F. Marchini, G. Rousse, R. Dugas, and J-M. Tarascon. "In Search of the Best Solid Electrolyte-Layered Oxide Pairing for Assembling Practical All-Solid-State Batteries." *ACS Applied Energy Materials* 4, No. 12 (2021): 13575–13585. https://doi.org/10.1021/acsaem.1c02187.

[4] Han, Y., S. H. Jung, H. Kwak, S. Jun, H. H. Kwak, J. H. Lee, S-T. Hong, and Y. S. Jung. "Single- or Poly-Crystalline Ni-Rich Layered Cathode, Sulfide or Halide Solid Electrolyte: Which Will Be the Winners for All-Solid-State Batteries?" *Advanced Energy Materials* 11, No. 21 (2021): 2100126.

Patents/Publications/Presentations

The project has no patents, publications, or presentations to report this quarter.

Task 1.9 – Polyester-Based Block Copolymer Electrolytes for Lithium-Metal Batteries (Nitash Balsara, University of California, Berkeley)

Project Objective. The project objective is to design and synthesize polyester-based block copolymer electrolytes that can enable full-cell cycling at 1 mA/cm^2 or greater for 300 cycles. The cell comprises Li-metal anode, 4.5 V Ni-Mn-Co (NMC) cathode, and thin separators (20-50 µm) casted from the block copolymer.

Impact. Polymer electrolytes offer increased stability in lithium batteries in comparison to more widely used liquid electrolytes. Block copolymer-based electrolytes containing both soft, ion-conducting domains and rigid, nonconducting domains offer the opportunity to tune both mechanical and electrical properties separately. Most block copolymer electrolytes studied thus far comprise poly(ethylene oxide) (PEO) as the conducting domain. The team hopes to develop polyester-based electrolytes that exhibit much higher transport properties and limiting currents than PEO-based electrolytes. An all-solid full cell with this new block copolymer electrolyte, a Li-metal anode, and an NMC cathode will have much higher energy density than current Li-ion technology.

Approach. The team will begin by synthesizing several series of polyester homopolymers and fully characterizing their blends with lithium salts as polymer electrolytes in Li-Li symmetric cells. Next, they will make block copolymer electrolytes based on the most promising candidate and measure the electrochemical and mechanical properties thoroughly. Finally, they will assemble full cells with the optimum block copolymer electrolytes together with lithium metal and a 4.5 V NMC cathode.

Out-Year Goals. In the first year, the team will establish an efficient synthesis and characterization platform for polyester electrolytes. Several polyesters will be synthesized, and electrolytes will be made by blending each polymer with lithium salt. Transport properties (such as conductivity and current fraction) and limiting current of resulting electrolytes will be measured in Li-Li symmetric cells. The highest performing polymer electrolyte will be used as the conducting phase in the block copolymer design in the second year.

Collaborations. There are no active collaborations this quarter.

Milestones

1. Limiting current: Measure limiting current of at least one polyester electrolyte. (Q1, FY 2023; Completed)
2. Molecular weight: Explore the effect of molecular weight of polyester electrolytes on Li-ion transport. (Q2, FY 2023; In progress)
3. Block copolymer synthesis: Try at least two approaches for synthesizing polystyrene-polyester-polystyrene (PS-PES-PS) block copolymers. (Q3, FY 2023)
4. Physical properties: Study physical properties of at least one PS-PES-PS block copolymer, including morphology, mechanical properties, and conductivity. (Q4, FY 2023)

Progress Report

This quarter, the team measured the limiting current (i_L) of three poly(pentylene malonate) / lithium bis(trifluoromethanesulfonyl)imide (PPM/LiTFSI) electrolytes using Li-Li symmetric cells. Figure 24a-b shows the voltage (V) as a function of time (t) for various applied current densities for electrolytes with a salt concentration or r value of 0.02 and 0.04, respectively. For this study, it is useful to determine the largest current density that results in a stable voltage response and the smallest current density that results in an unstable voltage response. These two values are averaged to find the limiting current. As seen in Figure 24a, an applied current density of 0.25 mA/cm^2 results in a stable voltage response where over time the voltage goes to a constant value. An applied current density of 0.3 mA/cm^2 results in an unsteady voltage response. In Figure 24b, the same phenomenon is seen for current densities of 0.9 mA/cm^2 and 1.1 mA/cm^2.

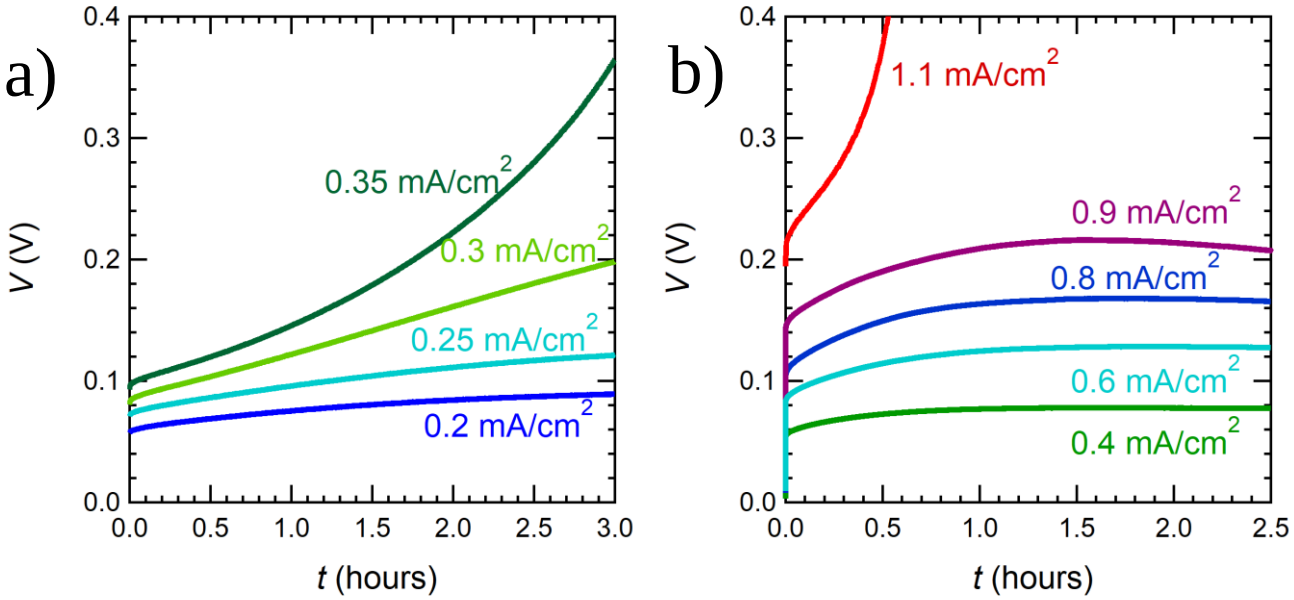

Figure 24. Voltage (V) behavior as a function of time (t) for various applied current densities at 90°C for PPM/LiTFSI electrolytes with salt concentrations of (a) r = 0.02 and (b) r = 0.04.

In the team's studies, they also measured the limiting current of PPM/LiTFSI electrolytes of salt concentration r = 0.06. The limiting current of these three electrolytes allows for a comparison of the performance limitations of PPM/LiTFSI electrolytes and PEO/LiTFSI electrolytes.

Figure 25 shows the normalized limiting current, where the limiting current density is multiplied by the thickness of the electrolytes, to compare the limiting current of PPM/LiTFSI electrolytes to previously determined limiting currents of PEO/LiTFSI electrolytes.[1] At the lowest salt concentration of r = 0.02, the limiting current of the two systems is very similar. However, at higher salt concentrations, the limiting current of the PPM/LiTFSI electrolytes is more than double that of PEO/LiTFSI. This shows that PPM/LiTFSI electrolytes can be subjected to higher currents compared to PEO/LiTFSI electrolytes, making this material more attractive for real world applications when compared to PEO.

According to concentrated solution theory, the limiting current should be a linear function of salt concentration. In Figure 25, linear fits of the limiting current data are shown, with the intercept held at zero since no current will be passed through a neat polymer. For PPM/LiTFSI electrolytes, $i_L L = 1.16r$, and for PEO/LiTFSI electrolytes, $i_L L = 0.42r$. Again, this is indicative that PPM/LiTFSI electrolytes can operate under higher applied currents than PEO/LiTFSI electrolytes for most salt concentrations above the lower limit of r = 0.02.

Next quarter, the team will examine how the molecular weight of their polyester electrolyte affects Li-ion transport properties.

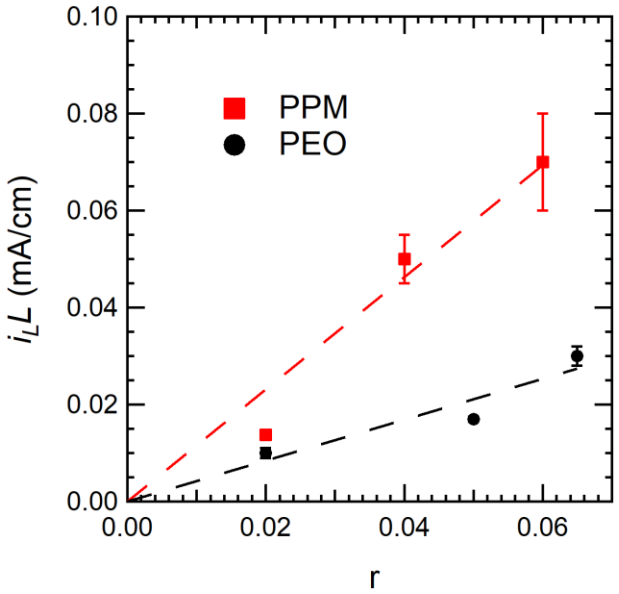

Figure 25. Normalized limiting current, $i_L L$ of PPM/LiTFSI and PPM/LiTFSI electrolytes as a function of salt concentration, r. The dashed lines are linear fits of the data with the intercept constrained at zero. The red data represent PPM/LiTFSI electrolytes, and the black data represent PEO/LiTFSI electrolytes. All data were collected at 90°C.

Reference

[1] Gribble, D. A., L. Frenck, D. B. Shah, J. A. Maslyn, W. S. Loo, K. I. S. Mongcopa, D. M. Pesko, and N. P. Balsara. "Comparing Experimental Measurements of Limiting Current in Polymer Electrolytes with Theoretical Predictions." *Journal of Electrochemical Society* 166 (2019): A3228−A3234.

Patents/Publications/Presentations

The project has no patents, publications, or presentations to report this quarter.

Task 1.10 – Advanced Polymer Materials for Batteries (Zhenan Bao and Yi Cui, Stanford University)

Project Objective. This project will develop new polymer materials for batteries. The team will develop polymer coatings with specific mechanical properties that can accommodate the volume expansion and contraction of the Li-metal anode associated with deposition and stripping (charging and discharging).

Project Impact. The cycling stability and Coulombic efficiency of Li-metal electrodes will be increased by implementation of a polymer-based protective layer that functions as an artificial solid electrolyte interphase (SEI) with desired properties. The improved performance will enable further development toward practical utilization of Li-metal anodes with higher cycling efficiency and less susceptibility to dendrite-based failure.

Approach. The project uses soft polymer coatings with dynamic crosslinking to give the resulting polymers liquid-like rheological properties and stretchable, self-healing properties. In previous work, the team has shown that such coatings resulted in uniform deposition/stripping of lithium metal and improved cycling stability of Li-metal electrodes. To understand the design rules for effective polymer coatings, they chose a few representative polymers to systematically understand structure property relationships. Here, they investigate the correlation between surface energy of the polymer and exchange current for lithium deposition.

Out-Year Goals. Work will progress toward the correlation between dielectric constant and exchange current. These findings will enable further understanding and development of various polymer coatings for protecting Li-metal anodes.

Collaborations. The team is collaborating with J. Qin at Stanford University.

Milestones

1. Fundamental understanding of an existing polymer design. Characterize the chemical composition of the coated interface with lithium metal in different electrolytes. (Q1, FY 2023; Completed)

2. Probing the lithium deposition mechanism under the polymer coating: build optical cells and conduct *in situ* microscopic imaging of coated copper electrode during lithium deposition. (Q2, FY 2023)

3. Characterizing coating performance in stringent cycling conditions: high-capacity cycling (5 mAh cm^{-2} cathode loading) in the lean electrolyte condition (~ 3 g Ah^{-1}). (Q3, FY 2023)

4. Coat the polymer on thin lithium anode (50 µm) and perform stable long-term cycling (≥ 400 cycles) with novel electrolytes. The goal is to examine coating performance when pairing with high performing, instead of standardized, electrolyte. (Q4, FY 2023)

Progress Report

Recently, the team developed a polymer coating capable of tuning SEI composition. When lithium is in contact with the electrolyte, it reacts with both the salt and the solvent. Recent research findings indicate that a salt-derived SEI is beneficial for battery performance. The aim of the team's materials design is to develop a polymer coating capable of selectively transporting salt over solvent molecules and tuning the SEI composition to be more salt-derived. They named this series of polymer SP^2 (salt-philic solvent-phobic). They have arrived at a desirable composition, SP^2_{perF}, with the "perF" indicating addition of a perfluorinated side chain (Figure 26).

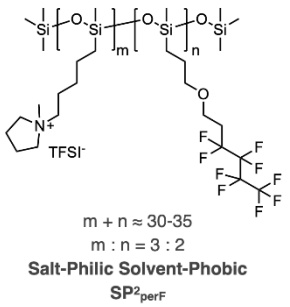

Figure 26. Chemical structure of SP^2_{perF}.

An effective way to characterize SEI composition is through X-ray photoelectron spectroscopy (XPS). The interfacial chemistry changes with different electrolyte environments. The team examined and compared the SEI chemistry under the influence of polymer coating with standard electrolytes. Recent literature has suggested that several factors affect the composition analysis of XPS. These factors include rinsing, sputtering, and sampling location. These are addressed in the following sections.

Rinsing. The rinsing protocol can change the composition of the SEI through dissolution. The team investigated the salt-derived SEI content in both rinsed and unrinsed samples. When there was no rinsing, SP^2_{perF} increased the salt-derived SEI content from 56% to 73%. When the sample was rinsed with 200 µL dimethoxyethane (DME), SP^2_{perF} coating increased the salt-derived SEI content from 14% to 31% (Figure 27a-b). Based on consistent results, they have concluded that the rinsing protocol does not affect interpretation of the XPS result, which suggests that SP^2_{perF} coating can increase the salt-derived SEI content.

Sampling Location. Inconsistent results can be derived from different sampling locations. This can be mitigated by following two strategies: (1) characterize the SEI on a rigid substrate (copper) instead of a soft substrate (lithium), as soft substrates are subject to deformation during sample handling, and (2) use cumulated SEI from several cycles, instead of the 1st cycle SEI, to build sample thickness and homogeneity. The team sampled the S/C elemental ratio at two different locations on the sample (1 M lithium bis(trifluoromethanesulfonyl)imide 1,3-dioxolane/dimethoxyethane, or LiTFSI DOL/DME, with 1 wt% $LiNO_3$ electrolyte, SP^2_{perF} coated copper, 0.5 mA cm^{-2}, 1 mAh cm^{-2} 10 cycles, rinsed with 200 µL DME, 2 kV µA). One is 0.376, and the other is 0.357. The two data points show consistent SEI composition at different sampling locations. By using a hard copper substrate and accumulating a thick layer of SEI through 10 cycles of strip-and-plate, they found consistent results of SEI composition at different locations.

Sputtering. Sputtering-induced inconsistency can also be mitigated by increasing sample thickness. By characterizing a thick layer of SEI from 10 cycles, instead of a thin layer of 1st cycle SEI, the team observed consistent SEI composition after different sputtering lengths for both carbonate and ether electrolyte. For 1 M $LiPF_6$ ethylene carbonate, dimethyl carbonate (EC/DEC) electrolyte, they reported consistent SEI composition at different sputtering times (Figure 28). The polymer coated sample has ~ 3 times higher F/C ratio than the bare sample at different sputtering times. For 1 M LiTFSI DOL/DME 1 wt% $LiNO_3$ ether electrolyte, they sampled the oxygen 1s spectrum at 2-minute and 3-minute sputtering times (Figure 27b-c). They separated out the SEI contribution from solvent and salt decomposition, and found similar percentages (29%, 31%) for the salt-derived contents of SP^2_{perF} coated samples at different sputtering times.

The team found that rinsing (or not) does not influence the conclusion that SP^2_{perF} coating increases the salt-derived SEI content. Through accumulating thick layers of SEI by cycling and using a rigid copper foil substrate, the inconsistency derived from sampling locations and sputtering time can be mitigated.

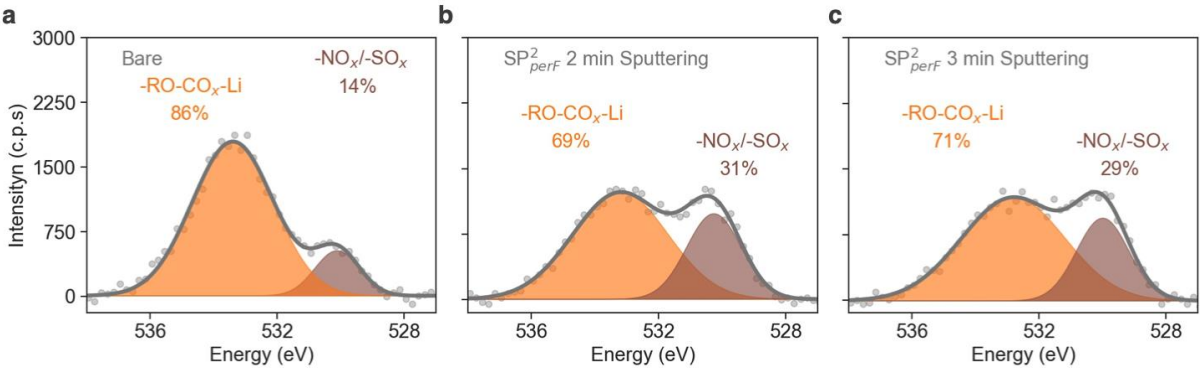

Figure 27. The oxygen 1s spectra of SEI from 1 M LiTFSI DOL/DME with 1 wt% $LiNO_3$ electrolyte with rinsing: (a) bare copper, sputtered for 2 minutes, (b) SP^2_{perF} coated copper after 2 minutes of sputtering, and (c) SP^2_{perF} coated copper after 3 minutes of sputtering. The sample was cycled at 0.5 mA cm^{-2}, 1 mAh cm^{-2} for 10 cycles. The sample was rinsed with 200 µL DME, sputtering power 2 kV µA.

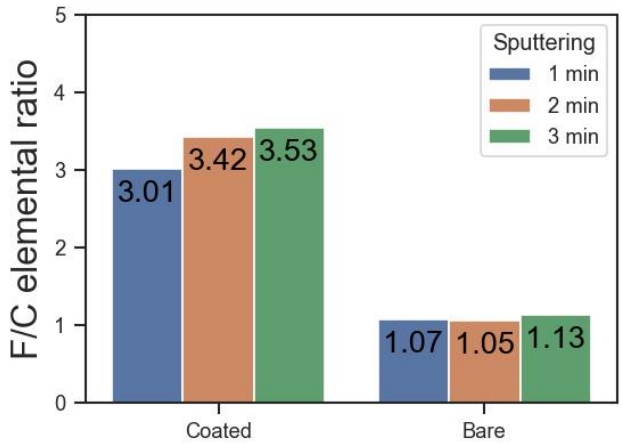

Figure 28. The F/C elemental ratio with 1 M $LiPF_6$ EC/DEC electrolyte at different sputtering times. The sample was coated with SP^2_{perF}, cycled at 0.5 mA cm^{-2}, 1 mAh cm^{-2} for 10 cycles, and rinsed with 200 µL DEC, 2 kV µA.

To examine the interfacial composition without the influence of an additive, the team cycled Li||Cu cell at 0.5 mA cm^{-2}, 1 mAh cm^{-2} for 10 cycles with two electrolytes: 1 M $LiPF_6$ EC/DEC and 1 M LiTFSI DOL/DME. The S/C elemental ratio can indicate the salt-derived SEI content. For samples with SP^2_{perF} coating applied, the S/C ratio was increased by ~ 3-fold (Figure 29). For carbonate-based electrolyte, the F/C elemental ratio can quantify the salt-derived SEI content, and increased F/C ratio was also observed in coated samples (Figure 30). Through XPS characterization, they found that SP^2_{perF} coating can increase the salt-derived SEI content in additive-free carbonate (1M $LiPF_6$ EC/DEC) and ether electrolytes (1M LiTFSI DOL/DME).

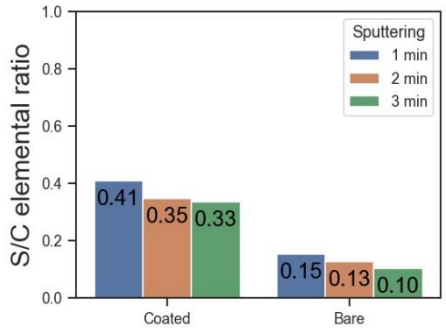

Figure 29. The S/C elemental ratio with 1 M LiTFSI DOL/DME electrolyte at different sputtering time. The sample was coated with SP^2_{perF}, cycled at 0.5 mA cm^{-2}, 1 mAh cm^{-2} for 10 cycles, and rinsed with 200 µL DME, 2 kV µA.

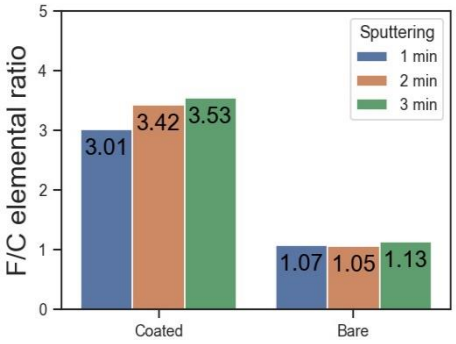

Figure 30. The F/C elemental ratio with 1 M $LiPF_6$ EC/DEC electrolyte at different sputtering time. The sample was coated with SP^2_{perF}, cycled at 0.5 mA cm^{-2}, 1 mAh cm^{-2} for 10 cycles, and rinsed with 200 µL DEC, 2 kV µA.

Patents/Publications/Presentations

Publications

- Boyle, D. T., S. Cheol Kim, S. T. Oyakhire, R. A. Vilá, Z. Huang, P. Sayavong, J. Qin, Z. Bao, and Y. Cui. "Correlating Kinetics to Cyclability Reveals Thermodynamic Origin of Lithium Anode Morphology in Liquid Electrolytes." *Journal of the American Chemical Society* 144, No. 45 (2022): 20717–20725. https://doi.org/10.1021/jacs.2c08182.
- Boyle, D. T., Y. Li, A. Pei, R. A. Vilá, Z. Zhang, P. Sayavong, M. Sek Kim, W. Huang, H. Wang, Y. Liu, R. Xu, R. Sinclair, J. Qin, Z. Bao, and Y. Cui. "Resolving Current-Dependent Regimes of Electroplating Mechanisms for Fast Charging Lithium Metal Anodes." *Nano Letter* 22, No. 20 (2022): 8224–8232. https://doi.org/10.1021/acs.nanolett.2c02792.

Presentations

- International Symposium of Stimuli Responsive Materials, Napa Valley, California (October 24, 2022): "Designing Polymer Coatings for Li Metal Anodes"; Z. Huang, Y. Cui, and Z. Bao.
- Electrochemistry Conference: Gordon Research Conference, Santa Barbara, California (September 10, 2022): "Polymer Materials Design for Li Metal Anode"; Z. Huang, Y. Cui, and Z. Bao.

Task 1.11 – Synthesis of Composite Electrolytes with Integrated Interface Design (Sanja Tepavcevic, Argonne National Laboratory)

Project Objective. This project aims to develop well-controlled, scalable $Li_7La_3Zr_2O_{12}$ (LLZO) nanofiber and composite polymer electrolyte (CPE) synthesis processes that will address the manufacturing challenges of current solid-state electrolytes (SSEs) and demonstrate the fabrication of large-area, thin CPE membranes with outstanding electro-chemomechanical properties.

Impact. The outcome of this proposal will be a transformative manufacturing solution that can create large-area, mechanically and (electro)chemically stable SSEs (0 V to 4.5 V versus Li/Li^+) with Li^+ conductivity of $\geq 10^{-3}$ S/cm at room temperature enabling ≥ 1C charging rates.

Approach. To commercialize all-solid-state Li-ion battery technology, further advances will require the application of knowledge, concepts, and tools from several fields including materials science, physics, engineering, theory, and interfacial electrochemistry. The team's research philosophy is to establish a synthesis-material characterization-computation cycle that advances synthesis, chemistry, microstructure, interfaces, and transport in CPEs by a coordinated, interdisciplinary approach. The team's diverse expertise will allow them to understand, create, and rapidly scale up composite electrolytes to meet ambitious conductivity, energy, and power density targets.

Out-Year Goals. The innovative design and synthesis of integrated SSE interfaces include the following goals: (1) achieve high room-temperature conductivity by optimizing composite microstructures, synthetically modifying the LLZO-polymer interface, and reducing CPE membrane thicknesses down to 20 µm; (2) create a stable and effective interface between the CPE and metallic lithium that yields low charge transfer resistance and enables high critical current density (CCD, > 3 mA/cm^2); and (3) modify the CPE-cathode interface to enable the use of different cathodes [that is, lithium iron phosphate, $LiCoO_2$, and Ni-Mn-Co] and achieve high energy and power density in batteries.

Collaborations. Computational researchers will further help the team to understand and design better all-solid-state batteries. They will work closely with L. A. Curtiss, P. Barai, K. Chavan, and V. Srinivasan (Argonne National Laboratory) to understand the molecular and mesoscopic characteristics and performance of the team's CPEs.

Milestones

1. Investigate with experimental and computational modeling the combined impact of conductivity and mechanical properties of the solid electrolyte interphase (SEI) layer in stabilizing lithium deposition. (Q1, FY 2023; Completed)
2. Optimize nanofiber and composite electrolytes chemistry and processability for ambient stability. (Q2, FY 2023)
3. Use experimental and computation methods at the continuum level to understand ion transport mechanism through LLZO / poly(ethylene oxide) (PEO) composites and determine optimal chemistries for LLZO-PEO interfacing. (Q3, FY 2023)
4. Optimize LLZO processing and investigate with computational modeling how to achieve good percolation, improve conduction pathways, and reach CPE conductivity of 5×10^{-4} S/cm at room temperature. (Q4, FY 2023)

Progress Report

In previous milestones, the team investigated the chemistry of the SEI in CPEs with and without LLZO nanofibers. They demonstrated that the LLZO plays no role in the SEI, and only the PEO polymer and lithium bis(trifluoromethanesulfonyl)imide (LiTFSI) salt decompose when exposed to lithium to generate the interphase. To optimize the SEI and increase charging rates and Coulombic efficiencies (CEs), they used computation of SEI mechanics and experimental design to improve the anode interface.

Mesoscale modeling was employed to compare two SEI characteristics: modulus and uniformity. A poor SEI will be heterogeneous in coverage, thin, and made of weak/soft chemical components; a high quality SEI will be thick and uniform and contain a large portion of hard components (Figure 31a). According to the developed computational framework, as current is applied and lithium metal plates, dendritic filaments can grow through defects in the SEI. These dendrites continue to grow at certain rates, which can be quantified as dendrite growth velocity. As seen in Figure 31b, high quality SEIs slow the effective dendrite growth velocity under all conditions relative to weak SEIs. Also of note in Figure 31b is that the growth velocity is constant and high until the shear modulus of the bulk electrolyte, G_{Elec}, approaches and exceeds that of lithium metal, G_{Li}. As shown, the moduli of all PEO-based composite electrolytes with and without LLZO nanofibers are well below the moduli of lithium metals.

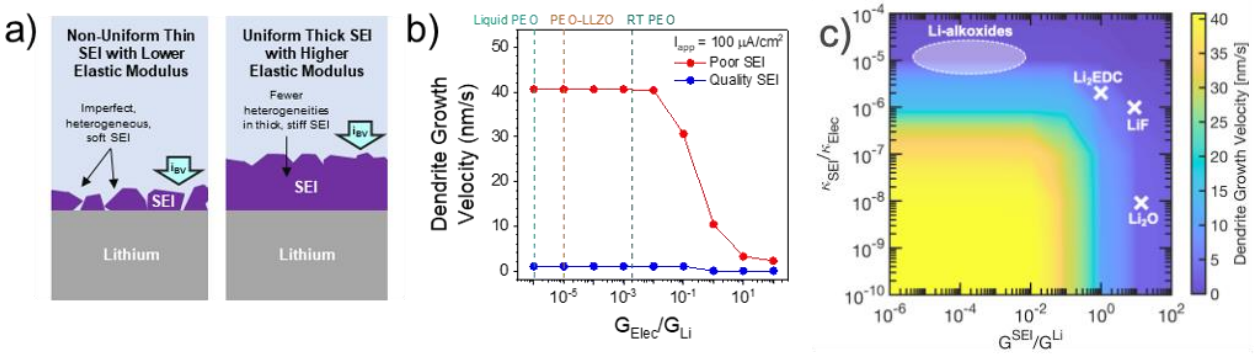

Figure 31. Modeling Ideal SEI Properties. (a) Schematic of the mesoscale model used for modeling lithium plating through soft and heterogenous SEI versus strong and uniform SEI. (b) Computed dendrite velocity as a function of relative bulk electrolyte modulus for the weak and strong SEIs. Notably, all composite electrolytes have moduli below lithium metal, so only a sufficiently strong SEI can prevent dendrite formation for the materials modeled here. (c) A phase map demonstrating the competition between the conductivity and elastic modulus of the SEI layer in determining the stability of lithium deposition process. Lower conductivity and stiffness promote dendrites, whereas larger magnitudes of SEI conductivity and SEI stiffness help to prevent their growth. Various SEI components in terms of their conductivity and shear modulus are shown within the phase map.

The conductivity of the SEI layer can also impact the propensity for dendrite growth by altering the reaction current density at the defect zone. Figure 31c is a phase map demonstrating the dendrite growth velocity as a function of conductivity and mechanical stiffness of the SEI layer. It is evident that increasing the overall conductivity of the SEI layer helps minimize the extent of current focused at the imperfections where dendrites are expected to initiate. This implies that either a sufficiently strong or a highly conductive SEI should be able to fully prevent dendrite growth in CPEs. Various commonly observed SEI components, such as Li_2O, LiF, di-lithium ethylene di-carbonate (Li_2EDC), and lithium alkoxides, are pointed out in the phase map shown in Figure 31c. Inorganic SEI components (Li_2O, LiF) deposited in a uniform fashion are expected to stabilize the lithium deposition process due to higher elastic stiffness. On the other side, uniform layers of organic SEI components (Li_2EDC, Li-alkoxides) may also reduce dendrite growth velocity due to a higher SEI ionic conductivity. Unfortunately, the actual SEI layer consists of both organic and inorganic components, which leads to inherent heterogeneities in both transport and mechanical properties of the SEI layer. These inhomogeneities act as hot spots for current focusing as well as fracture of the SEI layer, which can lead to dendrite growth and subsequent shorting of the cell.

For the current study, the team chose to focus on maximizing the inorganic SEI components with high elastic stiffness. Given the components of PEO and LiTFSI (since LLZO is not present at the interface under the normal fabrication conditions, as established in previous studies), a strong interface layer is only achievable with an SEI made from inorganic salt decomposition, generating species like LiF, Li_2O, Li_2S, and other compounds. With this in mind, they sought to improve the SEI characteristics in two ways. First, they varied the chemistry of the lithium salt to determine which anions lead to the best SEI and cell performance. Second, by using roll-to-roll slot-die coating, they generated different precursor layers to control the SEI through cell architecture in addition to salt chemistry.

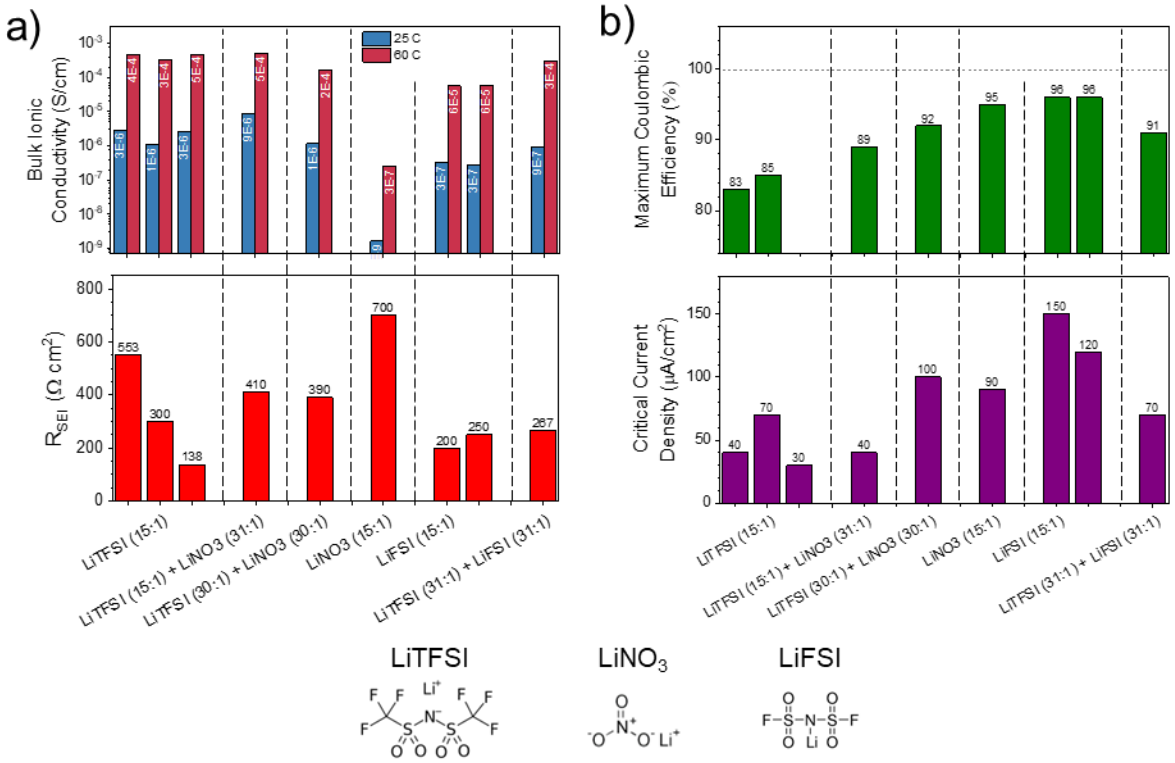

Figure 32. Controlling SEI with Salt Chemistry. (a) Bulk ionic conductivity at 25°C and 60°C and SEI resistance at 60°C of Cu|PEO-Li$_x$|Li cells. (b) Highest observed Coulombic efficiency and critical current density before shorting in the same cells at 60°C. Numbers in parentheses correspond to monomer-to-salt molar ratio (EO:Li$_x$).

LiTFSI is known to reductively decompose into LiF, Li_2O, Li_2S, Li_xSO_y, and Li_3N components; it also produces organic species from the decomposition of CF_3 groups along with the reduction of PEO. To determine how much LiTFSI—a costly material—can be replaced by an inexpensive salt yet still generate a good SEI, they partially and fully replaced the LiTFSI in PEO with lithium nitrate ($LiNO_3$) and lithium bis(fluorosulfonyl)imide (LiFSI). The EO:Li molar ratios for the tested salts are listed in Figure 32; for example, LiTFSI (30:1) + $LiNO_3$ (30:1) is a PEO electrolyte with 30:1 monomer units per LiTFSI and 30:1 monomer units per $LiNO_3$, a total 15:1 EO:Li^+ ratio for the mixture. In Cu||Li half cells, cyclic voltammetry was used to electrochemically form the SEI before testing with galvanostatic cycling in 10 μA/cm^2 steps. This allowed the team to quantify the bulk conductivity and SEI resistance (Figure 32a) as well as CE and CCD (Figure 32b).

It is clear that replacing LiTFSI lowers the bulk conductivity, as LiFSI dissociates less than LiTFSI, and $LiNO_3$ barely dissociates at all in PEO except at higher temperatures. This is not a long-term concern, since the goal is to achieve bulk conductivity with LLZO nanofibers, leaving room to tune the salt chemistry in the polymer phase. Additionally, the SEI resistances are similar across the board when LiTFSI is used in any amount at ~ 250-400 Ω cm^2. LiFSI produced slightly lower SEI resistances, which is interesting considering the lower Li^+ conductivity of the polymer phase with LiFSI; this shows the promise of LiFSI. The most important changes are seen in CE and CCD values. Cells with fully inorganic salts $LiNO_3$ and LiFSI show > 95% CE at their

greatest current densities, while TFSI-containing electrolytes barely reach 90%. Additionally, electrolytes with partial or full replacement of LiTFSI show higher current densities (70-150 µA/cm^2) than pure LiTFSI alone (typically ~ 50 µA/cm^2). Based on these observations and the lower cost than LiTFSI, the team is pursuing LiFSI as a salt of interest in further SEI studies.

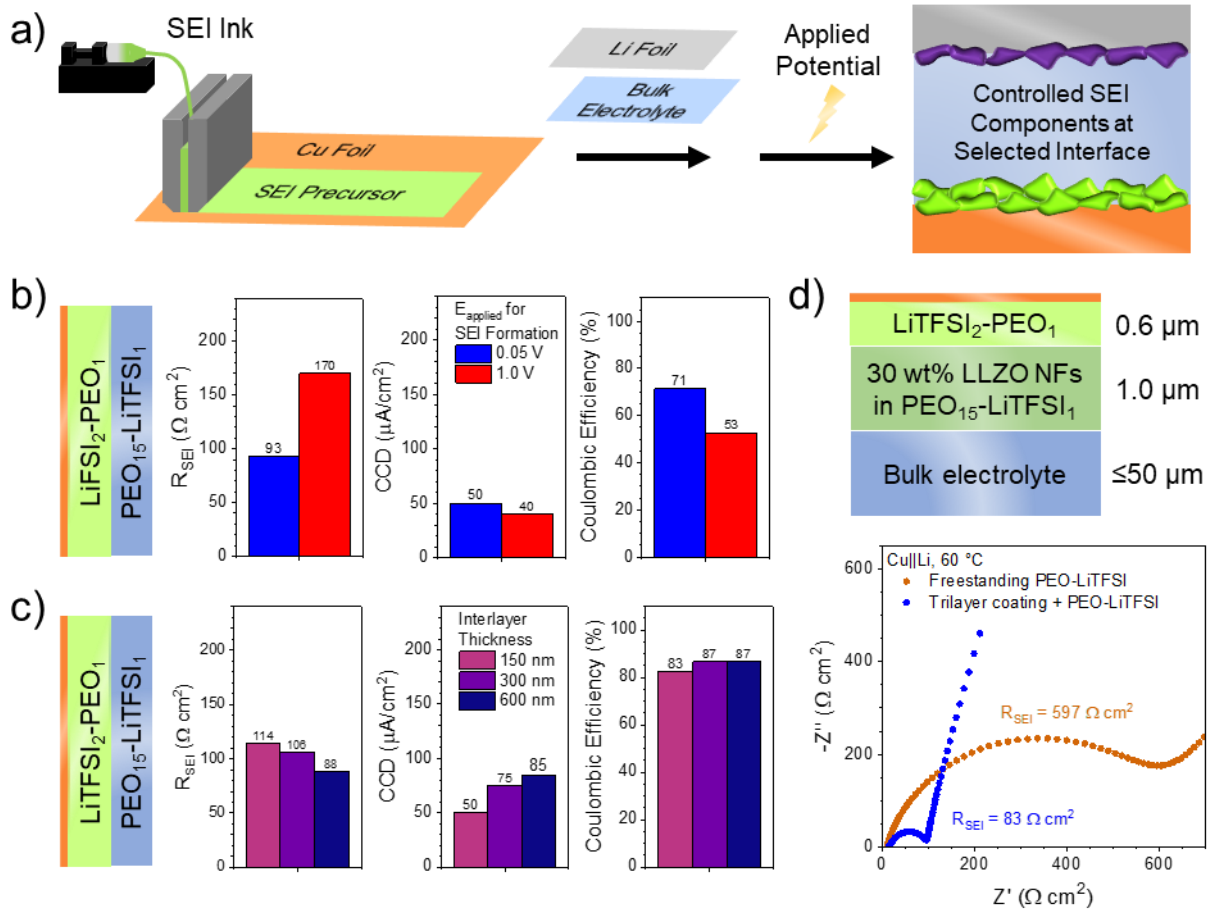

Figure 33. Controlling SEI with Cell Architecture. (a) Schematic of slot-die coating salt-rich SEI precursor layers and generating SEI under controlled conditions on copper electrodes. (b) Applying potentials of 0.05 V and 1.0 V for 2 hours at 25°C with LiFSI-rich interlayers shows that lower potentials generate better cell characteristics. (c) Varying the thickness of LiTFSI-rich interlayers shows that thicker 600-nm layers have better performance. (d) Incorporating LLZO nanofibers in a coated trilayer structure can decrease the effective interface resistance by > 85% compared to typical cells assembled with freestanding membranes.

To further ensure inorganic SEI characteristics, the team developed salt-rich thin film coatings on copper foil electrodes. Putting these in contact with freestanding bulk electrolyte membranes with lower salt contents and controlling the temperature and potential of SEI formation should allow control over inorganic versus organic SEI components (Figure 33a) while limiting the cost of using large salt quantities. Their hypothesis is that SEI formed electrochemically (in the absence of lithium metal) at higher potentials would yield more inorganic species and improve cell characteristics. Using a LiFSI-PEO coated interlayer with 2:1 Li:EO ratio, potentials of 0.05 V and 1.0 V were applied at room temperature (Figure 33b). Surprisingly, cells with SEI formed at lower potentials performed better with lower SEI resistance, higher CCD, and better CE before shorting. Notably, cell shorting seems to still be determined by the bulk electrolyte, PEO-LiTFSI, indicating the need for more SEI studies.

To optimize other characteristics of this interlayer, the team adjusted the thickness of the coating from 150 nm to 600 nm, which is achievable in uniform layers with their slot-die technique. Interestingly, thicker layers of LiTFSI-PEO with 2:1 Li:EO showed enhanced performance, with lower SEI resistance and higher CCD (Figure 33c). This may be due to more salt being present in the diffusion layer during SEI formation,

leading to more salt-derived SEI. Finally, they incorporated LLZO nanofibers as an additional interfacial layer between the salt-rich coatings and bulk PEO-LiTFSI electrolyte followed by SEI formation at 0.05 V. This produced the lowest interface resistance in their cells to date, with an 86% decrease in impedance compared to the typical freestanding samples (Figure 33d). Slot-die coating directly onto copper anodes will be their approach for cell fabrication for the near future, as this provides lower cell resistance in half cells. They will continue to investigate the best salt chemistries, concentrations, and SEI formation conditions to optimize resistance, CE, and CCD. Connecting with future milestones, they will also incorporate optimized LLZO nanofibers into the coatings to improve Li^+ conductivity at lower temperatures.

Patents/Publications/Presentations

The project has no patents, publications, or presentations to report this quarter.

Task 1.12 – Polymer Electrolytes for Stable, Low-Impedance, Solid-State Battery Interfaces (X. Chelsea Chen, Oak Ridge National Laboratory)

Project Objective. The overall project objective is to develop stable polymer/cathode and polymer/anode interfaces with low interfacial impedance for integration of a thin solid composite electrolyte into a battery, to achieve chemical stability at the electrodes, high energy density (500 Wh/kg), high rate (1 mA/cm^2), and long cycle life (80% capacity retention for 300 cycles), demonstrated in pouch cells.

Impact. Achieving stable, low-impedance interfaces at both the cathode and anode sides is critical to achieve high energy density with excellent safety, lifetime, and cycling efficiency. This project will identify key design strategies needed to prepare a polymer electrolyte (PE) to achieve stable, low-impedance polymer/cathode and polymer/Li interfaces and to develop processing procedures to integrate a thin composite electrolyte into a solid-state battery. Success will enable U. S. Department of Energy (DOE) technical targets: energy density of 500 Wh/kg with 80% capacity retention for at least 300 cycles.

Approach. The team's main design principle is to use an oxide ceramic as the main ion transporting phase in the electrolyte and a fluorinated polyether-based PE to form optimized interfaces as well as to provide flexibility to the electrolyte membrane. Compared with inorganic electrolytes, PEs are soft and flexible and capable of maintaining good contact at interfaces. However, several technical barriers remain. On the Li-metal side, the interface between PEs and thin-Li and Li-free anodes is still at an early stage of investigation. Interface optimization using thin-Li and Li-free designs is crucial to reaching the DOE 500 Wh/kg target. On the cathode side, studies on the polymer/cathode interface are scarce. The interface resistance between polymer (catholyte) and cathode active material is not well understood. In addition, with a target voltage stability of 0-4.5 V versus Li/Li^+, a polymer with oxidative stability up to 4.5 V is needed. Fluorinated polyethers have the potential to form stable and low impedance interfaces at both the cathode side and the anode side. By systematically examining the effects of fluorine content, polymer chain length and structure, and plasticization on the interfacial resistance with the cathode and the anode, a balance between the desolvation kinetics of Li^+ and diffusion rate will be achieved to optimize the interface ion transport. A fundamental understanding of the origin of interfacial impedance with the cathode as well as Li-metal anode will be developed alongside the optimization process to generate design rules for polymers with optimized interfaces. The team will also develop a processing procedure to integrate a thin composite electrolyte that was previously developed into a full cell. The composite electrolyte features an interconnected ceramic structure with a thickness of 20 µm. It will be backfilled with the newly developed fluorinated PEs. The mechanical properties of the composite electrolytes will be optimized to accommodate roll-to-roll processing.

Out-Year Goals. In the second and third year of this project, the team will focus on optimizing the cathode/polymer as well as the Li-anode/polymer interface with maximized stability and minimized interfacial impedance. A fundamental understanding of parameters that determine the interfacial impedance and strategies to minimize the interfacial impedance will be developed. The fourth and fifth year of the project will be focused on integration of a thin composite electrolyte into a full cell to achieve high energy density, high rate, and long cycle life, as stated in the overall project objectives. Processing techniques and procedures for electrolyte integration will be investigated to achieve this goal.

Collaborations. Work is being conducted by B. Armstrong, S. Kalnaus, R. Sahore, X. Tang, A. Ullman, and X. C. Chen.

Milestones

1. Synthesize single-ion-conducting PEs with two ion concentrations. Quantify ionic conductivity and Li^+ transference number. (Q1, FY 2023; Completed)

2. Develop processing protocol to form interconnected composite electrolyte with a single-ion-conducting polymer. (Q2, FY 2023)
3. Use modeling to predict concentration gradient and limiting current density in the interconnected composite electrolyte. (Q3, FY 2023)
4. Quantify interfacial resistance and stability between model PE and electrodes. Gain understanding of interface chemical composition, and study lithium dendrite growth mechanism. (Q4, FY 2023)
5. Demonstrate performance with interconnected composite electrolyte. (FY 2023 Annual Milestone)

Progress Report

Due to the unsatisfactory ionic conductivity, Li^+ transference number, and oxidative stability of the fluorinated polyether PEs the team developed in FY 2022, this fiscal year they will modify Task 1 to synthesize a model single-ion-conducting PE. This quarter, they synthesized three single-ion-conducting PEs and evaluated their ionic conductivity and Li^+ transference number. The three electrolyte membranes are referred to as 60VEC-SIC, 80VEC-SIC, and 60EC-SIC, respectively. First, the monomers were mixed in an Ar-filled glovebox. Then, the polymerization reaction was carried out between two glass plates separated by cover glass slips with a thickness of 0.17 mm, on a hotplate inside the glovebox. After the desired reaction time, the membrane was peeled off from the glass plates and stored in the glovebox. Measurements were done without further treatments. Among the three membranes synthesized, 60VEC-SIC and 80VEC-SIC had the same monomers with different compositions; 60EC-SIC had a different monomer than 60VEC-SIC and 80VEC-SIC.

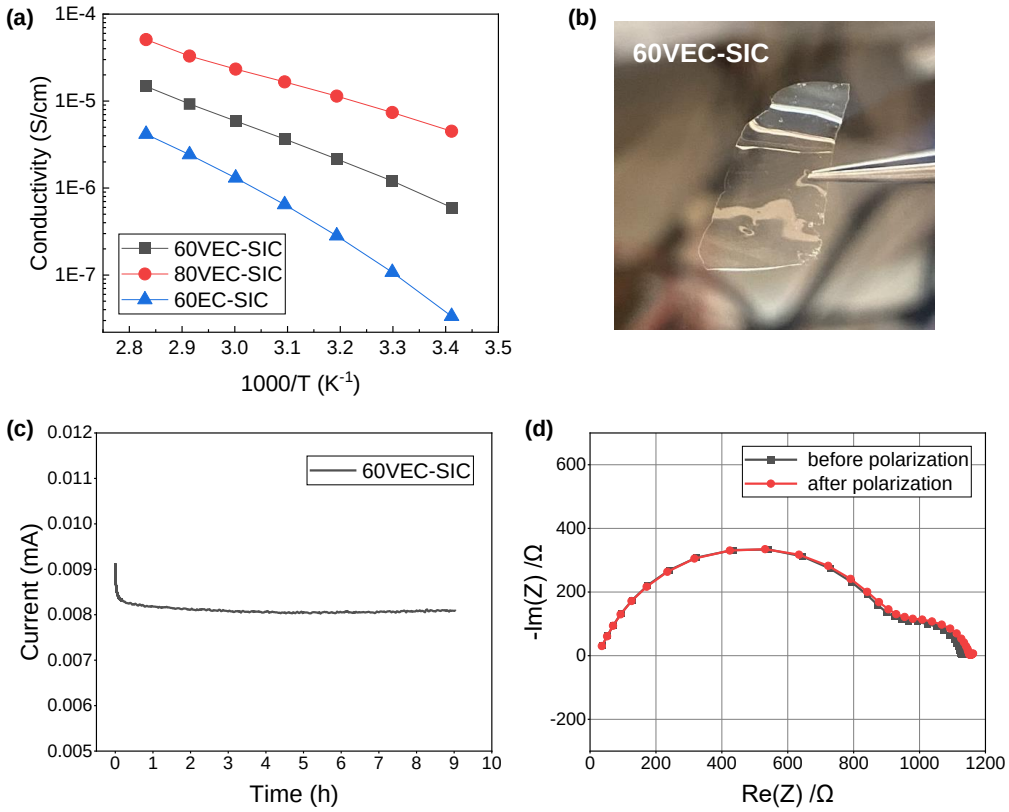

Figure 34. (a) Ionic conductivity of 60VEC-SIC, 80VEC-SIC, and 60EC-SIC as a function of inverse temperature. (b) Digital photograph of 60VEC-SIC membrane. (c-d) Li^+ transference number (t_+) measurement results of 60VEC-SIC at 70°C. (c) Chronoamperometry with an applied potential of 10 mV. (d) Impedance spectra before and after the applied potential.

Figure 34a shows the ionic conductivity of the three membranes. 60EC-SIC had much lower ionic conductivity than 60VEC-SIC (3.4×10^{-8} versus 6.0×10^{-7} S/cm at 20°C), indicating that it is advantageous to use the monomers in 60VEC-SIC. Comparing 60VEC-SIC and 80VEC-SIC, 80VEC-SIC had ~ 5× higher ionic conductivity. However, the high conductivity is the result of low degree of polymerization and large amounts of unreacted monomers. The resulting membrane was not a complete solid. 60VEC-SIC, on the other hand, appears to be a solid membrane with good flexibility and integrity (see photograph in Figure 34b).

The team measured the Li^+ transference number (t_+) of 60VEC-SIC in a lithium symmetric cell at 70°C using the Bruce-Vincent method. The results are shown in Figure 34c-d. In the chronoamperometry measurement, the steady-state current showed little decay from the initial value, indicating a very low concentration gradient has formed in the electrolyte. The t_+ obtained for 60VEC-SIC is 0.92. Further, the interfacial impedance with lithium is relatively small (290 $\Omega \cdot cm^2$), compared to the fluorinated polyether PE (~ 8000 $\Omega \cdot cm^2$) and crosslinked PEO-LiTFSI (350 $\Omega \cdot cm^2$) at the same temperature, as reported last quarter. Next quarter, the team will explore more compositions of the single-ion-conducting PEs to optimize ionic conductivity while maintaining film integrity. They will then focus on developing a processing protocol to form an interconnected composite electrolyte with a single-ion-conducting polymer.

Patents/Publications/Presentations

Presentations

- 242nd Electrochemical Society Meeting, Atlanta, Georgia (October 9–12, 2022): "A Three-Dimensionally Interconnected Composite Polymer Electrolyte for Solid-State Batteries"; R. Sahore, B. L. Armstrong, C. Liu, and X. Chen.
- University of Crete, Virtual Lecture (October 2022): "Ion Transport and Segmental Dynamics of Polymer Electrolytes at Interfaces"; X. C. Chen. Invited.

Task 1.13 – Ion Conductive High Li^+ Transference Number Polymer Composites for Solid-State Batteries
(Bryan McCloskey, University of California, Berkeley)

Project Objective. This project seeks to develop polymer-inorganic composites that have an optimal combination of conductivity, processability, and low interfacial resistance at both a Li-metal anode and a porous Li[Ni, Mn, Co]O_2 (NMC) cathode. To enable Li-metal anodes, mechanically rigid solid-state Li^+ conductors, such as $Li_7La_3Zr_2O_{12}$ (LLZO), $Li_{1+x}Al_xTi_{2-x}(PO_4)_3$ (LATP), and Li_2S-P_2S_5 (LPS) glasses, have been employed due to their high Li^+ ion conductivity and, when engineered to eliminate interfacial defects, appropriate stiffness to suppress Li-metal dendrite formation. However, for these materials to result in batteries that compete against current commercial cells in terms of energy density and cost per kWh, they would need to be manufactured at no more than 50-µm thickness and cost no more than $5 per square meter. These metrics are daunting for pure thin-film inorganic ion conductors, particularly when a porous, thick cathode also needs to be used to achieve competitive cell energy densities. To overcome these challenges, this project aims to develop polymer-inorganic composites, where high Li^+ transference number polymer electrolytes (PEs) serve as a binder for inorganic ion conducting particles.

Impact. By optimizing the composition of this composite electrolyte, the team aims to marry the processability and interfacial mechanical compliance of polymers with the impressive transport properties of inorganic composites, thereby enabling roll-to-roll manufacturing to allow thin (< 50 µm) layers of high-conductivity solid-state conductors to be cost-effectively incorporated into batteries.

Approach. The project approach relies on the following key steps: (1) using monomers with (trifluoromethanesulfon)imide anions appended to them, synthesize and characterize polyanionic PEs with high Li^+ transference number and conductivity; (2) through systematic material structure-property characterization, understand how to reduce interfacial ion transport impedance between inorganic ion conductors (specifically, thin-film inorganic conductors such as Li-La-Zr-Ta-O (LLZTO), LATP, and LPS) and high Li^+ transference number PEs; and (3) characterize electrode-polymer and electrode-inorganic conductor interfacial resistances at a Li-metal anode.

Out-Year Goals. The overall project goal is to develop an optimized polymer-inorganic Li-ion conductor with superior conductivity (> 1 mS/cm), thin-film processability, and low electrode interfacial impedance. Of particular interest in the out years is development of a process to fabricate thick, porous, and electrochemically stable NMC cathodes using the polymer-inorganic composite as both the binder and electrolyte. The team aims to integrate the optimized high-loading cathode with a 25-µm thin-film polymer-inorganic electrolyte to create an "anode-less" battery with 500 Wh/kg and 80% capacity retention after 300 cycles.

Collaborations. While this project has a single principal investigator (PI), B. McCloskey will leverage the collaborative battery research environment at Lawrence Berkeley National Laboratory (LBNL) and coordinate with other LBNL PIs in the BMR Program for materials and experimental development.

Milestones

1. Quantify carbonate content of LLZO powders procured from suppliers. (Q1, FY 2023; Completed)
2. Finalize optimization of polymer composition (monomer ratio, trace additive). *Go*: Select polymer composition with best transport and film-forming capabilities; *No-Go*: all others. (*Go/No-Go*: Q2, FY 2023; In progress)
3. Hire a summer intern to work on this project. (Q3, FY 2023; In progress)
4. Design and fabricate cell to characterize bi- and tri- layered electrolytes. (Q4, FY 2023; In progress)

Progress Report

To satisfy this quarter's milestone, the team confirmed that their titration mass spectrometry (TiMS) techniques can be used to quantify carbonates in LLZO powders. TiMS is a capability they have developed that relies on known acid-carbonate-CO_2 equilibria, where carbonate exposure to acid will result in quantitative (stoichiometric) CO_2 evolution from any carbonate present in a sample. CO_2 evolved can then be accurately quantified using their mass spectrometry setup. As-received LLZO powder from Ampcera was analyzed using TiMS, where it was found that roughly 5.5 wt% of the powder was Li_2CO_3. The origin of such a high carbonate content in nominally pure LLZO powder remains unknown; however, it is likely a result of the well-known reactivity of LLZO with CO_2 in the atmosphere. Caution should be used when synthesizing and handling LLZO powders to eliminate exposure to air. They are working on procedures to remove the carbonate from the particle surfaces, attempting to improve ion transport through the particle interface. Understanding the impact of carbonate impurities on ion transport through particle interfaces will be the focus of future studies.

Last quarter, the team synthesized methacrylate-based plasticizers to aid in the film formation of their poly((trifluoromethane)sulfonimide lithium methacrylate) (PLiMTFSI) films. This quarter, they moved their attention to using polyethylene glycol (PEG) of various molecular weights as a film-forming agent. Adding PEG to the PLiMTFSI polymers resulted in successful formation of free-standing films that they were able to electrochemically characterize. PEG content as low as 15 wt% relative to PLiMTFSI resulted in thin films that were sufficiently flexible to handle. As PEG content increased to over 50 wt%, the blend transitioned to the mechanical strength of a gel rather than a flexible film, so they used 15-50 wt% PEG in characterizing these blends.

There are two competing effects in these blends—adding more PEG results in lower Li-ion content that would decrease conductivity, while adding more PEG should improve both segmental motion and ion dissociation in blends, increasing conductivity. As a result, understanding the impact PEG content would have on overall conductivity was an important direction. The team presents film conductivity as a function of PEG wt% in Figure 35a. It is seen that that PEG content did not have a significant impact on the blend conductivity, likely due to the competing effects canceling each other out. They tested two PEG molecular weights (2 kDa and 20 kDa), which confirmed no significant molecular weight dependence. Temperature sweeps showed an Arrhenius-type dependence of conductivity on temperature, implying no phase change or change in crystallinity occurs over the temperature range tested (30-80°C); see Figure 35b.

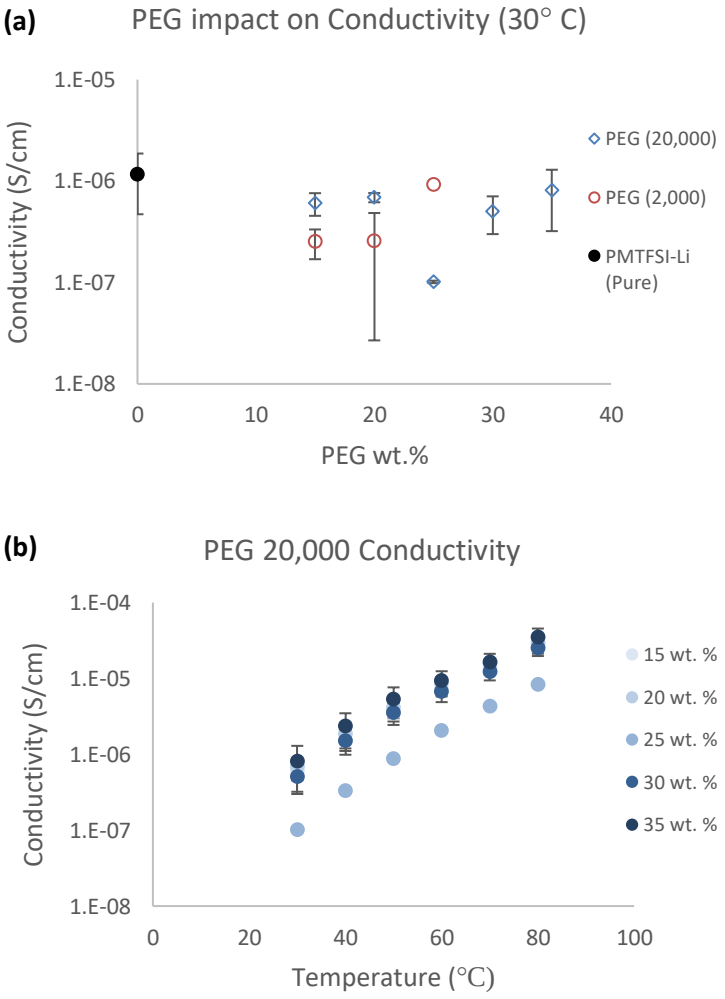

Figure 35. (a) Conductivity data at room temperature shows insignificant change to conductivity as PEG content increases. (b) Temperature sweeps of conductivity suggest no phase transition occurs in this range.

Once the team had a procedure allowing for consistent film formation, they began incorporating their ceramic (LLZO) into the polymer blends to create composite films. The literature suggests an initial increase in conductivity followed by a critical ceramic composition, after which adding more high-conductive ceramic actually decreases the sample's conductivity. Their most recent conductivity data are shown in Figure 36. It appears that there is a critical composition of 40 wt% LLZO where conductivity hits a maximum. They will continue to characterize additional LLZO compositions to get a better idea of the shape of this conductivity versus LLZO composition curve. These films are similar to the pure polymer films in that temperature sweeps revealed no phase transitions occurring in the same temperature range as above (30-80°C).

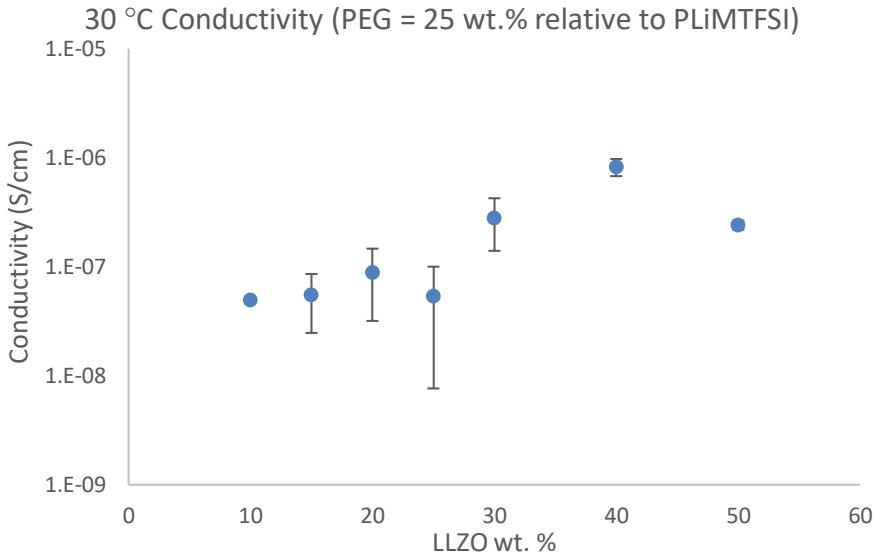

Figure 36. Current conductivity data over a range of LLZO content. 40 wt% appears to be the critical content after which conductivity begins to decrease. All data were collected at the same PEG content and molecular weight (20,000).

Next quarter, the team has several characterizations to implement. They plan to run conductivity measurements on different LLZO types (as-received, washed, air-exposed) after incorporating them into composite films to understand how carbonate at the particle interface impacts ion conductivity. They also plan to run differential scanning calorimetry measurements for their films to quantify how adding PEG and LLZO to PLiMTFSI impacts the glass transition temperature and, by extension, the segmental motion of the films.

Patents/Publications/Presentations

Presentation

- American Institute of Chemical Engineers (AIChE). Annual Conference, Phoenix, Arizona (November 22, 2022). Poster presentation.

Task 1.14 – Inorganic-Polymer-Composite Electrolyte with Architecture Design for Lithium-Metal Solid-State Batteries
(Enyuan Hu, Brookhaven National Laboratory)

Project Objective. This project targets the following goal: the composite electrolytes will be thin (< 100 μm) and have high Li-ion conductivity (≥ 10^{-3} S/cm at room temperature), low interfacial impedance, and desirable mechanical properties. When used in the solid electrolyte (SE) Li-metal battery, a current density > 1 mA/cm^2 and an areal capacity of 2-3 mAh/cm^2 can be achieved with more than 300 cycles. The constructed $LiNi_xMn_yCo_{1-x-y}O_2$ (NMC) / $LiCoO_2$ || composite electrolyte || Li-metal cell can be operated at up to 4.5 V versus Li^+/Li. The SE will also be compatible with high loading cathodes in achieving high energy density at the coin or pouch-cell level.

Impact. The results of this project will lead to advancement of solid-state batteries (SSBs), a beyond Li-ion battery option with better safety characteristics and higher energy density. The project will also provide valuable knowledge to U. S. industries in scaling up SSB production for vehicle applications, thus providing solutions to the clean energy strategy.

Approach. The project approaches are as follows: (1) design and synthesize polymer with an anion-tether strategy for high transference number, (2) through theories and experiments, design hierarchical inorganic electrolyte for suppressing lithium dendrite penetration, (3) optimize the composite electrolyte composition and structure, (4) use additives for Li-metal anode and NMC cathode protection, and (5) use synchrotron and cryogenic electron microscopy characterization to understand the bulk electrolyte and interphases.

Out-Year Goals. The out-year goals are to synthesize single ion conducting solid polymer electrolyte (SIC-SPE) with high transference number and conductivity; to design hierarchical inorganic electrolyte with high ionic conductivity and good mechanical/electrochemical stability; and to use synchrotron total scattering to study the structure of ceramic/polymer electrolyte.

Collaborations. The principal investigator (PI) will work closely with co-PIs H. Xin of University of California, Irvine, and X. Li of Harvard University.

Milestones

1. Optimize the composition of SIC-SPE to achieve interfacial resistance < 200 Ω cm^2, limiting current density > 1 mA/cm^2, and membrane thickness < 20 μm under stacking pressure < 0.1 MPa. (Q1, FY 2023; Completed)
2. Complete synchrotron-based characterization of polyvinylidene (di)fluoride polymer-based SE to understand its stability against lithium metal and NMC cathode. (Q2, FY 2023)
3. Increase cathode loading in NMC || hierarchical ceramic electrolyte || Li cells to 8 mg/cm^2 and test performance of cells using various electrolytes. (Q3, FY 2023)
4. Complete synchrotron-based *in situ* / *ex situ* studies of the ceramic-based solid-state cells to understand the stability of electrode-electrolyte interphases. (Q4, FY 2023)

Progress Report

This quarter, the first fiscal year milestone was successfully accomplished. Figure 37a shows an ultra-thin, SIC-SPE prepared by a modified ultraviolet polymerization approach. Typically, a 20-µm-thick Celgard® polypropylene (PP) separator was employed as the mechanical reinforcement to ensure compatibility with conventional battery fabrication technology. The SPE chemistry was also carefully tuned for better wettability toward the PP reinforcement as well as avoiding macroscopic phase separation. The achieved thickness of 20-µm is comparable to state-of-the-art liquid electrolytes and is significantly reduced compared with other reported solid-state electrolytes.[1] More excitingly, the team further demonstrate in Figure 37b that the 20-µm SIC-SPE still possesses excellent dendrite blocking capability, as evidenced by a high critical current density (CCD) of 2.4 mA/cm^2. For comparison, the CCD for inorganic SEs[2] is typically ~ 1 mA/cm^2. In addition, a low charge transfer resistance of 100 µ·cm^2 (Figure 37c) also suggests excellent interfacial stability with the Li^0 anode. Limiting current density (LCD) is the largest sustainable current density that can be drawn across the electrolyte. Above this value, the concentration of lithium salt near the cathode reaches zero and causes cell failure.[3] They investigated the LCD of the mixed ion conducting SPE (MIC-SPE, both the Li$^+$ and anion are mobile) by applying step-up current densities to a Li^0-Li^0 cell and then recording the time-dependence of cell potential (Figure 37d). At small current densities (< 1.2 mA/cm^2), the voltage gradually ramps up with charging time and then reaches a steady value. At a higher current density of 1.6 mA/cm^2, the potential first exponentially increases with time due to salt accumulation near the anode and depletion near the cathode. After reaching a maximum value, a voltage drop was observed, suggesting soft-shorting inside the battery. This trend became more obvious with increasing current densities; thus, the LCD of MIC-SPE was determined to be 1.2 mA/cm^2. For the SIC-SPE (Figure 37e), a higher LCD of 2 mA/cm^2 was observed due to the homogenous distribution of covalently tethered anion within the membrane matrix (that is, no concentration gradient). In Figure 37g-h, they further tested the durability of the 20-µm SIC-SPE. At 0.2 mA/cm^2, the Li^0-Li^0 cell shows a low overpotential of < 100 mV, and the cycling life is > 550 hours. The preliminary full-cell result using a Li-LiFePO$_4$ configuration shows a high initial capacity of 161 mAh/g, which is close to the theoretical value of 170 mAh/g. The capacity retention after 65 cycles is 96.3%, and the stable charge-discharge curves in Figure 37f suggest no short-circuiting occurred.

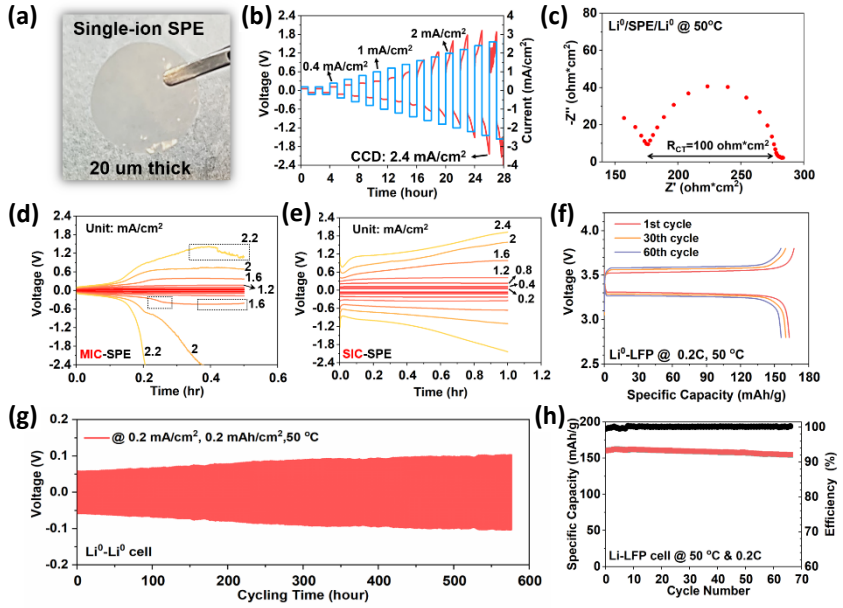

Figure 37. (a) Photograph of 20-µm-thick single ion conducting solid polymer electrolyte (SIC-SPE). (b) Critical current density of SIC-SPE measured at 50°C. (c) Electrochemical impedance spectroscopy plot of a Li^0/SIC-SPE/Li^0 cell showing the charge transfer resistance. (d-e) Limiting current density of (d) mixed ion conducting solid polymer electrolyte (MIC-SPE) and (e) SIC-SPE, measured at 50°C. (f) Selected charge-discharge curves of Li-LiFePO$_4$ cell. The cathode loading is 2.2 mg/cm^2. (g) Long-term cycling performance of SIC-SPE tested under Li^0-Li^0 symmetric cell configuration. (h) Cycling stability of Li-LiFePO$_4$ cell at 50°C and 0.2C.

References

[1] Wu, J., Yuan, L., Zhang, W., Li, Z., Xie, X., and Huang, Y. "Reducing the Thickness of Solid-State Electrolyte Membranes for High-Energy Lithium Batteries." *Energy & Environmental Science* 14, No. 1 (2021): 12–36.

[2] Han, F., A. S. Westover, J. Yue, X. Fan, F. Wang, M. Chi, D. N. Leonard, N. J. Dudney, H. Wang, and C. Wang. "High Electronic Conductivity as the Origin of Lithium Dendrite Formation within Solid Electrolytes." *Nature Energy* 4, No. 3 *(*2019): 187–196.
[3] Hoffman, Z. J., A. S. Ho, S. Chakraborty, and N. P. Balsara. "Limiting Current Density in Single-Ion-Conducting and Conventional Block Copolymer Electrolytes." *Journal of the Electrochemical Society* 169, No. 4 (2022): 169.

Patents/Publications/Presentations

The project has no patents, publications, or presentations to report this quarter.

Task 1.15 – Solid-State Batteries with Long Cycle Life and High Energy Density through Materials Design and Integration
(Haegyum Kim, Lawrence Berkeley National Laboratory)

Project Objective. This project aims to create solid-state Li-metal batteries (SSLMBs) with high specific energy, high energy density, and long cycle life using scalable processing techniques. The team will achieve this by addressing fundamental challenges associated with (1) interfacial reactivity, (2) Li-metal plating, and (3) cathode loading. Addressing these challenges supports the broader Vehicle Technologies Office goal of solid-state batteries (SSBs) with increased cycle life and energy density.

Impact. Ultimately, this project will develop an understanding of how to prevent interfacial reactions, make uniform Li-metal plating, and increase cathode loading significantly. The knowledge obtained from this project will be used to design SSLMBs with high specific energy of 500 Wh/kg, 80% capacity retention for at least 300 cycles, and critical current density (CCD) > 1 mA/cm^2.

Approach. This project addresses several fundamental challenges and makes the SSLMB competitive, surpassing the specific energy, energy density, and cycle life of Li-ion batteries:

- Create homogeneous lithium deposition on the anode without penetration of lithium metal through the separator to achieve high cycle life and high safety. The team will achieve this with the use of an active buffer layer (ABL) that combines active and inactive components to homogenize lithium plating and to keep the lithium plating potential away from the solid electrolyte (SE) separator.
- Limit chemical reactivity and mechanical decohesion between the SE, carbon, and cathode material in the composite cathode so that high cycle life can be achieved. The team will limit chemical reactivity by protecting the carbon from the SE, by using novel cathode coatings designed to be stable to high voltage and that do not react with the SE, by using novel solid halide catholyte conductors, and by using inorganic/organic solid composite electrolytes in the cathode.
- Achieve high volumetric loading of the active cathode material in the composite cathode to achieve high energy density and high specific energy. The team will achieve high volumetric cathode loading by creating thin highly porous conductor scaffolds that are infiltrated with cathode, by tailored particle size distributions of deformable lightweight conductors, and by the use of organic/inorganic hybrids.
- Create inexpensive materials and processes to fabricate SSBs so that they can be cost-competitive with Li-ion batteries. The team will create solution-processable organic/inorganic hybrids to be used as separators and to blend in the composite cathode; they will use inexpensive, scalable ceramics processing techniques to create high loading composite cathodes.

Out-Year Goals. The ultimate project goal is to develop SSLMBs that achieve high specific energy of 500 Wh/kg, 80% of capacity retention after 300 cycles, and > 1 mA/cm^2 of CCD.

Collaborations. The principal investigator's (PI's) team collaborates with the following co-PIs: H. Kim, V. Battaglia, G. Chen, M. M. Doeff, G. Liu, M. Scott, M. Tucker, and J. Urban, all at Lawrence Berkeley National Laboratory (LBNL).

Milestones

1. Li_6PS_5Cl (LPSCl) polymer composite glass with ionic conductivity of 0.1-1 mS/cm. (Q1, FY 2023; *Go/No-Go*: Completed)
2. Demonstrate 100 cycles without noticeable lithium dendrite growth. (Q2, FY 2023; In progress)

3. 1st discharge capacity in cell with graphite or indium anode > 90% of liquid cell. (Q3, FY 2023; In progress)
4. Scaffold-less cathode design with thin, dense Li-La-Zr-O (LLZO) separator. Stop if too fragile or scale-up too difficult. (Q4, FY 2023; *Go/No-Go:* In progress)

Progress Report

Buffer Layers to Stabilize the Li/SE Interface and Create Uniform Lithium Plating (H. Kim, G. Ceder, V. Battaglia, M. Scott)

The broad project goal is to improve anode performance of SSLMBs by incorporating an ABL that prevents formation/propagation of Li-metal dendrites. The team's effort is aimed at expanding previous work by Samsung on understanding the mechanism by which the ABL functions and thereby optimizing performance through improvements in composition and fabrication processes. The ABL in the Samsung paper is comprised of a mixture of carbon black and silver nanoparticles bound together with polyvinylidene difluoride binder. LBNL is looking to replace the silver with less expensive metals; however, the team first aspires to reproduce the Samsung work, as not all fabrication details were provided in the paper. They have successfully cast and calendered an ABL on stainless steel (hereafter referred to as SUS) to a thickness of 10 µm. Figure 38a shows a picture of this casted ABL electrode after calendering. While the team has successfully made a slurry, cast it, and calendered it to the targeted thickness, scanning electron microscopy (SEM) images (Figure 38b) of the ABL surface show that there are 1-µm and greater-sized clumps of silver nanoparticles seen as lighter portions of the images. The team employed energy dispersive X-ray spectroscopy (EDS, Figure 38c) to confirm that these lighter sections are clusters of silver. A cross-sectional SEM further confirms that these clumps are present through the depth of the ABL (Figure 38d). Since they do not have a clear understanding of how the ABL prevents dendrite growth, it is unclear whether this clustering of silver will be beneficial. The team suspects that a more homogeneous distribution of silver particles would be preferable. Thus, they will continue to optimize their fabrication process with silver particles before expanding to other metals such as magnesium.

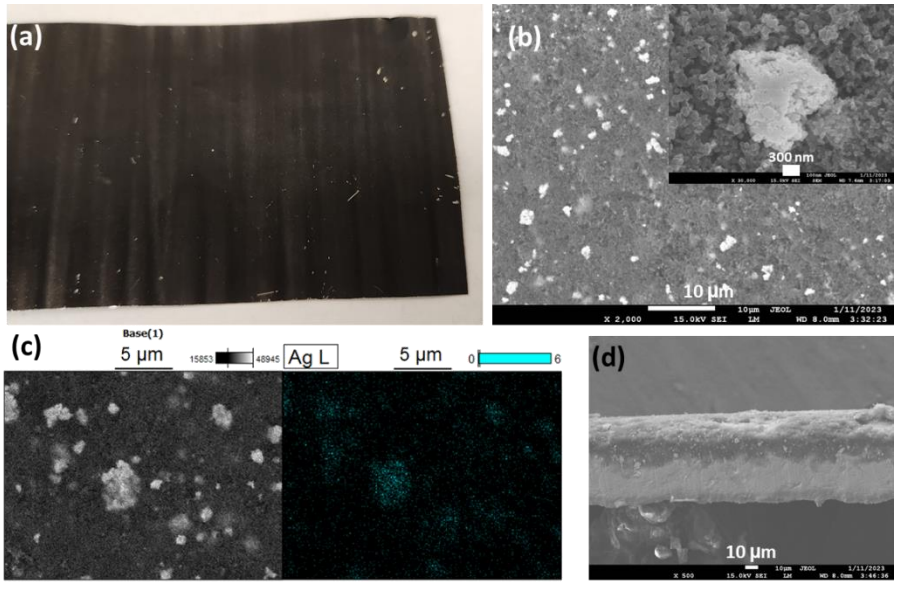

Figure 38. (a) Photograph of active buffer layer (ABL) after calendering. The ABL composition is 38:16:46 C:Ag:PVDF by weight. The vertical lines seen in the photo are a result of the calendering process. (b) Scanning electron microscopy (SEM) image of ABL surface showing silver clusters as lighter spots. Inset: SEM image of ABL surface showing a single silver cluster as the lighter portion in the center. (c) SEM (left) and corresponding energy dispersive X-ray spectroscopy (right) images of ABL surface showing the location of silver in the film. (d) Cross-sectional SEM image of the ABL (darker top layer) on the stainless–steel current collector (lighter bottom layer). Note that because of the perspective, part of the surface is visible in addition to the cross-section, which makes the ABL layer look thicker than it is. The thickness of ~ 10 µm was determined by measurement with a micrometer.

The LBNL team also has been testing several metallic components (that is, silver, tin, magnesium, and silicon nanoparticles) to investigate what materials can replace expensive silver in the ABL and to understand what properties enable uniform Li-metal plating and prevent dendritic Li-metal formation. In their experiments, all metallic components were mixed with carbon (75 wt% of carbon and 25 wt% of metallic component) by dry ball milling. ABL electrodes were prepared by mixing with polytetrafluoroethylene binder (10 wt%), and thin films (~ 30 μm) were fabricated. To test the electrochemical performance of ABLs, the team assembled a symmetric cell, as shown in Figure 39a. The LPSCl SE and ABL were pelletized at 300 MPa. Then, lithium metal was attached on both sides of the stacked pellet and pressed at 20 MPa. Figure 39b-c shows the charge and discharge profiles of the SSBs using amorphous carbon ABL and amorphous C/Mg ABL, respectively. The charge-discharge experiments were conducted at a constant current density of 0.17 mA/cm^2 (2 hours charge and 2 hours discharge for each cycle) at 50°C. Both amorphous carbon ABL and amorphous C/Mg ABL exhibit low overpotentials < 0.02 V without noticeable short-circuit behaviors over 80 cycles and 200 cycles, respectively. They are testing other metallic components including tin and silicon nanoparticles.

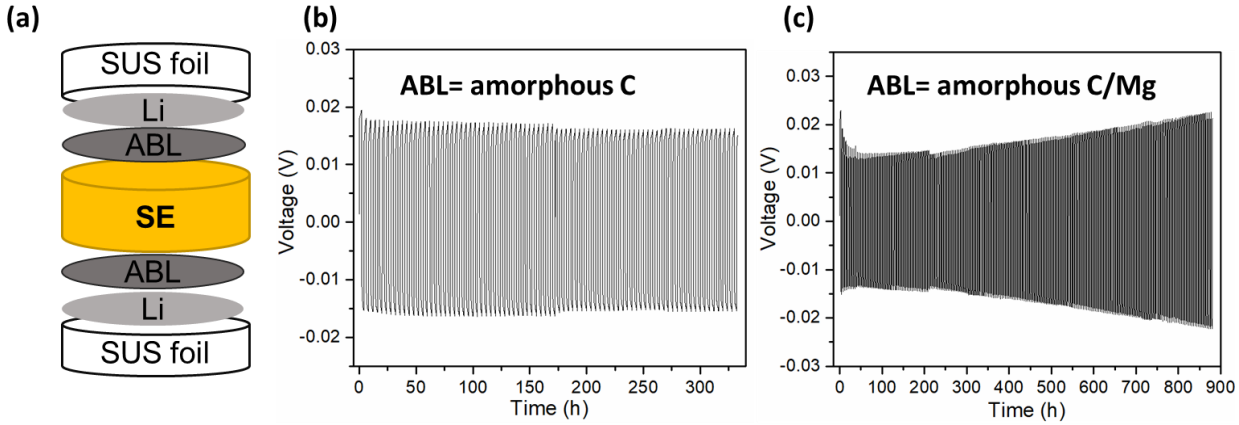

Figure 39. (a) Schematic of stacked pellet cell. Charge-discharge profiles of (b) amorphous carbon active buffer layer (ABL) and (c) amorphous C/Mg ABL.

Composite Cathode: High Voltage Stability and Chemical/Mechanical Degradation Issue (G. Chen, H. Kim, J. Urban, G. Ceder, M. Scott)

The team is searching the chemical space of amorphous and crystalline halides for novel lithium superionic conductors using a combined theoretical and experimental approach. Lithium halide superionic conductors have recently shown great promise to be used as a catholyte in an all-solid-state battery (ASSB). For example, they have good oxidation stability, soft mechanical response, and high ionic conductivity. These materials, when combined with existing oxide/sulfide-based SE separators, can solve the contact issue with Li-metal anode and help realize a high-performing ASSB. An interesting amorphous halide SE, containing LiCl and GaF_3, was recently synthesized by mechanically ball milling the two salts at room temperature by Samsung.[1] The resulting amorphous material was found to have a clay-like soft mechanical response with a storage and loss moduli < 1 MPa, and a high room-temperature ionic conductivity of 3.6 mS/cm. The objective is to understand how the mixing of two hard salts can create a clay-like soft matter with such high ionic conductivity. The team has investigated the microscopic features, which are responsible for soft-mechanical response and high ionic conductivity in the Li-Cl-Ga-F system. The understanding developed here will be used to create a design strategy to predict other similar clay-like soft superionic conductors.

To begin, the team followed a previously reported synthesis technique to create the amorphous compound. Figure 40a shows the picture of the resulting experimentally synthesized $LiCl+2GaF_3$ compound. They found that the material is soft like clay and can be deformed into different shapes. Symmetric cells ($SUS/LiCl+2GaF_3/SUS$) were fabricated to evaluate ionic conductivity. The Nyquist plot at room temperature (T = 25°C) from the electrochemical impedance spectroscopy (EIS) is plotted in Figure 40b. They found that the ionic conductivity is 2.9 mS/cm. This value is close to that reported in prior work.

After confirming the synthesis and high ionic conductivity of the material, the team next wanted to understand why this material shows a soft mechanical response. Since the material is amorphous, modeling its properties with conventional density functional theory based *ab initio* molecular dynamics (AIMD) is not tractable. They thus employed a multiscale theoretical approach to study the properties. They first trained an interatomic potential energy model of the Li-Cl-Ga-F chemical system using deep learning. The training was performed on over 1 million AIMD trajectories. The potential energy model was subsequently used to construct a representative amorphous structure with more than 10,000 atoms. Figure 41a shows the constructed amorphous structure. The structure was equilibrated in a classical molecular dynamics (MD) simulation at a high temperature of T = 850 K for t = 20 ps to allow anion exchange and enhanced mixing. Thermodynamically, it is expected that when LiCl and GaF_3 react, the thermodynamic driving force is maximum for the reaction: $2LiCl + 3GaF_3 \rightarrow 2LiF + 3GaCl_3$. They found as expected that anion exchange occurs and that $GaCl_3$-like units are formed.

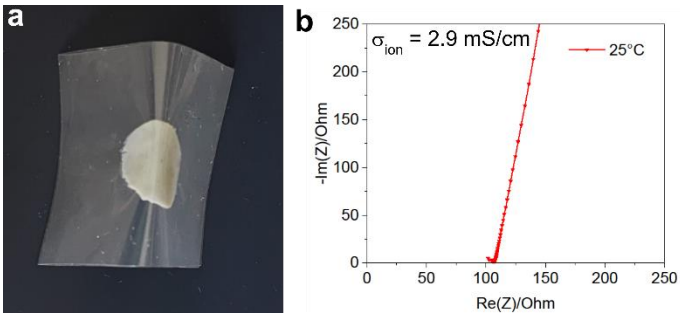

Figure 40. (a) Picture of synthesized $LiCl+2GaF_3$ material with clay-like mechanical property. The material can be deformed into different shapes. (b) Nyquist plot.

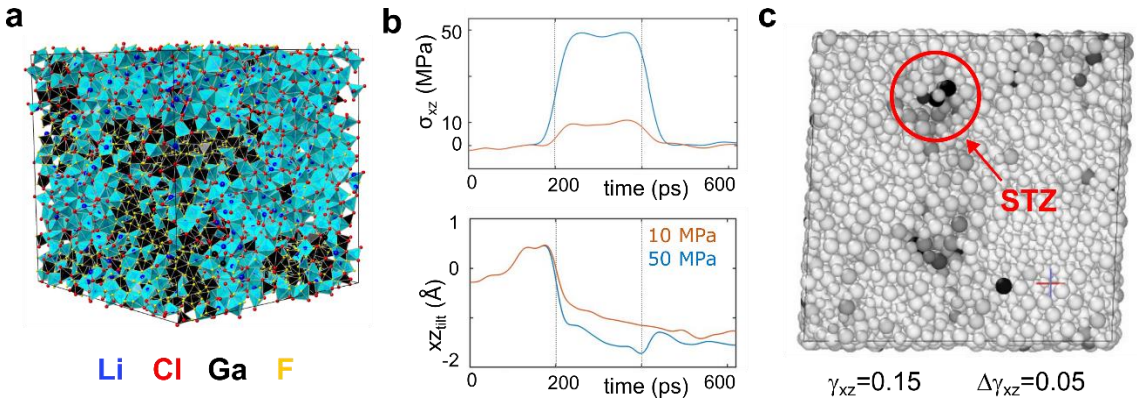

Figure 41. (a) Amorphous Li-Cl-Ga-F structure constructed for theoretical modeling. (b) Evolution of the applied external shear stress (σ_{xz}) and xz-tilt distance of the amorphous structure as a function of time in the classical molecular dynamics simulation. The xz-tilt distance is representative of shear strain. A maximum of 10 MPa and 50 MPa of external periodic stress was applied to the amorphous structure to study its mechanical response. (c) Snapshot of the amorphous structure at an external shear strain γ_{xz} = 0.15. The grayscale color (white-low and black-high) represents value of non-affine displacement, at an interval of $\Delta\gamma_{xz}$ = 0.05. The shear transformation zone (STZ) formed is circled in red.

The team next explored the mechanical properties of the amorphous structure by performing classical MD simulations with the trained potential energy model. To understand if the structure is mechanically soft as in experiments, they explored the shear response of the amorphous structure under a low periodic external stress of 10 Mpa and 50 MPa. Figure 41b shows the time evolution of the periodic external shear stress and the resulting change in xz-tilt distance, which is representative of shear strain. The xz-tilt distance does not revert to its original value even when the external stress is removed. This permanent deformation corresponds to plastic deformation behavior. It is interesting to see plastic behavior at low stresses of 10 MPa, which is in agreement with the experimental observations. The team then studied the microscopic features that are responsible for such soft-plastic behavior. It is widely known that plastic behavior in amorphous materials occurs through the formation of shear transformation zones (STZ). STZs are usually a collection of a few molecular units that get activated during onset of plastic deformation. Non-affine displacement, which is a measure of deviation from elastic deformation, is routinely used to track plastic behavior. Figure 41c shows a snapshot of the amorphous structure at a shear strain of 0.15, where the color represents the value of non-affine

displacement. The dark regions are the formed STZs. On closely looking at the atomic structure, they found that these STZs are $GaCl_3$-like molecular units. $GaCl_3$ is a molecular solid and, in comparison with LiCl and GaF_3, is very soft. $GaCl_3$ bulk solid is an aggregate of Ga_2Cl_6 molecules connected by a weak van der Waals bond. Their results show that the formation of these weakly bonded molecular solids is linked to the clay-like soft mechanical response. These molecular solids formed during anion exchange ($2LiCl + 3GaF_3 \rightarrow 2LiF + 3GaCl_3$) get activated at low stresses to form STZs and are responsible for the soft plastic behavior. Even in natural clay, the soft water molecules lead to the soft plastic response, and the mechanisms for the soft mechanical behavior in both these systems are very similar. Since the formation of molecular solids is responsible for clay-like mechanical response, finding other salt combinations where there is a maximum thermodynamic driving force for molecular solid formation might also show similar behavior. Apart from thermodynamics, the kinetics of the anion exchange are also important; for example, a complete anion exchange will lead to phase separation of molecular solid units and will not lead to clay-like material. In subsequent quarters, the team will explore the detailed role of synthesis kinetics on the properties of these systems.

High-Loading Composite Cathodes (M. Tucker, M. Doeff, G. Chen, G. Ceder)

This effort aims to achieve high energy density and specific energy by developing thick cathode using scalable processing techniques. In previous work, the LBNL team developed thin LLZO SE. This quarter, they developed and installed the fixture for the mechanical testing to evaluate the mechanical properties of the thin LLZO SE. In this experiment, they will use the 3-point bending test, one of the representative methods for measuring the maximum force a specimen can withstand without fracturing (Figure 42a). The fixture for this 3-point bending test was installed in a dynamic mechanical analyzer as shown in Figure 42b. Rectangular-shaped thin LLZO (thickness of 100 μm) electrolytes for this test were fabricated through tape casting, as shown in Figure 42c. The test will be carried out with several repetitions to obtain reliable data in following quarters.

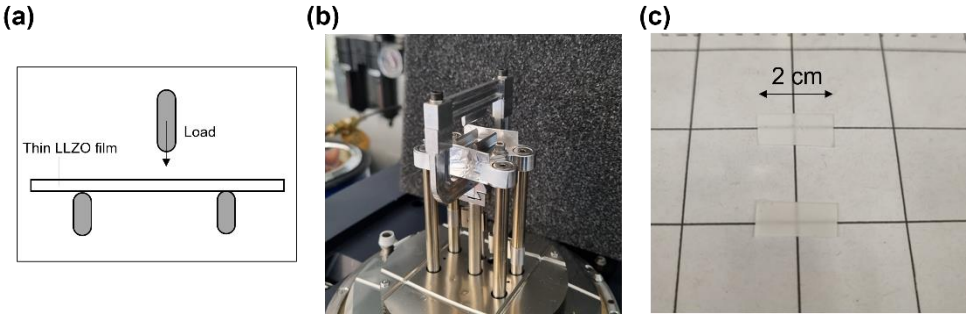

Figure 42. Mechanical property testing for the thin LLZO electrolyte. (a) Schematic diagram of 3-point bending test. (b) 3-point bending test fixture installed in a dynamic mechanical analyzer. (c) Prepared rectangular-shaped thin LLZO electrolytes.

The team also investigated two succinonitrile (SN) – lithium salt mixtures for use as catholytes in LLZO-based ASSBs. The mixtures were prepared as shown in Figure 43a: LiTFSI+SN (5 mol%), LiBOB+SN (3 mol%). The SN and lithium salts were mixed at 80°C in the glove box. The mixtures then were cooled to room temperature. The mixtures are in a plastic crystal phase, as shown in Figure 43b. Then, they evaluated the required properties of the catholyte, including ionic conductivity, oxidative stability, and compatibility with LLZO. The ionic conductivities of the mixtures were evaluated in symmetric cells (SUS/SN+Li salts mixture/SUS) using EIS. Figure 44a shows the Nyquist plots of the two mixtures. The LiBOB+SN exhibits a distinguishably higher impedance than LiTFSI+SN, and its conductivity was 5.58×10^{-5} S/cm, which is ~ 100 × lower than that of LiTFSI+SN (3.46×10^{-3} S/cm).

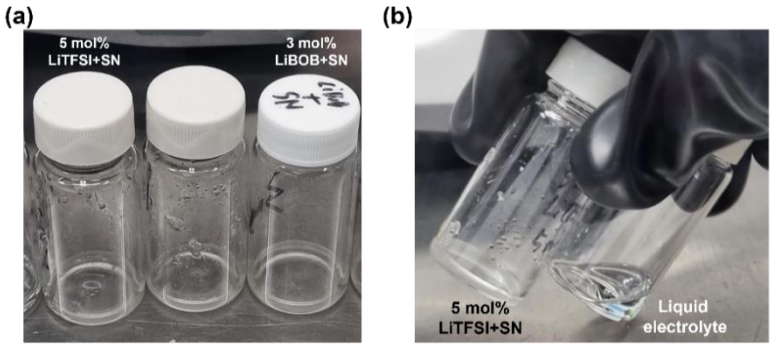

Figure 43. Prepared SN+Li salt mixtures. (a) SN+Li salts after cooling to room temperature. (b) Tilted vials containing SN+Li salt and typical liquid electrolyte.

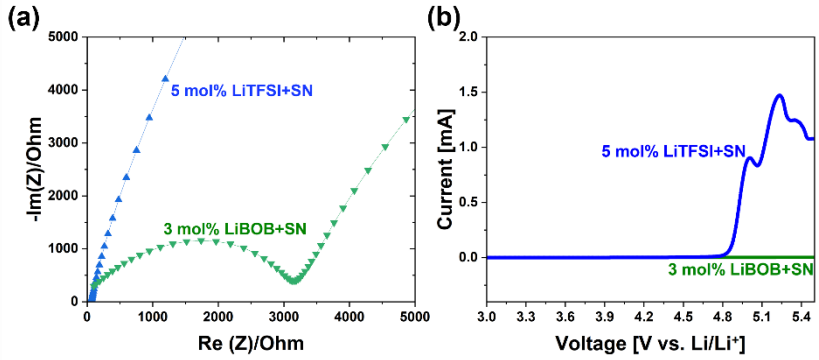

Figure 44. Ionic conductivity and oxidation stability test. (a) Nyquist plots of SN+Li salts mixtures. (b) Linear sweep voltammetry of the SN+Li salts mixtures in the range of 3.0 ~ 5.5 V versus Li/Li$^+$.

The oxidation stability was tested in a coin cell (SUS/SN+Li salts mixture/Li metal) using the linear sweep voltammetry (LSV) method in Figure 44b. The scanned voltage range was 3.0~5.5 V versus Li/Li$^+$ with a scanning speed of 1 mV/sec. For the LSV plot of LiTFSI+SN (Figure 44b), little current was detected (< 10 μA) before ~ 4.7 V, which implies that it is stable to oxidation up to ~ 4.7 V. The plot also showed a noticeable current flowing at > 4.7 V, suggesting that the LiTFSI+SN can be oxidized at such a high voltage (> 4.7 V). In contrast, the LiBOB+SN exhibited negligible current flowing until the end of the measurement (5.5 V). Throughout this oxidation stability test, the team observed that both LiTFSI+SN and LiBOB+SN have excellent oxidation stability (> 4.7 V versus Li/Li$^+$), indicating compatibility with high-potential cathode active materials.

LLZO-based all-solid-state cell testing with the LiTFSI+SN mixture was conducted, as shown in Figure 45. The cell consists of $LiNi_{1/3}Mn_{1/3}Co_{1/3}$ (NMC-111) as a cathode active material (CAM), 5 mol% SN+LiTFSI as a catholyte, LLZO pellet as SE, and lithium metal as an anode. The testing was carried out at 0.1 C-rate and 25°C. Figure 45a shows the voltage profile of the cell during cycling. The cell has cycled for the 15th cycle with a stable voltage profile without voltage fluctuation or short circuits. This implies that the SN+LiTFSI worked properly as a catholyte in the cell. However, it is notable that the cell shows high polarization. This high polarization is attributable to some possible reasons, including thick LLZO, high interface resistance, and chemical compatibility issues of the SN+LiTFSI with CAM or LLZO. Because of this high polarization, the cell reached a voltage cut-off earlier than typical liquid cells, resulting in a lower capacity. The typical cell shows ~ 150 mAh/g, but their all-solid-state cell (Figure 45) showed ~ 90 mAh/g. The first discharge capacity was 92 mAh/g, and the 15th cycle discharge capacity was 81.7 mAh/g. This capacity fading was also faster than typical liquid cells, and the reasons will be investigated.

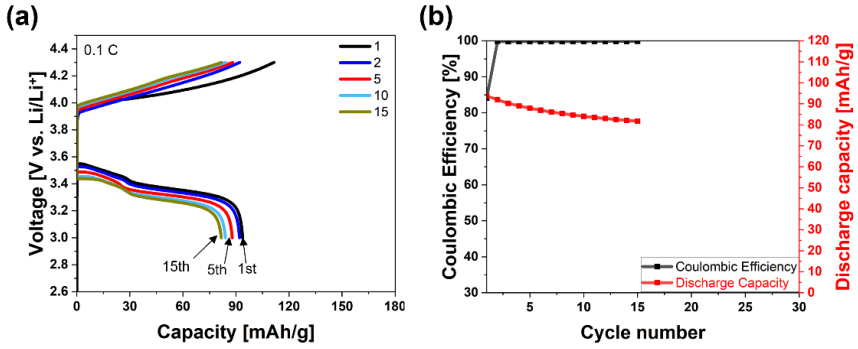

Figure 45. (a) Charge and discharge voltage profile. (b) Cycle retention of the all-solid-sate cell with SN+LiTFSI as catholyte.

In the following quarters, the team will conduct mechanical testing on the prepared thin LLZO electrolytes and fabricate strong thin LLZO electrolytes with strategies to enhance mechanical properties (for example, adding fibers). All-solid-state cell tests will be expanded to other SN+Li salts mixtures.

Glass Composite SE by Low-Temperature Solution-Phase Synthesis (G. Liu)

This work aims to develop a sulfide glass separator that is both thin and resistant to lithium dendrite penetration from the Li-metal anode side. Solution processable separators would be more easily integrated with SSBs through low-cost processing. In addition, solution processable SEs could be directly integrated with cathode materials to form a composite cathode through conventional slurry coating. The team's objective is therefore to develop the processes to synthesize hybrid SEs from inorganic conductors and polymer through solution-based processes, combining high ionic conductivities (>10^{-3} S cm^{-1}) and high fracture toughness (> 10 MPa $m^{1/2}$). This quarter, the team investigated the properties of LPSCl – polyphenylene oxide (PPO) composites prepared by the solution-precipitation method. Owing to the higher thermal stability of PPO than that of the poly(ethylene oxide) (PEO), they expected to achieve a higher crystallinity of LPSCl by allowing a higher temperature (400°C) for an annealing process. The observed morphology of the LPSCl-PPO composite via SEM analysis is quite similar to the LPSCl-PEO composites; their crystal grain size ranges from 1 µm to 10 µm, and the polymer phase is not distinguishable in SEM images. Thus, they performed elemental mapping using transmission electron microscopy – EDS to monitor the polymer distribution in the composites. Figure 46a-b shows a good distribution of the oxygen element that represents the polymer phase and the phosphorus element that belongs to the LPSCl phase, regardless of the PPO content. There are also small portions of the free polymer phase observed in the image, which is sometimes seen in high polymer-loaded composites (both PEO and PPO). As a downside of this method, they found the segregated chlorine region, expected to be LiCl, indicating LPSCl decomposition during the process (denoted by blue arrows in Figures 46a-b). The decomposition could be originated from the dissolution of LPSCl in ethanol, where some of the crystals are completely dissolved and cannot reform back to the same structure. This effect can be minimized by the reduction of ethanol exposure time as mentioned in the earlier quarterly report.

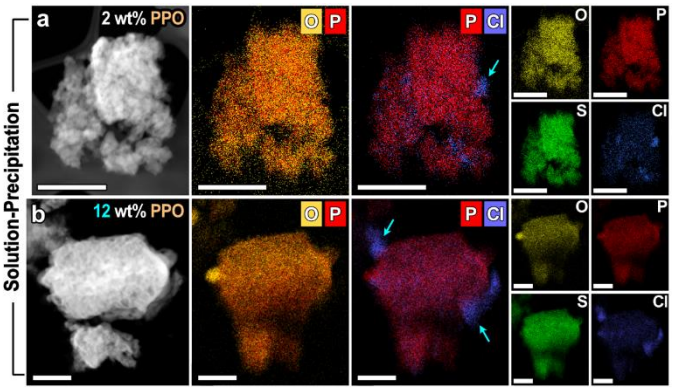

Figure 46. Chemical and mechanical evaluations of LPSCl-PPO composite. (a-b) Elemental mappings (O, P, S, Cl) in LPSCl-PPO composites with different polymer content: (a) 2 wt% and (b) 12 wt%. Note that the observed LiCl phase regions are denoted by blue arrows.

The effects of polymer species and their content on the Li-conductivity were evaluated using EIS. The result summary is shown in Figure 47. The conductivity decreases when the PEO content increases for both dispersion and solution-precipitation methods. Note that the solution-precipitation method shows a more significant decrease in conductivity as the polymer content increases (10^{-2} mS/cm versus 1 mS/cm of pristine LPSCl). The low conductivity could be originating from the LPSCl becoming smaller crystals or an amorphous phase after the solution-precipitation reaction. Therefore, thermal treatment at a higher temperature is required to improve the crystallinity of LPSCl SEs. The conductivities of LPSCl-PPO composites after 400°C treatment are all between 0.1 mS/cm and 1 mS/cm. For LPSCl-PPO composites, the mechanical mix and dispersion samples displayed similar conductivity and trends in which the increase of polymer content lowers the conductivity of the materials. Interestingly, the conductivity of PPO composites from solution-precipitation exhibits a more negligible effect on the polymer content (from 2 wt% to 12 wt%). This could be due to the well-distributed polymer in which there is no large polymer domain to block ion-conductive channels.

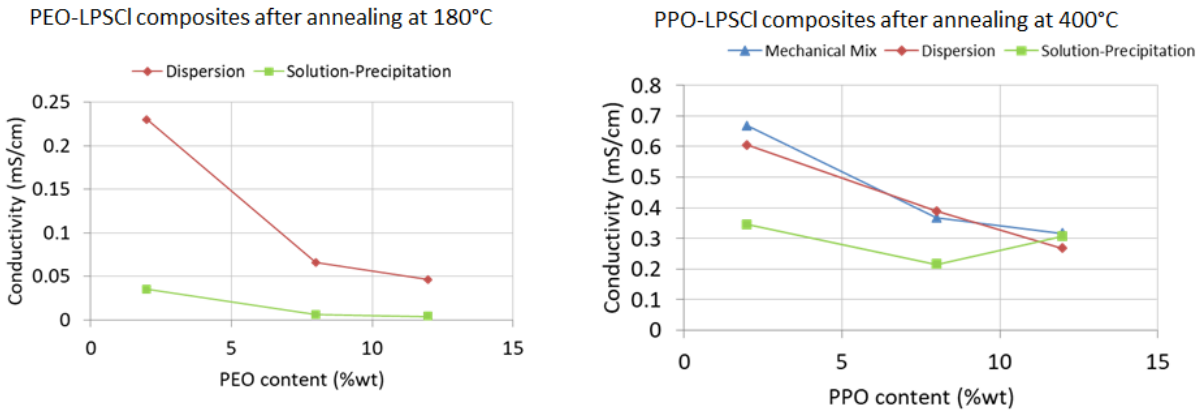

Figure 47. Conductivity of PEO-LPSCl composites after 180°C annealing (left) and PPO-LPSCl composites after 400°C (right).

Reference

[1] Jung, S-K.,* H. Gwon,* G. Yoon, L. J. Miara, V. Lacivita, and J-S. Kim. "Pliable Lithium Superionic Conductor for All-Solid-State Batteries." *ACS Energy Letters* 6, No. 5 (2021): 2006-2015 (Letter). https://doi.org/10.1021/acsenergylett.1c00545.

Patents/Publications/Presentations

Publication

- Jonson, R., V. Battaglia, and M. Tucker. "Lithium Batteries with Small-Molecule Quinone Cathode Enabled by Lithium Garnet Separators." ACS *Applied Energy Materials* 6, No. 2 (2023): 745–752. https://doi.org/10.1021/acsaem.2c02932.

Presentation

- 242nd Electrochemical Society Meeting, Atlanta, Georgia (October 2022): "The Impact of Residual Solvent on the Performance of Catholyte for Solid-State Batteries"; F. Shen, R. Jonson, and M. Tucker.

Task 1.16 – Low-Pressure All-Solid-State Cells (Anthony Burrell, National Renewable Energy Laboratory)

Project Objective. The goal of this project is to develop all-solid-state batteries (ASSBs) using four classes of solid-state electrolytes, and/or electrode modifiers, that can be used to achieve the final 500 Wh/kg cell target. These materials will be down selected using full-cell testing and advanced characterization to achieve cell targets at cell pressures less than 100 psi.

Impact. Many factors limit ASSB performance, and this project seeks to address the interface stability of both the lithium interface and the high-voltage cathode. The combination of multiple ionic conductors coupled is specifically targeted to allow solution processing, and low-pressure cell outcome will enable lower cost deployment of solid-state cells in automotive applications.

Approach. To achieve the goal of low-pressure ASSBs, the team is utilizing three classes of solid ion conductors, sulfide materials, melt-processable lithium carboranes, and multinary metal halides. These materials can be chemically modified to optimize ionic conductivity and voltage stability in single conductor modes or in combinations to effect interface modification for full-cell development. Specifically, the use of flexible ionic conductors at the cathode interface will enable the mechanical effects of cathode expansion and contraction to be mitigated. In combination with the materials discovery work, the project has an extensive characterization team to help determine the impacts of interface, chemical, electrochemical, and mechanical factors on system performance. Full-cell assembly and development, targeting approaches that are readily scalable and compatible with roll-to-roll process, will drive the materials innovation and development.

Out-Year Goals. The out-year goal is demonstration of 2 Ah cells that achieve 500 Wh/kg and lifetimes exceeding 300 cycles at functional pressures below 100 psi.

Collaborations. There is a joint effort for this project between National Renewable Energy Laboratory, M. Toney at the University of Colorado, and A. Maughan at the Colorado School of Mines.

Milestones

1. Determine the conductivity of high purified lithium carbaboranes. (Q1, FY 2023)
2. Demonstrate composite electrolytes in an electrochemical cell and determine compatibilities and interfacial resistance issues. (Q2, FY 2023)
3. Determine pressure-performance dependance of new sulfur-based electrolytes. (Q3, FY 2023)
4. Demonstrate 80% utilization of a high nickel cathode in a full-cell configuration. (Q4, FY 2023)

Progress Report

Enabling Low Pressure Cell Testing

An updated high-pressure test rig for cycle testing ASSBs has been developed, constructed, and tested (Figure 48). The updated rig, designed for low- to medium-pressure cycling (5-100 MPa) adapted a previous cell design with modified electrical isolation that improves pressure uniformity/better electrical connections. This was achieved through installing insulating washers and bushings on the top pressure plate, thus electrically isolating the top and bottom halves of the pressure cell. This conferred several benefits. One of these is eliminating the need for insulating PEEK plastic top and bottom caps for the application of pressure. The stainless-steel plates are now in direct contact with the coin cell, yielding a more homogenous pressure distribution. Another benefit is that the updated design eliminates the need for comparatively complex electrical attachment to the cell terminals using metal foils, wires, or soldering. Faster electrical connection is achieved through banana clips or screw terminals on either half of the cell. Cycling pressure is set through the conventional method of compressing springs by a predetermined distance.

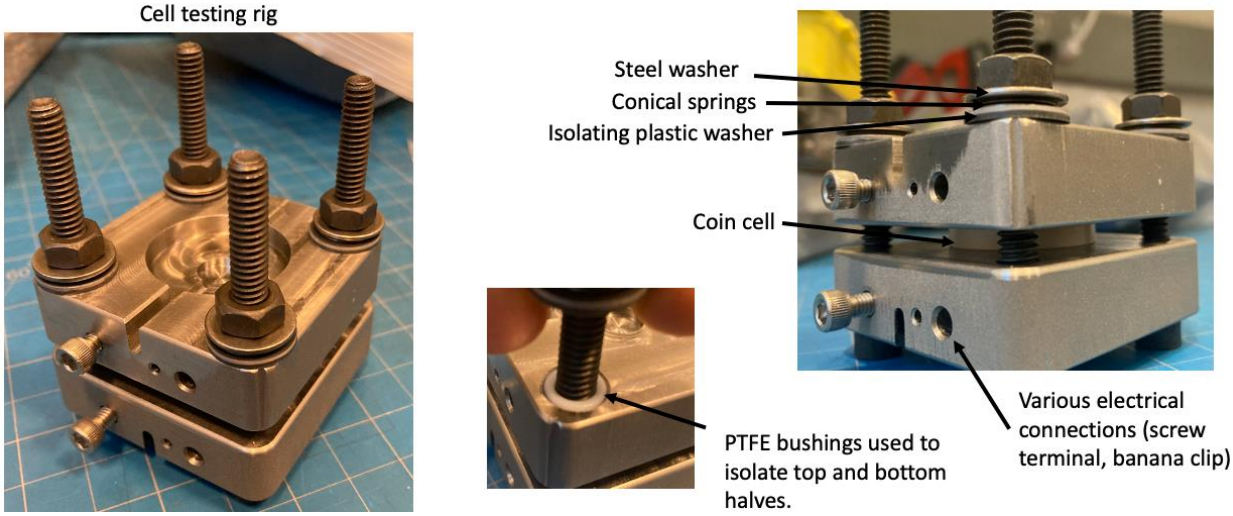

Figure 48. Images of the updated high-pressure cell testing rig. The various modifications and additions are annotated above.

During previous quarters, the team developed methods to coat a sulfide-based argyrodite Li_6PS_5Cl (LPSCl) solid electrolyte powder with a novel ionically conductive sulfur polymer (polyS) that can be solubilized in non-polar solvents, that is chemically compatible with LPSCl, and that improves ionic conductivity at low pressures. In the last quarter of FY 2022, the team assembled cathodes using a polyS binder and lithium cobalt oxide (LCO). Next, they assembled these cathodes into cells with In-metal anodes.

This quarter, the team expanded these efforts by designing and fabricating a new high-pressure solid-state cell system that is an evolution of the state-of-the-art methods that have been described previously in the literature.[1-3] This cell design also concurrently simplifies the methods required to conduct the pressure-dependent studies that they have reported and builds on previous success designing and utilizing low-pressure solid-state battery systems. Figure 49 shows optical images of the new cell design. Specifically, Figure 49a shows the disassembled parts of the system. Figure 49b shows the assembled cell system mounted in a hydraulic press for initial cell lamination at a pressure of 760 MPa. Figure 49c shows the final cell assembly ready for cycling at a pressure of 1.6 MPa. Figure 49d-e shows voltage profiles and cycling data for the LCO cathode (3 wt% polyS, 27 wt% LPSCl, 60 wt% LCO, 10 wt% vapor-grown carbon fibers) and graphite anode (3 wt% polyS, 27 wt% LPSCl, 60 wt% graphite, 10 wt% vapor-grown carbon fibers) cell. Both electrodes utilize polyS-coated LPSCl to achieve effective ionic conductivity at low cell stack pressures. This full cell was

assembled using the new system and was cycled at 1.6 MPa at a temperature of 70°C. These results further demonstrate that it is possible to fabricate a low-pressure, metal-anode, solid-state cell with the sulfur polymer as an enabling technology.

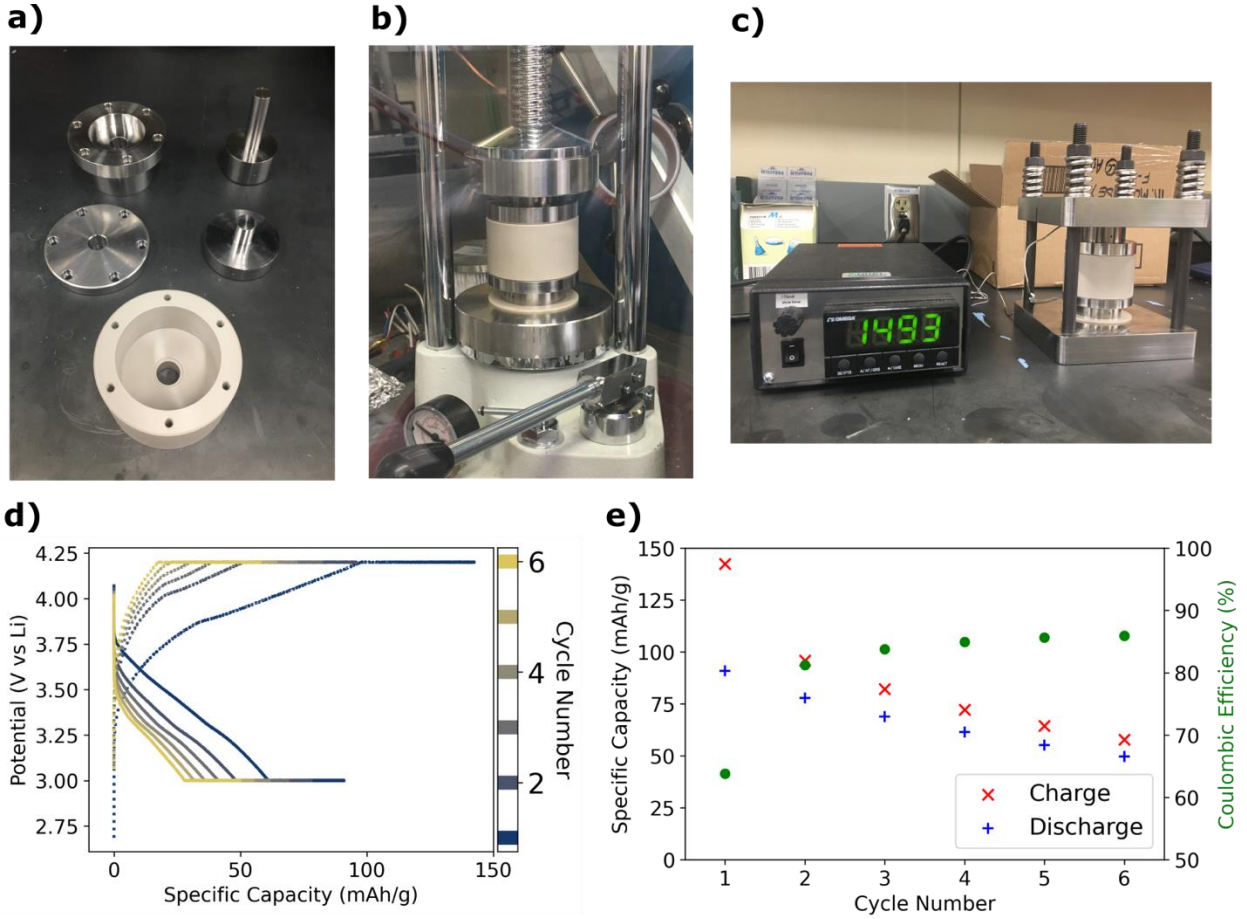

Figure 49. (a-c) New high-pressure solid-state cell testing hardware. All-solid-state graphite/LCO cell with sulfur polymer/argyrodite solid electrolyte. (d) Voltage versus specific cathode capacity. (e) Specific capacity and Coulombic efficiency versus cycle number.

References

[1] Tan, D. H., et al. "Carbon-Free High-Loading Silicon Anodes Enabled by Sulfide Solid Electrolytes." *Science* 373, No. 6562 (2021): 1494–1499. https://doi.org/10.1126/science.abg7217.

[2] Banerjee, A., H. Tang, X. Wang, J. H. Cheng, H. Nguyen, M. Zhang, D. H. S. Tan, T. A. Wynn, E. A. Wu, J. M. Doux, T. Wu, L. Ma, G. E. Sterbinsky, M. S. D'Souza, S. P. Ong, and Y. S. Meng. "Revealing Nanoscale Solid-Solid Interfacial Phenomena for Long-Life and High-Energy All-Solid-State Batteries." *ACS Applied Materials & Interfaces* 11, No. 46 (2019): 43138–43145.

[3] Fang, C., B. Lu, G. Pawar, M. Zhang, D. Cheng, S. Chen, M. Ceja, J. M. Doux, H. Musrock, M. Cai, B. Liaw, and Y. S. Meng. "Pressure-Tailored Lithium Deposition and Dissolution in Lithium Metal Batteries." *Nature Energy* 6, No. 10 (2021): 987–994.

Patents/Publications/Presentations

The project has no patents, publications, or presentations to report this quarter.

Task 1.17 – Precision Control of the Lithium Surface for Solid-State Batteries (Andrew Westover, Oak Ridge National Laboratory)

Project Objective. The overall goal of this project is to understand and engineer the surface and purity of thin Li-metal anodes to enable batteries with an energy density of 500 Wh/kg and a cycle life > 300 cycles.

Impact. The knowledge of lithium surface engineering and the implications for cell design of Li-metal batteries will improve commercialization efforts for solid-state Li-metal batteries. There is very little standard knowledge about variations in the impurity level in different lithium sources, the surface chemistry of different lithium surfaces, and their impact on performance. Furthermore, the strategies developed to engineer the surface of the lithium metal for integration into Li-metal batteries will provide significant performance increases, ideally enabling successful commercialization.

Approach. This project is broken into two parts. First, the team is focused on thoroughly understanding the purity, mechanics, and surface chemistry of multiple lithium sources and how these parameters impact performance. Second, they will focus on intentional engineering of the lithium purity and surface chemistry to control the mechanical properties, electrochemical stability, and electrochemical performance. They will explore three approaches to engineer the surfaces: gas-phase passivation, deposition of thin metal coatings, and deposition of thin inorganic coatings. To test electrochemical performance, they will use standard ceramic and polymer electrolytes to demonstrate the impact of purity and surface chemistry. The program will also employ a range of standard and specialized characterization techniques, including a significant focus on understanding the mechanics of lithium metal using nanoindentation and adhesion measurements using surface probe microscopy (SPM).

Out-Year Goals. In FY 2023, the program plans to finish gaining a deep understanding of different lithium sources, purity, and surface conditions, and of how they affect performance in Li-metal cells with both ceramic and polymer electrolytes. In FY 2024 through FY 2027, the primary goal is to develop strategies to carefully control and engineer the surface of lithium metal to optimize performance, enabling batteries that can achieve 500 Wh/kg and cycle for more than 300 cycles at mid-to-high current densities.

Collaborations. The project also includes E. Herbert, W-Y. Tsai, R. Sahore, S. Kalnaus, and R. Sacci of Oak Ridge National Laboratory (ORNL). The team anticipates the BMR program will also foster significant collaborations with other teams who have a complementary focus on lithium metal.

Milestones

1. Complete chemical characterization of different native lithium surfaces and correlate to cycle life and rate capability with various electrolytes. (Q1, FY 2023; In progress)
2. Measure adhesion of lithium metal to solid electrolytes (SEs) with various surfaces and solid-state electrolyte (SSE) using SPM. (Q2, FY 2023; In progress)
3. Demonstrate intentional passivation/coating of clean lithium surfaces. (Q3, FY 2023; In progress)
4. Identify the best lithium surface / SSE combination for at least one SE with a performance target of at least 50 cycles, at a capacity >1 mAh/cm^2, and current density of > 0.5 mA/cm^2 with no electrical shorting. (Q4, FY 2023)

Progress Report

The goal this fiscal year is first and foremost to connect the performance of different lithium sources with SEs in terms of surface composition, microstructure, and mechanics. Last quarter, the team established that the thickness of the surface layer directly correlated to the interfacial resistance of standard poly(ethylene oxide) – lithium bis(trifluoromethanesulfonyl)imide electrolytes. Surprisingly, the cleanest lithium surface performed the worst in terms of cycling performance before shorting. The data suggest that the microstructure also plays a key role in the performance. This quarter, the team's focus was on testing the performance of different lithium sources with an argyrodite SE Li_6PS_5Cl purchased from NEI corporation. To this end, they developed Li/argyrodite/Li cells in collaboration with G. Yang and J. Nanda's ORNL project team (Task 1.4). The cells were made by taking half-inch lithium discs and placing them in the PEEK die first. This was followed by 200 mg of argyrodite powder poured on top. With a stainless-steel plunger, the powder was pressed to 50 bars of pressure for ~ 15 seconds. Then, the plunger was taken out, and the second lithium disc ($^7/_{16}$ inch) was placed on top. The whole stack was then pressed with a stainless-steel plunger on top at 200 bars (~ 80 MPa) for 5 minutes. These cells were then tested at 5-6 MPa, and room temperature. The cells were cycled at a current density of 100 µA/cm^2 for 10 hours per cycle for a total capacity of 1 mAh/cm^2. In total, the team compared three different lithium sources. To maintain the quality of the comparison, all three sources consisted of lithium deposited on battery grade copper foil ~ 10-µm thick. For the evaporated lithium, they compared lithium of 10-µm and 30-µm thickness. For the commercial source, they used a source that is rolled onto copper foil and was ~ 40-µm thick. In the data, the team can clearly see that both evaporated Li-metal sources fail first. Notably, the failure mechanism is not dendritic shorting, but rather a sharp rise in the overpotential. This overpotential results from a loss of lithium contact with the SE. This can occur due to voiding at the lithium surface, or due to continuous reactions between the SE and lithium metal, or due to a combination of both. As there is a difference in the lithium thickness, the first possibility is that voiding is exacerbated because there is less pressure in the cells with the evaporated lithium. To rule this out as a possible explanation, the team performed a similar set of tests, but with a higher pressure of 17 MPa versus 5 MPa of the standard tests. There was very little difference in performance for the 10-µm evaporated lithium tested at higher pressure from the initial tests at 5 Mpa, suggesting that pressure is not the reason for the difference in performance. With the difference in pressure due to the thicker lithium ruled out, there are two possible reasons for the difference in performance. The first is that the surface layer on the commercial lithium, which is characterized by a silicone signature, helps to mitigate the reactions between the lithium metal and the SE. A second possibility is that the different microstructures among the three different lithium sources result in a different lithium self-diffusion and the subsequent ability of the lithium metal to replace the stripped lithium at the Li/SSE surface. Understanding the exact origin of these performance differences will be a primary focus in the next few quarters.

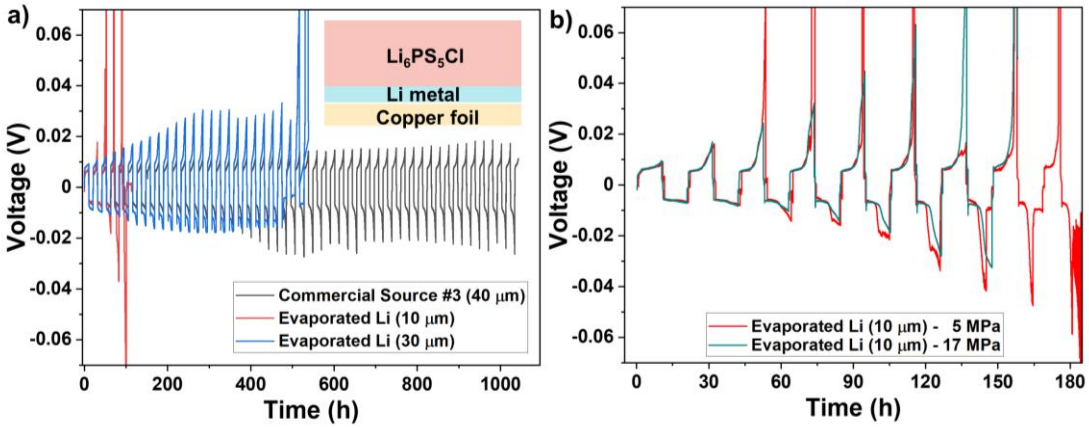

Figure 50. (a) Cu/Li/Li_6PS_5Cl/Li/Cu cells tested with three different types of lithium: a commercial source, dubbed #3 in prior quarterly reports on copper, and evaporated lithium of two thicknesses (that is, 10 µm and 30 µm). (b) Two cells tested at 5 MPa and 17 MPa, both with the 10-µm-thick lithium metal.

Patents/Publications/Presentations

Publication

- Self, E. C., W-Y. Tsai, A. S. Westover, K. L. Browning, G. Yang, and J. Nanda. "Benchmarking Solid-State Batteries Containing Sulfide Separators: Effects of Electrode Composition and Stack Pressure." *Journal of The Electrochemical Society* 169 (2022): 100510.

Presentation

- 242nd Electrochemical Society Fall Meeting, Atlanta, Georgia (October 2022): "How Does One Enable High Energy Li Metal Batteries: A Case Study with Lipon"; A. S. Westover, S. Kalnaus, N. Dudney, K. Browning, G. M. Veith, and R. L. Sacci.

Task 1.18 – Developing Materials for High-Energy-Density Solid-State Lithium-Sulfur Batteries (Donghai Wang, Pennsylvania State University)

Project Objective. The project objectives are to develop materials involving advanced S-C composite materials, solid additives, and sulfide-based solid-state electrolytes (S-SSEs) and to acquire knowledge for all-solid-state Li-S batteries (ASSLSBs). These batteries—with large areal sulfur loading (≥ 5 mg cm^{-2}) and high sulfur content (≥ 50 wt% in cathode), and paired with lithium or Li-alloy anodes—will deliver a high initial specific capacity > 1200 mAh g^{-1} at high charge/discharge rate (> 0.3 C) for 500 cycles with over 80% capacity retention.

Project Impact. This project aims to develop new materials to enable ASSLSBs with high energy density, excellent cycling stability, and good rate performance, and thus to build knowledge for fabrication of prototype ASSLSBs. Specifically, the developed new materials will greatly increase the specific capacity of sulfur and sulfur utilization at high areal sulfur loading, alleviate the interfacial problem between S-C composite and SSE within sulfur cathode, boost Li-ion conductivity, and improve moisture stability of glass and glass-ceramic S-SSEs. Meeting the technical targets will potentially promote development of high-energy-density ASSLSBs and their practical application in electric vehicles (EVs) and plug-in hybrid EVs and will also reduce petroleum consumption in the transportation sector by helping battery-powered vehicles become more accepted by consumers as a reliable source of transportation.

Approach. The project goal will be accomplished through developing new materials, together with in-depth characterization of sulfur cathodes. Specifically, approaches to realize the project objectives include the following: (1) development of new carbon material with unique structure, high surface area, and large pore volume; (2) development of new S-C and S-C-M_xS_y materials (M = Li, Co, Ti, Mo, etc.) to facilitate electron/ion transport; (3) development of novel additives to tune interfacial behavior among components in the cathode; (4) development and optimization of new SSE through cation and anion doping with superior properties such as high ionic conductivity, good moisture resistance, and stability; and (5) diagnostics, characterization, and cell tests on the developed new material or advanced sulfur cathode.

Out-Year Goals. The out-year goals are as follows: (1) develop and optimize sulfur cathode materials and synthesize new solid electrolytes (SEs; ionic conductivity > 5 mS cm^{-1} at room temperature), and (2) conduct characterization and performance tests on both material and electrode levels. The final demonstration will be all-solid-state sulfur cathodes with > 1200 mAh g^{-1} discharge capacity at 0.3 C discharge rate and 50 wt% sulfur content for 500 cycles at room temperature.

Collaborations. There are no active collaborations.

Milestones

1. Demonstrate new solid electrolyte (SE) with ionic conductivity > 3 mS cm^{-1} at 25°C. (Q1, FY 2023; Completed)
2. Demonstrate sulfur cathode with high areal sulfur loading (5 mg cm^{-2}) and > 50 wt% sulfur content over 1000 mAh g^{-1} discharge capacity at 0.3C rate at 25°C for 50 cycles. (Q3, FY 2023; In progress)
3. Demonstrate sulfur cathode with high sulfur content (> 50 wt%) over 1200 mAh g^{-1} discharge capacity at 0.3C rate at 25°C for 500 cycles. (Q4, FY 2023; In progress)

Progress Report

Electrochemical Characterization of Sulfur Cathodes

In previous quarters, the team found that the new SSE they prepared could effectively improve performance of high-sulfur-content cathodes (60 wt% of sulfur). To explicate the electrochemical behaviors of sulfur cathodes during charge/discharge, they performed the galvanostatic intermittent titration technique using ASSLSBs with sulfur cathodes using conventional $75Li_2S$-$25P_2S_5$ (LPS) solid electrolyte (S-C-LPS) and the new SE they prepared (S-C-SSE). As shown in Figure 51, S-C-SSE cathode delivered significantly higher specific capacity and lower overpotential than S-C-LPS cathode, suggesting more active sulfur, lower reaction resistance, and improved Li^+ transport kinetics. The above analysis demonstrates that sufficient Li^+ transport pathways and fast Li^+ transport kinetics are achieved in the S-C-SSE cathode.

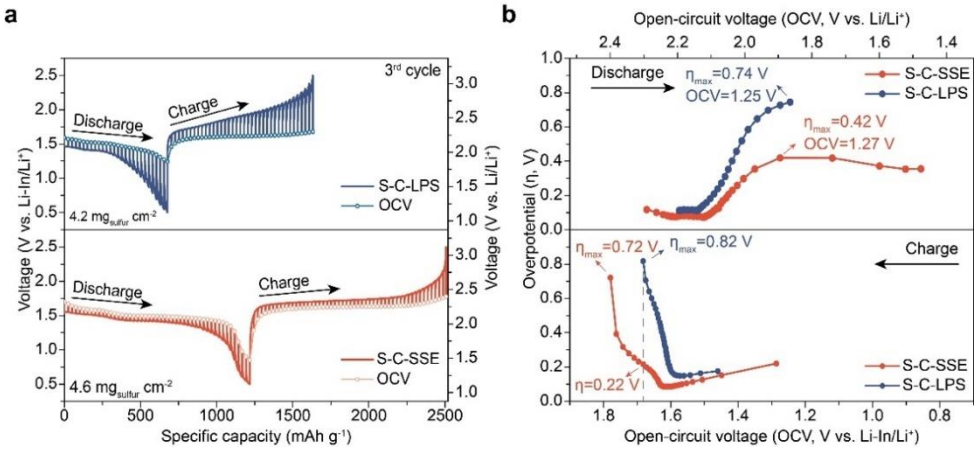

Figure 51. (a) Galvanostatic intermittent titration technique (GITT) and open circuit voltage (OCV) curves of S-C-SSE and S-C-LPS cathodes at the third cycle. Current pulses of 0.03 C for 30 minutes were employed, followed by 4-hour resting. (b) Overpotential profiles of S-C-SSE and S-C-LPS cathodes from the GITT measurement. Capacities are based on the mass of the sulfur.

Development of New Additive for Sulfur Cathodes

Based on the team's previous findings, they identified a new additive for sulfur cathodes to improve the ionic conductivity of sulfur cathodes. As shown in Figure 52, within a limited electrochemical voltage window of 1.0-2.5 V versus Li-In/Li^+ (or 1.62-3.12 V versus Li/Li^+), the sulfur cathode with an areal sulfur loading of 2.175 mg cm^{-2} and a high sulfur content of 50 wt% exhibited a high discharge specific capacity over 1200 mAh g_{sulfur}^{-1} at 0.1 C. They will incorporate the additive to their previously developed cathode to further improve battery performance toward meeting the project milestone.

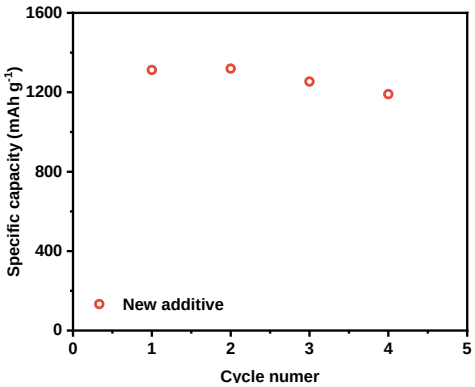

Figure 52. Cycle performance of sulfur cathode with new additive at 0.1 C (1 C=1675 mAh g_{sulfur}^{-1}).

Lithium Alloy Anodes for ASSLSBs

Additionally, to prolong the lifetime of all-solid-state Li-S batteries and increase their energy density, the team synthesized different types of Li-alloy anodes to replace Li-In anode. Utilizing the high-energy ball-milling method, they could fabricate lithium alloys with different lithiated states, which possess various electrochemical potentials versus lithium metal. They found that the electrochemical potentials play an important role in preventing lithium dendrite formation and propagation. Also, to improve the interfacial issues such as side

reactions between SSEs and lithium metal, using alloy anodes could not only suppress undesired products, but also improve interfacial contact between the two. The team developed three types of lithium alloys and performed a series of electrochemical testing. For the long-cycling performance (Figure 53), the lithium alloy-2 with a moderate lithiated state outperforms the lithium alloy-1 and lithium alloy-3. It can cycle stably and enable ASSLSBs with high discharge capacities over 200 cycles and sustain a high capacity retention of ~ 90%. However, lithium alloy-1 suffers from short-circuiting after 20 cycles, while lithium alloy-2 and lithium alloy-3 could deliver high discharge capacities and prevent dendrite formation. This implies that suitable lithiated state of the applied alloy anode could avoid short-circuiting, and still maintain high energy density. The mechanism and root causes of short-circuiting are still under investigation to obtain knowledge of how different alloy anodes affect the full cell's performance, which will shed light on prolonging the lifetime of Li-S batteries.

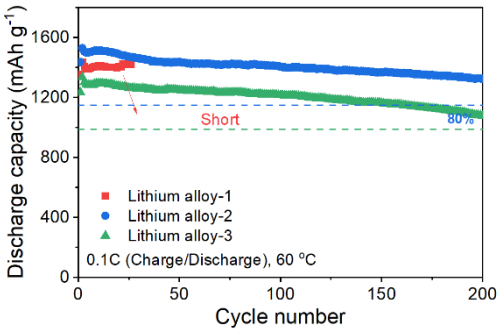

Figure 53. Cycling performance of the Li-S all-solid-state batteries with alloy anodes. The cells were tested at 0.1C under 60°C, and the specific capacity is based on the weight of sulfur.

Patents/Publications/Presentations

The project has no patents, publications, or presentations to report this quarter.

Task 1.19 – Hot Pressing of Reinforced Lithium-NMC All-Solid-State Batteries with Sulfide Glass Electrolyte
(Thomas Yersak, General Motors, LLC)

Project Objective. The project will research, develop, and test lithium – Ni-Mn-Co (Li-NMC) all-solid-state batteries (ASSBs) capable of achieving program performance metrics by implementing sulfide-glass solid-state electrolytes (SSEs) and hot-press processing in a dry-room environment. The performance of ASSBs with sulfide SSEs is limited because they are essentially green tapes with up to 20% porosity. In composite cathodes, the porosity limits energy density and power, while porosity in the separator acts as a conduit for Li-metal deposits if cycling conditions (C-rate, operating temperature, and pressure) are not strictly controlled. The project goal is to demonstrate that the hot-pressing method and appropriately formulated sulfide-glass SSEs can eliminate porosity to enable Li-NMC ASSBs with energy density of > 350 Wh/kg.

Project Impact. The hot-press processing method and appropriately formulated sulfide-glass SSEs may enable Li-NMC ASSBs with improved energy density > 350 Wh/kg. The General Motors (GM) processing technology depends on heating a sulfide-glass SSE above its transition temperature, at which point it can consolidate via viscoplastic flow. In the composite cathode, hot-pressing provides liquid-like contact between the NMC cathode and SSE to increase energy density and power by enabling thick composite cathodes with high active material loading. Furthermore, cathode-supported sulfide-glass separators can be made dense and thin by hot-pressing. A dense separator enables the use of Li-metal anodes because lithium deposits may be more effectively blocked, preventing cell shorting.

Approach. The sulfide SSE used in the composite cathode, otherwise known as the catholyte, will dictate the processing specifications for ASSB hot-pressing. Thermal stability can be achieved by NMC passivation and proper catholyte formulation. This project will systematically evaluate different NMC coatings, catholyte formulations, and hot-press processing specifications (that is, temperature, time, and pressure). The performance of hot-pressed ASSBs will be compared to green baseline ASSBs and hot-pressed control ASSBs consisting of the β-Li_3PS_4 and Li_6PS_5Cl model SSEs. Electron microscopy will be employed to understand interfacial phenomena and track composite cathode microstructure before and after hot-pressing.

Out-Year Goals. In the second year of this project, a sulfide-glass SSE will be formulated specifically for use as the separator. The separator glass SSE formulation will be designed to achieve full densification under the hot-press processing specifications determined for the catholyte. Separator glass formulation design will also consider cathodic stability, moisture stability, and ionic conductivity. Once a system of separator glass SSE and catholyte has been determined, the third year of the project will demonstrate hot-pressed full cells at the coin-cell and single-layer pouch-cell levels, meeting program target performance metrics.

Collaborations. GM will lead this project with no subrecipients.

Milestones

1. Report performance of hot-pressed coin cell. (Q1, FY 2023; Completed)
2. Report performance of hot-pressed single layer pouch cell. (Q2, FY 2023; In progress)
3. Report performance of hot-pressed pouch cell. (Q3 FY 2023; In progress)

Progress Report

This report describes the performance of hot-pressed coin cells using a cathode and catholyte system optimized for processability. Previously, the team reported the performance of coin cells with hot-pressed NMC cathode composites. Two issues were revealed. First, SSE was susceptible to thermal degradation in the presence of high voltage (HV) cathode during hot pressing. This led the team to prioritize thermal stability over processability, which led to a negligible improvement in cell-level energy density. Second, high-nickel NMC is susceptible to microcracking during consolidation, which reduces cycle life. Here, they show that cathode composites with low voltage (LV) cathode materials are better suited for consolidation by hot pressing.

The cathode composite studied here is composed of a natural pyrite (FeS_2) active material, an oxysulfide catholyte ($Li_7P_3S_{11-x}O_x$), and an optional carbon black conductive additive in a mass ratio of 10:20:2, respectively. FeS_2 was chosen because it is thermally stable versus (oxy)sulfide SSE since its voltage (~ 1.8 V) is lower than the oxidative limit of these SSEs (~ 2.5 V). The FeS_2 high specific capacity of 894 mAh/g makes up for the lower voltage.[3] The cathode composite pellets were pressed at 1 metric ton (1.3273 cm^2 cross sectional area) for 10 minutes at either room temperature (cold-pressed, CP) or 240°C (hot-pressed, HP). The porosities of these samples are provided in Figure 54. The porosities of CP samples are > 30%, whereas the porosities of HP samples are reduced to nearly 20%. For comparison, the optimal HV cathode composite consisting of NMC and β-Li_3PS_4 had a CP porosity of 29.7% and HP porosity of only 26.7%.[1] They could achieve lower porosity because $Li_7P_3S_{11-x}O_x$ has superior processability compared to β-Li_3PS_4.[2] Ongoing focused ion beam – scanning electron microscopy imaging seeks to characterize cathode composite microstructure; however, schematics (Figure 54b-c) are provided in the interim.

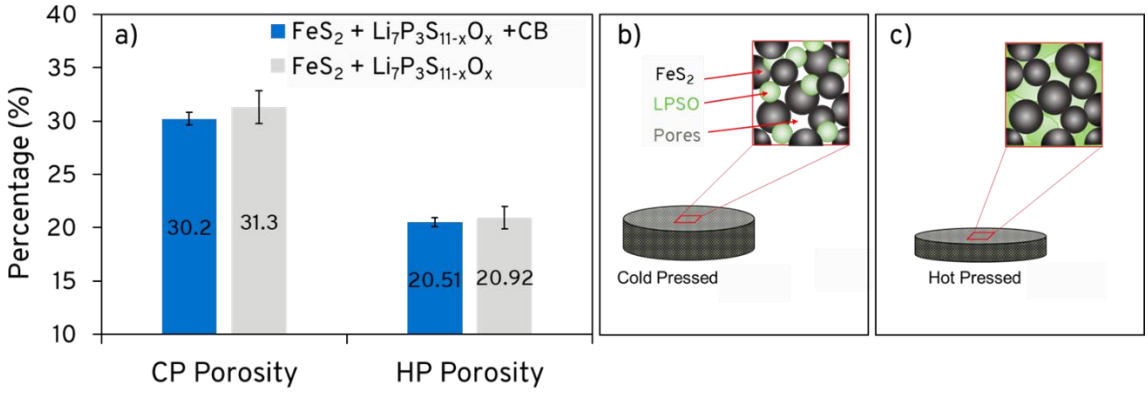

Figure 54. (a) Porosities of FeS_2 composite cathodes after consolidation at room temperature (cold-pressed, CP) and 240°C (hot-pressed, HP) with and without carbon black (CB) conductive additive. (b) Schematic of CP FeS_2 cathode composite showing high porosity. (c) Schematic of HP FeS_2 cathode composite showing reduced porosity.

Coin cells were then prepared with the FeS_2 composite cathode described above, and the preliminary electrochemical data are provided in Figure 55. Figure 55a provides the impedance spectra for a CP cell and HP cell. The total resistances of the CP and HP cells are 4000 Ω and 75 Ω, respectively. To determine why the resistance of the HP cell was so much lower than the CP cell, there are two factors to consider: namely, electrode microstructure and SSE ionic conductivity. During heat treatment, it is common for (oxy)sulfide glass SSEs to devitrify and in many cases the ceramic phase has a higher ionic conductivity than the mother glass. Glassy $Li_7P_3S_{11-x}O_x$ has an ionic conductivity of 0.20 ± 0.003 mS/cm, while fully devitrified $Li_7P_3S_{11-x}O_x$ has an ionic conductivity of 1.22 ± 0.118 mS/cm. However, hot-pressed $Li_7P_3S_{11-x}O_x$ has an ionic conductivity of only 0.23 ± 0.157 because it is 11.7 % devitrified.[2] In other words, it takes longer than 10 minutes to fully devitrify $Li_7P_3S_{11-x}O_x$ to maximize ionic conductivity. Therefore, the difference in cell resistance is not explained by a change in SSE ionic conductivity. Rather, the difference can be explained by the well-formed FeS_2/SSE interface achieved by hot pressing. Indeed, the HP cell delivered a 3rd cycle discharge capacity of 800 mAh/g

(Figure 55c), whereas the CP cell delivered only 650 mAh/g (Figure 55b). Both cells were cycled at 60°C; however, ongoing tests are evaluating the performance of fully annealed test cells at room temperature. In conclusion, the remainder of work to be completed during this project will focus on cell designs utilizing LV cathode for the reasons described above.

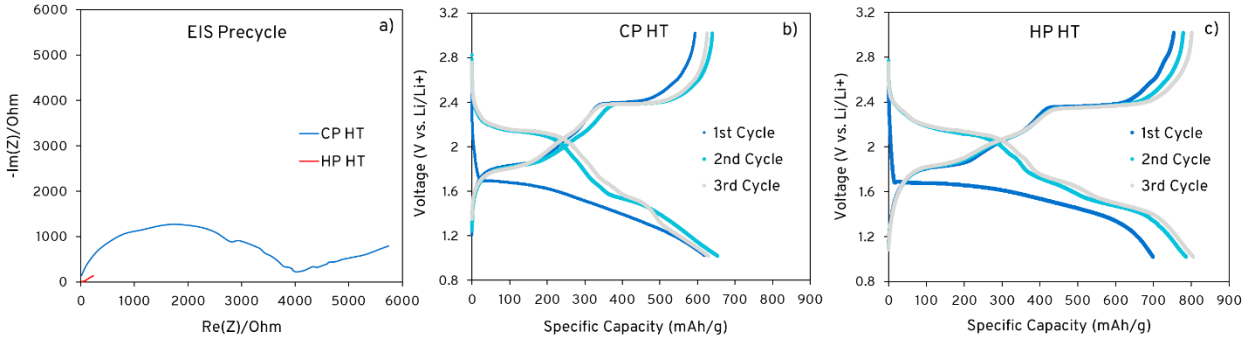

Figure 55. (a) Nyquist diagram with impedance spectra of the cells prior to cycling. The HP cell has a much lower impedance than the CP cell, which is attributed to better interfacial contact between the FeS_2 and SSE as facilitated by hot pressing. (b) First three cycles of CP FeS_2/In_xLi cell. (c) First three cycles of HP FeS_2/In_xLi cell.

References

[1] Yersak, T., et al. "Consolidation of Composite Cathodes with NCM and Sulfide Solid-State Electrolytes by Hot Pressing for All-Solid-State Li Metal Batteries." Journal of Solid State Electrochemistry 26, No. 3 (2022): 709–718.
[2] Gonzalez Malabet, H. J., T. Yersak, et al. (In preparation)
[3] Yersak, T., et al. "Solid State Enabled Reversible Four Electron Storage." Advanced Energy Materials 3, No. 1 (2013): 120–127.

Patents/Publications/Presentations

The project has no patents, publications, or presentations to report this quarter.

Task 1.20 – Low Impedance Cathode/Electrolyte Interfaces for High-Energy-Density Solid-State Batteries (Eric Wachsman and Yifei Mo, University of Maryland)

Project Objective. The project objective is to research, develop, and test Li-metal-based batteries that implement solid Li-ion conductors equipped with Ni-Mn-Co (NMC) cathodes integrated into the Li-metal / Li-La-Zr (LLZ) tri-layer architecture. Specifically, the team will achieve the following: (1) identify and demonstrate interfacial layers to achieve low-impedance and stable NMC/LLZ interfaces; (2) develop novel processing techniques to fabricate NMC/LLZ composite cathodes with low interfacial resistance; and (3) enable high-performance all-solid-state batteries (ASSBs) with an energy density of 450 Wh/kg and 1400 Wh/L and negligible degradation for 500 cycles.

Project Impact. Instability or high resistance at the interface of high-energy cathode materials with Li-garnet solid electrolytes limits the high-energy-density all-solid-state lithium batteries. This project will lead to a fundamental understanding of solid-electrolyte/solid-cathode interfaces and a unique and transformative LLZ framework to enable high-energy-density, safe Li-metal batteries approaching ~ 400 Wh/kg.

Approach. In this new project, the team will build on their demonstrated expertise with garnet electrolytes and ASSB cells to accomplish the following: (1) engineer interfaces to overcome high NMC/LLZ interfacial impedance and interfacial degradation; (2) develop processing and fabrication techniques to achieve high-loading NMC/LLZ composite cathodes with low resistance and high cyclability; and (3) integrate the NMC/LLZ cathodes into all-solid-state Li-metal/LLZ cells to achieve high-energy-density batteries.

Out-Year Goals. The project will solve the current challenges of integrating garnet SE with a cathode to achieve a high-performance ASSB using a high-energy-density Li-metal anode. The resultant high energy density and stability using both high-energy-density Li-metal anodes and NMC cathodes will open new applications in portable electronics, electric vehicles, and beyond.

Collaborations. This project funds work at University of Maryland. The principal investigator (PI), E. Wachsman, will have management responsibility and will lead experimental efforts including garnet synthesis, interface processing, cell fabrication, and testing. The Co-PI, Y. Mo, will lead computational efforts on understanding stability between garnet and cathode and on identifying promising coating materials. In addition, Wachsman is actively collaborating with several universities and national laboratories through the U.S.–German cooperation on solid-state battery interfaces.

Milestones

1. Thermochemical stability between LLZ and interface-coated NMC experimentally determined. (Q3, FY 2022; Completed)
2. Experimental results compared with computational results and model refined for side reactions and process optimization. (Q4, FY 2022; Completed)
3. 10× reduction in interfacial impedance between coated LLZ/NMC and uncoated LLZ/NMC interfaces demonstrated by co-sintering. (Q4, FY 2022; Completed)
4. Fabricate trilayer cell with composite NMC-LLZ cathode layer and measure. (Q1, FY 2023; In progress)
5. *Go/No-Go Decision*: Demonstrate final cell with achieved performance. (Q2, FY 2023; In progress)

Progress Report

The thermochemical stability and interfacial impedance improvements gained by coating $LiNi_{0.6}Mn_{0.2}Co_{0.2}$ (NMC-622) with various interlayer materials are summarized in Figure 56. The data show that the NMC phase % increases when coated with Li_5AlO_4 or Li_4SiO_4 coatings, most notable at higher excess lithium contents in the Li-La-Zr-Ta-O (LLZTO). This confirms the increase in thermochemical stability.

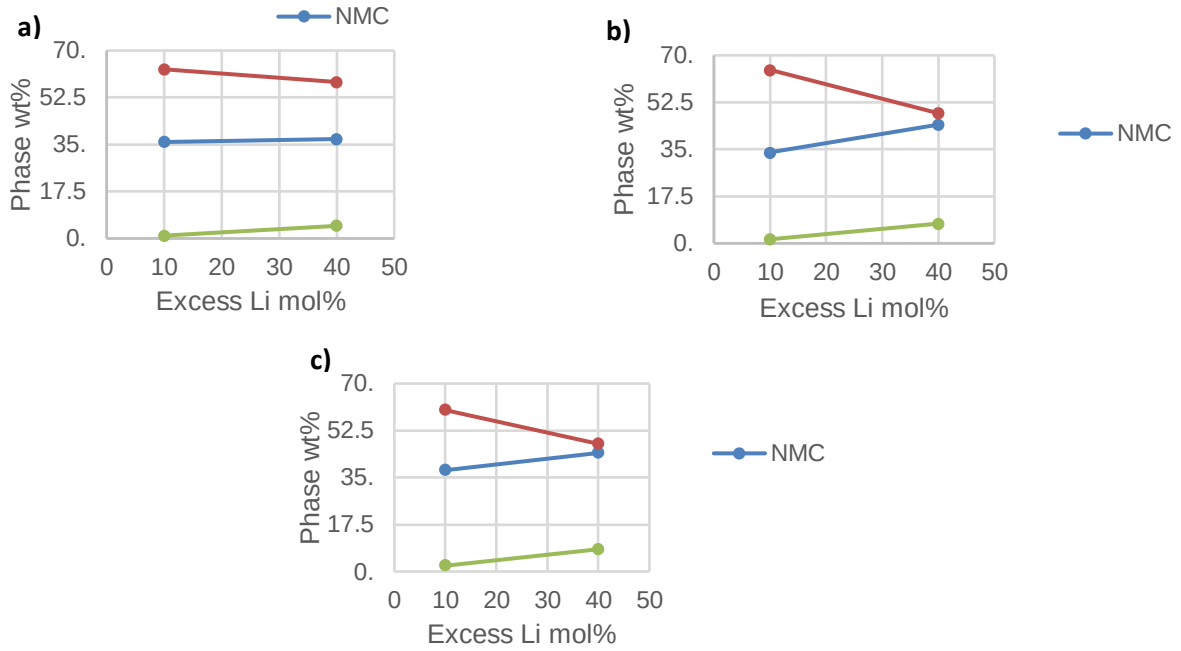

Figure 56. Phase percentages versus the excess lithium molar content of the LLZTO obtained by Rietveld Refinement of X-ray diffraction of 1:1 weight ratios of NMC-622 and LLZTO sintered in O_2 at 900°C for 3 hours. The data are shown for samples that are (a) uncoated NMC-622, (b) Li_5AlO_4-NMC-622, and (c) Li_4SiO_4-NMC-622.

Figure 57 displays the symmetric cell electrochemical impedance spectroscopy results of the most promising coating materials as analyzed by distribution of relaxation times analysis, demonstrating that a 10 mol% coating of Li_5AlO_4 reduces interfacial impedance by 5× and a 10 mol% coating of Li_4SiO_4 reduces it by 10×.

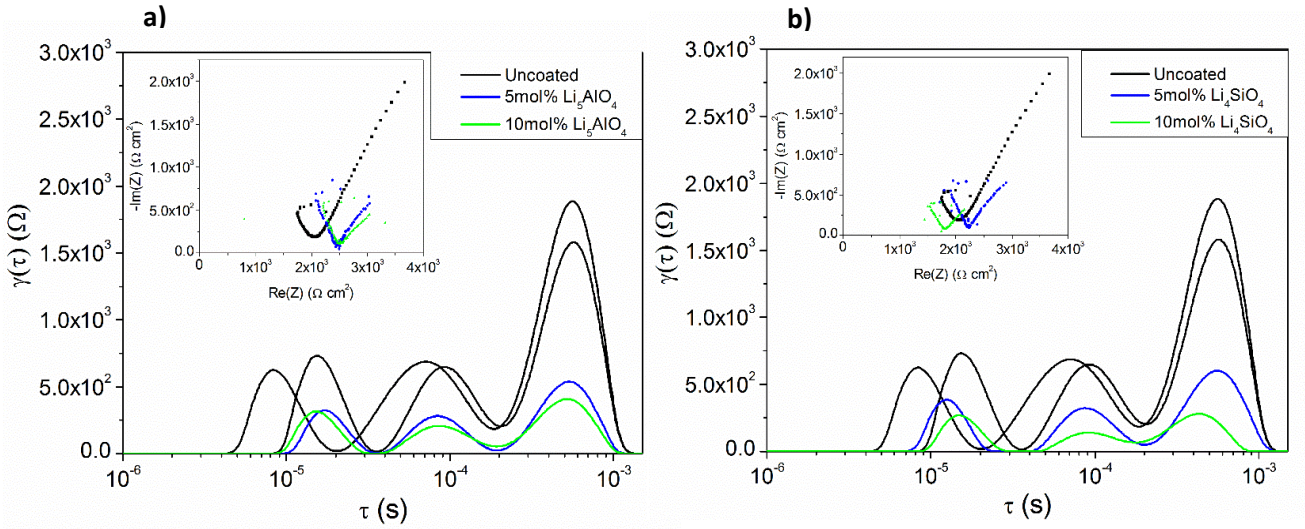

Figure 57. Distribution of relaxation times (DRT) plots with corresponding Nyquist plots (inset) of symmetric composite (1:1 weight ratio of NMC:LLZTO) NMC-622 cathode cells for top two interlayer compositions: (a) Li_5AlO_4 and (b) Li_4SiO_4.

Table 2 summarizes the reduction in interfacial impedance results for all synthesized coating materials. The lithium silicate and lithium aluminate coatings were the most effective, with the high lithium compositions being the best. This supports the conclusions from previous computational results that decreasing the lithium gradient between NMC and LLZTO reduces the formation of resistive decomposition phases.

Table 2. Summary of the reduced impedance from each interlayer material as collected by electrochemical impedance spectroscopy of NMC symmetric cells and analyzed by distribution of relaxation times analysis.

Coating	Li_2ZrO_3	Li_3PO_4	$LiAlO_2$	Li_5AlO_4	Li_2SiO_3	Li_4SiO_4
mol%	2.5	10	10	10	10	10
EIS Reduction	2x	1.33X	4x	5x	4x	10x

Figure 58 contains a Nyquist plot of NMC|LLZTO|Li-metal full cells with both Li_4SiO_4 coated NMC-622 and uncoated NMC-622. The impedance drops by nearly an order of magnitude, highlighting the ability of this interfacial coating to improve the interface between LLZTO and NMC-622. Cycling data are forthcoming for these cells.

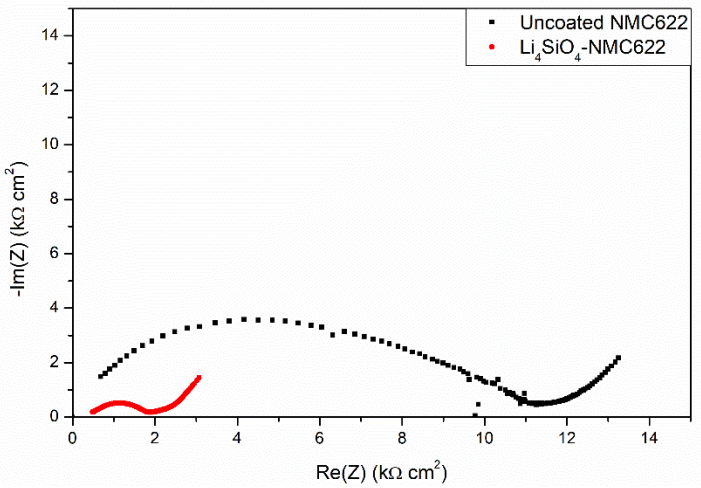

Figure 58. Nyquist plot of electrochemical impedance spectroscopy of uncoated and Li_4SiO_4-coated NMC-622 Li-metal full cells co-sintered in a 1:1 wt ratio with $Li_{6.75}La_3Zr_{1.75}Ta_{0.25}O_{12}$ (LLZTO) onto LLZTO trilayers at 1050°C in O_2.

Patents/Publications/Presentations

Publications

- Ren, Y., T. Danner, A. Moy, M. Finsterbusch, T. Hamann, J. Dippell, T. Fuchs, M. Müller, R. Hoft, A. Weber, L. A. Curtiss, P. Zapol, M. Klenk, A. T. Ngo, P. Barai, B. Wood, R. Shi, S. Wan, T. Wook, M. Engels, J. Nanda, F. Richter, A. Latz, V. Srinivasan, J. Janek, J. Sakamoto, D. Fattakhova-Rohlfing, and E. D. Wachsman. "Oxide-Based Solid-State Batteries: A Perspective on Composite Cathode Architecture." *Advanced Energy Materials* 13, No. 1 (2023): 2201939. https://doi.org/10.1002/aenm.202201939.
- Ren, Y., and E. D. Wachsman. "All Solid-State Li/LLZO/LCO Battery Enabled by Alumina Interfacial Coating." *Journal of The Electrochemical Society* 169 (2022): 040529. https://doi.org/10.1149/1945-7111/ac644f.

Presentation

- 22nd Advanced Automotive Battery Conference, San Diego, California (December 5–8, 2022): "Enabling High Rate Metal Anodes by Tailored Structures and Interfaces"; E. D. Wachsman.

Task 1.21 – Molecular Ionic Composites: A New Class of Polymer Electrolytes to Enable All-Solid-State and High-Voltage Lithium Batteries (Louis A. Madsen, Virginia Polytechnic Institute and State University)

Project Objective. Based on a newly discovered class of solid polymer electrolyte materials, that is, molecular ionic composites (MICs), the overall objective is to develop solid-state lithium conductors targeted for use in transportation applications. MICs form a mechanically stiff, electrochemically stable, and thermally stable matrix. Specific objectives include the following: (1) development of robust MIC electrolyte thin films (~ 20 µm) to serve as simultaneous nonflammable separators and dendrite-blocking Li^+ conductors, (2) electrochemical quantification of key performance metrics including electrolyte stability, interfacial reactions, and suitability/compatibility with a range of electrode materials, and (3) comprehensive investigation of ion transport mechanisms and electrode-electrolyte interfacial reactivity under practical operating conditions using nuclear magnetic resonance (NMR) and synchrotron X-ray analyses.

Project Impact. Commercialization of solid-state Li-metal batteries is hampered by lack of a functional nonflammable solid electrolyte (SE) that can provide high ionic conductivity, a wide electrochemical window, favorable mechanical properties to inhibit lithium dendritic growth, and low interfacial resistance. The tunable MIC materials platform has potential to fulfill these requirements with relatively simple fabrication techniques, and thus shows promise for enabling nonflammable solid-state batteries that can be optimized for low cost and high energy density.

Approach. MICs rely on a unique polymer that is similar to Kevlar® in its strength, stiffness, and thermal stability, but with densely spaced ionic groups that serve to form an electrostatic network that permeates mobile ions in the MIC. The team can tailor the ion concentrations and types to yield MIC electrolyte films that are electrochemically compatible with Li-metal anode as well as a range of high-voltage layered cathodes. They are searching the composition space of lithium salts, electrochemically compatible ionic liquids, and polymer [poly(2,2′-disulfonyl-4,4′-benzidine terephthalamide), or PBDT] molecular weight to determine best composition windows for MIC electrolytes. The team is also investigating best methods for casting thin films in terms of temperature, solvent/evaporation conditions, and control over the initial liquid crystalline gel formation point. Concurrently, they are testing MIC films in various electrochemical cells, quantifying transport and structural/morphology parameters with NMR and X-ray techniques, and measuring key mechanical (dynamic mechanical thermal analysis, stress-strain) and thermal (differential scanning calorimetry, thermal gravimetric analysis) properties.

Out-Year Goals. This year, the team will generate a predictive model to understand the relationship between the mobility of all ions and the MIC synthesis parameters. They will establish the testing protocol for NMR measurements under operating conditions. They will also study the surface chemistry of the MIC electrolyte before and after cycling. The team will identify methods to mitigate interfacial degradation. They will then test the final project electrolyte in a full cell and develop specifications.

Collaborations. The team is collaborating with T. J. Dingemans' group at University of North Carolina (UNC), Chapel Hill, in which they are forming composites based on PBDT polymer and carbon materials such as graphene oxide and are beginning to develop charged rigid-rod polymers building on the PBDT structure. The team is exploring shear rheology and broadband dielectric spectroscopy in collaboration with R. H. Colby at Pennsylvania State University. They are collaborating with D. Nordlund and Y. Liu at SLAC National Accelerator Laboratory and S-M. Bak at Brookhaven National Laboratory (BNL) to conduct synchrotron X-ray studies on MIC films.

Milestones

1. Multivariant analysis of experimental parameters and electrochemical properties. (Q1 FY 2022; Completed)

2. In situ experiments implementing NMR spectroscopy and diffusometry at different cell states of charge. (Q2, FY 2022; Completed)
3. Spectroscopic surface analysis of cathode, anode, and MIC electrolyte after various cycling history. (Q3, FY 2022; Completed)
4. Area specific resistance: MIC/Li ≤ 10 Ω cm2 and cathode/MIC ≤ 50 Ω cm2 / cells. (Q4, FY 2022; In progress)

Progress Report

This quarter, the team reported on the fundamental investigation of interfacial processes in the Li | MIC | Ni-Mn-Co cells. The work was done at NSLS-II at BNL. They have successfully collected preliminary data for the cross-section of the SE after various stages of battery cycling. Figure 59 shows a schematic representation of the beamline experiments. They are now able to chemically resolve the species at the electrode-electrolyte interface. In particular, the team has made more progress since the report of this technique in a previous quarter. With these new insights, the team has developed a solid understanding of the anodic and cathodic side reactions in this new solid battery cell. They plan to use such understanding to implement compositional changes to improve battery performance.

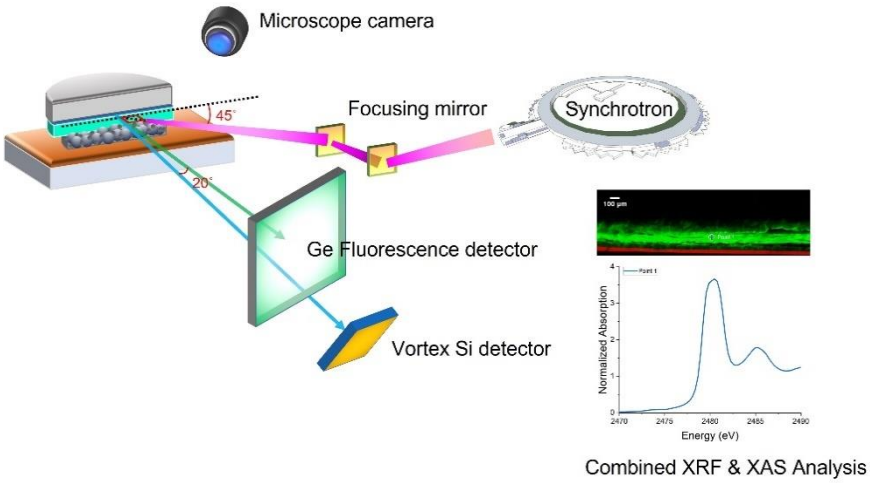

Figure 59. Schematic representation of the combined X-ray fluorescence (XRF) and X-ray absorption spectroscopy (XAS) experiments, which allow identification of the local concentration and chemical structure of the interested element at the cross-section.

The team has also made further progress on a new formulation of this solid-state rigid polymer electrolyte. They use both Li/Li and Li/$LiFePO_4$ cells to evaluate the limiting current density of the prepared rigid polymer electrolyte. For the Li/$LiFePO_4$ cells, the cathode, containing 3 wt% PBDT, 10 wt% carbon additive, and 87 wt% $LiFePO_4$, is used directly here. Figure 60a shows the voltage profile of a Li/Li cell cycled at 22°C at different current densities. When the applied current density is below 0.3 mA cm^{-2}, the cell cycles stably. After 2.5 cycles (10 hours) at 0.3 mA cm^{-2}, the voltage increases drastically and eventually reaches the safety limit (5 V), indicating that the limiting current density is about 0.3 mA cm^{-2} at 22°C for the rigid polymer electrolyte membrane. Li/$LiFePO_4$ cells demonstrate similar results (Figure 60b-c). Increasing the cycling current density from 0.05 mA cm^{-2} to 0.3 mA cm^{-2} leads to the specific capacity decreasing from 150 mAh g^{-1} to 120 mAh g^{-1}. Further increasing the current density causes significant polarization and drastic capacity decay. The limiting current density of an electrolyte is closely related to its thickness. Under the same salt polarization profile, the

obtainable current density is inversely proportional to the thickness of the electrolyte. Since the rigid polymer electrolyte used in this study is very thick (130 ± 20 μm), reducing its thickness to 25 μm should lead to an increase of the limiting current density by a factor of about 5.

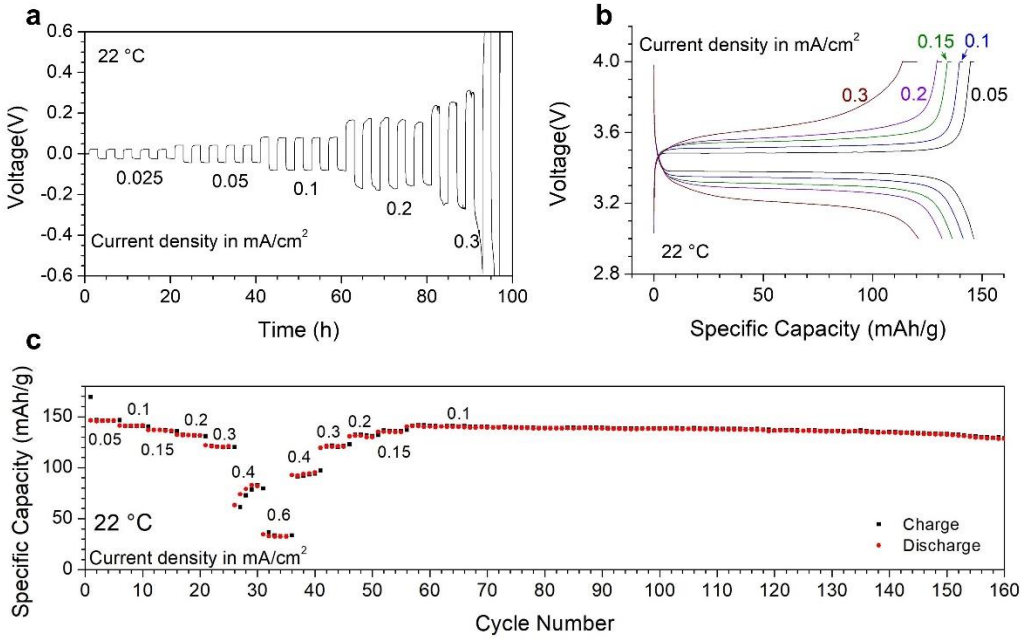

Figure 60. Rate capability of Li/Li and Li/$LiFePO_4$ cells using the new formulation for the solid-state rigid polymer electrolyte at 22°C. (a) Voltage profile of a Li/Li cell cycled at various current densities. Both charging and discharging time are 2 hours for each cycle, and the current density increases from 0.025 mA cm^{-2} to 0.3 mA cm^{-2} with 5 cycles for each step. (b) Typical voltage profiles of the Li/$LiFePO_4$ cell cycled at different current densities. (c) Specific charge and discharge capacities of $LiFePO_4$ when cycled at various current densities. The thickness of the rigid polymer electrolyte used in this study is 130 ± 20 μm, and the $LiFePO_4$ mass loading in the cathode is 3.6 ± 0.4 mg cm^{-2}. Li/Li and Li/$LiFePO_4$ cycling tests reveal a limiting current density of ~ 0.3 mA cm^{-2} and stable long-term cycling at 0.1 mA cm^{-2} of the rigid polymer electrolyte at 22°C.

Patents/Publications/Presentations

Patent

- Full U. S. international patent application filed: "Rechargeable Solid State Lithium Batteries Working Over A Wide Temperature Range"; PCT/US22/39656.

Presentations

- UNC, Department of Applied Physical Sciences, Chapel Hill, North Carolina (November 15, 2022): "Transport and Structural Phenomena in Molecular Ionic Composite Solid Electrolytes"; L. A. Madsen.
- UNC–Asheville, Department of Chemistry, Asheville, North Carolina (October 14, 2022): "A Safe Solid Battery Electrolyte Based on a Rigid Double Helical Polymer"; L. A. Madsen.
- International Symposium on Polymer Electrolytes (ISPE-17), Niagara-on-the-Lake, Ontario, Canada (October 2–7, 2022): "Transport and Structural Phenomena in Molecular Ionic Composite Solid Electrolytes"; L. A. Madsen. Invited keynote lecture.

Task 1.22 – Development of Thin, Robust, Lithium-Impenetrable, High-Conductivity, Electrochemically Stable, Scalable, and Low-Cost Glassy Solid Electrolytes for Solid-State Lithium Batteries (Steve Martin, Iowa State University of Science and Technology)

Project Objective. The project objective is to develop new Li^+-conducting mixed oxy-sulfide nitride (MOSN) glassy solid electrolytes (GSEs) that are impermeable to lithium dendrites, have high conductivities, are scalable through low-cost glass manufacturing, are chemically and electrochemically stable, and will enable low-cost, high-energy-density all-solid-state lithium batteries (ASSLBs). The ASSLBs constructed from these new GSEs will meet and exceed all program objectives: usable specific energy @ C/3 ≥ 350 Wh/kg, calendar life of 15 years, cycle life (C/3 deep discharge with < 20% energy fade) of 1000, and cost ≤ $100/kWh.

Project Impact. This project will enable the team to demonstrate the following: (1) thin MOSN GSE films yield superior performance in a much safer, lower-cost, and Li-dendrite impenetrable form, and (2) high rate and long cycle life can be achieved in ASSLBs using thin-film MOSN GSEs. The new GSEs in ASSLBs are anticipated to increase energy density (anode basis) from ~ 300 mAh/g to ~ 4,000 mAh/g, enabling replacement of internal combustion engines in both light-duty and heavy-duty vehicles. Each 20% reduction in the ~ 1.6 billion l of gasoline used per day in the United States would reduce CO_2 emissions by ~ 4 billion kg or 2×10^{12} l of CO_2 per day. The team will also increase scientific and engineering knowledge of thin-film GSEs in ASSLBs.

Approach. The MOSN mixed glass former (MGF) glasses used for the GSEs in this project were developed in previous work to have the necessary thermal stability and high ionic conductivity for successful use as a drawn-film electrolyte. In this project, the glass chemistry will be tuned for even more desirable properties, by investigating structure-property relationships and testing variations in glass chemistry.

Out-Year Goals. Work will progress toward developing a glass capable of being drawn to 100-µm thickness, while having high conductivity and electrochemical stability and good cycling ability.

Collaborations. The team is collaborating with S. Kalnaus and G. Veith (Oak Ridge National Laboratory) on the physical and mechanical properties of oxy-nitride glasses and with Y. Cui (Stanford University) and A. Sendek (Avionics) on new classes of polycrystalline lithium thioborate solid electrolyte. The team is also collaborating with T. Versak (General Motors) on testing of the GSEs in their solid-state cells.

Milestones

1. Accomplish: Large MOSN MGF GSE preforms (10 cm × 0.5 cm × 30 cm) demonstrate < 1 vol% crystallization at 90°C above the glass transition temperature (T_g). (Q1, FY 2022; Completed)
2. Accomplish: Optimize draw conditions for MOSN GSE to achieve 5 m × 5 cm × < 50 µm thin films. (Q2, FY 2022; In progress)
3. Accomplish: Fabricate MOSN MGF Li|GSE|Li cells in intermediate area format, ~ 2 cm^2. (Q3, FY 2022; In progress)
4. *Go/No-Go Decision*: Fabricate MOSN MGF GSE cells in large format ~ 5 cm^2. Cells achieve targeted performance metrics. Analysis indicates technical approach capable of achieving performance targets. (Q4, FY 2022; In progress)

Progress Report

Develop Optimized High Li^+ Conductivity MOSN MGF GSEs

Develop Preforms of MOSN MGF GSEs that do not Crystallize

Compositional development was continued to introduce nitrogen into the glasses described in previous quarterly reports. Work to further understand the glass series $0.58Li_2S + 0.42\ [(1\text{-}x)SiS_2 + xLiPO_3]$ has led to the development of a newer series of glasses that display high ionic conductivities and large working ranges. Materials up to $x = 0.4$ could be prepared as crystallization free glasses, while from $0.4 < x < 0.7$ partially crystallized glass ceramics were produced, and batches synthesized with $x > 0.7$ were fully crystallized ceramics. The $x = 0$ composition is a pure sulfide glass that is then doped with $LiPO_3$ to increase the oxygen, lithium, and phosphorous content of these glasses. Figure 61a shows that as $LiPO_3$ is incorporated into these glasses, there is an increase in the T_g, glass crystallization temperature (T_c), and working range, ΔT, at around $x = 0.2$ and then a steady decline. The maximum working range observed was ~108°C for the $x = 0.2$ composition. In addition to the change in the thermal properties, there was also a similar trend observed in the ionic conductivity. Specifically, Figure 61b shows that there is a maximum observed at $x = 0.1$ yielding a conductivity of $1.4 \cdot 10^{-3}$ S/cm, followed by minimum value at $2.0 \cdot 10^{-4}$ S/cm for the $x = 0.3$ to $x = 0.5$ glasses. These materials are promising, as they can be used to further develop and study the mixed-oxy-sulfide schema and thus further study the incorporation of nitrogen.

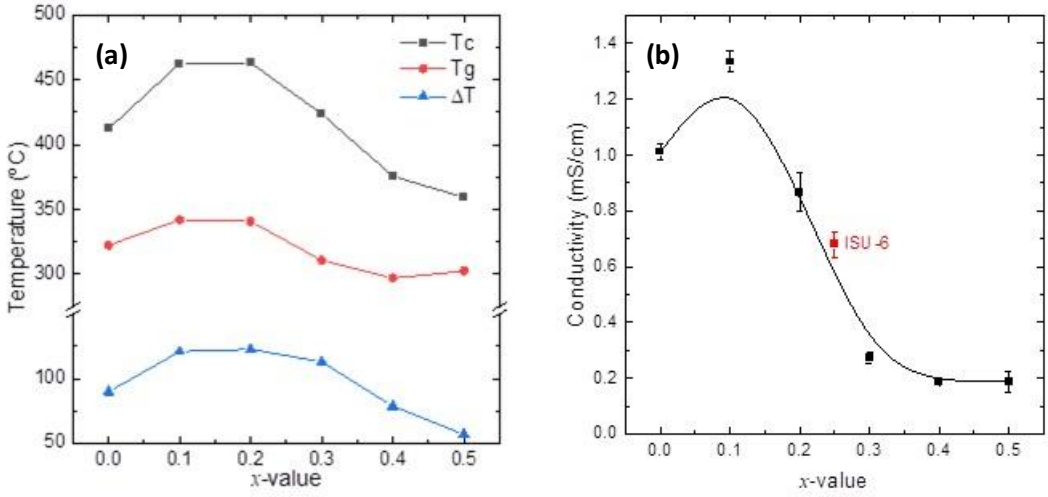

Figure 61. (a) Thermal properties of the glasses in the $0.58Li_2S + 0.42\ [(1\text{-}x)SiS_2 + xLiPO_3]$ series. (b) Conductivity of the glasses in the $0.58Li_2S + 0.42\ [(1\text{-}x)SiS_2 + xLiPO_3]$ series.

Using knowledge generated from the MGF series displayed above, work has begun to incorporate nitrogen into these glasses. Specifically, the glass composition of $x = 0.1$ was selected due to its high conductivity of > 1 mS/cm. Therefore, the composition explored is $58\ Li_2S + 37.8\ SiS_2 + 4.2[(1\text{-}y)LiPO_3 + xLiPO_{2.53}N_{0.31}]$ where $0 < y < 0.6$ and there is still potential to further incorporate more LiPON into these glasses. Figure 62a shows that T_c and ΔT decrease, while T_g increases with more nitrogen incorporation. Figure 62b shows that as more LiPON is incorporated into these glasses, the ionic conductivity reaches a minimum value at $y = 0.3$ and then increases slightly with more LiPON incorporation. Work will be continued to further synthesize and characterize these MOSN GSEs.

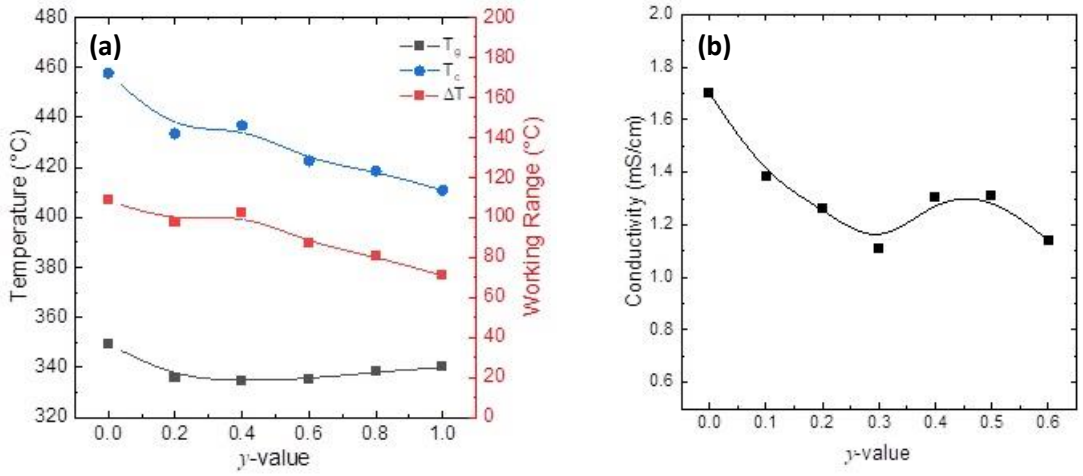

Figure 62. (a) Thermal properties of the 58 Li_2S + 37.8 SiS_2 + 4.2[(1-*y*)$LiPO_3$ + *x*$LiPO_{2.53}N_{0.31}$] glass series. (b) Conductivity of the 58 Li_2S + 37.8 SiS_2 + 4.2[(1-*y*)$LiPO_3$ + *x*$LiPO_{2.53}N_{0.31}$] glass series.

In the team's previous work, they showed that previous glass preforms demonstrated several issues while attempting to be drawn, including thermal shocking, higher viscosity, and early crystallization. As such, a new preform is in the process of being synthesized through small-scale (10 g) batches. To have the highest quality preform, rigorous testing is being conducted on each 10-g batch to confirm the chemistry and crystallization properties prior to combining the batches into one single preform. Any sample that shows poor crystallization or undesirable glass structural units will be set aside and not used for the new high quality preform. They have so far synthesized ~ 260 g of new ISU-6 glass and have begun extensive testing of the glass.

Each batch is undergoing a set of differential scanning calorimetry experiments to determine the crystallization behavior through the Johnson-Mehl-Avrami-Kolmogorov method, as discussed in previous reports. From this, a glass is considered good enough for the preform if it can withstand at least 3 hours at the draw temperature of 355°C prior to reaching 1% crystallized. Furthermore, Raman spectroscopy is being conducted on each sample. Each spectrum is being compared to an accepted spectrum for high quality ISU-6, and any deviations are noted. The common deviations that are being seen are excess sulfur found at ~ 470 cm^{-1} and the P^{1P} defect structure found at ~ 390 cm^{-1}, as can be seen in Figure 63. Batch 1 shows minimal deviation from the expected spectra, while Batch 2 shows excess sulfur, and Batch 3 shows the P^{1P} defect structure. More work is being done to determine the exact metrics to quality test each glass prior to making the full preform. The new preform will be synthesized and drawn next quarter.

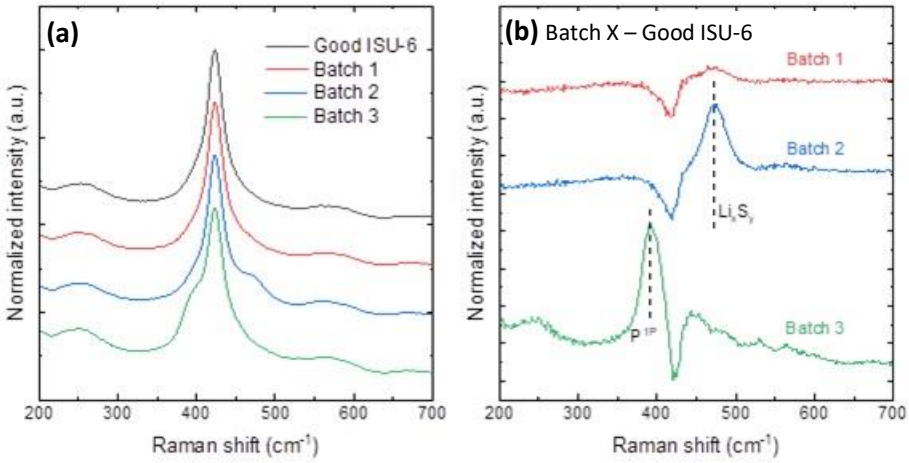

Figure 63. (a) Raman spectra of a good, accepted ISU-6 glass, along with three new synthesized samples. (b) Differential Raman spectra of the same batches where the good ISU-6 spectrum was subtracted from each batch to emphasize differences.

Develop Micro-Sheet Glass Ribbon Processing Facility for GSEs

Develop and Optimize GSE Micro-Sheet Glass Ribbon Processing Facility (Completed)

No work was done to optimize the processing facility. All effort is being concentrated on generating preforms and pulling thin films.

Develop Processing Conditions Micro-Sheet Ribbons of MOSN MGF GSEs

Complete Optimization of Draw Conditions for Optimized Mixed Oxy-Sulfide (MOS) MGF GSEs < 50 µm

It was determined that the old preform was unsuitable for drawing due to poor crystallization and viscosity behaviors, and as such, effort was put into synthesizing a new high quality preform for thin film drawing.

Fabricate and Test ASSLBs using GSEs in Large Area Planar Formats

Complete Testing of Optimized MOSN MGF GSE in Intermediate Cell Format ASSLBs

In the continued effort to develop batteries utilizing drawn-film MOS glassy electrolytes, full cells were fabricated using drop-cast cathodes via methods described by He et al.[1] A slurry was made by mixing carbon coated $LiFePO_4$, vapor grown carbon fibers, poly(vinylidene fluoride), $Li(CF_3SO_2)_2N$, and succinonitrile into 1-methyl-2-pyrrolidinone. This slurry was drop cast directly onto drawn film of ISU-6 and dried to the surface to create a cathode-electrolyte composite. Using a Li-metal foil anode, full cells were built in size 2032 coin cells. Electrochemical impedance spectroscopy and cycling data (galvanostatic cycling with potential limitation) of these cells is shown in Figure 64. The impedances of these cells remain high, but the steady cycling behavior indicates that if these interfacial resistances can be reduced, casting a slurry onto a drawn film presents itself as an efficient and scalable process for producing thin-film GSE-based full cells.

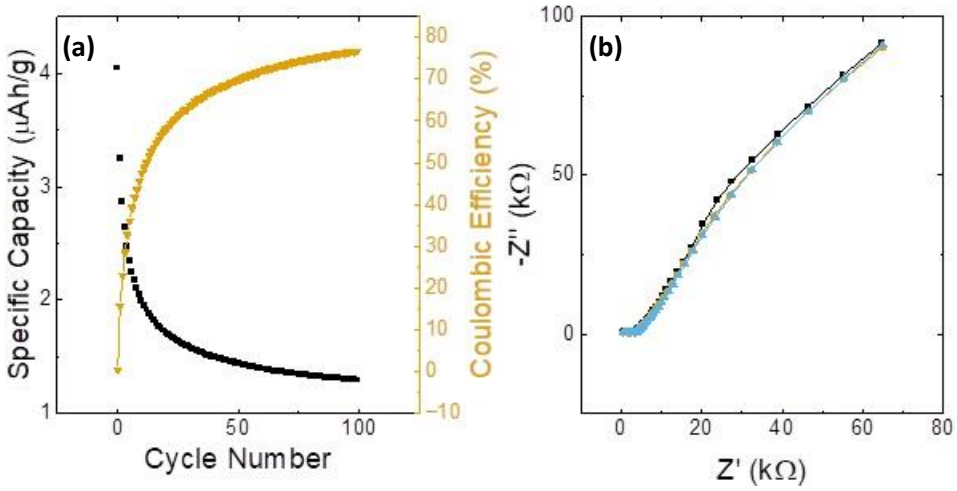

Figure 64. (a) Specific capacity and Coulombic efficiency of drop-cast full cells over 100 cycles. (b) Electrochemical impedance spectroscopy of the full cell pre-cycling.

Reference

[1] He, M., Z. Cui, F. Han, and X. Guo. "Construction of Conductive and Flexible Composite Cathodes for Room-Temperature Solid-State Lithium Batteries." *Journal of Alloys and Compounds* 762 (2018): 157–162.

Patents/Publications/Presentations

Publication

- Wheaton, J., M. Olson, V. M. Torres, and S. W. Martin. "Glassy Solid-State Electrolytes for All-Solid-State Batteries." *ACerS Bulletin* 102, No. 1 (2023): 25–31. Available online: https://ceramics.org/wp-content/uploads/2022/12/JanFeb-2023_Feature.pdf

Task 1.23 – Lithium Dendrite-Free Li_7N_2I-LiOH Solid Electrolytes for High-Energy Lithium Batteries (Chunsheng Wang, University of Maryland)

Project Objective. The objective of this project is to research, develop, and test Li-metal-based batteries that implement solid Li-ion conductors equipped with Li_7N_2I-LiOH solid electrolyte (SE) capable of achieving cell performance of 350 Wh/Kg energy density for 1000 cycle life with a cost of ≤ $100/kWh.

Impact. Lithium dendrite growth during charge/discharge cycles limits the use of all-solid-state Li-metal batteries (ASSLMBs). A criterion for lithium dendrite suppression that is developed through systematical investigation on thermodynamics and kinetics of lithium dendrite growth will guide the electrolyte design. Li_7N_2I-LiOH and Li_3YCl_6 solid-state electrolytes (SSEs) with high ionic conductivity and low electronic conductivity will be used to validate the criterion for lithium dendrite suppression, to achieve the project objective.

Approach. The team will establish the relationship among interface energy, lithium plating/stripping overpotential, interface resistance, SSE stability with lithium, and critical current density (CCD). The dendrite suppression criterion will be developed based on the relationship. The dendrite suppression capability for the Li_7N_2I-LiOH pellet will be evaluated by testing the CCD. ASSLMB will be prepared to demonstrate the overall interface stability.

Out-Year Goals. The project will refine Li_7N_2I-LiOH and Li_3YCl_6 electrolytes and fabricate Li/Li_7N_2I-LiOH/Li_2S cells and Li|Li_7N_2I-LiOH/Li_3YCl_6|NCM-811 cells to achieve 350 Wh/Kg with 1000 cycle life.

Collaborations. There are no reported collaborations this quarter.

Milestones

1. Optimize $Li_3Y(In)Cl_6$ to reach ionic conductivity of > 5×10^{-4} S/cm, anodic stability > 4.5 V. (Q1, FY 2022; Completed)
2. Develop scaffold as the supporter to fibrate < 100 µm Li_7N_2I-LiOH/$Li_3Y(In)Cl_6$ bi-layer electrolytes and evaluate the electrochemical performance of thin-film electrolyte. (Q2, FY 2022; Completed)
3. Use three-dimensional aluminum foam as a supporter to fabricate thick $LiNi_{0.8}Mn_{0.1}Co_{0.1}O_2$ (NCM-811) – $Li_3Y(In)Cl_6$ cathodes and Li_7N_2I-LiOH-Li_2S cathodes, and evaluate their electrochemical performance. (Q3, FY 2022; Completed)
4. Achieve the performance targets of a Li-metal battery (Li/Li_7N_2I-LiOH/Li_2S cells or Li|Li_7N_2I-LiOH/$Li_3Y(In)Cl_6$|NCM-811 cells) with high energy density (> 350 Wh/kg) and long cycle life of 1000. (Q4, FY 2022; In progress)

Progress Report

Designing High-Performance Cathode for Solid-State Batteries (SSBs)

To achieve the energy density target of 350 Wh/kg and cycle life of 1000 cycles, modifications for both the Li-SE interface and cathode components are required. Previously, the team reported that they built a stable Li/SE interface by introduction of a thermodynamically stable Li_7N_2I-based interlayer; more efforts are devoted to the cathode design in this report. NCM-811 is employed as the cathode active material because of its high specific capacity. The particle size of NCM-811 significantly affects performance of the SSBs. Two sizes of NMC-811 (5 µm and 10 µm, denoted as SNMC-811 and LNMC-811) were explored. NMC-811 was synthesized using a hydroxide coprecipitation method. LNMC-811 is the product after coprecipitation for 15 hours, while SNMC-811 is obtained from coprecipitation for a shorter time. As shown in the scanning electron microscopy (SEM) images in Figure 65a-b, both NMC have uniform particle size. The NMC-811 particles were mixed with Li_6PS_5Cl SE with a weight ratio of 7:3 and used as the composite cathode in the SSB. For both kinds of cells, the SSB was cycled at 0.1 C for the first three cycles, and then cycled at 0.33 C, as depicted in Figure 65c-d. For the initial cycle, as shown in Figure 65e, the SSB with LNMC-811 particles achieved an initial Coulombic efficiency (CE) of ~ 78%. In contrast, the employment of SNMC-811 particles can deliver an initial CE above 80%. In addition, the charge curve of SSB with SNMC-811 starts charging at 3.55 V, ~ 0.05 V lower than that with LNMC-811, which indicates that an SSB with SNM C-811 has smaller polarization. The 1st cycle charge/discharge capacities of the two sizes of NMC-811 are 216.6/168.8 mAh g^{-1} and 232.6/ 187.8 mAh g^{-1} at 0.1 C, respectively. The increased initial CE and initial specific capacities can be attributed to better interfacial contact between SE and SNMC-811 particles than that between SE and LNMC-811. When cycled at 0.33 C from the 4th cycle, the capacity of SSB with SNMC-811 dropped from 156.8 mAh g^{-1} to 142.7 mAh g^{-1} after 40 cycles, while that with LNMC-811 dropped from 135.1 mAh g^{-1} to 109.9 mAh g^{-1}. The capacity retentions for SNMC-811 and LNMC-811 are 91.0% and 81.3%, respectively. Electrochemical impedance spectra of both cells were recorded as shown in Figure 65f. The cell resistances for the SSB with SNMC-811 and LNMC-811 are 107.4 Ω and 129.7 Ω, respectively, which suggests small particle sizes of active particles can improve the interfacial contact inside the cathode. All these results demonstrate that the utilization of small-particle-size NMC-811 is a good choice to achieve high energy density and long cycle life for SSB.

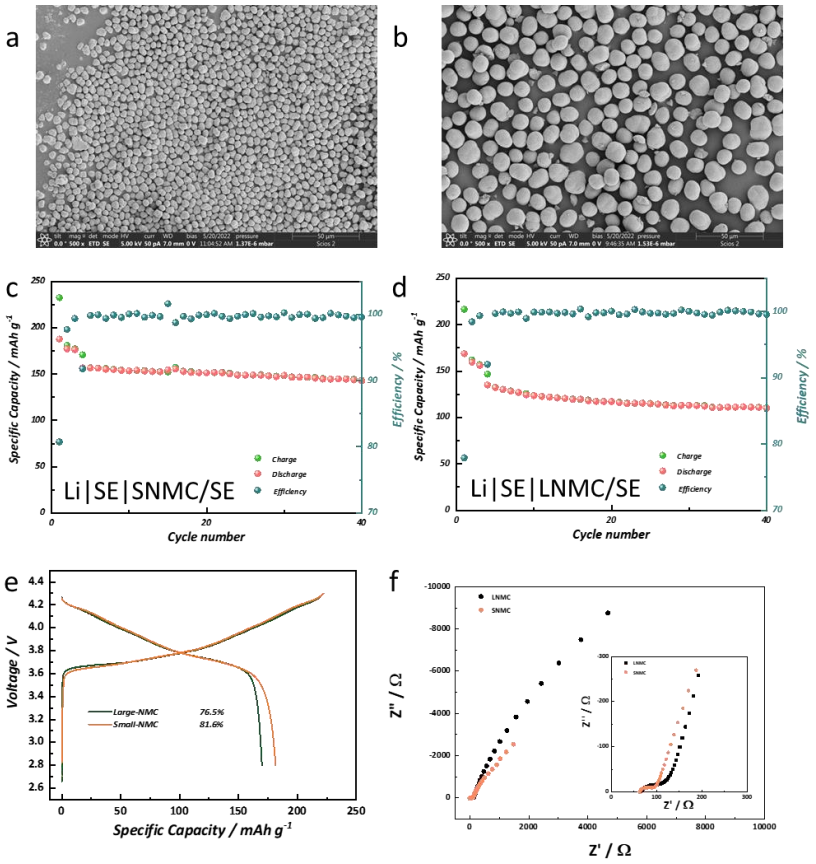

Figure 65. Scanning electron microscopy images of NMC-811 with particle size around (a) 5 µm and (b) 10 µm. (c-d) Cycle performance of the all-solid-state Li-metal cells with corresponding NMC-811 particles. (e) Initial cycle charge/discharge curves and (f) corresponding Nyquist plots of SSBs with SNCM-811 and LNCM-811.

Optimizing Thickness and Ionic Conductivity of Thin Film Electrolyte

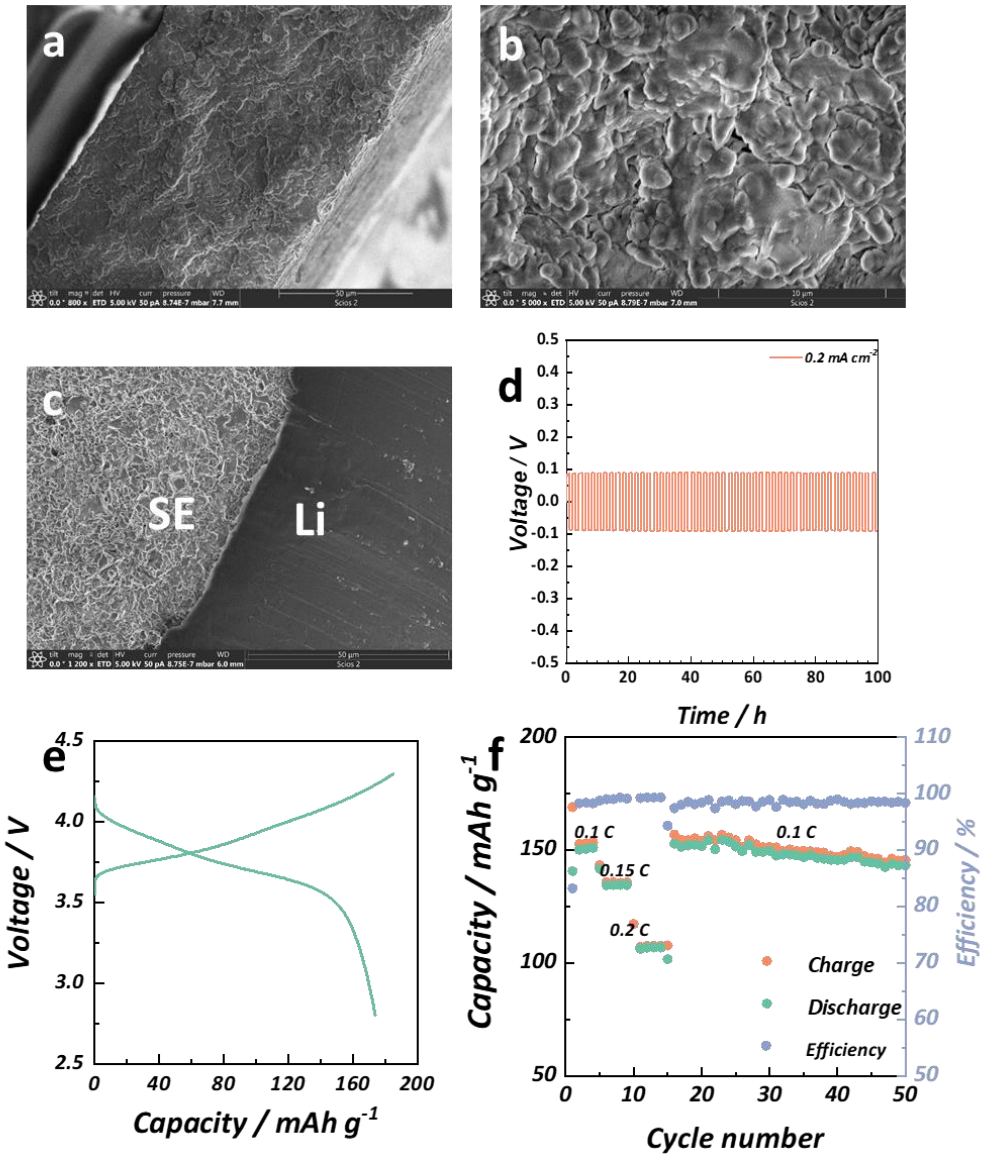

Figure 66. (a) Cross-sectional and (b) front scanning electron microscopy images of composite thin film electrolyte. (c) Cross-sectional image of interface between lithium and solid electrolyte. (d) Cycling curves of lithium symmetric cell using thin film electrolyte. (e) Charge and discharge curve of solid-state battery with thin film electrolyte at 0.1 C and (f) corresponding cycling performance.

As illustrated in the previous report, the team has realized the energy density above 250 Wh/kg for NMC-811||Li full cell, which can provide a high capacity of 7.9 mAh/cm^2 at a current density of 1 mA/cm^2 and temperature of 80°C. However, to achieve the final goal of 350 Wh/kg, the battery structure must be further modified. The thickness of the electrolyte membrane, which occupied the most weight ratio of the whole battery, needs to be reduced. Here, they successfully fabricated a thin-film electrolyte composed of Li-P-S-Cl (LPSCl) electrolyte and nitrile butadiene rubber (NBR) binder. The thickness of the thin film can be less than 100 μm by controlling the weight amount of the powder, as shown in Figure 66a. Figure 66b depicts the front SEM image of the SE film, which clearly shows that the SE particles are well connected by the NBR binder. To evaluate the electrochemical performance, the SE film was tested in the lithium symmetric cell. The SE film was first pressed at a pressure of 1.0 ton and then pressed together with lithium metal at a lower pressure to obtain a flat surface of the SE film and improve the interfacial contact between SE film and lithium. The cross-sectional image in

Figure 66c shows the intimate contact between the SE film and lithium. The cell tested at 0.2 mA cm^{-2} (Figure 66d) exhibited stable cycle performance over 100 hours, indicating the stability of the SE film. The SE film was then further evaluated in the full cell with a structure of Li|SE|NMC/SE. The cells cycled at 0.1 C, 0.15 C, and 0.2 C show a capacity of about 153 mAh g^{-1}, 135 mAh g^{-1}, and 107 mAh g^{-1} (Figure 66f), respectively. The cell cycled at 0.1 C afterward decreased from 153 mAh g^{-1} to 142 mAh g^{-1} after 50 cycles. These results demonstrated the feasibility of using NBR and LPSCl to fabricate thin-film electrolytes for high energy density. The electrochemical performance of the SE film can be further improved by reducing the thickness, incorporating high conductive SE particles, and using lithium salt to enhance the lithium mobility in the polymer binders.

Modeling Lithium Plating in SSBs

Two possibilities can lead to the short-circuit in ASSLMBs. First, lithium penetrates the pore of the electrolyte. Second, lithium nucleates inside the pore of the electrolyte driven by Li-metal overpotential. Herein, the team proposes that high interface energy could be used as an effective approach to mitigate both cases of electrolyte degradation. As shown in Figure 67a-b, lithium that penetrate into electrolytes with different interface energy are believed to have quite different behavior. Since lithium will spontaneously creep toward the tip of the crack due to capillary force, electrolytes with low interface energy against lithium will suffer from the following: stress accumulation, ion focusing effect, and Li-electrolyte reaction and electron ejection (Figure 67b). However, electrolytes with high interface energy with lithium can avoid all three effects. The team performed quantitative analysis and phase field simulations to demonstrate this idea as follows.

The detailed quantitative analysis of capillary force exerted on the deposited lithium that relates to the interfacial energy of electrolyte is shown in Figure 67c-d. The analysis is based on the relationship that increased interfacial energy due to lithium protrusion is equal to the mechanical work of the associated reaction:

$$W_{pressure} = E_{interface} \quad (1)$$

Here, the mechanical work of the associated reaction is a product of pressure, contact area (A), and protrusion length (ΔL=L2-L1):

$$W_{pressure} = Pressure \times A \times (L2 - L1) \quad (2)$$

Then, the increased interfacial energy can be expressed as

$$E_{interface} = \left(\gamma_{Li-electrolyte} - \gamma_{Li}\right) \times A \quad (3)$$

So, they establish the relationship between the reaction pressure and the diameter of the channel size.

$$Pressure = \frac{4 \times (\gamma_{Li-electrolyte} - \gamma_{Li})}{D} \quad (4)$$

Assuming a lithiophobic electrolyte with triangle-shaped defects is presented in the Li-electrolyte boundary, as shown in Figure 67d, the diameter of channel size as a function of penetration depth (d) can be expressed as

$$D = (h - d) \times 2\,tan\left(\frac{\theta}{2}\right) \sim (h - d) \times \theta \quad (5)$$

Plugging into the previous equation, they obtain the relationship between penetration depth d and capillary force F_c:

$$F_c = \frac{4 \times (\gamma_{Li-electrolyte} - \gamma_{Li})}{(h - d) \times \theta} \quad (6)$$

Here, the pressure increased with the increase of d. Therefore, they believe that high interfacial energy of electrolytes can lead to an increased capillary force that is exerted on lithium metal during lithium deposition to avoid the physical penetration of lithium across the electrolyte.

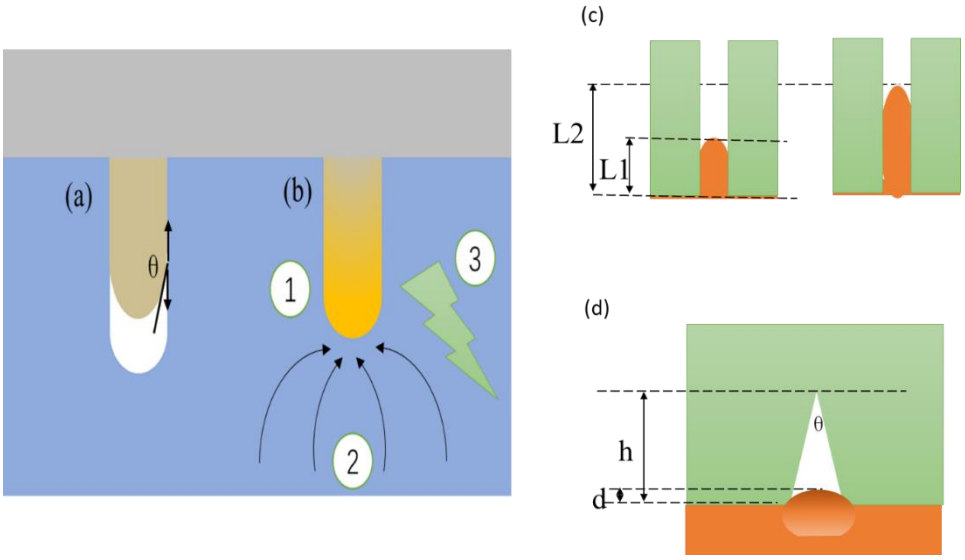

Figure 67. Schematic of lithium penetration into electrolyte with: (a) high interface energy, and (b) low interface energy. Electrolyte with low interface energy against lithium suffers from (1) stress accumulation, (2) ion focusing effect, and (3) Li-electrolyte reaction and electron ejection. (c) The quantitative analysis of capillary force exerted on lithium due to interfacial energy of electrolyte. (d) Increased capillary force during lithium penetration into lithiophobic electrolyte.

The team performs phase field simulations to investigate the influence of interfacial energy to lithium plating. To simulate lithium plating in the SSE, the total energy related to lithium plating, including chemical energy, interfacial energy, and electrochemical energy was considered in the phase field model as Eq. 7.

$$f = f_{chem} + f_{intf} + f_{elec} \quad (7)$$

The chemical energy term is formulated as a double well function.

$$f_{chem} = A * \zeta^2 * (1-\zeta)^2 + \frac{B}{2}\zeta^2 {\phi_g}^2 \quad (8)$$

Here, ζ is the phase field parameter of Li-metal phase ($\zeta = 1$ for lithium metal), and ϕ_g is the phase field parameter for electrolytes ($\phi_g = 1$ for electrolyte). A and B were the barrier height of phase transition and equal to 3.75×10^6 J m^{-3}.

The interfacial term is a function of the order parameter gradient.

$$f_{intf} = \frac{1}{2}k_\zeta(\nabla\zeta)^2 - k_{Li-grain}\sum_{g=1}^{N}\nabla\zeta\,\nabla\phi_g + \frac{1}{2}k_\phi(\nabla\phi_g)^2 \quad (9)$$

Where k_ζ and k_ϕ are the gradient coefficient associated with the surface energy of lithium metal and SE, respectively, set as 5×10^{-5} J m^{-1}. $k_{Li-grain}$ is associated with the interfacial energy between lithium metal and SE. For lithiophobic electrolyte, $k_{Li-grain}$ = 5×10^{-5} J m^{-1}; for lithiophilic electrolyte, $k_{Li-grain}$= -5×10^{-5} J m^{-1}.

The electrochemical term is related to local potential.

$$f_{elec} = F * \varphi * c_{Li+} \quad (10)$$

F is Faraday's constant, φ is the overpotential, c_{Li+} is the concentration of Li^+.

Therefore, the total energy can be expressed as:

$$f = A * \zeta^2(1-\zeta)^2 + \frac{D}{2}\zeta^2{\phi_g}^2 + \frac{1}{2}k_\zeta(\nabla\zeta)^2 - k_{Li-grain}\sum_{g=1}^{N}\nabla\zeta\,\nabla\phi_g + \frac{1}{2}k_\phi(\nabla\phi_g)^2 + F * \varphi * c_{Li+} \quad (11)$$

The governing equation for phase field model is Allen-Cahn equation.

$$\frac{\partial\zeta}{\partial t} = -L_\sigma\left(\frac{\partial f_0}{\partial\zeta} - k_\zeta\nabla^2\left(\zeta - \frac{k_{Li-grain}}{k_\zeta}\phi_g\right) - L_\eta RTh'(\zeta)\left[exp\left(\frac{(1-\alpha)F\eta}{RT}\right) - \frac{c_{Li+}}{c_0}exp\left(-\frac{\alpha F\eta}{RT}\right)\right]\right) \quad (12)$$

Here, t is time. L_σ is interfacial mobility and equal to 2.5×10^{-6} m·s kg^{-1}. f is total energy. κ is the interfacial coefficient, which will be tailored in lithium deposition. L_η is the electrochemical reaction constant and equal to 1 s^{-1}. $h(\zeta) = \zeta^3(6\zeta^2 - 15\zeta + 10)$, $h'(\zeta) = 30 \times \zeta^2(1-\zeta)^2$. α is the symmetry factor of lithium deposition/ stripping reaction and was set as 0.5. F is Faraday's constant. R is the ideal gas constant. η is the applied potential (-1 mV).

Figure 68a shows the evolution of lithium protrusion driven by interfacial energy. Initially, lithium with a triangle-shaped protrusion (red region) was set in contact with the electrolyte (blue region), representing the uneven Li-electrolyte contact. The uneven Li-electrolyte contact widely occurs in the SSB due to the presence of flaws or impurities on the surface of the electrolyte, and grain boundary with weak mechanical strength. However, the shape of lithium protrusion gradually becomes smooth after interaction with the lithiophobic electrolyte for 1 second and 5 seconds. The change of protrusion shape can significantly reduce its detrimental effect on electrolyte degradation including stress accumulation, ion focusing effect, and Li-electrolyte reaction and electron ejection. When the evolution time is 20 seconds, the interface of lithium and electrolyte becomes nearly flat. In other words, the sharpening of lithium protrusion due to the ion-focusing effect during lithium plating can be recovered by interfacial energy. Therefore, the team proposes a criterion for lithium stable plating, that is, the characteristic time of ion focusing due to privileged lithium plating on the tip should be larger than the characteristic time of the smooth effect caused by the interfacial energy. Increasing the lithiophobicity of electrolytes, reducing the size of lithium protrusion, or reducing the overpotential of lithium plating is helpful to achieve this goal. Usually, electrolytes with high lithiophobicity can withstand higher current density during lithium plating.

Figure 68b-c shows the simulated lithium growth in ionic conductive dense SSEs with high lithiophobicity or lithiophilicity. The mechanical properties of electrolytes were incorporated into this simulation. Initially, a flat lithium was set in contact with an electrolyte with a triangular flaw. The lithium plating was driven by an

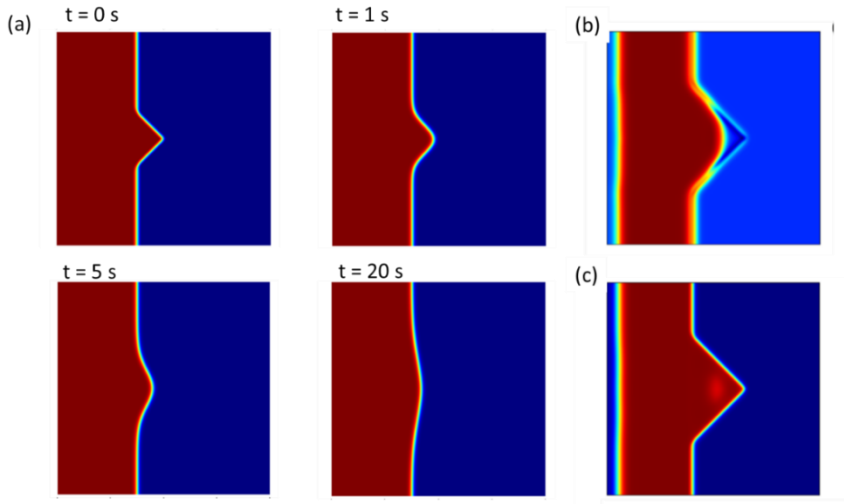

Figure 68. (a) The evolution of lithium protrusion driven by interfacial energy. Stable structure of lithium in contact with (b) lithiophobic (c) lithiophilic solid-state electrolyte during lithium plating. The red color represents the lithium metal. The blue region represents the electrolyte.

overpotential of 1 mV at the anode side. For lithium to grow in lithiophobic electrolyte, the pressure due to lithium plating pushes lithium anode toward the flaw of the electrolyte. However, the more lithium penetrates the flaw, the larger the capacity force from the electrolyte will be created to balance the force due to lithium plating. As a result, lithium growth was mechanically suppressed by the lithiophobic interlayer even if the flaws exist in the lithiophobic electrolyte surface (Figure 68b). The equilibrium penetration depth is a function of electrolyte lithiophobicity and lithium plating overpotential (Figure 67d). Therefore, the capillary force from lithiophobic electrolytes can help to avoid lithium dendrite penetration. In contrast, when lithium plates at a lithiophilic electrolyte, the capillary force cannot avoid promoting penetration of the lithium dendrite. As shown in Figure 68c, lithium easily penetrates into the flaw of lithiophilic electrolytes and keeps intimate contact with electrolytes at flaw tips. The presence of lithium inside the flaw of a lithiophilic electrolyte will further change the lithium diffusion pathway, which not only enhances the tips-focusing effects of Li^+ diffusion, but also boosts the Li-electrolyte reaction. Both will boost lithium dendrite growth.

Patents/Publications/Presentations

The project has no patents, publications, or presentations to report this quarter.

TASK 2 – ADVANCED DIAGNOSTICS

Team Lead: Guoying Chen, Lawrence Berkeley National Laboratory

Summary

To meet the goals of the Vehicle Technologies Office programs on next-generation electric vehicles, low-cost and abuse-tolerant batteries with higher energy density, higher power density, better safety, and longer lifetimes are needed. In pursuit of these goals, high cell operating voltages and demanding cycling conditions are used, which leads to unprecedented chemical and mechanical instabilities in cell components. Successful implementation of promising electrode materials (such as silicon anode and high-voltage cathodes) and new cell chemistry (such as high-energy Li-metal cells combined with solid-state electrolytes, or SSEs) requires better understanding of fundamental processes, especially those at the interface/interphase of both anode and cathode. Identifying and understanding structure-property-electrochemical performance relationships in materials and various failure modes in cell chemistry are therefore more pressing than ever, not only in guiding battery development activities but also the scale-up efforts needed for commercialization.

Task 2 takes on these challenges by combining model systems—*ex situ*, *in situ*, and *operando* approaches—with an array of state-of-the-art analytical and computational tools. Numerous subtasks are tackling the chemical processes and reactions at the electrode/electrolyte interfaces in Li-metal batteries. Researchers at Lawrence Berkeley National Laboratory (LBNL) use surface- and bulk-sensitive techniques, including Fourier transform infrared (FTIR), attenuated total reflectance – FTIR, near-field infrared and Raman spectroscopy/microscopy, and scanning probe microscopy to characterize changes in materials and the physio-chemical phenomena occurring at the interface of Li-metal electrode. General Motors is developing *in situ* diagnostic techniques, including atomic force microscopy (AFM), nano-indentor, dilatometer, and stress-sensor, to be combined with atomic/continuum modeling schemes to investigate the coupled mechanical/chemical degradation of the solid electrolyte interphase (SEI) layer as well as the microstructural evolution at the interface/interphase of Li-metal anode. Argonne National Laboratory aims to develop high-conductivity ceramic electrolytes through cation doping and to identify mechanistic barriers that limit chemical, mechanical, and electrochemical durability of solid/solid interfaces. University of Houston (UH) is developing multidimensional diagnostic tools, including focused ion beam – scanning electron microscopy (SEM), time-of-flight secondary ion mass spectrometry (TOF-SIMS), and *in situ* SEM nanoindentation, to probe structural, chemical, and mechanical evolution at the interfaces of solid-state lithium batteries. At LBNL, model systems of electrode, SSE, and their interfaces with well-defined physical attributes are being developed and used for advanced diagnostic and mechanistic studies at both bulk and single-particle levels. These controlled studies remove the ambiguity in correlating a material's physical properties and reaction mechanisms to its performance and stability, which is critical for further optimization. Subtasks at Brookhaven National Laboratory (BNL) and Pacific Northwest National Laboratory (PNNL) focus on the understanding of fading mechanisms in electrode materials, with the help of synchrotron-based X-ray techniques (diffraction and hard/soft X-ray absorption) at BNL and high-resolution transmission electron microscopy / scanning transmission electron microscopy and related spectroscopy techniques at PNNL. The final subtask at Stanford / SLAC National Accelerator Laboratory develops and utilizes an integrated X-ray characterization toolkit to investigate and generate insights on solid-state batteries (SSBs), by tracking the evolution of nanoscale chemistry as well as structure, microstructure, and transport properties. The diagnostics team not only produces a wealth of knowledge key to developing next-generation batteries, but they also advance analytical techniques and instrumentation with a far-reaching effect on material and device development in various fields.

Highlights

The highlights for this quarter are as follows:

- The UH group (Y. Yao) developed a diagnostics platform combining TOF-SIMS with AFM to investigate the effect of chemo-mechanical coupling in SSBs. The technique is capable of simultaneously monitoring chemical, morphological, and mechanical evolution with a high spatial resolution and an ultra-low detection limit.
- The PNNL group (C. Wang) corroborated electrochemistry of lithium stripping with the morphological evolution features of the Li/SEI layer at low current densities. The study reveals that preferential lithium stripping leads to formation of localized SEI layers, which interrupts electron pathways and consequently induces formation of isolated lithium.

Task 2.1 – Characterization and Modeling of Lithium-Metal Batteries: Model-System Synthesis and Advanced Characterization
(Guoying Chen, Lawrence Berkeley National Laboratory)

Project Objective. This project will use a rational, non-empirical approach to design and develop solid-state electrolyte (SSE) materials and interfaces for next-generation Li-metal batteries. Combining a suite of advanced diagnostic techniques with carefully prepared model-system samples, the project will perform systematic studies to achieve the following goals: (1) obtain understanding on the role of SSE grain and grain boundaries (GBs) on ion conduction and dendrite formation, (2) obtain fundamental knowledge on rate-limiting and stability-limiting properties and processes in SSEs when used in Li-metal batteries, (3) investigate reactivities between SSE and electrodes, and gain insights on the dynamic evolution of the interfaces, and (4) design and synthesize improved SSE materials and interfaces for safer and more stable high-energy Li-metal batteries.

Impact. The project will focus on fundamental understanding of SSE and relevant interfaces to enable its use in Li-metal batteries. Knowledge gathered from model-system-based studies will guide the design and engineering of advanced materials and interfaces. The use of the non-empirical, rational-design approach will develop high-energy battery systems with improved commercial viability.

Approach. The project will combine model-system synthesis and advanced diagnostic studies to investigate ion conduction and interfacial chemistry of SSE in Li-metal batteries. Single crystalline, polycrystalline, and amorphous model SSE samples with various grain and GB properties will be synthesized. Model interfaces between the SSE and electrodes with controlled properties will also be developed. Both bulk-level and single-grain-level characterization will be performed. Global properties and performance of the samples will be established from the bulk analyses, while the single-grain-based studies will utilize time-resolved and spatially-resolved analytical techniques to probe the intrinsic redox transformation processes and failure mechanisms under battery operating conditions.

Out-Year Goals. The project will deliver fundamental knowledge on the role of SSE microstructure in Li^+ conduction and lithium dendrite formation/propagation. Insights on performance-limiting physical properties and phase transition mechanisms as well as dynamic evolution of SSE/electrode interfaces will be obtained. Mitigating approaches, such as use of surface coating or a "buffer layer" in stabilizing SSE/electrode interfaces, will be evaluated. Further, advanced SSE materials and interfaces for improved high-energy Li-metal batteries will be designed and synthesized.

Collaborations. This project collaborates with the following principal investigators: G. Ceder, K. Persson, M. M. Doeff, B. McCloskey, R. Kostecki, and R. Prasher (Lawrence Berkeley National Laboratory); W. Yang (Advanced Light Source); D. Nordlund and Y. Liu (Stanford Synchrotron Radiation Lightsource); C. Wang (Pacific Northwest National Laboratory); and J. Nanda (SLAC National Accelerator Laboratory).

Milestones

1. Complete comparative studies of all-solid-state battery (ASSB) anode interfacial reactivities between halide solid electrolyte (SE) and Li/In alloy versus lithium metal. (Q1, FY 2023; Completed)
2. Obtain mechanistic understanding and develop strategies to mitigate reactivities at the anode interface. (Q2, FY 2023; On schedule)
3. Investigate at least two approaches to stabilize the interface between halide SE and Li-metal based anode. (Q3, FY 2023; On schedule)
4. Develop and evaluate performance of ASSB cells with the modified anode interface. (Q4, FY 2023; On schedule)

Progress Report

While Li_3MCl_6-family halide SEs have been shown to have good stability toward 4-V-class cathode materials, their thermodynamic instability toward Li-metal anode remains a significant challenge. Theory studies indicate that on direct contact with lithium metal, Li_3YCl_6 (LYC) decomposes to LiCl, YCl_3, and metallic yttrium, leading to dendrite growth, internal shorting, and safety issues. To experimentally evaluate the reactivities at the anode-electrolyte interface, the team carried out comparative studies of LYC SE interfacing a Li-metal anode versus a Li-In alloy (3:7 molar ratio) anode. Li|LYC|Li and Li-In|LYC|Li-In symmetrical cells were assembled and galvanostatically charged and discharged at a current density of 0.2 mA/cm^2. As shown in Figure 69a, the lithium cell experienced a gradual increase in potential during the first 12 cycles, reaching ~ 150 mV after 25 hours. Following that, the potential gradually decreased and reached ~ 2 mV after 60 hours, which remained constant afterwards. The electrochemical results suggest rapid reactions at the LYC/Li interface, which was followed by cell internal shorting. Further evidence is shown by the scanning electron microscopy (SEM) image collected on the anode electrolyte interphase (AEI) region of the recovered LYC SE pellet where a large amount of black deposits is clearly present (Figure 69b). While the X-ray diffraction (XRD) pattern of the same sample (Figure 69c) is dominated by LYC peaks, LiCl was found to be the main decomposition product in the AEI. Due to the poor detection limit of XRD, it is unclear whether metallic yttrium was also present.

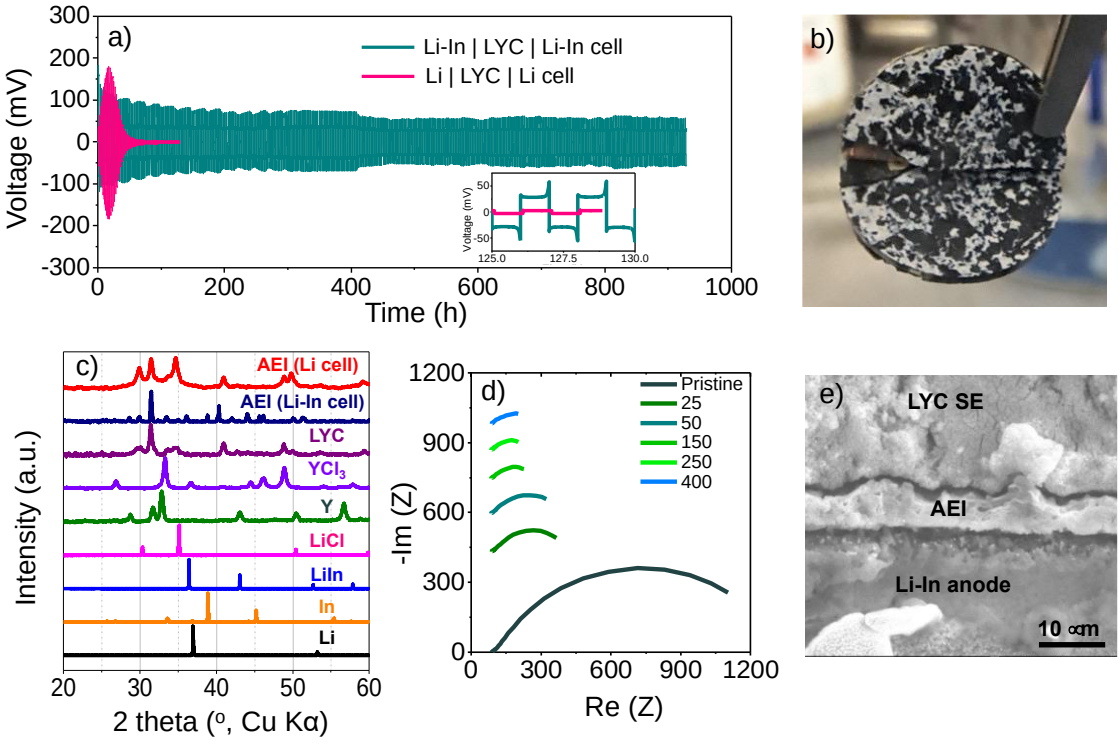

Figure 69. (a) Voltage profiles of Li|LYC|Li and Li-In|LYC|Li-In symmetrical cells when cycled at a constant current density of 0.2 mA/cm^2. (b) Scanning electron microscopy (SEM) image collected from the recovered anode electrolyte interphase (AEI) region of the cycled Li|LYC|Li cell. (c) X-ray diffraction patterns collected on various samples as indicated. (d) Electrochemical impedance spectroscopy data collected at the open circuit voltage of the Li-In|LYC|Li-In cell after various cycles, in the frequency range of 1 MHz – 100 mHz. (e) Cross-sectional SEM image collected from the recovered AEI region of the cycled Li-In|LYC|Li-In cell.

In comparison, the voltage response of the Li-In symmetrical cell is also shown in Figure 69a. At 0.2 mA/cm^2, the cell quickly reached a constant voltage of ~ 35 mV during both charge and discharge. The potential increased slightly at the end of each step, reaching ~ 50 mV. However, the process is highly reversible and stable cycling

was maintained throughout the test, suggesting the presence of a passivating AEI between LYC and the Li-In alloy anode. The team further performed electrochemical impedance spectroscopy (EIS) to monitor the evolution of the AEI during cycling. The data were collected at the open circuit voltage after various cycles, using a constant voltage of 10 mV. As shown in the Nyquist plot (Figure 69d), a depressed semi-circle was obtained from the pristine Li-In|LYC|Li-In cell. The size of the semi-circle decreased quickly on initial cycling, then stabilized and remained constant during the rest of cell testing, confirming the formation of a stable AEI following the initial reactions between LYC and Li-In in early cycles. In contrast, the impedance responses from the lithium symmetrical cell were largely unstable, especially after 50 hours; EIS data were not collectable due to the internal shorting in the cell.

Figure 69e shows the cross-sectional SEM image collected on the recovered interface region of LYC and the Li-In anode. After ~ 460 cycles, the presence of an AEI layer with an average thickness of ~ 8-10 μm is clearly shown. A comparison of the XRD patterns collected at the AEI regions of LYC/Li and LYC/Li-In (Figure 69c) shows significant differences in reaction products. Further chemical and structural analysis of the AEI formed between LYC and Li-In alloy is under way; results will be presented in a future report.

Patents/Publications/Presentations

Publication

- Kim, S. Y., H. Cha, R. Kostecki, and G. Chen. "Composite Cathode Design for High-Energy All-Solid-State Lithium Batteries with Long Cycle Life." *ACS Energy Letters* 8, No. 521 (2023). https://doi.org/10.1021/acsenergylett.2c02414.

Presentation

- 242nd Electrochemical Society Meeting, Atlanta, Georgia (October 2022): G. Chen. Invited.

Task 2.2 – Interfacial Processes – Diagnostics
(Robert Kostecki, Lawrence Berkeley National Laboratory)

Project Objective. The project objective is to establish specific design rules toward the next generation of low-impedance Li-metal rechargeable batteries that are capable of performing 1000 deep discharge cycles at Coulombic efficiency > 99.9% and suppressing lithium dendrite formation at high current densities (> 2 mA/cm^2). This project aims at the following: (1) establishing general rules between Li^+ transport properties in novel liquid/solid electrolytes, and (2) determining the mechanism of the solid electrolyte interphase (SEI) layer (re)formation. The other goal is development and application of far- and near-field optical probes and synchrotron-based advanced X-ray techniques to obtain insight into the mechanism of Li^+ transport and interfacial reactions in lithium/liquid model systems. Through an integrated synthesis, characterization, and electrochemistry effort, this project aims to develop a better understanding of lithium / liquid electrolyte (LE) interface so that rational decisions can be made as to their further development into commercially viable Li-metal cells.

Project Impact. Chemical instability and high impedance at the interface of Li-metal electrodes limit electrochemical performance of high-energy-density batteries. A better understanding of the underlying principles that govern these phenomena is inextricably linked with successful implementation of high-energy-density materials in Li-metal-based cells for plug-in hybrid electric vehicles (PHEVs) and electric vehicles (EVs). New state-of-the-art techniques to identify, characterize, and monitor changes in materials structure and composition that take place during battery operation and/or storage will be developed and made available to BMR participants. The work constitutes an integral part of the concerted effort within the BMR Program, and it supports development of new electrode materials for high-energy, Li-metal-based rechargeable cells.

Approach. Pristine and cycled composite electrode and model thin-film electrodes will be probed using various surface- and bulk-sensitive techniques, including Fourier transform infrared (FTIR), attenuated total reflectance (ATR) – FTIR, near-field infrared and Raman spectroscopy/microscopy, and scanning probe microscopy to identify and characterize changes in materials structure and composition. Novel *in situ / ex situ* far- and near-field optical multifunctional probes in combination with standard electrochemical and analytical techniques are developed to unveil the structure and reactivity at interfaces and interphases that determine electrochemical performance and failure modes of materials.

Out-Year Goals. In the out-years, the project aims to achieve the following: (1) understand factors that control performance and degradation processes, (2) unveil structure and reactivity at hidden or buried interfaces and interphases that determine electrochemical performance and failure modes, and (3) propose effective remedies to address inadequate Li-metal-based battery calendar/cycle lifetimes for PHEV and EV applications.

Collaborations. Diagnostic studies will be carried out in sync with other diagnosticians (that is, G. Chen, B. McCloskey, R. Prasher, and L-W. Wang) and theory/computational scientists (that is, G. Ceder and K. Persson).

Milestones

1. Optimize Li-metal sample preparation to enable surface nanoscale characterization of the passivation layer. (Q1, FY 2023)
2. Optimize fabrication of a buried graphene-LE interface compatible with the *in situ* cell developed in FY 2022. (Q2, FY 2023)

3. Collect biased nano-FTIR data from Li-metal/electrolyte interface. (Q3, FY 2023)
4. Observe the changes in SEI layer of lithium at different stages of cell operation. (Q4, FY 2023)

Progress Report

This quarter, the team focused attention on efforts establishing a sample preparation protocol for studying the SEI on lithium metal created by interaction with GEN 2 electrolyte (ethylene carbonate / ethyl methyl carbonate, or EC/EMC, 1.2 M $LiPF_6$) with nano-FTIR spectroscopy. In the experiment, they used their unique approach to create a clean lithium surface that was developed last fiscal year. The process is illustrated in Figure 70. Briefly, a piece of lithium metal was cut out of cleaned lithium rod in a solvent-free glovebox via razorblade wrapped in Celgard®. The choice of Celgard® is explained by its presence as a separator in many battery systems; therefore, this will introduce minimum contaminants. Then, lithium metal was rolled between two plastic plates wrapped in Celgard®. In this way, they reproducibly obtained shiny metallic lithium surfaces, as can be seen in Figure 70 (left). Lastly, they transferred the prepared lithium surface in a sealed bag into the glovebox containing the electrolyte.

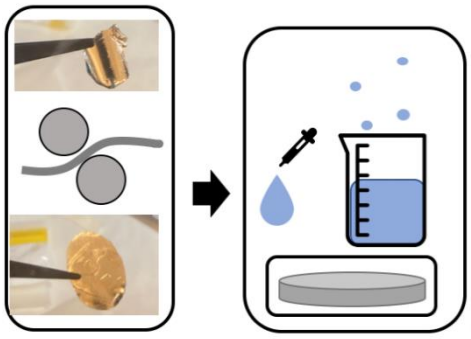

Figure 70. Schematic of process for creating clean lithium surfaces to enable studying reactions between lithium and Gen 2 electrolyte.

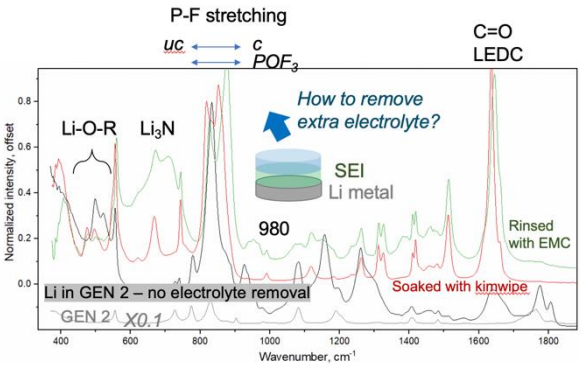

Figure 71. Attenuated total reflectance – Fourier transform infrared spectra of Li-metal surface reacted with GEN2 with electrolyte removed by (black) drying (red) soaking Kim wipe with excess of electrolyte (green) rinsing with 30 µL EMC (grey) spectrum of Gen 2 electrolyte dried on copper.

It is important to note that on the surface of lithium metal, together with the products of reaction between lithium metal and Gen 2 electrolyte, there is often excess electrolyte present. In such a case, the decomposition products are buried under the excess electrolyte, making it challenging to study them. ATR-FTIR spectra of lithium after interacting with GEN 2, where electrolyte was dried under low vacuum (glovebox antechamber), contain a mix of electrolyte and lithium ethylene dicarbonate (LEDC). Strong EC peaks indicate a significant presence of EC on the surface. Surprisingly, EMC peaks were observed, which corresponds to the known phenomena of electrolyte trapping inside the SEI layer. In the literature, the most common method of getting rid of electrolyte is washing with organic solvents with similar properties to the electrolyte.

Thus, the team performed systematic attempts at washing the surface to remove excess electrolyte without complete removal of SEI components. A good indication of that is the presence of a peak at ~ 1650 cm^{-1}, which is a C=O vibration of LEDC. EC and EMC, whether coordinated or not, show the C=O vibration at ~ 1800 cm^{-1}. Furthermore, in the lower frequency region, Li-O bonds could be found that are not present in dried electrolyte. They have found that 30 µL of EMC preserves LEDC; however, the rise of a broad peak at ~ 700 cm^{-1} shows the growth of Li_3N, a product of reaction between lithium metal and the N_2 atmosphere, where the ATR-FTIR instrument is located. This is an indication of removing too much of the SEI, disrupting the passivation layer. On the other hand, when the electrolyte is removed with a Kimwipe™ (gently soaked from the surface), the peaks of SEI components are present and no peaks of EC/EMC are observed. Therefore, they went with this method to prepare samples for nano-FTIR.

On the microscale, an iridescent film was found on top of the Li-metal surface. When attempting to perform non-contact atomic force microscopy (AFM) measurements, the tip was contaminated, indicating that loosely bound particles of electrolyte, or its organic decomposition products, are being scratched from the surface. In the spot with no iridescent film, it was possible to collect AFM topography (Figure 72c) and a corresponding white light (WL) image. The WL image shows a distribution of near-field FTIR reflection, which could be correlated with electronic density of the material. The area appears to be uniformly covered with a film possessing a peak at 834 cm^{-1} (Figure 72e), which is attributed to P-F vibration. The absence of any other peaks is an indication of insufficient electrolyte removal, which brought them to investigate the effect of drying Li-metal surface post electrolyte removal.

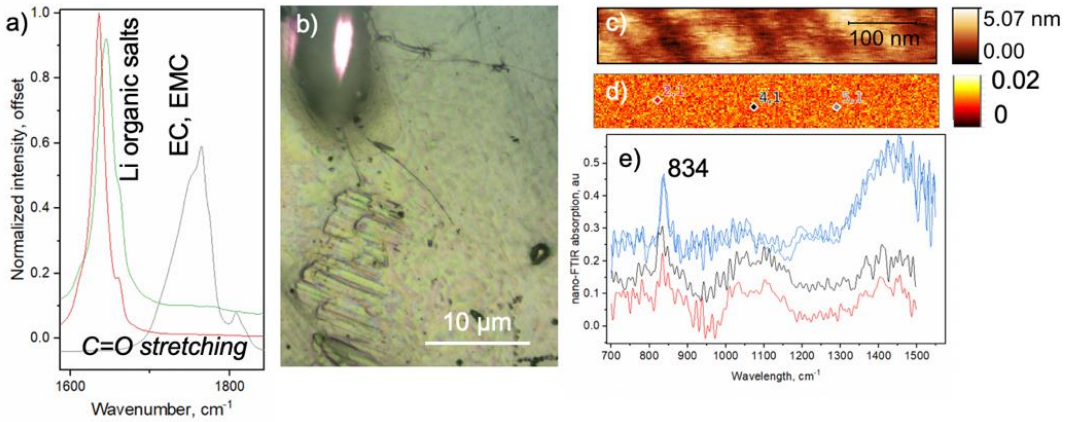

Figure 72. Characterization of dried lithium surface after reaction with Gen 2 electrolyte. (a) Attenuated total reflectance – Fourier transform infrared (FTIR) spectra C=O region of differently dried samples: both Kimwipe™ and rinsing removed EC and EMC on macro scale. (b) Optical image of lithium surface after drying electrolyte with Kimwipe™. (c) Atomic force microscopy topography image of lithium surface NOT covered by iridescent film. (d) White light image corresponding to (c). (e) Nano-FTIR spectra from three locations on the sample.

After prolonged drying under low vacuum (10^{-3} Torr, 48 hours), ATR-FTIR spectra of the lithium surface, after reacting with Gen 2, look identical. However, on the microscale, the lithium surface does not have the same iridescent film previously observed. The AFM topography measurements reveal a surface structure of a collection of quasi-spherical particles with sizes that range from ~ 50-300 nm (Figure 73c). WL imaging shows nanoscale heterogeneities in infrared reflectivity. The WL image is correlated with the topography image. The nano-FTIR spectra reveal broad features in the 830-890 cm^{-1} region, indicating the presence of P-F or POF_3 vibrations in various degrees of coordination.

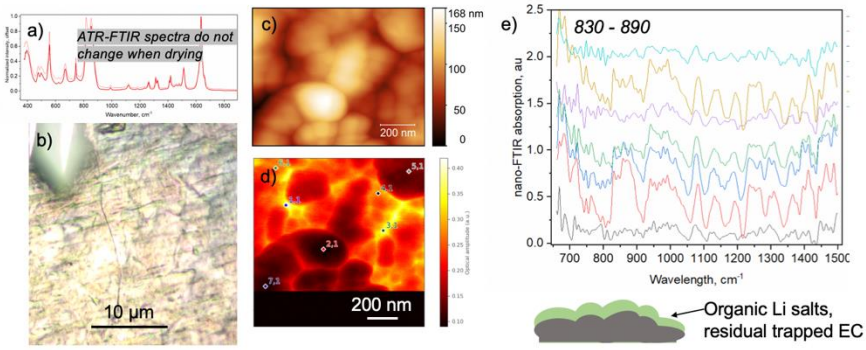

Figure 73. Characterization of a lithium surface after reaction with Gen 2 electrolyte: effect of vacuum drying. (a) Attenuated total reflectance – Fourier transform infrared (FTIR) spectra of lithium sample after 30 minutes of drying and 48 hours of drying under vacuum. (b) Optical image of the lithium surface after drying electrolyte with Kimwipe™ and drying for 48 hours under vacuum. (c) Atomic force microscopy topography image of the lithium surface after reaction with Gen 2. (d) White light image corresponding to (c). (e) Nano-FTIR spectra from seven locations on the sample.

The uncovered sample preparation protocols, which are invaluable at preserving the SEI structure and chemistry, will be employed on forthcoming *ex situ* lithium electrodes post cycling.

Patents/Publications/Presentations

The project has no patents, publications, or presentations to report this quarter.

Task 2.3 – Advanced *In Situ* Diagnostic Techniques for Battery Materials (Xiao-Qing Yang and Enyuan Hu, Brookhaven National Laboratory)

Project Objective. The primary objective of this project is to develop new advanced *in situ* material characterization techniques and to apply these techniques to support development of new cathode and anode materials with high energy and power density, low cost, good abuse tolerance, and long calendar and cycle life for beyond Li-ion battery systems to power plug-in hybrid electric vehicles (PHEVs) and battery electric vehicles. The diagnostic studies will focus on issues relating to capacity retention, thermal stability, cycle life, and rate capability of beyond Li-ion battery systems.

Project Impact. The Vehicle Technologies Office Multi-Year Program Plan describes the goals for battery: "Specifically, lower-cost, abuse-tolerant batteries with higher energy density, higher power, better low-temperature operation, and longer lifetimes are needed for development of the next-generation of HEVs [hybrid electric vehicles], PHEVs, and EVs [electric vehicles]." The results of this project will be used for development of technologies that will significantly increase energy density and cycle life and will reduce cost. This will greatly accelerate deployment of EVs and reduce carbon emission associated with fossil fuel consumption.

Approach. This project will use a combination of synchrotron X-ray diffraction and pair distribution function and of neutron diffraction and pair distribution function; X-ray spectroscopies including hard/soft X-ray absorption spectroscopy (XAS), X-ray photon emission spectroscopy; and imaging techniques including X-ray fluorescence microscopy, transmission X-ray microscopy (TXM), and transmission electron microscopy.

Out-Year Goals. The out-year goals are to develop spectro-tomography, X-ray diffraction, XAS, and pair distribution function (PDF) techniques, and to apply these techniques on Li-ion battery cathode, and beyond Li-ion batteries including lithium metal, Na-ion, and solid-state batteries.

Collaborations. The Brookhaven National Laboratory team will work closely with Pacific Northwest National Laboratory for the S-based cathode and Li-metal anode materials. This project will also collaborate with industrial partners, as well as with international collaborators.

Milestones

1. Complete PDF studies of the amorphous components in solid electrolyte interphase (SEI) for Cu||Li, Ni-Mn-Co (NMC) || Li, and NMC||Cu cells using low-concentration 1 M lithium bis(fluorosulfonyl) imide (LiFSI) in 1,2 dimethoxyethane (DME) electrolyte. (Q1, FY 2023; Completed)
2. Complete studies of sulfur mapping on Li-metal anode (in NMC||Li cell using LiFSI-based electrolyte) to understand spatial distribution of interphase species in SEI. (Q2, FY 2023)
3. Complete the study of the beam damage phenomenon in *in situ* TXM experiment of NMC||Li coin cells and its implications on data analysis. (Q3, FY 2023)
4. Complete the study of mitigating beam damage for *in situ* TXM experiment of NMC||Li cells by manipulating the cell configurations. (Q4, FY 2023)

Progress Report

This quarter, the first milestone was successfully completed. The team used PDF to characterize the SEI on Li/Cu in Cu||Li, NMC||Li, and NMC||Cu cells. The electrolyte used is 1M LiFSI in DME. PDF probes both the crystalline and amorphous phases, and the peaks correspond to atomic pairs that can be either chemical bonds or two indirectly-connected atoms. The left panel of Figure 74 shows measured PDF of SEI from Cu||Li cells, with the calculated PDF patterns of possible SEI components also shown for data analysis. It clearly indicates that the SEIs on copper foil and on lithium foil have basically the same crystalline and amorphous components. The only difference is the residue copper that was accidentally introduced into SEI during sample collection. The first peak in the blue region corresponds to carbon-based bonds that are relatively short. These include C=O bond in Li_2CO_3 and C-O and C-O bond in DME oligomers. The second peak in the blue region corresponds to S-based bonds that are longer than the carbon-based bonds. These include S-F, S-N, and S-O in the chemical species resulting from FSI^- anion decomposition. For example, it could be $Li_2(FSI_{(-F)})_2$ (-F means one fluorine atom is lost from FSI^-). The first peak in the red region corresponds to the Li-O bond that can only be originated from inorganic SEI components such as Li_2O, LiF, Li_2CO_3, and LiOH. Because of its uniqueness, this peak is a good indication of the relative content of inorganic species in the SEI. The second peak in the red region corresponds to the indirect O-O pair in the CO_3^{2-} motif, which is from Li_2CO_3. It can be concluded that 1 M LiFSI in DME electrolyte is not fully stable on lithium or copper electrode. It can decompose, leading to the SEI having a similar amount of organic and inorganic species. LiFSI is very likely decomposed during the process. While SEI components are the same for lithium and copper in Cu||Li cells, they are quite different in Li||NMC and Cu||NMC cells, which is indicated by the center panel and right panel in Figure 74. In Li||NMC cells, the SEI on lithium foil has large amount of organic species resulting from anion decomposition, which is indicated by the dominant peak in the blue region. The amount of inorganic species, which is indicated by the peak in the red region, is relatively small. In Cu||NMC cells, the organic species in SEI come from decompositions of both solvents and anions. In contrast to the SEI on lithium foil in Li||NMC cells, the SEI on copper foil in Cu||NMC is dominated by inorganic species, which is indicated by the strong peak in the red region. This study demonstrates PDF is capable of probing both crystalline and amorphous phases in SEI, revealing the relative content of organics from solvent decomposition, organics from anion decomposition, and overall inorganics.

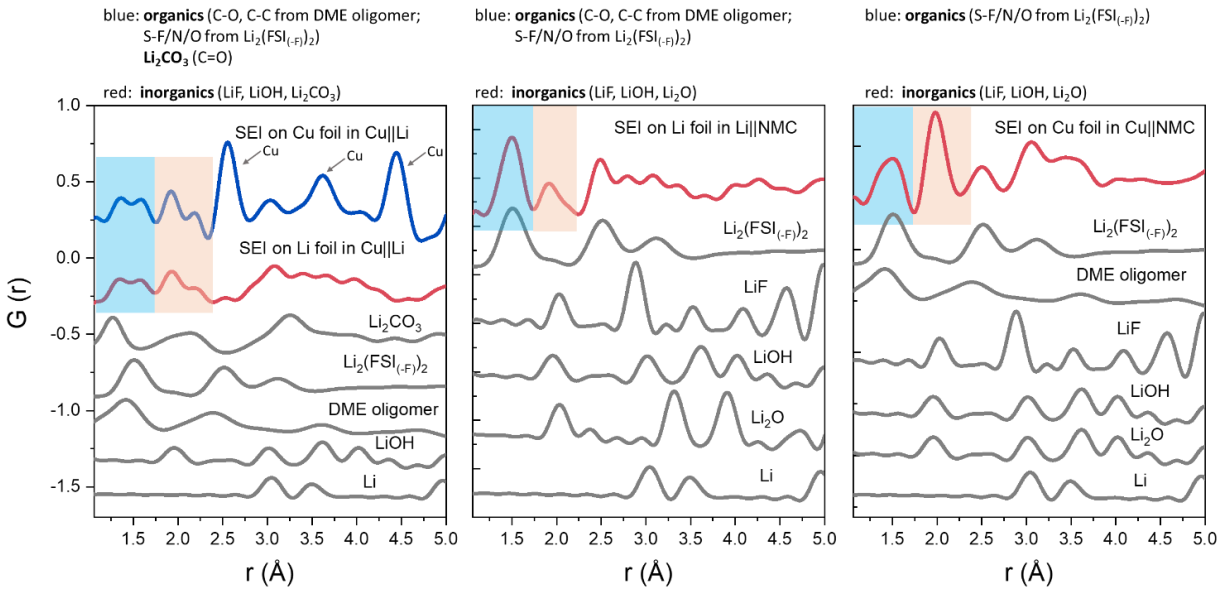

Figure 74. (left) Measured pair distribution function (PDF) data of SEIs on copper foil and on lithium foil in Cu||Li cells. (center) PDF data of SEI on lithium foil in Li||NMC cells. (right) PDF data of SEI on copper foil in Cu||NMC cells. Calculated PDF patterns of possible SEI components are also shown for data analysis.

Patents/Publications/Presentations

The project has no patents, publications, or presentations to report this quarter.

Task 2.4 – Probing Interfacial Processes Controlled Electrode Stability in Rechargeable Batteries (Chongmin Wang, Pacific Northwest National Laboratory)

Project Objective. The main objective is to explore interfacial phenomena in rechargeable Li-ion batteries of both solid-state electrolyte (SSE) and liquid electrolyte (LE) configuration to identify the critical parameters that control the stability of interface and electrodes as well as solid electrolyte (SE). The outcome will be establishing correlations between structural-chemical evolution of active components of batteries and their properties. These correlations will provide insight and guidance to battery materials development groups for developing high-performance battery materials.

Project Impact. The proposed characterization work focuses on atomic-level structural and chemical analysis and direct correlation with battery fading properties. The work can be directly used to guide design of electrode materials with tailored microstructure and chemistry for enhanced properties of increasing the energy density of Li-ion batteries and to accelerate market acceptance of electric vehicles (EVs), especially for plug-in hybrid electric vehicles as required by the EV Everywhere Grand Challenge.

Approach. The project will use integrated advanced microscopic and spectroscopic techniques, including *in situ* and *ex situ* scanning transmission electron microscopy (STEM), environmental STEM, cryogenic electron microscopy, and *in situ* liquid secondary ion mass spectrometry, in collaboration with theoretical modeling, to directly probe the structural and chemical information of active materials in rechargeable batteries. Cryogenic STEM with analytical tools, such as energy dispersive X-ray spectroscopy (EDS) and electron energy loss spectroscopy (EELS), will be used to gain chemical and electronic structural information at the interface between lithium metal and electrolyte of both solid-state and liquid configuration, which will allow direct correlation between the morphology and chemistry. STEM – high-angle annular dark-field atomic-level imaging and EDS/EELS will be used to probe the interface and bulk lattice stability of cathode and SE in solid-state batteries (SSBs). The work will be in close collaboration with the battery development group within the BMR and U. S. – Germany Collaboration on Energy Storage.

Out-Year-Goals. This project has the following out-year goals:

- Reveal critical insights as to how the solid electrolyte interphase (SEI) layer governs electron leakage and Li-ion transport characteristics, leading to optimized tailoring of SEI layer structure and chemistry through electrolyte chemistry toward enhanced performance of battery.
- Develop new *in situ* and *ex situ* STEM capability for probing challenging questions related to energy storage technology for both SSE and LE energy storage systems.

Collaborations. This project collaborates with G. Chen (Lawrence Berkeley National Laboratory, LBNL); J. Nanda (SLAC National Accelerator Laboratory); Y. Yao (University of Houston); K. Amine (Argonne National Laboratory); D. Wang (Pennsylvania State University); A. Manthiram (University of Texas, Austin); W. Tong (LBNL); Y. Cui (Stanford University); Y. Xu, J. Zhang, J. Liu, P. M. L. Le, W. Xu, X. Jie, and D. Lu (Pacific Northwest National Laboratory); X. Xiao (General Motors); and M. S. Whittingham (State University of New York, Binghamton); and the U. S. – Germany Collaboration on Energy Storage.

Milestones

1. Reveal cation dissolution poison effect on SEI layer electrical properties. (Q1, FY 2023; Completed)
2. Quantitative determination of Li-ion transport characteristic in SEI layer. (Q2, FY 2023)
3. Identification of the electron leakage path in SEI layer. (Q3, FY 2023)
4. Reveal structural and chemical evolution of interface in SSBs. (Q4, FY 2023)

Progress Report

Li-metal anodes paired with LEs have gained much attention in the search for next-generation high-energy-density batteries. Recently, there has been much progress in monitoring the Li-metal structure during cycling. A general consensus is that controlling the Li-metal surface during cycling is critical for stable cycling of Li-metal anodes. The low durability of Li-metal anode originates from the continuous growth of SEI and the formation of isolated lithium that is electronically disconnected from the current collector. These deteriorating effects for lithium metal are found to closely correlate with surface features of lithium metal, such as irregularities, nonplanar features, and high-surface-area structures of the lithium anode. Typically, during discharge, parts of the lithium are not stripped reversibly and remain isolated from the current collector. The isolated lithium is trapped in the insulating SEI shell and contributes to the capacity loss. Therefore, a fundamental understanding of why isolated lithium forms and how it can be mitigated is critical for potential deployment of Li-metal anode.

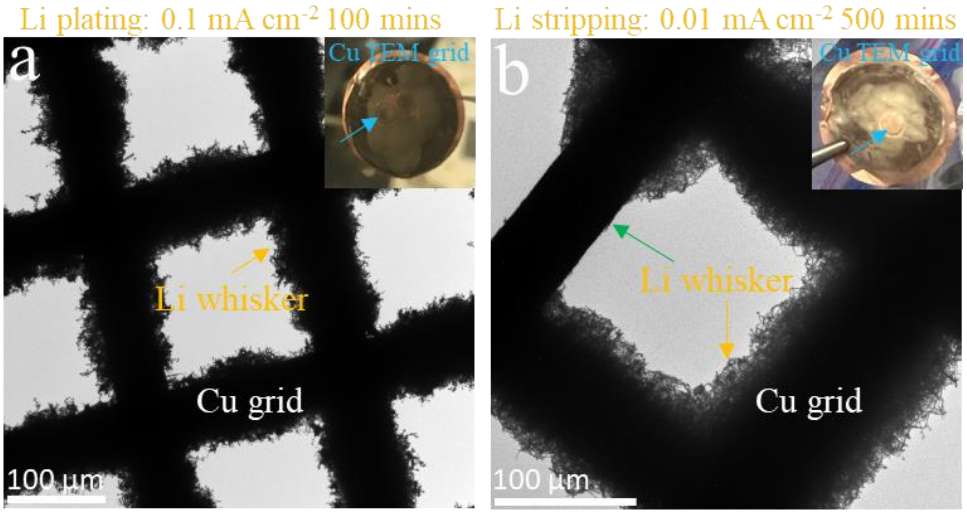

Figure 75. Cryogenic transmission electron microscopy (cryo-TEM) images of lithium spatial distribution at large scale: (a) after 100 minutes plating at a current density of 0.1 mA cm^{-2} and (b) after 500 minutes stripping at a current density of 0.01 mA cm^{-2}. The non-uniform stripping of lithium can be seen from the number density of lithium whiskers in (b), by which some region is totally stripped off (green arrow), while the other region shows high density of lithium whisker (yellow arrow). The insets show optical images of the TEM grid in a coin-cell.

The objective of this work is to investigate the topographic feature of lithium metal during the stripping of Li-metal anodes and the origin of formation of isolated lithium. The team uses cryogenic transmission electron microscopy (cryo-TEM) to study the stripping behavior of lithium at low stripping current density. Lithium was plated at 0.1 mA cm^{-2} for 100 minutes in Li||Cu coin cell with 1.2 M $LiPF_6$ in ethylene carbonate / ethyl methyl carbonate (3:7 by weight) with 5 wt% vinylene carbonate electrolyte. Lithium was stripped at 0.01 mA cm^{-2} for 500 minutes. To understand the stripping behavior of lithium at different length scales simultaneously, they placed copper TEM grid on the surface of copper current collector (Figure 75a, inset). In this setup, they can visualize the stripping features at scales ranging from several hundred microns (Figure 75a) down to a few nanometers (Figure 76c).

At micrometer scale as shown in Figure 75, in the case of stripping at a low current density of 0.01 mA cm^{-2}, the team notices a non-uniform lithium dissolution, which is featured by the localized area completely stripped off of the lithium on the TEM grid (indicated by green arrow in Figure 75b), while the other part of the TEM grid is still fully covered with the lithium deposition (indicated by yellow arrow in Figure 75b). It is unclear if such a large scale non-uniform stripping of lithium is associated with localized electrical field distribution. A more detailed exploration is needed.

At nanoscale, they investigate the microstructural features of lithium deposits and SEI on lithium plating and stripping. As shown in Figure 76a, the cryo-TEM image of the deposited lithium formed on copper grid at low current density (that is, 0.1 mA cm^{-2}) exhibits whisker-like morphology. The lithium whisker is covered with an SEI layer of uniform thickness (Figure 76b). The atomic resolution cryo-TEM image (Figure 76c) indicates the deposited lithium is crystalline lithium metal. The SEI layer has amorphous structure.

The team has noticed that the morphology feature of the lithium and SEI layer from the region that has not been fully stripped off still possesses the characteristics of the originally deposited lithium (Figure 76d-f). This observation indicates that some lithium whiskers are not stripped at all, demonstrating non-uniform stripping of lithium.

To gain information on the lithium stripping at each whisker, the team focuses on imaging the lithium whiskers in the areas with a low number density following the stripping, as shown in Figure 76g-l. In particular, they can identify if isolated lithium forms in this stripped region. They reveal that preferential stripping occurs at the kink and tip region of the whisker, as representatively shown in Figures 76h/k. It is apparent that the preferential dissolution of lithium at the tip and kink regions of lithium whisker leads to the localized crumpling of the SEI layer at the preferentially stripped regions. The crumpled SEI layer is shown as dark contrast in the cryo-TEM images in

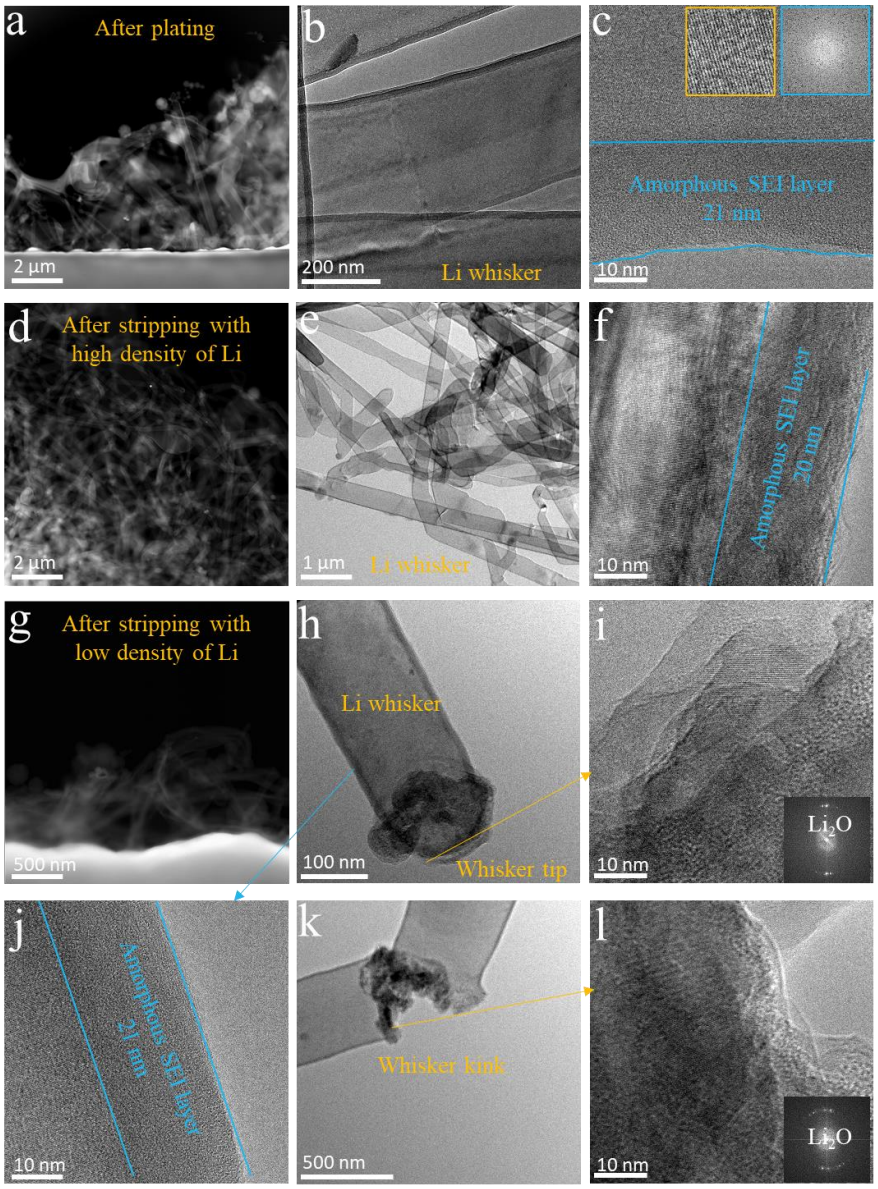

Figure 76. Microstructure of deposited lithium and features of SEIs following the plating and stripping in a coin cell. (a) Cryogenic scanning transmission electron microscopy high-angle annular dark-field (cryo-STEM-HAADF) image shows the general features of the deposited lithium. (b) Bright-field transmission electron microscopy (TEM) images show the structure of lithium whisker. (c) Atomic resolution TEM images of the lithium deposits and corresponding SEI layer on lithium following the plating. (d) Cryo-STEM-HAADF image showing the morphology of lithium deposits after lithium stripping by which the lithium whisker still possesses a high number density. (e) Bright-field TEM image shows the morphology of lithium whisker after stripping. (f) Atomic resolution TEM image showing the lithium whisker and SEI layer after lithium stripping. (g) Cryo-STEM-HAADF image shows the morphology of lithium at the region where the lithium number density is very low following the stripping. (h) Bright-field TEM image shows the preferential stripping of lithium from the tip of the whisker, leading to the crumpling of SEI layer at the tip region. (i) Atomic resolution TEM images showing the crumpled SEI layer at the tip of lithium. (j) Atomic resolution TEM image shows the SEI layer on the stem region of lithium metal. (k) Bright-field TEM image shows preferential stripping of lithium from a kink in lithium whisker, leading to crumpling of the SEI layer. (l) Atomic resolution TEM image shows the crumpled SEI layer at the kink.

Figure 76i/l, as compared with the uniform layer of SEI layer at the stem region of the whisker (Figure 76j).

It is apparent that the preferential dissolution of lithium at the kink will lead to separation of one part of the whisker from the other part, essentially inducing electronical disconnection of a section of lithium whisker from the other section; this consequentially induces the formation of isolated lithium.

The team used EELS to reveal the chemical composition and spatial distribution of SEI layers. Figure 77a-c illustrates the EELS elemental maps, showing the spatial distribution of elements in the SEI layers on the lithium whisker after lithium plating. Based on elemental maps, the SEI layer is mainly composed of lithium, oxygen, and carbon, with dilute concentration of fluorine. In comparison, they analyze the composition of the crumpled SEI at the tip (Figure 77d-f) and kink (Figure 77g-j) regions following the preferential stripping of lithium from these regions. The crumpled SEI layer following preferential lithium stripping is compositionally featured by oxygen enrichment, non-uniform distribution of carbon, and low concentration of fluorine. Morphologically, it is apparent that preferential localized stripping of lithium from the kink and tip region leads to the crumpling of the SEI layer at these two regions, while it is not clear how such a crumpling SEI leads to the localized chemical composition redistribution. More work is needed.

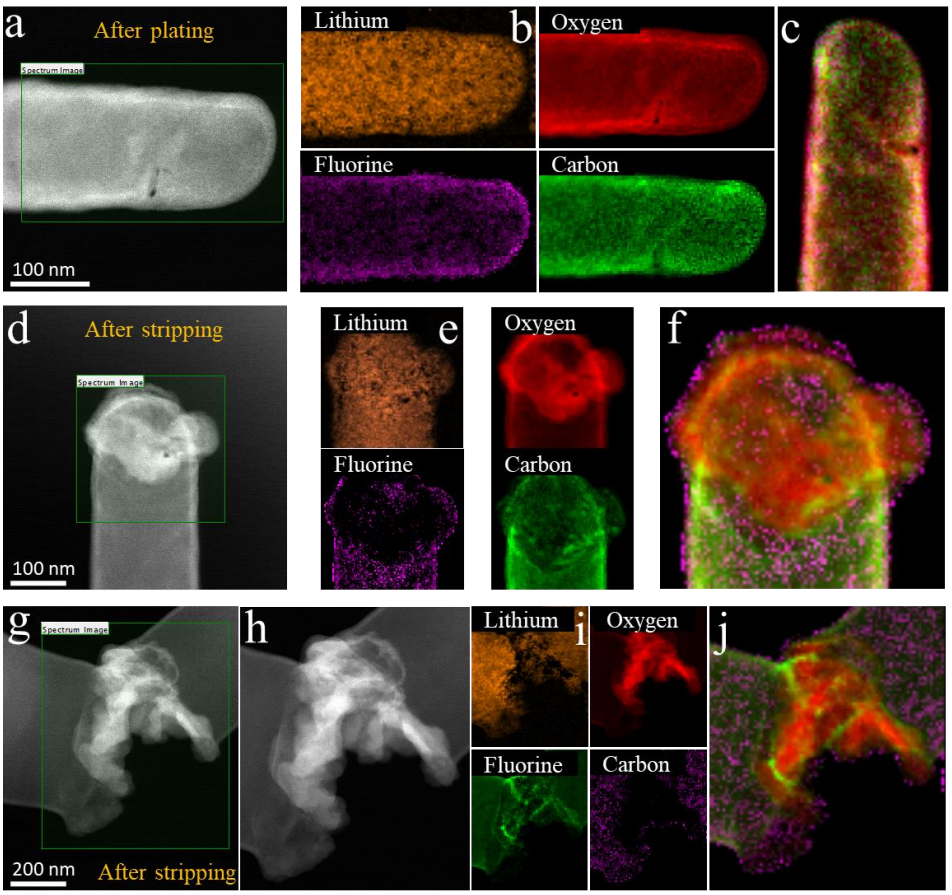

Figure 77. Composition and elements spatial distribution of SEI layer on lithium following deposition and stripping in coin cell. (a) Cryogenic scanning transmission electron microscopy high-angle annular dark-field (cryo-STEM-HAADF) image reveals the SEI layer on the lithium particle formed in Li||Cu coin cell. (b) Electron energy loss spectroscopy (EELS) elemental maps show the element distribution of SEI. (c) The EELS composite map of oxygen, carbon, and fluorine shows spatial correlation of each element. (d) Cryo-STEM-HAADF image reveals the SEI layer on the lithium whisker tip after lithium stripping. (e) EELS elemental maps show elemental distribution at the lithium whisker tip after lithium stripping. (f) EELS composite map of oxygen, carbon, and fluorine to illustrate the spatial correlation of elements. (g) Cryo-STEM-HAADF image reveals the structure of SEI at kink after lithium stripping. (h) Enlarged image of (g) to show the crumpled SEI at the kink after lithium stripping. (i) EELS elemental maps to show the elemental distribution around kink. (j) EELS composite map of oxygen, carbon, and fluorine to show the spatial correlation of elements in the crumpled SEI layer.

In summary, the team investigated the stripping behavior of lithium at low stripping current densities and correspondingly the morphological evolution features of the Li/SEI layer. Preferential stripping of lithium from the geometrically distinct spots, such as the tip or kinks, leads to the interruption of electron path by the formation of localized crumpling of SEI layers, which correspondingly induces the formation of isolated lithium. The effect of these defects on preferential stripping of lithium will be amplified with a low current

density stripping, which is in accordance with the dominance of either thermodynamic or kinetic factors. In a general term, non-uniform stripping of lithium could be closely associated with defective structure of deposited lithium and non-uniform SEI layer.

Patents/Publications/Presentations

Publications

- Zhang, X. H., P. Y. Gao, Z. H. Wu, M. H. Engelhard, X. Cao, H. Jia, Y. B. Xu, H. D. Liu, C. M. Wang, J. Liu, J-G. Zhang, P. Liu, and W. Xu. "Pinned Electrode/Electrolyte Interphase and Its Formation Origin for Sulfurized Polyacrylonitrile Cathode in Stable Lithium Batteries." *ACS Applied Materials & Interfaces* 14 (2022): 52046–52057.
- Jia, H., Z. J. Yang, Y. B. Xu, P. Y. Gao, L. R. Zhong, D. J. Kautz, D. G. Wu, B. Fliegler, M. H. Engelhard, B. E. Matthews, B. Broekhuis, X. Cao, J. Fan, C. M. Wang, F. Lin, and W. Xu. "Is Nonflammability of Electrolyte Overrated in the Overall Safety Performance of Lithium Ion Batteries? A Sobering Revelation from a Completely Nonflammable Electrolyte." *Advanced Energy Materials* (2022): 2203144.

Presentation

- Materials Research Society Fall Meeting & Exhibit, Boston, Massachusetts, (November 27–December 2, 2022): "Unveiling the Role of Electrolyte on Solid-Electrolyte Interphase Formation and Structure of Li Deposit"; Y. B. Xu.

Task 2.5 – Integrated Atomic-, Meso-, and Micro-Scale Diagnostics of Solid-State Batteries (Yi Cui, William Chueh, and Michael Toney; Stanford University / SLAC National Accelerator Laboratory)

Project Objective. By developing a characterization toolkit that tackles length scales (Å to mm), cell pressure (1-100 bars), and dynamics (during synthesis, fabrication, and cycling), the project aims to generate insights to engineer solid-state batteries (SSBs) for deployment in electric vehicles. This interdisciplinary team aims to achieve this objective by merging a broad range of characterization approaches as well as modeling to track the evolution of nanoscale chemistry and structure, microstructure, and transport.

Project Impact. The project will have an impact in several areas: (1) accelerate rational design of coatings and artificial solid electrolyte interphases (SEIs) in SSBs; (2) inhibit the root causes leading to cell shorting, and enable high current cycling; (3) accelerate design of cathode coating and composite electrode architectures; and (4) reduce degradation and variability during SSB manufacturing via composition and surface engineering.

Approach. The project has a multifold approach that will encompass the following: (1) resolve nanoscale structure and chemistry of SEIs via cryogenic transmission electron spectroscopy (cryo-TEM); (2) track solid electrolyte (SE) and lithium microstructure evolution in three dimensions via X-ray micro and diffraction tomography; (3) visualize nanoscale ionic and electronic transport at grain boundaries via conducting atomic force microscopy; (4) map current distribution in cathodes via scanning transmission X-ray microscopy; and (5) monitor nanoscale SE evolution with gas impurity via *in situ* environmental TEM.

Out-Year Goals. The project will develop an integrated characterization toolkit to characterize SSBs within a single cycle and over hundreds of cycles, spanning a wide range of relevant length scales.

Collaborations. Project collaborations include work with Stanford Synchrotron Radiation Lightsource, Advanced Light Source, and Advanced Photon Source synchrotron light sources.

Milestones

1. Identify three metallic coating materials and the heat treatment routes to promote uniform lithium plating. (Q1, FY 2023)
2. Perform *operando* microprobe scanning emission microscopy (SEM) imaging to characterize lithium plating in Li-La-Zr-O (LLZO) cells with metallic coatings. (Q2, FY 2023)
3. Characterize the depth profiles of hydrogen, lithium, and other elements in LLZO that develop during cell making. (Q3, FY 2023)
4. Demonstrate that biaxial stress suppresses dendritic growth in LLZO. (Q4, FY 2023)

Progress Report

The team developed a mathematical model to extract the size of plated lithium whisker using a microprobe in contact with SE. This model establishes the exact contact area during the *operando* SEM experiments to image lithium plating, stripping, and mechanical fracture in SSBs. The goal of their electrochemical model is to estimate the lithium whisker diameter as a function of the applied potential from current-voltage measurements. For a symmetric cell, since the reference and working electrodes are both lithium metal, the total cell potential is composed of three overpotential components:

$$V_{app} = \eta^{Ohm} + \eta^{WE} + \eta^{CE}$$

where V_{app} is the applied potential across the entire cell, η^{WE} and η^{CE} are the electrochemical overpotentials due to charge transfer kinetics at the working and counter electrodes, respectively, and η^{Ohm} is due to ohmic Li-ion transport across the SE. For their microprobe platform, they measured a short circuit resistance of < 20 Ω for the probe and sample holder apparatus, which allows them to neglect any extra electronic ohmic overpotential in their analysis once lithium whisker growth has begun.

The first assumption of the team's model is that the overpotential on the counter electrode is much smaller than the overpotential on the working electrode. The second assumption is that due to the microelectrode geometry of the plated lithium metal, they can represent the resistance of the electrolyte as $R_c = \frac{1}{2\sigma_{ion} d}$, where σ_{ion} is the ionic conductivity of the SE, and d is the effective diameter of the lithium whisker. In this case, they assume that the lithium whisker has a circular cross-section. This formula for the resistance is valid if the thickness of the electrolyte is more than ~ 2× the diameter of the microelectrode, which is satisfied in this case with the electrolyte being several mm in thickness. The final assumption of the model is that the electrochemical kinetics can be described by a Butler-Volmer type relationship with a symmetric charge transfer coefficient. This is given by:

$$\eta^{WE} = \frac{2RT}{F} \operatorname{arcsinh}\left(\frac{j}{2j_0}\right)$$

where RT/F is a constant of 25 mV at room temperature, j is the current density, and j_0 is the exchange current density. The current density is given by:

$$j = \frac{4i}{\pi d^2}$$

where i is the measured current. In the case of lithium deposition, the diameter of the lithium whisker changes dynamically with applied potential. Based on the assumptions above, they use the applied potential and measured current to estimate the diameter of the whisker at every point along the voltage sweep using a numerical solver and the final equation below:

$$V_{app} = \frac{i}{2\sigma_{ion} d} + \frac{2RT}{F} \operatorname{arcsinh}\left(\frac{2i}{j_0 \pi d^2}\right)$$

Patents/Publications/Presentations

Presentations

- Halliburton Labs, Houston, Texas (November 30, 2022): "Approaching Grid Energy Storage as a System"; W. C. Chueh.
- 13th International Conference on Advanced Lithium Batteries for Automobile Applications (ABAA-13), Marrakesh, Morocco (October 19, 2022): "Point Defects in Layered Oxides"; W. C. Chueh.
- Research Network on Electrochemical Energy Storage (R2SE) Meeting, Collège de France and National Centre for Scientific Research (CNRS), Montpellier, France (October 12, 2022): "Point Defects & Local Redox Chemistry in Layered Oxides"; W. C. Chueh.

Task 2.6 – Fundamental Understanding of Interfacial Phenomena in Solid-State Batteries (Xingcheng Xiao, General Motors)

Project Objective. The project objective is to develop a comprehensive set of *in situ* diagnostic techniques combined with atomic/continuum modeling schemes to investigate and understand the coupled mechanical/chemical degradation associated with dynamic interfacial phenomena in solid-state batteries (SSBs). Specifically, *in situ* observations and characterizations of lithium plating-stripping processes, lithium dendrite formation, interphase formation, and the induced interfacial stresses, as well as the mechanical and electrochemical properties of interfaces and interphases, are paramount. The study will provide useful guidelines for optimizing cell structure design and engineering interfaces and interphases to enable SSBs.

Project Impact. The project will provide fundamental understanding of the dynamic interfacial phenomena and the coupled mechanical and chemical degradation. In addition, it will establish a critical guideline to design safe and durable SSBs with energy density > 500 wh/kg for electric vehicle (EV) applications.

Approach. The multiscale *in situ* diagnostic tools, including atomic force microscopy, nanoindentation, dilatometer, stress sensors, and pressure cells, will be used to investigate mechanical behavior and microstructure evolution at interface/interphase during lithium plating and stripping. The information (along with Li-ion transport properties and microstructure evolution obtained using the advanced spectroscopic ellipsometry, and *in situ* transmission electron microscopy) will be correlated with electrochemical performance toward high cycle efficiency and dendrite-free SSBs. The goal of this understanding is to develop strategies for surface and interface engineering, apply them to commercially available solid electrolytes (SEs) including powder, pellets, and foils, and assemble SSBs for further validation and optimization, eventually extending cycle life for EV application.

Out-Year Goals. The project seeks to develop SSB model systems to capture critical mechanical properties and probe the coupled mechanical-chemical degradation by further developing comprehensive *in situ* diagnostic tools. All results obtained from these *in situ* studies, combined with advanced postmortem analysis and modeling, will be correlated with the cycling stability of SSBs. The *in situ* tools developed will be applied to the following two periods to deeply understand the coupled mechanical and chemical degradation of interface/interphase.

Collaborations. The principal investigators involved in experiments and simulation will be as follows: B. W. Sheldon and Y. Qi (Brown University), and Y-T. Cheng and A. Seo (University of Kentucky).

Milestones

1. Artificial interlayer can regulate mechanical/chemical properties of interfaces. (Q1, FY 2022; Completed)
2. Artificial interphase has good ionic conductivity and chemical stability. (Q2, FY 2022; Completed)
3. Model to predict the governing mechanical and material properties of interfaces responsible for failures. (Q3, FY 2022; Completed)
4. Pouch cells of SSBs with optimized interlayers with energy density > 350 Wh/kg and cycle life > 500 cycles. (Q4, FY 2022; In progress – will be completed in no-cost extension period)

Progress Report

Development of Kinetic Monte Carlo (KMC) Stripping Code for Li/SE Interface

The KMC code has been employed to simulate the vacancy evolution near different Li/SE interfaces using the density functional theory (DFT) calculated lithium hopping barriers. To gain more accurate insight for the surface morphology after stripping, the implementation of stripping in the KMC simulation is further developed to impose the constant current density at the interface in this quarter. The developed code is tested among Li/LiF, Li/Li_2O, and Li/Li-La-Zr-O interfaces, which can provide input for the simulation of the contact loss at the interface at larger length scale and time scale on the continuum level.

Implementation of Stripping Code. In the KMC simulation, the lithium diffusion within the anode, SE, and the stripping of lithium atoms from the anode to the SE are assisted by the lithium vacancy hopping. As the number of lattice sites in the simulation cell is fixed and the shortest hopping is considered, the lattice diffusion model can help explain the hopping events in the KMC simulation. In the lithium anode, assuming the lithium surface is the first plane (j=1), the lithium flux across a plane j considering the 2-direction hopping events is calculated using

$$\frac{dLi_j}{dt} = \frac{1}{2N_0}(k_f^{i+1}N_{i+1}V_i + k_b^{i-1}N_{i-1}V_i - k_f^{i}N_iV_{i-1} - k_b^{i}N_iV_{i+1}), \quad (1)$$

where N_0 is the total number of lattice sites on the plane j, k_f^i and k_b^i are the forward and backward hopping rates for the forward (toward the interface) and backward (away from the interface) hopping event, and N_i and V_i are the number of lithium atoms and vacancies on the plane i, where $N_0 = N_i + V_i$.

The hopping events in KMC simulation are also related to the numbers of both lithium atoms and vacancies. In the anode, a hopping event is when a lithium atom moves from its current position to the nearest vacancy along the (111) direction (~ 3Å). The DFT calculated hopping barriers (E_a) were converted to the hopping rate (k_i, i stand for the intergers between 1 and 10.) for each possible hopping event within the anode according to the transition state theory

$$k_i = v_0 \exp\left(\frac{-E_a}{k_B T}\right), \quad (2)$$

where v_0 is the jumping frequency, and k_B and T are the Boltzmann constant and the temperature, respectively. For hopping events in the interface region (except for the first two layers), the hopping barriers were fitted to exponential functions and then converted to hopping rates.

At the interface, the diffusion model can be applied to the first plane according to

$$\frac{dLi_1}{dt} = \frac{1}{2}(k_f^2 N_2 \frac{V_1}{N_0} - k_b^1 N_1 \frac{V_2}{N_0} - k_s N_1 \frac{V_s}{N_s}), \quad (3)$$

where k_s is the rate for each stripping event, V_s is the number of vacancy sites on the anode surface and N_s is the number of lattice sites on the anode surface. N_s is around $1.56N_0$ in the current SE reservoir. In the KMC simulation, since the lithium ions in the SE are removed before the simulation, V_s is equal to the lithium sites in the SE reservoir. A stripping/hopping event here is when a lithium atom on the anode surface jumps to the nearest vacancy site on the SE surface. The cutoff distance for this kind of hopping is 3.5 Å.

To apply the constant current density at the interface, $\frac{dLi_1}{dt}$ (or the flux in the SE, $\dot{N}$, ms^{-1}) can be calculated from the current density (i_s, mA/cm^2) using

$$\dot{N} = \frac{I_s A}{1000q}, \quad (4)$$

where A is the area of the interface cross section and q is the electric charge for one electron.

For testing purposes, the lithium hopping was firstly neglected to focus on the stripping process at the interface, which can be verified by the number of stripped lithium atoms and the stripping time. Assuming all the stripping events are equivalent, it leads to the condition

$$\dot{N} = \frac{k_s N_1 V_s}{2N_s}. \quad (5)$$

For lithium hopping within the SE reservoir, only the diffusion to vacancy sites within the cutoff distance (3.5 Å) on adjacent planes are considered, which also has the hopping rate k_s ($k_s = k_9$). The backward hopping ($k_{10} = 0$) was set to be 0.

The KMC code was developed based on the Bortz-Kalos-Lebowitz algorithm. Each KMC step consists of 5 operations: (1) all possible hopping events (cutoff distance 3.5 Å) are determined in the evolving structure, (2) the corresponding hopping rates are assigned to the hopping events, (3) the qth event is picked to occur according to the criteria $\sum_{m=1}^{q} k_m \geq \rho_1 k_{tot} \geq \sum_{m=1}^{q-1} k_m$, where ρ_1 is a random number between 0 and 1, (4) the positions of the lithium atom and the vacancy in the jth event are switched to update the evolving structure, and (5) the simulation time is evolved by $\Delta t = -\frac{ln\rho_2}{k_{tot}}$, where ρ_2 is another random number between 0 and 1. The KMC simulation is finished after 10^4 steps for current densities larger than 10^3 A/cm^2.

Effect of Dimethyl Ether – Trimethylolpropane – Lithium Nitrate (DTL) Coating Layer on Hot-Pressed $Li_{6.24}Al_{0.24}La_3Zr_2O_{11.98}$

To investigate the DTL coating as the interlayer in SSBs, bare and coated lithium electrodes were studied in symmetrical cells with $Li_{6.24}Al_{0.24}La_3Zr_2O_{11.98}$ (LLZO) solid-state electrolyte pallets. Lithium symmetrical cells were assembled using split test cell (MTI) for electrochemical characterization. Electrochemical impedance spectroscopy was performed 7 MHz-1Hz with 10 mV perturbation. Critical current density (CCD; Jc) test was performed starting at 10 μA/cm^2 with 10 μA/cm^2 increment. For each current density, there were 5 minutes of stripping or plating process for 5 cycles.

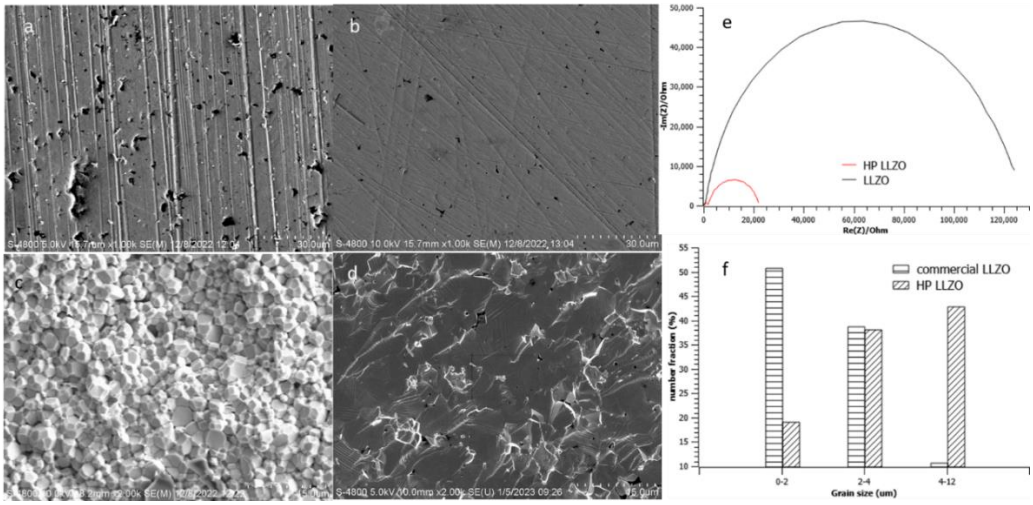

Figure 78. Scanning electron microscopy surface image of (a) commercial LLZO and (b) hot-pressed LLZO. Fracture image of (c) commercial LLZO and (d) hot-pressed LLZO. (e) Nyquist plots obtained from electrochemical impedance spectroscopy. (f) Grain size distribution.

As shown in the surface scanning electron microscopy image of LLZO (Figure 78a-b), more dark spots were noted as pore for the commercial LLZO. No matter how intensively the polish process is performed, these intrinsic pores will cause contact loss and lead to large contact resistance and low CCD. Even though the DTL coating layer could fill the void of pellets and improve contact resistance, as reported previously, the cell total impedance is still too large to perform CCD test or long-time cycling. Thus, the team decided to use

hot-pressed LLZO instead of commercial LLZO for future experiments. A clear difference was evident from impedance measurement, as shown in Figure 78e. With same surface polishing method, total impedance of the cell with commercial LLZO showed six times higher than the cell with hot-pressed LLZO.

Another important aspect of the microstructural difference was the fracture mode, as shown in Figure 78c-d. The commercial LLZO showed intergranular fracture, while most of the hot-pressed LLZO showed intragranular fracture; this indicated strong grain boundaries (GB) for the hot-pressed LLZO pellets. Relative densities were calculated based on the ratio between measured density and theoretical density. Relative density for commercial LLZO is 90.6%, while the hot-pressed LLZO could achieve 95%. The increase in grain size (Figure 78f) and decrease in porosity at GB would lead to an increase in percentage of intragranular fracture.

Patents/Publications/Presentations

Patent

- General Motors Invention Number, P103667: "A Process to Reduce the Interfacial Impedance in All-Solid-State Batteries"; X. Xiao.

Publication

- Feng, M., C-T. Yang, and Y. Qi. "The Critical Stack Pressure to Alter Void Generation at Li/Solid-Electrolyte Interfaces during Stripping." *Journal of The Electrochemical Society* 169 (2022): 090526.

Presentation

- Best Poster Award – 2022 Materials Research Society Fall Meeting, Boston, Massachusetts (November 29, 2022): "Investigating Chemo-Mechanical Phenomena in All-Solid-State Lithium Metal Batteries Using *In Situ* Curvature Measurements"; J. H. Cho, K. Kim, S. Chakravarthy, X. Xiao, J. L. M. Rupp, and B. W. Sheldon.

Task 2.7 – Multidimensional Diagnostics of the Interface Evolutions in Solid-State Lithium Batteries (Yan Yao, University of Houston)

Project Objective. The project objective is to develop a platform combining focused ion beam – scanning electron microscopy (FIB-SEM) tomography, time-of-flight secondary ion mass spectrometry (TOF-SIMS), and *in situ* scanning electron microscopy (in-SEM) nanoindentation-based stiffness mapping for structural, chemical, and mechanical characterizations in solid-state lithium batteries (SSLBs). Assessment of the influence of cell design and testing conditions (that is, external pressure, current density, and temperature) on the evolutions of interfaces will be performed.

Project Impact. The consolidated *in situ* structural–chemical–mechanical diagnostic platform established in this project will provide unprecedented insights into the failure mechanisms of SSLBs.

Approach. Space- and time-resolved structural, chemical, and mechanical characterizations of the cathode-electrolyte and anode-electrolyte interfaces will be performed on lithium all-solid-state batteries using FIB-SEM, TOF-SIMS, and in-SEM nanoindentation. Tasks include the following: (1) development of solid-state cell thin stacks and test-cell configurations that are suitable for *in situ* characterizations; (2) quantitative characterization and *in situ* tracking of interfacial voids formation within composite cathode and electrolyte layer; (3) identification and *in situ* tracking of the chemical composition, spatial distribution, and mechanical properties of electrolyte decomposition products at the lithium- and cathode-electrolyte interfaces; and (4) visualization, chemo-mechanical properties detection, and *in situ* tracking of lithium dendrites grown within the solid electrolyte layer.

Out-Year Goals. In the out years, the project will develop thin-stack solid-state cells, micro-cells, in-SEM nanoindentation, and testing protocols. The correlation among structural evolution, electrolyte decomposition, and interfacial resistance increase will be investigated.

Collaborations. The University of Houston team (that is, Y. Yao, Z. Fan, and Y. Liang) works closely with the Rice University team (that is, J. Lou and H. Guo).

Milestones

1. Multiscale structural investigations. (Q1, FY 2022; Completed)
2. Composition and spatial distribution study. (Q2, FY 2022; Completed)
3. Selected region mechanical property probing. (Q3, FY 2022; Completed)
4. Real-time monitoring of structural evolutions. (Q4, FY 2022; Completed)
5. Real-time monitoring of chemical products evolutions. (Q1, FY 2023; Completed)
6. Real-time monitoring of chemical products evolutions. (Q2, FY 2023; In progress)

Progress Report

The effects of chemo-mechanical coupling on solid-state batteries (SSBs) were investigated by using the IONTOF TOF-SIMS NCS instrument, which combines a time-of-flight – secondary ion mass spectrometer (TOF-SIMS) with an atomic force microscope (AFM). As shown in Figure 79, a polished open-cell SSB (Ag-C / Li-P-S-CL (LPSCl) / Li) was mounted on the team's custom-made TOF-SIMS stage for chemical and mechanical analysis. The ultra-low detection limit (ppm-ppb) of Li-related species in the TOF-SIMS allowed for acquisition of chemical evolution at the electrolyte-anode interface in the as-prepared sample. Figure 79a shows a surface secondary ion mapping of the pristine Ag-C/LPSCl interface, where the Ag^+ (blue) mapping displays the distribution of the Ag-C layer, and the Li^+ (red) mapping indicates the presence of Li-related species (LPSCl) in the sample. *In situ* topography and stiffness mapping on a selected region were also performed using AFM. Figure 79b shows the AFM topography of selected Ag-C region, providing insight into the morphological evolution of the Ag-C layer during electrochemical operation.

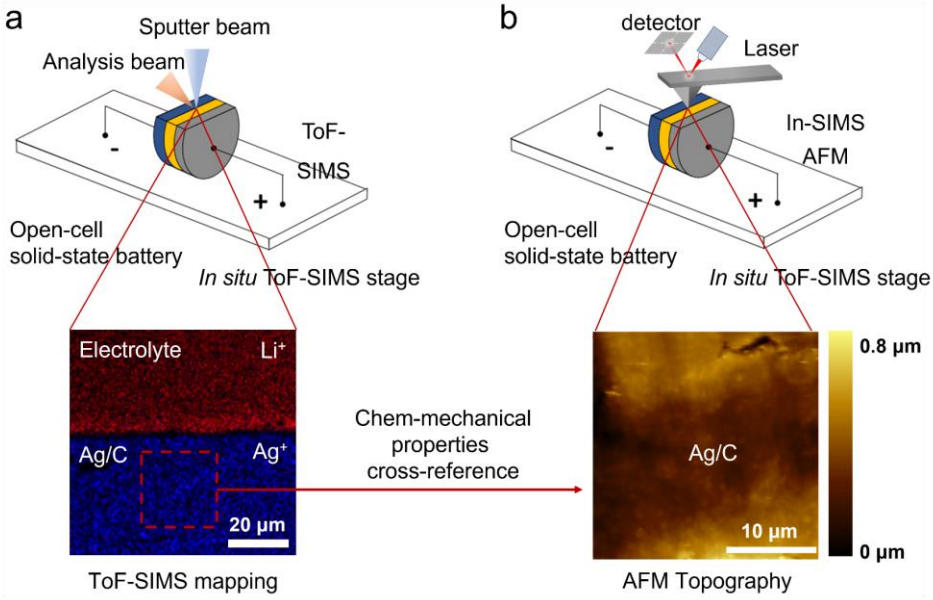

Figure 79. Illustration of *in situ* time-of-flight – secondary ion mass spectrometry (TOF-SIMS) and *in situ* scanning electron microscopy atomic force microscopy (AFM) measurements. (a) Schematic of TOF-SIMS analysis on Ag-C/LPSCl interface. (b) Schematic illustration of AFM measurement on selected Ag-C region.

The stiffness of the Ag-C layer is measured using force-distance curves obtained with AFM. The AFM tip is moved in a vertical direction rather than scanning along the surface, as shown in Figure 80a. The force between AFM probe and sample is collected as the tip approaches and retracts from the surface. Figure 80b shows a single-point force-distance curve on the Ag-C sample, where the stiffness can be obtained from the retraction curve. The AFM tip can probe an extremely small interaction area (tip radius ~ 5-50 nm) with a high force sensitivity, allowing for mapping of microstructure evolution in the Ag-C layer with high spatial resolution. Here, a 5-μm line scan of stiffness measurements was performed on the Ag-C layer, with a 100-nm interval between each force-distance test, as shown in Figure 80c. The team observes a stiffness difference along the scanning line, plotted in Figure 80d, which may originate from inhomogeneous composition and microstructure. As

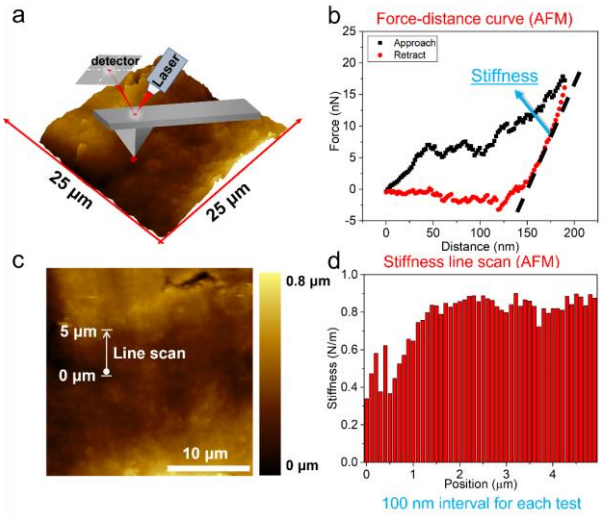

Figure 80. Stiffness measurements of selected Ag-C region. (a) Schematic illustration of single-point stiffness measurement. (b) Force-distance curve on Ag-C layer. (c) Line scan of stiffness measurements on Ag-C layer. (d) Stiffness plot along the scan line displays in (c), with 100 nm interval for each test.

previously reported in *in situ* TOF-SIMS tests, the team observed a gradient distribution of Li-related species in the Ag-C layer during lithiation, indicating a gradual and possibly multi-step lithiation process. Therefore, more effort will be devoted to performing the chemical-structural-mechanical mapping measurements on lithiated Ag-C samples to better understand the lithiation mechanism of Ag-C interlayer, which will be reported next quarter. The combined TOF-SIMS and AFM technique could also be implemented to investigate the chemical, morphological, and mechanical evolution in cathode, anode, and related interfaces in SSBs, providing insight into their operation mechanisms.

Patents/Publications/Presentations

Presentations

- Materials Research Society Fall Meeting, Boston, Massachusetts (November 28, 2022): "Multidimensional Characterizations for All-Solid-State Batteries"; Y. Yao. Invited.
- Ford Motors, Virtual (October 18, 2022): "Multidimensional Characterizations for All-Solid-State Batteries"; Y. Yao. Invited.
- Department of Industrial and Systems Engineering Seminar, Hong Kong Polytechnic University, Virtual (September 15, 2022): "Next-Generation Batteries for Electric Vehicles and Stationary Storage"; Y. Yao. Invited.

TASK 3 – MODELING

Team Lead: Venkat Srinivasan, Argonne National Laboratory

Summary

Achieving the performance, life, and cost targets outlined by the Vehicle Technologies Office will require moving to next-generation chemistries, such as higher capacity Li-ion intercalation cathodes, silicon and other alloy-based anodes, Li-metal anode, and sulfur cathodes. However, numerous problems plague development of these systems, from material-level challenges in ensuring reversibility to electrode-level issues in accommodating volume changes, to cell-level challenges in preventing cross talk between the electrodes. In this task, a mathematical perspective is applied to these challenges to provide an understanding of the underlying phenomenon and to suggest solutions that can be implemented by the material synthesis and electrode architecture groups.

The effort spans multiple length scales, from *ab initio* methods to continuum-scale techniques. Models are combined with experiments, and extensive collaborations are established with experimental groups to ensure that the predictions match reality. Efforts also focus on obtaining parameters needed for the models, either from lower-length scale methods or from experiments. Projects also emphasize pushing the boundaries of the modeling techniques used to ensure that the task stays at the cutting edge.

A major focus of the effort is around Li-metal-based solid-state batteries. While these chemistries hold promise, numerous challenges such as reactivity, conductivity, and mechanical stability prevent their commercialization. Mathematical models are ideal to provide the guidance and insights needed to solve these issues.

In the area of Li-metal anodes, the focus is on understanding how materials can be designed to prevent dendrite growth using continuum modeling approaches, combined with calculations on mobility in solid conductors. The results are used to guide materials development by providing the properties needed to prevent dendrites, while also achieving the energy and power goals. Models examine the role of the solid electrolyte interphase on the morphology of the dendrite and describe the mechanical-electrochemical coupled effects that are critical for dendrite formation. Finally, efforts are focused on discovery of new solid ion conductors with properties that far exceed existing materials. The focus is on using these models as a guide before embarking on extensive experimentation.

Lithium metal with solid electrolytes will be paired with cathode materials, often intercalative in nature. Models are being developed to examine the solid-cathode interface in Li-metal-based systems, where side reactions and interface debonding issues are known to limit cycling. These models are being used to understand how to prevent chemo-mechanical failure at the interface. Coatings, an effective strategy for high-voltage operation, are being explored with the aim of providing a rational design approach for new coating materials. In addition, focus is paid to porous electrodes with cathode particles to predict the impact of heterogeneities on electrode behavior.

Highlight

Cathode coatings play an essential role in preventing undesired reactions and have become crucial for the commercialization of next-generation cathode materials. Coatings needs to have both fast Li^+ diffusion and be able to block O^{2-} diffusion to limit oxygen-loss-induced cathode surface reconstruction. The Lawrence Berkeley National Laboratory group (K. Persson) has been developing a high throughput computation screening platform for amorphous coatings. The group has been using *ab initio* molecular dynamics simulations to calculate ionic diffusivity, flux, and transport time through the coating materials. Using this methodology, the team has developed a map that ranks coatings that promise low impedance and high stability to oxygen loss. The map shows a number of promising candidates that can serve as cathode coatings.

Task 3.1 – Characterization and Modeling of Lithium-Metal Batteries: First-Principles Modeling and Machine Learning
(Kristin Persson, Lawrence Berkeley National Laboratory)

Project Objective. This project supports Vehicle Technologies Office programmatic goals by developing next-generation, high-energy cathode materials and enabling stable cathode operation at high voltages through target particle morphology design, functional coatings, and rational design of electrolytes. The end-of-project goals include the following: (1) understanding of the factors that govern charge transport in nonaqueous, superconcentrated liquid electrolytes (LEs), (2) critical surface and coating design and optimization strategies that will improve cycling of Li-ion battery cathodes by reducing cathode degradation from oxygen loss, and (3) simulation and machine learning (ML) of the early formation of the solid electrolyte interphase (SEI) on Li-metal electrodes.

Project Impact. This project is aimed at providing fundamental insights into the atomistic mechanisms underlying surface reactivity and performance of Li-ion cathode materials and electrolytes, with the goal being to suggest improvement strategies, such as coatings, surface protection, novel electrolyte formulations, and particle morphology design. Transport modes as a function of solvent and salt concentrations will be clarified, and a data-driven reaction network framework will be designed and implemented to predict early SEI formation on lithium metal.

Approach. First-principles calculations, both static and dynamic approaches, are used to model solid-state electrolyte material thermodynamics and kinetics. LEs are modeled through coupled classical molecular dynamics (MD) and first-principles methods to accurately capture solvation structure as well as reactivity of the liquid system. The reaction network is built on large-scale first-principles data, using graph theory and ML models.

Out-Year Goals. Electrolyte work will be aimed toward understanding the atomistic interactions underlying performance of lithium electrolytes, specifically elucidating conductivity (as a function of salt concentration) and impact on the charge transport mechanisms at play. Amorphous coatings will be evaluated based on ionic transport metrics and thermodynamic stability. The reaction network will be tested against known interfacial species forming on lithium metal in $LiPF_6$ / ethylene carbonate (EC) electrolytes.

Collaborations. This project is highly collaborative among several BMR principal investigators: G. Chen (Lawrence Berkeley National Laboratory), G. Ceder (University of California, Berkeley), and R. Kostecki (Argonne National Laboratory). Improved coating formulations will be examined by Chen and Ceder, and interfacial reactivity insights will be corroborated by Kostecki.

Milestones

1. Correlate electrolyte chemistry, and Li/SEI compositional structure determined for Li-EC-based electrolyte. (Q1, FY 2022; Completed)
2. Determine sensitivity of molecular dynamics parameters to diluent effect on transport in at least one superconcentrated electrolyte. (Q2, FY 2022; Completed)
3. Develop high-throughput (HT) infrastructure for MD simulations. (Q3, FY 2022, Completed)
4. Determine chemistry and structural motifs that control cathode amorphous coating performance, screening over 50,000 compositions. (Q4, FY 2022; Completed)

Progress Report

This quarter, the team reports recent progress in high-throughput computational screening of amorphous cathode coatings for Li-ion battery applications. Besides providing facile Li^+ diffusion pathways, an optimal cathode coating should block O^{2-} diffusion such that the oxygen-loss-induced cathode surface reconstruction can be mitigated. Therefore, to evaluate Li^+ and O^{2-} transport in the screened amorphous coatings, they calculate ionic diffusivity, flux, and transport time through the coating materials using *ab initio* molecular dynamics simulations and Onsager transport models.

Figure 81 illustrates the distribution of $D_{\mathrm{rt}}^{\mathrm{Li}}$ and $D_{\mathrm{rt}}^{\mathrm{O}}$ of 20 selected compounds. The team's calculations show that in general, Li^+ and O^{2-} diffusion is correlated, that is, a compound with a higher $D_{\mathrm{rt}}^{\mathrm{Li}}$ also has a higher $D_{\mathrm{rt}}^{\mathrm{O}}$. In addition, they find that for compounds consisting of the same species, a compound with a higher Li^+ concentration also has a higher Li^+ and O^{2-} diffusion. For example, comparing $Li_3B_{11}O_{18}$ and LiB_3O_5, they find that LiB_3O_5, which has a higher Li^+ concentration, exhibits a higher $D_{\mathrm{rt}}^{\mathrm{Li}}$ and $D_{\mathrm{rt}}^{\mathrm{O}}$. Similar behavior is found in $LiPO_3$ and Li_3PO_4, relating to their $D_{\mathrm{rt}}^{\mathrm{Li}}$ and $D_{\mathrm{rt}}^{\mathrm{O}}$.

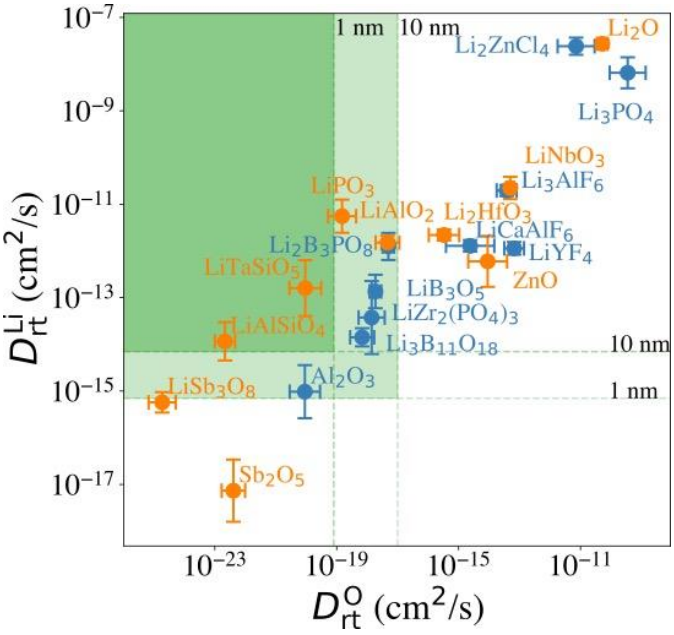

Figure 81. Calculated room-temperature self-diffusion coefficients of Li^+ ($D_{\mathrm{rt}}^{\mathrm{Li}}$) and O^{2-} ($D_{\mathrm{rt}}^{\mathrm{O}}$) in the selected compounds. Dash lines represent approximated $D_{\mathrm{rt}}^{\mathrm{Li}}$ and $D_{\mathrm{rt}}^{\mathrm{O}}$ limits based on a coating thickness between 1 nm and 10 nm. The green region represents favorable $D_{\mathrm{rt}}^{\mathrm{Li}}$ and $D_{\mathrm{rt}}^{\mathrm{O}}$ values. Blue and orange compounds indicate the compounds pass and do not pass screening criteria, respectively.

From the calculated $D_{\mathrm{rt}}^{\mathrm{Li}}$ and $D_{\mathrm{rt}}^{\mathrm{O}}$, the team evaluates the coating suitability of the selected compounds in terms of their ability to facilitate Li^+ transport while blocking O^{2-} transport. They estimate the overpotential, ΔV, at the cathode surface. They set the criterion for overpotential imposed by the coating as $\Delta V \leq 0.1$ V, above which the Li^+ transport across the coating will be significantly compromised. Figure 82a shows that for 1-nm surface coatings, all the selected compounds, except Sb_2O_5 (23 V) and $LiSb_3O_8$ (0.18 V), result in overpotentials below 0.1 V, which indicates a sufficient Li^+ transport in these compounds. The overpotential of the Al_2O_3 coating is found to be 0.07 V. When coating thickness is increased to 10 nm, the overpotentials of Sb_2O_5, $LiSb_3O_8$, and Al_2O_3 coatings increase to 230 V, 1.8 V, and 0.7 V, respectively, while the overpotentials of other compounds are still below 0.1 V. Next, they estimate the minimum Li^+ diffusivity $D_{\mathrm{rt}}^{\mathrm{Li}}$ to meet the overpotential criterion of $\Delta V \leq 0.1$ V, which is represented by the horizontal dashed lines in Figure 81.

To evaluate the effectiveness of these coatings in blocking O^{2-} transport, they estimate the O^{2-} flux J^O and the time t required for O^{2-} to diffuse through the coating. Figure 82b shows the calculated O^{2-} diffusion time t in the selected compounds. They select the compounds with an estimated O^{2-} diffusion time longer than 1 hour such that not all O^{2-} ions that are evolved from surface NiO_2 layer have diffused through the coating under 1C rate. They find that $LiSb_3O_8$, $LiAlSiO_4$, Sb_2O_5, Al_2O_3, $LiTaSiO_5$, $LiPO_3$, $Li_3B_{11}O_{18}$, $LiZr_2(PO_4)_3$, and LiB_3O_5 exhibit an estimated O^{2-} diffusion time longer than 1 hour. Next, they estimate the upper limit of O^{2-} diffusivity to have $t \geq 1$h, which is represented by the vertical dashed lines in Figure 81. Therefore, the green region in Figure 81 represents the favorable Li^+ and O^{2-} diffusivity window, and a compound falling on the top left area is more desirable in terms of facilitating Li^+ transport while blocking O^{2-} transport.

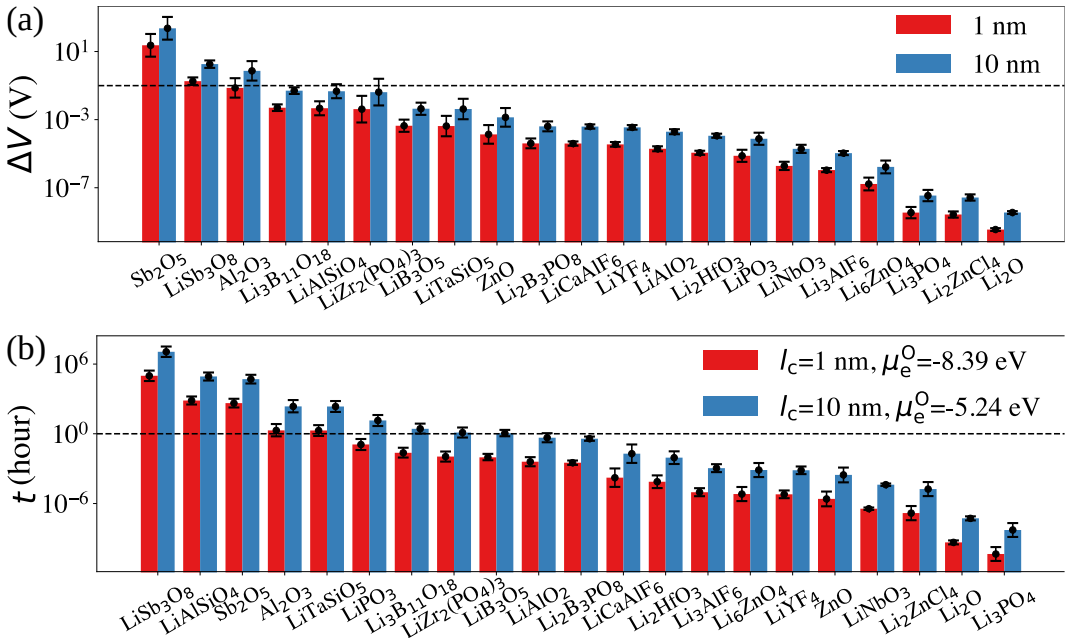

Figure 82. (a) Calculated overpotentials (ΔV) for a current density of 0.044 mA cm^{-2} across room-temperature cathode coatings of $l_c = 1$ nm band 10 nm. The dashed line represents $\Delta V = 0.1$ V. (b) Calculated O^{2-} diffusion time t in the selected compounds assuming an $r = 1\ \mu m$ primary particle and an $l_s = 2$ nm surface rocksalt phase. The dashed line represents $t = 1$ h. The green regions represent favorable ΔV and t.

Patents/Publications/Presentations

Publication

- Cheng, J., K. D. Fong, and K. A. Persson. "Materials Design Principles of Amorphous Cathode Coatings for Lithium-Ion Battery Applications." *Journal of Materials Chemistry A* 10 (2022): 22245.

Task 3.2 – Electrode Materials Design and Failure Prediction (Venkat Srinivasan, Argonne National Laboratory)

Project Objective. The main project objective is to develop computational models for understanding the various degradation mechanisms for next-generation Li-ion batteries. This year's goal is to use the continuum-based mathematical model to investigate interfacial stability between Li-metal electrodes and solid electrolytes (SEs) during deposition and dissolution of lithium with different interfacial conditions, such as presence of alloying or composite type anodes as well as interfacial voids and imperfections. Instabilities observed at the cathode/SE interface due to interdiffusion of atoms will also be investigated. SEs are expected to enable high-energy-density and liquid-free, safe, next-generation Li-ion batteries, while combined with thin Li-metal anodes. Abilities of both hard and soft inorganic and organic SEs will be studied to stabilize lithium deposition on Li-metal anodes. During charge, lithium dendrites are observed through the SEs, which are supposed to occur because of the non-uniform current distribution at the Li/electrolyte interface. Due to their lack of conformability, hard-ceramic-based SEs (such as $Li_7La_3Zr_2O_{12}$ and Li-Al-Ti-P) are expected to experience loss of electrochemically active surface area during lithium plating and stripping, which can eventually lead to current focusing and subsequent dendrite growth. Sulfide-based soft ceramics Li-P-S and Li-P-S-Cl, and/or polymer-ceramic composite electrolytes are expected to maintain better contact with the Li-metal electrode because of their higher deformability, but formation of lithium dendrites is observed in them as well. Application of external pressure has been considered and extensively implemented to stabilize the lithium deposition process with limited success. Other possibilities involve adoption of alloying or composite type anodes that can react with the depositing lithium much before it plates and forms dendrites. Enabling a solid catholyte material that is stable against the cathode over a wide range of potential windows is a huge challenge due to the interdiffusion- and delamination- induced issues, which is also being studied here.

Project Impact. Findings from this research will give a better understanding of the lithium deposition mechanism at the lithium/SE interface with different alloying and composite type anodes and protective layers. Strategies to stabilize the cathode/SE interface will also be elaborated.

Project Approach. In the present project, mesoscale models are developed based on mass conservation, charge balance, and force balance relations at the continuum level to describe the physical processes occurring in the electrochemical systems during charge and discharge, which is then compared with the experimental observations for appropriate validation. The models are then used to provide insights and guidance for strategizing new design concepts for the stabilization of Li-metal anodes and cathode/SE interfaces.

Out-Year Goals. In this project, a computational framework will be presented that can capture the lithium deposition at the electrode/electrolyte interface and predict the extent of interdiffusion at cathode/SE interface.

Collaborations. This project collaborates with L. A. Curtiss, A. T. Ngo, S. Tepavcevic, and Y. Zhang at Argonne National Laboratory and Jürgen Janek from Justus Liebig University, Giessen, Germany.

Milestones

1. Develop computational model for lithium deposition and stripping with alloying anodes. (Q1, FY 2023; Completed)
2. Model the interdiffusion of ions at the cathode/SE interface. (Q2, FY 2023)
3. Investigate lithium deposition at a Li|electrolyte interface with pre-existing voids. (Q3, FY 2023)
4. Study the effect of external materials (such as carbon nanotube) on the overall lithium stripping phenomena. (Q4, FY 2023)

Progress Report

Develop Computational Model for Lithium Deposition and Stripping with Alloying Anodes. To stabilize lithium deposition at the anode side during the charging process, various metals have been attempted as the anode capable of alloying with lithium and possibly eliminating the growth of dendrites. However, depending on the open circuit potential of the alloying anode, and the extent of lithiation experienced by the alloying metal, it is possible to obtain either alloying of lithium, or plating of lithium, on top of the anode. In the present context, a computational model is developed capable of predicting the propensity of alloying or plating reactions. The alloying reaction shows some positive value of the open circuit potential, whereas the lithium plating reaction occurs under zero volts. Lithiation of the alloying anode is assumed to occur through a solid solution mechanism. The concentration dependent variation in open circuit potential of the alloying anode material is assumed to follow the Nernst equation, where the impact of the activity coefficients is neglected. The computationally predicted voltage versus time curve during the lithium deposition on top of the alloying anode is shown in Figure 83, where both alloying and plating is successfully captured. Changes in the computational domain during the alloying and plating process are shown on the left by the images marked A – F.

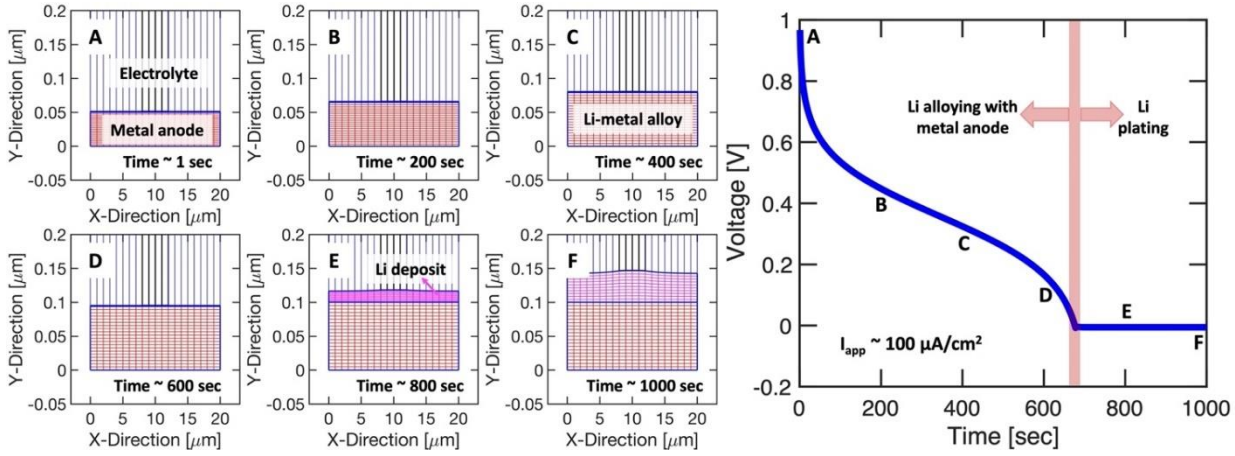

Figure 83. Computationally predicted voltage versus time curves for lithium alloying and plating phenomena. Time evolution of the domain containing Li-metal alloy (red) and deposited lithium (magenta) is shown in the left. The electrolyte on top is also denoted in blue. The applied current density is 100 μA/cm².

A separate one-dimensional model is developed for capturing the stripping process that occurs after the deposition of lithium. Figure 84 shows the voltage versus capacity curves obtained during plating and stripping of lithium for different thickness of the alloying anode material. Development of a computational model that captures the alloying, plating, and stripping process of lithium completes the first quarter milestone.

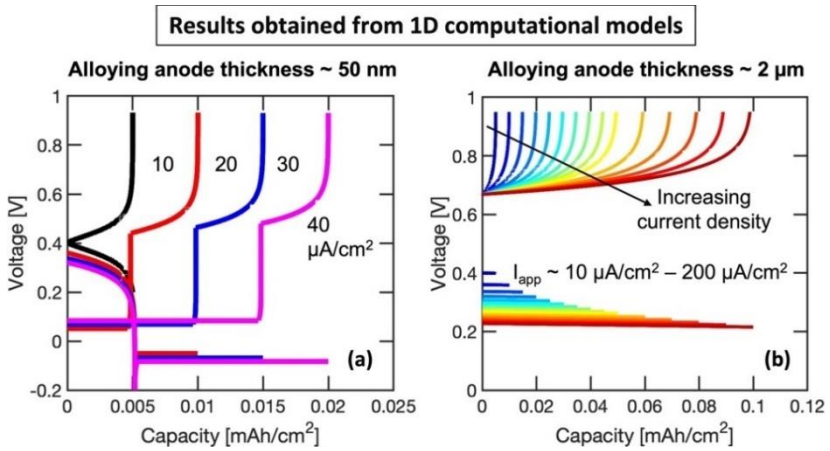

Figure 84. Computation predicted voltage versus capacity curves obtained during plating and stripping of lithium with alloying metal anodes. (a) Thinner alloying anode layer is used with thickness ~ 50 nm, which experiences both alloying and plating reactions. During stripping, the plated lithium strips first and the dealloying process starts later. (b) With 2-μm-thick metal foil, all the deposited lithium ends up alloying with the metal. No plating of lithium is observed. During stripping, only dealloying is observed.

Patents/Publications/Presentations

Presentations

- 242nd Electrochemical Society Fall Meeting 2022, Atlanta, Georgia (October 9–13, 2022): "Computational Modeling of Void Formation Mechanism at the Lithium/Solid-Electrolyte Interface"; P. Barai, T. Fuchs, J. Janek, and V. Srinivasan. Invited.
- Materials Research Society Fall Meeting, Boston, Massachusetts (November 27 – December 2, 2022): "Theoretical Understanding of Heterogeneous Nucleation During Lithium Electrodeposition"; A. Mistry and V. Srinivasan.

Task 3.3 – Modeling of Amorphous Solid-State Conductors (Gerbrand Ceder, University of California, Berkeley)

Project Objective. Solid-state batteries are promising to achieve high energy density. The project objective is to determine the design principles needed to create solid-state electrolytes (SSEs) with high Li-ion conductivity, while also achieving stability against common Li-ion cathodes and Li-metal anodes.

Project Impact. The project will lead to understanding the factors that control Li-ion motion in crystalline and amorphous solids and will develop strategies to create stable interfaces against lithium metal and high-voltage cathode materials. The understanding of such processes is necessary to determine design principles to develop reliable all-solid-state batteries (ASSBs).

Approach. High-throughput (HT) computation is used to screen suitable solid electrolytes (SEs) with high electrochemical stability and high ionic conductivity, by incorporating nudged elastic band and an *ab initio* molecular dynamics method. Meanwhile, density functional theory (DFT) is used to calculate bulk elastic constants of materials, surface energies, and interface decohesion energies of grain boundaries. Thermodynamic interface stability is assessed from *ab initio* computed grand potential phase diagrams in which the lithium voltage can be controlled. Kinetic limits for SE decomposition are assessed by topotactic lithium insertion and removal from the SE.

Out-Year Goals. Future goals include the following: (1) gain insight into what creates high Li-ion conduction in sulfide and oxide solids, and (2) develop stable, processable solid-state conductors that can be applied in ASSBs.

Collaborations. There are no collaborative activities this quarter.

Milestones

1. Computationally explore novel Li-ion conductors in the space of overlithiated rocksalts. (Q1, FY 2023; Completed)
2. Design and synthesize novel overlithiated ionic conductor. (Q2, FY 2023; In Progress)
3. Experimentally investigate ionic conductivity in novel ionic conductor and optimize to > 10^{-4} S/cm. (Q3, FY 2023; In progress)
4. Evaluate anodic and cathodic stability of novel conductor and test against lithium metal and cathode materials. (Q4, FY 2023; In progress)

Progress Report

Designing Overlithiated Rocksalt-Based Lithium Superionic Conductors

Li-metal oxides with a face-centered cubic (*fcc*) anion sublattice constitute a large family of compounds, but their potential for serving as superionic conductors has not been explored. Recently, formation of distorted face-sharing lithium polyhedra at intermediate states on lithium insertion has emerged as a key mechanism to account for the fast kinetics observed in several Li-ion anodes (for example, $Li_4Ti_5O_{12}$[1], $Li_3V_2O_5$[2]). The team proposes that constructing a face-sharing lithium configuration, in which lithium ions simultaneously occupy an octahedral site and its face-sharing tetrahedral site (Figure 85a), could be a general strategy to enhance the Li-ion conductivity in *fcc*-type oxides. Such a face-sharing configuration leads to strong Li-Li interactions, which will lift the lithium site energy and potentially activate ion migration with low barriers. However, the face-sharing lithium environment is typically absent in stoichiometric *fcc* oxides such as rocksalt. To create a face-sharing lithium configuration, they propose to introduce over-stoichiometric lithium in the rocksalt lattice, which may naturally drive lithium to occupy the tetrahedral sites that are face-sharing with the octahedral lithium.

The team performed HT DFT calculations to evaluate the phase stability of various redox-inactive metal couples in the presence of over-stoichiometric lithium. The calculated compositions share the general formula of $Li_{1+x+2y}M1_zM2_{1-x-z}O_2$, where y is the overlithiation level (y = $\frac{1}{6}$ or $\frac{1}{12}$) and x is the Li-excess level (x = 0, $\frac{1}{6}$, $\frac{1}{3}$). Sixteen redox-inactive metal cations that are commonly used in SSEs were selected. The resulting metal compatibility heatmap is shown in Figure 85b, where each pixel represents the average E_{hull} of all the computed compounds for the selected metal pairs. A lower E_{hull} value suggests that the metal couples can better accommodate the face-sharing configuration induced by over-stoichiometric lithium. From this heatmap, it can be inferred that larger metal cations (for example, In^{3+}) generally lead to better phase stability. This trend occurs because larger cations can better tolerate structure distortions caused by face-sharing configuration, except for La^{3+}, which is too large to stabilize a six-fold coordination. Based on these HT results, they will further investigate the In-based overlithiated rocksalt system and examine the Li-ion conductivity both computationally and experimentally.

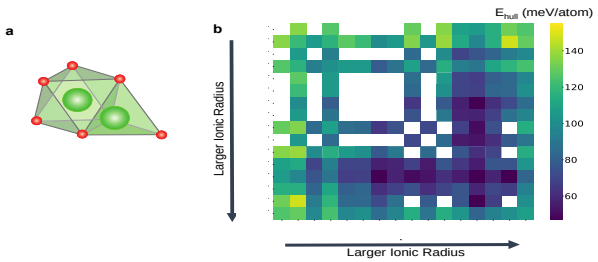

Figure 85. (a) Schematic of tetrahedral-octahedral face-sharing lithium configuration. (b) Metal compatibility heatmap extracted from high-throughput density functional theory calculations.

References

[1] Zhang, W., et al. "Kinetic Pathways of Ionic Transport in Fast-Charging Lithium Titanate." *Science* 367 (2020): 1030.

[2] Liu, H. et al. "A Disordered Rock Salt Anode for Fast-Charging Lithium-Ion Batteries." *Nature* 585 (2020): 63–67.

Patents/Publications/Presentations

Presentation

- Sun, Y., B. Ouyang, Y. Wang, Y. Zhang, S. Sun, Z. Cai, and G. Ceder. "Enhanced Ionic Conductivity and Lack of Paddle-Wheel Effect in Pseudohalogen-Substituted Li Argyrodites." *Matter* 5, No. 12 (2022): 4379–4395.

Task 3.4 – *In Situ* and *Operando* Thermal Diagnostics of Buried Interfaces in Beyond Lithium-Ion Cells
(Ravi Prasher, Lawrence Berkeley National Laboratory)

Project Objective. Transport at various interfaces in beyond Li-ion cells will play a major role in electrochemical performance and reliability. It has not yet been possible to thermally profile a Li-metal cell during operation to provide a spatially resolved map of thermal transport properties throughout the cell. The objective of this research is to create a metrology capable of spatially resolved *in operando* thermal property profiling, and then to relate thermal property to the quality of electrodes and interfaces, and to use the developed thermal metrology to understand electrochemical processes in Li-metal batteries, such as dendrite growth, interface kinetics, and ionic transport.

Project Impact. Characterizing electrochemical processes in Li-metal cells such as lithium deposition and dendrite growth at interfaces is of great significance for understanding and enhancing their electrochemical performance and reliability. *In situ* and *operando* micro electrothermal sensors can provide significant information regarding the impact of buried interfaces as a function of time, material, voltage, current, temperature, etc. Therefore, it is important to develop *operando* micro electrothermal sensors and develop models relating those signals to electrochemical performance for beyond Li-ion cells. The physics-based model relating thermal and electrochemical properties based on these measurements can facilitate future design of Li-metal batteries.

Approach. To accomplish project goals, the team will utilize an in-house adapted 3-omega (3ω) technique to probe thermal properties of a Li-metal cell while it is in operation, without affecting the operation of the cell. The 3ω sensors will be deposited and fabricated on Li-metal cells based on previous learning on 3ω sensor fabrication. The characteristic depth of the thermally probed region is defined by the wave's "thermal penetration depth," $\delta_p = \sqrt{D/2\omega}$, where D is the sample's thermal diffusivity, and 2ω is the heating frequency of the thermal wave. By depositing the project's 3ω sensors on the battery's outer surface and adjusting ω, the team controls δ_p to span the full range from the top to the bottom layer, thereby noninvasively probing the thermal transport in subsurface layers and interfaces within the bulk of the battery. Thermal transport can be related to quality of the interfaces. By doing concurrent thermal transport and electrochemical performance measurements, the team plans to relate thermal transport to electrochemical performance. As frequency-based thermal measurement techniques provide excellent spatial resolution within the cell, the team also plans to study heat generation at the electrolyte/Li-metal interface and to relate the thermal signals to the interface kinetics and ionic transport. The frequency dependence of heat generated due to transport resistance is different from that due to kinetic resistance. The team plans to utilize this difference to separate the contributions of kinetic and transport resistance at the interface, which will enable understanding of interface kinetics and transport at the Li-metal / solid-state electrolyte interface.

Out-Year Goals. The project will design, build, and implement the adapted 3ω metrology to examine thermal properties and a general frequency-dependent thermal metrology to examine heat generation. This will involve developing and testing the metrology itself along with accompanying theory, designing compatible battery samples, and applying the technique to live cells. The team will measure thermal transport properties of battery materials provided by collaborators. Combined with the electrochemical performance measurement, this will provide significant information relating the thermal signal to the electrochemical process.

Collaborations. This project collaborates with two Lawrence Berkeley National Laboratory groups: V. Battaglia's for cell assembly for 3ω studies, and R. Kostecki's for pristine battery active material growths for studies of thermal signals related to electrochemical process.

Milestones

1. Validation of multiharmonic electro-thermal spectroscopy (METS), an electrochemical-thermal method to resolve transport and kinetic overpotential at the electrochemical interfaces. (Q1, FY 2023; Completed)
2. Resolution of kinetic and transport overpotential at the lithium – Li-La-Zr-O (LLZO) interface using METS. (Q2, FY 2023)
3. Study of the effect of self-heating/temperature rise on the combined and individual components of interface electrochemical resistance. (Q3, FY 2023)
4. Study of effect of stack pressure on thermal and electrochemical interface resistance at the Li-LLZO interface. (Q4, FY 2023)

Progress Report

This quarter, the team worked on validating METS for spatially resolved electrochemical measurements. METS works on the principle that different electrochemical processes have thermal signatures in different harmonics of the alternating current passed through an electrochemical cell. It also utilizes the concept of thermal penetration depth to achieve spatial resolution.

To verify METS, the team designed a model system (an electrochemical cell) with a Li-foil electrode and electrodeposited lithium electrode. They performed METS measurement using a sensor near the electrodeposited electrode and tried to resolve the contribution of electrode kinetics versus the transport overpotential at the interface due to the presence of surface passivation layer (solid electrolyte interphase, SEI). To show the effect of SEI growth on the interface overpotential, they performed METS and electrochemical impedance spectroscopy (EIS) simultaneously on a cell freshly after preparation (pre-SEI growth) and after cycling the cell and letting the SEI grow under 40°C for 12 hours (post-SEI growth). Both EIS and METS showed increase in the interface resistance attributable to the SEI growth. However, since the information from EIS is limited, the team could not differentiate or quantify the amount of the increase in SEI resistance to any particular electrode. Unlike with EIS, METS provides spatial information as well; thus, they were also able to resolve the contribution of each electrode on the apparent interface resistance.

Figure 86a shows the schematic of the fabricated model cell and Figure 86b shows the EIS spectra before and after SEI growth. As seen in Figure 86a, although the two electrodes are chemically identical (lithium), one is electrodeposited, whereas the other is foil lithium. They expect the electrodeposited lithium to be more pristine, while the foil lithium should contain surface contaminants and therefore should have a higher interface resistance. In the EIS plots (Figure 86b), they do see two semi-circles possibly pertaining to the two electrodes. However, there is no certain way of quantifying the apparent interface resistance to any particular electrode.

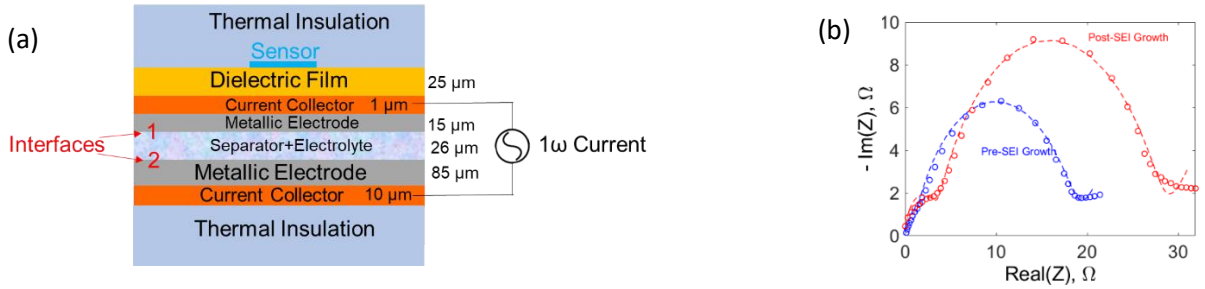

Figure 86. (a) Schematic of model cell with electrodeposited and foil lithium electrodes. The multiharmonic electro-thermal spectroscopy sensor is deposited on the dielectric film with a thin-film copper current collector on which 15-µm lithium is electrodeposited. (b) Electrochemical impedance spectroscopy (EIS) spectra of the cell measured after cell assembly (pre-SEI, blue) and after cycling to allow SEI growth (post-SEI, red). Two semi-circles are visible on both spectra; however, attributing each semi-circle to particular electrodes is ambiguous because of the lack of spatial information with EIS.

Unlike in the case of EIS, from the frequency dependence of the thermal penetration depth, and from the non-linearity in the generation of thermal signature, METS can resolve both the kinetic overpotential versus transport overpotential at the interface and the contribution of each electrode toward the transport and kinetic overpotential. Figure 87 shows the experimentally obtained METS spectrum for different current magnitudes for the model cell pre-SEI growth (top) and post-SEI growth (bottom).

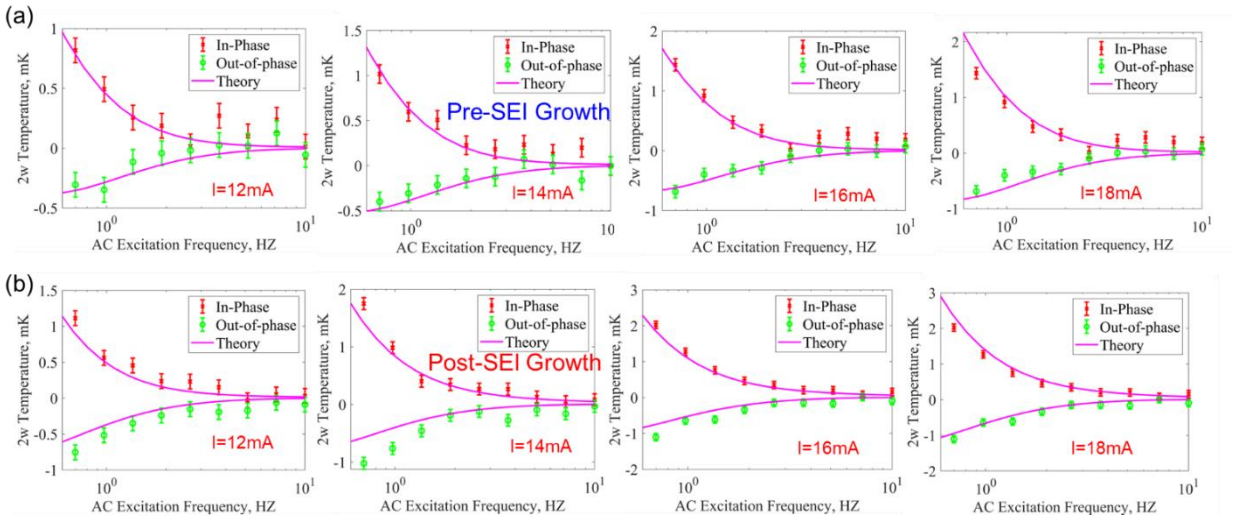

Figure 87. Multiharmonic electro-thermal spectrum and the best-fit lines (purple) at different current magnitudes for pre-SEI growth (a, top) and post-SEI growth (b, bottom) cases. From the frequency dependence of the thermal penetration depth, the spatial resolution, that is, resolution of the contribution of each electrode, is achieved. From the non-linear dependence of electrode kinetics on the current, the resolution of transport (SEI resistance) and the kinetic overpotential is achieved.

From the best-fit to METS spectrum at different current magnitudes, the team was able to deduce the contribution of kinetics and transport overpotentials at each electrode (summarized in Table 3 and Table 4). The total resistance due to kinetics and SEI at both the electrodes should sum up to the apparent low frequency impedance in the EIS spectra. As seen in the comparison (Table 3), the total impedance measured from EIS and METS agree well and therefore validate the METS method.

Table 3. Summary of impedances related to kinetic and transport overpotentials at the interface measured using multiharmonic electro-thermal spectroscopy (METS) and electrochemical impedance spectroscopy (EIS) for the cell *pre-SEI* growth.

	Electrode 1, Transport	Electrode 1, Kinetics	Electrode 2, Transport	Electrode 2, Kinetics	Total
METS	1.9 Ω	0.1 Ω	17.2 Ω	0.8 Ω	**20 Ω**
EIS	Unknown	Unknown	Unknown	Unknown	**18.8 Ω**

Table 4. Summary of impedances related to kinetic and transport overpotentials at the interface measured using multiharmonic electro-thermal spectroscopy (METS) and electrochemical impedance spectroscopy (EIS) for the cell *post-SEI* growth.

	Electrode 1, Transport	Electrode 1, Kinetics	Electrode 2, Transport	Electrode 2, Kinetics	Total
METS	5.9 Ω	0.2 Ω	23.7 Ω	0.8 Ω	**30.6 Ω**
EIS	Unknown	Unknown	Unknown	Unknown	**28.2 Ω**

Patents/Publications/Presentations

Presentation

- 242nd Electrochemical Society Meeting, Atlanta, Georgia (October 9–13, 2022): "Multi-Harmonic Electrothermal Spectroscopy (METS), A New Technique for Spatially Resolved Electrochemical Measurements"; D. Chalise, J. Schaadt, A. Dhar, V. Srinivasan, S. Lubner, S. Kaur, and R. Prasher.

Task 3.5 – Multiscale Modeling of Solid-State Electrolytes for Next-Generation Lithium Batteries (Anh Ngo, Larry A. Curtiss, and Venkat Srinivasan, Argonne National Laboratory)

Project Objective. This project is part of a multiscale modeling effort to obtain an in-depth understanding of the interaction of the electrode and the solid electrolyte (SE) aimed at developing highly efficient solid-state electrolyte (SSE) batteries for vehicle applications. Input parameters needed for mesoscale (continuum) level calculations are being obtained from atomistic calculations including density functional theory (DFT) and classical molecular dynamics (MD) simulations. This atomistic input will enable a multiscale computational procedure for SSEs that is capable of successfully capturing the physicochemical aspects during charge and discharge process, including lithium transport mechanisms, interfacial phenomena during the insertion and extraction of lithium ions, and mechanical deformation of SSE.

Project Impact. A major safety concern experienced with commercially available Li-ion batteries under some scenarios is leakage of the liquid electrolyte (LE), which can potentially catch fire. Replacement of the LE is necessary to decrease the fire hazard and improve safety associated with present-day Li-ion batteries. In addition, use of SEs provides a path to prevent dendrites in Li-metal anodes, thereby leading to batteries with significantly higher energy density. The impact of this project will be to help in development of good SSEs as a replacement for the commercially used organic LEs to improve safety and energy density in Li-ion batteries.

Approach. Parameters needed for mesoscale modeling of grain interior, grain boundary (GB), and electrode-electrolyte interface will be calculated by DFT-based calculations along with Monte Carlo and MD simulations. The calculations will be used to determine properties of the electrode with the SE as well as in GB regions of the SE. This will include calculations of structure, stability, ionic conductivity, Young's modulus, fracture toughness, exchange current density, and other properties.

Out-Year Goals. The out-year goals of this work are to calculate other properties such as fracture toughness and include other SSEs and coatings in the multiscale modeling.

Collaborations. This project collaborates with Y. Cui at Stanford University.

Milestones

1. Development of reactive force field (ReaxFF) for $LiCoO_2$ (LCO) || Li-Ge-P-S (LGPS) interface systems using DFT calculations. (Q1, FY 2023; Completed)
2. Development of ReaxFF for LCO || Li-Nb-Ti-O (LNTO) interface systems through DFT calculations. (Q2, FY 2023; Initiated)
3. Investigate lithium transport across LCO||LGPS and LCO||LNTO interface with reactive MD calculations. (Q3, FY 2023; Initiated)
4. Mesoscale calculations for interdiffusion of transition metal ions between cathode and SEs. (Q4, FY 2023; Initiated)

Progress Report

Two solids in direct contact with each other exchange atoms (or ions) to reach an equilibrium among themselves. The exchange of atoms (or ions) is mostly driven by the chemical and/or electrochemical potential gradient at the interface. This particular phenomenon is prevalent in solid-state lithium-ion batteries, mostly at the interface between the cathode (such as LCO and Ni-Mn-Co) and the SE (such as Li-La-Zr-O, LGPS). Interdiffusion of ions can lead to the destruction of the desired lattice structures at the electrode/electrolyte interface, which can substantially increase the energy barrier (a decrease in exchange current density) associated with charge transfer between the cathode and SE. Formation of a new phase is also possible at the cathode/SE interface due to exchange of ions, which can lead to the formation of resistive cathode electrolyte interphase films capable of detrimentally influencing the interfacial ion transport mechanism. Interdiffusion of ions can be either chemical or electrochemical in nature. Chemical form of interdiffusion occurs during the synthesis process where the composite of the cathode and SEs are subjected to elevated temperatures. Due to the faster diffusion kinetics at elevated temperatures, the chemical interdiffusion is accelerated, and substantial amount of ion exchange is observed, which leads to formation of a very resistive interphase layer that can substantially impact overall cell performance. Some interdiffusion phenomena can become more prominent during cell cycling where the electrode/electrolyte interface is subjected to a potential gradient. However, it is assumed that the applied potential gradient causes transfer of only the desired ions (such as lithium cations in a Li-ion cell, and oxygen ions in solid oxide fuel cells), and the interdiffusion of the undesired ions from the cathode or the electrolyte leads to a net zero flow of current. However, the chemical configuration of a cathode in a fully charged condition ($Li_{0.5}CoO_2$) is very different from a cathode in the discharged condition ($LiCoO_2$). Lack of lithium in charged conditions can provide multiple empty sites for the undesired cations from the electrolyte to move into the cathode domain. Also, due to a large variation in the energy landscape, it is possible to have the formation of alternate phases when the cathode exists in a charged condition, as compared to a discharged one. Due to the deleterious effect of the interdiffusion of ions at the cathode/SE interface, it is helpful to understand the ion transport mechanism and the speed at which this transport occurs, to calculate the extent of the formation of the interphase layer. Rate of transport of ions can be obtained from the self-diffusion coefficients of each of the atoms (or ions) within the cathode and SE of interest.

Since interdiffusion of ions among the cathode and SE leads to formation of the resistive interphase layers, it is desirable to somehow minimize the intermixing of the various atoms. The most common strategy is the incorporation of interphase layers capable of slowing down the rate of ion transport between the cathode and the SE. $LiNbO_2$ has been used extensively in various experiments to minimize the interdiffusion of ions between layered oxide cathodes (LCO) and sulfide-based SEs (LGPS). In the present research, effectiveness of these $LiNbO_2$ layers in preventing the interdiffusion of ions during long-term operation (such as hundreds of cycles), will be investigated using a multiscale computational methodology.

This quarter, the team focused on obtaining the ReaxFF for LCO||LGPS interface systems using *ab initio* molecular dynamics (AIMD) simulation and DFT calculations. An in-house *C++* code integrated with a large-scale atomic/molecular massively parallel simulator (LAMMPS) was used to minimize the difference in electronic structure parameters between the reference DFT calculations and a target ReaxFF. The process of parametrization is shown in the flowchart (Figure 88), starting from the DFT calculation that was used as a starting/reference point, followed by ReaxFF parametrization, and testing of the accuracy of results for the solid structure and diffusion process obtained with the parametrized potential parameters. Increasing the complexity of the inputs to be parametrized and controlling the weight error are part of the plan. The validity of the output parameters was tested through the MD simulation technique as implemented in LAMMPS by the comparison of the lattice vector parameters, interatomic distances, and energy evolution of the cell deformations, with the same structures optimized using reference DFT calculations or AIMD simulation under target thermodynamic conditions, while directly comparing ion diffusivity in charge, discharge, and equilibrium with experimental

measurements. Once the validity of the ReaxFF potential parameters is confirmed by both theory and experiment, a large-scale system can be assembled to collect the statistics along the ensemble of particles and, hence, increase the accuracy of the simulated properties.

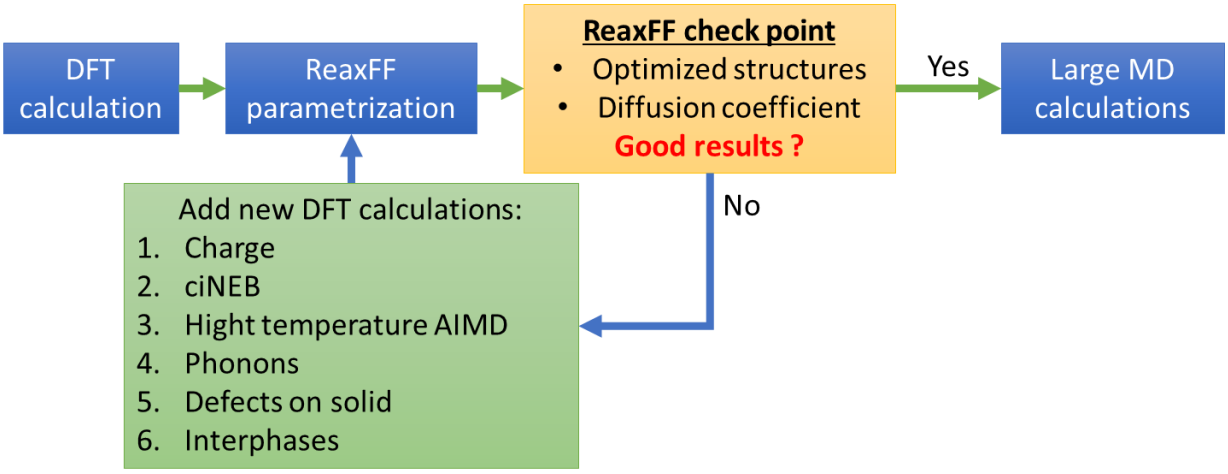

Figure 88. Flowchart of ReaxFF parameterization protocol.

The DFT calculations were carried out with the Perdew-Burke-Ernzerhof functional with a plane wave basis and both generalized gradient approximation (GGA) and GGA+U calculations were performed using the Vienna *Ab initio* Simulation Package (VASP) code. Additionally, a quenching surface generated by AIMD between LCO and $Li_{10}GeP_2S_2$ will be assembled, followed by further optimization for reference. The optimized quenched surface, single-point frames from the AIMD calculations every 50 fs in a total of 20 ps, and the formation energy will be obtained from DFT calculations and will be used to support force field parameterization. Those calculations will be added to the parametrization as a contingent plan to improve the force field accuracy.

Following the parametrization protocol described above (Figure 88), the potential parameters of ReaxFF were obtained. To check the reliability of the obtained set of parameters, the evolution of the cohesive energy on cell deformation was calculated. A short summary is illustrated in Figure 89, where the unit cells for CoO, GeS_2, GeP, and P_2O were compressed and expanded along the [111] direction; the energy profiles calculated with the DFT approach coincide well with those obtained using the parametrized force field parameters from MD simulations. This is especially pronounced for the cohesive energy near the equilibrium values of the lattice vector, while at the lower scales the difference is noticeably higher, which might be a subject of additional revision by means of the AIMD simulations. Nevertheless, for all the considered cases in the framework of LCO||LGPS interface, the comparison of the lattice parameters also shows insignificant deviations (not exceeding 10%) between the DFT optimized structures and those obtained using MD simulation.

The team is performing a series of DFT, climbing image nudged elastic band calculations to determine ReaxFF for LCO||LNTO interface and will report on the results next quarter.

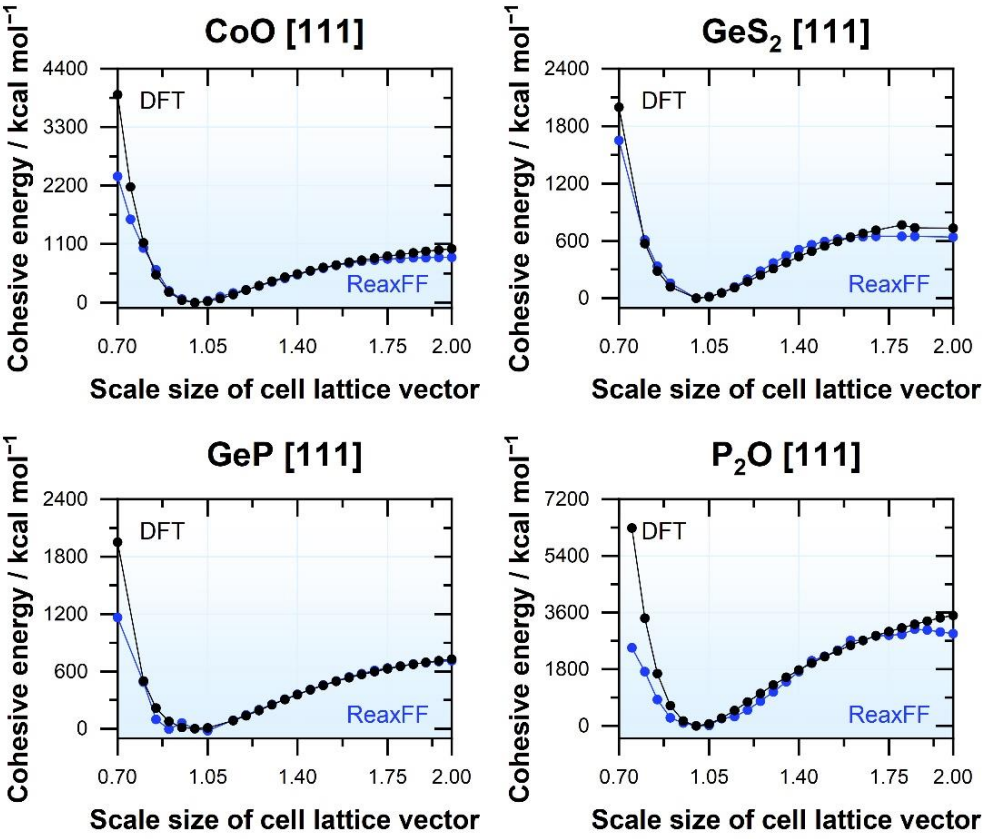

Figure 89. Illustration of the cell deformation difference expressed by the evolution of the cohesive energy against the compression (lower values) and expansion (higher values) along [111] direction of the unit cell vector for CoO, GeS_2, GeP, and P_2O obtained by means of density functional theory calculations and molecular dynamics simulation using the parameterized ReaxFF potentials.

Patents/Publications/Presentations

The project has no patents, publications, or presentations to report this quarter.

Task 3.6 – First-Principles Modeling of Cluster-Based Solid Electrolytes (Puru Jena, Virginia Commonwealth University)

Project Objective. The objective of the project is to use cluster-ions, which are stable atomic clusters that mimic the chemistry of individual atoms, as the building blocks of new solid electrolytes (SEs) for Li-ion batteries and the corresponding battery system. The advantages of using cluster-ions to replace elemental ions is that the size, shape, and composition of the former can be tailored to achieve higher superionic conductivity, electrochemical stability, and charge transfer across the solid-state ions than the conventional materials. More specifically, the goal is to develop superior SEs based on cluster-ions and to model these SEs and their interfaces with electrodes, especially with the Li-metal anode, for successful integration into high-performance solid-state batteries (SSBs) for electric vehicles (EVs). The team will model and screen cluster-based solid-state electrolytes (CSSEs) that, compared to conventional SEs, have low activation energies, practical room-temperature ionic conductivities, wide electrochemical stability windows, and desired mechanical properties that, for example, can inhibit Li-metal anode dendrite growth. They will provide a fundamental understanding of the ionic conduction mechanism in the newly developed CSSEs and will identify means to further improve property metrics via chemical and defect engineering. The team will model the interfacial properties, such as the structural, chemical, electrochemical, and ion/charge transfer properties, between the CSSEs and electrodes at the atomic level, as well as find the interfacial coating materials with desired properties. Based on accumulated data from modeling, they will establish links between the basic parameters of the cluster-ions and the bulk/interface properties, which can directly guide experiments. Meanwhile, the team will work closely with experimentalists in the BMR Program to complement the project's theoretical efforts and to guide them in focused development of the predicted CSSEs and the interfaces.

Project Impact. The proposed project will open a new avenue for guiding experiments in the synthesis of SSBs equipped with CSSEs and capable of operating over a wide temperature range. Modeling and understanding of the ionic conduction of CSSEs and their interfacial properties with electrodes, especially with Li-metal anode, will enrich current battery science and also train the future workforce in SSB development for next-generation EVs by supporting postdoctoral fellows.

Approach. This project will employ multiscale theoretical methods and computational techniques.

Out-Year Goals. The out-year goals involve modeling development of new CSSE materials and database.

Collaborations. The team is working with J. Nanda of SLAC Stanford Battery Research Center (formerly of Oak Ridge National Laboratory), Y. Wu of Ohio State University, and D. Mitlin of University of Texas, Austin, on SEs.

Milestones

1. Complete phase analysis for interfaces between the CSSE and electrodes. (Q1, FY 2022; Completed)
2. Model structural properties of CSSE interfaces. (Q2, FY 2022; Completed)
3. Model chemical/electrochemical and transport properties of CSSE interfaces. (Q3, FY 2022; Completed)
4. Identify potential coating materials, and model electrolyte-coating-electrode interfaces. (Q4, FY 2022; Completed)
5. Complete multiple papers for the project based on analysis of data obtained previously. (Q1, FY 2023; In progress)

Progress Report

All milestones have been completed. As planned, the team is completing a number of new papers based on analysis of previously obtained data. This quarter, two papers have been finished. One is on understanding the ionic conductivity of a mixed phase with both cluster and halogen ions. A new program is developed to characterize the dynamically changed channel space and Li-anion interactions in systems containing different ratios of cluster-ions and halogens. The dynamical channel space method is found to be a simple yet effective way to qualitatively evaluate the ionic conductivity and the activation energy of the CSSEs. In another paper, they reported on studying the kinetic effect of the cluster-ions on the SSE-Li interface, and showed that the cluster-ions can inhibit the detrimental reaction at the interface by *in situ* formations of interphases that are electronically insulating and ion-conductive. The paper was submitted to *PRX Energy* and is in revision.

The team's previous studies show that the ionic conductivity and activation energy of a CSSE with halogen dopants do not change monotonically with the dopant concentration. For example, for a $Li_6PS_5(BH_4)_{1-x}Cl_x$ system, the system exhibits the lowest activation energy and the highest ionic conductivity at x = 0.875. This is orders of magnitude higher than that at x = 0.125 or 0.675. This suggests that the ionic conductivity is independent from the concentration of the halogen and cluster ion. The ionic conductivity is closely related to the available channel space for Li-ion migration in the structure. For the channel space, conventional studies have focused on characterizing the "static" spaces in an SSE using topology analysis. However, given the presence of non-spherical cluster ions and their motional dynamics in the studied SSEs, it is necessary to characterize the dynamically changing channel space or the voids inside an SSE. They have developed a method to evaluate the dynamical channel space inside a given SSE by going through the "snapshots" from the molecular dynamics simulations. For each snapshot structure, the cell is first filled by dots, with each dot carrying a tiny volume unit. Then, the dots that can accommodate at least one lithium ion will be identified using a specific algorithm. The total void space in a structure that can hold at least one lithium ion is then determined. The channel spaces around each lithium ion and between the neighboring lithium ions are further evaluated, as shown schematically in Figure 90a.

The ionic conductivity is also closely related to the Li-anion and Li-cation interactions in the system. A lithium ion will deviate from its equilibrium position (at the ground state) against the anion during diffusions. The deviation will strain the Li-anion interaction and cost energy, which is related to the activation energy of an SSE. For a system with "soft" Li-anion interactions (small force constant of a Li-anion spring, per Figure 90a), large deviations can be accessible during the thermally excited Li-ion diffusion, corresponding to relatively low activation energy. For systems with "stiff" Li-anion interactions (large force constant of a Li-anion spring), relatively small deviations can be accessible, corresponding to relatively high activation energy. Reduction in the neighboring Li-Li distance from its equilibrium value (at the ground state) would suggest increased Li-ion correlation during the diffusion.

Figure 90b shows the calculated channel spaces and deviations against the Cl-doping concentration at room temperature. It is found that lithium ions always approach the Cl^- during the diffusion and reduce the Li-Cl distance from the equilibrium value at the ground state. As mentioned above, this will strain the Li-Cl interaction and cost energy. On the other hand, the Li-H ($@BH_4^-$) distance is largely maintained. This is because, although the lithium ions will approach BH_4^- during the diffusion, the anion cluster can accommodate the passing lithium ion using its large rotational and translational degrees of freedom, maintaining the equilibrium Li-H distance to lower the energy cost. This agrees well with the team's previous discoveries. They have found before that the dynamics of anion cluster can be categorized into two types. The first is called "responsive" dynamics, where the cluster can rotate and translate to accommodate a passing lithium ion to lower the pathway energy. The second is called "active" dynamics, where the clusters randomly rotate due to direct thermal excitations. These latter dynamics may inhibit the ion diffusion. Therefore, to make the high ionic conductivity in a CSSE is to introduce a "right amount" of cluster compositions and cluster dynamics. Excessive cluster dynamics can also lead to high activation energy and low ionic conductivity.

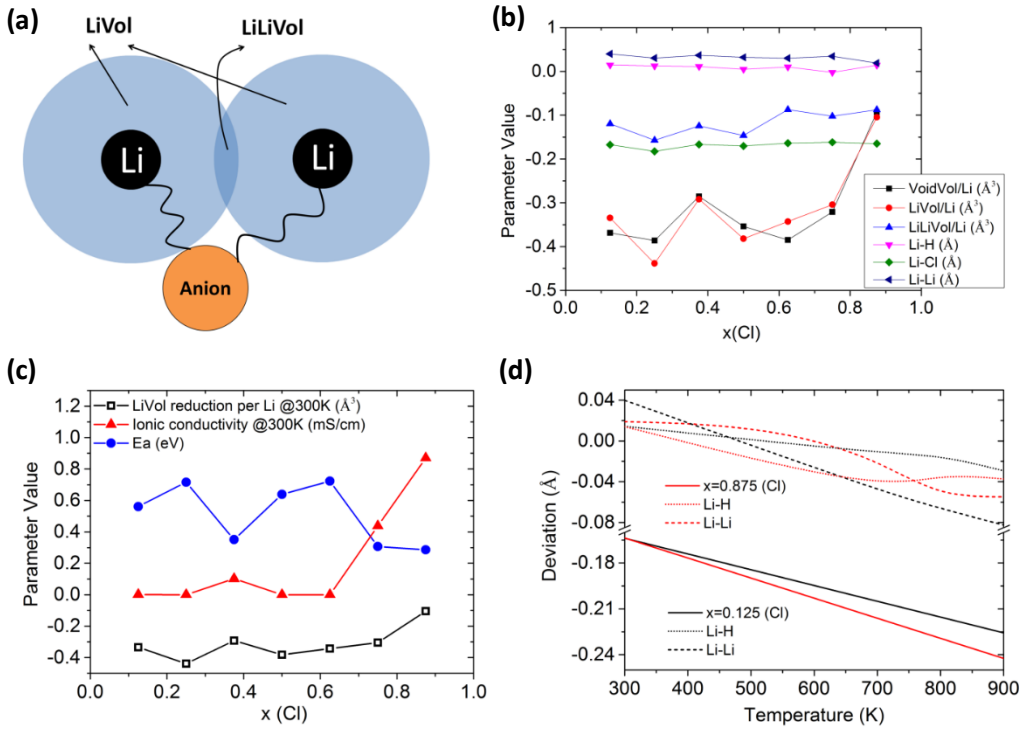

Figure 90. (a) Schematics show the channel spaces around each lithium ion (LiVol) and between the neighboring lithium ions (LiLiVol). It also shows the simple spring model capturing the Li-anion interaction in the system. (b) The calculated total void space (VoidVol), channel space surrounding each lithium ion (LiVol), channel space between neighboring lithium ions (LiLiVol), deviation of lithium ion from its equilibrium against BH_4^- (Li-H), deviation of lithium ion from its equilibrium against chlorine (Li-Cl), and deviation of the neighboring Li-Li distance from equilibrium. (c) Strong correlation between the channel space LiVol and the ionic conductivity/activation energy of the solid-state electrolyte. (d) Deviations of lithium ion from its equilibrium against Cl^- (solid lines), BH_4^- (dotted lines), and neighboring lithium (dashed lines) with elevated temperature at two chlorine concentrations, x = 0.875 and x = 0.125.

Figure 90c shows that the defined channel space surrounding each lithium (LiVol) correlates well with the ionic conductivity and activation energy of an SSE, and can serve as an effective descriptor for these quantities. Such dynamical channel space can be evaluated in a short time period and can be applied to qualitatively prescreen the compositions that can lead to high ionic conductivities. On the other hand, directly calculating the ionic conductivity at room temperature is extremely hard to converge, requiring a lengthy simulation time. Any shortage of simulation time may result in the computed ionic conductivities with orders of magnitude difference.

Figure 90d shows that the Li-Cl (solid lines) and Li-H (dotted lines) deviations for x = 0.875 are significantly greater than those of x = 0.125. This explains why the former exhibits the high ionic conductivity and low activation energy per Figure 90, that is, the system with x = 0.875 exhibits "soft" Li-anion interactions and small energy cost for the ion diffusion. The figure also shows that the Li-cluster (Li-H) distance deviates slightly from the equilibrium value (put at zero in the figure) with elevated temperature, due to the large deviation caused by the Li-ion diffusion that cannot be completely accommodated by the cluster dynamics at high temperatures. The reduction in the Li-Li distance also increases with elevated temperature, suggesting a stronger Li-Li correlation during the diffusion.

In the second paper, the team shows that explicit interface simulations at finite temperature are needed to understand the effects of the clusters on the stability of the SSE-Li interface with ion kinetics. As obtained from previous studies, the interface model between the CSSE and the Li-metal is built as a coherent heterointerface. These models are fully optimized and subject to *ab initio* molecular dynamics simulations at room temperature. Figure 91a shows an as-built interface of $Li_6PS_5(BH_4)$-Li with three possible terminal groups (H_2, B, and LiS) in contact with the lithium metal. They monitored the completeness of the cluster anions

PS_4^{3-} and BH_4^- at the interface throughout the simulation. The instability of the CSSE against lithium metal is attributed to the reduction of phosphorus in the poly-anion PS_4^{3-} contained in the original argyrodite composition, as suggested by the continuing P-S bond breaking in all cases in Figure 91b. In particular, PS_4^{3-} poly-anions in the lithium argyrodite Li_6PS_5Cl are reduced extremely fast, with the SSE structure reacting at the interface within only 5 ps. Meanwhile, the reduction reaction in the CSSE is significantly slower. With the terminal group of LiS, the reduction of PS_4^{3-} stops with about 90% of the poly-anions intact. The substitutional mono-anion BH_4^- for the halogen is found to be intrinsically stable against lithium metal, as shown in Figure 91b (red line). Radial distribution function (RDF) analyses reveal that a stable phase of $Li(BH_4)$ against lithium is formed at the interface. As shown in Figure 91c, the characteristic B-H peaks of $Li(BH_4)$ in the range of 3-5 Å start to appear at the interfaces with H_2 and LiS terminal groups. This corresponds to the sluggish reduction of PS_4^{3-} after 20 ps, shown in Figure 91b. The reduction stops at the LiS-terminated interface, which shows the strongest signals of the interphase $Li(BH_4)$ in its RDF (per Figure 91c), suggesting that the reduction reaction is effectively inhibited by the presence of $Li(BH_4)$, which is ionically conductive and electronically insulating. In contrast, there is no $Li(BH_4)$ formed at the B-terminated interface according to the corresponding RDF in Figure 91c, leading to progressive P-S bond breaking and reduction of PS_4^{3-}, as shown in Figure 91b (dashed line).

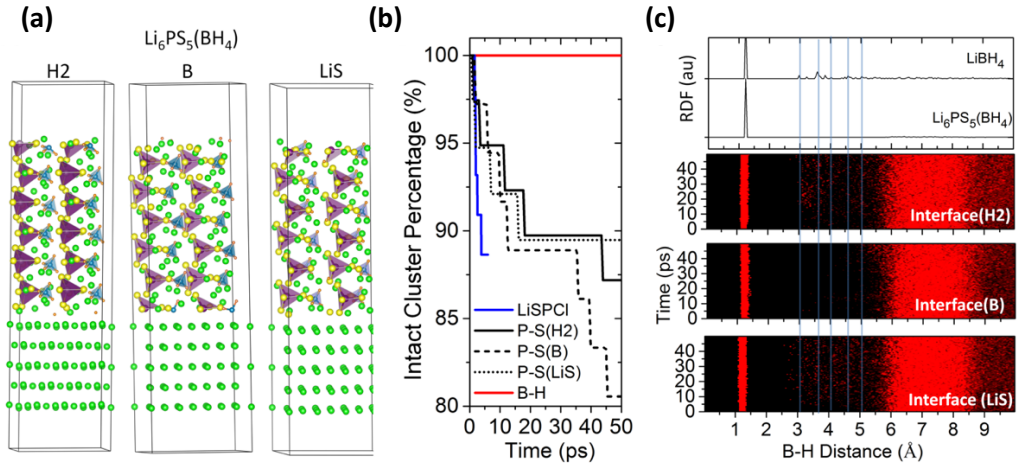

Figure 91. (a) Interface models with three possible terminal groups, with PS_4^{3-} units in purple tetrahedra, BH_4^- in blue tetrahedra, lithium in green, and sulfur in yellow. (b) Percentage of the intact clusters based on the *ab initio* molecular dynamics data. (c) Radial distribution function analyses at the interface.

Patents/Publications/Presentations

The project has no patents, publications, or presentations to report this quarter.

Task 3.7 – Predicting the Nucleation and Evolution of Interphases in All-Solid-State Lithium Batteries (Sabrina (Liwen) Wan, Lawrence Livermore National Laboratory)

Project Objective. The goal of this project is to develop and apply a suite of new computational tools to predict early-stage formation of metastable interphases in solid-state batteries (SSBs). To achieve this goal, this project focuses on meeting three primary objectives corresponding to different regimes within the early-stage interphase formation: (1) identify chemical motifs for pre-nucleation; (2) predict possible interphase structures; and (3) model the kinetics of interphase formation.

Project Impact. Degradation of solid-state electrolyte and formation of undesired secondary interphases at the solid electrolyte/electrode interfaces are some of the key issues that limit SSB technology from practical applications. The computational tools developed in this project will allow modeling of nucleation and formation of interphases with quantum-level accuracy as well as significantly improved efficiency compared to currently available methods. Completion of this project will also provide valuable insights into the correlation between local chemistry and interphase formation, which can be used to inform design of interfacial structures to lower interfacial resistance, and to extend cycling life of SSBs.

Approach. The project approach centers on close integration of *ab initio* molecular dynamics (AIMD) simulations, machine learning (ML), and stochastic methods to probe chemistry and nucleation across broad ranges of time and length scales. First, the team will identify chemical motif, which acts as chemical precursor for pre-nucleation based on ML and large-scale AIMD simulations. Second, they will predict possible interphase structures based on stochastic minimizations of population-weighted chemical motifs identified from the molecular dynamics (MD) simulations. Third, they will model the kinetics of interphase formation and evolution using metadynamics and solid-state nudged elastic band methods. To test the general applicability of the proposed computational methods, the team considers various commercially viable solid electrolyte (SE) and cathode materials, including cubic $Li_7La_3Zr_2O_{12}$ (LLZO) and LiPON SEs, and Li-Co-O (LCO) and Li-Fe-P (LFP) cathodes. These materials also represent a range of degrees of stability arising from their intrinsic properties—in particular, LiPON|LCO, LLZO|LCO, and LLZO|LFP are expected to form stable, less stable, and reactive interfaces, respectively.

Out-Year Goals. The future goal is to predict practical strategies either (1) to facilitate formation of the desired interphase that allows for fast Li^+ diffusion and is stable on cycling, or (2) to suppress formation of undesired interphase to reduce interfacial impedance of all-solid-state batteries.

Collaborations. There are no collaborative activities this quarter.

Milestones

1. Predict the structure and nucleation kinetics of secondary phases. (Q1 FY 2023; Completed)
2. Extract phase evolution kinetics from dynamic simulations. (Q2, FY 2023; In progress)

Progress Report

MD Simulations of La-Co-O Phase Nucleation at LLZO/LCO Interface. From the team's previous large-scale MD simulation of various LLZO/LCO interfacial models using ML interatomic potentials, they have observed lanthanum and cobalt interdiffusions. To better understand how the accumulated lanthanum and cobalt ions at the LLZO/LCO interface may lead to nucleation and formation of secondary phases, they have performed accelerated MD simulations to probe the pathways of such La-Co-O phase evolutions at the LLZO/LCO interface. They start the simulation by random packing of La, CoO_4 tetrahedra and CoO_6 octahedra building units in an empty cell, where the ratio of these clusters is chosen from preliminary AIMD simulations that were performed and analyzed previously. The atomic positions and lattice vectors of the interface model (Figure 92a) are then relaxed at 0 K using density functional theory. To accelerate the simulation of La-Co-O phase evolution, they have trained neural network interatomic potentials (NNP) using disordered La-Co-O structures and various La-Co-O crystal phases including $LaCoO_3$, $La_2Co_3O_7$, $La_2Co_3O_6$, and La_2CoO_4. The trained NNP have energy root-mean-square-error (RMSE) of 5.0 meV/atom and force RMSE of 0.29 eV/Å.

From the initial structure, the team carried out MD simulation with the NNP to probe possible crystalline seed formation and growth. First, a $LaCoO_3$ crystalline seed was created within the interface model under 1000 K, 0 GPa NPT [that is, constant number of atoms (N), pressure (P), and temperature (T)] ensemble (Figure 92b). Because Co-Co-Co-Co chain in the $LaCoO_3$ crystal has a square shape with Co-O coordination number of 6 (CoO_6 octahedral), the distance between the four cobalt atoms was adjusted by applying additional force to have a square shape. Next, the Co-O coordination number was changed by applying a metadynamic bias to the Co-O coordination number, while maintaining the Co-Co distance. As a result, $LaCoO_3$ crystalline seeds were successfully formed, and growth was observed after ~ 3 ns MD simulation at 1500 K and under 40 GPa pressure (Figure 92c). This is the first time of direct probing of phase transformation from disordered La-Co-O structure that is observed at the LLZO/LCO interface to a $LaCoO_3$-like structure at the atomistic scale. Further analysis is under way to extract characteristics of such phase evolution and correlation to the initial La-Co-O environment at the LLZO/LCO interface.

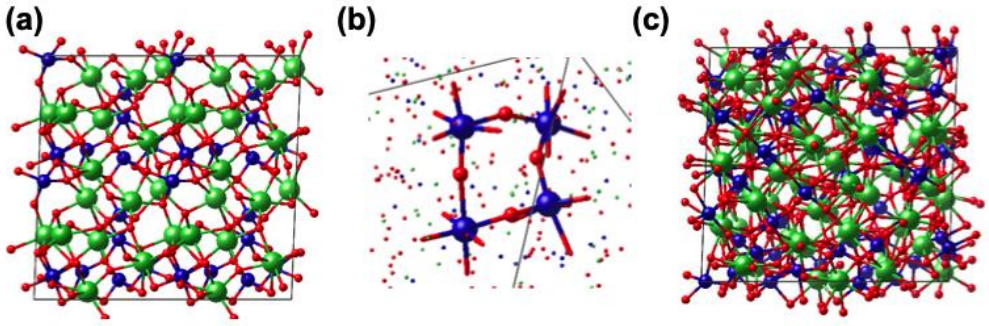

Figure 92. (a) Model La-Co-O structure formed at the LLZO/LCO interface. (b) $LaCoO_3$ nucleation seed. (c) Snapshot of model La-Co-O structure after ~ 3 ns of molecular dynamic simulations with NPT ensemble at 1500 K and 40 GPa, where $LaCoO_3$-like phase nucleation is observed. Here, lanthanum, cobalt, and oxygen atoms are represented as green, blue, and red spheres, respectively.

Development of Descriptors to Characterize La-Co-O Local Environment at LLZO/LCO Interface. To understand the impact of local structure of La-Co-O on its phase evolution, the team defined a bond orientational order parameter to better characterize the local structural disorders. As shown in Figure 93, the order parameters defined (q2 and q5) here can effectively distinguish local chemical environment in the La-Co-O phases. They are applying these descriptors to characterize the La-Co-O structures identified at the LLZO/LCO interface from previous AIMD simulations and extracting correlations between local chemical environment and phase evolution kinetics.

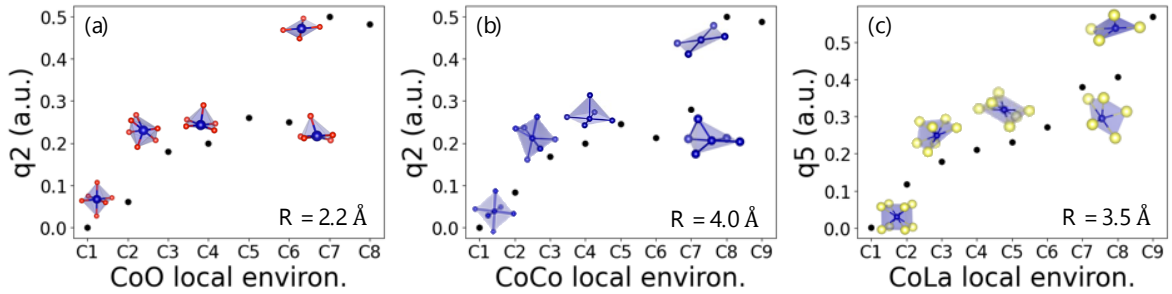

Figure 93. The bond orientational order parameters for (a) Co-O, (b) Co-Co, and (c) Co-La within the La-Co-O structures identified at the LLZO/LCO interface from *ab initio* molecular dynamic simulations. The local environment of configuration C1 corresponds to the local environment in the most stable $LaCoO_3$ phase predicted by Basin Hopping. R is the cutoff radius used in each order parameter calculation. For Co-O, Co-Co octahedral coordination, the q2 parameter is found to be most effective to capture local distortions, where for Co-La with 8-fold coordination environment, the q5 parameter is found most sensitive to local structural variations. Here, lanthanum, cobalt, and oxygen atoms are represented in yellow, blue, and red, respectively.

Patents/Publications/Presentations

Presentations

- Materials Research Society Fall Meeting, Boston, Massachusetts (November 27 – December 2, 2022): "Development of Machine-Learning Force Fields for Simulating Interfaces in Solid-State Batteries"; K. Kim, A. Dive, A. Grieder, N. Adelstein, S. Y. Kang, B. Wood, and L. Wan.
- Royal Society Meeting on Understanding Fast-Ion Conduction in Solid Electrolytes, Lancaster, UK (November 2022): "Paradigms of Structural, Chemical, and Dynamical Frustration in Superionic Conductors"; B. C. Wood.

Task 3.8 – Design of Strain Free Cathode – Solid-State Electrolyte Interfaces Using Chemistry-Informed Deep Learning
(Hakim Iddir, Argonne National Laboratory)

Project Objective. The main objective of this project is to use state-of-the-art machine learning (ML) techniques and high-performance computing (HPC) to model complex oxide materials that will allow the team to develop cathode / solid electrolyte interfaces that exhibit minimal or no strain as well as provide chemical stability at the interface between the cathode material and the solid-state electrolyte (SSE). A deep understanding and control of the cathode/SSE interface (including its chemical and mechanical stability) is needed to develop an effective solid-state battery (SSB). The active cathode material changes volume during cycling, particularly at high state of charge (SOC). This volume change leads to strained interfaces triggering loss of contact and delamination, and hence reduction/elimination of electron and ion transport pathways. The increased strain could also generate cracks within the SSE, creating new paths for lithium dendrite growth channels. These structural changes degrade the electrochemical performance of the battery. Several strategies have had limited success in alleviating these drawbacks, including mixed SSE, buffer layers between the cathode and the SSE, and dopants to improve chemical stability of the interface. These approaches, although promising, could not resolve issues with both the chemical and mechanical stability of the interface. In this project, the team proposes a new approach that takes advantage of well-established ML techniques and HPC to screen for candidate dopants of high-Ni-content Ni-Mn-Co (NMC) cathodes that would both reduce the volume expansion and the chemical reactivity (mixing) at the interface, with minimum impact on electrochemical performance and energy density of the cathode.

Project Impact. Structure-property relationships are at the heart of most fundamental scientific approaches. However, the link between structure and property remains a challenge in the materials science of complex systems, such as the oxides that form battery components. In particular, the chemical and mechanical stability of the cathode-SSE interface presents a challenge to development of SSBs. High-performance density functional theory (DFT) calculations provide the necessary framework to understand such systems. Unfortunately, given the limited number of atoms and time scales accessible by the method, along with the myriad calculations required to achieve satisfactory results, the computational cost of simulating all the possible configurations of a multicomponent oxide is prohibitive. In this work, the team augments the DFT data with ML (especially deep learning) techniques that allow them to access the large system sizes and longer time scales necessary to build thermodynamic models. They focus on understanding the nature of benchmark $Li_{1-\alpha}Ni_{1-x-y-z}Mn_xCo_yM_zO_2$ structures (M dopant, α, x, y, z < 1), their volume change with lithium content, the nature and concentration of the dopants, and chemical stability of the SSE-cathode interface. The DFT and ML approach will provide new cathode compositions that will reduce the strain of the SSE-cathode interface and hence improve its mechanical and chemical stabilities.

In this project, the team aims at developing a methodology that will allow them to explore and expand the configurational space using HPC approaches in a systematic and efficient way. The methodology will encompass DFT, *ab initio* molecular dynamics, molecular dynamics (MD), and ML. The methodology will also take advantage of various software already developed at Argonne National Laboratory (ANL) and at other U. S. Department of Energy laboratories (for example, Balsam) to automate, manage, and control the large number of calculations needed to achieve the project goal.

Approach. All calculations will be performed by spin-polarized DFT as implemented in the Vienna *Ab initio* Simulation Package (VASP). After geometry optimization within the DFT+U framework, electronic relaxation will be performed using a single-point calculation with the hybrid functional HSE06. For production calculations, they will use the message-passing interface (MPI) parallelized version of VASP.

Exploration of the potential energy surface is needed to predict the structure of solid materials and interfaces. Such calculations are infeasible using MD or DFT calculations alone. Thankfully, the potential energy surface of a system can be represented by the sum of the energies of the local neighborhoods surrounding each atom.

This enables the use of ML surrogate models trained with DFT calculations to capture the energies in local neighborhoods. The input to the ML surrogate must be a unique representation of the system under study. Consequently, the local environment of each ion is described using a local environment descriptor that renders the atomic configuration invariant to rotations, translations, and permutations of the atoms. In recent years, several different descriptors have come to prominence with advantages and disadvantages. Once the ML surrogate is trained, the total energy and forces over all the ions of any structural configuration can be determined. Such information can be used for atomistic simulations, namely, MD and Monte Carlo.

In this project, the team proposes to use the open-source DeepMDkit python/C++ package to construct the ML potential energy surface and force fields. The promise of DeepMDkit in this work is to provide near-DFT accuracy at orders-of-magnitude lower computational expense, comparable to traditional MD simulations. Efficiency in training is facilitated through integration with TensorFlow and MPI / graphics processing unit support.

One of the challenges of developing ML potential energy surface is achieving accurate predicted forces and energies across the entire configurational space, while minimizing the total number of calculations required for training. In recent years, active learning has been highlighted for its ability to target training examples most likely to improve the model quality or to achieve some other objective (that is, maximizing a predicted material property). DP-GEN, an open-source python package based on DeepMDkit, implements a similar active learning scheme with HPC support, and has been employed to construct ML potential energy surface with accuracy approaching DFT and sometimes exceeding embedded atom potential for experimentally measured properties of interest. In this work, the team proposes to leverage DeepMDkit and DP-GEN to efficiently generate ML potential energy surfaces for cathode-electrolyte systems including a variety of dopants.

Out-Year Goals. One out-year goal involves developing a DFT-trained ML model on NMC / $Li_7La_3Zr_2O_{12}$ interface, ready to use for large screening of new cathodes, SSE compositions, and cathodes/SSE interfaces. A second is to provide fundamental understanding on critical parameters limiting performance and stability of the cathode/SSE interface and hence of the SSB.

Collaborations. Project collaborators include J. Croy, C. Johnson, and E. Lee from ANL Chemical Sciences and Engineering Division for the synthesis phase of the project.

Milestones

1. Synthesize the most effective dopant (lanthanum) of high-Ni cathode materials (Ni > 0.9) and characterization. (Q1, FY 2023; Completed)

Progress Report

Modeling data suggest that substitution of large metal cations (for example, lanthanum, yttrium, calcium, or cerium) into NMC material will reduce the unacceptable volume reduction of the NMC crystal structure at high SOCs. The purpose of this study is to determine if one or a combination of larger cations would provide crystal stabilization on charging the cathode to high SOC.

Two batch sets were made to determine the following: (1) the solubility of lanthanum, and (2) if mixed elements would improve the solubility of large cation metals. An NMC 90-5-5 precursor: $(Ni_{0.90}Mn_{0.05}Co_{0.05})(OH)_2$ was obtained from the ANL Materials Engineering Research Facility. The first batch consisted of NMC 90-5-5 Baseline, 1%, 3%, and 5% by molar lanthanum addition. The second batch consisted of 0.5 mol% each of lanthanum and yttrium (0.5%LaY) sample and 0.25 mol% each of lanthanum, yttrium, calcium, and cerium (0.25%LaYCaCe). Appropriate amounts of metal nitrates were dissolved into water and then mixed with the precursor in a planetary mixer at 2000 rpm for 2 minutes. Freshly ground lithium hydroxide was then mixed in the material using the planetary mixer at the same rate and time. The mixtures were dried at least 5 hours in flowing N_2 at 100°C and then calcined at 720°C / 12 hours in flowing O_2.

Laboratory X-ray diffraction (XRD) disclosed the expected pattern of R-3m layered phase in each sample, with increasing amounts of impurity phase with increasing lanthanum substitution. The solubility of lanthanum was found to be < 1%. The impurity phase in the La-substituted samples was identified as $La_2Li_{0.5}Ni_{0.5}O_4$. In the 1%La sample, the impurity level was determined to be 1 wt%. The multi-element batches were made at the 1 mol% total amount.

Laminates and cells were made from the Baseline, 1%La, 0.5%LaY, and 0.25%LaYCaCe materials. Three cells were made from each material. Two cells were cycled using the standard Realizing Next Generation Cathodes (RNGC) rate protocol.[1] One of each cell was held for 12 hours at open circuit voltage and charged to 4.8 V at a C/10 rate (1C = 200 mA/g). The cut-off limit for capacity was set at 220 mAh/g. The cells were disassembled, and the cathode foil was wrapped in Kapton® tape for XRD examination.

The determination of the a and c lattice parameters and unit cell volume in the pristine and charged states is illustrated in Figure 94 and Figure 95, respectively.

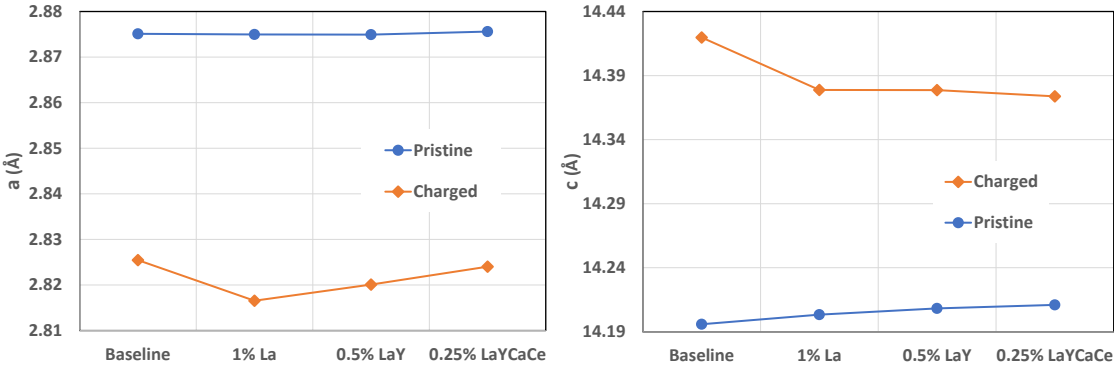

Figure 94. Lattice parameters of substituted NMC 90-5-5 in the pristine and charged states.

The a and c parameters are seen to nominally increase as substitution of large ions proceed from the Baseline, to 1% La, to 0.5% LaY, and to 0.25% LaYCaCe. This implies that the solubility of the large ions increases as more metals are added to the mixture. It is instructive to consider the average radius of the combinations is La = 1.03, La & Y = 0.97, and La, Y, Ca, & Ce = [1]0.99, which explains the improved solubility of 0.5% LaY;

however, the 0.25% LaYCaCe has a larger average than 0.5% LaY. The increased entropy of the system introduces bonding relaxation due to increased disorder, allowing increased solvation of the large metal ions into the lattice. The unit cell volume is shown to follow the effect of the a-parameter comparison (Figure 95).

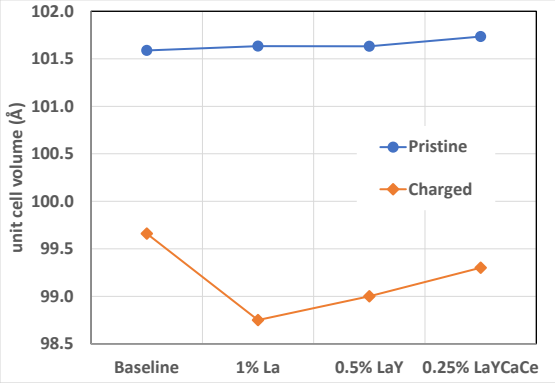

Figure 95. Unit cell volume of substituted NMC 90-5-5 in the pristine and charged states.

It is difficult to make sense of the charged state lattice parameters and unit cell volume. The a-parameter is expected to decrease as the cathode is delithiated during charge, as shown in the left panel of Figure 94. However, it was unexpected that the substituted samples contracted more than the Baseline material. The c-parameter was expected to increase to a point and then contract severely at high SOC. In this case, the c-parameter (Figure 94, right panel) has expanded 1%, with the Baseline being the greatest. It seems that the charge did not reach a high enough SOC (> 85%) for the large contraction to occur.

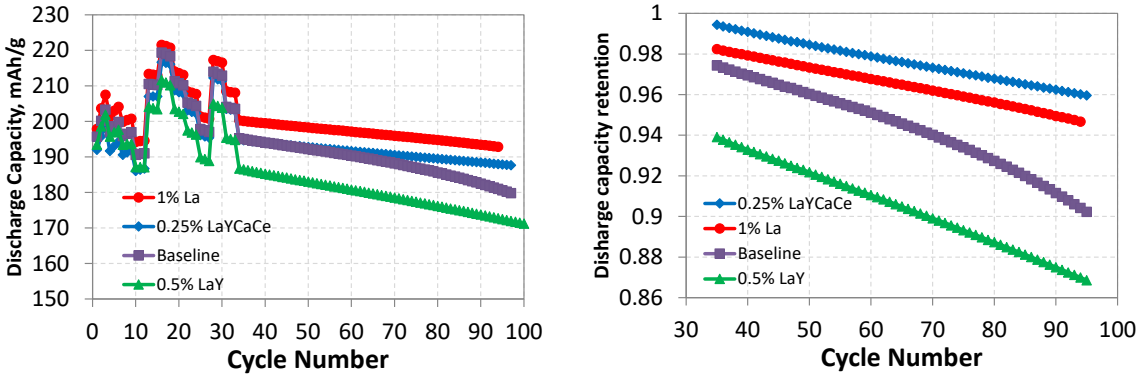

Figure 96. Cell discharge capacity (left) and discharge capacity retention (right): effects of large ion substitution.

There is, however, a clear beneficial effect from the large ion addition to NMC 90-5-5. As shown in Figure 96, the cell capacity and capacity retention demonstrate improved performance when 1%La and 0.25%LaYCaCe are substituted into the material. The 0.5%LaY seems to have performance issues. These promising results merit further investigation. An *in situ* high-energy XRD experiment would provide valuable insight.

Reference

[1] Long, B. R., S. G. Rinaldo, K. G. Gallagher, D. W. Dees, S. E. Trask, B. J. Polzin, A. N. Jansen, D. P. Abraham, I. Bloom, J. Bareño, and J. R. Croy. "Enabling High-Energy, High-Voltage Lithium-Ion Cells: Standardization of Coin-Cell Assembly, Electrochemical Testing, and Evaluation of Full Cells." *Journal of the Electrochemical Society* 163, No. 14 (2016): A2999. https://doi.org/10.1149/2.0691614jes

Patents/Publications/Presentations

Publication

- Low, J. J., H. Iddir, and J. Garcia. "On Proton Defects and the Phase Transformation of NiO_2." *Journal of Physical Chemistry C*. https://doi.org/10.1021/acs.jpcc.2c06738.

Task 3.9 – Tackling Solid-State Electrochemical Interfaces from Structure to Function Utilizing High-Performance Computing and Machine-Learning Tools

(Shinjae Yoo, Feng Wang, and Deyu Lu, Brookhaven National Laboratory; Nongnuch Artrith and Alexander Urban, Columbia University)

Project Objective. This project aims at elucidating the structural evolution and other dynamic properties of the interphases at the solid-state ions (SSIs) in solid-state batteries (SSBs) under processing and electrochemical cycling conditions that strongly impact cell performance. By leveraging synergies of first-principles theory, high-performance computing, machine learning (ML), and computational/experimental spectroscopy, this project involves a comprehensive investigation of solid electrolyte (SE) systems and SSIs that may enable the practical use of lithium anodes and high-Ni Ni-Mn-Co cathodes in SSBs. Specific project objectives are as follows: (1) develop realistic atomic-scale structure models of the heterostructural SSIs, (2) determine the impact of structural evolution on stability and transport properties of SSIs, and (3) identify the coating/doping chemistry that may stabilize SSIs during formation and electrochemical cycling.

Project Impact. Interfacial properties and the dynamical evolution of interphase structures are crucial for the stability and performance of SSBs. This project will lead to fundamental understanding of current materials limits and will identify key materials parameters for optimizing the performance of SSBs. By corroborating atomic-scale theory with experiment, the project will identify structure–property relationships of the heterostructural SSIs in SSB systems that are relevant for electric vehicles (EVs). The outcomes of this project will therefore accelerate development of high-energy-density, safe SSBs for EVs.

Approach. Accurate ML potentials will be trained on an extensive database from density functional theory (DFT) calculations to simulate the structure evolution and electrochemical properties of the SSIs. Using a second ML model, key physical descriptors will be extracted from electron energy loss spectroscopy and X-ray absorption spectroscopy (XAS) measurements. This spectral fingerprinting will enable the automated interpretation of spectroscopy measurements, thereby bridging between atomistic modeling and experiment. An experimental platform will be developed to integrate experimental/computational spectroscopy and modeling of SSIs. In combination, the two ML models and the spectroscopic data will facilitate the construction of a physics-based model to unravel the structure-property relationships of the SSIs.

Out-Year Goals. The project will progress toward establishing dynamic composition-structure-property relationships for interface stability and transport within and across the electrochemical SSIs in SSBs. The ML approach will be further developed to a general model for thermodynamic and transport properties of dynamic heterostructural electrochemical interfaces and will eventually be applied to the practical SSB systems.

Collaborations. The project is collaborating with Y. Du at Brookhaven National Laboratory.

Milestones

1. Conduct spectroscopic characterization of the electrochemical decomposition reactions of Li_6PS_5X (LPSX) electrolytes; develop atomic-scale structure models associated with the dynamic process of the formation and growth of the SSI layer on the heterostructure interface; compare the results with baseline Li-P-S (LPS) behavior. (Q1, FY 2023; Completed)
2. Determine effect of coating on cathode-SE interphase during SSI formation and battery operation. (Q2, FY 2023; In progress)
3. Develop manuscript on atomic-scale delithiation process of LPS SE. (Q3, FY 2023; In progress)
4. Manuscript development on the effects of halide doping approach of LPSX electrolyte on interface stability. (Q4, FY 2023; In progress)

Progress Report

This quarter, the team has employed XAS to study the electrochemical decomposition reactions of the argyrodite electrolytes LPSX (X = Cl, $Cl_{0.5}Br_{0.5}$, or Br). In addition, they have used first-principles DFT calculations to obtain computational phase diagrams of Li-P-S-Cl (LPSCl) and Li-P-S-Br (LPSBr) at different lithium stoichiometry. By analyzing the phosphorus, sulfur, chlorine, and bromine K-edge XAS spectra, they have found that LiX forms during delithiation, followed by sulfur local motif change with the formation of S-S bonds. The change in the phosphorus spectra and distortion of PS_4 local structure are smaller than for Li_3PS_4 (β-LPS, see previous reports). The spectral changes are partially reversible during the lithiation process. The type of halide dopant species has an effect on the chemical stability of the electrolyte, and LPSBr is the most stable among the three electrolytes. This is consistent with the DFT calculations that LPSBr has higher oxidation potential.

Computational Delithiation of LPSX

The team is developing atomic-scale models to understand the structural change and spectral evolution through first-principles DFT calculations. The argyrodites exhibit substitutional disorder in which the lithium sites are fractionally occupied, and a subset of the sulfur sites are statistically shared with the halide dopant. They employed the following protocol to obtain an initial estimate of the ground-state phase diagram. First, starting from the experimental crystal structure, all lithium sites were fully occupied, and all S/X sites were decorated with X atoms, temporarily creating structures with the composition $Li_{12}PS_3X_3$. Next, all symmetrically distinct Li/vacancy and S/X orderings were enumerated to obtain structures with the composition $Li_{12-x}PS_5X$, where $x = 6$ corresponds to the ideal argyrodite composition, $x < 6$ corresponds to lithiation (electrochemical reduction), and $x > 6$ corresponds to delithiation (electrochemical oxidation). For all enumerated structures, DFT calculations were performed.

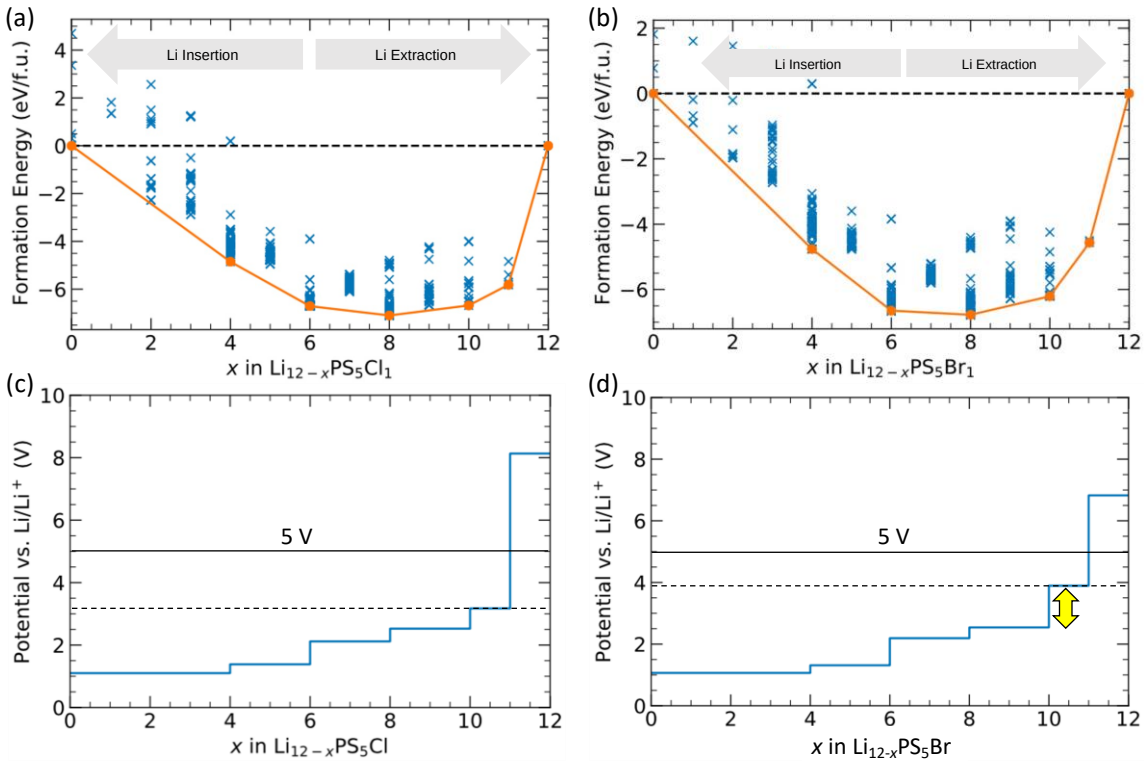

Figure 97. Computed (a-b) formation-energy diagrams and (c-d) equilibrium voltage profiles corresponding to the electrochemical reduction (lithium insertion) and oxidation (lithium extraction) of Li_6PS_5Cl and Li_6PS_5Br.

The resulting computational phase diagrams of LPSCl and LPSBr are shown in Figure 97a-b, and the derived equilibrium voltage profiles are shown in Figure 97c-d. As seen, both argyrodites are predicted to show similar electrochemical behavior. The most significant difference is seen for lithium extraction, where compositions with lithium content below Li_2PS_5X can be accessed at an equilibrium potential of ~ 3 V versus Li/Li^+ for LPSCl, but require ~ 4 V versus Li/Li^+ for LPSBr. Note that the actual oxidation potentials are subject to the kinetics of bond rearrangement and can therefore lie significantly above the predicted equilibrium potentials. Hence, based on these computational data, they would expect to observe in electrochemical experiments a greater stability against oxidation in LPSBr than in LPSCl. Apart from this difference, the two argyrodites can be expected to behave similarly.

Spectroscopic Characterization of LPSX Electrolytes during Electrochemical Decomposition

The team performed XAS experiments on Cl- and Br-doped argyrodite electrolytes LPSX (X = Cl, $Cl_{0.5}Br_{0.5}$, or Br) to study the formation and growth of the solid-solid interphase layer. In LPSX-C | LPSCl | Li-In cells, LPSX-carbon composite electrodes were cycled to different states of delithiation using cyclic voltammetry (CV). The scan rate of the CV experiments was 0.1 mV/s. The cell fabrication and sample preparation were described in the first quarter report in FY 2022. Details about the electrochemistry profiles can be found in the second quarter report in FY 2022.

Figures 98-101 show the measured XAS data from LPSX samples cycled to different states. The team measured K-edge XAS of phosphorus (2.15 keV), sulfur (2.47 keV), and chlorine (2.82 keV) at the 7-ID-2 beamline at NSLS-II in electron yield (EY) mode, and at 8-BM beamline in fluorescence yield (FY) mode. The only difference of the EY and FY results arises from the different probe depths (~ 10 nm in EY mode and ~ 5 μm in FY mode). This report presents only the EY results for conciseness. In addition, they measured the XAS of the bromine K-edge (13.47 keV) at 8-ID in transmission mode.

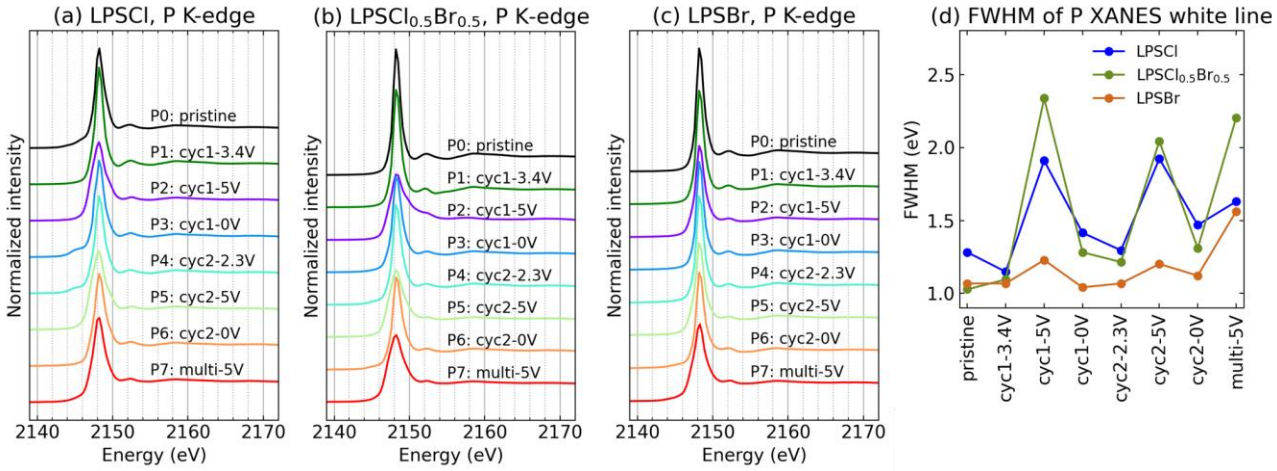

Figure 98. (a-c) Phosphorus K-edge X-ray absorption near-edge structure (XANES) data of LPSX (X = Cl, $Cl_{0.5}Br_{0.5}$, Br) electrolytes cycled to different states. The data were measured at the 7-ID-2 beamline at NSLS-II in electron yield mode. (d) Full width at half maximum (FWHM) of the white line peaks in phosphorus K-edge XANES spectra of the three LPSX electrolytes at different charge states.

Figure 98a-c shows the phosphorus K-edge X-ray absorption near edge structure spectroscopy (XANES) data for LPSCl, $LPSCl_{0.5}Br_{0.5}$, and LPSBr. At cycle 1 – 3.4 V (spectrum P1), none of the electrolytes show observable change. At the end of the first delithiation, cycle 1 – 5 V, the white line peak at 2148 eV decreases and broadens. The change in the white line peak is reversible on lithiation (cycle 1 – 0V and cycle 2 – 2.3 V) and reappears at the second delithiation (cycle 2 – 5 V). The full width at half maximum values of the white line peaks are plotted in Figure 98d. The analysis of phosphorus K-edge XANES data based on the team's LPS delithiation database (see the third quarter FY 2022 report) shows that the broadening of the white line peak indicates the distortion of the PS_4 tetrahedra. In contrast to Li_3PS_4 (see the third quarter FY 2022 report), LPSX shows no new peak after multiple delithiation, indicating a more stable PS_4 structure without large distortions. Comparing

the different halide doped LPSX electrolytes, the broadening in LPSCl and $LPSCl_{0.5}Br_{0.5}$ is more prominent than in LPSBr, indicating that LPSBr maintains more stable PS_4 motifs on delithiation to 5 V.

Figure 99 shows the sulfur K-edge XANES data of the three LPSX samples cycled to different states of charge. Unlike the phosphorus spectra, the sulfur spectra slightly change at cycle 1 – 3.4 V, showing an increase in intensity at the dip at ~ 2472.3 eV, as indicated by the arrow in Figure 99a. This suggests a decrease in the lithium neighbors, as explained in last quarter's report. On delithiation to 5 V, a new peak at 2472.5 eV forms, as shown in cycle 1 – 5V, cycle 2 – 5V, and multicycle – 5V spectra. This new peak is a fingerprint of the S-S bridging bond formation. The behavior of the sulfur spectra of LPSX is similar to that of Li_3PS_4.

Combining the results for sulfur and phosphorus, LPSBr shows less spectral change and is, therefore, more stable than the other two electrolytes. This stability stems from the different halide species of the dopant, but the mechanism needs further investigation.

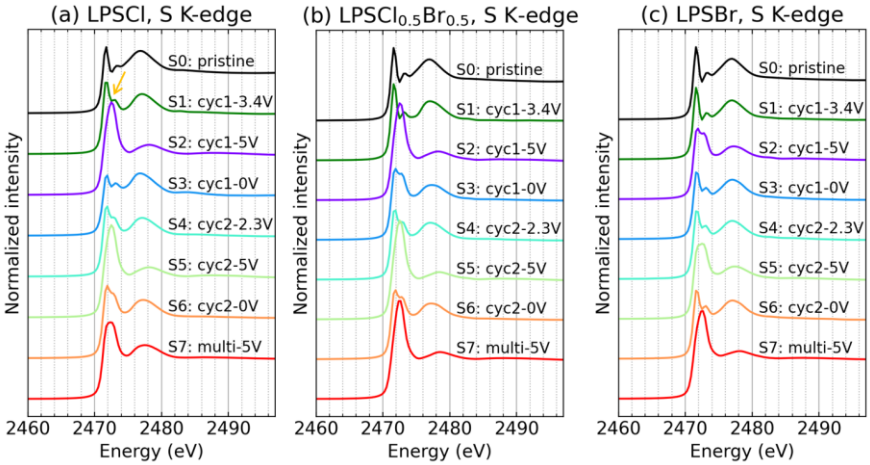

Figure 99. Sulfur K-edge X-ray absorption near-edge structure data of LPSX electrolytes, measured at the 7-ID-2 beamline at NSLS-II in electron yield mode.

Chlorine K-edge XANES data for LPSCl and $LPSCl_{0.5}Br_{0.5}$ are shown in Figure 100. The team also measured the chlorine spectrum of the LiCl standard sample at 7-ID-2, plotted in each subplot as a reference. The delithiated LPSX samples show similar characteristic features to the LiCl spectrum. Taking the spectrum of

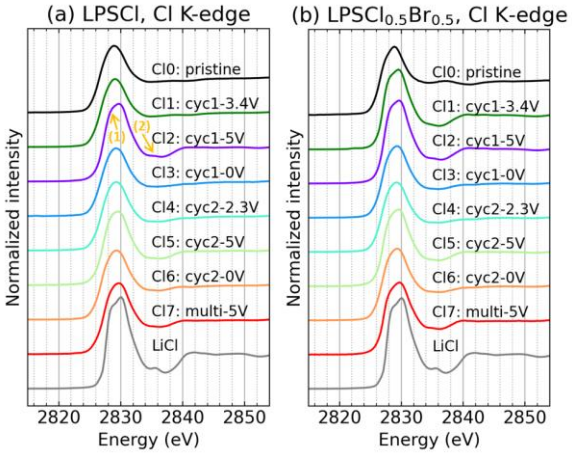

Figure 100. Chlorine K-edge X-ray absorption near-edge structure data of LPSCl and $LPSCl_{0.5}Br_{0.5}$, measured at the 7-ID-2 beamline at NSLS-II in electron yield mode.

LPSCl, cycle 1 – 5 V as an example, the white line peak at 2830 eV shows a similar peak shape with a shoulder at about 2828 eV (arrow (1)) and a decrease in intensity at the 2836 eV dip (arrow (2)). Thus, LiCl is a delithiation product of LPSCl and $LPSCl_{0.5}Br_{0.5}$. Bromine K-edge XAS results provided in the next paragraph will show that LiBr also forms during the delithiation of $LPSCl_{0.5}Br_{0.5}$. The formation of LiCl is partially reversible on lithiation. A side-by-side comparison of the cycle 1 – 3.4 V spectra shows that the characteristics of LiCl are not observed in LPSCl, but are very evident in $LPSCl_{0.5}Br_{0.5}$. This may be due to different halide dopants, but they cannot rule out the possibility of sample-to-sample variation, so further experimental and theoretical studies are needed. Comparing the phosphorus, sulfur, and chlorine spectra of $LPSCl_{0.5}Br_{0.5}$ at cycle 1 – 3.4 V, which were measured on the same sample, the change in the chlorine spectrum is more prominent, while the changes in phosphorus and sulfur are minimal. Hence, they conclude that the change in chlorine local structure occurs at lower voltages and precedes the change in phosphorus and sulfur local structures.

Figure 101 shows the bromine K-edge XANES of $LPSCl_{0.5}Br_{0.5}$ and LPSBr, as well as the LiBr spectrum measured at 8-ID. The team first notes that the bromine K-edge energy (13.47 keV) is in the hard X-ray regime, and the attenuation length of LPSBr at 13 keV is 273 μm, so XAS measures bulk information. Fortunately, in their sample preparation, by mixing LPSX with carbon black into composite electrodes, the surface-to-volume ratio is largely increased, and the reaction can be expected to occur at each LPSX particle's surface. Thus, the XAS signal from the interface reaction can still be observed, although this change is mostly masked under the bulk signal. The main difference is that the multi-cycle spectrum shows slightly lower intensity at the dip at 13486 eV, indicating signs of LiBr formation. This change is partially reversible on lithiation. Further quantitative analysis will be conducted by linear combination fitting.

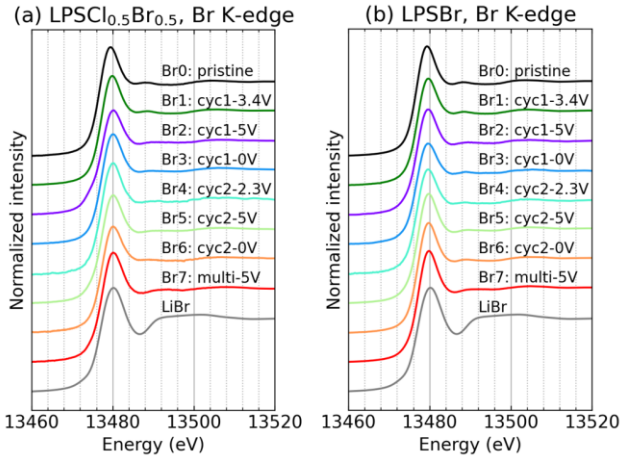

Figure 101. Bromine K-edge X-ray absorption near-edge structure data of $LPSCl_{0.5}Br_{0.5}$ (a) and LPSBr (b), measured at the 8-ID beamline at NSLS-II in transmission mode.

To summarize the team's findings in the XAS experiments, they have found that S-S bonds form in LPSX electrolytes on delithiation and that PS_4 tetrahedra in LPSX electrolytes are more stable than those in β-LPS. Furthermore, LiX forms during delithiation, likely prior to forming S-S bonds. Additionally, LPSBr appears to be more stable than LPSCl and $LPSCl_{0.5}Br_{0.5}$ on delithiation to 5 V versus Li^+/Li. Further theoretical studies on the origin of PS_4 stabilization, the effect of different halide species on electrolyte stability, and how LiX formation affects the decomposition process of LPSX are in progress.

Patents/Publications/Presentations

Publication

- Guo, H., M. R. Carbone, C. Cao, J. Qu, Y. Du, S-M. Bak, C. Weiland, F. Wang, S. Yoo, N. Artrith, A. Urban, and D. Lu. "Simulated Sulfur K-Edge X-Ray Absorption Spectroscopy Database of Lithium Thiophosphate Solid Electrolytes." https://doi.org/10.48550/arXiv.2302.00126.

Task 3.10 – Integrated Multiscale Model for Design of Robust, Three-Dimensional, Solid-State Lithium Batteries
(Brandon Wood, Lawrence Livermore National Laboratory)

Project Objective. This project is developing and applying multiscale, multiphysics models that connect composition, microstructure, and architecture to mechanical integrity in three-dimensional (3D) solid-state batteries (SSBs). The models integrate multiple computational methods, informed and validated through collaborations with complementary experimental efforts. The project scope addresses three objectives: (1) develop multiphysics, multiscale chemomechanics models; (2) assess interface- and microstructure-induced mechanical failure thresholds; and (3) simulate chemomechanical evolution under battery operating conditions.

Impact. This project will deliver multiscale, multiphysics models that connect composition, microstructure, and architecture to mechanical integrity in 3D SSBs. The tools will be used to examine common interfaces in commercially viable electrolyte and cathode materials and to provide design principles for maintaining mechanically robust operation. The modeling framework will address the shortcomings of existing modeling strategies that either lack coupling of the multiphysics nature of various processes active in 3D batteries or fail to incorporate processes at different length scales to understand function. Connections will be made to understand the limits of operability and to co-optimize ionic conductivity and mechanical robustness in solid electrolyte-cathode matrix composites.

Approach. The project approach integrates atomistic, mesoscale, and continuum simulation methods to predict chemomechanical properties of interfaces in ceramic (Li-La-Zr-O, or LLZO) and halide-based solid electrolytes (SEs). Both internal grain boundaries (GBs) and interfaces with $LiCoO_2$ (LCO) and Ni-Mn-Co (NMC) cathode materials are considered. The project is aligned along three tasks, each of which uses simulations to probe a different fundamental length scale relevant to the performance of 3D-SSB architectures. First, atomic-scale interfacial properties are computed using density functional theory and machine learning (ML) approaches. These include local bond strength and mechanical response, as well as stress distributions associated with formation of cracks. Second, using digital reproductions of 3D electrodes and electrolytes, the local stress distributions and stress hotspots in SEs and cathode-electrolyte composites are computed within a mesoscale model. Third, materials performance is coupled to cycling conditions within an operating device by incorporating phase-field models that can simulate rate-dependent fracture likelihood under cycling and extract microstructure-fracture-transport relationships.

Out-Year Goals. The team will focus on the following out-year goals: use *ab initio* methods to generate models for GBs and cathode electrolyte interphases; compute local bond strength and mechanical response of model interfaces; reconstruct microstructures of electrodes and electrolytes using phase-field models; and develop a phase-field model for cathode-induced volume evolution on cycling.

Collaborations. This project collaborates with N. Adelstein from San Francisco State University on atomistic diffusion modeling, and J. Ye from Lawrence Livermore National Laboratory (LLNL) on 3D printing of SSB materials. They also partner with T. Danner and A. Latz from Deutsches Zentrum für Luft- und Raumfaurt on impedance modeling and electro-chemo-mechanical interface models, with P. Zapol from Argonne National Laboratory on modeling of interfaces in LLZO, and with D. Fattakhova-Rohlfing from Forschungszentrum Jülich and E. Wachsman from University of Maryland on properties of LLZO with varying densities and microstructures as part of the U. S.–Germany partnership on SSB research.

Milestones

1. Train machine learning force fields (MLFF) for cathode/electrolyte interfaces. (Q1, FY 2023; In progress)
2. Generate model microstructures of cathode/electrolyte composites. (Q2, FY 2023; Completed)

3. Implement phase-field model for cathode evolution. (Q3, FY 2023; On schedule)
4. Determine threshold stress for bond breaking. (Q4, FY 2023; On schedule)

Progress Report

ML Interatomic Potentials for Accelerated Atomistic Simulations. It has been observed experimentally, including by the team's partners within the U.S.-Germany collaboration on SSBs, that cobalt ions can migrate from LCO into LLZO through the solid electrolyte (SE) / cathode interfaces and form Co-rich secondary phases at the GBs of LLZO. To elucidate this cobalt diffusion mechanism, the team performed large-scale molecular dynamics (MD) simulations of the ∑13(230)/[001] symmetric tilt GB of $[Li_{6.625}Co_{0.125}]La_3Zr_2O_{12}$ using their previously developed interatomic potentials. Figure 102a shows the migration pathway of cobalt ions (yellow isosurface), which indicate Co-ion diffusion in cubic LLZO follows Li-ion diffusion pathways. The diffusivity of cobalt ions was predicted to be about one to two orders of magnitude lower than that of lithium ions above 1000 K, implying that Co-ion diffusion could be sufficiently fast to be observed at the experimental timescales during co-sintering of LLZO-LCO at high temperatures. Moreover, they found that cobalt ions, which were placed at grain interior on initializing the MD simulation, have segregated at the GB, as shown in Figure 102b. The segregated cobalt ions did not migrate along the GB, but were instead trapped at the GB after segregation, likely due to the structural disorder at the GB that disrupts Co-ion migration pathways. A joint experiment-theory manuscript on these findings is under way, with planned submission next quarter.

The team is also retraining the MLFFs for disordered LLZO to study its mechanical response under various loading conditions, which will be used to assess susceptibility to crack initiation and propagation. In addition to the existing data of 5500 structures, they have collected 1300 additional structure data from *ab initio* molecular dynamics simulations for two slab models of a (100) facet with lithium termination and a (111) facet with zirconium termination at a wide range of temperatures. These data will provide necessary information of

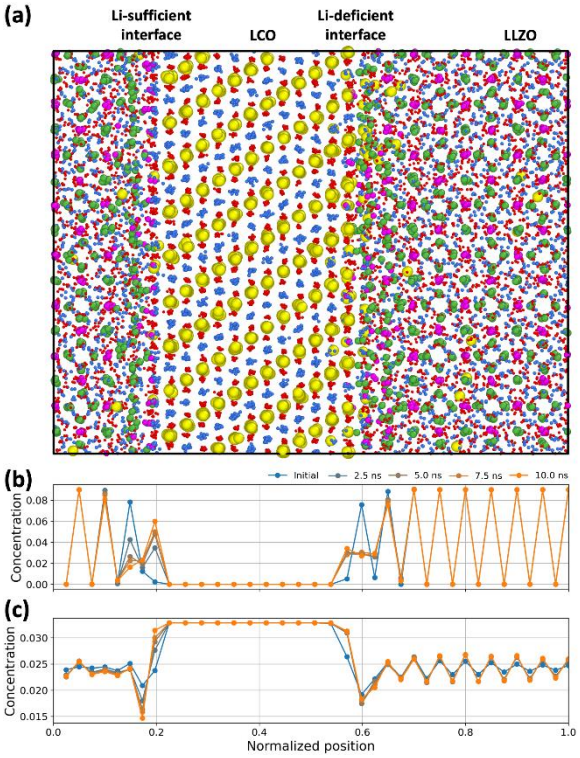

Figure 102. (a) LLZO(001)|LCO(104) interface after 10 ns of large-scale molecular dynamics simulation at 1500 K using the developed machine-learning force field. The atomic model shows two interfacial regions with different initial chemical compositions. Lithium is in blue, lanthanum is green, zirconium is magenta, oxygen is red, and cobalt is yellow. The concentration profiles of (b) zirconium and (c) oxygen ions are also presented as a function of position normal to the interface.

surface atomic environments so that the trained MLFFs can model surfaces, voids, and cracks that are relevant during mechanical deformation of the material. Once the MLFFs are trained and validated, the team will perform large-scale MD simulations to study crack opening and propagation behavior within LLZO.

Mesoscale Modeling of Bi-Continuous and Hierarchical Composite Microstructures for Co-Sintered SE-Cathode Particles. This quarter, the team's mesoscale modeling effort was focused on improving the existing workflow and developing new techniques to generate more representative digital microstructures for the co-sintered SE-cathode particles mixture. Some of the results are summarized in Figure 103. They first analyzed the morphological features of the experimentally characterized microstructure of CO_2 laser co-sintered 25 wt% Li-La-Zr-Ta-O (LLZTO) / 75 wt% LCO pellets, which was fabricated by the LLNO group led by J. Ye. The scanning electron microscopy image of the microstructure of the co-sintered composite show bi-continuous morphology of both the LLZTO and LCO phases and polycrystalline (PC) structures within each particle, as shown in Figure 103a. The bi-continuous and PC nature of the composite microstructure were not considered in the previous version of the workflow, which was based on a stochastic microstructure generation approach. To account for these realistic microstructural features, which are expected to play critical roles in determining the effective properties, the team improved their workflow for reconstructing the digital microstructures.

A new approach was debuted to account for the bi-continuous feature of the digital representations of two-phase composite microstructures by combining the physics-based spinodal microstructure simulator, image analysis toolkits, and the stochastic microstructure generation method. Specifically, they first generated a bi-continuous spinodal microstructure by leveraging the LLNL phase-field model for simulating the spinodal decomposition process in generic phase-separating systems. Figure 103b shows an example of the bi-continuous spinodal microstructure in which the red and blue colors represent two distinct phases. The skeleton of each phase is then extracted by performing an image analysis technique known as the skeleton transform, as shown in Figure 103c. The spatial coordinates of each point along the skeletons are then used as the centers for stochastically generated particles. In contrast to the previous approach based on stochastically locating particles over the entire domain, this new approach confines the positions of particle centers to the connected pathways (that is, skeletons), incorporating the spatial correlation and thus the bi-continuity for the SE and cathode phases. Note that this microstructural feature is experimentally more relevant, representing realistic ionic conduction pathways in the LLZTO-LCO particles mixture, as suggested in Figure 103d. Although a two-dimensional (2D) spinodal microstructure is presented here, the phase-field simulation can also efficiently generate 3D microstructures with more complex morphological features.

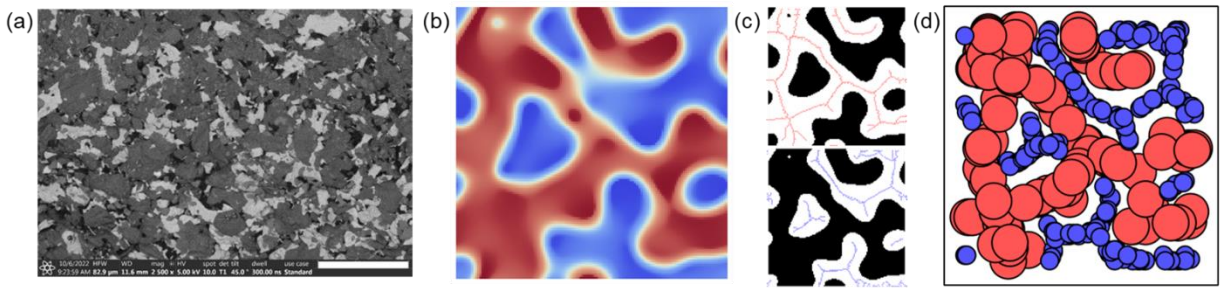

Figure 103. Experimental characterization and mesoscale modeling of the microstructure of solid electrolyte-cathode composites. (a) Scanning electron microscopy image of CO_2 laser co-sintered 25 wt% LLZTO / 75 wt% LCO pellets. The white scale bar represents 20 μm. (b-d) Generation of a bi-continuous two-phase particulate microstructure using a combined method. (b) 2D bi-continuous spinodal microstructure generated by phase-field simulation. (c) Image processing of the binarized spinodal microstructure to obtain the skeletons of each phase. (d) Bi-continuous two-phase particulate microstructure created by stochastic generation of disks centered at the skeletons.

In the coming quarters, the team plans to utilize the bi-continuous and hierarchical composite microstructures to perform mesoscale effective property calculations to assess the impacts of more realistic microstructural features on the effective ionic transport properties of the composites. For more quantitative analyses, the microstructure-aware models will be further parameterized by implementing the interfacial transport parameters

derived from their atomistic simulations. Sensitivity analysis will be performed on several microstructural metrics, including the grain orientation and size of LLZO and LCO particles, the porosity, and the connectivity of each phase, to systematically establish microstructure-effective property relationships.

Mesoscale Simulation of Chemo-Mechanical Stress Evolution during Delithiation Process of Isolated LCO Primary Particle Embedded within LLZO. This quarter, the team also extended a mesoscale microstructure-aware model to simulate the lithiation/delithiation-induced mechanical stress evolution in the active cathode materials during the discharging/charging processes. They focused on the chemo-mechanical stress evolution in an isolated PC LCO particle (consisting of ~ 150 small crystallites) surrounded by dense LLZO SE during delithiation. For simplicity, it was assumed that the surrounding LLZO is as follows: (1) homogeneous, (2) in coherent contact with LCO, and (3) free of volume change during delithiation. The elastic modulus of LLZO is obtained from MLFF-based atomistic calculations performed last quarter, while the elastic modulus and Li-induced volumetric strain of LCO are obtained from experiments and first-principles calculations found in literature. The mechanical properties at the GBs of LCO and the interface between LCO and LLZO are interpolated. Note that LCO is known to exhibit volume expansion on delithiation to $Li_{0.6}CoO_2$. Preliminary 2D simulation results are summarized in Figure 104.

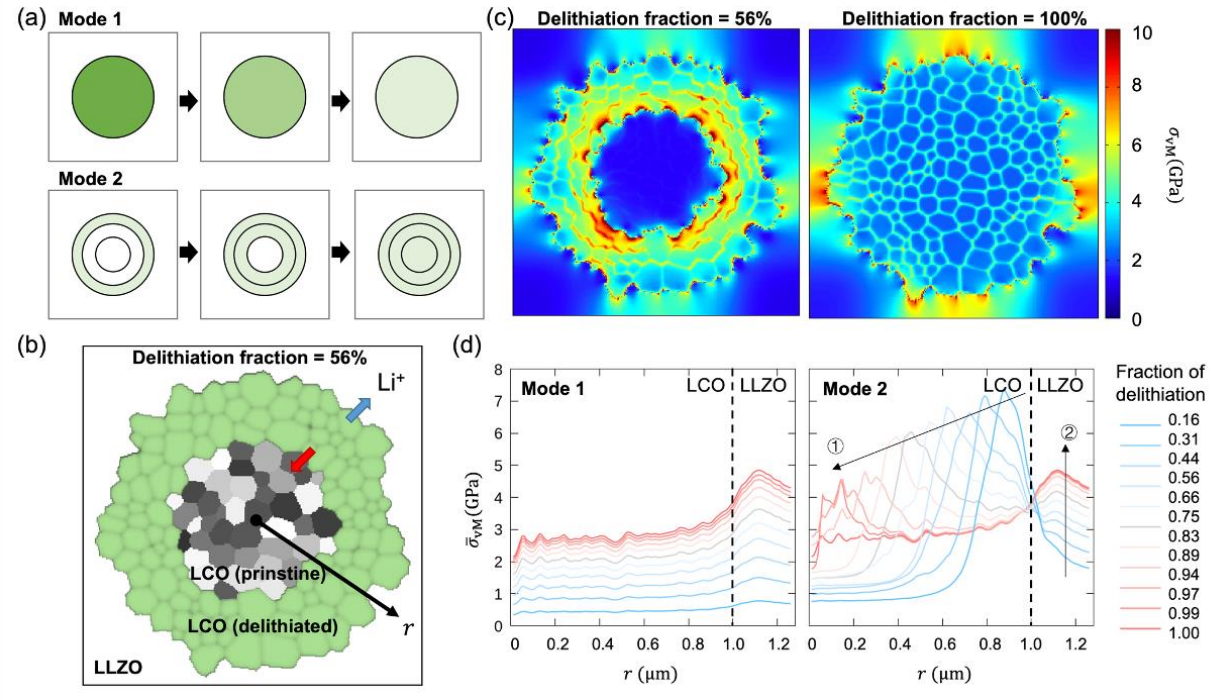

Figure 104. Mesoscale simulation of chemo-mechanical stress evolution during delithiation in an isolated LCO primary particle surrounded by LLZO. (a) Schematics of Mode 1 (uniform delithiation) and Mode 2 (radial delithiation). (b) Digital grain structure of an LCO primary particle consisting of ~ 150 secondary particles with the delithiation fraction = 56% (Mode 2) embedded by LLZO solid electrolyte, generated by phase-field grain growth simulation. The red arrow denotes the moving front between the delithiated and pristine regions. The blue arrow denotes the delithiation direction. The black arrow denotes the polar coordinate direction for performing the radial statistics. The radius of the primary particle is ~ 1 μm. (c) Stress hotspot analysis based on distributions of von Mises stress (σ_{vM}) for the embedded LCO particle at delithiation fraction = 56% and 100%. (d) Comparison between the evolution of the radially-averaged von Mise stress distributions ($\bar{\sigma}_{vM}$) using Mode 1 and 2.

To account for microstructural variability during the delithiation process, two possible modes were considered for the temporal evolution of lithium distribution inside the PC LCO particle (Figure 104a). As illustrated, Mode 1 assumes uniform delithiation over the LCO particle. On the other hand, Mode 2 assumes delithiation with a core-shell microstructure; delithiation starts to occur from the crystallites at the outer shell and then proceeds radially into the core of the particle. Figure 104b shows an example of the generated digital microstructure of the PC LCO particle for Mode 2 with ~ 56% delithiation. The LCO crystallites in delithiated regions (in light green) are subject to volumetric expansion of 3%, while those inside the pristine region

(in grayscale) remain unchanged. For each microstructure with a different stage of delithiation, micromechanics analysis was performed by solving the mechanical equilibrium equation to obtain the von Mises stress distribution. The computed stress profiles for the two selected delithiation stages (that is, 56% delithiation and 100% delithiation) are shown in Figure 104c as examples. It was found that at the intermediate stage, stress hotspots develop not only near the interface between the LCO and LLZO, but also at the LCO GBs surrounding the inner front between the delithiated and pristine regions. In contrast, at the fully delithiated stage, the hotspots tend to concentrate at the interface between LCO and LLZO, even though the GBs of LCO are also subject to relatively larger stress than the bulk grain interiors.

To examine the impacts of the delithiation microstructure on the simulated stress evolution in the LCO particle for the two assumed microstructural modes, additional statistical analysis was performed for each mode to obtain the radial distributions of the von Mises stress ("radial stress" hereafter) during delithiation by averaging over a region with a given radius *r* from the center of the particle (Figure 104d). It was found that the two modes exhibit quite different radial stress behavior. Mode 1 leads to uniform increase of von Mises stress as a function of the extent of delithiation, with the peak stress occurring near the LCO-LLZO interface. In contrast, Mode 2 exhibits nontrivial behavior. The peak stress moves from the outer to the inner shell of the LCO particle, but with a decayed magnitude (denoted by black arrow ①). Meanwhile, the stress near the LCO-LLZO interface increases as delithiation proceeds (denoted by black arrow ②). This analysis suggests that the evolution of chemomechanical stress during the delithiation of the active cathode material is highly sensitive to the evolving delithiation microstructure and its mechanical interaction with the surrounding SE.

Next quarter, the team will further elaborate the microstructure-aware micromechanics model to perform 3D simulations based on the Mode 2 for LCO primary particles, which is assumed to be more realistic. Moreover, they will incorporate the PC features into the LLZO SE, as well as the defective (or incoherent) interface between LLZO and LCO grains. After elucidating the chemomechanical stress evolution in an isolated LCO particle and its interaction with the surrounding LLZO electrolyte, a homogenized model will be developed to assess the chemomechanical behavior of the composite cathode with multiple LLZO and LCO particles at a larger length scale. In addition, the same chemomechanical stress analysis approach will be adopted to study other cathode materials of interest (for example, NMC).

Patents/Publications/Presentations

Publication

- Ren, Y., T. Danner, A. Moy, M. Finsterbusch, T. Hamann, J. Dippell, T. Fuchs, M. Müller, R. Hoft, A. Weber, L. A. Curtiss, P. Zapol, M. Klenk, A. T. Ngo, P. Barai, B. C. Wood, R. Shi, L. F. Wan, T. W. Heo, M. Engels, J. Nanda, F. H. Richter, A. Latz, V. Srinivasan, J. Janek, J. Sakamoto, E. D. Wachsman, and D. Fattakhova-Rohlfing. "Oxide-Based Solid-State Batteries: A Perspective on Composite Cathode Architecture." *Advanced Energy Materials* 13 (2022): 2201939. https://doi.org/10.1002/aenm.202201939.

Presentations

- Materials Research Society Fall Meeting, Boston, Massachusetts (November 27 – December 2, 2022): "Development of Machine-Learning Force Fields for Simulating Interfaces in Solid-State Batteries"; K. Kim, A. Dive, A. Grieder, N. Adelstein, S. Y. Kang, B. Wood, and L. Wan.
- Royal Society Meeting on Understanding Fast-Ion Conduction in Solid Electrolytes, Lancaster, UK (November 2022): "Paradigms of Structural, Chemical, and Dynamical Frustration in Superionic Conductors"; B. C. Wood.
- Royal Society Meeting on Understanding Fast-Ion Conduction in Solid Electrolytes, Lancaster, UK (November 2022): "Simulating Li-Diffusion in Amorphous and Crystalline LLZO"; N. Adelstein.

TASK 4 – METALLIC LITHIUM

Team Lead: Jagjit Nanda, SLAC Stanford Battery Research Center

Summary

The use of a metallic lithium anode is required for advanced battery chemistries like Li-ion, Li-air, and Li-S to realize dramatic improvements in energy density, vehicle range, cost requirements, and safety. However, use of metallic lithium with liquid and solid polymer or ceramic electrolytes has so far been limited due to parasitic solid electrolyte interphase (SEI) reactions and dendrite formation that eventually short circuit the battery. Adding excess lithium to compensate for such losses negates the high-energy-density advantage of a Li-metal anode and leads to further concern for battery safety. For a long lifetime and safe anode, it is essential that no lithium capacity is lost either (1) to physical isolation by roughening, dendrites, or delamination processes, or (2) to chemical isolation from side reactions. The key risk, and current limitation, for this technology is the gradual loss of lithium over the cycle life of the battery. To address these issues, there is need for a much deeper analysis of the degradation processes and new strategies to maintain a dense, fully connected lithium and a dendrite-free electrolyte so that materials can be engineered to fulfill the target performance metrics for electric vehicle application, namely 1000 cycles and a 15-year lifetime, with adequate pulse power. Projecting the performance required in terms of just the lithium anode, this requires a high rate of lithium deposition and stripping reactions, specifically about 30 µm of lithium per cycle, with pulse rates up to 10 nm/s and 20 nm/s (15 mA/cm^2) charge and discharge, respectively, with little or no excess lithium inventory.

The efficient and safe use of metallic lithium for rechargeable batteries is then a great challenge, and one that has eluded research and development efforts for years. This project takes a broad look at this challenge for both solid-state batteries and batteries continuing to use liquid electrolytes (LEs). Electrolytes reported here include conventional LEs such as localized high-concentration electrolytes, gel type polymer-in-a-salt, composites of ceramic polymer phases, common and novel polymer electrolytes, and both oxide and sulfide ceramic electrolytes. Researchers are typically working toward cycling of full cells with relevant and balanced capacities using both thin lithium metal and anode-free configuration, prelithiation methods, and post-cycling observation of the disassembled cell components to assess stability of the Li-metal/ electrolyte interface.

Highlights

The highlights for this quarter are as follows:

- The SLAC National Accelerator Laboratory / Stanford University group (Y. Cui) report a one-step thermal annealing process to incorporate lithium in copper. The process allows lithium atoms to diffuse into copper lattice as observed by change in their crystal structure from the X-ray diffraction analysis and changes in the physical color. This novel approach allows utilization of current collectors, which are electrochemically inactive and considered as “dead weight,” to store lithium and to be used as dry prelithiation agent.
- The Pacific Northwest National Laboratory group (W. Xu) has developed single and bi-layer coatings on Li-metal as an artificial SEI layer to prevent side reactions between Li-metal anode and the electrolyte. These coatings are expected to improve the cycling stability of Li-metal anode at high charge current densities. Electrochemical test results showed that bi-layer coating (cross-linked polymer and Li-glycerol) had better capacity retention at lower current (C/10), while single layer (only Li-glycerol) demonstrated better stability at high rate (C/2).

Task 4.1 – Lithium Dendrite Prevention for Lithium Batteries (Wu Xu, Pacific Northwest National Laboratory)

Project Objective. The objective of this project is to enable lithium metal to be used as an effective anode in Li-metal batteries with good thermal stability and safety. The investigation in FY 2023 will focus on the following aspects: (1) continuing development of three-dimensional (3D) structured, lightweight, flexible current collectors for Li-metal anode and Li-metal batteries, (2) developing a stable dual-layer (DL) as an artificial protection layer for Li-metal anode to be used as an effective anode in Li-metal batteries, and (3) obtaining mechanistic insight on Li-metal deposition/stripping behavior.

Project Impact. Lithium metal is an ideal anode material for next-generation, high-energy-density, rechargeable batteries. However, the application of Li-metal anode has been hindered by concern for safety and short cycle life. The safety concern regarding Li-metal batteries mainly arises from lithium dendrite growth and electrolyte flammability; the short cycle life is largely associated with the high reactivity of lithium metal with electrolyte and the lithium loss due to formation of solid electrolyte interphase (SEI) and electrochemically inactive or "dead" lithium during cycling. Although much progress has been achieved in suppressing lithium dendrites and increasing lithium Coulombic efficiency in liquid electrolytes in recent years, the intrinsic problems of Li-metal anode still exist. This fiscal year, the Pacific Northwest National Laboratory (PNNL) team will continue to develop 3D porous current collectors for Li-metal anode to suppress lithium dendrite growth, increasing the utilization of lithium metal and consequently enhancing the safety and cycle life of Li-metal batteries. Th team will also develop artificial DLs to protect Li-metal anode and further investigate mechanisms affecting lithium deposition and stripping behaviors to lay the groundwork for future improvement of electrolytes (salts, solvents, and additives) for Li-metal batteries. The success of this project will increase safety and cycle life of lithium batteries and accelerate market acceptance of electric vehicles (EVs), as required by the EV Everywhere Grand Challenge.

Approach. The approach will encompass the following areas: (1) continue development of current collectors with 3D structure for Li-metal anode to suppress lithium dendrite growth, increase lithium utilization, and extend cycle life of Li-metal batteries, (2) develop artificial protection layers on Li-metal anode to improve the cycling stability of Li-metal batteries [Li||$LiNi_xMn_yCo_{1-x-y}O_2$ (NMC)], and (3) conduct mechanistic studies on lithium deposition behavior to lay groundwork for future improvement of Li-metal batteries.

Out-Year Goals. The long-term goal of the proposed work is to enable Li-metal batteries with a specific energy of > 350 Wh/kg (in cell level), 1000 deep-discharge cycles, 15-year calendar life, and less than 20% capacity fade over a 10-year span to meet the goal of the EV Everywhere Grand Challenge.

Collaborations. This project collaborates with C. Wang of PNNL on characterization by transmission electron microscopy; Y. Zhang and J. Lee of Argonne National Laboratory on electrospinning polyimide, polysulfone, and polycarbonate porous membranes; X. Meng of University of Arkansas on molecular layer deposition (MLD); and X. Shan and G. Xia of University of Houston on studying SEI formation using *in situ* reflection interference microscope.

Milestones

1. Optimize preparation conditions to make flexible 3D-structured current collectors with full coverage of thin copper film. (Q1, FY 2023; Completed)
2. Evaluate lithium deposition morphology and cell performance of 3D-structured current collectors in Li||NMC cells. (Q2, FY 2023)

3. Fabricate DL-protected Li-metal anode and investigate its effect on deposited lithium morphology. (Q3, FY 2023)
4. Evaluate cell performance of DL-protected lithium in Li||NMC cells. (Q4, FY 2023)

Progress Report

Last quarter, lithium (4 mAh cm^{-2}) deposited on a 3D current collector consisting of copper-coated polyimide fibers (Cu@PI) was investigated by scanning electron microscopy (SEM). Although the uniformity of copper coating on the polyimide fibers was confirmed by its SEM images, lithium did not deposit through all thickness direction at a current density of 0.4 mA cm^{-2}. Therefore, the copper was mainly detected on the back of the Cu@PI by energy dispersive X-ray spectroscopy (EDS) mapping, as shown in Figure 105a. To improve the lithium deposition, the current densities were adjusted to 0.2 mA cm^{-2} and 0.13 mA cm^{-2}. The EDS mapping images indicate that lithium tends to deposit more uniformly when a current density is lower (Figure 105b). When lithium deposition rate was further reduced to 0.13 mA cm^{-2}, the back of Cu@PI substrate was almost fully covered by lithium, and copper is only barely detected by EDS mapping, indicating lithium was deposited through the thickness direction (Figure 105c). These results indicate that the electronic conductivity of current Cu@PI substrate needs to be further improved to get uniform lithium deposition through the thickness direction at a relatively higher current density. New results on this further optimization will be updated next quarter.

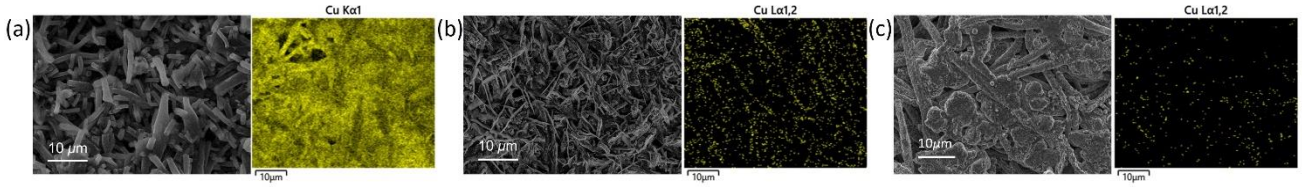

Figure 105. Scanning electron microscopy images and energy dispersive X-ray spectroscopy mapping images for backside of lithium deposited Cu@PI mat at a current density of (a) 0.4 mA cm^{-2}, (b) 0.2 mA cm^{-2}, and (c) 0.13 mA cm^{-2}.

Single or double coating layers have been investigated as an artificial SEI layer to prevent side reactions between Li-metal anode and the electrolytes. A single layer of lithium glycerol (GL) coated lithium metal (GL@Li) was realized by using MLD on 50 μm of Li-metal surface, and a top layer (TL) coated lithium metal (TL@GL@Li) was prepared by coating a crosslinked polymer layer on the GL@Li. These coatings are expected to improve the cycling stability of Li-metal anode at high charge current densities. To investigate the effect of GL and TL@GL coating layers on the cycling performance of Li-metal batteries, the cycle performance and charge rate capability of Li || $LiNi_{0.6}Mn_{0.2}Co_{0.2}$ (NMC-622) coin cells using the bare and coated Li-metal anodes were assembled, with 75 μL electrolyte of Li-bis(fluorosulfonyl)imide – 1,2-dimethoxyethane – 1,1,2,2-tetrafluoroethyl-2,2,3,3-tetrafluoropropyl ether (LiFSI-DME-TTE) at

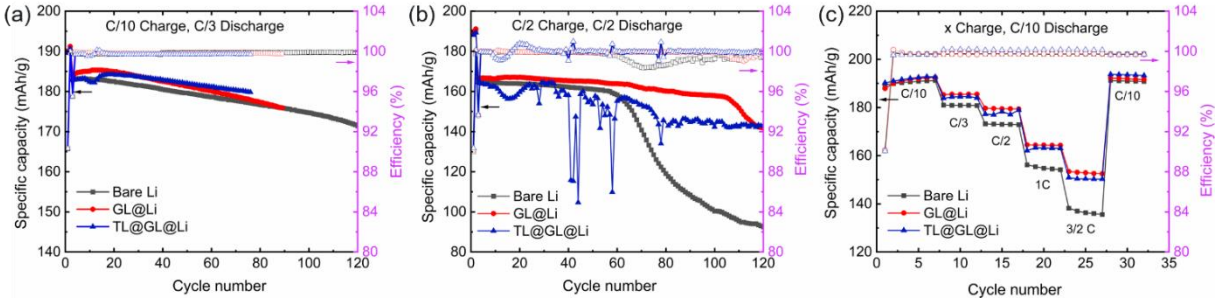

Figure 106. Cycling performance of Li||NMC-622 cells at (a) C/10 for charging and C/3 for discharging, (b) C/5 for charging and discharging, and (c) various charge current densities (x) with a constant discharge current density (C/10). The cells were first conducted with two formation cycles at C/10, where 1C = 4.0 mA cm^{-2}. The voltage range is from 2.8 to 4.4 V (versus Li/Li^+).

1:1.2:3 by mol. At a current density of C/10 for charging and C/3 for discharging, TL@GL@Li delivers a better capacity retention of 98.6% after 70 cycles compared to GL@Li (97.1%) and bare lithium (97.2%) (Figure 106a). While at a current density of C/2 for both charging and discharging, GL@Li showed more stable cycling performance with capacity retention of 94.8% after 100 cycles than bare lithium (60.9%), while TL@GL@Li did not show stable cycling (Figure 106b). More testing on TL@GL@Li is needed. In the charge rate capability testing, both GL@Li and TL@GL@Li show improved charge rate capability compared with bare lithium, as shown in Figure 106c. These results demonstrate that GL@Li and TL@GL@Li could be promising candidates for high electrochemical performance of Li-metal batteries. The performance of GL@Li and TL@GL@Li will be further optimized next quarter.

Patents/Publications/Presentations

The project has no patents, publications, or presentations to report this quarter.

Task 4.2 – Prelithiation for High-Energy Lithium-Ion Batteries (Yi Cui, Stanford University)

Project Objective. Prelithiation of high-capacity electrode materials is an important means to enable those materials in high-energy batteries. This study pursues three main directions: (1) development of facile and practical methods to increase 1st-cycle Coulombic efficiency (CE) of anodes, (2) synthesis of fully lithiated anode to pair with high-capacity, Li-free cathode materials, and (3) prelithiation from the cathode side.

Project Impact. Prelithiation of high-capacity electrode materials will enable those materials in the next generation of high-energy-density Li-ion batteries. This project's success will make high-energy-density Li-ion batteries for electric vehicles.

Approach. Silicon electrode film will be prepared by coating the slurry of silicon nanoparticles, carbon black, and binder mixture on copper foil through a doctor-blading method. The silicon electrode film will be prelithiated by pressing a Li-metal foil on top of it and heating it in an argon glovebox for a certain time. Then, Li_xSi electrode film can be obtained by removing the redundant lithium foil through a peeling-off approach. The redundant lithium foil is reusable for the next prelithiation. The structure, morphology, and other properties can be analyzed by scanning electron microscopy, transmission electron microscopy, X-ray photoelectron spectroscopy, Raman spectroscopy, X-ray diffraction (XRD), etc. In the first year, the team aims to fabricate Li_xSi freestanding electrode film and improve its air stability. In the second year, the team aims to improve the electrochemical stability in full cells.

Out-Year Goals. Materials containing a large quantity of lithium will be synthesized for pre-storing lithium ions inside batteries. Materials and processes will be developed to be compatible with battery electrode and cell fabrication. First-cycle CE of anodes will be improved and optimized by prelithiation materials. Materials for prelithiation from the cathode side will be developed.

Collaborations. This project engages in collaboration with the following: BMR principal investigators; SLAC National Accelerator Laboratory: M. Toney *(in situ* X-ray); and Stanford University: W. Nix (mechanics).

Milestones

1. Demonstrate Li-containing current collectors as new dry prelithiation materials. (Q1, FY 2023; Completed)
2. Investigate the time influence on forming Li-containing current collectors. (Q2, FY 2023)
3. Study the optimal temperature for forming Li-containing current collectors. (Q3, FY 2023)
4. Demonstrate the improved initial CE through prelithiation from Li-containing current collectors. (Q4, FY 2023)

Progress Report

Substantial improvements on energy density of Li-ion batteries require development of high-capacity electrodes. Silicon anodes that have high theoretical capacities (3579 mAh/g)—ten times higher than the conventional graphite anodes (372 mAh/g)—hold great potential for application in high-energy Li-ion batteries. However, silicon anodes exhibit a low initial CE of 50-80%, which means 20-50% of battery capacity will be lost after 1st cycle due to side reactions. Therefore, a strategy to compensate the initial active lithium loss and improve initial CE is urgently needed to prevent battery initial capacity degradation.

Previously, the team presented Li-rich compounds for both anode and cathode prelithiation. However, the challenge associated with anode prelithiation is the high reactivity of prelithiation materials, which has difficulty surviving multiple processing steps during battery electrode fabrication. They further presented *in situ* prelithiation to minimize processing steps and achieve one-step dry prelithiation. Here, they demonstrate a Li-containing copper current collector that they transfer from dead weight to a promising dry prelithiation reagent.

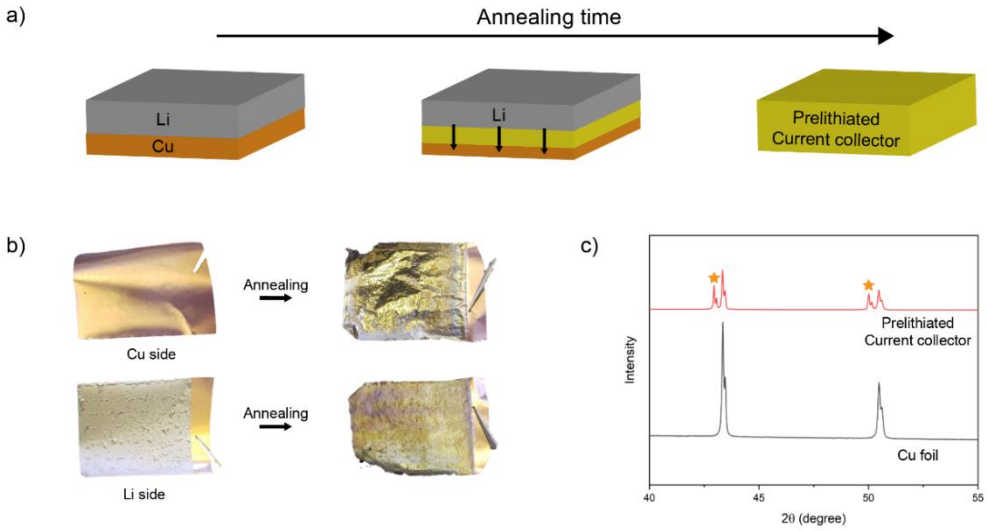

Figure 107. (a) Schematic of preparing Li-containing copper current collector by annealing. (b) Digital photos of lithium on copper foil before (left) and after (right) prelithiation by annealing. (c) X-ray diffraction analysis results of bare copper foil and prelithiated current collector. New peaks observed from Li-containing current collector are marked with yellow symbols.

The Li-containing current collectors are prepared by annealing lithium and copper foil (Figure 107a). First, thin lithium foil of desired capacity is placed on top of copper foil, a conventional current collector for anodes. Then, aligning foils, they place this set of foils into an oven for annealing and observed changes. During annealing, lithium foil on top starts to liquify due to temperature above its melting temperature, and lithium atoms start to diffuse into the copper current collector (Figure 107a, center). This process allows lithium atoms to transport into copper lattices and change their crystal structure. After annealing, the prelithiated current collector is collected from the oven and cooled down for further experiments (Figure 107a, right). As depicted in Figure 107b, the layered foils exhibit a goldish color on both sides; this change implies possible formation of a new phase. The XRD analysis results in Figure 107c show a direct evidence of changes in copper crystal lattices. Compared to XRD peaks of copper foil, those of prelithiated current collectors are shifted toward lower angle of diffraction. Since 2θ is inversely proportional to interplanar spacing under the same incident beam, these data indicate that lattice parameters have increased after annealing, possibly due to insertion of lithium into lattices. Therefore, the team could suggest that lithium atoms can be stored inside the copper current collector for prelithiation. The most important part of this work is that they were able to utilize current collectors, which are electrochemically inactive and considered as dead weight, to store lithium by one-step thermal reactions.

Patents/Publications/Presentations

The project has no patents, publications, or presentations to report this quarter.

Task 4.3 – Anode-Free Lithium Batteries
(Ji-Guang Zhang and Xia Cao, Pacific Northwest National Laboratory)

Project Objective. The main objective of this project is to explore the feasibility of anode-free lithium batteries (AFLBs) for high-energy-density energy storage systems. An AFLB is an extreme case of Li-metal battery and Li-ion battery, where all active lithium is stored in cathode in the as-assembled batteries. Because of the many similarities among AFLBs, Li-metal batteries, and Li-ion batteries, extensive experiences and approaches developed for Li-metal and Li-ion batteries can be applied to AFLBs. Likewise, new approaches and knowledge to extend the cycle life and calendar life of AFLBs can also be used for development of Li-metal and Li-ion batteries, thus accelerating the market penetration of Li-based rechargeable batteries.

Project Impact. The ever-increasing need for electric vehicles (EVs) continually pushes the boundary of high-density energy storage systems. To date, the state-of-the-art Li-ion batteries consisting of graphite anode and high-voltage lithium intercalation cathodes cannot satisfy the energy demand from these applications. By replacing graphite anode with Li-metal anode, the specific energy density of Li-metal batteries can increase by more than 50% because Li-metal anode has a much higher specific capacity (3820 mAh g^{-1}) than that of graphite (372 mAh g^{-1}). To further increase the energy density of lithium batteries, the concept of AFLBs has been explored. An as-assembled or fully discharged AFLB consists of a cathode and an anode current collector (such as copper). All lithium source is stored in cathode. This cell design not only increases energy density of the battery, but also improves battery safety because no lithium metal is present in the battery in its as-assembled or discharged state. However, the cycle life of AFLBs is still very limited due to loss of active lithium during the cycling process. Therefore, there is an urgent need to understand the correlation between lithium Coulombic efficiency (CE), cathode CE, and electrolyte (including its electrochemical properties and consumption), as well as lithium dendrite growth and the formation of "dead" lithium, so that AFLBs and Li-metal batteries can be designed to achieve desired energy density and cycle life. In the end, the combination of these two efforts will accelerate the understanding and application of high-energy-density rechargeable batteries for EV applications.

Approach. This task will investigate the main factors affecting performance of AFLBs and identify solutions to enable long-term cycling and safety of these batteries. The lithium loss due to solid electrolyte interphase (SEI) formation and "dead" lithium generation by dendrite growth in the lithium deposition and stripping processes will be analyzed. The lithium dendrite suppressing principles and strategies for both liquid and solid-state AFLBs, ranging from materials design (that is, electrolytes, cathodes, and current collectors), cell fabrication, and operation controls (that is, pressure, temperature, and cycling protocol) will also be investigated.

Out-Year Goals. The long-term goal of the proposed work is to enable lithium batteries with a specific energy of > 350 Wh/kg (in cell level), 1000 deep-discharge cycles, 15-year calendar life, and less than 20% capacity fade over a 10-year span to meet the goal of the EV Everywhere Grand Challenge.

Collaborations. This project collaborates with the following: C. S. Wang of University of Maryland on approaches to improve the CE of lithium cycling; C. M. Wang of Pacific Northwest National Laboratory on characterization by transmission electron microscopy / scanning electron microscopy; and Battery500 principal investigators on understanding and approaches to improve the calendar life of lithium batteries.

Milestones

1. Quantify SEI formation and SEI dissolution at different voltages and temperatures. (Q1, FY 2023; Completed)
2. Identify electrolytes that enable a lithium CE of 99.8% and formation of SEI layer with minimum SEI dissolution in the electrolyte. (Q2, FY 2023; In progress)

3. Optimize anode substrate to minimize lithium loss. (Q3, FY 2023; In progress)
4. Increase CE of AFLB to > 99.8%, capacity retention of 80% for 100 cycles. (Q4, FY 2023; In progress)

Progress Report

This quarter, the team investigated the effect of internal pressure on lithium deposition under the optimized voltage range of 3.5-4.5 V obtained during previous work. It is found that the morphology of the deposited lithium layer is very sensitive to the internal pressures applied on the copper electrode in the 2032-type coin cells. The uniformity/density of lithium deposition and associated SEI quality vary significantly under different internal pressures. During the coin-cell assembling process, different amounts of stainless-steel spacers (SSS) and/or different thicknesses of SSS were used, as shown in Figure 108a. Because the total thickness of the coin cells is fixed by the assembling mold, the internal pressure of the cells increases with increasing stack thickness of SSS. Figure 108b-c shows that thickness of lithium layers deposited on the copper electrode decreases with increasing pressure. The cell assembled with optimized pressure (SSS – 2t) shows the best cycling stability with a capacity retention of 72% after 100 cycles, while cells assembled with lower internal pressures (SSS – 1t and SSS – 1.5t) have a faster capacity decay. The cell assembled with too high of a pressure (SSS – 3t) without a spring leads to unstable cycling and early cell failure after ~ 40 cycles (Figure 108g). Although the most compact lithium deposition was obtained at the highest pressure, too high of an internal pressure may lead to mechanical/physical failure of the cell components (especially separator) in the coin cells. An ideal cell design also needs a spring to accommodate volume changes during lithium deposition/stripping.

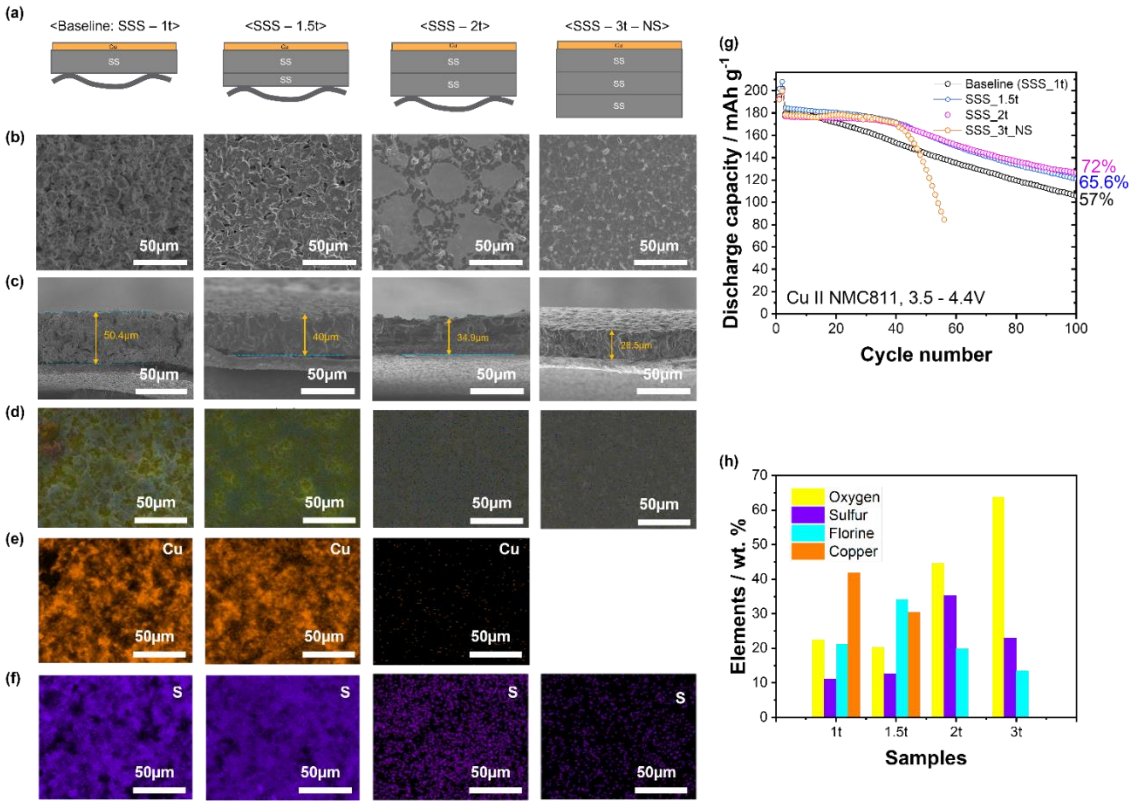

Figure 108. (a) Schematic illustration for internal pressure effect on density and uniformity of lithium deposited on copper electrode in 2032-type coin-cells. Corresponding scanning electron microscopy images for the top (b) and cross-sectional (c) views of copper electrodes after the first lithium deposition. Energy dispersive X-ray spectroscopy mappings for SEIs: (d) all elements, (e) copper element, and (f) sulfur element after 1st cycle lithium deposition and stripping. (g) Cycling performance of NMC-811||Cu cells with different internal pressures cycled between 3.5 V – 4.4 V. (h) Quantified elements distribution in SEIs formed at different internal pressures.

The energy dispersive X-ray spectroscopy mapping results shown in Figure 108d-f indicate that higher internal pressure leads to better SEI qualities. The uniform lithium deposition at high pressure (SSS – 2t and SSS – 3t) leads to uniform SEI distribution even after lithium stripping. Figure 108e (copper mapping) shows that copper is barely seen in the samples deposited at high pressures (SSS – 2t and SSS – 3t), indicating a good coverage of lithium deposition. However, more copper is found in the samples deposited at low pressures (SSS – 1t and SSS – 1.5t), indicating poor coverage of lithium deposition at lower pressures. In addition, the element distributions of the SEIs formed under different conditions are compared in Figure 108h. The SEI layer formed under optimized pressure of SSS–2t exhibits the highest sulfur element content of 36% (which is derived from the salt decomposition) and led to the best cycling stability of AFLBs, as shown in Figure 108g.

Patents/Publications/Presentations

The project has no patents, publications, or presentations to report this quarter.

TASK 5 – LITHIUM-SULFUR BATTERIES

Team Lead: Prashant N. Kumta, University of Pittsburgh

Summary

The collected work of the projects in this Task encompasses the following areas:

- Conducting focused fundamental research on the mechanism of "shuttle effect" inhibition for rechargeable Li-S batteries.
- Developing electrode and electrolyte systems that can mitigate the "shuttle effect" so the low self-discharge and long cycle life can be achieved.
- Synthesizing sulfur composite materials with an emphasis on polymer sulfur composite materials.
- Developing creative electrode-making processes to improve processability and areal capacity; for example, polymeric sulfur composites may not be suitable for the traditional slurry casting process.
- Developing a novel S_xSe_y cathode material for rechargeable lithium batteries with high energy density and long life, as well as low cost and high safety.
- Delivering an electrochemically responsive self-formed hybrid Li-ion conductor as a protective layer for Li-metal anodes, enabling them to cycle with high efficiency.
- Developing high-energy, low-cost Li-S batteries with long lifespan.

Highlights

The highlights for this quarter are as follows:

- Task 5.1 led by K. Amine's group at Argonne National Laboratory continued their studies in the Li-S system to improve cycling performance utilizing Se-S compositions in the cathode. Specifically, they have utilized $S_{22.2}Se$/microporous carbon composite, denoted as the ordered microporous sulfur host (OMSH) – Se/S system, in which the carbon host is embedded with Co-N-C single atoms and ZnS nanoparticles to suppress the polysulfide shuttle effect and improve the reaction kinetics. They have studied the system with hydrofluoroether (HFE) based electrolyte [1 M lithium bis(trifluoromethanesulfonyl)imide (LiTFSI) / 1,3-dioxolane + 1,2-dimethoxy-ethane (v/v) + 0.1 M $LiNO_3$] at low (0°C) and high (55°C) temperature conditions. At low temperatures, they are able to demonstrate areal capacities of > 4.2 mAh cm^{-2} after 100 cycles at 100 mA g^{-1}. At 55°C, the cell delivers 1215.97 mAh g^{-1}, stabilizing at 750.94 mAh g^{-1} after 50 cycles at 5 mg cm^{-2} sulfur loading. They also demonstrated pouch-cell results using 200-µm Li-foil anode, with the system exhibiting initial capacity of 830.76 mAh g^{-1} and stabilizing to 650.23 mAh g^{-1} after 50 cycles at electrolyte to sulfur (E/S) ratio conditions of 10 µL mg^{-1}. Using 40-µm lithium foil, with E/S ratio of 7 µL mg^{-1}, the cell can deliver initial capacity of 931.12 mAh g^{-1}, dropping to ~ 600 mAh g^{-1} after 70 cycles. X-ray photoelectron spectroscopy studies revealed the presence of LiF formation on the anode surface. These results validate the concept of using OMSH host and HFE-based electrolyte in high-energy-density Li-S batteries.
- The Task 5.2 group led by D. Lu and J. Liu at Pacific Northwest National Laboratory has attempted to study the impact of the cathode structure on lithium growth and cycling of the electrodes. They have used patterned sulfur cathodes having a patterned surface structure to represent the amplified rough surface and studied them at high sulfur loading of 6 mg cm^{-2} by applying a double-layer coating of the sulfur electrode slurry on aluminum mesh template for the second-layer coating. Using surface profilometry, they see diamond-shaped peak regions and linear valley regions, with the former showing ~ 60 µm higher peaks

than the latter, giving an average roughness of ~ 25 μm. The baseline sulfur cathode, on the other hand, had an average surface roughness of ~ 20 μm. They tested both under lean electrolyte conditions of E/S = 4 mL g^{-1}. The patterned cell, however, encountered internal short circuit and failed after 303 hours of cycling, which demonstrates the influence of surface patterning. The team therefore performed a mild calendering with a smoother surface, applying 10% compression and lowering the average roughness by 20%. They observed that this new mild calendered electrode showed improved cycle life from 557 hours for the baseline electrode to 790 hours at the same E/S of 4 mL g^{-1}. With a lower areal loading of 4 mg cm^{-2}, the cycle life improved to 1251 hours, representing a 124% increase. These results show the influence of surface topography of the sulfur electrodes on cycle life of the Li-S battery.

- Task 5.3 led by Y. Cui's group at Stanford University continued their work in developing all-solid-state lithium-sulfur batteries (ASSLSBs). They demonstrated formation of single atom catalysts of cobalt atoms by hydrogen substituted graphdiyne (HGDY) aerosol assisted ultra-fast sparking synthesis providing ample active sites for enhancing the sluggish Li-S redox reaction kinetics in ASSLSBs. They have used this approach to synthesize cobalt single atoms by generating the HGDY aerogel containing cobalt salt precursors, which was then brought in contact with a hot plate kept at 450°C to initiate a sparking reaction transforming HGDY to a black colored powder following a rapid heating and cooling to generate the metastable single cobalt atom precursor. The team claims this is a facile, scalable, and low-cost reagents approach with promise for large-scale commercialization. They have characterized the synthesized HGDY-derived cobalt single atoms by high-angle annular dark-field scanning transmission electron microscopy to resolve single atoms further validated by cobalt K-edge extended X-ray absorption fine structure and wavelet analysis showing no Co-Co formation in the Co/HGDY material, indicating formation of single atom cobalt on graphdiyne for potential application in ASSLSBs.
- Task 5.4 led by E. Hu's group at Brookhaven National Laboratory in partnership with D. Qu at the University of Wisconsin, Milwaukee, continued studies on their new bio-inspired N-doped carbon host with a unique pore structure. They have used *in situ* high-performance liquid chromatography – electrochemical technique to show that the N-doped carbon can convert the polysulfides in the electrolyte to elemental sulfur and possibly Li_2S_x ($x \leq 2$). They showed this by comparing the absorption of polysulfides by adding a baseline solution of 5 mM Li_2S_6 to the baseline high surface area carbon (PWA) and their new bio-inspired N-doped carbon (NC-800). The NC-800 shows no detectable polysulfides remaining in the solution, but a large amount of dissolved elemental sulfur suggests the possibility of NC-800 participating in disproportionation reaction of the polysulfides to elemental sulfur. They demonstrated the use of NC-800 in minimizing the shuttle effect in Li-S battery by analyzing for presence of polysulfide ions in the separator of a cell made with PWA carbon and NC-800 cells, respectively, after 3 cycles; the former showed polysulfide ions of all different chain-lengths, whereas few polysulfide ions were detected in the NC-800-containing cell. The latter also showed capacities of ~ 1000 mAh g^{-1} with little fade, showing the promise of this NC-800 system for high-energy-density Li-S batteries.
- Task 5.5. led by G. Liu's group at the University of California, Berkeley, has studied the conversion reaction of sulfur to Li_2S in the presence of their new prepared micellar electrolyte solutions. They studied different electrolyte solutions containing different amounts of the additive, F_4EO_2, by conducting cyclic voltammetry (CV) cycling the S/C electrode in the voltage range (1.8 V to 2.8 V) employing a scan rate of 0.1 mA/s, and they indicate that only broad reduction current peak was observed in the cathodic scan representing the solid-solid phase transition of sulfur in carbon to Li_2S. On the other hand, in the standard electrolyte, two reduction peaks are observed at 2.3 V and 2.0 V corresponding to the solid-liquid (elemental sulfur to dissolved Li_2S_8) and liquid-solid (dissolved Li_2S_6 to Li_2S_2 or Li_2S) phase transition. Therefore, they claim that the prepared electrolyte solutions suppress polysulfide dissolution. They also observe that LiFSI-containing electrolytes exhibited marginal overpotential in the initial cathodic and anodic sweeps due to polarization caused by the phase transition in the conversion-dissolution-diffusion process of sulfur and polysulfides. Alternatively, the electrolyte containing LiTFSI with different amounts of F_4EO_2 with 1,1,2,2-tetrafluoroethyl 2,2,2-trifluoroethyl ether (TTE), particularly, TF(5:1) DLiTFSI electrolyte solution containing TTE: F_4EO_2 in 5:1 ratio exhibited less polarization and very good cyclability and no change in

the impedance spectra after CV cycling, demonstrating positive effects of the F_4EO_2 additive and LiTFSI salt on both sulfur electrode and Li-metal anode, which suggests the likelihood of the electrolyte resulting in better cell performance. These results indicate the promise of these amphiphilic micellar electrolytes in high-energy density Li-S batteries.

- Task 5.6 led by Y. S. Meng's group at the University of California, San Diego, continued their work to demonstrate the efficacy of the new hexaazatrinaphthylene (HATN) polymer-sulfur composite electrode architectures in Li-S batteries. One major activity was to optimize synthesis of the HATN monomer (lab trial of 10-g batch) by Ampcera. The team has shown ability to make the material with a high yield of ~ 85%. They also updated the cyclability of the hexaazatrinaphthylene / carbon nanotube polymer – sulfur composite (HATN/CNT-S) cathode with a high cycling areal capacity of ~ 5.5 mAh cm^{-2} for Li-S batteries (coin cell) under lean electrolyte (< 5 g Ah^{-1}) and low N/P ratios [< 2.6; capacity ratio between anode (negative electrode) and cathode (positive electrode)]. Quantifying the lithium and sulfur inventory loss of the cycled lithium and HATN/CNT-S cathode in the above cells by titration gas chromatography and thermal gravimetric analysis, respectively, giving a sulfur inventory loss of 68.2% and lithium inventory loss of 34.58%. The team reports a high areal capacity of the HATN/CNT-S cathode (> 10 mAh cm^{-2}) with a stringently low N/P ratio of 1.85 in coin-cell tests; however, polysulfide dissolution and corrosion of the anode remain a challenge. In further activity, the team is unveiling the limiting factor of polysulfide corrosion in lean-electrolyte-based Li-S batteries with a low N/P ratio. They are also updating a new batch of the General Motors (GM) C-S cathode with a fairly smaller sulfur loading of ~ 3.56 mg cm^{-2} and its electrochemical performance by GM internal evaluation. In addition, they are fabricating robust HATN/CNT-S electrode sheets (~ 5 cm × 5 cm) with a sulfur loading of > 6 mg cm^{-2} that were demonstrated for testing at GM. These results demonstrate the potential of this system for high-energy-density Li-S batteries.
- Task 5.7 led by P. N. Kumta's group at the University of Pittsburgh, Pennsylvania, demonstrated use of additives in the electrolyte to stabilize cycling performance of the sulfur electrodes. They showed that by adding 1 wt% of an organic chemical additive, the SEI on the anode and cathode is stabilized, and the cells containing low (3.5 mg cm^{-2}) and high (7.8 mg cm^{-2}) sulfur loadings show stable capacities ~ 520 m Ah g^{-1} and ~ 569 m Ah g^{-1} after 95 cycles with Coulombic efficiencies (CEs) of greater than 98.8% and 97.8%, respectively. They also studied the influence of this new organic additive on the cycling of the Li-metal anode. Accordingly, they fabricated cells with Li-metal anode and bare copper as the cathode with this modified electrolyte containing 1 wt% of the organic additive at 1 mA current for 1 hour. The cells cycled for more than 100 cycles, delivering an areal capacity of 0.793 m Ah cm^{-2} for over 100 cycles with an average CE of 99.97%. Finally, the team studied novel multicomponent alloys (MCAs) serving as both a dendrite-free anode material and current collector synthesized by high-energy mechanical milling and alloying processes. This MCA3 alloy was cycled at different current rates to explore rate capability, namely 1 mA for 1 hour alloying and dealloying, 1 mA for 2 hours alloying and dealloying, 1 mA for 4 hours alloying and dealloying, 1.5 mA for 4 hours alloying and dealloying, and 2 mA for 4 hours alloying and dealloying for 30 cycles each, followed by exploring cycling stability at 2.5 mA for 4 hours alloying and dealloying for another 100 cycles. The cycling results show excellent cycling stability of MCA2 alloy even after 150 cycles of rate capability, affording stable areal capacity of ~ 8 m Ah cm^{-2} for a continuous 100 cycles. These results on the cathode, electrolyte additives, and novel dendrite-free anodes show the potential of these new systems for fabricating high-energy-density Li-S batteries.
- Task 5.8 led by D. Wang's group at Pennsylvania State University, based on their earlier work on optimized sulfur polymerized composite (SPC) derived active materials, utilized electrolytes and binders to achieve SPC-based batteries under high areal loading, low E/S ratio and limited Li-metal anodes. The team attempted to test the SPC-based cathodes at relatively lean electrolyte conditions of E/S of $\leq$ 5 μL mg^{-1} with conventional carbonate electrolytes. The cell demonstrated high initial areal capacity of ~ 4.3 m Ah cm^{-2}, but then failed. With new electrolytes using two different diluents, the cells showed lower areal capacities of ~ 2.2 m Ah cm^{-2} and ~ 3.5 m Ah cm^{-2}, respectively. To further increase overall energy density, binders for cathode fabrication were optimized for higher areal capacity. Application of binder 2 afforded enhanced

cycling stability; binder 3 showed promise to act as a binder as well as a conductive agent. Binder 3 showed promise for affording high mass ratio and enhanced initial areal capacity of ~ 5 m Ah cm^{-2}. They plan to demonstrate sulfur cathode using sulfur composite active materials with an initial discharge capacity > 700 m Ah g^{-1} (based cathode weight) at an E/S ratio < 10 μL mg^{-1} as well as optimize the synthetic parameters of sulfurized polyacrylonitrile baseline cathode materials for the next quarter. Results to date show the promise of these SPC systems for Li-S batteries.

Task 5.1 – Novel Chemistry: Lithium Selenium and Selenium Sulfur Couple (Khalil Amine, Argonne National Laboratory)

Project Objective. The project objective is to develop novel S_xSe_y cathode materials and advanced liquid electrolytes for rechargeable lithium batteries with high energy density and long life, as well as low cost and high safety.

Project Impact. Development of a new battery chemistry is promising to support the goal of plug-in hybrid electric vehicle and electric vehicle applications.

Approach. The dissolution of lithium polysulfides (LiPS) in nonaqueous electrolytes has been the major contribution to the low energy efficiency and short life of Li-S batteries. In addition, insulating characteristics of both end members during charge/discharge (sulfur and Li_2S) limit their rate capacity. To overcome this problem, sulfur or Li_2S is generally impregnated in a carbon-conducting matrix for better electronic conductivity. However, this makes it difficult to increase the loading density of practical electrodes. It is proposed to solve these barriers using the following approaches: (1) partially replace sulfur with selenium, (2) nano-confine the S_xSe_y in a nanoporous conductive matrix, and (3) explore advanced electrolytes with suppressed shuttle effect.

Out-Year Goals. This new cathode will be optimized with the following goals:

- A cell with nominal voltage of 2 V and energy density of 600 Wh/kg.
- A battery capable of operating for 500 cycles with low capacity fade.

Collaborations. This project engages in collaboration with the following: C. Sun, W. Xu, and X. Zuo of Advanced Photon Source at Argonne National Laboratory (ANL), Y. Liu of the Center for Nanoscale Materials at ANL, and L. Cheng of the Materials Science Division at ANL.

Milestones

1. Demonstrate stable Li/SeS pouch cells under high areal loading (≥ 5 mg/cm^2), lean electrolytes (≤ 7 µl/mg), and thin lithium metal (< 50 µm). (Q1, FY 2023; Completed)

2. Complete investigation of the interface and polysulfides dissolution by time-of-flight secondary ion mass spectrometry and *in situ* X-ray diffraction / X-ray absorption spectroscopy. (Q2, FY 2023; In progress)

3. Optimization of selenium ratio in SeS cathode to improve capacity/voltage retention under higher current densities. (Q3, FY 2023; In progress)

4. Design novel interlayer to improve cycling of high-loading (≥ 5 mg/cm^2) Li/S batteries at high current densities. (Q4, FY 2023; In progress)

Progress Report

This quarter, the team has evaluated the electrochemical performance of $S_{22.2}Se$/macroporous carbon composite [denoted as ordered microporous sulfur host (OMSH) – Se/S] in which the carbon host is embedded with Co-N-C single atoms and ZnS nanoparticles to suppress the shuttle effect and improve the reaction kinetics.

To evaluate the practical application potential of OMSH-Se/S cathode with fluorinated (HFE, that is, hydrofluoroether)-based electrolyte [1 M lithium bis(trifluoromethanesulfonyl)imide / 1,3-dioxolane + 1,2-dimethoxyethane (v/v) + 0.1 M $LiNO_3$], the team further conducted the electrochemical characterizations under more harsh conditions. First, they tested the OMSH-Se/S cathode with high areal loading (~ 5 mg cm^{-2}) under both low (0°C) and high (55°C) temperature conditions to evaluate the wide-temperature operating performance. At low temperature, the ion diffusion coefficient and the redox kinetics will decrease and deteriorate the electrochemical performance, particularly for thick electrodes. Meanwhile, the accumulation of LiPSs and polyselenides (LiPSes) intermediates during cycling caused by the slower redox kinetics will also lead to the loss of active material and thus affect the cycling stability of Li-S cells. As a result, most of the previously reported low-temperature Li-S cells were still based on thin sulfur cathode.

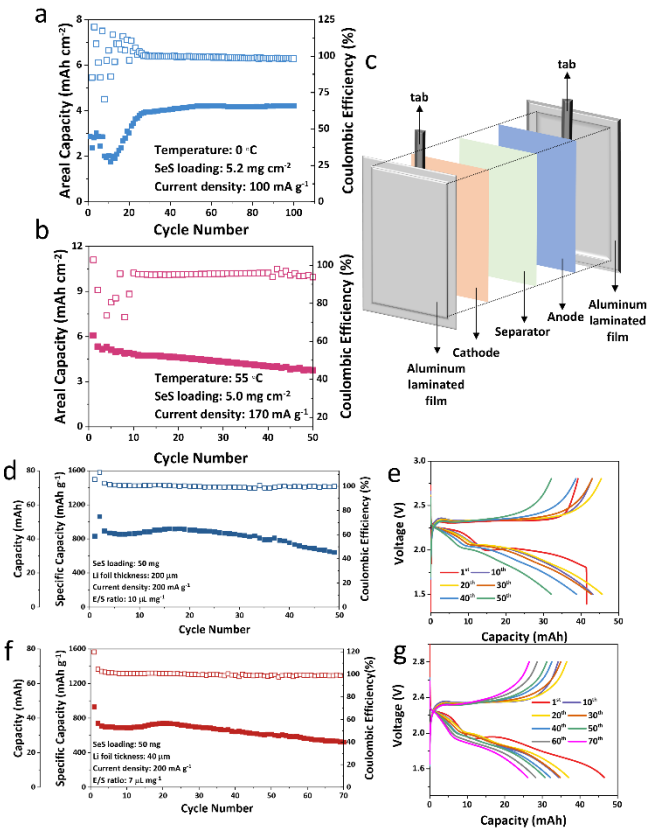

Figure 109. Practical application validation for the combination of OMSH Se/S cathode with HFE-based electrolyte. Cycling performance of OMSH-Se/S cathode in HFE-based electrolyte under (a) 0°C condition and (b) 55°C condition. (c) Schematic graph of Li-Se/S pouch-cell configuration. (d) Cycling performance of Li-Se/S pouch cell with thick Li-metal anode (200 µm). (e) Charge/discharge voltage profiles of various cycles of Li-Se/S pouch cell with 200 µm Li-metal anode. (f) Cycling performance of Li-Se/S pouch cell with thin Li-metal anode (40 µm). (g) Charge/discharge profiles of various cycles of Li-Se/S pouch cell with 40 µm Li-metal anode.

In contrast, due to the introduction of the OMSH and selenium doping, the electrochemical redox kinetics of the OMSH-Se/S cathode are effectively boosted. As shown in Figure 109a, when cycling the thick OMSH-Se/S cathode (5.2 mg cm^{-2}) under 0°C, the cathode can still deliver and maintain a reversible high areal capacity of > 4.2 mAh cm^{-2} after 100 cycles at a current density of 100 mA g^{-1}. Nevertheless, the low-temperature condition will affect both the electrochemical redox and the solid electrolyte interphase (SEI) formation kinetics. In addition, the electrolyte's physical properties, such as ionic conductivity, will also be affected by the low-temperature condition. Thus, it will take a longer time for SEI formation and stabilization under low-temperature condition, leading to abnormal performance at early cycles. Nevertheless, once the SEI is well formed after several cycles, cycling performance can resume normally. The team then evaluated the electrochemical performance of thick OMSH-Se/S cathode (5.0 mg cm^{-2}) in HFE-based electrolyte at an elevated temperature of 55°C. As shown in Figure 109b, the higher temperature can further enhance the electrochemical redox kinetics of the OMSH-Se/S cathode, resulting in a high specific capacity of 1215.97 mAh g^{-1}, and it can maintain a specific capacity of 750.94 mAh g^{-1} after 50 cycles even with high areal Se/S loading. Since the high-temperature condition will result in thermal deformation of the polypropylene separator, and it will also enhance the side reaction kinetics, stabilization process was also observed at early cycles. Nevertheless, once the inner environment was stabilized after several cycles, the performance resumed normally.

Furthermore, the team then investigated the electrochemical performance of OMSH-Se/S cathode in HFE-based electrolyte using a practical pouch-cell configuration. The pouch-cell configuration is shown in Figure 109c. The team first evaluated the performance of the Li-Se/S pouch cell based on OMSH-Se/S cathode and HFE-based electrolyte with 200-µm-thick Li-metal foil as the anode, and the electrolyte-to-sulfur (E/S) ratio was controlled to be 10 µL mg^{-1}. As shown in Figure 109d-e, the as-assembled Li-Se/S pouch cell can deliver an initial specific capacity of 830.76 mAh g^{-1} at a current density of 200 mA g^{-1}. Meanwhile, it can well maintain a specific capacity of 650.23 mAh g^{-1} after 50 cycles, corresponding to a capacity retention rate of 78.27%. The sudden voltage dip in the initial cycle was mainly caused by the insufficient electrical/ionic contact within the pouch cell due to the lack of uniform external pressure. Previous work has revealed the importance of anode swelling in stabilizing Li-metal pouch cells. Thus, cell-level engineering and optimization should also be taken into consideration in future development of a practical Li-S pouch cell.

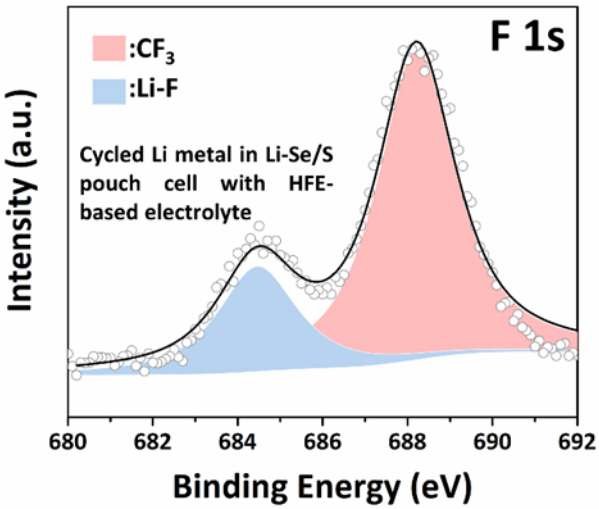

Figure 110. High-resolution X-ray photoelectron spectrum of fluorine 1s of cycled Li-metal anode in Li-Se/S pouch cell with HFE-based electrolyte.

To deliver a high realistic cell specific energy, the amount of Li-metal anode and electrolytes should also be carefully controlled. However, since the parasitic reaction in a practical pouch cell is much more severe than that of a small-scale coin cell, it remains challenging to achieve a stable cycling performance in a Li-S pouch cell. And most of the reported Li-S pouch cells utilized Li-metal anode with thickness > 100 µm. As a result, the team applied thin Li-metal foil (40 µm) as the anode and controlled the E/S ratio to 7 µL mg^{-1} of the Li-Se/S pouch cell to validate the effectiveness of the sulfur host in limiting the parasitic reaction and thus to enhance stability of the Li-Se/S pouch cell. As shown in Figure 109f-g, the as-assembled Li-Se/S pouch cell can deliver an initial specific capacity of 931.12 mAh g^{-1} at 200 mA g^{-1}. Moreover, the cell can well maintain a high Coulombic efficiency of > 99.3 % for 70 cycles. The team further conducted X-ray photoelectron spectroscopy characterization of the cycled anode. As shown in Figure 110, the fluorine 1s spectra of cycled Li-metal anode revealed a high content of Li-F on the cycled anode surface, and the formation of robust F-rich SEI in HFE-based electrolyte can explain the stable cycling performance even with thin Li-metal anode. The stable cycling performance of Li-Se/S pouch cell with thin Li-metal anode and low E/S ratio further validates the team's concept of applying OMSH host material and HFE-based electrolyte in limiting parasitic reaction inside the cell.

Patents/Publications/Presentations

Patent

- Patent Invention (ANL-22-150): "Method of Electrolyte-Less Batteries"; C. Zhao, G-L. Xu, and K. Amine.

Task 5.2 – Development of High-Energy Lithium-Sulfur Batteries (Dongping Lu and Jun Liu, Pacific Northwest National Laboratory)

Project Objective. The project objective is to develop high-energy, low-cost Li-S batteries with long lifespan. All proposed work will employ thick sulfur cathode (≥ 4 mg/cm^2 of sulfur) at a relevant scale for practical applications. The diffusion process of soluble polysulfide out of thick cathode will be revisited to investigate cell failure mechanism at different cycling. The fundamental reaction mechanism of polysulfide under the electrical field will be explored by applying advanced characterization techniques to accelerate development of Li-S battery technology.

Project Impact. The theoretical specific energy of Li-S batteries is ~ 2300 Wh/kg, which is almost three times higher than that of state-of-the-art Li-ion batteries. The proposed work will design novel approaches to enable Li-S battery technology and accelerate market acceptance of long-range electric vehicles (EVs) required by the EV Everywhere Grand Challenge.

Approach. The project proposes the following approach: (1) to identify and address key issues of applying high-energy sulfur cathodes including materials, binders, electrode architectures, and functional electrode additives, (2) to advance the mechanism study of sulfur cathode and electrolyte by using *in situ* / *ex situ* techniques and custom-designed hybrid cell setup, and (3) to verify effectiveness of the new approaches with coin/pouch cells by using high-loading electrodes (> 4 mg/cm^2), limited lithium (< 200% lithium excess), and lean electrolyte (electrolyte-to-sulfur, or E/S, ratio < 4 µL/mg).

Out-Year Goals. This project has the following out-year goals:

- Fabricate Li-S pouch cells with thick electrodes to understand sulfur chemistry/electrochemistry in environments similar to those witnessed in real application.
- Leverage the Li-metal protection project funded by the U. S. Department of Energy and Pacific Northwest National Laboratory (PNNL) advanced characterization facilities to accelerate development of Li-S battery technology.
- Develop Li-S batteries with a specific energy of 400 Wh/kg at cell level, 1000 deep-discharge cycles, improved abuse tolerance, and less than 20% capacity fade over a 10-year period to accelerate commercialization of EVs.

Collaborations. This project engages in collaboration with the following: X-Q. Yang (Brookhaven National Laboratory), M. Cai (General Motors), Y. Fu (PNNL), and Z. Liu (Thermo Fisher Scientific).

Milestones

1. Fabricate model electrodes with controlled architecture/topography to study their effects on sulfur reactivity and reaction uniformity at high-mass-loading electrode and lean electrolyte conditions (> 4 mg/cm^2, E/S < 4). (Q1, FY 2023; Completed)
2. Investigate effects of cathode architecture on lithium plating/striping and cell cycling stability at practical conditions and mechanism behind. (Q2, FY 2023; In progress)
3. Build three-dimensional electrode models to understand electrolyte transport and sulfur reactions in high-loading and low-porosity electrodes. (Q3, FY 2023; On schedule)
4. Introduce secondary-phase electrolyte reservoir into the dense electrode to extend cell cycle > 100 cycles in high loading electrodes (> 4 mg/cm^2) at lean electrolyte conditions. (Q4, FY 2023; On schedule)

Progress Report

It is well known that lithium plating during the charging of Li-S batteries is affected by the local current density, Li-ion concentration gradient, and electrolyte mass transfer, etc. Thus, any change in these factors would affect the morphology of the lithium plating and cell cycle life. This is particularly true in Li-S cell, because sulfur cathodes are not only highly rough and porous, but also involve dynamic redistribution of sulfur species during discharging/charging. To study the impact of the cathode structure on lithium growth and cycling, the patterned sulfur cathodes (PSCs), which have patterned surface structures, were prepared to represent the amplified rough surface, and were studied at practical high sulfur loading and lean electrolyte conditions. The PSC with a sulfur loading of 6 mg cm^{-2} was prepared by applying a double-layer coating using aluminum mesh as a template for the second-layer coating (Figure 111a). Copying the aluminum mesh template, the PSC showed diamond-shaped peak regions (PR) and linear valley regions (VR) (Figure 111b-c). The optical profilometry measurement indicates that the PR resides ~ 60 µm higher than the VR, and the average roughness of the whole electrode is ~ 25 µm (Figure 111d/g). For comparison, the baseline sulfur cathode (BSC) without any patterns was also prepared, with an overall flatter surface (Figure 111e) and an average surface roughness of 20 µm (Figure 111f). The BSC and PSC were assembled into coin cells and tested under lean electrolyte conditions (E/S = 4 mL g^{-1}), as seen in Figure 111h. It was found that compared to PSC, the BSC showed higher specific capacity and a longer cycle life under the lean electrolyte conditions. The charge failure occurred after 563 hours of cycling. However, in the PSC cell, the cell failure occurred much earlier during the fourth cycle (~ 70 hours), featuring an internal short circuit (ISC), as highlighted in gray in Figure 111h. The cell was recovered after a prolonged and fluctuated charge cycle, indicating the occurrence of a micro or soft ISC. Despite the recovery, the cell failed after 303 hours of cycling. Increasing the electrolyte amount (E/S ratio) helped extend the cycle life for both electrodes (results are not shown here), but the trend in charge failure, that is, PSC had much shorter cycle life than BSC, remained the same. This suggests the prevailing role of sulfur electrode topography in cell cycling, where a rougher surface leads to quicker formation of lithium dendrites and, thus, earlier cell failure.

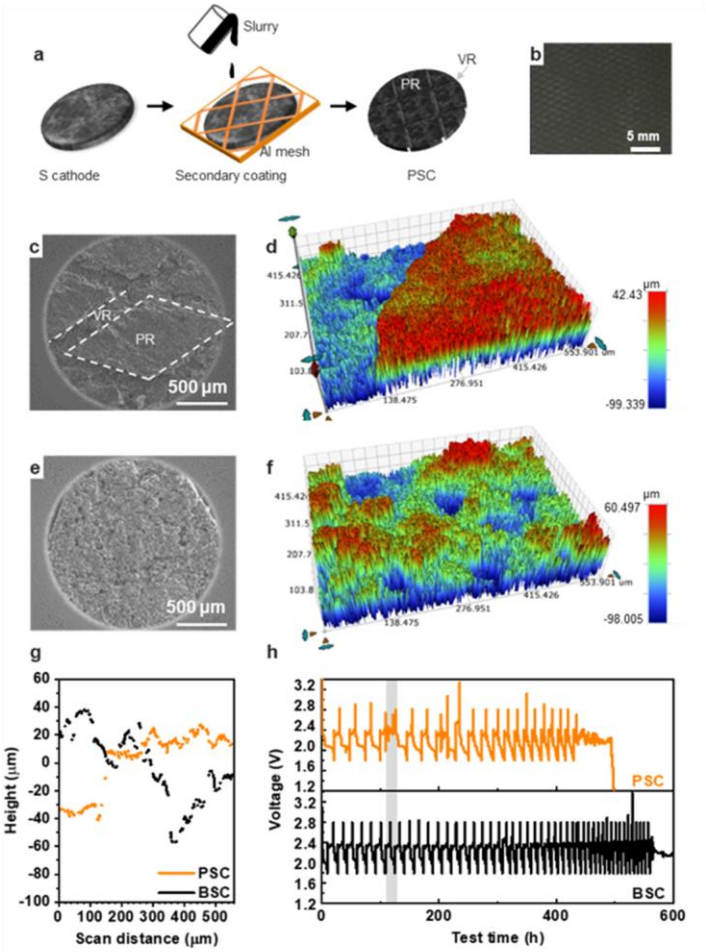

Figure 111. (a) Schematic illustration of patterned sulfur cathode (PSC) preparation. (b) Digital photograph of PSC, scanning electron microscope, and surface profilometric images of (c-d) PSC and (e-f) baseline sulfur cathode (BSC). The color from blue to red represents the height from low to high. (g) X line-scan profiles of PSC and BSC. (h) Discharge and charge profiles of the PSC and BSC on cycling at an E/S of 4 mL g^{-1}. The gray bar highlights the early occurrence of internal short circuit in PSC.

Based on the study, any approaches that could homogenize cathode reactions and lower the variation of local currents would help to delay or even eliminate an ISC event, thereby extending cell cycle life. Control of electrode topography is one of the most straightforward ways to accomplish this. To verify its effectiveness, a

mild calendered electrode with a smoother surface was prepared. Only 10% compression was used to prepare the compressed sulfur cathode (CSC), and the measured average roughness was decreased by 20% compared to that of BSC (Figure 112a). Without calendering, the BSC failed by ISC at 557 hours and 570 hours (Figure 112b/d) at a sulfur loading of 6 mg cm^{-2} and 4 mg cm^{-2}, respectively. Promisingly, the CSC shows a significantly improved cycle life from 557 hours to 790 hours at the same E/S of 4 mL g^{-1} (Figure 112b). By lowering the areal loading from 6 mg cm^{-2} to 4 mg cm^{-2}, the cycle life improvement was even more profound, improving by 124% to 1251 hours (Figure 112b-d). This further proves the importance of electrode topography on cell cycle life, where high electrode uniformity and low roughness are desired for long cycling lithium batteries. These understandings and improvement have been incorporated to the Li-S pouch cell assembly and test.

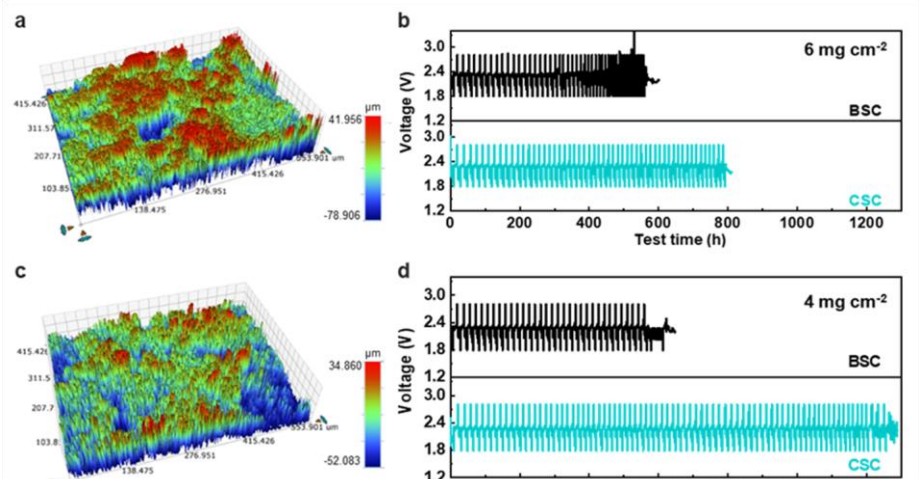

Figure 112. Optical profilometric images of compressed sulfur cathode (CSC) at sulfur loading of (a) 6 mg cm^{-2} and (c) 4 mg cm^{-2}. Discharge and charge profiles of the baseline sulfur cathode (BSC) and CSC at sulfur loading of (b) 6 mg cm^{-2} and (d) 4 mg cm^{-2} in E/S = 4 mL g^{-1}.

Patents/Publications/Presentations

The project has no patents, publications, or presentations to report this quarter.

Task 5.3 – Nanostructured Design of Sulfur Cathodes for High-Energy Lithium-Sulfur Batteries (Yi Cui, Stanford University)

Project Objective. The charge capacity limitations of conventional transition metal oxide cathodes are overcome by designing optimized nano-architectured sulfur cathodes. This study aims to enable sulfur cathodes with high capacity and long cycle life by developing sulfur cathodes from the perspective of nanostructured materials design, which will be used to combine with Li-metal anodes to generate high-energy Li-S batteries. Novel sulfur nanostructures as well as multifunctional coatings will be designed and fabricated to overcome issues related to volume expansion, polysulfide dissolution, and the insulating nature of sulfur.

Project Impact. The capacity and cycling stability of sulfur cathodes will be dramatically increased. This project's success will allow Li-S batteries to power electric vehicles and decrease the high cost of batteries.

Approach. The approach involves three main efforts:

- Advanced nanostructured sulfur cathodes design and synthesis, including (1) engineer empty space into sulfur cathode to solve the problem of electrode volume expansion, (2) develop novel sulfur nanostructures with multifunctional coatings for confinement of S/Li polysulfides to address issues of active materials loss and low conductivity, (3) develop/discover optimal nanostructured materials that can capture the polysulfide dissolved in the electrolyte, (4) develop space-efficiently-packed nanostructured sulfur cathode to increase volumetric energy density and rate capability, and (5) identify interaction mechanism between sulfur species and different types of oxides/sulfides, and find optimal materials to improve capacity and cycling of sulfur cathode.
- Structure and property characterization, including *ex situ* scanning electron microscopy, X-ray photoelectron spectroscopy analysis, and *in operando* X-ray diffraction and optical microscopy.
- Electrochemical testing including coin cells and pouch cells as well as a set of electrochemical techniques.

Out-Year Goals. The cycle life, capacity retention, and capacity loading of sulfur cathodes will be greatly improved (that is, 200 cycles with 80% capacity retention, > 0.3 mAh/cm^2 capacity loading) by optimizing material design, synthesis, and electrode assembly.

Collaborations. This project collaborates with the following: BMR principal investigators; SLAC National Accelerator Laboratory: M. Toney *(in situ* X-ray); and Stanford University: W. Nix (mechanics) and Z. Bao (materials).

Milestones

1. Designing and synthesizing single atom catalyst to facilitate Li-S conversion in all-solid-state Li-S batteries (ASSLSBs). (Q1, FY 2023; Completed)

2. Demonstrating ASSLSBs with designed single atom catalyst. (Q2, FY 2023; In progress)

3. Exploring the working mechanism of single atom catalyst in ASSLSBs, experimentally and theoretically. (Q3, FY 2023; In progress)

4. Enabling ASSLSBs with high capacity and high-rate ability. (Q4, FY 2023; In progress)

Progress Report

Single atom catalysts with the maximum usage of atom efficiency and metal-support interaction have been used for catalytic-related applications. So far, the studies of single atom catalysts for Li-S batteries have been focused on liquid electrolytes. Using single atom catalysts to enhance ASSLSBs is challenging and unexplored, owing to the limited catalytic activity in the solid-state systems. This quarter, the team prepared cobalt single atoms by hydrogen substituted graphdiyne aerogel assisted ultra-fast sparking synthesis (GAUSS), which provides abundant active sites for enhancing the sluggish Li-S redox reaction kinetics in ASSLSBs.

For the GAUSS process (Figure 113a), hydrogen substituted graphdiyne (HGDY) aerogel is designed to provide micro-explosions. HGDY aerogels have high surface area, high volume to mass ratio, micropores, and unique acetylenic carbon chemistry, which provides high density sites of micro-explosions to realize ultra-high temperature. When the HGDY aerogel touches the hotplate (set to 450°C), a sparking reaction occurs. During this reaction, red flames spread from origin quickly through the entire aerogel, transforming the HGDY from a light brown to a black color. This reaction produces a large amount of heat and pressure. Synthesis of Co/HGDY with the team's GAUSS platform is achieved by soaking the HGDY aerogel in ethanol with dissolved metal salts and then drying to achieve a metal-infused HGDY aerogel. The metal-infused HGDY aerogel is then placed in contact with a hotplate (set to 450°C), quickly initiating the spark reaction, which provides the fast heating and cooling rates necessary to achieve the metastable states. The facile, scalable nature, and low costs of reagents of the GAUSS platform endow the method with promise for large-scale commercialization.

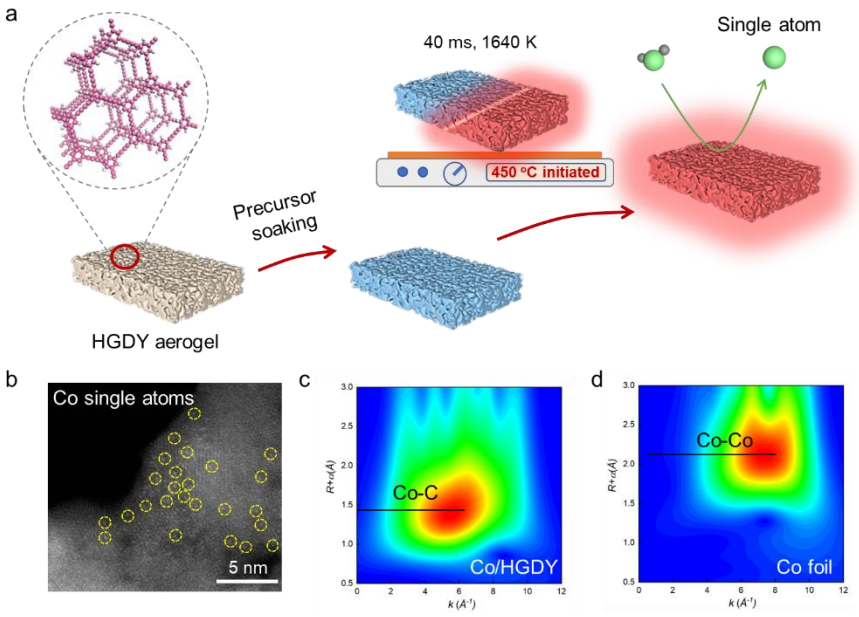

Figure 113. Single atoms by graphdiyne aerogel assisted ultra-fast sparking synthesis (GAUSS) for all-solid-state Li-S batteries. (a) Schematic of GAUSS for cobalt single atoms. Precursors are first dissolved in ethanol and soaked on hydrogen substituted graphdiyne (HGDY) aerogel. Solvated HGDY aerogel is dried and placed on the hotplate set at a temperature of 450°C. Immediately, sparking reaction happens and spreads quickly through the entire aerogel, achieving an ultra-high temperature up to 1640 K within 40 milliseconds. (b-d) Characterizations of single atoms by GAUSS. (b) Scanning transmission electron microscopy image of cobalt single atoms on HGDY. Wavelet transforms for (c) Co/HGDY and (d) cobalt foil reference.

To characterize single atoms produced by their GAUSS platform, the team used aberration corrected high-angle annular dark-field scanning transmission electron microscopy (HAADF-STEM) to resolve single atoms owing to large atomic number difference between metal atoms and carbon atoms in the HGDY support. The HAADF-STEM image showed localized bright spots on the HGDY support, indicating single atom cobalt sites are well dispersed on the HGDY support (Figure 113b). Cobalt K-edge extended X-ray absorption fine structure further supports the HAADF-STEM measurement. Wavelet analysis clearly shows no Co-Co formation in the Co/HGDY material, indicating the successful synthesis of single atom sites on GDY (Figure 113c-d). The cobalt loading is determined as 0.23 wt% by inductively coupled plasma analysis.

Patents/Publications/Presentations

The project has no patents, publications, or presentations to report this quarter.

Task 5.4 –Investigation of Sulfur Reaction Mechanisms (Enyuan Hu, Brookhaven National Laboratory; Deyang Qu, University of Wisconsin, Milwaukee)

Project Objective. The primary objectives are as follows:

- To synthesize, optimize and down select small organo-sulfur electrode for all solid-state Li-S batteries.
- To investigate the interface and physical compatibility, for example, elasticity between the small organo-sulfur electrode and solid-state electrolyte (SSE).
- To develop surface protective lithium anode so it can be compatible with polytetrafluoroethylene (PTFE) binder.
- To continue investigating the interaction of polysulfides in the cathode solid phase.

Project Impact. The results of this project will be used for development of technologies that will significantly increase energy density and cycle life and will reduce the cost of beyond Li-ion battery systems. This will greatly accelerate deployment of electric vehicles and reduce carbon emission associated with fossil fuel consumption and help in the direction of building the U. S.-based energy storage manufacture chains.

Approach. This project will encompass the following: (1) continue to investigate and improve the interphase between the sulfur (including organo-sulfur) cathode and the electrolyte, (2) continue to develop hosting and catalytic materials to limit the migration of long-chain polysulfide, and (3) collaborate with Brookhaven National Laboratory (BNL), continuing to investigate the sulfur redox reaction in the solid phase taking advantage of synchrotron-based techniques at BNL and electrochemical analytical techniques at University of Wisconsin, Madison.

One-Year Goals. In FY 2023, the interim goal is to develop a Li-sulfur battery with sulfur-containing cathode of 600-800 mAh/g capacity with mitigation of the "shuttle effect" in the liquid electrolyte and in all-solid-state electrolyte.

Collaborations. The principal investigator (PI) works closely with beamline scientists at synchrotron facilities to develop novel Li-S characterization tools. The PI and co-PI collaborate closely with top scientists at Argonne National Laboratory, Lawrence Berkeley National Laboratory, and Pacific Northwest National Laboratory, as well as U. S. industrial collaborators at General Motors, Ford, Clarios, etc. The PI and co-PI also collaborate with scientists in China, Japan, and South Korea. These collaborations will be strengthened and expanded to give this project a vision on both today's state-of-the-art technology and tomorrow's technology in development, with feedback from the material designer and synthesizers upstream and from industrial end users downstream.

Milestones

1. Synthesize and downselect small organosulfur compounds and testing in all-solid-state Li-S cells. (Q1, FY 2023; Completed)
2. Develop surface protected lithium anode and test with SSE of PTFE binder. (Q2, FY 2023; In progress)
3. Complete interfacial investigation of both small organo-sulfur and protected lithium with SSE. (Q3, FY 2023; In progress)
4. Complete testing full cell with selected small organo-sulfur surface protected lithium anode and SSE. Complete investigation of polysulfide in solid-phase. (Q4, FY 2023; In progress)

5. Complete investigations of interface of small organo-sulfur electrode, surface protected anode with SSE. Complete studies of redox reaction mechanism in the solid phase in cathode and the interplay between dissolved polysulfide ions in electrolyte and sulfide compounds in the solid. Complete and continue testing of small organosulfur cathode and surface protected lithium anode in all-solid-state electrolyte Li-S full cell. (Annual milestone; In progress)

Progress Report

In late FY 2022, the team reported the synthesis and testing of a novel bio-inspired N-doped carbon with a unique pore structure. The carbon was used a sulfur host material and tested in both coin cells and pouch cells. Excellent performance was demonstrated in both cell formats. *In situ* high-performance liquid chromatography – electrochemical technique was applied to investigate the mechanism of the reactions. The team concluded that the N-doped carbon can convert the dissolved polysulfides in the electrolyte to elemental sulfur and possibly Li_2S_x ($X \leq 2$).

Figure 114 shows the change of polysulfide distribution in a baseline solution of 5 mM Li_2S_6 (stoichiometry) after adding PWA carbon and the bio-inspired N-doped carbon (NC-800). Clearly, after adding NC-800, no detectable dissolved polysulfides remain in the solution, but a large amount of dissolved elemental sulfur appeared. Based on the experimental evidence shown in Figure 114, it is worth pointing out that NC-800 did not act as a catalyst, but rather participated in the sulfur "disproportionation reaction." By definition, it should not be referred to as disproportionation, either. A catalyst can only change the activation energy of a reaction, but not shift the chemical equilibrium. Evidently, the chemical equilibrium of the polysulfide ions shifted toward the formation of elemental sulfur induced by the NC-800. Although the detailed reaction mechanism is still unclear, the interaction of NC-800 with polysulfides can be ascribed to their relatively higher nitrogen content on the carbon surface.

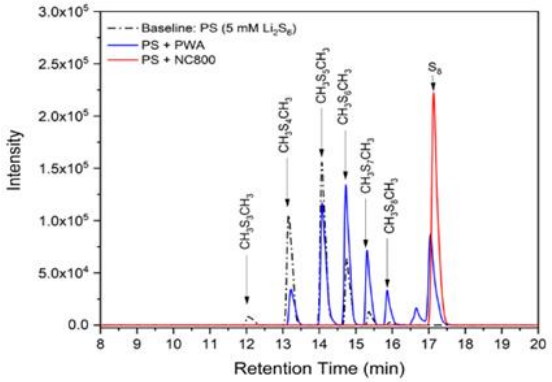

Figure 114. Distribution of polysulfide in the baseline solution containing 5 mM Li_2S_6 (stoichiometry); the solution after adding PWA carbon and NC-800 carbon.

The shuttle effect in a Li-S battery results from the interaction between lithium anode and dissolved polysulfide ions. Efforts have been made to absorb polysulfides in a porous carbon through physical absorption or to localize polysulfides on a polymer backbone through chemical bonds, for example, sulfurized polyacrylonitrile. The results the team presents open a new avenue to remediate the shuttle effect in a Li-S battery. Since most of the dissolved polysulfide ions were converted to elemental sulfur, then the shuttle effect can be substantially depressed. The hypothesis is proven, as shown in Figure 115. It shows that abundant polysulfides with various chain lengths are formed in the Li-S cell using a regular high surface area carbon (PWA). In comparison, little polysulfide can be found in the Li-S cell using NC-800. Also shown in Figure 115, after 100 deep cycles, the specific capacity of the sulfur cathode in the cell made with NC-800 retains ~ 1000 mAh/g of capacity. Little capacity fade was observed.

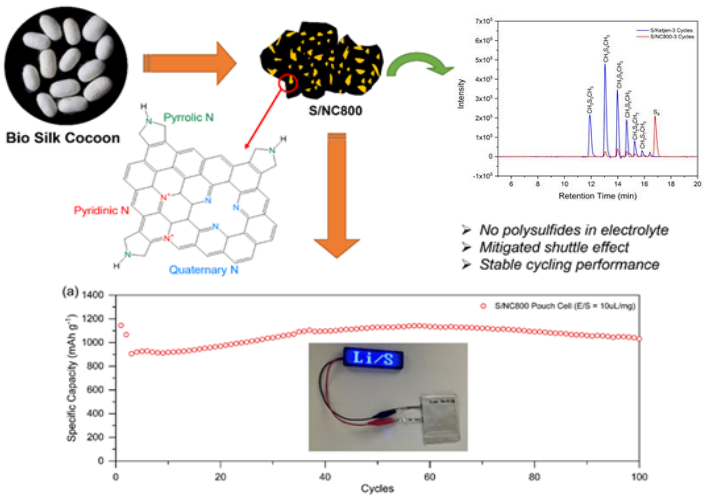

Figure 115. The synthesis and possible structure of the NC-800, cycling of a Li-S pouch cell made with NC-800, and distribution of dissolved polysulfide ions recovered from the separators after three cycles of Li-S cells made with KG black carbon and NC-800.

Patents/Publications/Presentations

The project has no patents, publications, or presentations to report this quarter.

Task 5.5 – New Electrolytes for Lithium-Sulfur Battery (Gao Liu, Lawrence Berkeley National Laboratory)

Project Objective. The project objective is to develop new electrolytes, additives, and electrode compositions for Li-S battery with high ion-conductivity, stable toward polysulfide, and promoting the polysulfide affiliation with the electrode substrate to prevent polysulfide dissolution.

Project Impact. This work will address the high cost and low energy density of Li-ion rechargeable batteries. The emerging Li-S batteries could feature both high energy density and low cost. This project enables applications of the low-cost, abundant sulfur element as a major chemical component for electrical energy storage. This project will develop new approaches for electrolytes and electrode compositions of Li-S rechargeable batteries.

Approach. This project aims to develop new electrolytes and additives for Li-S battery. The properties of the ideal electrolyte for sulfur electrode would be high ion conductivity, stable toward polysulfide, and promoting the polysulfide affiliation with the electrode substrate to prevent polysulfide dissolution. The project is designed to first understand the electrode substrate interaction with the polysulfides in different electrolytes. This will lead to better understandings of the polysulfide nucleation and precipitation mechanisms in common electrolytes. The second stage of the project will focus on chemically modifying the structures of the solvent and salt electrolyte molecules to increase electrolyte stability and ionic conductivity, to prevent polysulfide dissolution, and to promote polysulfide precipitation.

Out-Year Goals. The team will also investigate the contribution of Li-metal electrodes to overall Li-S battery performance and will develop methods to stabilize Li-metal surface.

Collaborations. This project collaborates with J. Guo and C. Zhu (Advanced Light Source / Lawrence Berkeley National Laboratory, LBNL), A. Minor (National Center for Electron Microscopy at LBNL / University of California, Berkely), G. Nagy and W. Heller (Neutron National Science User Facility / Oak Ridge National Laboratory), and P. B. Balbuena (Texas A&M University).

Milestones

1. Synthesis and formulation of a series of electrolytes including new amphiphilic additives and combination of solvents and lithium salts. (Q1, FY2023; Delayed, with completion by Q2 due to chemicals availability)
2. Using synchrotron national user facility to study the aggregation morphology of the series of electrolytes. (Q2, FY 2023)
3. Fabricate both Li-metal anode and lithiated alloy anode, and sulfur cathode rechargeable Li-S batteries, and test cell performance. (Q3, FY 2023; In progress)
4. Use advanced diagnostics to study interface properties of the anode and cathode interfaces of the cycled electrodes using the amphiphilic electrolyte. (Q4, FY 2023)

Progress Report

The cyclic voltammetry (CV) results of the Li-S batteries with the prepared electrolyte solutions are shown in Figure 116. The voltage range was 1.8-2.8 V, and the scan rate was 0.1 mA/s. The Li-S batteries with the prepared electrolyte solutions showed one broad reduction current peak in the cathodic scan, which is associated with the solid-solid phase transition (S/C to Li_2S). On the other hand, the Li-S battery with the standard electrolyte solution showed two reduction peaks at ca. 2.3 V and 2.0 V, which corresponded to the solid-liquid (elemental sulfur to dissolved Li_2S_8) and liquid-solid (dissolved Li_2S_6 to Li_2S_2 or Li_2S) phase transition. Therefore, the prepared electrolyte solutions suppress polysulfide dissolution. The slight overpotential in the initial cathodic and anodic sweep in the Li-S batteries with the TF(5:1)DLiTFSILiFSI and TF(5:1)DLiFSI electrolyte solution (see Table 5 for electrolyte compositions) is due to the polarization caused by the phase transition in the conversion-dissolution-diffusion process of sulfur and polysulfides. More importantly, the electrochemical impedance spectroscopy (EIS) of the Li-S batteries with TF(5:1)DLiTFSILiFSI and TF(5:1)DLiFSI (see Table 5 for electrolyte compositions) electrolyte solutions changed significantly after CV cycling, which is caused by the presence of the less stable bis(fluorosulfonyl)imide (FSI) anion in the electrolyte solutions. However, the Li-S batteries with the TF(5:1)DLiTFSI (see Table 5 for electrolyte compositions) electrolyte solution showed excellent cycling performance, with well-overlapping anodic and cathodic scans in the CV curves and no changes observed in EIS after CV cycling, indicating low polarization and high reversibility in subsequent cycles. Additionally, as the amount of F_4EO_2 additive in the electrolyte solution increases, the Li-S battery shows less polarization and good reversibility in the CV cycles, demonstrating the positive effects of the F_4EO_2 additive and lithium bis(trifluoromethanesulfonyl)imide (LiTFSI) salt on both sulfur electrode and Li-metal electrode to yield better cell performance.

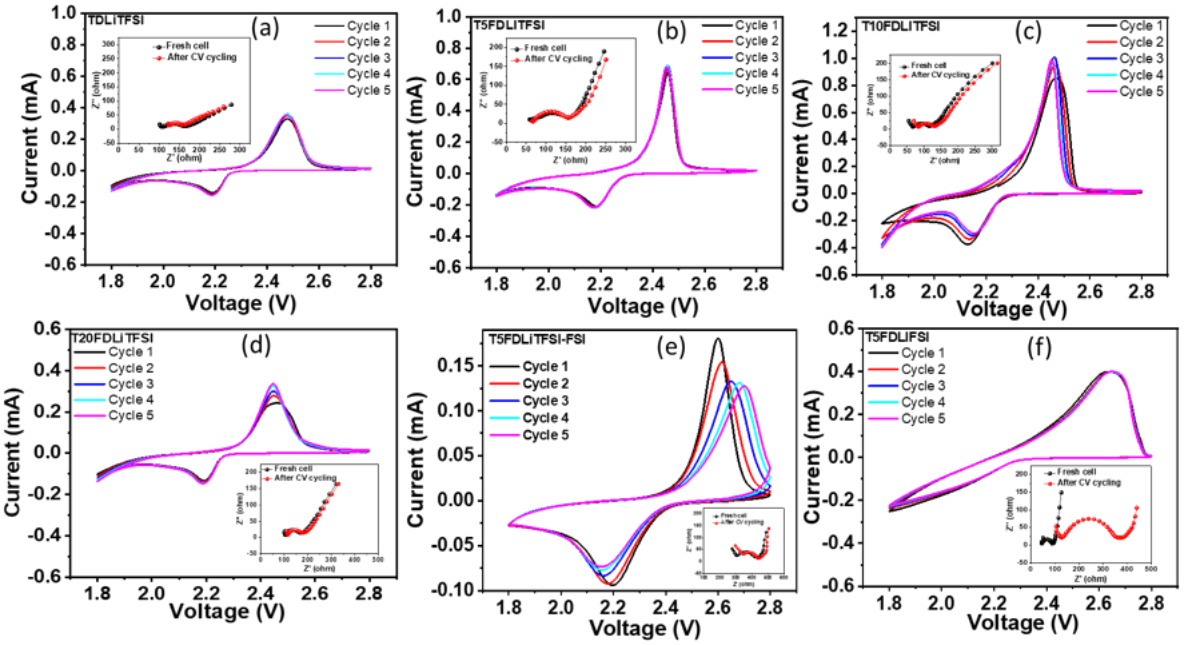

Figure 116. Cyclic voltammetry (CV) curves of the (a) TDLiTFSI, (b) TF(5:1)DLiTFSI, (c) TF(10:1)DLiTFSI, (d) TF(20:1)DLiTFSI, (e) TF(5:1)DLiTFSILiFSI, and (f) TF(5:1)DLiFSI electrolyte solutions with the Li // electrolyte // S/C cell configuration at 0.1 mV/s.

Table 5. Compositions of the prepared electrolyte solutions.

Electrolyte Solution	Ratio of 1,1,2,2-tetra-fluoroethyl-2,2,3,3-tetra-fluoropropyl ether (TTE) and F_4EO_2 in Solution A		Amount of 1,3-dioxolane (DOL, vol%) with respect to Solution A	Molar Concentration of lithium bis(trifluoromethane-sulfonyl)imide (LiTFSI)	Molar Concentration of lithium bis(fluoro-sulfonyl)imide (LiFSI)
	TTE	F_4EO_2			
TDLiTFSI	5	-	10%	0.5 M	-
TF(5:1)DLiTFSI	5	1	10%	0.5 M	-
TF(10:1)DLiTFSI	10	1	10%	0.5 M	-
TF(20:1)DLiTFSI	20	1	10%	0.5 M	-
TF(5:1)DLiTFSILiFSI	5	1	10%	0.25 M	0.25 M
TF(5:1)DLiFSI	5	1	10%	-	0.5 M

Patents/Publications/Presentations

The project has no patents, publications, or presentations to report this quarter.

Task 5.6 – Strategies to Enable Lean Electrolytes for High Loading and Stable Lithium-Sulfur Batteries (Y. Shirley Meng, University of California, San Diego)

Project Objective. The project aims to develop high energy density (> 500 Wh/kg) and low cost (< 65 $/kWh) Li-S pouch cells.

Impact. The project focuses on addressing the fundamental bottleneck in enabling high-energy-density Li-S batteries. This has been identified as the need to reduce liquid electrolyte excess and enable high areal loading electrodes. The challenges are overcome via the use of a dense polymer – sulfur electrode composite, which significantly reduces electrode porosity in conventional C-S systems while improving capacity retention. These capabilities, combined with project collaborator Ampcera's material scale up and collaborator General Motor's (GM's) pouch prototyping capability using thin lithium metal, will result in breakthroughs in next-generation Li-S battery chemistries that meet the energy density (> 500 Wh/kg) and cost goals (< $65/kWh) of this project.

Approach. Novel electrode architectures using hexaazatrinaphthylene polymer – sulfur (HATN-S) composite electrode will be explored to reduce the porosity and increase the active loading of the composite electrode. Additionally, advanced electrolyte systems and optimization of Li-metal anode will be applied to further increase energy density of the Li-S pouch cell. If successful, the proposed HATN-S electrode should have less than 30% porosity with high areal capacities of > 10 mAh cm^{-2}, which will enable lean electrolyte conditions < 2 g/Ah^{-1} in the full Li-S pouch cell.

Out-Year Goals. The out-year goals involve demonstration of baseline cell chemistries with reduced cathode porosity and increased cathode areal loading pairing with limited electrolyte and lithium inventory. The conventional electrode drying process (solvent evaporation) limits sulfur loading in the electrode, as higher loading leads to cracking. Thus, the HATN-S electrode will be prepared by optimizing the electrode architecture to increase sulfur loading and reduce electrode porosity. The electrolyte system will be optimized to reduce excessive lithium usage [low N/P ratio; that is, capacity ratio between anode (negative electrode) and cathode (positive electrode)] and improve cell stability.

Collaborations. Project collaborators include GM and Ampcera. This quarter, the work was accomplished by University of California, San Diego (UCSD). Ampcera has optimized the synthesis of hexaazatrinaphthylene (HATN) monomer and polymer with an improved yield of ~ 80%. GM has provided thin lithium metal (100 μm) and is working on the conventional C-S cathode with a sulfur loading of 3.56 mg cm^{-2} for this project.

Milestones

1. Conduct laboratory-scale characterization to identify limiting factors in performance and to establish mitigation strategies. (Q1, FY 2023; Completed)
2. Complete scalable fabrication of electrode materials. (Q2, FY 2023; In progress)
3. Decrease cost of raw materials to meet the final goal of $68/kWh. (Q3, FY 2023; In progress)
4. Optimize HATN-S composite full cell. Achieve large-scale production of materials. (Q4, FY 2023; In progress)

Progress Report

Introduction

The project objective is to develop high-energy-density (> 500 Wh/kg) and low-cost (< $68/kWh) Li-S pouch cells. To achieve that, novel electrode architectures using the HATN-S composite electrode will be explored to achieve the low cathode porosity and high sulfur active loading of the composite electrode. Additionally, advanced electrolyte systems and the optimization of the Li-metal anode will be applied to further increase the energy density of the Li-S pouch cell. If successful, the proposed HATN-S composite electrode will achieve less than 20% porosity, significantly decreasing electrolyte usage with high areal capacities of > 10 mAh cm^{-2}, enabling lean electrolyte conditions < 2 g Ah^{-1} in the full Li-S pouch cell. This quarter, major activities include the following:

- optimizing synthesis of HATN monomer (laboratory trial of 10-g batch) by Ampcera;
- updating the cyclability of the hexaazatrinaphthylene / carbon nanotube polymer – sulfur composite (HATN/CNT-S) cathode with a high cycling areal capacity of ~ 5.5 mAh cm^{-2} for Li-S batteries (coin-cell) under lean electrolyte (< 5 g Ah^{-1}) and low N/P ratios (< 2.6);
- quantifying the lithium and sulfur inventory loss of the cycled lithium and HATN/CNT-S cathode in the above cells by titration gas chromatography (TGC) and thermal gravimetric analysis (TGA), respectively;
- reporting a high areal capacity of the HATN/CNT-S cathode (> 10 mAh cm^{-2}) with a stringently low N/P ratio of 1.85 in coin-cell tests;
- unveiling the limiting factor of polysulfide corrosion in lean-electrolyte-based Li-S batteries with a low N/P ratio;
- updating a new batch of the GM C-S cathode with a fairly smaller sulfur loading of ~ 3.56 mg cm^{-2} and its electrochemical performance by GM internal evaluation; and
- fabricating the robust HATN/CNT-S electrode sheets (~ 5 cm × 5 cm) with a sulfur loading of > 6 mg cm^{-2}.

Specifically, the synthetic setup was installed at Ampcera during an on-site visit from UCSD last quarter. A laboratory trial of a 10-g batch of HATN monomer has been synthesized at Ampcera this quarter, with a high yield of ~ 80% under optimized conditions. The as-prepared HATN monomer was validated by nuclear magnetic resonance (NMR) and Fourier transform infrared, and a 5-g batch was shipped to UCSD. The team's HATN/CNT-S cathode was prepared by mixing HATN/CNT with bulk sulfur instead of the conventional sulfur melt infusion (Q4, FY 2022). The HATN/CNT-S cathode consists of bulky particles (~ 15 µm), presenting a low porosity of 30% and a super low average two-dimensional (2D) tortuosity of 1.22 within 1.57 of a semicircle (Figure 118a). This facilitates electrolyte wettability and the diffusion of liquid-state active sulfur species under the lean electrolyte condition. By using a lean baseline electrolyte (that is, electrolyte-to-sulfur (E/S) ratio of ~ 6 µl mg_{sulfur}^{-1} or electrolyte-to-capacity (E/C) ratio of ~ 5 g Ah^{-1}) and pairing with 100-µm Li-metal foils (N/P ratio of 2.6) received from the team's collaborators at GM, the HATN/CNT-S cathode delivers a high cycling areal capacity of ~ 5.5 mAh cm^{-2} at 0.1 C in Li-S batteries (coin cell). The cells run for 76 cycles with a capacity loss of ~ 45%, but the voltage profiles of the HATN/CNT-S cathode are well maintained without any over-charge issues, indicating the $LiNO_3$ reservoir is sufficient (Q1, FY 2023). In this quarter, the lithium and sulfur inventory loss of the cycled lithium and HATN/CNT-S cathode in the above cells (after 76 cycles) was quantified by TGC and TGA, respectively. The results show that the HATN/CNT-S cathode has a sulfur inventory loss of 68.8% and a lithium inventory loss of 34.58%, which is better than a sulfur inventory loss of 80.6% and a lithium inventory loss of 47.0% for the conventional C-S cathode whose capacity drastically drops after 68 cycles, using a higher E/S ratio of ~ 10 µl mg_{sulfur}^{-1} and much higher N/P ratio of ~ 5.7 (Q2-Q3, FY 2022). Thus, it is demonstrated that the team's dense bulky HATN/CNT-S cathode can achieve improved electrochemical performance under lean electrolyte and lean lithium conditions.

However, to achieve high energy density of Li-S batteries with long cycling stability, the current performance is still limited. Thus, it is of utmost importance to pinpoint the root causes of the short cycle life of lean-electrolyte-thin-lithium-based Li-S batteries apart from the $LiNO_3$ depletion issue. This quarter, UCSD reports a high areal capacity of the HATN/CNT-S cathode (> 10 mAh cm^{-2}, ~ 8.48 mg_{sulfur} cm^{-2}) with a stringently low N/P ratio of 1.85 in coin-cell tests. The S-specific capacities of the HATN/CNT-S (no sulfur melt infusion) were evaluated by using E/S of ~ 6 µl mg_{sulfur}^{-1} at 0.25 mA cm^{-2} and 0.5 mA cm^{-2}. The areal current density of 0.25 mA cm^{-2} is equivalent to 0.17 C of $LiFePO_4$ with the same active loading. It is shown that the HATN/CNT-S cathode presents high S-specific capacities (high sulfur utilization) of > 1000 mAh g_{sulfur}^{-1} under the lean electrolyte condition. As a result, an extremely low N/P ratio of 1.85 was obtained using such a high cathode areal capacity of HATN/CNT-S cathode, which is the prerequisite of the targeted energy density of ~ 500 Wh kg^{-1}. The cell capacity drops quickly within 40 cycles, showing dramatic degradation of electrodes. It is foreseen that larger sulfur utilization in the cells using higher areal sulfur loadings paired with the same amount of lithium (100 µm) generates a higher concentration of polysulfide in the Li-S system, which accelerates the reaction between lithium and polysulfide, especially under lean-electrolyte conditions. The lithium corrosion by concentrated polysulfide was further validated by the fast vanishment of a fresh lithium chip (100 µm) put into a 0.5 M Li_2S_6 solution (Figure 120e). The limiting factor of longer cycle life might be the corrosion of lithium by the concentration polysulfide solution. The future strategies will focus on lithium protection and alleviating the corrosion of concentrated polysulfide in lean-electrolyte-based Li-S batteries. Lastly, GM has established a batch of C-S cathode using their new coater with a sulfur loading of ~ 3.56 mg cm^{-2}; they evaluated the electrochemical performance before sending it to UCSD. UCSD also fabricated electrode sheets with a larger area of 5 cm × 5 cm to assemble a small pouch cell to make the most use of the electrolyte for high energy density.

Optimized Synthesis of HATN Monomer and Design for Scaling-Up (Ampcera)

In previous quarters, Ampcera determined that the HATN purity and yield inconsistency between trials was caused by the method shortfalls and reagent quality. Additionally, it was hypothesized that this reaction might be pH dependent because it is acid catalyzed, and the reaction also generates water, which increases the pH. With these considerations in mind, Ampcera has adjusted the laboratory-scale process and developed a scalable method for synthesizing the HATN monomer. Ampcera has produced 10 g of a pure product (single batch) with a yield greater than 85%. The following ^{13}CNMR (Figure 117) and ^{1}HNMR (Figure 117b) spectra of the product were obtained by Ampcera at the University of Arizona and are provided for reference.

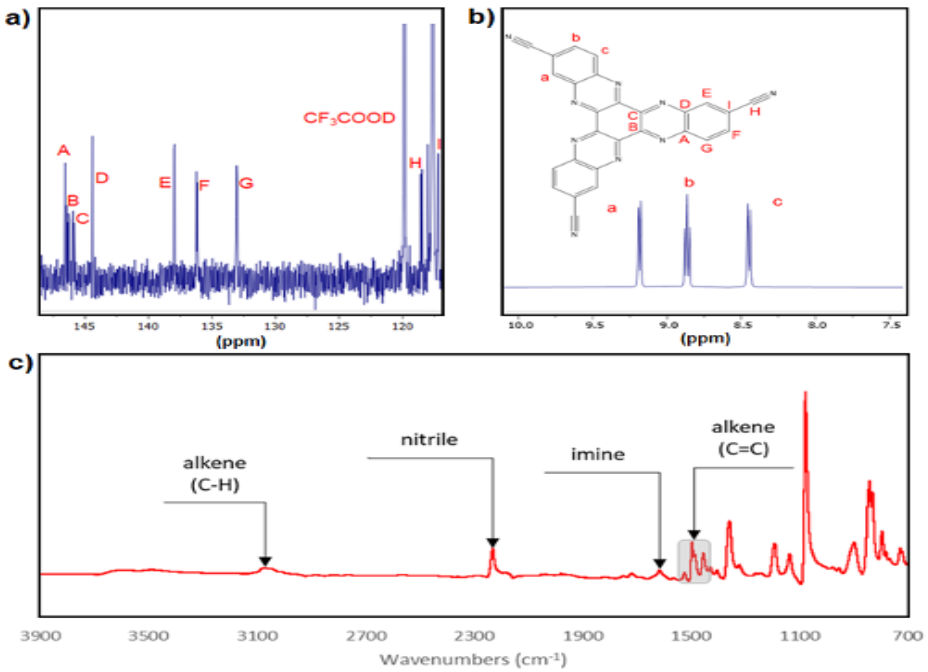

Figure 117. ^{13}CNMR (a), ^{1}HNMR (b), and infrared (c) spectra of the HATN monomer obtained at University of Arizona

The proton NMR result (Figure 117b) shows chemical shifts consistent with the HATN spectra obtained from UCSD. The expected signal splitting between the three types of protons present in the product is also observed. The locations of the protons are shown on the structure to the left by the red lowercase letters associated with the respective chemical shifts in the NMR result (Figure 117b) above. Because of the threefold symmetry of HATN, it can be assumed that the protons and carbons in geometrically congruent positions will have the same chemical shift. The carbon NMR result (Figure 117a) shows the nine chemically distinct carbons present in the product. Based on the chemical shifts observed in the data, the red capital letters on the image to the left indicate the position of each carbon. The chemical structure obtained in the NMR analysis is validated by infrared in Figure 117c, with key functional groups highlighted. A 5-g batch of HATN monomer has been shipped to UCSD for lab-scale polymerization to prepare the HATN/CNT composite and the HATN/CNT-S cathode. Ampcera and UCSD discussed the required instruments for chemical storage and the polymerization process (Q4, FY 2022). Ampcera will work on the scaled-up synthesis of the HATN polymer and the HATN/CNT composite in the coming quarters.

Updating Cyclability of HATN/CNT-S Cathode with High Cycling Areal Capacity (UCSD)

The HATN/CNT composite was prepared to construct a good ion and electron conduction network (Q3, FY 2022). The HATN/CNT-S electrode was introduced by simply mixing bulk sulfur with the as-prepared HATN/CNT. This strategy was initially designed for better wettability of electrolyte, and active polysulfide solution (Q4, FY 2022). After preparation of the electrolyte, an electrochemical sulfur infusion will be performed by simply discharging the cell to its full capacity. The C=N active sites on the HATN will chemically absorb the polysulfide and restrain the diffusion of the sulfur species. As a result, the active sulfur species undergoes fast reaction kinetics within the HATN/CNT matrix, and the cathode is expected to boast high S-specific capacity (high sulfur utilization) under the lean electrolyte condition (Q4, FY 2022; Q1, FY 2023). Figure 118a shows the cryogenic focused ion beam scanning electron microscopy (cryo-FIB SEM) image of the cross-section of the HATN/CNT-S cathode via electrochemical infusion featuring a bulky particle size of > 15 μm (Figure 118a) with a low porosity of ~ 30%. Furthermore, the 2D average tortuosity (τ) of this optimized HATN/CNT-S cathode is calculated to be 1.22 based on $\tau_1 = 1.14$, $\tau_2 = 1.15$, and $\tau_3 = 1.37$ within 1.57 of a semicircle path. The energy dispersive X-ray spectrum of Figure 118b corresponds to the uniform S-element distribution of the HATN/CNT-S cathode. Its low cathode porosity decreases the electrolyte usage, and the low cathode tortuosity facilitates electrolyte wettability, which ultimately yields a high sulfur utilization and a high working voltage. As a result, the active sulfur species undergoes fast reaction kinetics within the HATN/CNT matrix, and the cathode is expected to boast high S-specific capacity (high sulfur utilization) under the lean electrolyte condition (Q4, FY 2022; Q1, FY 2023).

To achieve high-energy-density Li-S batteries, the cathode porosity of HATN/CNT-S needs to be decreased, and the sulfur loading needs to be increased. Previously, the milestone of a starting areal capacity of 5 mAh cm^{-2}, recommended by the U. S. Department of Energy, has been completed by increasing the sulfur loading to 6.30 mg_{sulfur} cm^{-2} of the HATN/CNT-S cathode (Q4, FY 2022). The areal discharge capacity can reach up to ~ 7.4 mAh/cm^2 initially under the first 0.05 C (0.315 mA cm^{-2}) formation cycle with a low N/P ratio of 2.6 and a low E/S ratio of 6 μl mg_{sulfur}^{-1} or E/C ratio of 5 g Ah^{-1}, which quickly stabilized at 5.5 mAh/cm^2 after switching to the 0.1 C discharge current rate for the following cycles (Figure 118c). Notably, the initial discharge plateaus are consistent with the subsequent, which reflects the good wettability and polysulfide diffusion in the HATN/CNT cathode. The cells run for 76 cycles with a capacity loss of ~ 45% (Figure 118d), but the voltage profiles of the HATN/CNT-S cathode are well maintained without any over-charge issues (Figure 118c), indicating the $LiNO_3$ reservoir is sufficient (Q1, FY 2023).

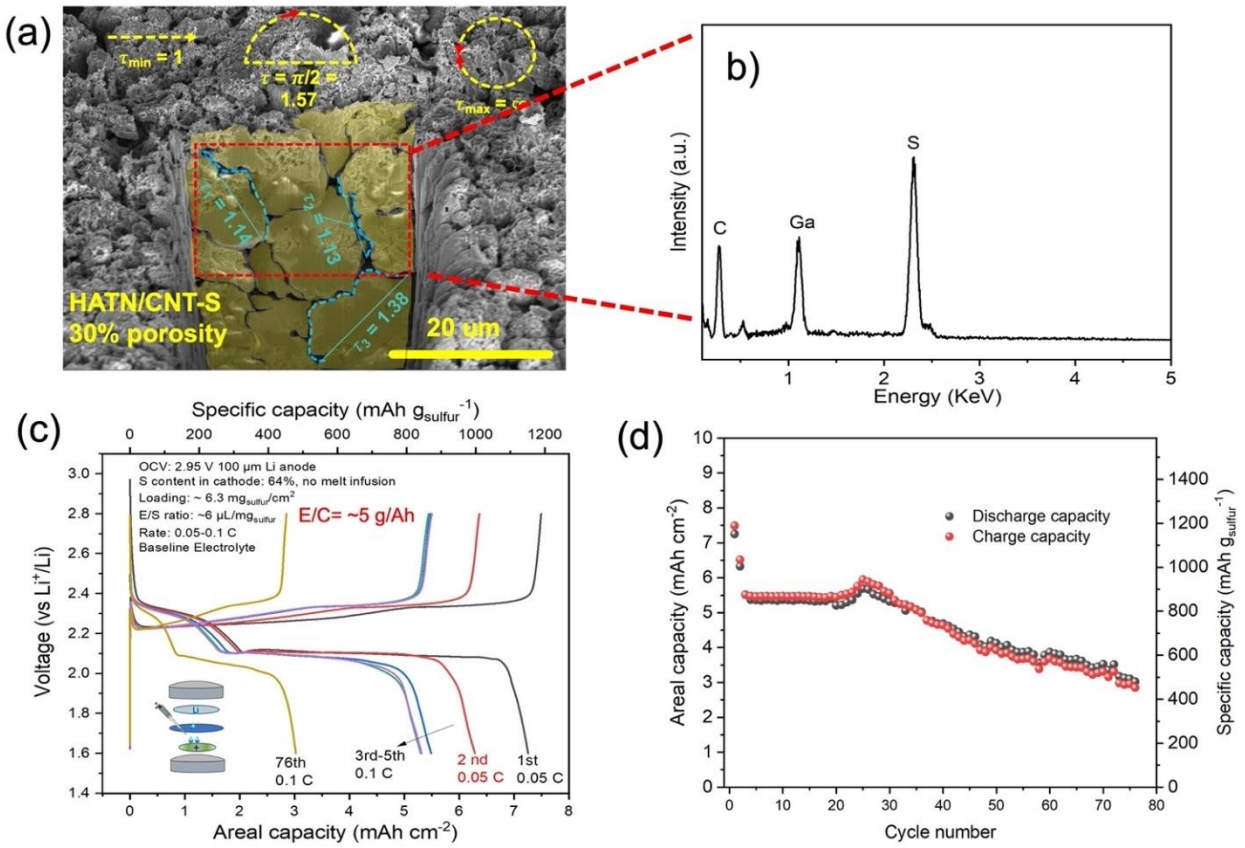

Figure 118. (a) The cryogenic focused ion beam scanning emission microscopy image of the cross-section of the HATN/CNT-S cathode via electrochemical infusion, which is highlighted with a low average 2D tortuosity (τ) of 1.22 and a bulky particle size of > 10 µm. (b) Energy dispersive X-ray spectrum of the selected area (red rectangle in panel a), showing the successful electrochemical sulfur infusion. (c) Voltage profiles of the HATN/CNT-S cathode with 6.30 mg_{sulfur} cm^{-2} with a low E/S ratio of 6 µl mg_{sulfur}^{-1} or an E/C ratio of 5 g Ah^{-1}. The inset schematics illustrate cell assembly. (d) Cycling behavior of the optimized HATN/CNT-S cathode at 0.1 C, 1 C = 1000 mAh g^{-1}.

Quantifying Lithium and Sulfur Inventory Loss of Cycled Lithium and HATN/CNT-S Cathode (UCSD)

To further understand the limiting factor in the cycle life of the high loading Li-S cells, this quarter, the lithium and sulfur inventory loss of the cycled lithium and HATN/CNT-S cathode in the above cells was quantified by TGC and TGA, respectively. To do so, the cycled electrode at the charged state from Figure 118d was extracted, and its sulfur content was analyzed using TGA in an Ar-protected environment. From an initial sulfur mass of 6.4 mg at the pristine state, only 2.0 mg of active sulfur was found after 76 cycles, as shown in Figure 119a. The TGA measured for the HATN/CNT-S cathode illustrates a sulfur inventory loss of 68.2%, which is smaller than 80.6% of the conventional C-S cathode after 68 cycles using a higher E/S ratio of ~ 10 µl mg_{sulfur}^{-1} and much higher N/P ratio of ~ 5.7 (Q2-Q3, FY 2022). To quantify the lithium inventory, the remaining metallic lithium mass in the cycled Li-metal electrode from the HATN/CNT-S Li-S cells was divided into three samples to be quantified by TGC (Figure 119b-c). Figure 119d shows that the cycled lithium metal undergoes a lithium inventory loss of 34.58. This is better than 47.0% of the cycled lithium paired with the conventional C-S cathode, with a total C-S cathode capacity of only ~ 2 mAh cm^{-2}, indicating that the polysulfide shuttle can be much alleviated in the HATN/CNT-S cathode. However, the current cycling performance is still to achieve a high energy density of Li-S batteries with long cycling stability. Figure 119c also shows the reacted lithium after the TGC experiment (dark brown solution) indicating a large amount of trapped sulfur species within the Li-metal matrix. Therefore, the team infers that the lithium anode side was indeed corroded by polysulfide. Thus, it is of utmost importance to find a way to stop lithium corrosion and prolong the short cycle life of lean-electrolyte-Li-based Li-S batteries apart from the $LiNO_3$ depletion issue.

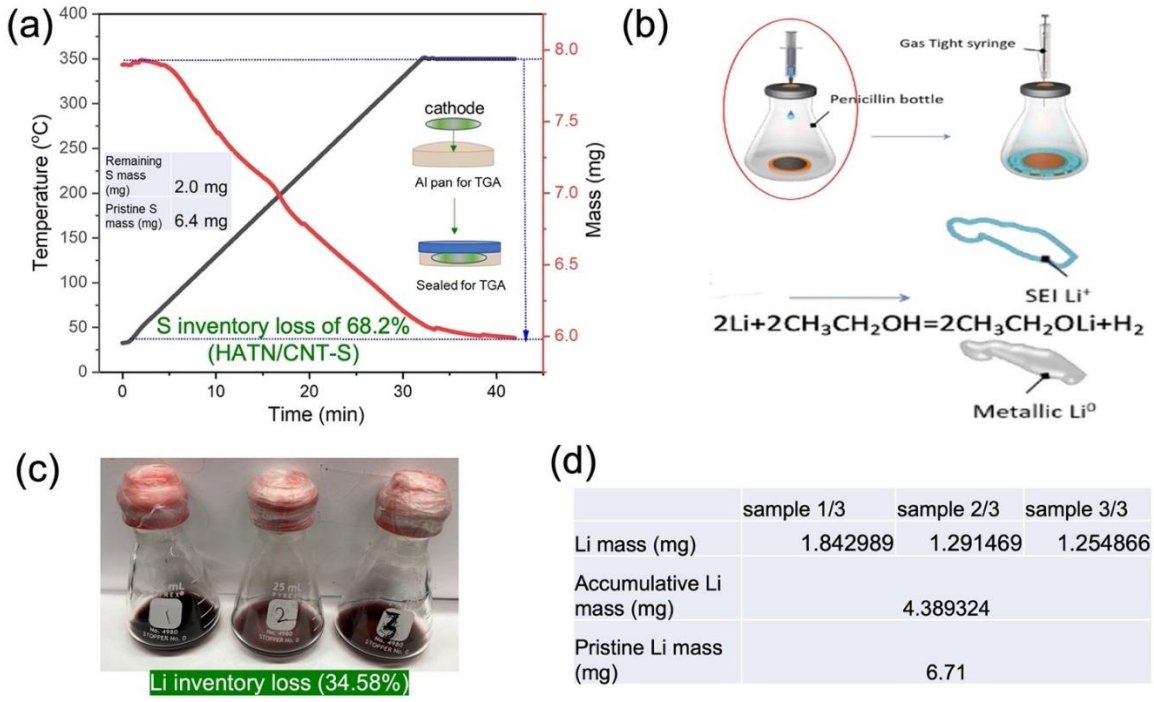

	sample 1/3	sample 2/3	sample 3/3
Li mass (mg)	1.842989	1.291469	1.254866
Accumulative Li mass (mg)	4.389324		
Pristine Li mass (mg)	6.71		

Figure 119. (a) Thermal gravimetric analysis curve of the HATN/CNT-S cathode from the disassembled cell after 76 cycles (washed by DOL/DME). (b) Schematic of titration gas chromatography (TGC) quantification of lithium metal loss. (c) Photo of reacted lithium solutions for TGC measurement with overall lithium inventory loss. (d) Table summarizing the metallic lithium mass of each lithium sample quantified by TGC.

Unveiling Key Factor of Polysulfide Corrosion in Lean-Electrolyte-Based Li-S Batteries with a Low E/S Ratio and Low N/P ratio (UCSD)

To approach a high energy density close to 500 Wh kg^{-1}, this quarter UCSD reports a high areal capacity of the HATN/CNT-S cathode (> 10 mAh cm^{-2}, ~ 8.48 mg_{sulfur} cm^{-2}) with a stringently low N/P ratio of 1.85 in coin-cell tests. This demonstrates the feasibility of the high areal capacity of the team's HATN/CNT-S cathode. The S-specific capacities of the HATN/CNT-S (no sulfur melt infusion) were evaluated by using E/S of ~ 6 µl mg_{sulfur}^{-1} at 0.25 mA cm^{-2} and 0.5 mA cm^{-2}. The areal current density of 0.25 mA cm^{-2} is equivalent to 0.17 C of $LiFePO_4$ with the same active loading. It is shown that the HATN/CNT-S cathode presents high S-specific capacities (high sulfur utilization) of > 1000 mAh g_{sulfur}^{-1} under the lean-electrolyte condition (Figure 120a). It delivers a high initial areal capacity of 10.8 mAh cm^{-2} at 0.25 mA cm^{-2}, which keeps at 9 mAh cm^{-2} at 0.5 mA cm^{-2}. The cell capacity drops quickly within 40 cycles (Figure 120b), showing dramatic degradation of electrodes. It is noted that higher areal sulfur loadings with high sulfur utilization generate a larger amount of polysulfide in the Li-S system when paired with the thin lithium (100 µm), which accelerates the reaction between lithium and polysulfide, especially under lean-electrolyte conditions. Figure 120c shows the scanning electron microscopy (SEM) image of the cycled lithium metal extracted from the above cells under the cryogenic condition and Ar-protected sample transfer. There is severe lithium pulverization, indicating severe corrosion by the concentrated polysulfide (Figure 120d) under the above cell testing conditions.

Thus, it is crucial to identify the effect of polysulfide in practical Li-S batteries using lean electrolyte and lean lithium. Herein, a simple calculation can be done to mimic the potential concentration of polysulfide under lean-electrolyte conditions by converting the utilized sulfur of the cathode (1000 mAh g^{-1}/1675 mAh g^{-1} = ~ 60%) into polysulfide (6 S ~ Li_2S_6) based on the electrolyte volume according to the E/S ratio (6 µl mg_{sulfur}^{-1}). Taking 5 mg sulfur in the cathode as an example, the utilized sulfur is 3 mg (32 g mol^{-1}) and the electrolyte volume is 30 µl; thus, the polysulfide concentration is calculated to be > 0.52 mol/L (> 0.52 M). Then, a 0.5 M Li_2S_6 solution was prepared by UCSD, and the chemical reactivity of lithium in this polysulfide solution

was investigated (Figure 120e). The fresh lithium vanished after 3 days, showing that lithium is vulnerable in such a high concentration of polysulfide.

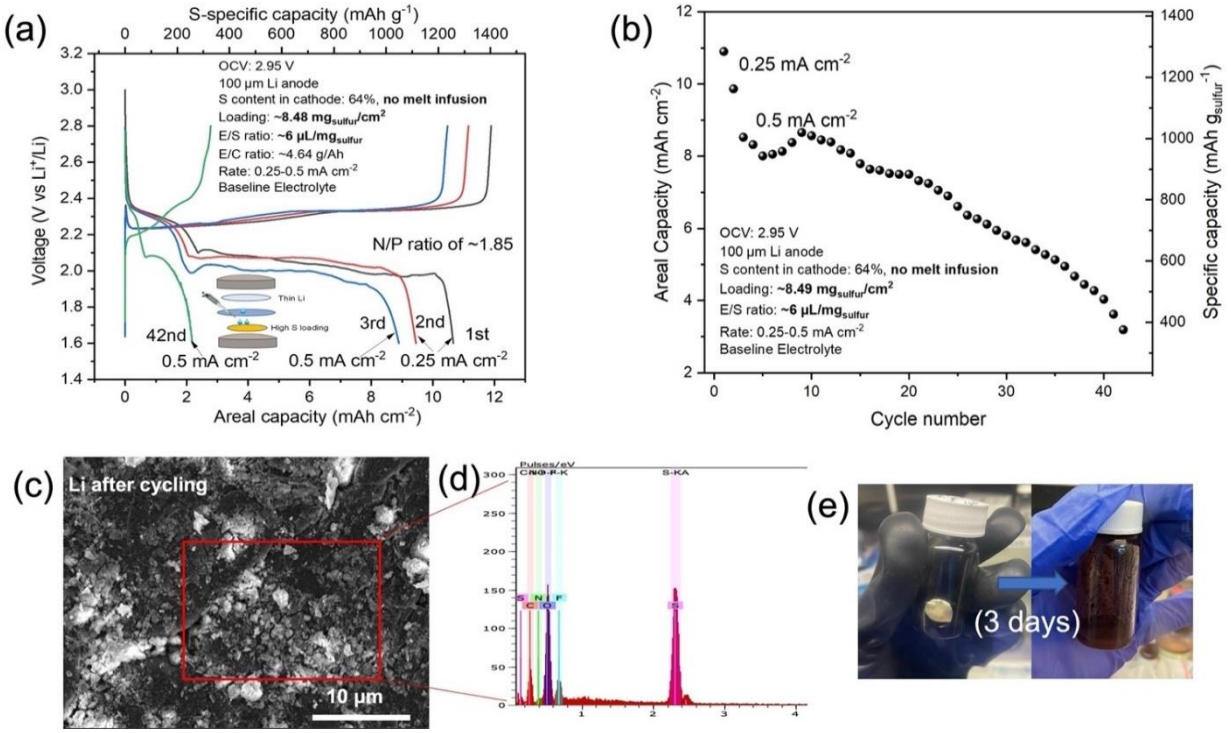

Figure 120. (a) Voltage profiles of the HATN/CNT-S cathode with ~ 8.48 mg_{sulfur} cm^{-2} with a low E/S ratio of 6 µl mg_{sulfur}^{-1} or a calculated E/C ratio of 4.64 g Ah^{-1}. The cells were assembled by pairing against 100-µm lithium anodes in baseline electrolyte. (b) Cycling behavior of the optimized HATN/CNT-S cathode at 0.5 mA cm^{-2}. (c) Cryogenic scanning electron microscopy images of the cycled lithium anode in the above cell. (d) Energy dispersive X-ray spectrum of the selected area (red rectangle in panel c), showing the polysulfide corrosion to lithium metal. (e) Photos showing the lithium chip immersed into 0.5 M Li_2S_6 before and after 3 days.

Notably, polysulfide can be constrained within the cathode host structures to some extent, but for a practical high energy density Li-S cell, polysulfide concentration will be higher at an even lower E/S ratio. Therefore, the polysulfide corrosion issue cannot be ignored, which is the limiting factor of the cycle life of Li-S batteries with a high energy density. The strategies are to protect the lithium anode and to alleviate the causticity of polysulfide. The corresponding performance will be evaluated in coming quarters.

New Batch of GM C-S Cathode with Sulfur Loading of ~ 3.56 mg cm^{-2} and Electrochemical Performance (GM)

Previously, the UCSD team requested a thinner conventional C-S cathode for fundamental study of the failure mechanism of the Li-S system. This quarter, a more moderate sulfur mass loading of 3.5 mg cm^{-2} was provided for testing, and test cells have demonstrated good capacity retention for over 50 cycles (Figure 121a-b).

Continuous quality improvements to improve robustness and repeatability of the baseline C-S composite electrode are being implemented, including changes to carboxymethyl cellulose (CMC) binder, aluminum foil, and replacement of the coating machine. The supplier of CMC binder was changed to a large battery grade supplier to exclude large batch-to-batch variation in both viscosity and dissolution behavior experienced with the previous vendor. An aluminum foil thickness variation of 8.4% was identified from one vendor that can extend into variation of the slurry coating thickness. The foil from an alternate vendor exhibited less than 2.9% variation, and this vendor material is now the standard foil in use to improve coating uniformity. Uniformity checks are now conducted on foils to identify excessive variation prior to production. A new coating

machine was brought online to replace previous equipment and reduce downtime and repair issues. Additional testing is continuing to maintain and improve coatings used for the project, and applicable improvements will be applied to baseline C-S composite cathode production and incorporated into pouch-cell prototyping work.

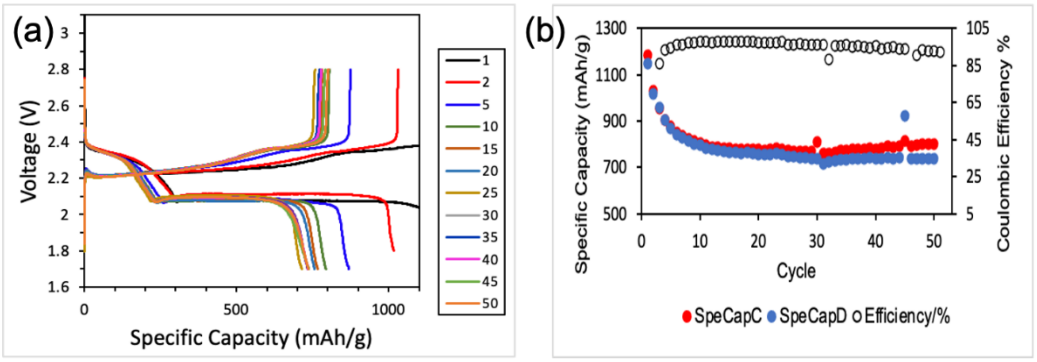

Figure 121. GM Data: Electrochemical performance of C-S cathode (a) charge-discharge profiles and (b) discharge-charge capacities and Coulombic efficiency versus cycle number. Notes — Loading: 3.56 mg$_S$ cm^{-2}; Electrolyte: LiTFSI $LiNO_3$ in DOL-DME 1:1 vol; Cycling Protocol: 2 @ C/20, C/10 cycling; and Set Up: C-S cathode/separator/600 µm lithium.

Fabricating Robust HATN/CNT-S Electrode Sheets

It has been discussed that single-layer or few-layer pouch cells will be assembled to test the electrochemical performance of the HATN/CNT-S cathode under lean-electrolyte conditions (Figure 122a). This quarter, the HATN/CNT-S electrode sheets were fabricated with a large area (5 × 5 cm^2) with a sulfur loading of > 6 mg cm^{-2} for future small pouch cell evaluation at GM (Figure 122b). It is evidenced that the electrode sheet is robust since there is no peel-off issue after rolling up. The cryo-SEM image of Figure 122c shows that the HATN/CNT-S cathode consists of bulky HATN/CNT and bulky sulfur particles without sulfur melt infusion. The brightness contrast of the SEM image suggests the electrically conductive HATN/CNT and non-conductive sulfur particles. The particles are further verified by the energy dispersive X-ray spectra (Figure 122d-e) of the selected areas of Figure 122c, showing a high intensity of carbon signal and sulfur signal for HATN/CNT and sulfur particles, respectively. The electrode recipe and casting protocol were adjusted and will be used for casting the electrode sheets for preliminary evaluation at GM.

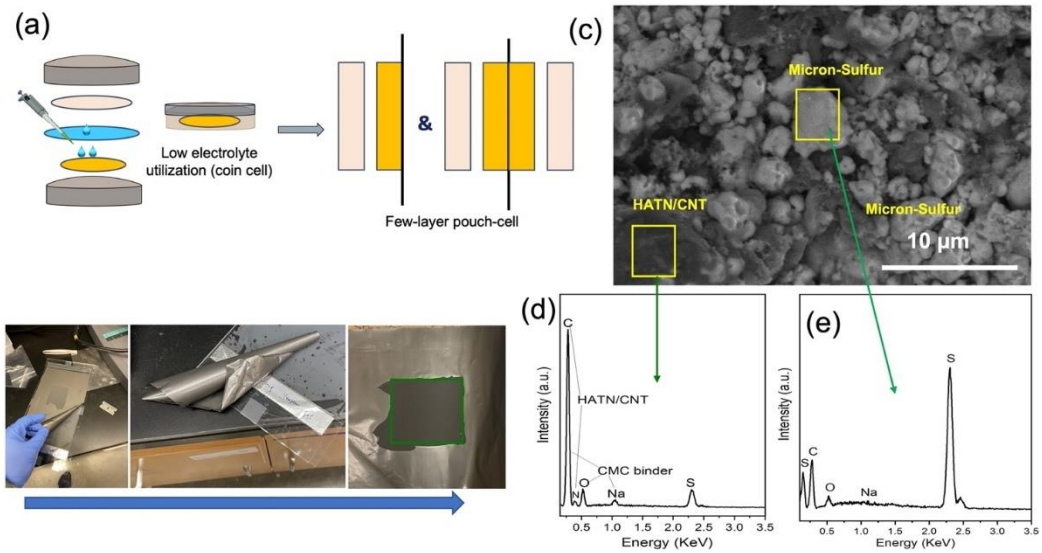

Figure 122. (a) Low utilization of electrolyte due to coin-cell setup and design of few-layer pouch-cell setup. (b) HATN/CNT-S electrode casting improvement process. (c) Scanning electron microscopy images of as-prepared HATN/CNT-S electrode. Energy dispersive X-ray spectroscopy of (d) HATN/CNT particle and (e) sulfur particle.

Patents/Publications/Presentations

Patent

- The project has a non-disclosure invention in preparation (under modification) regarding the new electrolyte additive and formula.

Presentation

- Materials Research Society Fall Meeting, Boston, Massachusetts (November 30, 2022): "Build a High Energy Density Li-S Battery with Long Lifespan"; X. Wang. Poster.

Task 5.7 – New Engineering Concepts to High-Energy-Density Lithium-Sulfur Batteries (Prashant N. Kumta, University of Pittsburgh)

Project Objective. The major objectives of this project are to develop a Li-S pouch cell with a cell capacity > 300 mAh with energy density ≥ 500 Wh/kg, ≥ 750 Wh/L with cycling over 1000 cycles @C/3 rate, cycle life of 1000 at C/3 and ≤ 20% fade in energy @ C/10-C/3, and ≤ $80/kWh. To achieve the proposed objectives, the following major goals will be successfully attained over the first year of the project: (1) identification of effective electrocatalysts and Li-ion conductors (LICs) lowering the activation barrier; (2) *in situ* synthesis of electrocatalysts and LIC dispersed complex carbon-based framework material (CFM) and sulfur nanocomposite with sulfur content ≥ 90 wt%; (3) ~ 15 mAh/cm^{-2} areal capacity of sulfur electrode with sulfur loading ≥ 10mg/cm^{-2}; (4) Li-containing structurally isomorphous alloy (Li-SIA) of ≥ 1000 cycles with 15 mAh/cm^{-2} areal capacity @C/3 rate; and (5) identification of optimal electrolyte compositions giving Li^+ conductivities ~ 10^{-2} S/cm and polysulfide dissolution < 1 ppm.

Impact. The work from this project will have a strong impact on development of high-energy-density Li-S batteries. The results of this work will lead to new knowledge on identification and generation of high-capacity sulfur cathodes and dendrite-free Li-metal anodes using scalable synthesis and fabrication approaches. Both fundamental and applied knowledge will be gathered from the study. Systematic characterization will provide new scientific insights into the mechanisms contributing to the corresponding response in coin-cell and pouch-cell formats. Results of this work also will likely have an impact on other fields such as electrocatalysts for water splitting and fuel cells and other fields engaged in electrochemistry. Plans are also in place to engage under-represented minority undergraduate students to gain research experience in various aspects of the project. With new materials identified as the project is executed, opportunities will emerge for filing invention disclosures, and provisional/non-provisional patent applications. The training and opportunities presented by this project to undergraduate and graduate students as well as postdoctoral research associates will foster next-generation work force training, equipping workers with the necessary skillsets to transform the quality of life all over the globe by generating high-energy-density systems that can be deployed in electric vehicles as well as in laptops and cell phones including innumerable portable and wireless devices, opening the doors to a new green and sustainable energy environment improving overall quality of life.

Approach. Work involves executing a theory-driven study directed at identification of electrocatalysts for efficient conversion of polysulfides to Li_2S during the forward discharge process and backward charge process to elemental sulfur and lithium. Also, first-principles computational approaches will be applied to identify solid-state LICs with conductivity > 10^{-4} S/cm. Employing expertise in the principal investigator's laboratory, suitable low-temperature (< 240°C) scalable synthesis techniques will be used to generate theoretically identified electrocatalysts and LICs. Low polysulfide solubility and stable solid electrolyte interphase (SEI) forming electrolytes will then be prepared from commercially available solvents, additives, and salts. The effectiveness of the electrocatalysts and LICs to improve the polysulfide to Li_2S transformation kinetics and the ability to achieve the targeted specific capacity by trapping polysulfides, including desired structural transformation during charging/discharging, will be assessed; accordingly, suitable modification of electrocatalysts and LICs will be performed to generate the ideal microstructures. Suitable modification, if required, of lithium alloy as anode will also be performed by alloying with other metals to improve the Li-ion diffusivity kinetics and the Gibbs-Thomson parameter. The scalable approaches developed will be further refined to optimize sulfur utilization in the cathode, engineer the surface and bulk structure of the novel Li-SIA and lithium multicomponent alloy (Li-MCA) anodes to yield the desired areal capacity with optimal Coulombic efficiency (CE), and finally optimize the electrolyte structure to minimize and eliminate polysulfide dissolution with desired Li^+ conductivities. Finally, the developed systems will be scaled up, fabricated, and tested in pouch-cell configurations.

Out-Year Goals. The following goals will be achieved in subsequent years: (1) determine optimal cell component design parameters such as electrode thickness and porosity exhibiting minimal polarization while maintaining cathode capacity ≥ 1500 mAh/gS, (2) demonstrate excellent cycle life of > 1000 cycles with > 80% capacity retention, (3) electrochemically test cells with dendrite-free Li-alloy anodes comprising Li-SIA and Li-MCA of areal capacity of ~ 15 mAh/cm^2, (4) electrochemically test cells with modified electrolytes at charge-discharge rages of C/3 as well as other C-rates of C/10-C/3, (5) fabricate > 300-mAh pouch cell giving energy density greater or equal to 500 Wh/kg at C/3 rate and demonstration of acceptable performance at other C-rates of C/10-C/3, and (6) demonstrate cyclability of a minimum of 1000 charge/discharge cycles with < 20% fade rate for operation in -40°C to +40°C temperature ranges, with temperature measured external to the pouch cell.

Collaborations. The project involves collaboration with G. E. Blomgran of Blomgren Consulting Services, Ltd.

Milestones

1. Devise optimized sulfur cathodes with optimal porosity and thickness. (Q1, FY 2023; In progress, with completion expected in April 2023)

2. Assemble and test cells of optimized cathodes, anodes, and electrolytes containing new additives under lean-electrolyte conditions. (Q2, FY 2023; In progress, with completion expected in July 2023)

3. Full-cell cyclability testing for 1000 cycles @ C/3 and complete evaluation at C/10 – C/3 current rates. (Q3, FY 2023; In progress, with completion expected in October 2023)

4. Electrode performance quantification in ~ 20-mm coin-cell configuration. (Q4, FY 2023; In progress with completion expected in January 2024)

Progress Report

This quarter, preliminary work began to modify the chemistry of standard electrolyte [that is, 1.0 M lithium bis(trifluoro-methanesulfonyl)imide, 2 wt.% $LiNO_3$ in 1,3-dioxolane : 1,2-dimethoxyethane) by adding appropriate additives to improve the electrochemical performance of Li-S batteries. Several additives were explored. To identify the best-performing additives and their corresponding amounts that influence the SEI layers on both the electrodes, namely, the Li-anode and the baseline sulfur cathode, to positively enhance the electrochemical performance of the Li-S cell, 1 wt% of an organic chemical additive (CA) was considered. The hypothesis is that this additive not only fine-tunes and interacts with the lithium polysulfides, preventing their dissolution, but also serves to modify the electrode interface forming a multifunctional SEI over the electrodes. The addition of CA is anticipated to form a multifunctional, robust, and stable SEI layer on both the electrodes, which is capable of conforming to the Li-anode surface while also regulating a uniform lithium deposition inhibiting dendrite formation and causing extremely low polarization during cycling. Therefore, this quarter the team reports the preliminary studies on the effect of the addition of 1 wt% of CA in the standard electrolyte on the electrochemical performance of the baseline CFM cathode developed by the team and the Li-metal anode, respectively.

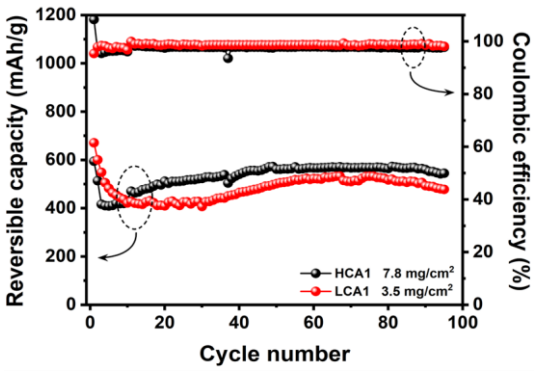

Figure 123. Cycling performance of baseline electrode with modified electrolyte (1 wt% of chemical additive) as additive at low and high sulfur loadings.

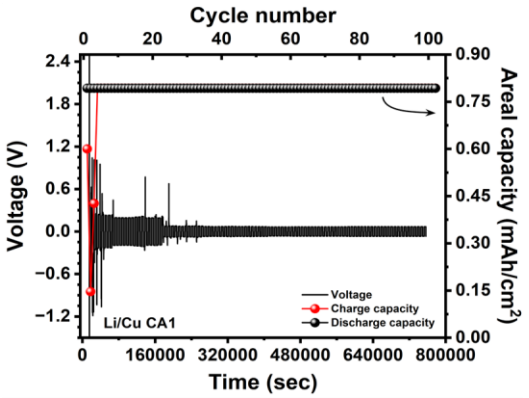

Figure 124. Lithium cycling with modified electrolyte (1 wt% chemical additive) at 1 mA current for 1 hour for 103 cycles.

The electrochemical cycling performance of the Li-S cell with baseline CFM and the modified standard electrolyte containing 1 wt% CA additive was evaluated with different sulfur loadings; the result is presented in Figure 123. The electrodes were prepared by the standard slurry casting method by mixing the active material, conductive carbon, and polyvinylidene (di)fluoride (PVDF) in a 72:18:10 ratio using N-methyl-pyrrolidone (NMP) as the solvent. Lean electrolyte with an electrolyte-to-sulfur ratio of 8µl mg^{-1} was used to fabricate all the cells. The cell with a moderate sulfur loading of 3.5 mg cm^{-2} is termed LCA1, and the cell with more than two-fold higher sulfur loading of 7.8 mg cm^{-2} is labeled HCA1 The cells were cycled at 0.05 C-rate for the initial 10 cycles for stabilization, followed by cycling at 0.1 C-rate for the entire test. All the cells showed an initial drop in the discharge capacity, likely due to the formation of an SEI layer over the electrodes, which stabilizes after a few cycles. The LCA1 and HCA1 cells stabilize and display a discharge capacity of 520 m Ah g^{-1} and 569 m Ah g^{-1} after 95 cycles with CEs of more than 98.8% and 97.8%, respectively.

To examine the effect of the additive on the stabilization of the Li-anode, coin cells with Li-metal as anode and bare copper as the cathode were fabricated and tested again with modified electrolyte (1 wt% CA) at 1 mA current for 1 hour. The cells were flooded with 60 µL of modified electrolyte. The cells were cycled for more than 100 cycles, and the results are presented in Figure 124. The lithium plating and stripping behavior stabilized after 3 cycles, and the cells delivered a stable areal capacity of 0.793 m Ah cm^{-2} throughout the 103 cycles with an average CE of 99.97%. Initially, the cells showed instabilities in lithium cycling and a high overpotential (0.2 V) is observed due to an unstable SEI layer. However, the lithium cycling stabilizes after ~ 22 cycles, and the overpotential is significantly reduced (0.073V), likely due to SEI layer stabilization and desirable Li-ion conduction in the modified electrolyte. Initial results presented in this report suggest that

CA significantly influences cell chemistry by possibly forming a stable SEI layer in both electrodes and interacting with lithium polysulfides. Additionally, electrochemical testing of other plausible electrolyte additives that influence the SEI layer, Li-ion conduction, and restrict polysulfide dissolution is ongoing, which would enable the team to further narrow down the preferred electrolyte additive. These results will be reported in subsequent quarterly reports.

The team also studied the system of multicomponent alloy (MCA) serving as both a dendrite-free anode material and current collector that was synthesized by a high-energy mechanical milling and alloying process. The structurally isomorphous system, termed as MCA3, having a similar lattice registry (*bcc phase*) to metallic lithium, prevents lithium dendrite growth by forming a solid solution with the reacting Li-ions electrochemically presented to it from the metallic lithium serving as the counter electrode. The ensuing electrochemical alloying reaction allows a significant amount of lithium to solubilize into the parent MCA3 alloy, causing a minimal change in volume due to the solid solution formation preserving the crystallographic registry and crystal symmetry. The crystallographic arrangements of atoms in the MCA3 alloy being identical to that of lithium enable preserving the overall crystallographic symmetry and allow formation of a solid solution with optimal interfacial energy. The MCA3 alloy also improves the Li-ion diffusion, preventing surface segregation while continuing to maintain dendrite-free cycling, and, hence, serving as effective anodes as well as current collectors in Li-S batteries. The MCA3 alloy was prepared by high-energy alloying, and the anode electrode for electrochemical testing was prepared by standard slurry casting method (95 wt% MCA3 and 5 wt% PVDF) in NMP solvent followed by electrochemical testing in a coin cell, as shown in Figure 125. The cells were flooded with 60 μL of standard electrolyte. The MCA3 cells with an average electrode loading of 3.2 mg cm^{-2} were initially cycled for rate capability at different current rates, namely, 1 mA for 1 hour alloying and dealloying, 1 mA for 2 hours alloying and dealloying, 1 mA for 4 hours alloying and dealloying, 1.5 mA for 4 hours alloying and dealloying, and 2 mA for 4 hours alloying and dealloying for 30 cycles each, followed by exploring cycling stability at 2.5 mA for 4 hours alloying and dealloying for another 100 cycles. The cycling stability of MCA3 after 150 cycles of rate capability is depicted in Figure 125, revealing excellent lithium plating/stripping behavior affording a stable areal capacity of ~ 8 m Ah cm^{-2} for a continuous 100 cycles. The propensity of the MCA3 alloy electrode to demonstrate reversible lithium cycling (plating/stripping) is evidenced in Figure 125, as the overpotential of the cell remains constant even after cycling for more than 250 cycles. Further electrochemical testing of the cells with the various other MCA electrodes is also in progress. Additionally, efforts are being directed at fabricating free-standing dense pellets of the MCAs to serve as dendrite-resistant anode current collectors for reversibly cycling lithium ions. Results of these ongoing current studies conducted on the MCA electrodes and the electrochemical testing results of the dense pellets of MCAs serving as current collectors and anodes will be reported in subsequent quarterly reports.

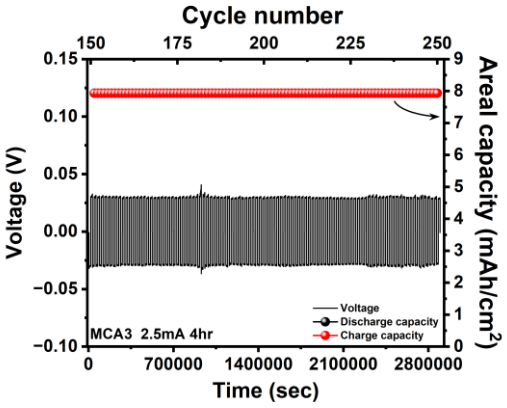

Figure 125. Electrochemical cycling performance of MCA3 electrode along with areal capacities cycled at 2.5 mA current for 4 hours for alloying and de-alloying, respectively, from 150 to 250 cycles after rate capability test.

Patents/Publications/Presentations

Presentation

- 242nd Electrochemical Society Meeting, Research and Development of Primary and Secondary Batteries Symposium, Atlanta, Georgia (October 9–13, 2022): "From Lithiated Transition Metal Oxides to Silicon to Lithium-Sulfur: Evolution of Electrochemically Active Materials"; P. N. Kumta. Invited.

Task 5.8 – Development of Lithium-Sulfur Battery Cells with High Energy Density and Long Cycling Life (Donghai Wang, Pennsylvania State University)

Project Objective. The objective of this project is to develop a new soluble-polysulfide-free sulfur cathode with a high sulfur content (> 50 wt%) and high discharge specific capacity (> 700 mAh g^{-1}, based on the weight of the whole cathode), and to demonstrate performance of the sulfur electrode at high electrode capacity (> 7 mAh cm^{-2}), low N/P ratio [< 2; that is, capacity ratio between anode (negative electrode) and cathode (positive electrode)], and low electrolyte-to-sulfur (E/S) ratio (< 2.5 μL mg^{-1}). Prototype Li-S pouch cells with predicted energy density of 400 Wh kg^{-1} and 80% capacity retention for over 300 cycles using conventional electrolyte and Li-metal anodes with a protective layer developed by the team will be demonstrated.

Impact. This project aims to develop new sulfur composite active materials and functional polymer binders that enable polysulfide-free, high-performance, low-cost sulfur cathode. The use of these high-performance and low-cost sulfur cathodes, in turn, enables Li-S batteries with high energy density and long cycle life. Such Li-S batteries, made using the developed cathodes paired with a Li-metal anode, can lead to 50% greater energy density than conventional Li-ion batteries. Meeting the technical targets will potentially develop high-energy-density lithium batteries, promote increased adoption of electric vehicles and plug-in hybrid electric vehicles, and reduce petroleum consumption in the transportation sector by helping battery-powered vehicles become accepted by consumers as a reliable source of transportation.

Approach. The overall approach will focus on synthesizing and optimizing a novel polysulfide-free sulfur composite active material and functional binders. Specifically, approaches to realize the project objectives include the following: (1) development of novel polysulfide-free sulfur composite active materials, (2) development of new functional polymer binders to facilitate Li^+ transport and trap residual lithium polysulfide; and (3) diagnostics, characterization, theoretical simulation, and cell tests on the developed materials in Li-S batteries.

Out-Year Goals. The out-year goals are as follows: (1) develop new sulfur composite active materials, and (2) conduct characterization, simulation, and performance tests on material and electrode levels. The *Go/No-Go Decision* will be demonstration of Li-S batteries using the developed sulfur composite active materials with an initial discharge specific capacity > 600 mAh g^{-1} (based on cathode weight) at an areal capacity of 4 mAh cm^{-2} and E/S ratio < 8 μL mg^{-1}.

Collaborations. Pennsylvania State University will collaborate with the University of Illinois at Chicago on theoretical simulation.

Milestones

1. Demonstrate sulfur cathode using sulfur composite active material (generation 1) with an initial discharge capacity > 650 mAh g^{-1} (based on cathode weight), at E/S ratio < 10 μL mg^{-1}. (Q1, FY 2023; Completed)
2. Demonstrate sulfur cathode using sulfur composite active material (generation 2) with an initial discharge capacity > 700 mAh g^{-1} (based on cathode weight), at E/S ratio < 10 μL mg^{-1}. (Q2, FY 2023; In progress).
3. Demonstrate sulfur cathode using sulfur composite active material (generation 1) with an initial discharge capacity > 750 mAh g^{-1} (based on cathode weight), at E/S ratio < 5 μL mg^{-1}. (Q3, FY 2023; In progress)
4. Demonstrate sulfur cathode using sulfur composite active material (generation 2) with an initial discharge capacity > 800 mAh g^{-1} (based on cathode weight), at E/S ratio < 5 μL mg^{-1}. (Q4, FY 2023; In progress)

Progress Report

This quarter, based on the team's previously optimized sulfur polymerized composite (SPC) derived active material for Li-S batteries, the team mainly utilized the electrolytes and the binders to achieve SPC-based batteries under realistic conditions, that is, high areal loading of cathode materials, low E/S ratio, and limited Li-metal anodes. Based on the team's experimental results, after optimization of electrolytes, they demonstrated polysulfide-free SPC cathodes with a high initial discharge capacity of over 650 mAh g^{-1} (based on cathode weight) and areal capacity over 3.5 mAh cm^{-2} at an E/S ratio as low as 5 µL mg^{-1}. Moreover, apart from electrolytes, the team also worked on optimization of binders to construct SPC and sulfurized polyacrylonitrile (SPAN)-based cathodes with higher areal capacities for enhanced energy density at cell level. The team first worked on optimization of electrolytes for SPC-based cathodes on limited Li-anode condition and the evaluation of electrochemical performances for corresponding soluble polysulfide-free Li-S batteries.

Although carbonate electrolytes have been reported to yield a robust cathode electrolyte interphase layer for SPAN cathodes, the solid electrolyte interphase layers formed at lithium anode side in carbonate electrolytes generally demonstrate very limited stability. This would lead to poor cycling performances for resultant Li-S batteries, especially at realistic conditions with lean electrolyte and limited lithium metal. Previously, the team showed that SPC-based cathodes with much improved specific capacity could be obtained and stably cycled in flooded carbonate electrolyte (that is, E/S ratio > 10 µL mg^{-1}). Therefore, in this quarter, the team attempted to test the SPC-based cathodes at relatively lean electrolyte conditions (that is, E/S ratio ≤ 5 µL mg^{-1}); meanwhile, they optimized electrolytes for desirable performances at realistic conditions. As shown in Figure 126, the team first paired the high areal capacity SPC-based cathodes with limited lithium metal and then tested the cycling performances in conventional carbonate electrolyte (electrolyte 1) at low E/S ratio. The corresponding cell demonstrated a high initial capacity, but then suffered from an obvious decay. In this regard, the team used two kinds of diluents to mediate the pristine carbonate electrolyte as locally concentrated electrolytes denoted as electrolyte 2 and electrolyte 3. With new electrolytes, although the initial capacities were slightly lower, the Li-S batteries demonstrated improved cycling stability over 50 cycles under realistic conditions. Such discharge specific capacity fulfills the target for this reporting period; further optimization of electrolytes will be continued in next steps.

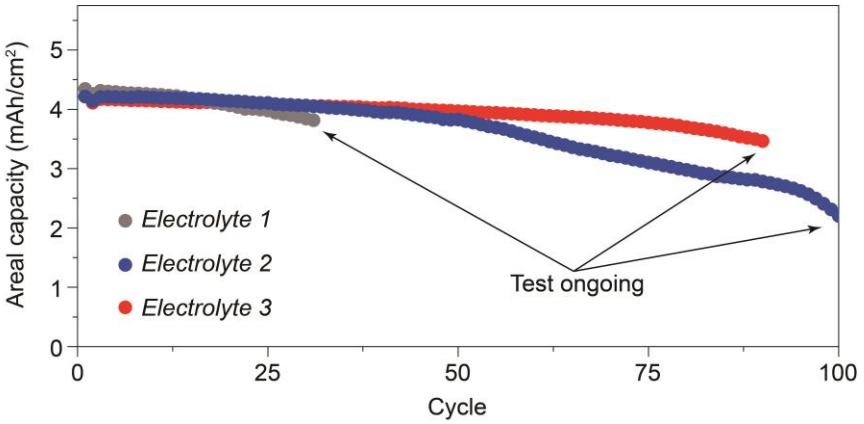

Figure 126. Cycling performances of optimized sulfur polymerized composite (SPC)-based cathodes in different electrolytes under realistic conditions of relatively low E/S ratio of 5 µL mg^{-1} and limited Li-metal anode at current density of 100 mA g^{-1}. Compared with previously used carbonate-based electrolytes (electrolyte 1), the optimized electrolytes (electrolyte 2 and electrolyte 3) afforded improved cycling stability and capacity retention for SPC cathode-based Li-S batteries.

To further increase the overall energy density of Li-S batteries at cell level, the binders of cathode fabrication were optimized for higher areal capacity. The resultant high areal capacity SPC-based cathodes were paired with excessive lithium metal and tested at low E/S ratio of 5 µL mg^{-1} in typical carbonate electrolyte

(electrolyte 1). As shown in Figure 127, the application of binder 2 afforded enhanced cycling stability compared with that of cathodes based on binder 1. The optimized binder 3 could simultaneously serve as binder and conductive agents for cathode preparation, thus a higher mass ratio of SPC-based cathode material could be achieved, which delivered an enhanced initial areal capacity. Such initial discharge capacity meets the target for this reporting period. However, the high initial discharge capacity based on binder 3 demonstrated limited cycling stability, which needed further optimization.

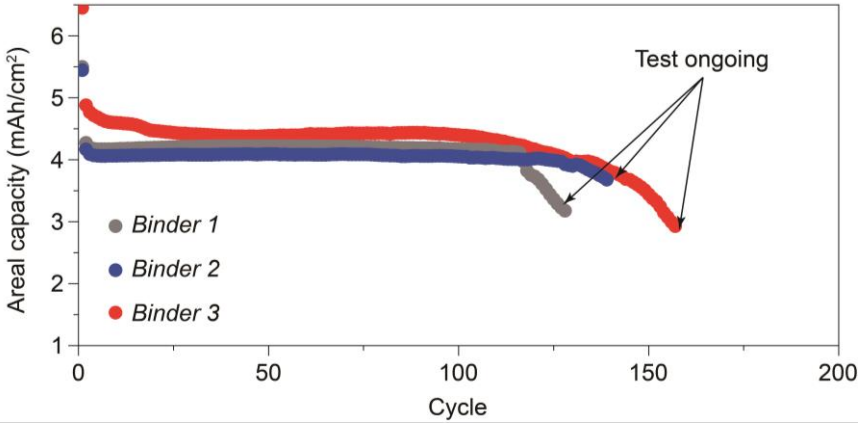

Figure 127. Cycling performances of optimized sulfur polymerized composite (SPC) cathodes fabricated with different binders tested at low E/S ratio of 5 µL mg^{-1} and excessive lithium metal. Compared with previously used binders (binder 1), on construction of high areal capacity SPC cathodes, the optimized binder 2 delivered improved cycling stability and the optimized binder 3 could afford higher areal capacity in Li-S batteries.

Next quarter, the team will continue to screen and optimize the electrolyte and binders for the optimized SPC materials for high areal capacity cathodes and further improve specific capacities of SPC materials. The milestone for next quarter will be demonstrating sulfur cathode using sulfur composite active material with an initial discharge capacity > 700 mAh g^{-1} (based on cathode weight) at an E/S ratio < 10 µL mg^{-1}. In addition, the team will continue optimizing synthetic parameters of SPAN baseline, SPC-1, and SPC-2 cathode materials.

Patents/Publications/Presentations

The project has no patents, publications, or presentations to report this quarter.

TASK 6 – LITHIUM-AIR BATTERIES

Team Lead: Ji-Guang Zhang, Pacific Northwest National Laboratory

Summary

The Task objective is to develop rechargeable Li-O_2 batteries with long-term cycling stability through in-depth research on more stable electrolytes and highly efficient catalysts for air electrodes, protection of Li-metal anodes, and deeper understanding on the oxygen reduction reaction (ORR) and oxygen evolution reaction (OER) mechanisms behind the electrochemical performance of Li-O_2 cells.

Highlights

The highlights for this quarter are as follows:

- The Argonne National Laboratory (ANL) team verified production of redox active species when cobalt single atom catalysts were used on the cathode using a three-electrode cell design. The reduction current indicates these species exhibit redox mediating properties that can be beneficial to the OER.
- The ANL / University of Illinois, Chicago, (UIC) team synthesized a new porous dichalcogenide catalyst ($SnIrS_{3.6}$ crystals) with bridging transition metal active sites by the chemical vapor transport method for use in a Li-O_2 cell to act as a catalyst for both ORR and OER. This new catalyst exhibits a one-dimensional nanoribbon texture and is being used in Li-O_2 batteries to determine whether it can lead to higher rates and lower charge rates.
- The UIC team further investigated the effect of the two-dimensional-based medium-entropy alloys as cathode catalysts comprised of sulfur and tellurium chalcogenides. They found that the nature of charge transfer for both CO_2RR and CO_2ER is similar. The catalyst with tellurium chalcogen shows much improved catalytic activities compared to that with sulfur chalcogen. Use of ionic liquid electrolyte leads to much improved battery cycling.

Task 6.1 – Lithium-Air Batteries
(Khalil Amine and Larry A. Curtiss; Argonne National Laboratory)

Project Objective. This project will develop new cathode materials and electrolytes for Li-air batteries for long cycle life, high capacity, and high efficiency. The goal is to obtain critical insight that will provide information on the charge and discharge processes in Li-air batteries to enable new advances to be made in their performance. This will be done using state-of-the-art characterization techniques combined with state-of-the-art computational methodologies to understand and design new materials and electrolytes for Li-air batteries.

Project Impact. The instability of current nonaqueous electrolytes and degradation of cathode materials limits performance of Li-air batteries. The project impact will be to develop new electrolytes and cathode materials that are stable and can increase energy density of electrical energy storage systems based on lithium.

Approach. The project is using a joint theoretical/experimental approach for design and discovery of new cathode and electrolyte materials that act synergistically to reduce charge overpotentials and increase cycle life. Synthesis methods, in combination with design principles developed from computations, are used to make new cathode architectures. Computational studies are used to help understand decomposition mechanisms of electrolytes and how to design electrolytes with improved stability. The new cathodes and electrolytes are tested in Li-O_2 cells. Characterization, along with theory, is used to understand the performance of materials used in the cell and to make improved materials.

Out-Year Goals. The out-year goals are to find catalysts that promote discharge product morphologies that reduce charge potentials and to find electrolytes for long cycle life through testing and design.

Collaborations. This project engages in collaboration with K. C. Lau (University of California, Norridge), Y. Wu (Ohio State University), and R. Shahbazian-Yassar (University of Illinois, Chicago).

Milestones

1. Develop electrochemical cell for *in situ* sampling of the electrochemistry of the electrolyte during cycling. (Q1, FY 2023; Completed)

2. Investigate non-precious metal alloy LiAl for lattice matching LiO_2 formation. (Q2, FY 2023; In progress)

3. Determine if the catalytic properties of single atom catalysts are solid-solid and/or solid-liquid. (Q3, FY 2023)

4. Determine the long-term stability of large LiO_2 particles formed by Ir_3Li catalysts. (Q4, FY 2023)

Progress Report

Lithium oxygen (Li-O_2) batteries have attracted extensive research interest due to their high energy density. Single atom catalysts hosted in carbon frameworks have been reported to show promising results for the cathode. However, their functioning mechanism has always been unclear. In a recent quarterly report, the team looked into the possibility that soluble homogenous catalyst can be produced from the solid cathode. These species can then help dramatically reduce the overpotential. This quarter, they report a cell design that can be used to detect the production of such species without significantly altering the transport properties of the cell.

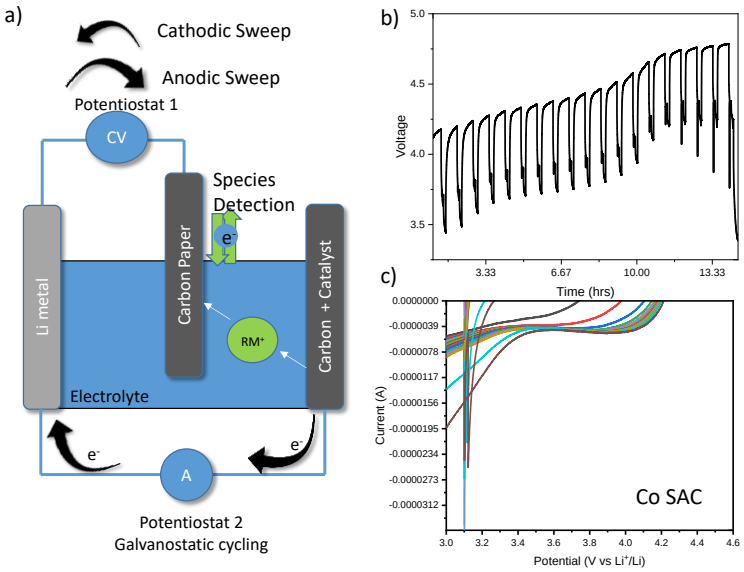

Figure 128. (a) Two working electrode cell design that was implemented in a Swagelok cell. The addition of an additional working electrode (that is, carbon paper) in the electrolyte and separated from the cathode, allows for the detection of electrochemical active species generated from the cathode. Note: RM stands for redox mediator. (b) Voltage profile during the intermittent galvanostatic charging executed between the cathode electrode and the Li-metal anode (reference and counter electrode). (c) Cyclic voltammograms observed at different states of charge sampled between the carbon paper electrode coated with cobalt single atom catalyst (SAC) and the Li-metal anode.

As seen in Figure 128a, they report a cell design that includes two working electrodes connected to two potentiostats. The premise of this design is to allow for the detection of electrochemically active species in the electrolyte that are generated from the cathode. This cell has been made by their in-house glass blower, with a 3-electrode connection. During operation, the carbon + catalyst cathode will be subjected to a galvanostatic charging current against the Li-metal reference and counter. At set intervals of times, the charging current will be halted, and cyclic voltammetry (CV) will be performed between the secondary working electrode (carbon paper) and the Li-metal reference and counter electrode. Figure 128b shows the charging profile observed in Potentiostat 2. Figure 128c shows the corresponding CV response, indicating some redox active species are present in the electrolyte on charging the cathode. Furthermore, the reduction current indicates that it has redox mediating properties that can be beneficial to the oxygen evolution reaction.

In conclusion, a new cell design was developed that allows for convenient electrochemical sampling of the electrolyte under relatively normal charging cell conditions. The team successfully applied this new design to probe the electrochemistry of the electrolyte for redox active species and has found such species when cobalt single atom catalysts were used on the cathode. This work points to changing how the Li-O_2 research community can understand solid-phase catalyst and also developing their relationship to liquid-phase catalysts.

Patents/Publications/Presentations

The project has no patents, publications, or presentations to report this quarter.

Task 6.2 – Lithium Oxygen Battery Design and Predictions
(Larry A. Curtiss / Anh Ngo, Argonne National Laboratory; Amin Salehi-Khojin, University of Illinois, Chicago)

Project Objective. The objective of this work is to develop new materials for Li-O_2 batteries that give longer cycle life and improved efficiencies in an air environment. New electrolyte blends and additives will be investigated that can reduce clogging and at the same time promote the cathode functionality needed to reduce charge overpotentials. New cathode and anode materials will be investigated that can work in conjunction with the electrolytes to improve cycle life in the presence of air components.

Project Impact. Li-air batteries are considered as a potential alternative to Li-ion batteries for transportation applications due to their high theoretical specific energy. The major issues with the existing Li-O_2 systems include degradation of the anode electrode, reactions with air components, clogging of the cathode, and electrolyte instability. Thus, this project is using a comprehensive approach to improve cycle life and efficiency through developing new materials for electrodes, anodes, and electrolytes that work in synergy.

Approach. The experimental strategy is to use cathode materials based on two-dimensional transition metal dichalcogenides that the team has found to be among the best oxygen reduction reaction (ORR) / oxygen evolution reaction (OER) catalysts. These cathode materials will be combined with new electrolyte blends and additives that work in synergy to reduce charge potentials and increase stability of the Li-air system. Density functional theory (DFT) and *ab initio* molecular dynamics simulations are used to gain insight at the electronic structure level of theory of the electrolyte structure, and function both in bulk and at interfaces with the cathode, anode, and discharge product. The team is using classical molecular dynamics to obtain understanding at longer length and time scales of processes occurring in the electrolyte and growth mechanisms of discharge products. They will also utilize a high-throughput (HT) screening strategy based on experiment and theory to develop a large database of properties and outcomes of electrolyte combinations that can be analyzed using machine learning to predict electrolytes and additives with the best performance.

Out-Year Goals. The out-year goals are to find electrolytes that give high capacities and long cycle life in an air atmosphere using HT screening.

Collaborations. This project engages in collaboration with R. Assary, J. G. Wen, and S. Tepavcevic of Argonne National Laboratory; B. Narayanan of University of Louisville; T. Li of Northern Illinois University; and F. Khalili-Araghi and R. Klie of University of Illinois, Chicago.

Milestones

1. Synthesis of new porous dichalcogenide catalysts with bridging TM active sites. (Q1, FY 2023; Completed)
2. Computational studies of stabilities of all possible surfaces of the new catalysts. (Q2, FY 2023; In progress)
3. Investigation of performance of new porous catalysts in cathodes for Li-O_2 batteries. (Q3, FY 2023)
4. Use of DFT for understanding discharge product results and redox mediator mechanisms. (Q4, FY 2023)

Progress Report

Li-air batteries are considered as strong candidates for the next-generation energy storage systems designed for electrical transportation. However, high charge potentials and low current rates are two major drawbacks that hinder these batteries from actual use as batteries. These issues necessitate discovery of novel electrocatalytic processes to significantly enhance the formation and decomposition of the products during battery cycling. The team is working on a synthesis of new classes of catalysts based on bi- and tri-metallic systems with dichalcogenides. This quarter, they synthesized new porous dichalcogenide catalysts with bridging TM active sites. Powders of $SnIrS_{3.6}$ crystals were synthesized by the chemical vapor transport (CVT) method for use in a Li-O_2 cell to act as a catalyst for ORR and OER. They believe such alloys will have high entropy and be more likely to withstand higher rates desired in a Li-O_2 battery. The powders of tin disulfide, iridium, and sulfur were mixed based on stoichiometric ratio and sealed into quartz ampoules. The synthesis process was started by heating the ampoule to 1050°C, keeping it at this temperature for ten days, and cooling it to room temperature naturally. A liquid-phase exfoliation method was used to exfoliate $SnIrS_{3.6}$ into nanoflakes.

Various characterizations were carried out on the as-synthesized $SnIrS_{3.6}$ to study its physical and electrochemical properties. Scanning electron micrograph of $SnIrS_{3.6}$ revealed a one-dimensional nanoribbon texture, as shown in Figure 129a, with a relative cross-sectional diameter ranging from 500 nm to 1 micron. The elemental mapping with energy-dispersive X-ray spectroscopy indicates a homogeneous distribution of sulfur, tin, and iridium in this material, as shown in Figure 129b. To find out the crystal structure, the three-dimensional electron diffraction dataset and atomic resolution scanning transmission electron microscopic image were acquired. The unit cell indicates the structure has never been discovered before for the whole chalcogenide compound family.

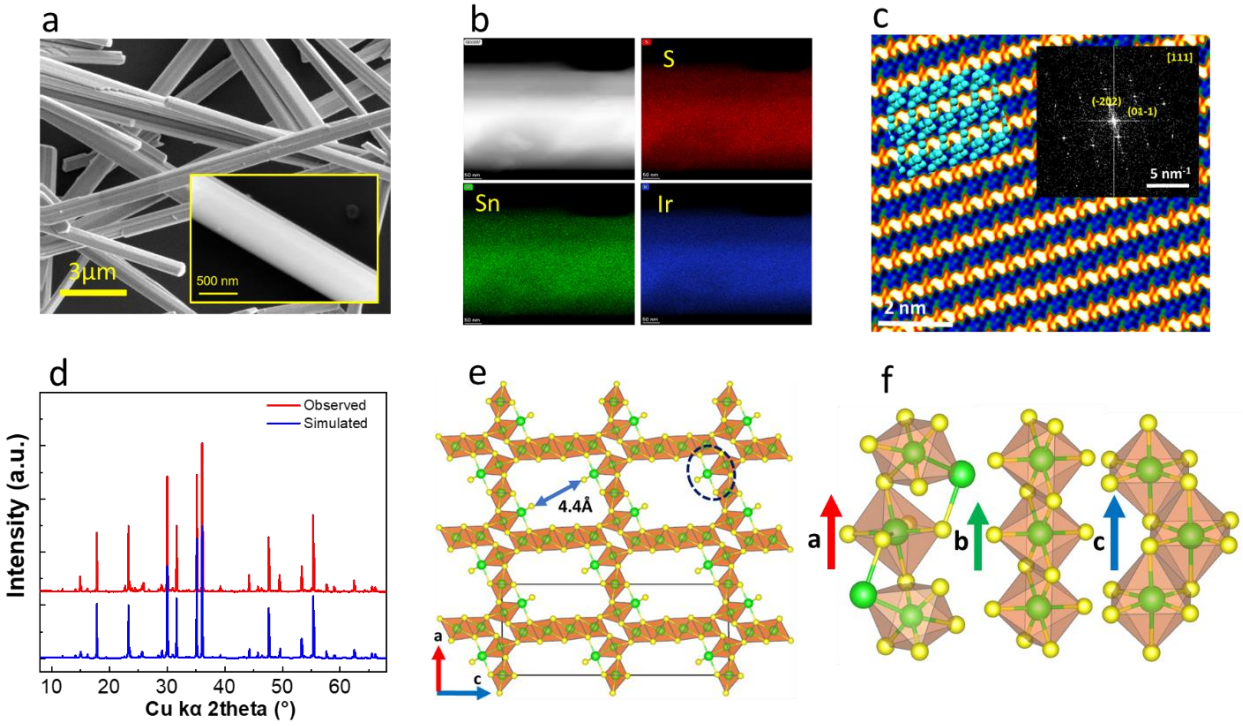

Figure 129. (a) Scanning electron microscopy images taken from as-synthesized $SnIrS_3$ nanorods. (b) Atomic resolution scanning transmission electron microscopic high-angle annular dark field (STEM HAADF) image and STEM energy dispersive X-ray spectrum image that shows the distribution of sulfur, tin, and iridium elements. (c) Atomic resolution STEM image was taken along the [111] direction. (d) A comparison plot between simulated and observed powdered X-ray diffraction patterns. (e) The 3D atomic structure determined from 3D electron diffraction datasets viewed along the b axis. The six coordinated metal atoms are highlighted as square bipyramids in the structure. (f) A magnified image shows a five-coordinated metal atom in the structure, showing the triangular bipyramid shape view along the a, b, and c axes.

The arrangement of the atoms fits well with the atomic model shown in Figure 129c. A powder X-ray diffraction (PXRD) pattern was collected and compared with the simulated PXRD pattern from the structure model, as shown in Figure 129d. The structure was composed of six- and five-coordinated metal atoms, forming octahedral and triangular bipyramids, respectively. Along the b-axis of the structure, a micropore with a size of 4.4 Å is presented (shown in Figure 129e). The formation of the porosity structure is intriguing since the synthesis method is CVT and does not involve the usage of any surfactants or structure-directing agents, which are the common chemical compounds to form micropores in the structure. The overall crystal structure was also viewed from other directions, as shown in Figure 129f. From the structure, they can also obtain the accurate stoichiometry for this material, which is $SnIrS_{3.6}$.

This new porous bimetallic dichalcogenide structure is being used in Li-O_2 batteries to determine whether bimetallic bridging type structure can give higher rates and lower charge rates. The results, along with computational results, will be reported in coming quarters.

Patents/Publications/Presentations

The project has no patents, publications, or presentations to report this quarter.

Task 6.3 – Development of a High-Rate Lithium-Air Battery Using a Gaseous CO_2 Reactant (Amin Salehi-Khojin, University of Illinois, Chicago)

Project Objective. The main objective of this project is to develop a novel strategy to enable operation of Li-CO_2 batteries at high-capacity high-rate with a long-cycle-life. The experiments will be performed in both Swagelok and pouch cells. In the former case, the team will use: (1) a novel co-catalyst system comprised of inexpensive and earth-abundant transition metal dichalcogenide (TMD) materials that work in synergy with ionic liquid (IL) – based electrolytes to enhance efficiency of reactions during discharge and charge processes, (2) a solution-based catalyst (redox mediator, or RM) to reduce charge overpotential and increase energy efficiency of the battery, (3) high-porosity cathode electrodes to increase electrode surface area, gas permeability, stability, electrical conductivity, and lifetime of battery operation, and (4) solid electrolyte interphase layer to protect the anode against oxidation without affecting the ionic transport of Li^+ species in the system. At the pouch-cell level, the team will design and construct a stackable pouch cell to deliver a capacity of > 200 mAh.

Impact. Li-air batteries are considered as a potential alternative to Li-ion batteries for transportation applications due to their high theoretical specific energy. Most work in this area focuses on use of O_2 as the reactant. However, newer concepts for using gaseous reactants (such as CO_2, which has a theoretical specific energy density of 1,876 Wh/kg) provide opportunities for further exploration. This project will produce a thorough understanding of key chemical and electronic parameters that govern the operation of Li-CO_2 batteries in realistic conditions. Achieving the project objectives will generate a library of fundamental properties of TMD- and IL-based electrolytes with the most promise for Li-CO_2 battery applications. The methodologies employed, and the insight generated, will also be valuable beyond advancing the field of Li-CO_2 batteries.

Approach. The above targets will be achieved through an integrated approach based on materials synthesis, testing, characterization, analysis, and computation. The team will synthesize catalysts and test them in cells along with developing new electrolytes and additives. These cathode materials with new electrolyte blends and additives will work in synergy to reduce charge potentials and increase battery stability. Density functional theory and *ab initio* molecular dynamics simulations will be performed to understand battery operation and make predictions of new materials for the Li-CO_2 battery.

Out-Year Goals. The out-year goals are to find novel two-dimensional (2D) catalysts and IL-based electrolytes that give high capacities and long cycle life in a CO_2 atmosphere.

Collaborations. This project collaborates with L. A. Curtiss (Argonne National Laboratory), F. Khalili-Araghi (University of Illinois, Chicago, or UIC), A. Subramanian (UIC), and Z. Huang (Stockholm University).

Milestones

1. Testing and analysis of four synthesized alloy catalysts in a Swagelok cell with CO_2 as reactant. (Q1, FY 2023; Completed)
2. Stability of TMD alloys in presence of electrolyte. (Q2, FY 2023; In progress).
3. Evaluation of four solvent blends for use with catalysts. (Q3, FY 2023).
4. Evaluation of four RMs for use with catalysts. (Q4, FY 2023)

Progress Report

Last quarter, the team reported a Li-CO_2 battery based on new 2D-based medium-entropy alloys as cathode catalysts comprised of sulfur and tellurium chalcogenides that work in synergy with an electrolyte blend of IL of 1-ethyl-3-methylimidazolium tetrafluoroborate and dimethyl sulfoxide (DMSO) with the volumetric ratio of 1:9, ZnI_2, lithium bis(trifluoromethanesulfonyl)imide. They found that the battery can run at high current density of 1 mA/cm^2 with capacities of 0.2 mAh/cm^2 and 0.4 mAh/cm^2 up to 150 cycles with Te-based catalyst, whereas the S-based catalyst was only able to operate for 70 cycles.

This quarter, they report further findings of this new catalytic system, which are key to operating the battery at high rates:

- The nature of charge transfer for both CO_2RR and CO_2ER is similar. Usually, the kinetics of reaction during CO_2ER are a sluggish process, and charge transfer in CO_2ER is much slower than CO_2RR. This is not the case in this new system.
- The role of chalcogen elements on the electronic and catalytic properties of the catalyst structures is significant where the catalyst with tellurium chalcogen shows much improved catalytic activities compared to that with sulfur chalcogen.
- The role of IL electrolyte is found to be deterministic in the basic reactions occurring during discharge and charge, resulting in much improved battery cycling.

The team performed linear sweep voltammetry (LSV) experiments on both catalysts within potential range of 2.4-4.5 V to determine the electrochemical activity of catalysts and in particular the role of chalcogenides (sulfur and tellurium) on CO_2RR and CO_2ER. Figure 130a illustrates the CO_2RR results with a current density of 23.5 mA/cm^2 for Te-based catalyst compared to 15.4 mA/cm^2 for S-based catalyst at the applied potential of 2.4 V. Figure 130b shows CO_2ER results, which indicate the CO_2ER current density of 23.7 mA/cm^2 for Te-based catalyst compared to 13.1 mA/cm^2 for S-based catalyst at 4.5 V. These results are much higher than those obtained for platinum and gold nanoparticles (NPs) under identical experimental conditions. Moreover, the results indicate that Te-based structure shows 1.5× and 1.8× higher activities for CO_2RR and CO_2ER, respectively. Figure 130c-d depicts the charge transfer resistance (R_{ct}) of the catalysts during CO_2RR and CO_2ER at two different overpotentials measured by electrochemical impedance spectroscopy (EIS). Results in Figure 130c indicate small R_{ct} for Te-based catalyst with values of 48.93 Ω and 50.53 Ω at overpotentials of 500 mV and 1000 mV, respectively, compared to 108.53 Ω and 144.84 Ω for S-based catalyst at same overpotentials during CO_2RR. EIS results during CO_2ER (Figure 130d) show the R_{ct} values of 50.21 Ω and 58.43 Ω at the overpotentials of 500 mV to 1000 mV for Te-based catalysts compared to 129 Ω to 164 Ω for S-based catalyst.

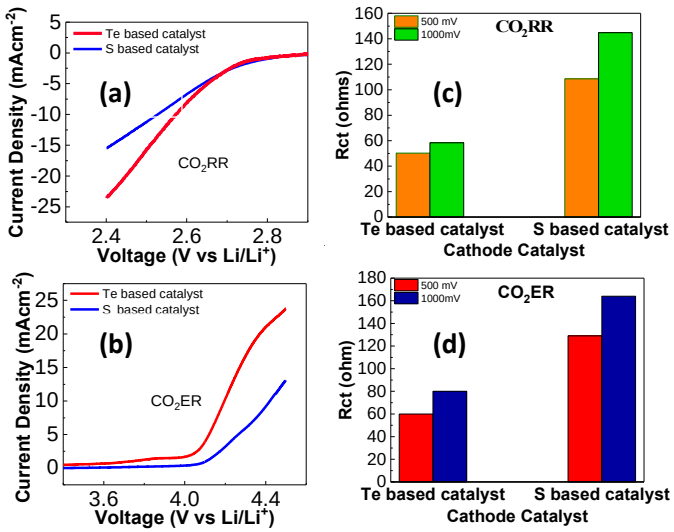

Figure 130. Linear sweep voltammetry results of tellurium- and sulfur-based catalysts during (a) CO_2RR and (b) CO_2ER. Electrochemical impedance spectroscopy measurements for both catalysts at two different overpotentials during (c) CO_2RR and (d) CO_2ER.

A unique feature of these catalysts is that the current density and R_{ct} values for both CO_2RR and CO_2ER are similar, as shown in Figure 130. Usually, these numbers are much smaller in CO_2ER, as they observed for platinum NPs and gold NPs. The sluggish kinetics during evolution reaction was also observed in

Li-O_2 chemistry which is attributed to the diabatic charge transfer process. However, results in Figure 130 suggest that the nature of charge transfer during CO_2RR and CO_2ER in both catalysts is similar, resulting in much improved electrochemical activity during CO_2ER.

To study the contribution of IL on the battery performance, the team first carried out LSV experiments with different IL to DMSO ratios (1:9, 4:6, and 9:1) using Te-based catalyst during CO_2RR/CO_2ER; results are shown in Figure 131a-b. The current density with 1:9 IL:DMSO is 23.2 mA/cm^2 at 2.4 V during CO_2RR, which is increased to 30.3 mA/cm^2 with 4:6 ratio and then decreased to 8.4 mA/cm^2 with 9:1 ratio (Figure 131a). Similarly, at 4.5 V during CO_2ER, the current density is increased from 23.7 mA/cm^2 with 1:9 IL:DMSO ratio to 33.2 mA/cm^2 with 4:6 ratio then decreased to 12 mA/cm^2 with 9:1 ratio (Figure 131b). Figure 131c-d depicts the R_{ct} results at two different overpotentials (500 mV and 1000 mV) and three IL:DMSO ratios. For instance, Figure 131c reveals that the IL:DMSO ratio of 6:4 gives the smallest R_{ct} of 48.93 Ω at the overpotential of 500 mV, compared to 57.32 Ω at 9:1 (IL: DMSO) ratio and 140.2 Ω at the ratio of 1:9. EIS results during CO_2ER (Figure 131d) also show the R_{ct} values of 50.21 Ω for 6:4 ratio compared to 60 Ω and 160 Ω for ratios of 1:9 and 9:1, respectively. This set of results suggests the ratio of 4:6 IL:DMSO produces the best LSV and R_{ct} results for both reaction compared to ratios 1:9 and 9:1. It is also suggests that the nature of charge transfer is similar for both reactions occurring during discharge and charge process.

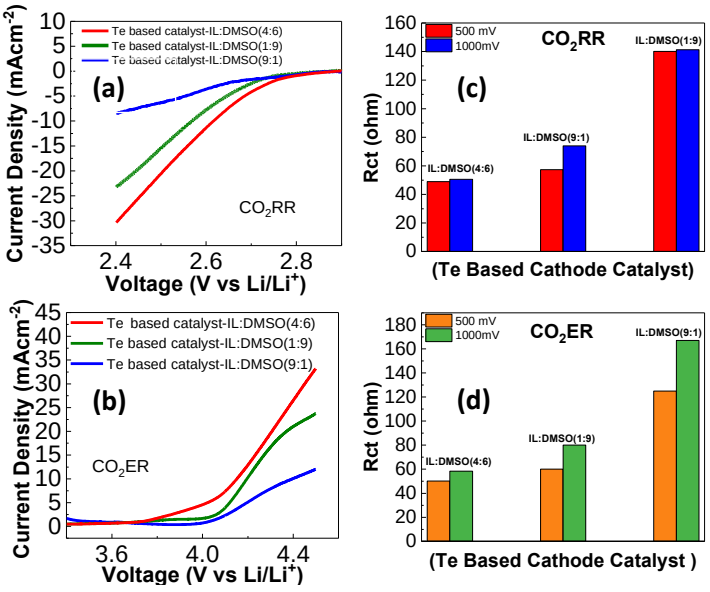

Figure 131. (left) Linear sweep voltammetry results of tellurium- and sulfur-based catalysts at three different ionic liquids (IL): DMSO ratios during: (a) CO_2RR and (b) CO_2ER. (right) Electrochemical impedance spectroscopy measurements at three different IL/DMSO ratios for both catalysts at two different overpotentials during: (c) CO_2RR and (d) CO_2ER.

Figure 132 shows cycling stability results of batteries at different IL:DMSO ratios. Consistent with the results of LSV and R_{ct} experiments, the highest cyclability (220 cycles) was obtained at IL:DMSO ratio, followed by 150 cycles at the ratio of 4:6 and a few cycles at 9:1 ratio. An early failure of the battery with IL:DMSO ratio of 9:1 is attributed to low salt solubility resulting in decreased electrolyte conductivity as well as high viscosity of the electrolyte. Higher cyclability at 4:6 ratio of IL:DMSO could be due to high CO_2 solubility in the electrolyte, which is under study by computational group.

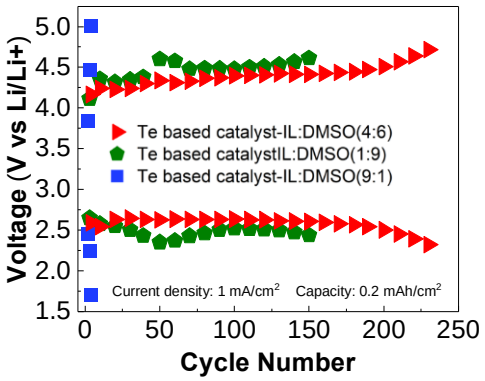

Figure 132. Cycling results for Te-based catalyst at different DMSO:IL ratios.

Patents/Publications/Presentations

The project has no patents, publications, or presentations to report this quarter.

TASK 7 – SODIUM-ION BATTERIES

Team Lead: Xiao-Qing Yang, Brookhaven National Laboratory

Summary

The Na-ion battery will require investigations to identify optimal electrode materials, electrolytes, separators, and binders to reach full potential. The BMR program will therefore have a limited effort directed toward identifying Na-ion battery materials that have potential value for vehicle applications. Progress on these projects this quarter is described in this report.

Highlights

The highlights for this quarter are as follows:

- The Argonne National Laboratory team developed full concentration O3 Ni-rich gradient layered oxide cathodes with 80% capacity retention for 300 cycles and P2-type Fe/Mn layered oxide cathode with 72.6% retention after 300 cycles.
- The Brookhaven National Laboratory team completed studies using pair distribution function (PDF) to characterize the solid electrolyte interphase (SEI) on Li/Cu in Cu||Li, Ni-Mn-Co (NMC) || Li, and NMC||Cu cells. It was found that in Li||NMC cells, the SEI on lithium foil has a large amount of organic species resulting from anion decomposition. The amount of inorganic species is relatively small. In Cu||NMC cells, the organic species in SEI come from decompositions of both solvents and anions. In contrast to the SEI on lithium foil in Li||NMC cells, the SEI on copper foil in Cu||NMC is dominated by inorganic species. This study demonstrates PDF is capable of probing both crystalline and amorphous phases in SEI, revealing the relative content of organics from solvent decomposition, organics from anion decomposition, and overall inorganics.
- The Lawrence Berkeley National Laboratory team completed optimization of best titanate anode in full-cell configurations. Several methods for carbon-coating sodium titanate (NTO) particles were studied. Carbon coating NTO heat-treated at 500°C resulted in much better capacity retention on cycling. This is attributed to changes in the surface chemistry induced by the coating.
- The Pacific Northwest National Laboratory team completed the selection of new cathode materials for Na-ion battery. Prussian Blue materials were selected to investigate as promising cathode for Na-ion batteries, with the variation of loading capacity from 1.5-2.0 mAh cm^{-2}. They also developed a new highly concentrated poly(ethylene oxide) / 1,2-dimethoxyethane / sodium bis(fluorosulfonyl)imide and diethylene glycol dimethyl ether based electrolytes showing the best compatibility with Prussian Blue cathode.

Task 7.1 – Exploratory Studies of Novel Sodium-Ion Battery Systems (Xiao-Qing Yang and Enyuan Hu, Brookhaven National Laboratory)

Project Objective. To meet the challenges of powering plug-in hybrid electric vehicles and battery electric vehicles, new rechargeable battery systems with high energy and power density, low cost, good abuse tolerance, and long calendar and cycle life need to be developed. The primary objective of this project is to develop new advanced synchrotron-based material characterization techniques and apply these techniques to study the new rechargeable battery systems beyond the Li-ion batteries, namely the Na-ion battery systems for electric vehicles (EVs).

Project Impact. The results of this project will be used for developing technologies that will significantly increase the energy density and cycle life and reduce the cost of beyond Li-ion battery systems. This will greatly accelerate deployment of EVs and reduce carbon emission associated with fossil fuel consumption and will help in the direction of building U. S.-based energy storage manufacture chains.

Approach. This project will use synchrotron-based *in situ* X-ray diagnostics such as *in situ* X-ray diffraction (XRD) and *in situ* X-ray absorption (XAS) tools, combined with transmission electron microscopy, scanning transmission electron microscopy, and transmission X-ray microscopy imaging techniques developed at Brookhaven National Laboratory (BNL) to evaluate the new materials and redox couples to obtain in-depth understanding of the reaction mechanisms of these materials, aiming to improve existing materials and to provide guidance for new materials and new technology development for Na-ion battery systems.

Out-Year Goals. The out-year goal is to complete synchrotron-based XRD, XAS, and resonant inelastic X-ray scattering (RIXS) studies of new cathode materials of P3 type $Na_{0.75}Li_{0.08}Cu_{0.25}Mn_{0.66}O_2$ for Na-ion batteries.

Collaborations. The BNL team has been closely working with top scientists on new material synthesis at Argonne National Laboratory, Oakridge National Laboratory (ORNL), and Pacific Northwest National Laboratory, with U. S. industrial collaborators at General Motors and Johnson Controls, and with international collaborators.

Milestones

1. Complete electrochemical characterization of P3-type $Na_{0.75}Li_{0.08}Cu_{0.25}Mn_{0.66}O_2$ cathode material. (Q1, FY 2023; Completed)
2. Complete *in situ* hard XAS studies on P3-type $Na_{0.75}Li_{0.08}Cu_{0.25}Mn_{0.66}O_2$ to investigate the charge compensation mechanism and local structural changes. (Q2, FY 2023)
3. Complete *in situ* XRD and *ex situ* soft XAS studies on P3-type $Na_{0.75}Li_{0.08}Cu_{0.25}Mn_{0.66}O_2$ to understand the evolution of structure and interphase during cycling. (Q3, FY 2023)
4. Complete *ex situ* RIXS studies on P3-type $Na_{0.75}Li_{0.08}Cu_{0.25}Mn_{0.66}O_2$ to study the oxygen redox behavior in this material. (Q4, FY 2023)

Progress Report

This quarter, the first milestone was successfully completed. In collaboration with scientists at ORNL, the team optimized the synthesis conditions and obtained P3-structured $Na_{0.75}Li_{0.08}Cu_{0.25}Mn_{0.66}O_2$ with high purity. Last fiscal year, they worked on P3-$Na_{2/3}Cu_{1/3}Mn_{2/3}O_2$ and concluded that it is possible to increase the capacity of this material by activating the oxygen redox. This may be fulfilled by substituting part of copper with lithium and therefore introducing the Na-O-Li structural motif that has been suggested as having influence on oxygen activity by theoretical studies. The synchrotron XRD pattern of $Na_{0.75}Li_{0.08}Cu_{0.25}Mn_{0.66}O_2$ is shown in Figure 133a. Rietveld refinement using a model structure having $P2_1/c$ space group symmetry leads to excellent fitting. The structure has orderings both within the Li/TM (transition metal; Cu, Mn) layer and the sodium layer. The XRD data have obvious anisotropic broadening, indicating there are possible stacking faults in the pristine material. The team first used the conventional 1 M $NaPF_6$ in ethylene carbonate/propylene carbonate as the electrolyte, but the $Na_{0.75}Li_{0.08}Cu_{0.25}Mn_{0.66}O_2$||Na cell cannot be cycled. Then, they changed the salt from $NaPF_6$ to $NaClO_4$ and added fluoroethylene carbonate into the electrolyte, which enables cycling of the cell; the electrochemical data are shown in Figure 133b. The electrochemical data of the non-substituted material $Na_{0.66}Cu_{0.33}Mn_{0.66}O_2$ are shown in Figure 133c for comparison. They clearly show that after introducing lithium substitution, the capacity is significantly increased. The 1st cycle discharge capacity increased from 80 mAh/g in $Na_{0.66}Cu_{0.33}Mn_{0.66}O_2$ to 130 mAh/g in $Na_{0.75}Li_{0.08}Cu_{0.25}Mn_{0.66}O_2$. The 1st charge process in $Na_{0.75}Li_{0.08}Cu_{0.25}Mn_{0.66}O_2$ features a long plateau at ~ 4.2 V, which is likely associated with the activation of oxygen redox. In comparison, such plateau is absent in $Na_{0.66}Cu_{0.33}Mn_{0.66}O_2$, even though it is charged to the same voltage. $Na_{0.75}Li_{0.08}Cu_{0.25}Mn_{0.66}O_2$ delivers considerable amount of capacity in the < 3 V region during discharge, while $Na_{0.66}Cu_{0.33}Mn_{0.66}O_2$ has little capacity in the same region. Such discharge capacity is likely to arise from the oxygen redox during discharge. The oxygen redox voltage difference between charge and discharge is likely caused by hysteresis. It is also noted that while lithium substitution successfully increases the capacity, the capacity fades more rapidly than the non-substituted material. More mechanistic studies will be carried out in this fiscal year.

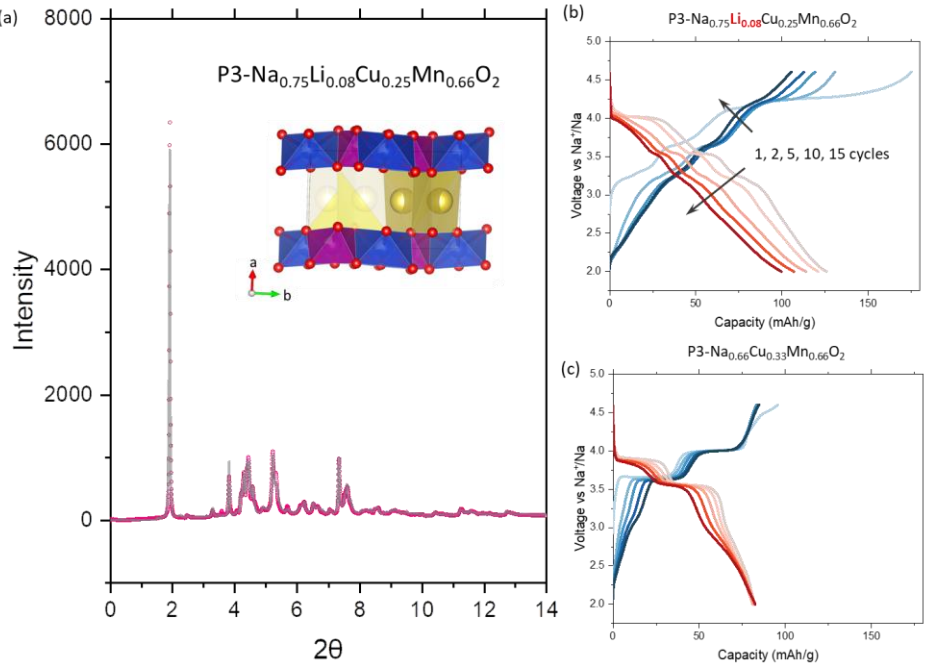

Figure 133. (a) X-ray diffraction data and Rietveld refinement of P3 $Na_{0.75}Li_{0.08}Cu_{0.25}Mn_{0.66}O_2$ with the inset graph showing the solved crystal structure. (b) Selected charge-discharge profiles of $Na_{0.75}Li_{0.08}Cu_{0.25}Mn_{0.66}O_2$ from the first 15 cycles. (c) Selected charge-discharge profiles of $Na_{0.66}Cu_{0.33}Mn_{0.66}O_2$ from the first 15 cycles.

Patents/Publications/Presentations

Publication

- Wang, Y., Z. Shadike, W. Fitzhugh, F. Wu, S-J. Lee, J-S. Lee, X. Chen, Y. Long, E. Hu,* and X. Li.* "Tuning Discharge Voltage by Schottky Electron Barrier in P2-$Na_{2/3}Mg_{0.205}Ni_{0.1}Fe_{0.05}Mn_{0.645}O_2$." *Energy Storage Materials* 55 (2023): 587–596. https://doi.org/10.1016/j.ensm.2022.12.027.

Task 7.2 – Development of a High-Energy Sodium-Ion Battery with Long Life (Chris Johnson and Khalil Amine, Argonne National Laboratory)

Project Objective. The project objective is to develop a high-energy Na-ion battery with long life. Moreover, the battery chemistry should utilize low-cost materials. The energy density target is 200 Wh/kg and/or 500 Wh/L, wherein the anode and cathode capacity targets are 600 $mAhg^{-1}$ and 200 $mAhg^{-1}$, respectively.

Project Impact. A Na-ion battery on par with the energy density of a Li-ion battery can have a high impact in the transportation sector with the assumption that the cost is significantly below $85/kWh and that the battery pack provides a 300-mile range. The consumer is not concerned about the battery chemistry employed if these metrics can be met. Development of these battery chemistries will situate the United States in a strong position as relates to new low-cost energy storage systems beyond lithium ion.

Approach. In a team approach, the Na-ion battery group will create a versatile Na-ion battery chemistry with beneficial advantages such as low cost, safety, recycling, and sustainability of materials used. The team will work synergistically so that the final design is the culmination of advances in phosphorus carbon composites mated with optimized lead or other highly dense metalloids, such as tin and/or antimony and derivatives thereof, for the recyclable anode. Synthesis and optimization of such blended composite anodes will be conducted in parallel to diagnostic characterization of structures, phase formation, and cycling stability. Cathode work will begin at the end of the first year and will involve gradient cathodes consisting of Fe-Mn compositions, as well as intergrowths of layer stacking sequenced oxides. If resources allow, the team also will attempt to stabilize cathode surfaces using atomic layer deposition methods, particularly for the benefit of staving off dissolution of manganese and iron / electrolyte reactivity. Electrolytes will be partly procured from H. Li at Pacific Northwest National Laboratory (PNNL).

Out-Year Goals. The state-of-the-art Na-ion battery in the literature has now been surpassed by this team, but performance is still too low for commercialization. Thus, the goal is to move forward and continually invent the most superior Na-ion battery chemistry that can compete worldwide through work output from this project.

Collaborations. Researchers from PNNL who are developing electrolytes for Na-ion batteries will provide this project with formulations to test with the various electrode combinations investigated at Argonne National Laboratory.

Milestones

1. Development of concentration gradient layered oxide cathode with 130 mAh/g and stable cycle life of > 200 cycles. (Q4, FY 2022; Completed)
2. Developing Ni-based or Fe/Mn-based cathodes with > 180 mAh/g and > 80% retention after 100 cycles. (Q1, FY 2023; Completed)
3. Developing novel electrolytes for the Ni- and Fe/Mn-based cathodes to achieve 2× improved stability. (Q2, FY 2023; In progress)
4. Surface coating for Co-free layered cathodes to achieve a reversible capacity of > 130 mAh/g after 200 cycles. (Q3, FY 2023; In progress)
5. Fabricating full cell / pouch cell using optimal layered cathodes and phosphorus or sodium metal anode with high areal capacity of 3 mAh/cm^2 and stable cycle life. (Q4, FY 2023; In progress)

Progress Report

This quarter, the team successfully developed two layered oxide cathodes with improved cycling stability for Na-ion batteries.

First, they have developed a full-concentration gradient layered O3 $NaNi_{0.8}Co_{0.1}Mn_{0.1}O_2$ (O3-FCG811) cathode by controlling the co-precipitation conditions. Figure 134a shows the cross-section scanning electron microscopy (SEM) images and the corresponding energy-dispersive X-ray analysis mapping of the O3-FCG811 cathode. As shown, the cathode exhibits a spherical particle shape with the concentration of nickel rich at core, while Co/Mn rich on the surface. Such design is intended to provide high specific capacity from redox reaction of nickel while suppressing surface reactivity with the electrolytes via using manganese. The team is mainly focused on the effect of such concentration gradient distribution with the cathode particle, while cobalt or even nickel will be eliminated in the future to reduce the use of critical elements in battery cathodes. Figure 134b shows the X-ray diffraction (XRD) pattern of O3-FCG811 cathode, which exhibits a typical layered $NaFeO_2$ structure without noticeable impurity. Figure 134c shows cycling performance of O3-FCG811 cathode during charge/discharge within 1.5-3.9 V at a current density of 75 mA g^{-1}. The cathode delivered an initial high specific capacity of ~ 15 mAh/g and can still maintain a reversible capacity of ~ 120 mAh/g after 300 cycles, resulting in a good capacity retention of 80%. Their results indicate that concentration gradient could pave a new way to stabilize high-capacity layered oxide cathodes for Na-ion batteries.

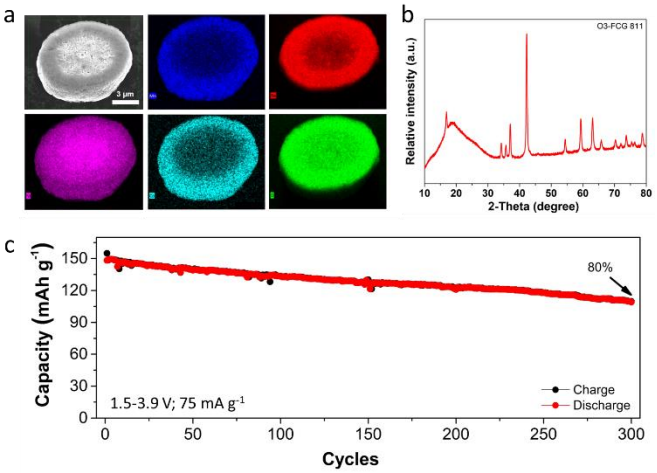

Figure 134. (a) Scanning electron microscopy and corresponding energy dispersive X-ray spectroscopy mapping. (b) X-ray diffraction pattern. (c) Cycling performance of developed O3 FCG $NaNi_{0.8}Co_{0.1}Mn_{0.1}O_2$ cathode.

On the other hand, to address the critical raw material supply chain challenge and improve sustainability of Na-ion battery, the team has further developed an earth-abundant layered P2 $Na_{0.67}Fe_{0.3}Mn_{0.5}O_2$ cathode for Na-ion batteries via Mg/Ti co-doping. The P2 $Na_{0.67}Fe_{0.3}Mn_{0.5}O_2$ w/o and w/ Mg/Ti co-doping are denoted as

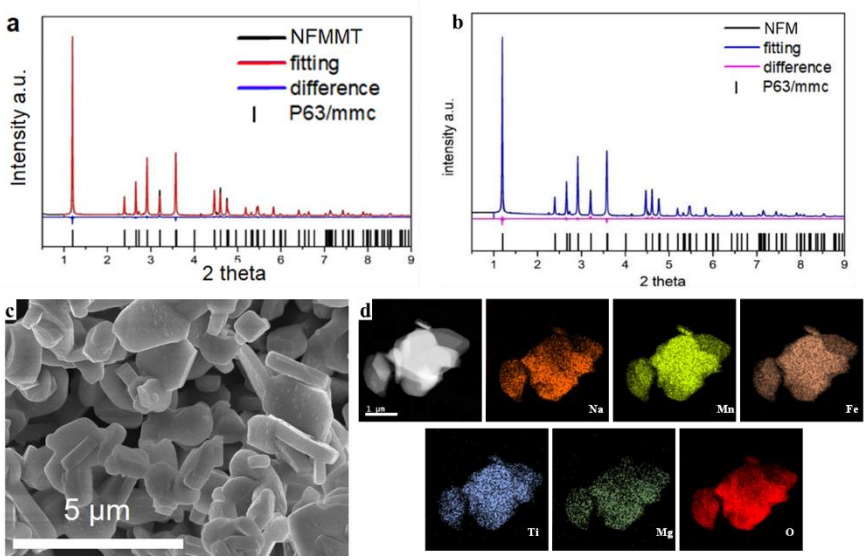

Figure 135. X-ray diffraction patterns of (a) NFMMT and (b) NFM. (c-d) Scanning electron microscopy images of NFMMT.

NFM and NFMMT, respectively. They were both synthesized through solid-state reactions by homogeneously mixing precursors followed by heat treatment. Figure 135a-b shows the XRD patterns of NFM and NFMMT, respectively. As shown, both materials exhibit a typical P2-type structure (space group P63/mmc (194)). In this structure, the "ABAB" stacking sequence of oxygen packing constitutes the main frame, transition metal (TM) ions are located in the center of TMO6 octahedrons, and Na^+ ions occupy the prismatic sites between TM layers. The Rietveld refinement results further indicate the P2 structure for both materials with no impurity phase. The obtained lattice parameters of NFM and NFMMT are a = 2.922(3) Å, c = 11.242(5) Å and a = 2.917(2) Å, c = 11.239(8) Å, respectively. The slight shrinkage of lattice parameters in NFMMT is originated from the smaller ionic radius of Mg^{2+} and Ti^{4+} than those of manganese and iron ions. The morphology of NFMMT was examined by SEM (Figure 135c), showing the typical particle size of 1-2 μm, and homogeneous distribution of sodium, iron, manganese, magnesium, and titanium within the particles.

The electrochemical performance of NFM and NFMMT cathode were evaluated in the coin cells using sodium metal as counter and reference electrode. The voltage range is 1.5-4.5 V versus sodium. Figure 136a-b shows the charge/discharge curves of NFM and NFMMT, respectively. The NFM cathode could deliver an initial high specific capacity of 216 mAh g^{-1} with an average working voltage of 2.6 V. However, on cycling, NFM exhibits a continuous loss in both capacity and working voltage. By sharp contrast, after Mg/Ti co-doping, the initial specific capacity of NFMMT cathode was slightly decreased to 209 mAh g^{-1}, while the voltage/capacity stability was significantly improved. After 50 cycles of charge/discharge at 20 mA g^{-1}, NFMMT cathode could still maintain a reversible capacity of > 160 mAh g^{-1}. The cycling performance of NFM and NFMMT cathode was further tested at a higher current density of 200 mA g^{-1}. As shown in Figure 136c, after the activation for the initial three cycles, the reversible capacity of NFM degrades rapidly on cycling, owing to the unfavorable phase transition and Jahn-Teller effect of Mn^{3+} ions, leading to a capacity retention of only 31.2±1.4% after 150 cycles at 200 mA g^{-1}. In sharp contrast, without any structural modification, NFMMT exhibits a promising capacity retention of 72.6±0.8% at 200 mA g^{-1} between 1.5-4.5 V after 300 cycles.

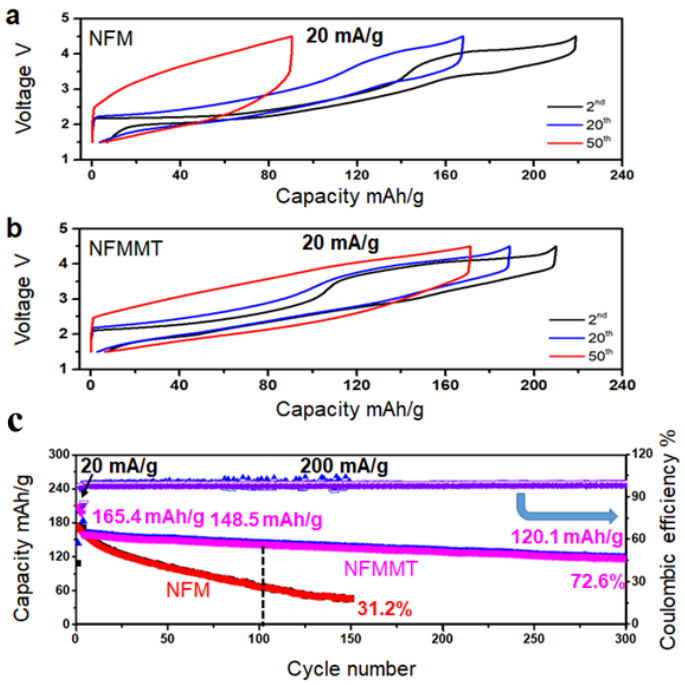

Figure 136. Electrochemical performance of NFM and NFMMT. (a-b) Charge and discharge profiles of NFM (a) and NFMMT (b) at 20 mA g^{-1} in the voltage range of 1.5-4.5 V. (c) Long-cycle performance of NFM and NFMMT at 200 mA g^{-1} between 1.5 and 4.5 V.

In summary, this quarter the team has developed two layered oxide cathodes with significantly improved cycling stability through concentration gradient and element doping. They will further explore surface coating and electrolyte modulation to improve cycling stability, particularly at high charge cut-off voltage to obtain higher reversible capacity.

Patents/Publications/Presentations

The project has no patents, publications, or presentations to report this quarter.

Task 7.3 – Tailoring High-Capacity, Reversible Anodes for Sodium-Ion Batteries (Marca M. Doeff, Lawrence Berkeley National Laboratory)

Project Objective. The project objective is to understand the role that vacancies, surface defects, and bulk structure play in determining electrochemical properties of high capacity, stepped layered titanate anodes.

Project Impact. Although several suitable cathode materials for Na-ion batteries exist, there are few suitable anode materials due to low potential instabilities. Sodium titanate anodes are a promising class of materials for this application. The electrochemical properties can be manipulated through structural and surface modifications.

Approach. The structure and surface properties of candidate stepped layered titanates will be modified through manipulation of synthetic parameters. Materials will then be characterized electrochemically and physically to understand the role that surface defects, vacancies, and bulk structure play in determining electrochemical behavior.

Out-Year Goals. The out-year goal is to achieve development of an electrode that can deliver 225 mAh/g at C/3 rate with good capacity retention (80% or better) for 100 cycles.

Collaborations. The team collaborates with beam line scientists at Stanford Synchrotron Radiation Lightsource and the Advanced Light Source at Lawrence Berkeley National Laboratory.

Milestones

1. Select best titanate for optimization in full-cell configurations. (Q1, FY 2023; Completed)
2. Complete full-cell testing. (Q2, FY 2023; In progress)
3. Examine feasibility of characterization of sodium nonatitanates by small-angle X-ray scattering or wide-angle X-ray scattering; stop if techniques are not useful. (Q3, FY 2023; In progress)
4. Conduct ambient pressure X-ray photoelectron spectroscopy experiments, *in situ* X-ray diffraction (XRD), and X-ray absorption experiments. (Q4, FY 2023; In progress)

Progress Report

This quarter, to select the best titanate anode for optimization in full-cell configurations, the team optimized the electrochemical performance of sodium titanates by surface carbon coating (this was a task and milestones carried over from FY 2022). Carbon coating on battery electrode materials is an effective approach to improve their low electronic conductivity and battery cycle life by limiting side reactions. They selected two promising sodium titanates ($Na_{0.74}Ti_{1.815}\square_{0.185}O_4 \bullet nH_2O$, NTO) for carbon coating study. The first, heated at 60°C, shows a large initial capacity of 228 mA h g^{-1}; however, it retains only 64.8% of its capacity over 50 cycles. The other, heated at 500°C, retains 94.3% of its initial capacity of 184 mA h g^{-1} over 50 cycles. Since 60°C-heated NTO undergoes structural changes at temperatures above 150°C, 60°C-heated NTO particles were coated with soft carbon (acetylene black) by dry ball-milling to preserve the layered structure. XRD revealed that the structure of the pristine material was preserved after the carbon coating (results not shown). One hour of ball-milling time was used to avoid undesired particle agglomeration during prolonged ball milling. Figure 137a-b compares the scanning electron microscopy images of 60°C-heated NTO before and after the carbon coating, showing no obvious change in the particle size after processing. The carbon-coated NTO shows much better capacity retention, with 92.8% of its initial capacity of 162.8 mA h g^{-1} over 50 cycles (Figure 137d). However, a lower initial reversible charge capacity is delivered for the carbon-coated NTO compared to the pristine material. The high-voltage plateau at ca. 1.2 V versus Na^+/Na is also absent after carbon coating. This result indicates that carbon coating modifies the surface chemistry of 60°C-heated NTO, deactivating some of the surface sodium storage sites that adversely affect the reversible capacity. The team further dispersed the carbon-coated sodium titanate in a carbon nanotube (CNT) network, which is expected to act as conductive wires to transport electrons to and from the carbon-coated titanate. A small increase in reversible capacity was observed due to the introduction of the CNT network. For the 500°C-heated NTO, they employed a wet carbon coating process using polyacrylonitrile (PAN) as carbon source. PAN was dissolved in N-methylpyrrolidone and hand ground with NTO thoroughly. The resulting mixture was then carbonized in argon atmosphere for 3 hours at 550°C at a heating rate of 2°C min^{-1}. The amount of carbon coating can be well controlled by the mass ratio of PAN to NTO (Figure 138c). A color change from white to black indicates successful carbon coating (Figure 138a-b). No obvious change in the particle size was observed after carbon coating. With only 4.9 wt% of carbon coating, the 550°C-heated NTO electrode cycles well without adding any additional carbon during electrode preparation (Figure 138d), suggesting that the surface carbon layer on NTO particles effectively improves electronic conductivity. More electrochemical characterization is in progress to find the optimized amount of carbon coating as well as the effects of surface carbon coating on the rate performance of 550°C-heated NTO electrode.

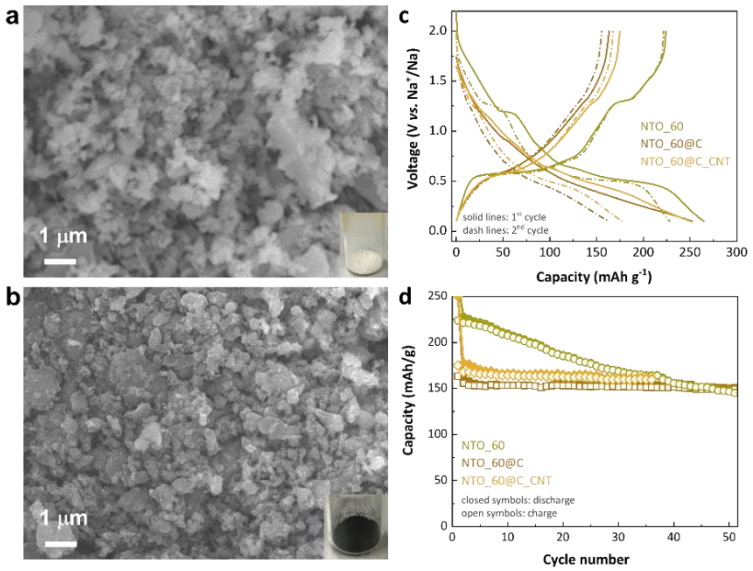

Figure 137. Scanning electron microscopy images of 60°C – heated NTOs (a) before and (b) after the carbon-coating process by dry ball milling. Optical images in the insets show a color-change from white to dark, indicative of successful carbon coating. (c) Initial two cycles and (d) capacity retention of sodium half-cells containing pristine (NTO_60), carbon-coated 60°C – heated NTOs (NTO_60@C), and carbon-coated 60°C – heated NTO dispersed in carbon nanotube framework (NTO_60@C_CNT) at 8 mA g^{-1} using an electrolyte of 0.5 M sodium tetraphenylborate in diethylene glycol dimethyl ether.

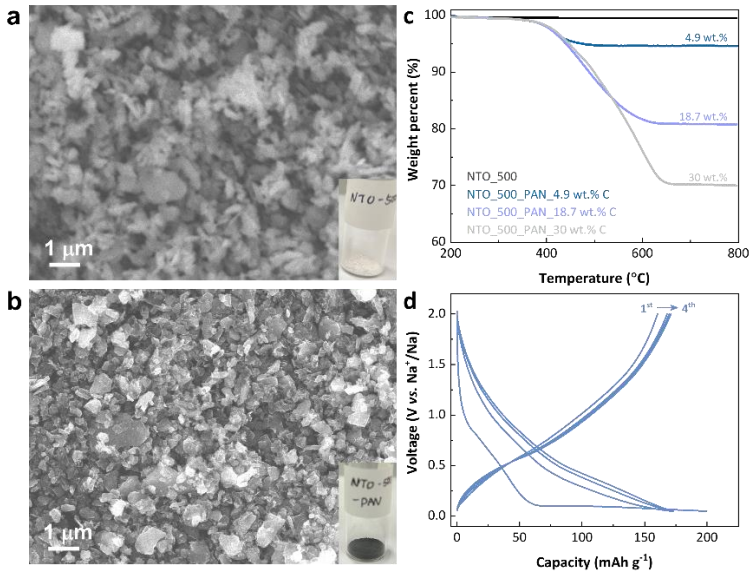

Figure 138. Scanning electron microscopy images of 500°C – heated NTOs (a) before and (b) after the carbon-coating process using polyacrylonitrile as carbon source. Optical images in the insets show a color-change from white to dark, indicative of successful carbon coating. (c) Thermogravimetry analysis of 500°C – heated NTOs before and after the carbon-coating process carried out in dry air with a heating rate of 10°C/min. (d) Voltage profiles of sodium half-cell containing carbon-coated 500°C – heated NTO (4.9 wt% carbon) at 8 mA g^{-1} using an electrolyte of 0.5 M sodium tetraphenylborate in diethylene glycol dimethyl ether; note that no additional carbon was used in the electrode.

Patents/Publications/Presentations

Publication

- Yin, W., G. Barim, X. Peng, E. A. Kedzie, M. C. Scott, B. McCloskey, and M. M. Doeff. "Tailoring the Structure and Electrochemical Performance of Sodium Titanate Anodes by Post-Synthesis Heating." *Journal of Materials Chemistry A* 47 (2022): 25178–25187. https://doi.org/10.1039/D2TA07403F.

Presentations

- 242nd Electrochemical Society Meeting, Atlanta, Georgia (October 9–13, 2022): "Developing Titanate Anodes for Sodium Ion Batteries"; M. M. Doeff, W. Yin, and G. Barim. Invited.
- Materials Research Society Meeting, Boston, Massachusetts (November 27 – December 2, 2022): "A Perspective on Sodium-Ion Batteries"; M. M. Doeff, W. Yin, and G. Barim. Invited.

Task 7.4 – Electrolytes and Interfaces for Stable High-Energy Sodium-Ion Batteries (Phung M. L. Le, Pacific Northwest National Laboratory)

Project Objective. The Na-ion battery is a potential alternative energy source for electric vehicles (EVs) and grid applications due to the low cost and the natural abundance of sodium. However, their energy density is still lower than that of commercial Li-ion counterparts. A promising solution toward higher energy is using high-voltage or high-energy-density cathode materials or replacing the insertion-type anodes in Na-ion batteries such as carbons with ultra-thin sodium metal (1,166 mAh g^{-1} and −2.71 V versus standard hydrogen electrode potential) to fabricate Na-metal batteries; another promising solution is exploring the concept of anode-free sodium batteries (AFSB). Either approach requires a good electrolyte to stabilize performance of the Na-ion cell to maintain long cyclability through the formation of stable solid electrolyte interphase (SEI) on the anode and formation of cathode electrolyte interphase (CEI) on the cathode. In addition, flammability of electrolyte also leads to safety concerns. Therefore, there is also an urgent need to develop more stable and safer electrolytes to enable applications in severe conditions (that is, high potential, high temperature). To reach this goal, a fundamental understanding of the nature of the dynamic interface between electrode and electrolyte is critical. The sluggish redox kinetics also remain challenging for high-power applications and needs to be improved.

Project Impact. This project will develop new electrolytes to enable long cycle life and safe operation of Na-ion batteries. If successful, the resulting improvements in energy, life, and safety will provide a solid contribution to the understanding of fundamental scientific questions and the development for Na-ion battery technology and promote its practical application as a competitive alternative to the current Li-ion batteries and greatly reduce the cost of energy storage systems for EVs.

Approach. This project will continuously focus on different electrolyte compositions (salt/solvent/additive) and will explore the electrolyte/electrode interphases using hard carbon (HC) as anode and the low-cost cathodes available in the market, with the aim to be cost-effective for future manufacturing of Na-ion batteries and to compete with Li-ion market. For high-energy Na-ion batteries, Prussian blue and white cathode ($Na_2Fe_2(CN)_6$) and $NaNi_{0.4}Fe_{0.2}Mn_{0.4}O_2$ (NFM) will be selected because of the high capacity and operational voltage (that is, 150 mAh/g and 3.4 V). For sodium batteries with extremely long cycle life, a polyanionic cathode ($Na_3V_2(PO_4)_3$ will be continuously used because this material is highly stable and standard for fundamental studies on anode-free sodium cell. Based on the cathodes available in market, the project will focus on developing a high-performance electrolyte to enable high-energy-density Na-ion batteries that are highly safe and have a long cycle.

Out-Year Goals. This project will select electrolyte compounds and identify formation of interfacial SEI layer on HC and CEI layer-on-layer oxide cathode and its effect on electrode materials. It will also guide electrolyte optimization and improve Coulombic efficiency of sodium deposition/stripping to be more than 99%.

Collaborations. This project will collaborate with leading scientists at Argonne National Laboratory, Lawrence Berkeley National Laboratory, and other organizations in the field of cathode and anode materials for Na-ion batteries. It will also collaborate with C. Wang and M. Engelhard of Pacific Northwest National Laboratory for transmission electron microscopy and X-ray photoelectron spectroscopy characterization.

Milestones

1. Develop nonflammable and safe electrolytes based on fluorinated solvent, new sodium salt, and polymer matrix for cathode materials (that is, Prussian blue and white, NFM). (Q1, FY 2023; Completed)
2. Investigate the thermal, physical, and chemical properties and the redox stability of developed electrolytes. (Q2, FY 2023)

3. Study different factors (that is, electrolyte composition, current collectors, cycling protocol, and temperature) affecting the efficiency of the sodium stripping/plating process and cycling performance of AFSB. (Q3, FY 2023)
4. Characterize CEI/SEI interphase properties in optimized electrolyte to probe the underlying mechanism of cycling stability of Na-ion batteries and AFSBs. (Q4, FY 2023)

Progress Report

Prussian Blue (PB) materials purchased from Altris (Sweden) have been selected to investigate as a promising cathode for Na-ion batteries due to their low cost, facile synthesis, and outstanding electrochemical performance. To reach a level of practical application comparable to Li-ion batteries, the high-loading-capacity PB cathode is essentially required for a high-energy-density Na-ion battery. However, the poor conductivity and a large volume change during the subsequent charge/discharge process might be harmful to the electrochemical properties of the PB electrode and its interface. Therefore, several efforts should be made to solve these issues, such as the electrode formation process and electrolyte formulations. This quarter, the team

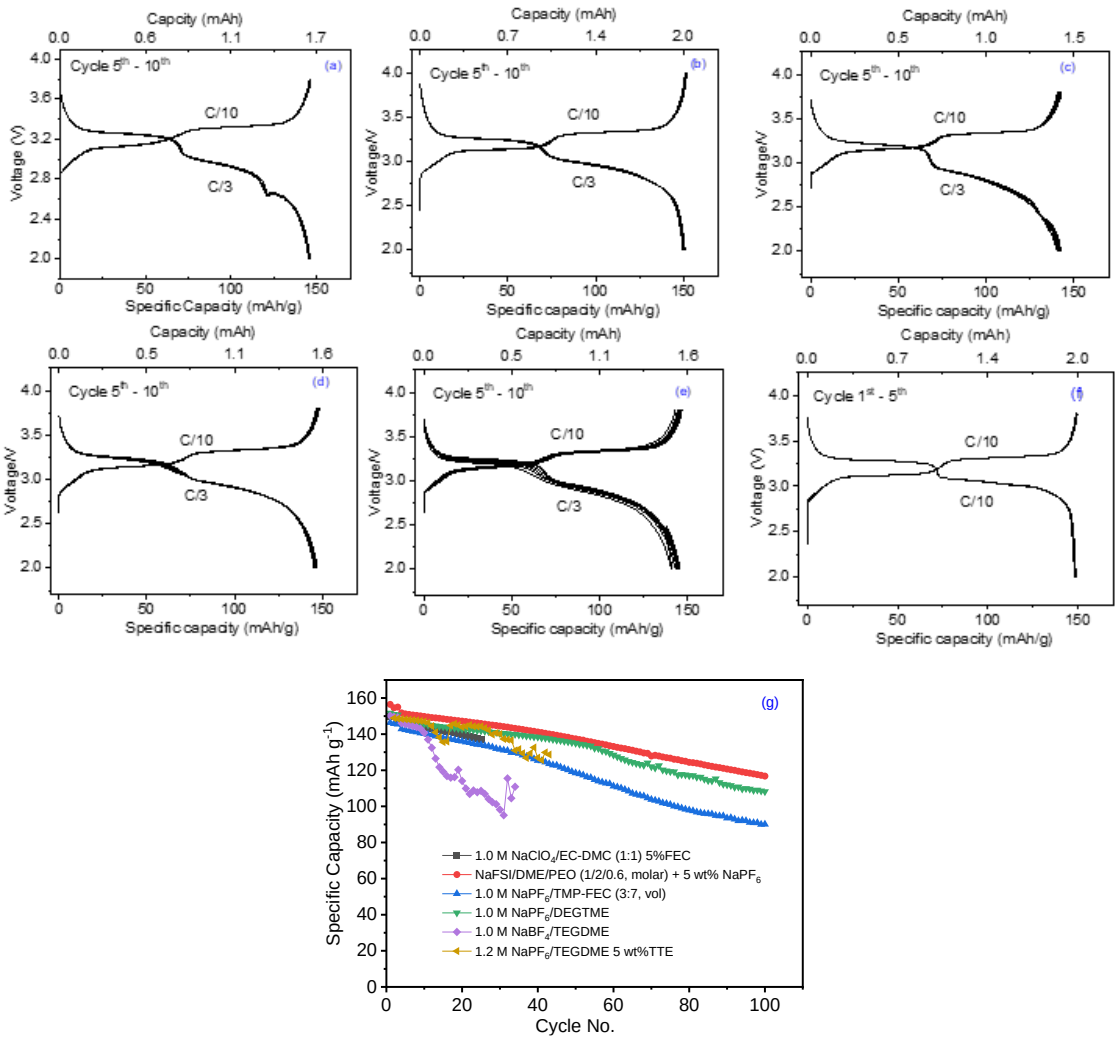

Figure 139. Charge – discharge profile of Prussian Blue (PB) cathodes in half-cell with sodium metal, 85% active material loading capacity: 1.5-2.0 mAh/cm^2; (a) baseline 1 M $NaClO_4$/EC-DMC (1:1 in vol) + 5 wt% FEC; (b) NaFSI/DME/PEO (1/2/0.6 molar ratio) + 5 wt% $NaPF_6$; (c) 1 M $NaPF_6$/TMP-FEC (3:7 in vol.); (d) 1 M $NaPF_6$/DEGDME; (e) 1 M $NaBF_4$/TEGDME; and (f) 1.2 M $NaPF_6$ in TEGDME 5 wt% TTE. (g) Cycling performance of PB cathodes in different electrolytes.

investigated the formulation of PB electrode at 85 wt% and 90 wt% active mass (in total cathode slurry) and electrode formation with and without calendering. Then, the PB electrodes were examined with different as-prepared electrolytes by using a half-cell configuration. Also, the new highly concentrated electrolyte using a poly(ethylene oxide) (PEO) matrix was developed and tested for compatibility with PB electrodes.

In general, PB cathode typically exhibited two plateaus of voltage at 3.35-3.25 V and 2.90-3.10 V, with the shoulder point at 3.2 V. Among the electrolytes, the tetraethylene glycol (TEG) dimethyl ether (DME) and PEO/DME based offers highest discharge capacity and highly symmetrical voltage profile in comparison with the others (Figure 139b/f). In addition, the cycling performance of all prepared electrolytes showed that NaFSI/DME/PEO electrolyte exhibited the highest initial discharge capacity (158 mAh g^{-1}) and capacity retention (~ 80% after 100 cycles) in comparison to others.

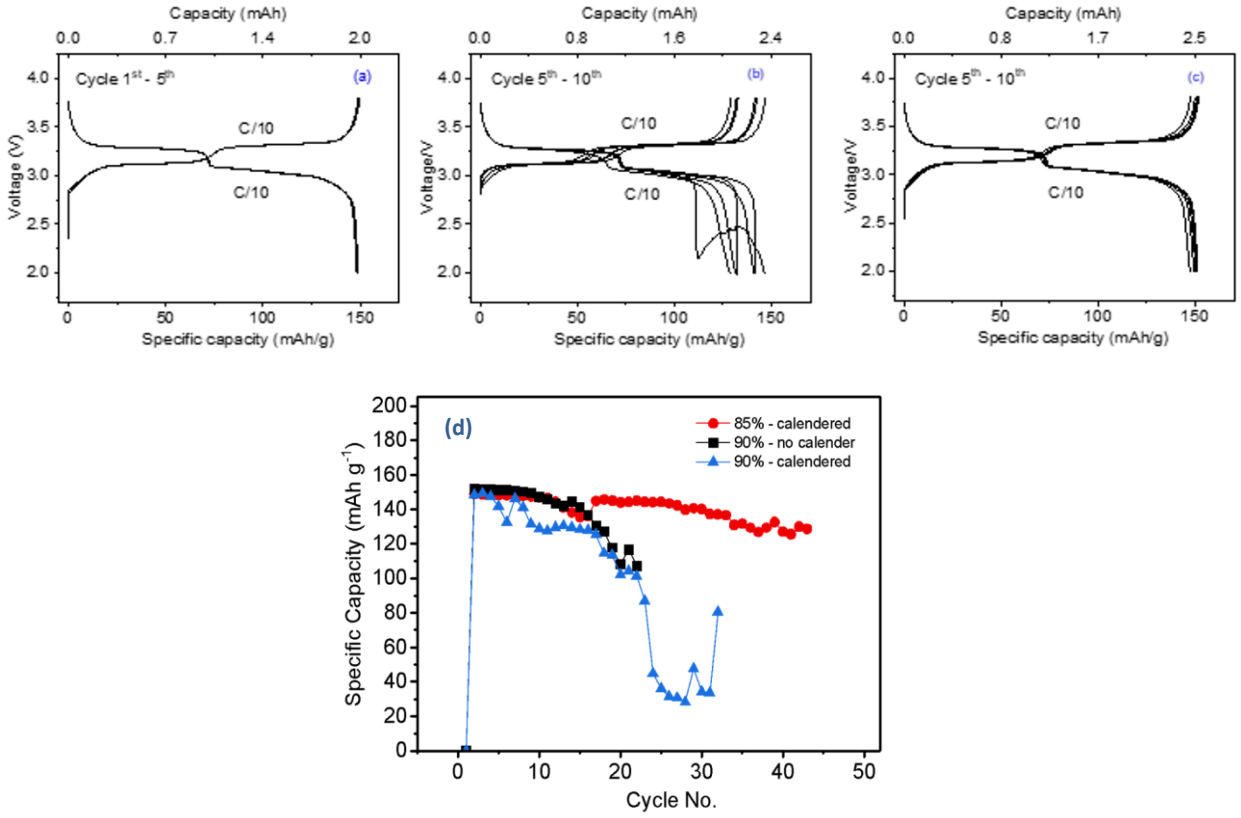

Figure 140. Charge – discharge profile of Prussian blue (PB) cathodes in half-cell with sodium metal at different percentage of active mass: (a) 85% active material, calendering electrode; (b) 90% active material, calendering; (c) 90% active material, non-calendering electrode, electrolyte of 1.2 M $NaPF_6$ in TEGDME 5 wt% TTE. (d) Cycling performance of different PB cathodes, loading capacity: 1.5-2.0 mAh/cm^2.

The variation of PB active material percentage in the slurry was also studied (Figure 140). It could be observed that the 90% PB active material induced a more dramatic capacity drop than the 85% active material due to the high oxidation rate of electrolyte on the electrode surface. The calendering and non-calendering electrodes exhibited fast capacity decline, only after 20 cycles. The increase of active material to 90 wt% requires a very stable electrolyte to stabilize long-cycling performance.

Patents/Publications/Presentations

The project has no patents, publications, or presentations to report this quarter.

Innovation Center for Battery500
(Jun Liu, Pacific Northwest National Laboratory; Yi Cui, Stanford University)

Project Objective. The overall goal of the consortium is to increase the energy density of advanced lithium batteries to beyond what can be achieved in today's state-of-the-art Li-ion batteries. The Battery500 Consortium aims to increase the specific energy (up to 500 Wh kg^{-1}) and achieve 1,000 charge/discharge cycles, with cost reduction of the cells to significantly less than $100 per kWh^{-1}. This goal directly addresses the U. S. Department of Energy priority to achieve a carbon-free electricity sector by 2035 and to decarbonize the transportation sector by developing and manufacturing the next-generation, high-energy, low-cost batteries to enable a wide deployment of electric vehicles (EVs) in the marketplace.

Project Impact. Battery500 will develop next-generation lithium battery technologies that will significantly increase energy density, improve cycle life, and reduce cost. This will greatly accelerate deployment of EVs and reduce carbon emission associated with fossil fuel consumption. The consortium will utilize first-class expertise and capabilities in battery research in the United States and develop an integrated and multidisciplinary approach to accelerate development and deployment of advanced electrode and electrolyte materials in commercially viable high-energy batteries. The advances made in this consortium will also benefit improvement of current Li-ion battery technologies. This project will provide tremendous opportunities for students and scientists for battery-related training that will enhance the workforce for the United States to maintain global leadership in the battery research and development field.

Approach. This project focuses on the two most promising battery chemistries: Li-metal anode with high-voltage/high-capacity metal oxide cathodes like $LiNi_xMn_yCo_{1-x-y}O_2$ (NMC), and lithium metal with sulfur cathodes. The project focus is to design novel electrode and cell architectures to meet the 500 Wh/kg goal. The consortium will work closely with battery/material manufacturers, suppliers, and end users / original equipment manufacturers in the United States to ensure the technologies being developed by this project are well aligned with industry needs, poised for transitioning to real production, and helpful in securing the supply chain in the United States.

Out-Year Goals. The out-year goals are to improve cycle life of the Li||NMC pouch cell with 400 Wh/kg energy density and cycle life of > 200, and to fabricate and test the pouch cells with 450 Wh/kg energy density and cycle life of > 100.

Collaborations. Collaboration among consortium team members will be well coordinated by the leadership team, which also includes four keystone project leads and co-leads along with principal investigators at all member institutions. Collaboration with the community outside of this consortium and with industry will be facilitated by the executive committee and the advisory board.

Milestones

1. Initiate baseline evaluation in small-cell format for C/S chemistry. Develop single-layer pouch cell for sulfurized polyacrylonitrile (SPAN) chemistry. (Q1, FY 2023; Completed)
2. Define voltage regimes leading to least capacity loss in high-Ni NMC, using electrochemistry and thermal loss. (Q2, FY 2023; In progress)
3. Complete single-layer pouch cell fabrication and testing protocols for NMC and sulfur system and prepare for sharing with B500 and industry. (Q3, FY 2023; In progress)
4. Demonstrate feasibility of 350 Wh/kg Li-metal pouch cell with up to 800 cycles. Demonstrate 450 Wh/kg pouch cells with 250 cycles. (Q4, FY 2023; In progress)

Progress Report

Keystone Project 1: Materials and Interfaces

Comparison of Reactivities of Different Commercial $LiNi_{0.8}Mn_{0.1}Co_{0.1}$ (NMC-811) Cathodes

NMC is the baseline material for the Battery500 Consortium. This quarter, the Binghamton team evaluated the reactivities of different commercial NMC-811 cathodes through both electrochemical tests and thermal studies.

As shown in Figure 141a, the commercial NMC-811 cathodes obtained from different vendors have different particle sizes and morphologies (EcoPro versus Targray); even for the same vendor (Targray), the different batches of products provided can have different modifications. These differences impact the reactivity of the NMC-811.

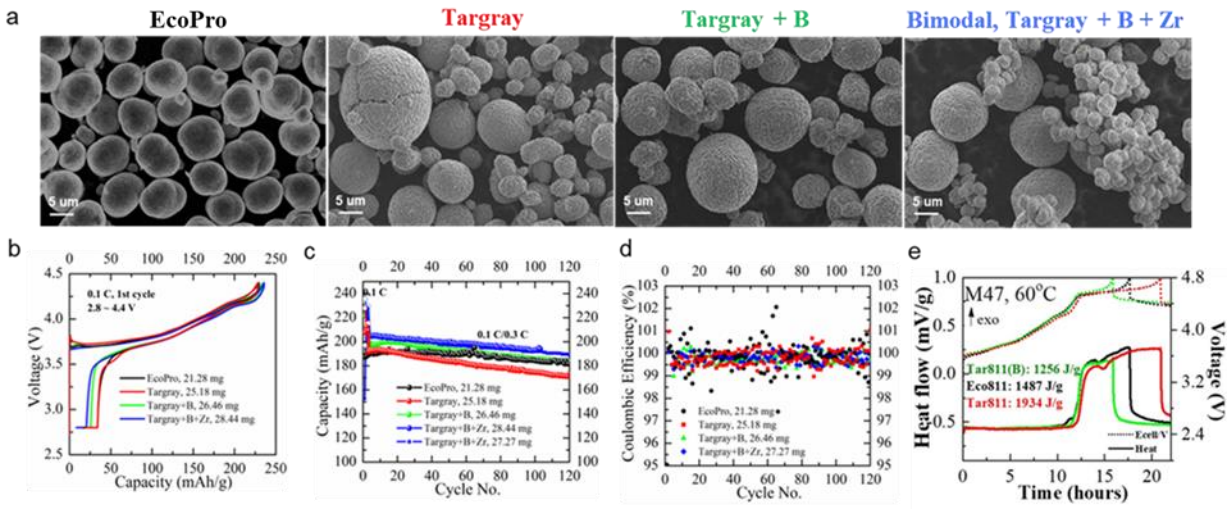

Figure 141. (a) Scanning electron microscopy images of different commercial NMC-811 cathodes. (b) 1st cycles. (c) Cycling performances. (d) Coulombic efficiencies of different commercial NMC-811 cathodes cycled between 2.8 ~ 4.4 V with the charge current of C/10 and discharge current of C/3 versus Li-metal anode tested inside coin cells with 50 µL LP30 electrolyte. (e) Heat evolved for three NMC-811s (EcoPro versus Targray versus Targray + B) with the M47 electrolyte using the aluminum protected Hohsen coin cells during the charging to 4.8 V at 60°C.

EcoPro NMC-811 has smaller primary particles and denser secondary particles (Figure 141a), which contributed to better cycling performance (Figure 141c) and thermal stability (Figure 141e) than the unmodified Targray NMC-811. However, surface modification with boron containing compound thoroughly enhanced the performance of Targray NMC-811 (Figure 141b-e): smaller first capacity loss, better capacity retention, more stable Coulombic efficiency (CE), and higher thermal stability, indicating the importance of surface modifications, which not only improves the interfacial kinetics but also suppresses the surface reactivity of the particles. The latest NMC-811 from Targray (Targray + B + Zr), which contains smaller secondary particles and B + Zr modification, gave even better electrochemical performance (Figure 141b-d). Its thermal stability is now being investigated and will be reported later.

Studies here show the critical role of particle size, morphology, distribution, and surface or bulk modification in suppressing undesired side reactions and structural degradation. Minimizing the latter two improves the capacity and capacity retention of the operating cells.

Electrolytes

This quarter, the University of Texas (UT), Austin, team investigated the mechanisms of the significantly improved cycling stability of high-Ni cathode (cobalt-free $LiNiO_2$) with the localized saturated electrolyte (LSE) that has been developed as the high-voltage electrolyte by this team. Figure 142a compares the anodic linear sweep voltammetry (LSV) measurement results from 3.0 V to 5.0 V at a scan rate of 0.05 mV s^{-1} for the LSE and the baseline LP57 electrolyte. The leakage current at 5.0 V is reduced from 2.0 (LP57) to 0.3 μA cm^{-2} (LSE). The improved high-voltage stability in the LSE can be attributed to its unique Li^+ solvation structure that is dominated by contact ion pairs and cation-anion aggregates due to the limited number of solvent molecules. Such a solvation structure can lower the highest occupied molecular orbital level of the solvent molecules, and thus improve the oxidative stability of the electrolyte.

Figure 142b compares the cycling stability of $LiNiO_2$ electrodes in the two electrolytes cycled in the voltage range of 2.8-4.4 V. The cell with LSE displays a slightly increased initial discharge capacity (223 mA h g^{-1}) compared to that with LP57 (217 mA h g^{-1}). The capacity retention after 400 cycles is greatly increased from 28% (LP57) to 85% (LSE). Figure 142c compares the charge curves at C/2, C/10, and C/100 for the two types of cells after 400 cycles. Most of the capacity is recovered by testing at low C-rates for the cell that was cycled in the LP57 electrolyte. Figure 142d further quantifies the charge capacities at low C-rates compared to the highest charge capacity during the three formation cycles. For the cell that was cycled in the LP57 electrolyte, the charge capacity at C/2 rate only retained 23% of its initial capacity, but 75% of its initial capacity at C/100 rate. The voltage plateau at 4.2 V also appears at an extremely low C rate (C/100), indicating that the kinetic barrier in the $LiNiO_2$ cathode is the major contributor to its severe capacity degradation. In comparison, for the cell tested in LSE, the capacity retention increased from 73% at C/2 rate to 92% at C/100 rate; both are significantly higher than the 23% and 75% retention for LP57 cell.

Structural degradation of the $LiNiO_2$ surface, along with the reduction of Ni^{4+} and oxygen loss, can lead to the formation of spinel-like structures and rock-salt phases during cycling, which is believed to be harmful to the overall performance of the electrode. Advanced high-angle annular dark-field scanning transmission electron microscopy (HAADF-STEM) was thus applied to investigate the surface structure of cycled $LiNiO_2$ using those two electrolytes. Five types of degraded phases were observed in the two cycled $LiNiO_2$: spinel $LiNi_2O_4$, spinel $Li_{1-x}Ni_{2+x}O_4$, spinel Ni_3O_4, rock-salt $Li_xNi_{1-x}O$, and rock-salt NiO. The distribution of these five phases on the surface of the two cycled $LiNiO^2$ particles is shown in Figure 142e-f. Figure 142g further compares the amount of the five degraded phases on the surface of the two cycled $LiNiO_2$ samples. The results indicate that the LP57 electrolyte promotes the formation of NiO and Ni_3O_4 on the surface of $LiNiO_2$, while the LSE helps in forming $LiNi_2O_4$ on the surface of the electrode. Compared to NiO and Ni_3O_4, $LiNi_2O_4$ with direct Ni-Ni interaction along the shared octahedral edges and no nickel in the tetrahedral sites of the three-dimensional (3D) spinel lattice has much higher Li^+-ion and electronic conductivity (Table 6). More importantly, Figure 142 shows that the conductive $LiNi_2O_4$ phase is distributed on the top surface of the cycled $LiNiO_2$ particle using the LSE (Figure 142f), while it is buried under the insulating NiO and Ni_3O_4 phases on the surface of the electrode with the LP57 electrolyte (Figure 142e). The quantity and distribution of these degraded phases on the surface of the two samples explain why the kinetics are better maintained in the cycled $LiNiO_2$ cell using the LSE (Figure 142c-d).

Table 6. Properties of phases formed on the surface of $Li_{1-x}NiO_2$.

Phase	$Li_{0.15}NiO_2$	$LiNi_2O_4$	Ni_3O_4	NiO
Structure	Layered	Spinel	Spinel	Rock salt
Li^+ Conductivity	Good	Excellent	Poor	Poor
Electronic Conductivity	Good	Excellent	Fair	Poor
Nickel Valence	+3.85	+3.5	+2.67	+2

Intergranular cracking in secondary particles has been considered a major cause of long-term capacity fade in high-Ni cathodes. Cross-section scanning electron microscopy (SEM) images were taken to study the effect of LP57 electrolyte and LSE on the intergranular cracking of cycled $LiNiO_2$ electrodes. Figure 142h-i shows the images of fully discharged $LiNiO_2$ electrodes after 400 cycles using these two electrolytes. Large cracks (red arrows) appear in almost all the imaged $LiNiO_2$ secondary particles when tested in the LP57 electrolyte (Figure 142h), while the cracks were limited to the edge regions of the particles with a short length when tested in the LSE (Figure 142g). The representative cracking of these images was also confirmed by the SEM images at other locations (not shown here). Therefore, the LSE suppresses intergranular cracking in the $LiNiO_2$ electrode during long-term cycling, correlated to the lower surface degradation shown in the STEM (Figure 142e-f). It is worth noting that the $LiNiO_2$ electrode tested in the LSE went through more repeated H2 - H3 phase transition at the high-voltage region than the electrode tested in the LP57 electrolyte during the continuous cycling. The reduced intergranular cracking in the $LiNiO_2$ electrode with the LSE indicates that there are other dominant factors to the cracking process besides the repeated H2 – H3 phase transition. These factors could be the improved surface stability and reaction homogeneity of the

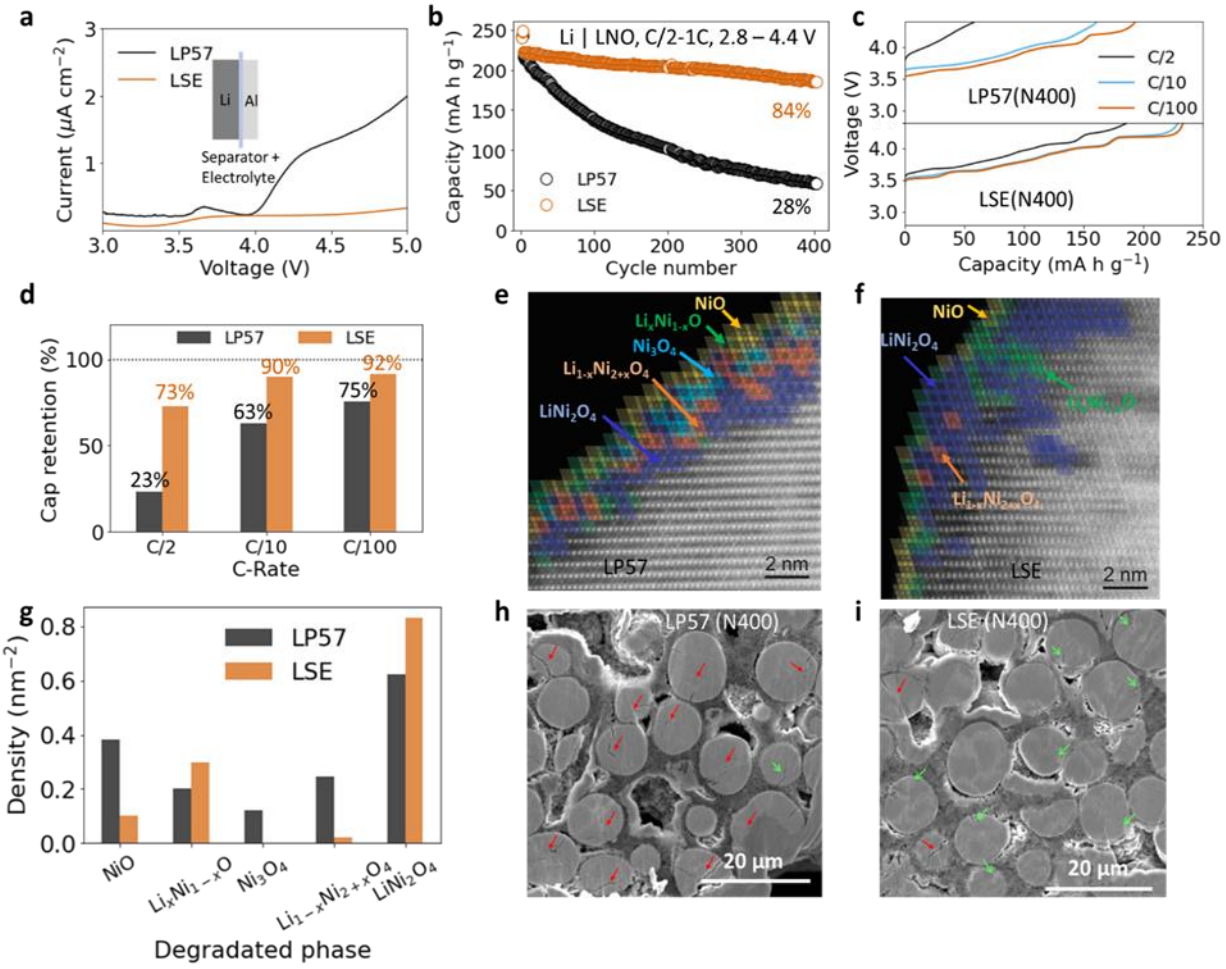

Figure 142. (a) Linear sweep voltammetry of Li|Al cells with LP57 electrolyte and LSE; the inset shows the components within the test cell. (b) Cycling performances of Li|$LiNiO_2$ cells at room temperature with the listed cycling parameters. (c) Charge curves at different C-rates after 400 cycles and (d) the corresponding capacity retention compared to the maximum charge capacity during the formation cycle. (e-f) High-angle annular dark field – scanning transmission electron microscopy images of cycled $LiNiO_2$ electrode with the (e) LP57 electrolyte and (f) LSE. Surface-degraded phases are identified and labeled. The diamonds represent the different atomic arrangements in each material based on the intensity profiles for those areas. Anything not indicated with a diamond has the standard layered oxide structure of $Li_{1-x}NiO_2$. (g) Semi-quantitative densities of the various atomic arrangements found in each sample. (h-i) Cross-section scanning electron microscopy images of cycled $LiNiO_2$ cathodes with the (h) LP57 electrolyte and (i) LSE. Green arrows and red arrows are used, respectively, to highlight small cracks (smaller than the radius of the particle) and large cracks (larger than the radius of the particle) within each secondary particle.

$LiNiO_2$ electrodes tested in the LSE. A similar phenomenon has been found in recent literature, which reported that advanced electrolytes reduce intergranular cracking in high-Ni cathodes during cycling. Therefore, the intergranular cracking in high-Ni layered oxide cathodes is affected by multiple competitive factors, and the team believes that improving surface stability is an effective way to inhibit the process during extended cycling.

The Pennsylvania State University (PSU) team continued to investigate the electrochemical performance of the Li||NMC-811 full cell under the conventional electrolyte E1, fluorinated saturated electrolyte (FSE), and fluorinated saturated electrolyte with additives (the AFSE, which is based on FSE with 0.1 wt% additive). The AFSE electrolyte is a new electrolyte formulation with solvents, salts, and additives optimized to achieve the target CE of 99.5% and was introduced in the last quarter. Figure 143a indicates that the FSE and AFSE significantly improved the cycling stability of NMC-811 with a cutoff voltage of 4.3 V. All cycling data were collected with CR- 2016 type coin cells with a high loading cathode of 4 mAh cm^{-2} (that is, 3.14 mAh/electrode) a 50-µm thin Li-metal anode, and a lean electrolyte usage of 5 µL mAh^{-1}. The data suggest that the NMC-811 cell with the FSE shows an initial discharge capacity of 2.78 mAh at 0.5C and retains 80% of its initial capacity after 265 cycles. AFSE enabled significantly improved cycling stability, delivering an 80% capacity retention of 2.66 mAh after 280 cycles. The average CE was nearly 99.9% for the cells tested with FSE and AFSE. By comparison, using the baseline electrolyte of E1, the cell decayed quickly and reached 70% of its original capacity of 2.79 mAh after only 50 cycles. The average CE was only 99.0% in the first 50 cycles (Figure 143a). A full cell with ultra-high loading cathode of 5 mAh g^{-1} (that is, 4 mAh/electrode) with leaner electrolyte condition of only 4 µL mAh^{-1} was conducted to further evaluate the advanced electrolyte under more practical conditions (Figure 143b). The cell showed initial capacity of ~ 4 mAh and a capacity retention of 80% after 120 cycles. The rate performance test (Figure 143c) shows the cell using the AFSE has higher capacity than the cell with E1 electrolyte and recovered to original capacity at 0.1C after a fast discharge at 3C. The improved rate performance could be attributed to the reduced interfacial charge-transfer resistance that is generally observed in localized high-concentration electrolyte (LHCE). Thus, it was crucial to add a fluorinated diluent to promote the Li^+ kinetics in the electrolyte. A Li-metal pouch cell was then assembled and tested toward achieving high energy density, with a high areal capacity (4.0 mAh cm^{-2}) NMC-811 cathode, a 50-µm thin Li-metal anode, and a lean electrolyte (3.0 g Ah^{-1}) (Figure 143d). The pouch cell demonstrated unprecedented cycling stability with 93% capacity retention after 30 cycles; the testing continues.

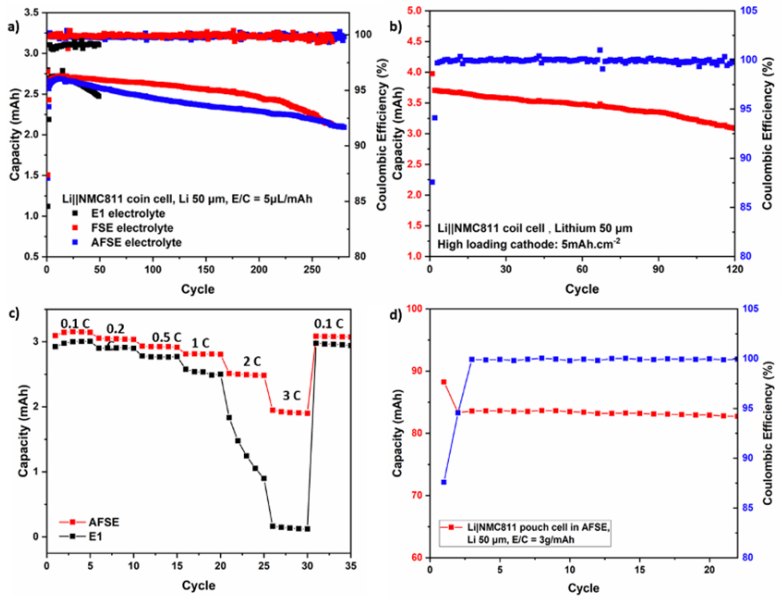

Figure 143. (a) Electrochemical performance of the Li||NMC-811 full cell tested in different electrolytes. (b) Electrochemical performance of the Li||NMC-811 full cell in AFSE at high loading cathode. (c) Rate capacity of the NMC-811||Li coin cells tested in different electrolytes. (d) NMC-811||Li pouch cell.

To study the solid electrolyte interphase (SEI) compositional difference between the three electrolytes, X-ray photoelectron spectroscopy (XPS) was performed on the cycled Li-metal anode after 10 cycles. As shown in Figure 144, the SEI that formed in the conventional electrolyte E1 contained a high content of $Li–CO_2^-$ (55 eV in the lithium 1s spectrum), $R–OCO_2R$ (289.8 eV in the carbon 1s spectrum) derived from fluoroethylene

carbonate (FEC), and $Li_xP_yOF_z$ (686.9 eV in the fluorine 1s spectrum). In contrast, for samples using FSE or AFSE electrolytes, the percentages of $Li_xP_yOF_z$ and $Li–CO_2^-$ were markedly lower, whereas the percentages of LiF and R-OCO_2R were significantly higher. LiF has been considered an excellent SEI component to suppress lithium dendrite growth and promote uniform lithium deposition owing to its high interfacial energy on lithium metal and its low surface barriers for Li-ion transport. The high content of LiF from AFSE electrolytes may be the main reason in the formation of stable SEI to deliver improved performance stability of Li-metal batteries over long-term cycling.

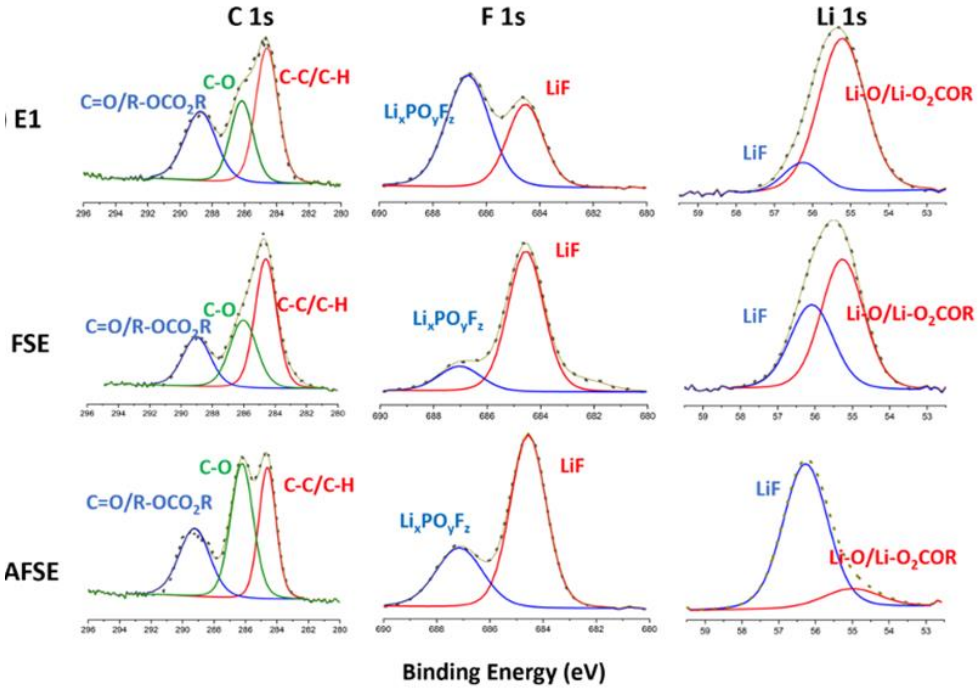

Figure 144. X-ray photoelectron spectroscopy characterization of Li-metal anodes after 10 cycles in E1, FSE, and AFSE.

The Pacific Northwest National Laboratory (PNNL) team continuously improves the performance of Li||NMC-811 (4 mAh cm^{-2}) cells by using a new diluent (DB) in their LHCE. The LHCE electrolytes using new diluent DB and different solvent to diluent ratios were named as LHCE-1 [lithium bis(fluorosulfonyl)imide (LiFSI) : 1,2-dimethoxyethane (DME) : DB = 1:1.25:2), LHCE-2 (LiFSI:DME:DB = 1:1.15:3), and LHCE-3 (LiFSI:DME:DB = 1:1.1:3). First, the average lithium CE of these electrolytes was measured in Li||Cu cells by using the Battery500 protocol. As shown in Figure 145a, all three electrolytes demonstrate a high average lithium CE of 99.4% to 99.6%, indicating the high reversibility of lithium deposition and stripping on the lithium anode. To evaluate the oxidation stability of the electrolytes, the Li||$LiMn_2O_4$ (LMO) cell was used. The potential was scanned from open circuit voltage (OCV; ~ 2.9 V) to 5.0 V with a scan rate of 0.05 mV s^{-1} in the LSV test. Figure 145b shows the delithiation process of LMO in the potential range of 3.9 V to 4.4 V, and the slight increase in current after 4.5 V could be associated with the oxidation process of the electrolytes on the LMO electrode. These results suggest that all as-prepared electrolytes with the new diluent could be stable up to 4.5 V and compatible with the Li-metal anode. The electrolytes were further evaluated in the Li||NMC-811 coin cell system (Al-Clad CR2032, MTI) in a voltage range of 2.8 V to 4.4 V. The cells were performed two cycles at C/10 to stabilize SEI formation, and then cycled at C/10 charge and C/3 discharge using different LHCEs. All the cells show similar voltage profiles during the formation cycle, and high discharge capacities of 194 mAh g^{-1}, 191 mAh g^{-1}, and 191 mAh g^{-1} for LHCE-1, LHCE-2, and LHCE-3 were obtained, respectively, as shown in Figure 145c. Figure 145d shows the cycling performance of the three electrolytes, which exhibit a capacity retention of > 90% after 195 cycles; all cells are still running at the time of this report. Notably, the LHCE-1 reveals a higher capacity at the initial cycles, but slightly lower capacity at the later cycles, suggesting that the solvent to diluent ratios could affect the cycling stability of the LHCE in Li||NMC-811 cells.

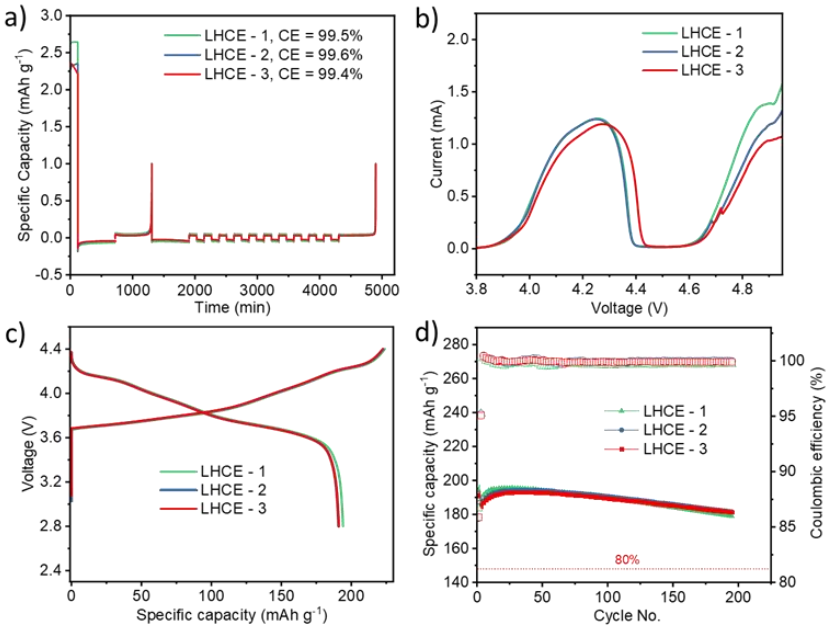

Figure 145. Electrochemical performance of Li||NMC-811 cells with different localized high-concentration electrolytes. (a) Lithium plating/stripping curves in Li||Cu cells. (b) Linear sweep voltammetry curves with scan rate 0.05 mV s^{-1} from open circuit voltage (~ 2.9 V) to 5.0 V. (c) 1st cycle charge/ discharge profiles at C/10. (d) Cycling performance of cells with charging at C/10 and discharging at C/3. Lithium metal (50-µm thick) on copper foil and 75 µL electrolyte were used for coin cells.

The University of Maryland (UMD) team continues studies on the electrolyte designing approach to obtain robust ceramic LiF-rich SEI to suppress lithium dendrite growth and enable long cycle life for Li-metal batteries. During a Battery500 biweekly meeting last quarter, the team reported a new ether-based electrolyte of 2.0 M LiFSI-D1 that could achieve a high lithium CE of 99.7%. Figure 146 summarizes the electrochemical performance of ether-based 2.0 M LiFSI-D1 electrolyte. Through molecule design, the anodic stability of ether electrolytes was extended to > 5.0 V (Figure 146a) with no sacrifice on anode stability. As shown in Figure 146b, compared to the same concentration DME electrolyte, the 2.0 M LiFSI-D1 electrolyte can effectively passivate the copper surface, demonstrating a LiF-rich SEI formation and low reduction potential in this new electrolyte through molecular design approach. High lithium CE of 99.53% and 99.68% was achieved at a capacity of 1.0 mAh cm^{-2} and current of 0.5 mA cm^{-2} in both full plating/stripping (Figure 146c) and lithium reservoir conditions (Figure 146d), respectively. The consistency with both Battery500 Li-Cu cycle protocols further confirms the superior reversibility of 2.0 M LiFSI-D1 electrolyte for smooth lithium plating/stripping. After demonstrating the lithium reversibility, a controlled lithium metal deposited on copper foil as anode (20 µm, ~ 4 mAh cm^{-2}) was paired with a high energy cathode $LiNi_{0.8}Co_{0.15}Al_{0.05}O_2$ (NCA) for full-cell test. Figure 146e-f demonstrates > 400 long cycles of the coin cell at 0.3C with a high cycle CE of > 99.9% and high capacity retention. The 2.0 M LiFSI-D1 electrolyte is further tested under harsh conditions in a large pouch cell with an increased areal capacity to 4.0 mAh cm^{-2}. As shown in Figure 146g-h, the 100 mAh laboratory-made pouch cell also guarantees a smooth cycle over 100 cycles with CE of > 99.9%, verifying the high compatibility of their designed electrolyte to high-voltage NCA‖Li full batteries. The discharge voltages of NCA at the 5th, 50th, and 100th cycles overlap well with each other, suggesting no significant structural change of the material nor continuous build-up of the cathode electrolyte interface (CEI) (Figure 146h). The initial capacity loss in the full cell (Figure 146h, black line) was probably caused by Li^+ consumption for SEI formation. The capacity loss is most rapid for the first three formation cycles and gradually slows down in the subsequent cycles at 0.3C. Full characterization of the 2.0 M LiFSI-D1 electrolyte will be performed next, and the mechanism of reversible lithium deposition and stripping will be studied using a series of surface characterization techniques.

Due to vulnerability toward high voltage of the ether molecule, especially in the presence of high oxidation state transition metal (TM, such as Ni^{2+}, Mn^{2+}, and Co^{2+}), the ether-based electrolyte is not suitable for the NMC-811 cathode cell. On the other hand, ester-based solvents, similar to the carbonate solvents used in conventional electrolytes, are usually anodic stable to high voltage up to 5 V. The team has designed and synthesized a new ester-based molecule, aiming at high lithium CE and high voltage compatibility to NMC-811 cathode. The electrochemical performance of the M1 electrolyte (2.0 M LiFSI dissolved in the new ester-based solvent) in both the lithium anode and NMC-811‖Li full cells was preliminarily investigated (Figure 147).

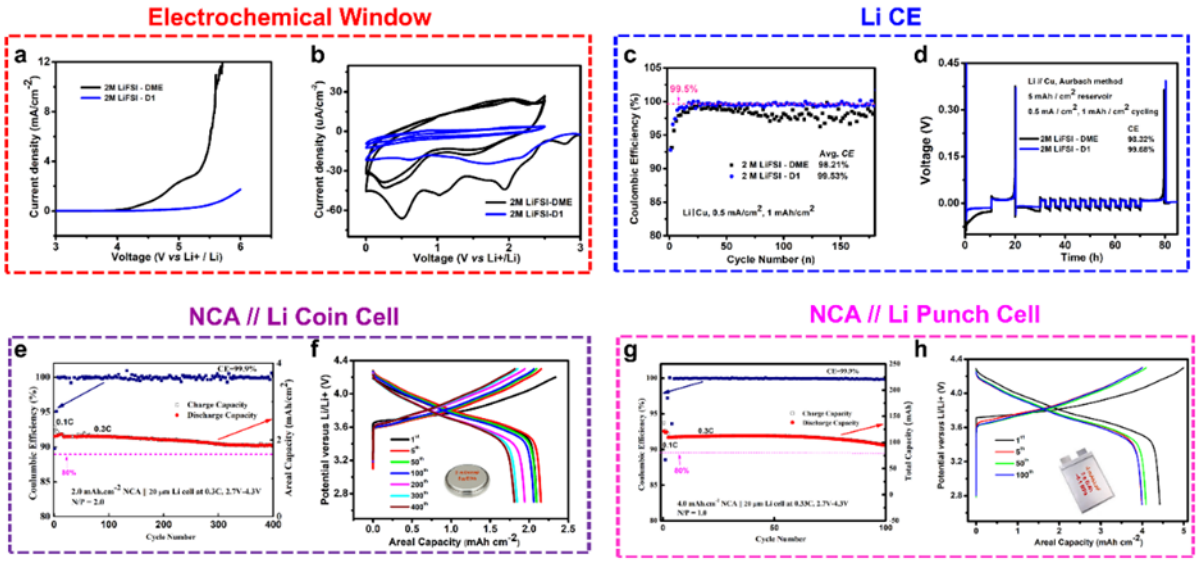

Figure 146. Electrochemical performance of 2.0 M LiFSI-D1 electrolyte. (a-b) Electrochemical window compared with 2.0 M LiFSI-DME electrolyte tested with Al||Li cell (a), and Cu||Li cell (b); the scan rate is 0.5 mV/s. (c-d) Lithium stripping and plating Coulombic efficiency under full plating/stripping conditions (c) and with 5 mAh lithium reservoir (d); the cycle current is 0.5 mA cm^{-2}, and capacity loading is 1 mAh cm^{-2}. (e-f) Full-cell NCA||Li performance with N/P ratio of 2, areal capacity of 2.0 mAh cm^{-2}. (g-h) 100 mAh homemade pouch-cell performance with NCA areal loading of 4.0 mAh cm^{-2}.

Under full discharge/charge conditions, reversible lithium deposition and stripping on copper foil can be realized in M1 electrolyte with a high initial CE of 94.8% at a current density of 0.5 mA.cm^{-2} and capacity of 1 mAh cm^{-2} (Figure 147a). At a higher loading of 2 mAh cm^{-2} and current density of 1 mA.cm^{-2}, the initial CE was improved to 97.1%, and the cycle CE ramps to 99.1% in 5 cycles with an average CE over 99.7% in 127 cycles (Figure 147a). The 4.5 mAh cm^{-2} NMC-811‖20-µm-Li full cell was first tested in a coin-cell configuration (Figure 147c-d). The cell was charged to 4.4 V and discharged to 2.8 V according to the Battery500 protocol. A two-cycle formation at 0.1C was given before the 0.3C long cycles. The discharge voltages of NMC-811 at the 5th, 50th, and 100th cycles overlap well with each other, indicating stable interfaces formed on both lithium anode (SEI) and NMC-811 cathode (CEI). The cell runs for > 150 cycles so far with no obvious capacity decays.

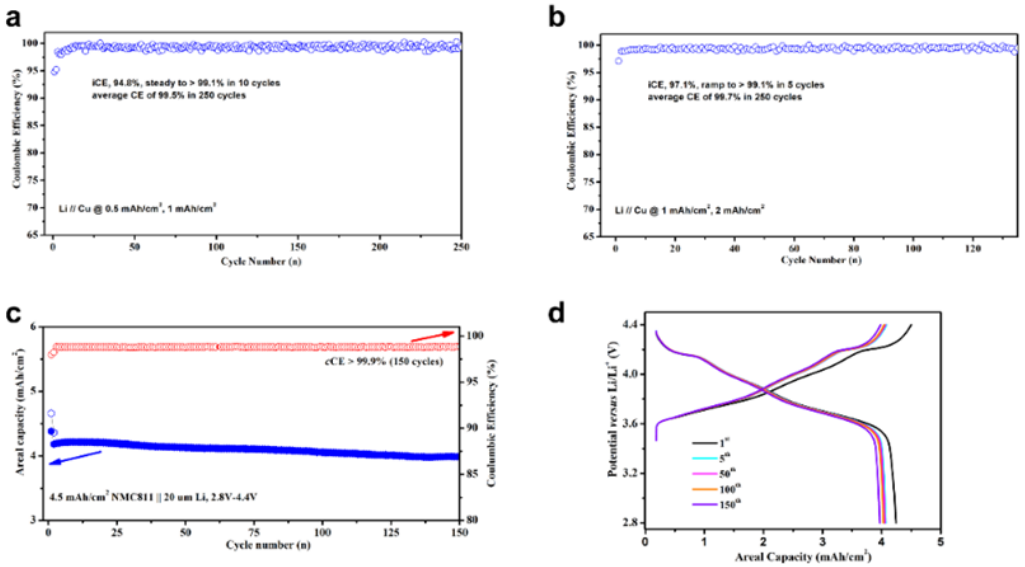

Figure 147. Electrochemical performance of M1 electrolyte. (a) Lithium stripping and deposition on copper foil at 0.5 mA cm^{-2} for 1 mAh cm^{-2}. (b) Lithium stripping and deposition on copper foil at 0.5 mA cm^{-2} for 2 mAh cm^{-2}. (c) Performance of 4.5 mAh cm^{-2} NMC-811//20 µm lithium coin cell cycled at 1.5 mA cm^{-2}. (d) Voltage profiles of lithium coin cell at various charge and discharge cycles.

The UT Austin team this quarter investigated the mechanism of organopolysulfide-based additives to stabilize Li-metal anode for use in Li-S batteries. The Li-metal stripping/plating performance in a Li||Ni cell with 1 M LiTFSI and 0.2 M $LiNO_3$ in DME and 1,3-dioxolane electrolyte using either lithium polysulfide (Li_2S_8, LiPS) as an additive or diallyl polysulfide (DAPS) as an additive is shown in Figure 148a, along with the corresponding SEM images. It is evident that the Li-metal anode cycles with a CE of 99.16% in the DAPS-containing electrolyte, which is higher than that of the LiPS-containing electrolyte that cycles with only 96.15% CE. Consequently, the Li-metal morphology is smoother and denser in the presence of DAPS. Characterization of the anode through techniques like XPS reveals that the presence of organic thiolates in the SEI stabilizes and protects the Li-metal anode.

To investigate the origin of the stabilizing effect of a thiolate-rich SEI, density functional theory (DFT) calculations were performed. Li_2S and CH_3SLi species were placed on top of a lithium slab and left to equilibrate. The potential difference between the slab with the species of interest and a pure lithium slab was calculated and is presented in Figure 148b. In the potential difference maps, the blue color indicates increased electron density, and the red color indicates the reduction of electron density. In the case of sulfide-rich SEI, strong electric field distortions exist through four layers of lithium atoms. When looking at the top-down perspective, large, widespread distortions are observed. With this non-uniformity, several electron-rich areas can act as the preferred site for the reduction of Li^+ to lithium metal during the plating process, thus increasing the propensity for dendrite formation. On the contrary, in the case of thiolate-rich SEI, the distortions are minimal after two layers of lithium atoms. Even the top-down perspective shows only minor potential differences. This arises as the covalent C-S bond withdraws most of the electron cloud away from sulfur, thus reducing the electrons withdrawn from the lithium slab. The improved uniformity of the electric field minimizes the potential to form dendrites.

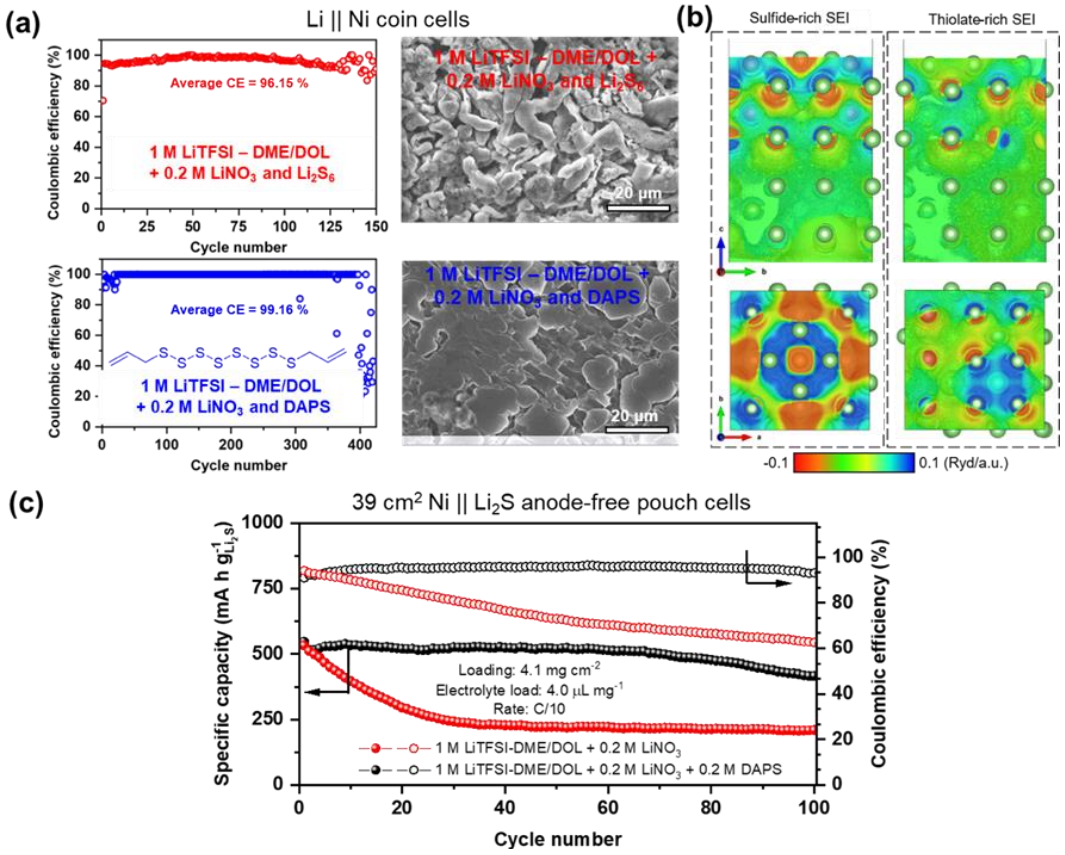

Figure 148. (a) Performance of Li||Ni symmetric cells with an electrolyte containing lithium polysulfide or diallyl polysulfide (DAPS) as an additive, along with the corresponding scanning electron microscopy images. (b) Visualization of the potential difference along the depth and on the surface of a lithium slab with a sulfide SEI and with a thiolate SEI. (c) Long-term cycling stability of anode-free Ni||Li_2S pouch cells.

As DAPS already consists of polysulfides, the Li-S system is suited to test the efficacy of this additive by studying the performance in anode-free Ni||Li_2S cells. As the anode-free systems start with a stoichiometric amount of lithium, the cycle life mirrors the effectiveness of lithium cycling. Pouch cells with a Li_2S loading of 4.1 mg cm^{-2} and a lean electrolyte amount of 4.0 µL mg^{-1}, paired with a bare nickel foil as the current collector, were fabricated and cycled at a C/10 rate. Both cells show identical material utilization in the first cycle (Figure 148c). However, in the control cell, the capacity drops by 50% in just 24 cycles and can retain only 39% of its initial capacity by 100 cycles. In sharp contrast, the DAPS-bearing cell can retain 76% of its initial capacity after 100 cycles. The monotonic drop in CE from 94.2% to 62.2% in a span of 100 cycles for the control cell showcases the ineffectiveness of sulfide-rich SEI in protecting the lithium metal. Meanwhile, the CE with DAPS is stable throughout, with an average of ~ 96%, showcasing the robustness of the thiolate-rich SEI. This makes organopolysulfide additives the ideal potential candidate for lithium metal protection in the Li-S system.

Current-Dependent Lithium Plating Morphology in the Presence of Residual SEI

Previously, the Stanford University team observed a strong dependence of Li||NMC-811 (4.5 mAh cm^{-2}) cycle life on charging current densities in three types of weakly solvating fluoroether electrolytes of 1 M LiFSI in fluorinated 1,4-dimethoxylbutane (FDMB), 1.54 M LiFSI in 1:3.6 (v/v) DME : (1,1,2,2-tetrafluoroethyl-2,2,3,3-tetrafluoropropyl ether) TTE, and 1 M LiFSI in 1:3 (v/v) 1,2-diethoxyethane (DEE) : fluorinated 1,4-diethoxybutane (FDEB), where soft shorting was observed above 2-5.2 mA cm^{-2}. This quarter, they further investigated the morphology dependence of lithium and residual solid electrolyte interface (rSEI) on plating current density. Thin lithium (50-µm thick) half cells were constructed with a piece of thick lithium as the counter electrode in DEE-FDEB electrolyte. All cells were activated at 0.4 mA cm^{-2} and 4 mAh cm^{-2} for 2 cycles, followed by 10 cycles at 0.4 mA cm^{-2} or 4 mA cm^{-2} plating current densities to form rSEI (low-current or high-current formation). In the final step, 0.2 mAh cm^{-2}, 0.5 mAh cm^{-2}, or 1 mAh cm^{-2} capacity lithium was plated at 4 mA cm^{-2} (high-current plating) or 0.4 mA cm^{-2} (low-current plating). These final plating capacities were less than 25% of the cycling capacity, which enabled the observation of initial lithium growth by SEM. The results of such morphology dependence on current profiles are shown in Figure 149.

Under the low-current formation and low-current plating condition, large lithium grains were observed, which are separated by rSEI (Figure 149a-c). Elemental mapping by energy dispersive X-ray spectroscopy (EDS) confirmed the different regions of lithium and rSEI, which are marked by yellow and green arrows, respectively, in Figure 149b. The lithium plating morphology observed here validated their previous hypothesis that in some weakly solvating fluoroether electrolytes, the plated lithium first grew through the porous rSEI layer before forming the typical pancake-like morphology on top of the rSEI. Under the slow-charging condition here, a minimum of 25% of cycled lithium (1 out of 4 mAh cm^{-2}) was surrounded by rSEI as evidenced by the lack of lithium plating above rSEI in Figure 149c.

Under the high-current formation and high-current plating condition, a very different surface morphology was observed (Figure 149d-f). The regions of lithium and rSEI were confirmed by EDS. A compact rSEI structure was formed (Figure 149d). At 0.2 mAh cm^{-2} deposition capacity, scarce and inhomogeneous lithium nucleation was observed on top of rSEI (Figure 149d). As deposition capacity increased, the lithium grain size continued to increase (Figure 149d-f), but remained smaller than those in Figure 149a-c. Importantly, unlike the morphology observed under the slow-charging condition, the plated lithium was not surrounded by rSEI after merely 0.2 mAh cm^{-2} capacity under the fast-charging condition. Since SEI should be electrically insulating, there must be a small amount of lithium growth within the rSEI (that is, < 0.2 mAh cm^{-2} or < 5% of cycling capacity) connecting the uncycled lithium underneath rSEI and the plated lithium above rSEI. Such scarce and dispersed points for lithium deposition led to significant inhomogeneity and hotspots for lithium growth.

As a control experiment, they formed rSEI at 4 mA cm^{-2} followed by plating lithium at 0.4 mA cm^{-2} (high-current formation, low-current plating) (Figure 149g-i) to investigate the relative contributions from current density and rSEI structure to lithium morphology. Compared to Figure 149d-f (high-current formation, high-current plating), the amount of lithium plated within rSEI was higher in Figure 149g-i, as evidenced by the lower coverage of lithium on top of rSEI. In addition, the lithium grain size was larger in Figure 149g-i.

These differences validated that the upward anisotropic growth of lithium is favored under higher current densities even in the presence of the same rSEI. Compared to the lithium morphology in Figure 149a-c (low-current formation, low-current plating), the plated lithium was less homogeneous and grew well above rSEI in Figure 149g-i. Therefore, the rSEI structure formed under high current densities can indeed guide undesirable lithium deposition morphology even after switching to lower plating current densities. This leads to the inhomogeneous electrochemically active surface for further lithium deposition above rSEI.

Next quarter, the team will investigate the current-dependent formation process of lithium and rSEI morphology. The knowledge gained from this study will guide design of electrolytes to enable fast-charging Li-metal batteries.

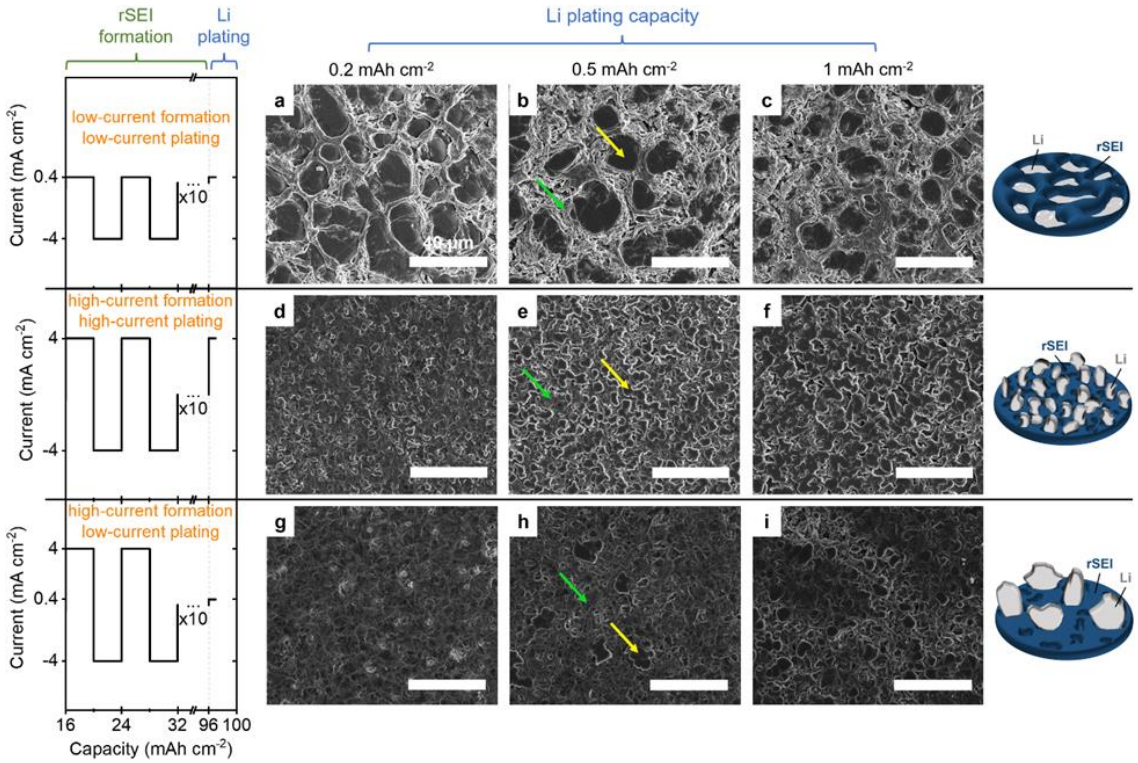

Figure 149. Scanning electron microscopy images of lithium plating morphology on 50-µm lithium electrode at various current densities and areal capacities in DEE-FDEB electrolyte. The residual solid electrolyte interface (rSEI) was formed by 10 cycles at either 4 mA cm^{-2} plating and stripping (high-current formation) or 0.4 mA cm^{-2} plating and 4 mA cm^{-2} stripping (low-current formation) for 4 mAh cm^{-2}. In the final step, 0.2 mAh cm^{-2}, 0.5 mAh cm^{-2}, or 1 mAh cm^{-2} capacity was plated at 4 mA cm^{-2} (high-current plating) or 0.4 mA cm^{-2} (low-current plating). The applied current profiles for rSEI formation and final lithium plating are shown on the left. The capacities of final lithium plating are labeled by columns on the top. Yellow and green arrows indicate lithium and rSEI, respectively. The scale bars are 40 µm. The schematics on the right illustrate the top surface morphology of lithium and rSEI.

Theoretical and Computational Analysis on Interfacial Evolution

The Texas A&M University team conducted the theoretical and computational analysis, which provides new insights into the CEI interactions on interfacial evolution. Electrolyte oxidative deprotonation reactions result in proton insertion in surface layers, and nickel reduction from +3 to +2 with subsequent Ni-O bond weakening. Ni^{2+} cations migrate to lithium vacancies initiating structural degradation. It is shown that proton insertion yields water and HF via salt hydrolysis, and nickel cation dissolution. Current studies address the effect of Ni-ion migration to the anode on the SEI formation on lithium metal.

The team is also addressing the thermal-driven degradation pathways of the SEI on Li-metal electrodes via first-principles methods in collaboration with experimentalists from the Binghamton University team. First, the SEI growth is modeled using a hybrid *ab initio* and reactive molecular dynamics simulation scheme that allows

the formation of extended organic and inorganic phases within the SEI along with the dissolution of remanent lithium metal into Li^+ ions. The simulation scheme produces an SEI structure that reproduces its main structural features. Next, they follow the SEI thermal evolution through *ab initio* molecular dynamics (AIMD) simulations following a linear heating ramp. Preliminary results from the team's simulations indicate that the destruction of the organic SEI precedes lithium leaching, and the inorganic SEI sustains the induced thermal stresses enforced within their achievable simulation window. Collaboration with the Binghamton research group is fundamental for fine-tuning the SEI composition. XPS and differential scanning calorimetry (DSC) data measured on SEI layers grown on lithium metal at OCV conditions allow them to modulate the electrolyte-to-anode ratio in their simulation cells to reproduce the SEI's structural and compositional features while leaving some unreacted lithium metal, which is essential to follow the SEI/Li-metal interface response in high-temperature regimes.

Highlights of Keystone Project 1

The highlights for this quarter are as follows:

- The Binghamton University team compared the reactivities of different commercial NMC-811 cathodes and found the critical role of the particle size, morphology, distribution, and surface or bulk modification, in suppressing undesired side reactions and structural degradation of NMC-811.
- The UT Austin team further investigated the mechanisms using advanced high-voltage electrolyte LSE to significantly improve the cycling stability of high-Ni cathode ($LiNiO_2$). The LSE not only enables the $LiNiO_2$ electrodes to show a better cycling and rate performance, but also helps to mitigate the surface structural degradation and intergranular cracking in secondary particles of the $LiNiO_2$ cathode. In addition, an organopolysulfide-based additive DAPS was developed to stabilize the Li-metal anode for use in Li-S batteries.
- The PSU team continued to investigate the electrochemical performance of new electrolyte AFSE at more practical conditions. The Li||NMC-811 coin cell using the AFSE can run 280 cycles with 80% capacity retention under a high areal capacity cathode (4.0 mAh cm^{-2}). Even at an ultra-high loading cathode of 5.0 mAh cm^{-2} and leaner electrolyte condition of only 4 μL mAh^{-1}, the cell showed a capacity retention of 80% after 120 cycles. The XPS studies reveal that the LiF-rich SEI from AFSE electrolytes may lead to stable SEI, enabling the Li-metal batteries with superior cycle and rate performance.
- The PNNL team developed a new diluent DB for the LHCE electrolytes to continuously improve performance of Li||NMC-811 (4 mAh cm^{-2}) cells. The three electrolytes LHCE-1/2/3 with different solvent ratios demonstrate a high average lithium CE of 99.4 – 99.6%, stable up to 4.5 V and compatible with the Li-metal anode. The Li||NMC-811 coin cells using all three LHCE electrolytes exhibit capacity retention of > 90% after 195 cycles.
- The UMD team developed a new ether-based electrolyte of 2.0 M LiFSI-D1 that could achieve a high lithium CE of 99.7%. To address the vulnerability toward high voltage of the ether molecule, especially in the presence of high oxidation state TM (such as Ni^{2+}, Mn^{2+}, and Co^{2+}), the ester-based electrolyte, anodic stable to high voltage up to 5 V, was designed and synthesized. The electrochemical performance of the ester-based electrolyte in both the lithium anode half-cells and NMC-811‖Li full cells was preliminarily investigated, showing stable interphases formed on both lithium anode (SEI) and NMC-811 cathode (CEI) in 150 running cycles.
- The Stanford team investigated current-dependent lithium plating morphology in the presence of rSEI. SEM images of lithium plating morphology on 50 μm lithium electrode at various current densities and areal capacities in DEE-FDEB electrolyte were studied. It is found that upward anisotropic growth of lithium is favored under higher current densities, even in the presence of the same rSEI. The rSEI structure formed under high current densities can guide undesirable lithium deposition morphology even after switching to lower plating current densities. This leads to the inhomogeneous electrochemically active surface for further lithium deposition above rSEI.

Keystone Project 2: Electrode Architecture

The goal of Keystone 2 is to design, model, fabricate, and characterize the effect of electrode architecture on the electrode and cell performance in support of reaching the project goal of 500 Wh kg^{-1} cell specific energy. Research conducted includes the understanding and optimization of high loading electrodes; 3D lithium anode architectures with and without surface chemical modification; the synthesis and optimization of SPAN; and the development of high-capacity sulfur composites. Research this quarter includes the following: effect of lithium iron phosphate (LFP) cathode thickness on rate capability (University of Washington, UW); demonstration of a SPAN composite cathode with higher capacity than SPAN (University of California, San Diego, UCSD); computational studies to identify catalysts for Li-S reaction (University of Pittsburgh, U-Pitt); computational analysis of the effect of electrolyte on discharge reactions in SPAN (Texas A&M); and the effect of chemically modifying the surface of two-dimensional (2D; USCD) and 3D (UW) substrates on Li-metal plating.

Oxide Cathode Thickness Optimization (UW)

The UW team continued work this quarter on examining the diffusion limits of thick cathode materials to determine optimal cathode thickness for high energy density and high capacity. Previously reported data from UW indicated that for high-Ni NMC cathodes with thicknesses of 50-200 µm, there does not appear to be a thickness dependence on the diffusion limit, counter to models in literature. This lack of dependence was noted in literature only for LFP cathodes. Therefore, this quarter, the same testing of capacity versus current density that was utilized last quarter for high-Ni NMC cells was used in cells using Li-foil anodes and LFP cathodes of thickness from 32 µm to 85 µm (Figure 150) as a parallel study. They observed the same lack of dependence of thickness on specific capacity in the LFP as the high-Ni NMC reported previously by UW.

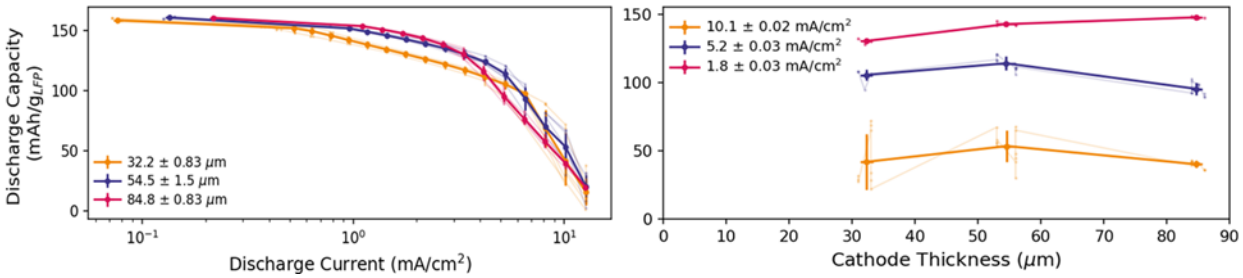

Figure 150. Data of LFP cathodes of various thicknesses show no significant impact of thickness on specific capacity, as was observed for high-Ni NMC cathodes.

Such lack of thickness dependence for both high-Ni NMC and LFP is hypothesized to result from the upper limit of thickness not being reached to observe diffusion-limited effects, particularly in the high-Ni NMC cathodes. Work will continue in fabricating and testing thicker cathode, both of NMC and LFP, to attempt to reach that limit. Additional tests are being developed to probe into the fundamental mechanism of diffusion in these thick electrodes.

SPAN Composite Cathode

Previously, the UCSD team developed SPAN that reached a capacity of over 720 mAh g^{-1}, which is higher than its theoretical capacity (650 mAh g^{-1}) based on a C_3NS stoichiometry. This phenomenon indicates that the nitrogen in the SPAN fused-pyridine matrix might host extra sulfur by forming a N-S bond. Based on this hypothesis, short-chain sulfur species could be integrated with SPAN, thus further enhancing the sulfur loading and capacity of SPAN. The theoretical capacity could reach over 940 mAh g^{-1}, assuming a composition of C_3NS_2. This proposed mechanism can guide new synthesis designs for higher capacity SPAN.

Based on this proposed mechanism, the UCSD team synthesized a SPAN composite, named as CS SPAN. This material has a sulfur loading of over 60%, much higher than that of SPAN (39 wt%). In a LHCE [2 M LiFSI in DME / bis(2,2,2-trifluoroethyl) ether (1:4 by weight)], the CS SPAN shows a much higher capacity than SPAN.

As shown in Figure 151a-b, after the 1st formation cycle, CS SPAN delivers a capacity of over 900 mAh g^{-1} at a 0.2C rate, even after 50 cycles. This represents a capacity improvement of ~ 200 mAh g^{-1}. It is noted that the discharge profile of CS SPAN after the formation cycle does not show the features of undesired soluble polysulfides, essential for its cycling stability.

The UCSD team will further optimize synthesis of the CS SPAN and perform detailed structural analysis to understand the mechanism for its enhanced capacity.

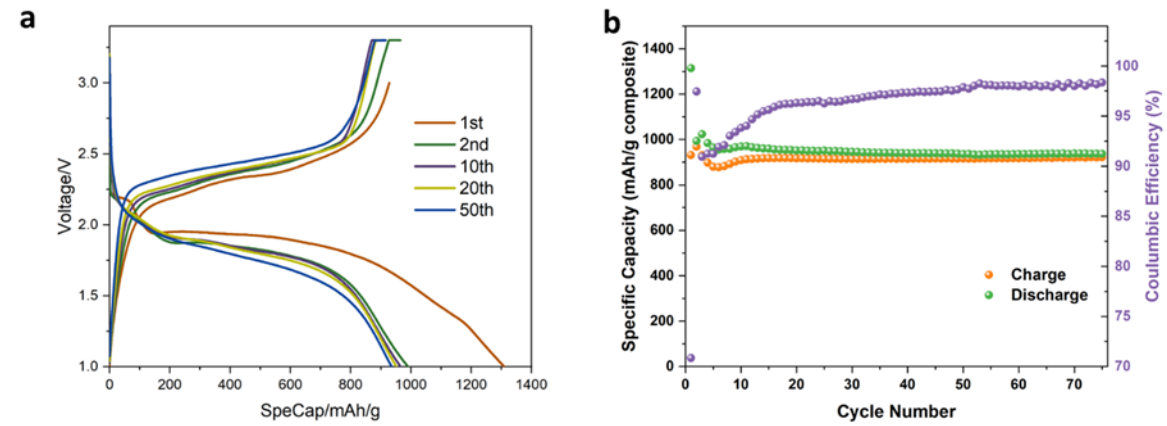

Figure 151. High-capacity SPAN composite (CS SPAN). (a) Battery curve and (b) cycling performance for CS SPAN composite with LDME electrolyte at 0.2C.

Computational Identification of Functional Electrocatalysts Enabling Conversion of Li_2S_2 to Li_2S

The U-Pitt team continued to conduct theoretical modeling to probe the conversion of Li_2S_2, the intermediate polysulfide phase, to Li_2S, the final phase. As discussed in previous reports, achieving the complete conversion of Li_2S_2 to Li_2S is of prime importance for the discharge process since the very sluggish kinetics of this reaction prevent the full utilization of sulfur in the sulfur cathode. The typical end products of the discharge process are Li_2S and Li_2S_2 mixtures, giving significantly lower capacity of almost 50% and, consequently, energy density commensurate with the lower sulfur utilization opposed to pure Li_2S due to the high activation barrier associated with the complete conversion of Li_2S_2 to the desired, final state of Li_2S. Thus, calculation of this kinetic reaction barrier and identification of appropriate electrocatalysts substantially decreasing or even leading to complete elimination of this activation barrier will result in efficient utilization of sulfur. Thus, the main aim of the present computational study is to identify functional electrocatalysts that can decrease the activation barriers and promote rapid conversion of Li_2S_2 to Li_2S during discharge and the corresponding backward reaction from Li_2S to Li_2S_2 during the charge process.

The team previously demonstrated that there are two principal reactions steps where functional electrocatalyst can make a difference. Reaction 1, $Li_2S^{(1)} \rightarrow LiS + Li$ in the discharge direction (from right to left), is almost spontaneous without registering any appreciable activation barrier, which indicates that the formation of Li_2S by seizing Li-ion during the discharge process does not hinder the overall kinetics of $Li_2S_2 \rightarrow Li_2S$ conversion. Reaction 2, $Li_2S_2 \rightarrow Li_2S^{(1)} + S$, on the other hand, has a considerable barrier in both the charge and discharge directions, thus rendering this reaction as the rate determining step in the overall conversion of Li_2S_2 to Li_2S and a focus of current study.

To obtain the thermodynamic properties, the DFT approaches implemented in the Vienna *Ab initio* Simulation Package (VASP) have been used, while a climbing image nudged elastic band (CI-NEB) method was utilized for determination of the activation energies and other pertinent kinetic parameters of the elementary reactions on the different prospective functional electrocatalytic surfaces. The model of the functional electrocatalyst considered consists of a surface slab with the most stable crystallographic orientation containing the attached Li_2S_2 or Li_2S molecules. The slab with a thickness of approximately 5-7 Å is separated from its image perpendicular to the surface direction by ~ 20 Å to avoid their mutual interaction. The bottom two-three layers

of the slab are then fixed with lattice parameters corresponding to the bulk state, while the remaining top layers, along with the attached polysulfide molecule, are allowed to completely relax. All of the species are adsorbed on the functional electrocatalyst surface, including the lithium and sulfur atoms.

The activation barriers for the elementary reactions were estimated using the CI-NEB method, where five intermediate points were chosen for calculations of the potential energy profile between the initial and final position of the Li-ion for the reaction 1 and sulfur atom for the reaction 2 at the functional electrocatalytic surface (totally seven points). All computations have been executed within the projector-augmented wave method and the generalized gradient approximation as the exchange-correlation energy functionals in a form described by J. P. Perdew and Y. Wang implemented in the VASP software. To maintain the desired high precision for all the total energy and electronic structure calculations, a plane wave cutoff energy of 520 eV was chosen. The relaxation procedure was used to optimize the internal positions as well as the lattice parameters of the supercell. Additionally, the Monkhorst-Pack scheme was used to sample the Brillouin zone and create the k-point grid for all the functional electrocatalytic surface slabs used in the current study. The selection of the appropriate numbers of k-points in the irreducible parts of the Brillouin zone was made on the grounds of the convergence of the total energy to 0.1 meV/atom.

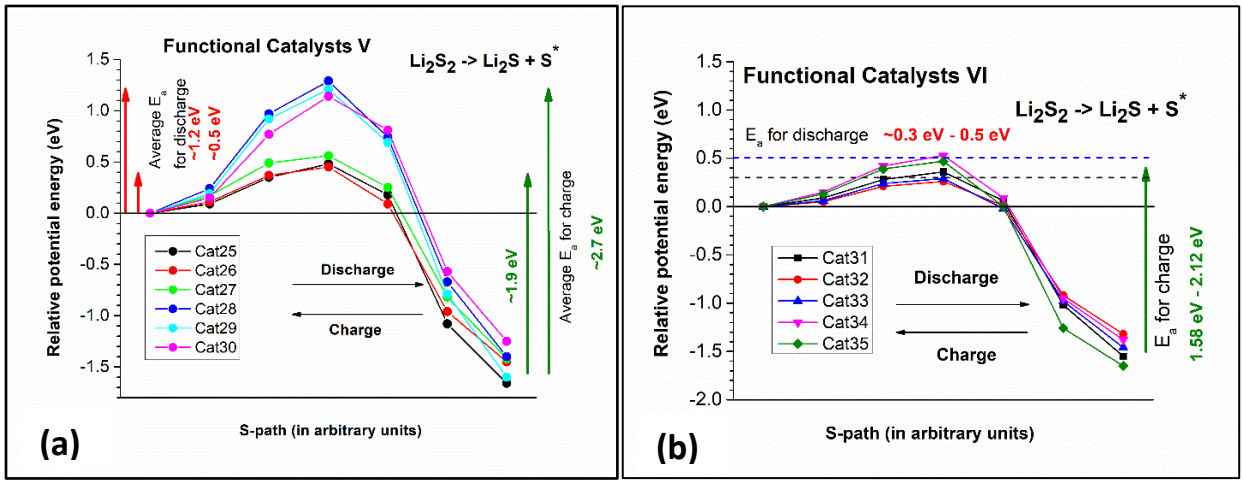

Figure 152. Potential energy profiles for Reaction 2 ($Li_2S_2 \rightarrow Li_2S + S^*$) for the two types of functional electrocatalysts considered.

In last quarter's report, the U-Pitt team demonstrated the potential energy profiles for Reaction 2 calculated for functional electrocatalysts comprising Functional Catalysts III – Type III family and Functional Catalysts IV – Type IV family. In this report, the potential energy profiles for Reaction 2 calculated for functional electrocatalysts comprising Functional Catalysts V – Type V and Functional Catalysts VI – Type VI are shown in Figure 152a-b, respectively. It can be observed that for all the probed materials of both functional electrocatalysts of types V and VI, Reaction 2 in the discharge direction is exothermic, as expected, with the final product (Li_2S + S) being more energetically favorable compared to Li_2S_2. However, in contrast to the spontaneous Reaction 1 discussed in the second quarter's report in FY 2022, this reaction is not spontaneous, with substantial activation barriers needed for the different electrocatalytic materials considered. The type V electrocatalysts are split into two subgroups with distinctly different average activation barriers: (1) Cat25, Cat26, Cat27 with the average barrier value of ~ 0.48eV, and (2) Cat28, Cat29, Cat30 with the average barrier value of ~ 1.2 eV. Type V is a multicomponent composition group of materials and demonstrates larger variation in the activation barriers values than those for Types I-IV studied and reported in earlier quarters. In the Type V functional electrocatalyst, as shown in Figure 152a, the lowest activation barrier is demonstrated by the multicomponent composition Cat26 with corresponding value of 0.45 eV, while the lowest barriers value in the Type VI, as shown in Figure 152b, belongs to another multicomponent composition Cat32 with the corresponding value of 0.26 eV. As of now, this is the lowest activation barrier determined by the team among the different types of functional electrocatalyst materials considered since the present project was initiated.

However, there is still the need to further decrease the activation barriers for Reaction 2, which will then likely yield much higher specific capacity values for sulfur in the S-cathode. These studies to further identify better functional electrocatalysts are proceeding as planned, and the research work is in progress. The team will provide results of the ongoing studies in upcoming reports, along with results of the corresponding experimental work to validate the findings of the theoretical calculations.

Computational Analysis of Effects of Electrolyte on Discharge Reactions in SPAN

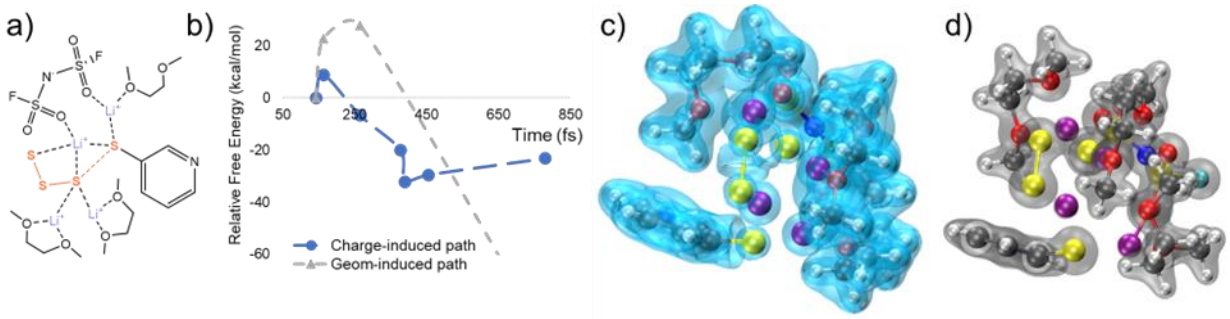

Figure 153. (a) Solvation structure, (b) free energy profile, (c) electronic Laplacian revealing the type of bonding, and (d) electron density isosurfaces. The key geometries obtained from *ab initio* molecular dynamics frames reveal two types of pathways, as shown in (b). The grey curve stands for the geometry-induced pathway that includes charge variation throughout the reaction; the blue one indicates the pathway where electron uptake happens prior to S-S cleavage. This event series takes place when Li:S = 1:2.

The Texas A&M team completed a theoretical-computational study this quarter that provides an overview of the lithiation reactions and solvation effects in different SPAN structures by comparing the lithiation energetics at different sites of SPAN. Two types of electrolytes were analyzed: a diluted solution of LiFSI, based on dimethyl carbonate (DMC) or DME as solvents, and LHCE with two fluorinated diluents. To further assess interactions between electrolyte species and reaction intermediates during electrochemical lithiation, AIMD simulations incorporating detailed electronic structure analysis of the key structures in major chemical events were employed. The thermodynamics of the SPAN structures were evaluated, using 4 pyridine units to serve as polyacrylonitrile backbone in DFT optimizations. After obtaining the vulcanization reaction energetics in forming different polysulfide chain categories, the lithiation free energy profiles of each feasible structure were also evaluated. It was found that when clustered with polysulfide chains, the electronic structures and binding energetics of solvated lithium cations are profoundly altered. The AIMD simulations provided details about the solvent, anion, and diluents stability during discharge. In both the DMC- and DME-solvated systems, Li-mediated solvent-SPAN interactions play significant roles in the S-S and C-S cleavage reactions. In DME-based electrolyte system, the electrolyte salt LiFSI is also involved in the sulfur chain cleavage pathways (Figure 153a). In the DMC-solvated system, solvent stabilization is less significant than DME, resulting in less dissolution of S_x chains. When four external lithium atoms enter the simulation slab, sulfur chain migration takes place. An S4-chain experiences cleavage, rearranges to bond with a neighboring S3-chain, leaving an individual sulfur atom not bonded to any neighboring sulfur atoms. Being consistent with the molecular geometries, Li-S has more electrostatic interaction properties than covalently shared electronic orbitals.

Surface Chemical Modification of 2D and 3D Substrates for Lithium Anodes

P. Liu's group at UCSD completed a study of growing single-crystalline lithium seeds on a 2D Fe/LiF substrate for fast-charging Li-metal batteries. Depositing lithium onto a copper substrate modified with a thin film of Fe/LiF resulted in formation of faceted, single-crystalline seeds (Figure 154a). This takes place despite the fact that Fe/LiF is a lithiophobic composite material. It is hypothesized that the uniformly distributed iron nanoparticles serve as nucleation sites, while LiF enables rapid lithium transport. This hexagonal seed layer facilities subsequent lithium growth without dendrite formation, even at high current densities. As shown in Figure 154b, lithium deposited on the Fe/LiF nanocomposite substrates is consistently denser than on copper at current densities from 0.5mA cm^{-2} to 3mA cm^{-2}. In fact, the advantages of the Fe/LiF substrate become more obvious at higher current densities. The cryogenic focused ion beam SEM images in Figure 154c also show that

the lithium deposited on Fe/LiF has much less porosity than the lithium deposited on copper. These results suggest that the crystalline seeds formed can induce subsequent dendrite-free and dense lithium deposition, even at fast charging rates.

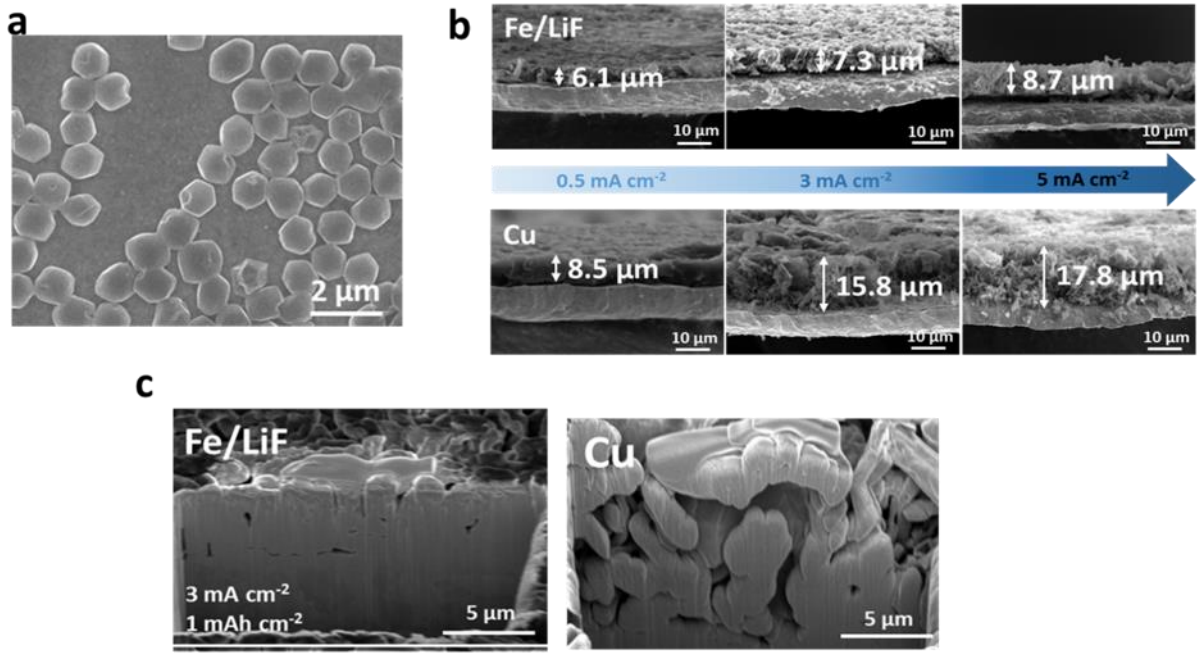

Figure 154. Morphology of deposited lithium layer on different substrate. (a) Scanning electron microscopy (SEM) images of top-view lithium crystalline seed deposited on the Fe/LiF substrate. (b) 1 mAh cm^{-2} lithium plated on the Fe/LiF nanocomposite and copper substrate, under 0.5 mA cm^{-2}, 3 mA cm^{-2}, and 5 mA cm^{-2}. (c) Cryogenic focused ion beam – SEM images of 1 mAh cm^{-2} lithium deposited on the Fe/LiF nanocomposite and copper substrate under 3 mA cm^{-2}.

The advantage of the new substrate also translates to performance advantages in full cells. Figure 155 shows the capacity retention of cells using a 3 mAh cm^{-2} NMC-811 cathode, 1-fold excess of lithium anode, and 3 g Ah^{-1} electrolyte. The cell with a lithium anode based on the Fe/LiF substrate is cycled at 1C rate for more than 130 cycles with 80% capacity retention, which is a 550% improvement over the baseline cells. Their findings advance the understanding of lithium nucleation and pave the way for realizing high-energy, fast-charging Li-metal batteries.

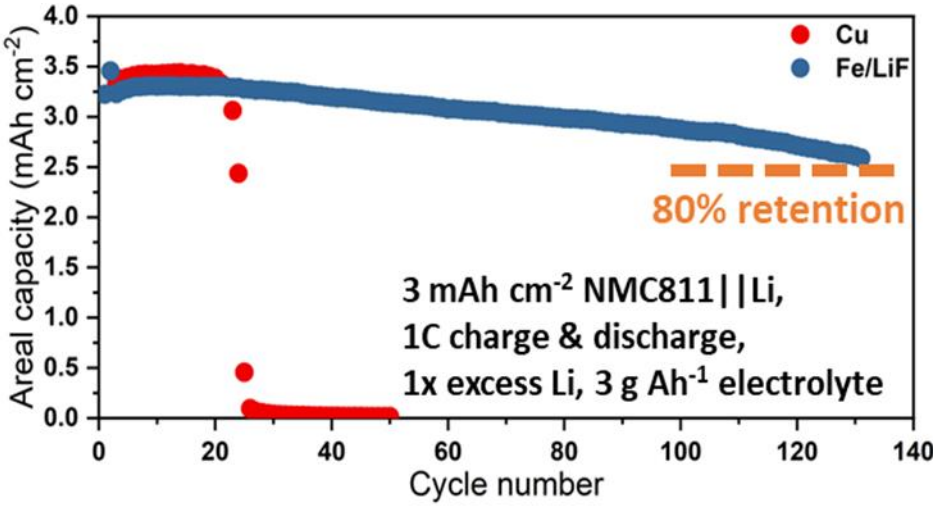

Figure 155. Electrochemical performance of full cell with different substrates. Capacity retention of full cell with 3 mAh cm^{-2} NMC-811 as the cathode, 3 mAh cm^{-2} lithium plated on different substrates as the anode. 3 g Ah^{-1} electrolyte is added to each cell.

The UW team continued their investigation of chemical modification of the surface of 3D anode architecture to determine whether a coating of lithiophilic material, in this case zinc, will cause lithium to plate deeper and more evenly within a 3D structure. Zinc was plated onto copper foil and 180-µm-thick copper foam by immersing zinc foil and the copper substrate in 1 M $ZnSO_4$ and holding the voltage at -1.5 V versus Ag/AgCl for 2 minutes for the copper foil and 15 minutes for the copper foam. The foam was plated for a longer period of time due to the greater true surface area of the structure. Then, 10 mAh/cm^2 of lithium was plated onto the bare and zinc plated structures in LHCE (LiFSE : 1.2 DME : 3 TTE), and SEM images were taken of the cross-section, shown in Figure 156).

Although the bulk lithium plating looks similarly even and dense for both the unmodified and modified substrates, there is a visible difference in density and adhesion at the surface of the substrate. The Zn-plated substrates (Figure 156b/d) appear to have much denser lithium plating at the substrate-lithium interface compared to the interface on the bare substrates (Figure 156a/c), which show a notable gap. This is likely due to alloying of the lithium with the zinc coating. Work continues to investigate the effect of the surface modification on CE and polarization as well as using EDS to analyze the composition of the substrate-lithium interface and verify or disprove the alloying theory.

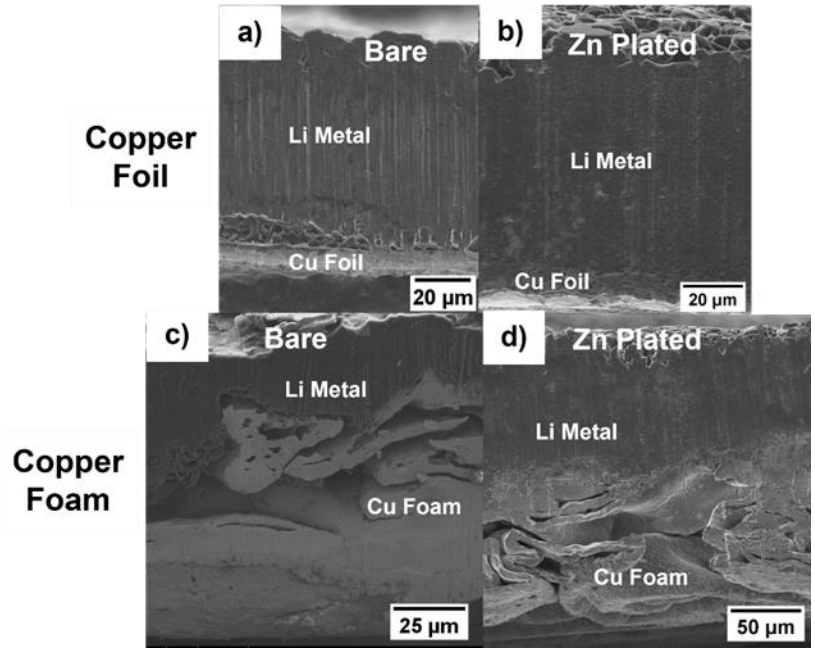

Figure 156. Scanning electron microscopy images of the cross section of 10 mAh/cm^2 of lithium plated on (a) bare copper foil, (b) copper foil plated with zinc, (c) bare copper foam, and (d) copper foam plated with zinc.

Highlights of Keystone Project 2

The highlights for this quarter are as follows:

- The UW team determined that specific capacity is not closely related to the thickness of cathode at the same current density for LFP cathodes. They also showed the benefits of zinc coating on copper foil and foam to improve lithium plating density and substrate adhesion.
- The UCSD team completed a study of growing single-crystalline lithium seeds on an Fe/LiF substrate for fast-charging Li-metal batteries. They discovered that depositing lithium onto a copper substrate modified with a thin film of lithiophobic Fe/LiF resulted in formation of faceted, single-crystalline seeds. Lithium deposited on the Fe/LiF nanocomposite substrates is consistently denser and has less porosity than that deposited on bare copper. The cell with a 3 mAh cm^{-2} NMC-811 cathode, lithium anode

based on the Fe/LiF substrate with 1-fold excess of lithium, and 3 g Ah^{-1} electrolyte cycled more than 130 cycles at 1C rate with 80% capacity retention. The team also demonstrated a SPAN composite cathode with higher capacity than SPAN.

- The U-Pitt team identified additional candidates by computational studies to lower the reaction barrier and promote electrocatalysis of the rate limiting step for Li_2S formation during the discharge process.
- The Texas A&M team used computational studies to show the less significant solvent stabilization of DMC compared to DME results in less dissolution of S_x when paired with SPAN.

Keystone Project 3: Cell Fabrication, Testing, and Diagnosis

Optimization of Li-S Batteries: Monitoring Specific Capacity Trends by Porosity Modulation

This quarter, the General Motors (GM) team conducted a series of experiments regarding electrode processing and cell assembly to further improve Li-S cells. Incongruencies in cathode testing data across the efforts of the GM team and their collaborators have demonstrated the need to pinpoint specific ways in which cathode performance can be improved and, oppositely, how performance could be compromised.

In the first phase of the program, the GM team conducted a series of evaluations on electrode porosities. The fresh uncalendered electrode always shows a porosity of about 65%, which was further reduced to lower porosity (in thickness for direct measurement). The design of the experiments was targeted to obtain the lowest porosity limit of the electrode that can still provide acceptable performance. The conclusion was that more than 50% porosity is necessary on the electrode level to provide enough reactive site for the sulfur conversion.

This quarter, the team checked minor porosity reduction from the fresh uncalendered samples. The sulfur electrodes with the porosities varying from 65%, to 64%, to 62%, to 60% were further evaluated in coin-cell format. As the voltage profiles show in Figure 157, all calendered samples show higher specific capacity than the uncalendered sample. The main discharge plateaus of all samples are at similar voltage, which suggests no significant differences in overpotential. This observation is also consistent with the first phase study, in which appropriate compression of the electrode would help with the conductivity. For the initial charging process, the samples with 62% and 60% porosity even showed fully overlapped voltage profile. In the 15th cycle, the capacity difference among all samples becomes more obvious. The samples with the porosities of 62% and 60% showed better capacity retention than the uncalendered sample. This observation suggested that reduction of electrode porosity, at a certain level, would be helpful for the cyclability. This behavior may be related to several factors, including carbon framework and/or active material integrity, electronic conductivity, and polysulfide confinement. Further characterization and testing are in progress to reveal more details.

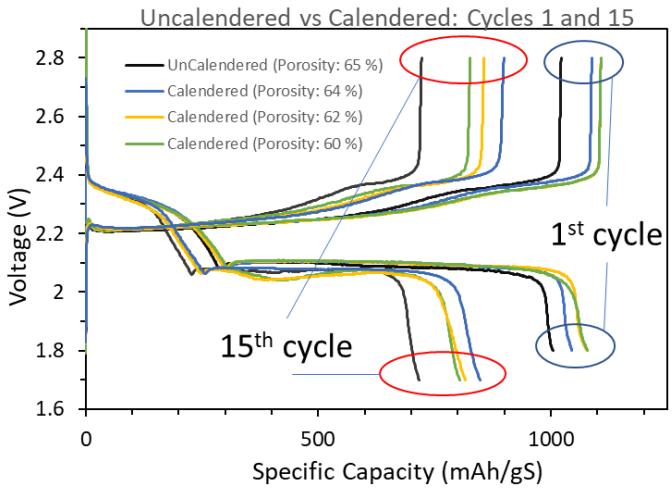

Figure 157. Electrochemical performance of a single cathode batch (loading: 4.05 mgS/cm^2) calendered from 65% to 64%, 62%, and 60%, with 8 µL/mg electrolyte amount control. 1st cycle is cycled at 0.05 C rate; the rest of the cycles at 0.1 C.

Effects of Low Internal Pressure Versus High Internal Pressure for Coin-Cell Assembly

Besides the electrode porosity, the GM team also checked the influence of the internal pressure, which was induced by different spacer thickness in the coin cell. The pressure influence on Li-metal batteries has already been well studied by many research institutes. For Li-S chemistry, some Battery500 teams [for example, the Idaho National Laboratory (INL) team] have also initiated studies using pouch cells. In this study, the GM team picked two spacer thickness selections to make the coin cells to check the difference of the performance caused by internal pressure.

The "high pressure" cell in Figure 158 uses a 1.0-mm spacer with a 600-µm lithium chip, which is standard in most current and past cell constructions. In comparison, a 0.5-mm spacer was used to present low pressure condition with the same lithium anode. The voltage profile of the first three cycles of both configurations is shown in Figure 158. It is clear that the "low pressure" cell only delivered ~ 900 mAh/gS specific capacity. The main discharge plateau was much lower than that of the "high pressure" case, which suggests much larger resistance. In the 2nd cycle, the "high pressure" cell showed normal voltage profile, while the "low pressure" cell showed distorted voltage profile with a "valley" in the main discharge plateau, which is similar to the behavior of the cell with deficient electrolyte. The specific capacity quickly decayed to lower than 400 mAh/gS for the "low pressure" cell in the 3rd cycle, while the specific capacity of the "high pressure" cell still maintained above 800 mAh/gS.

To understand the failure mechanism of the cell in the low pressure case, further investigation using additional characterization methods including microscopy will be carried out and reported later.

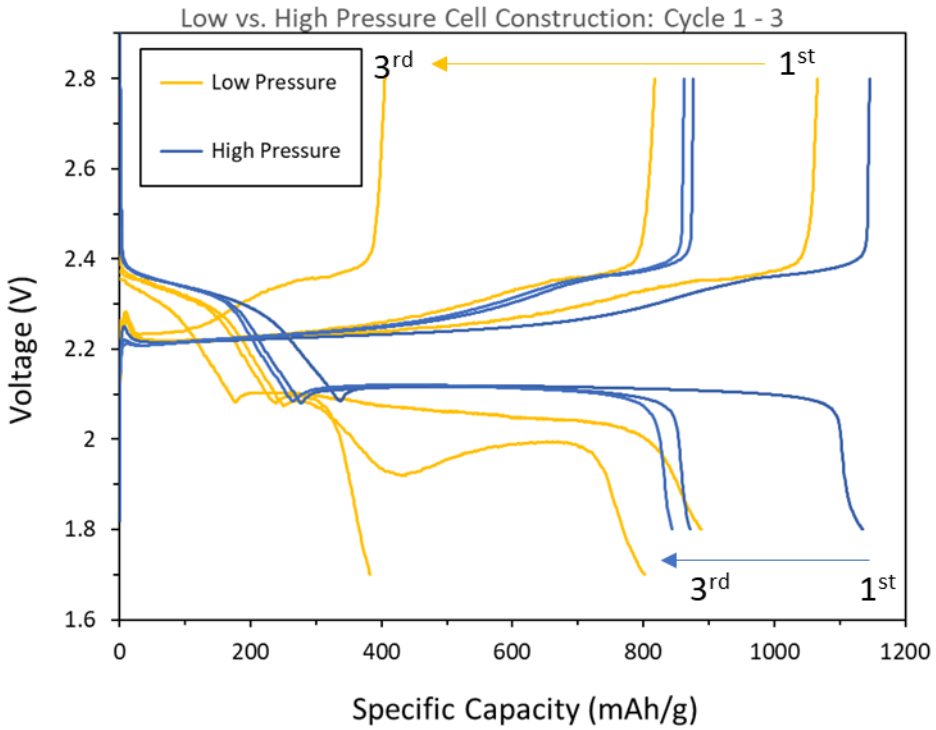

Figure 158. Electrochemical performance of coin-cell assembly with low and high pressure (loading: 3.82 mgS/cm^2). Low and high pressure cells differ only by the use of a 0.5-mm spacer and a 1.0-mm spacer, respectively.

Operation Optimization of Li-NMC-811 Single-Layer Pouch Cells (SLPCs)

The INL team focuses on the operation optimization of Li-NMC-811 SLPCs to improve their performance. As was reported by INL and other team members in Battery500, applying an appropriately high external pressure on the Li-metal pouch cells can benefit cycling performance by suppressing dendrite growth at the anode side.

In most cases, the pouch cells were sandwiched between two rigid plates, and the gap distance between the two plates was kept constant during cycling. Such a pressure fixture design is called "constant thickness" design. To further improve cell performance, the INL team proposed two other pressure fixture designs: "constant pressure" design and "constant thickness + foam" design. In the former design, springs were added on the top of one of the rigid plates to maintain almost constant pressure during cell cycling. In the latter design, soft foams were added at both sides of the pouch cells. The three kinds of pressure fixture designs are schematically shown in Figure 159.

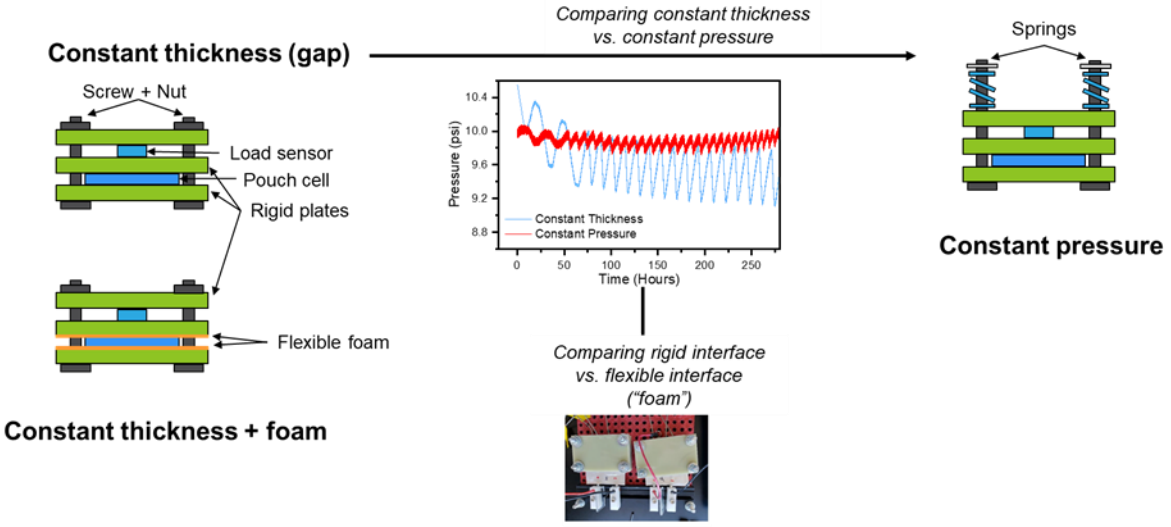

Figure 159. Three pressure fixture designs used in pouch cells to apply external pressures. The electrochemical performance of Li-NMC-811 single-layer pouch cells (SLPCs) was studied based on the three pressure fixture designs. In Li-NMC-811 SLPCs, a 50-µm-thickness Li-metal foil, an NMC-811 electrode with areal capacity of 4.2 mAh/cm², and LiFSI-DME-TTE (molar ratio: 1:1.2:3) were used as the anode, cathode, and electrolyte, respectively.

These cells were all cycled at C/10 during charge and C/3 during discharge under lean-electrolyte conditions (3.0 Ah/g electrolyte was added). For all three fixture designs, the initial external pressures were set to be 10 psi. It can be seen from Figure 160a that the "constant thickness + foam" design can help with longer lifespan. The addition of foams was expected to realize more uniform pressure distribution across pouch cells. The "constant pressure" design enables the cells to deliver the lowest initial specific capacity and shortest lifespan. The overpotentials of charge/discharge based on the three pressure fixture designs were calculated, as shown in Figure 160b One can see that the cell with the "constant pressure" design shows much faster growing charge/discharge overpotentials over cycling than the other two cells, suggesting larger cell resistances and shorter lifetime. The growth of charge/discharge overpotential for the cell with the "constant thickness + foam" design is slowest, implying longer lifetime. These results agree well with electrochemical performances of the cells shown in Figure 160a. The characterizations of SLPCs based on the three pressure fixture designs are under way, and the underlying mechanisms are being investigated and will be reported later.

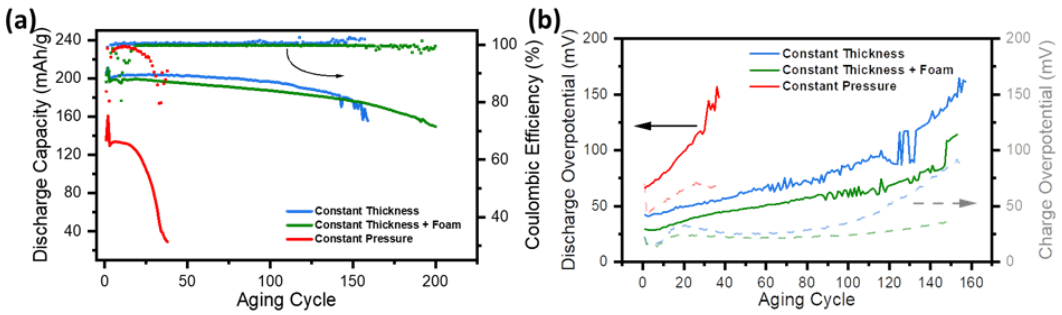

Figure 160. Cycling performances (a) and charge/discharge overpotentials over cycling (b) of the Li-NMC-811 single-layer pouch cells based on three pressure fixture designs.

Safety Properties of Li-Metal Batteries

Li-metal anodes are essential for developing next-generation high-energy-density batteries. Numerous concerns on the potential safety hazards of the lithium metal have been brought up before its massive application in commercialized battery packs. However, few investigations have been performed to systematically evaluate the reactivity of Li-metal anode at the full-cell level. Here, Y. S. Meng's group at UCSD reports their results aimed to quantitatively investigate the lithium metal reactivity and compare that with lithiated graphite (Li-Gr) and lithiated silicon (Li-Si) samples.

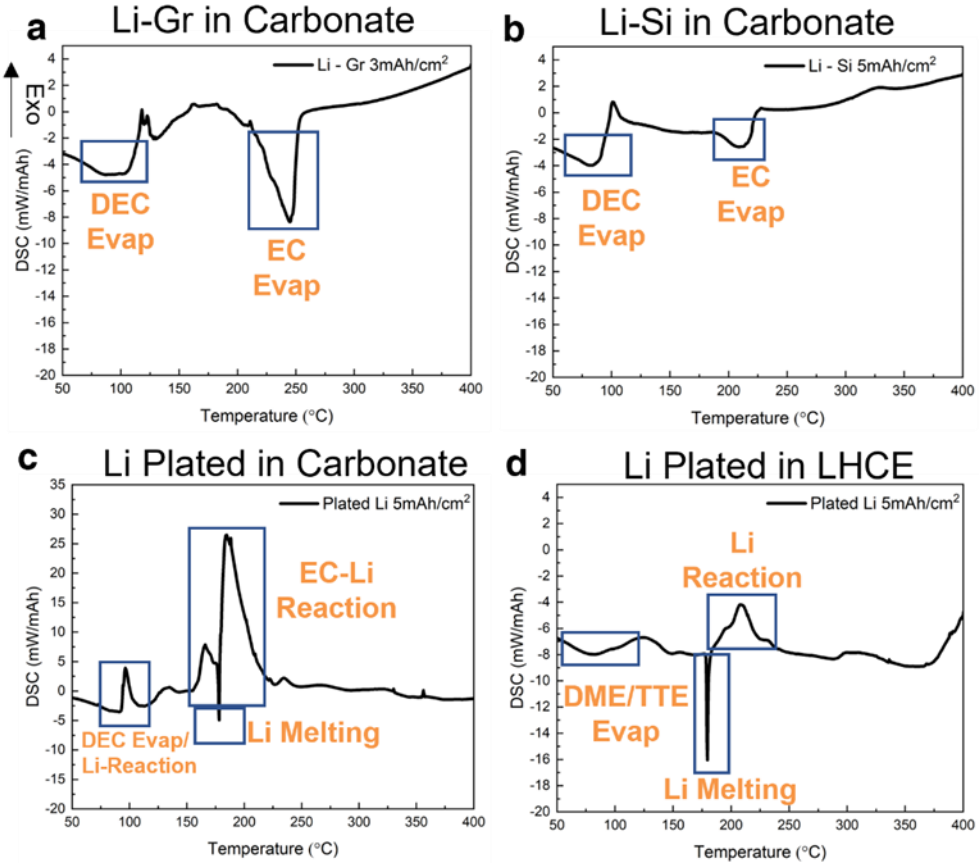

Figure 161. The differential scanning calorimetry (DSC) curves of (a) Li-Gr, (b) Li-Si, (c) lithium metal plated in carbonate, and (d) lithium metal plated in localized high-concentration electrolyte. Graphite and silicon anodes are lithiated to the desired capacity in half-cell setup with the rate of C/20. Lithium metal is plated in Li||Cu coin cell to the desired capacity at a current density of 0.5mA/cm².

Three anodes including graphite, silicon, and bare copper (no excess lithium) were charged with the controlled lithiation/plating amount of 3 mAh/cm^2 for graphite or 5 mAh/cm^2 for silicon and bare copper in the half cell. Instead of 5 mAh/cm^2, 3 mAh/cm^2 capacity is chosen for the graphite because it is the most widely available capacity among commercialized Li-ion cells. The prepared anodes were sealed in a DSC pan with a controlled amount of electrolyte (electrolyte/capacity ratio ~ 3 mg/mAh), and then transferred into the DSC Fourier transform infrared station for thermal analysis. All DSC tests were done at least twice to make sure that the obtained results are reproduceable. Figure 161 shows the DSC curves of Li-Gr, Li-Si, plated lithium in the carbonate-based electrolyte [that is, 1.2 M lithium hexafluorophosphate ($LiPF_6$) dissolved in ethylene carbonate (EC) : diethyl carbonate (DEC), (1:1 by weight) with 10% FEC). In addition, plated lithium in LHCE (that is, LiFSI, DME, and TTE with molar ratio 1:1.2:3) was also prepared. In both Li-Gr and Li-Si, most heat-absorbing peaks are associated with the evaporation of electrolyte solvents such as DEC and EC (Figure 161a-b). No significant heat-releasing peaks exist in the Li-Gr and Li-Si samples when heated to 400°C. However, when the plated lithium in the carbonate electrolyte was heated during the DSC measurement, two heat-releasing peaks

overlap with the evaporations of DEC and EC solvents, respectively (Figure 161c). When the lithium plated cell was heated at ~ 180°C, a sharp heat-absorbing peak appeared. The exothermic reactions might be caused by the melted lithium quickly reacting with the remaining EC solvent and $LiPF_6$ salt. Figure 161d shows the DSC curves of the plated lithium in LHCE electrolyte. The DME and TTE solvents are mostly evaporated before 100°C because of the low evaporation points, rather than reacting with the lithium. A sharp lithium melting peak is also shown ~ 180°C in Figure 161d, which indicates that the lithium was mostly melted rather than oxidized during the heating process. A small oxidation peak can be observed after the complete melting of lithium, which is associated with the decomposition of electrolyte salts. In the future, the lithium anode reactivity after long cycling will be further analyzed.

Highlights of Keystone Project 3

The highlights for this quarter are as follows:

- The GM team has optimized the porosity of sulfur electrodes with the value of 60% for enhanced specific capacity and capacity retention.
- The GM team found that higher pressure corresponding to the thicker spacer added in the Li-S coin cell showed normal discharge/charge curves with lower cell resistances and larger specific capacity.
- The INL team has developed three pressure fixture designs to apply external pressure onto Li-NMC-811 SLPCs. The addition of foams (constant thickness + foam) can benefit longer lifespan. However, the almost constant pressure during cycling can greatly increase cell resistances and reduce lifetime.
- The UCSD team has successfully quantitatively characterized the lithium metal reactivity by DSC. Plated lithium in LHCE electrolytes displayed weaker reaction than in other traditional carbonate electrolytes.

Keystone Project 4: Cross-Cutting Efforts

The goal of the Cross-cutting team is to develop and deploy advanced characterization tools in support of the other three Keystone efforts, with a focus on probing specific materials and interfaces for Keystone 1, probing individual electrodes for Keystone 2, and probing the whole cell for Keystone 3. This quarter, Brookhaven National Laboratory (BNL) investigated TM deposition on lithium metal using X-ray fluorescence (XRF) mapping, revealing nickel deposition nominates. The SLAC National Accelerator Laboratory and Texas A&M teams focused on the mechanical properties and growth mechanisms of SEI on lithium metal. Finally, the INL team carefully measured the OCV of NMC-811, paving the ground for advanced electrochemical diagnostics of NMC-811/Li full cells.

Quantifying TM Deposition on Lithium Anode at Electrode Scale

The BNL team characterized the electrochemistry and the TM dissolution behavior of cells prepared with novel electrolytes developed by Battery500 collaborators at SLAC. Three fluorinated ether electrolyte systems were tested: 1.2 M LiFSI in fluorinated-1,2-diethoxyethane electrolyte (F5DEE, or F5), 1.2 M LiFSI in F4DEE with difluoro(oxalate) borate (DFOB) additive (F4-DFOB), and 1.2 M LiFSI in FDMB. The molecular structures of F5, F4, FDMB, and DFOB are shown in Figure 162a.

The cyclability of NMC-811||Li cells using these electrolytes is shown in Figure 162b-c. The Battery500 coin cell test protocol was rigorously followed. Both FDMB and F5 deliver stable cycling in the voltage range of 2.8-4.4 V, while the cell using F4-DFOB electrolyte shows capacity fade after only 40 cycles. When increasing the charge voltage to 4.6 V, both FDMB and F5 electrolytes can still sustain long cycles, while the F4-DFOB electrolyte fails to do so. Such results are consistent with the data shown by the Stanford team and other Battery500 Consortium members.

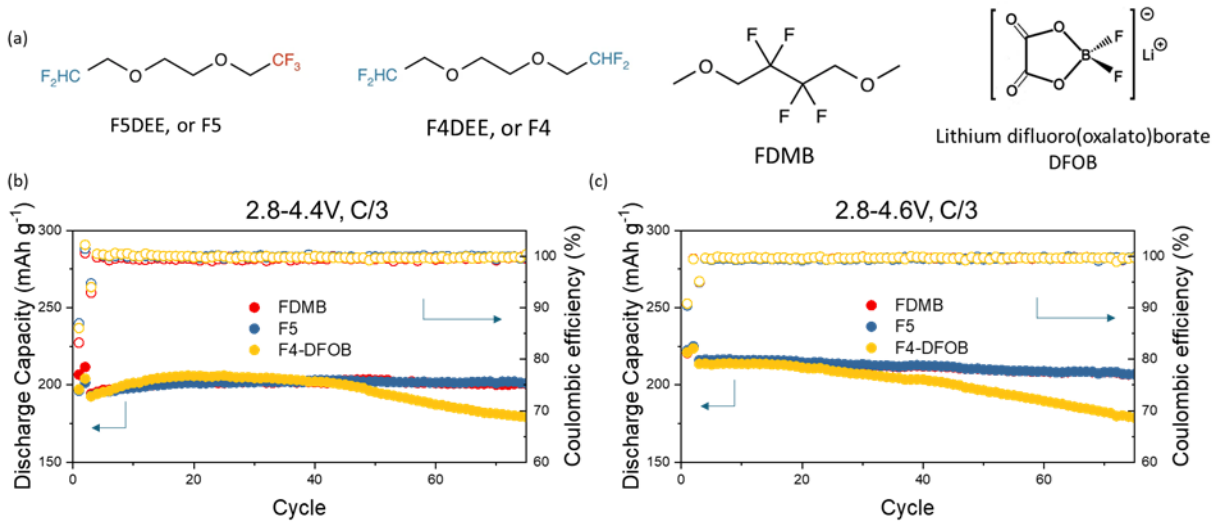

Figure 162. (a) Molecule structures of the solvents and additives used in the Stanford electrolytes. (b-c) Cycling data of coin cells using Stanford electrolytes in different voltage windows. The Battery500 coin-cell test protocol is followed.

To understand the TM dissolution behavior (and especially how this influences the Li-metal anode), the amount of TM deposited on Li-metal anode at electrode scale was quantified by the BNL team using synchrotron-based XRF mapping. The mapping results of Figure 163 indicate there is significant heterogeneity in TM deposition on Li-metal anode, emphasizing the importance of characterization at electrode scale, not just a small spot of the electrode. Such heterogeneity may result from nonuniformities in the local current density due to variations in the applied pressure or in the local composition and thickness of the interphase.

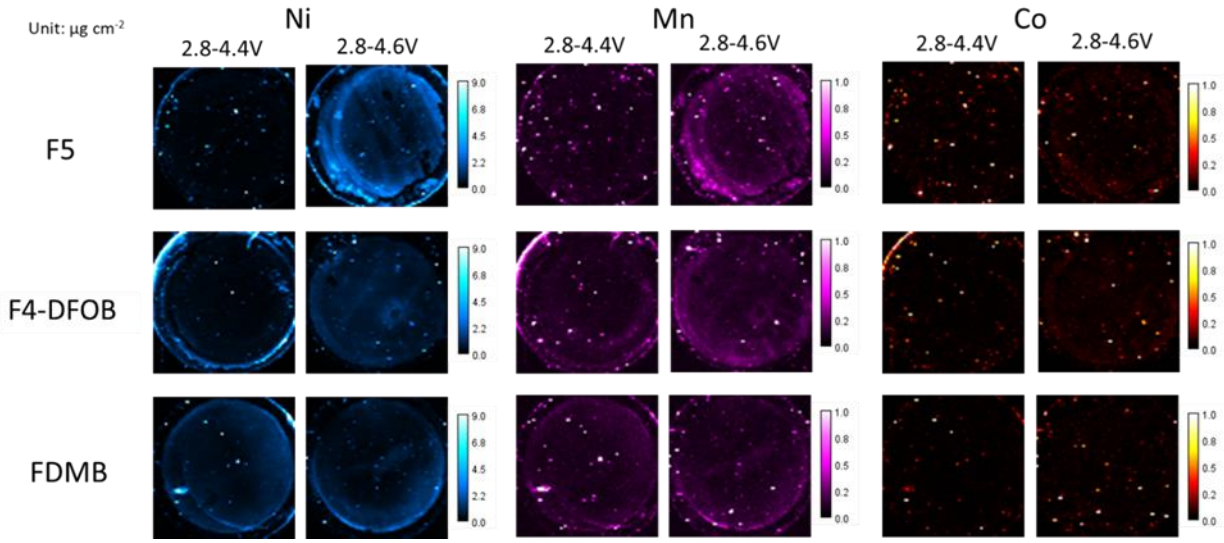

Figure 163. The X-ray fluorescence mapping of transition metal (TM) deposited on Li-metal anode harvested from cells going through 100 cycles. The color bar indicates the amount of TM deposition, with dark color and bright color corresponding to low and high values, respectively.

The deposited TM amount is quantified and analyzed in detail, as shown in Figure 164. In general, the deposited TM amount is on the scale of μg/cm^2. Considering the area of the electrode and the mass loading on the cathode side, this means the bulk cathode loses less than 0.1% of its TM after 100 cycles. Therefore, the negative effect of TM dissolution and deposition is more likely associated with surface and interphase damage, rather than TM inventory loss. The left panel in Figure 164 shows the absolute amount of TM deposition, indicating that nickel deposition is most serious, followed by manganese and cobalt. This is contrary to the popular belief that

manganese deposition is most serious among all the TMs. Figure 164 also shows that the deposited TM amount increases considerably when the charge voltage is increased. Generally, the F5 electrolyte seems to be most effective in suppressing TM dissolution and deposition, in accordance with its superior cycling performance. However, its capability of suppressing TM dissolution at high voltages (for example, 4.6 V) needs to be improved. Considering nickel, manganese, and cobalt are present in different fractions in NMC-811, the deposited TM amount should be normalized by stoichiometry, leading to results shown in the right of Figure 164. Interestingly, the normalized deposition is highest for manganese, followed by nickel and cobalt. This may suggest that after extended cycling, the relative ratio of TM on cathode surface is no longer the same as that in the pristine material. It is possible that the surface becomes Co-enriched since cobalt is the least dissolved and deposited TM.

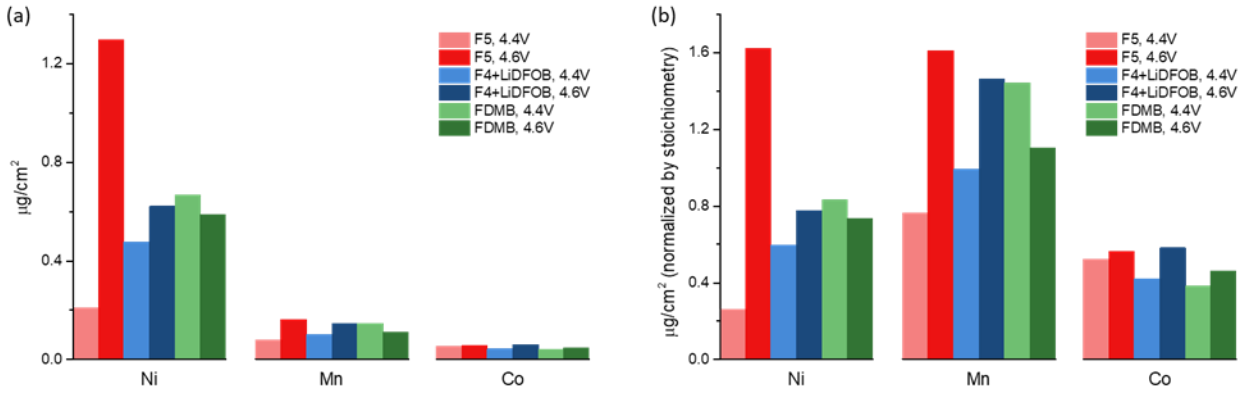

Figure 164. (a) The absolute amount of transition metal (TM) deposition quantified from X-ray fluorescence (XRF) mapping. (b) The normalized amount (normalized by TM stoichiometry in NMC-811) of TM deposition quantified from XRF mapping.

Mechanical Properties of SEI on Lithium Metal

Having wrapped up the work characterizing the SEI growth rate dynamics, the SLAC group's characterization work as part of the cross-cutting team has now shifted to performing mechanical measurements on the SEI. This set of measurements, leveraging the *in situ* capabilities of a glovebox atomic force microscope (AFM), develops understandings of how SEI grown on Li-metal surfaces plays a role in regulating lithium metal deposition and morphology, and ultimately cell performances. Building on work done by other teams within the Battery500 Consortium, they have probed local mechanics of the SEI grown in both conventional carbonate electrolytes (1:1 EC:DEC with 1 M $LiPF_6$) as well as SEI grown on LHCE. In addition to Young's modulus (Figure 165), they have also performed viscoelastic measurements by locally indenting the SEI under constant loading and then observing the resulting SEI creep.

Surprisingly, the plasticity of the SEI, measured by the amount of creep observed in one second of loading, proves to be a better predictor of cell performance than the more commonly reported modulus measurements. Because viscosity of the SEI is likely driven by the composition of the organic SEI phases, which are challenging to characterize with other nanoscale characterization techniques, they believe that this approach represents a novel and promising approach to electrolyte screening for future electrolyte engineering. To further characterize and understand the influence of the SEI nanomechanics on cell performance, they intend to perform further mechanical studies on more electrolytes as well as repeating the previous measurements *in situ* to capture the role of SEI chemistry and mechanics on battery performance.

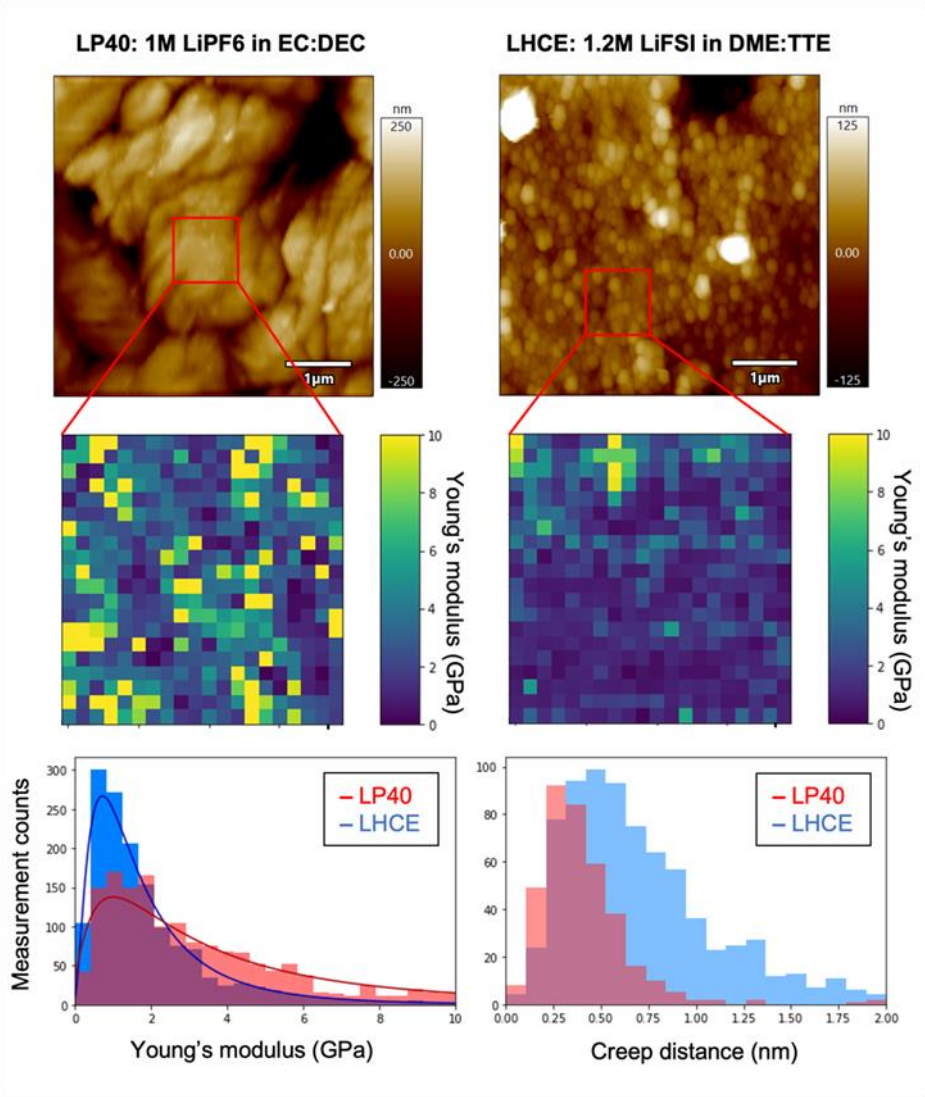

Figure 165. Nanoscale Young's modulus measurement performed on SEI formed on lithium metal in 1 M $LiPF_6$ in EC:DEC (left) and in 1.2 M LiFSI in DME:TTE electrolyte (right).

Growth of SEI at Surface of Lithium Metal

A new fundamental understanding of ion transport and deposition in complex interphases was obtained at Texas A&M using first-principles simulations. Depending on the state of charge (SOC) of the surface, clear differences are observed in the behavior and energy profile for ion transport at the interface. In the electron-rich environment provided by charged surfaces, the final charge transfer that leads to the ion reduction and deposition comes both from the partially charged solvation shell that assisted ion transport in the diffuse interfacial layer and from the Li-metal surface. When the lithium surface is partially covered by a Li_2O SEI, it is found that the ion motion occurs through the border of the SEI structure where the cation moves through coordination with oxygen anions and displacement of the lithium cations in the oxide surface (Figure 166). On the other hand, for LiOH SEIs, the lithium ion enters the SEI structure and substitutes one of the SEI lithium atoms with another lithium being released from the SEI to the electrolyte. Although the free energy profiles for the ion coming from the electrolyte into the lithium surface look similar to that of the ion traveling in the opposite direction, there is asymmetry in the magnitude of the barriers for solvation and desolvation, with the desolvation barrier for the ion to integrate with the SEI being higher than the solvation of the ion to enter the electrolyte phase. The LiOH structure offers better passivation properties than the Li_2O; this is evident from the reactivity of solvent properties on both surfaces. Inhomogeneous lithium deposits on pristine surfaces were

found to be unstable, triggering a surface self-healing mechanism. However, uneven lithium deposits were found to be stable if located near SEI nuclei. Depending on the chemistry, the SEI blockage might become the focus for further electrolyte reduction (observed in Li_2O), and ion motion is promoted through its border. This study also demonstrates that versatile computational chemistry tools allow elucidation of transport mechanisms in complex interphases, including SEI mixtures with various degrees of crystallinity. The results of this study have been published [see: Angarita-Gomez, S., and P. B. Balbuena. "Lithium-Ion Transport through Complex Interphases in Lithium Metal Batteries." *ACS Applied Materials & Interfaces* 14, No. 51 (2022): 56758−56766. https://doi.org/10.1021/acsami.2c16598].

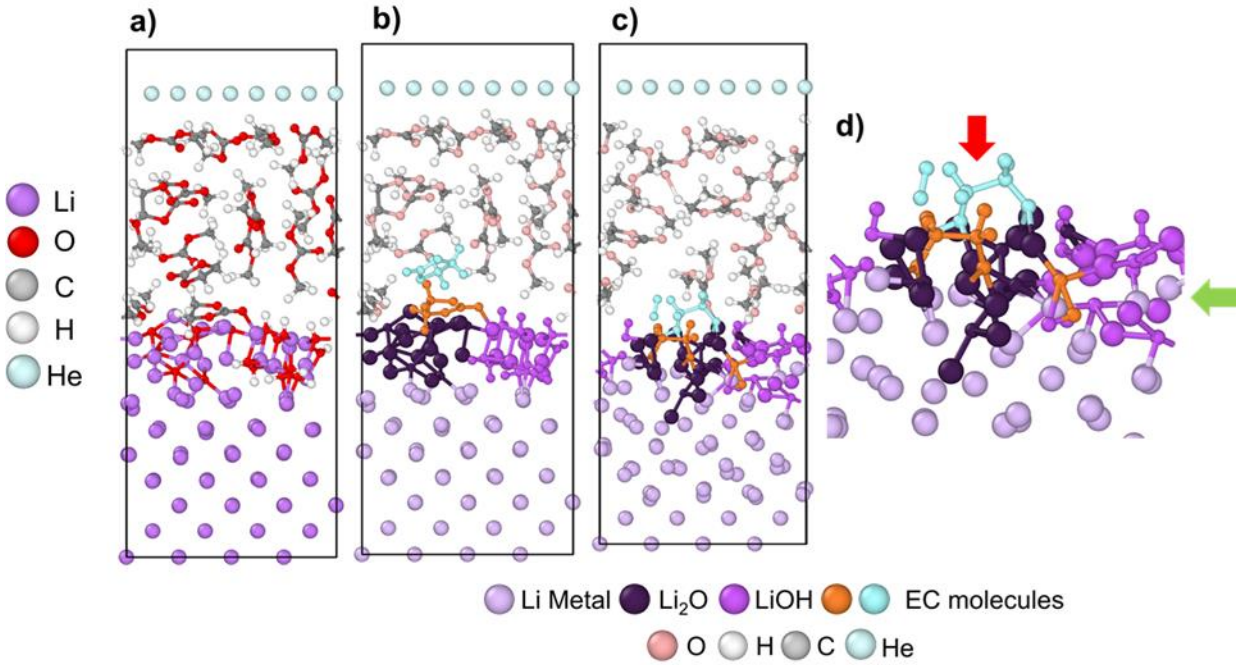

Figure 166. ***Ab initio*** **molecular dynamics (AIMD) simulation showing interfacial structural evolution for a Li-metal surface covered with SEI formed with Li_2O and LiOH, in contact with a 1:2 EC:DMC electrolyte. (a) Initial structure. (b) Initial structure color coded showing Li_2O and LiOH regions on the Li-metal surface. (c) Final structure after ~ 11 ps (AIMD at 300 K) showing EC molecules reacting preferentially on the Li_2O surface, and (d) close-up of structure shown in (c). The red arrow highlights reduced EC molecules, and the green arrow shows the motion of the Li-metal atoms toward the SEI surface.**

In addition, they are developing a kinetic Monte Carlo simulation code that addresses the growth of the SEI on Li-metal surfaces along with the lithium plating/stripping events. Their approach accurately describes the formation of a stratified SEI interphase that reproduces the main structural features of the organic and inorganic phases, similar to those proposed by E. Peled and other authors. First, they evaluate the lithium deposition rate impact on the formation of dendrites; second, they evaluate Li^+ ion mobility at the interface between inorganic SEI nanometer size clusters to investigate the Li^+ diffusion paths contributing to specific Li^+ deposition modes after repeated cycling.

Determining Relationship of Equilibrium Potential versus Lithium Content in NMC-811 Cathode for Battery Cell Performance Assessment and Diagnostics

The INL team recently developed a method to determine the equilibrium potential (V_{eq}) of NMC-811 cathode as a function of the lithium content in the NMC cathode active material (CAM) stoichiometry (that is, *x* in $Li_xNi_{0.8}Mn_{0.1}Co_{0.1}O_2$, or NMC-811). This V_{eq} versus *x* relationship can provide a reliable, consistent basis for assessing the utilization of CAM in the high-energy battery designs to achieve cell development goals.

The V_{eq} versus *x* relationship is often determined by the galvanostatic intermittent titration technique (GITT). The experiment is typically conducted by passing a certain amount of charge to the CAM composition in a stepwise manner incrementally and measuring the steady equilibrium potential of the electrode (V_{eq}) over a

sufficient rest period in each step of the charge increase. Thus, the V_{eq} as a function of the charge increment is the same as the V_{eq} versus *x* relationship with a presumption that the charge-composition correspondence is unity. The caveat is "if the CAM composition is fully utilized to assure that the presumption of a unified 'charge-composition correspondence' is validated."

Recently, through collaboration with Binghamton University, INL carefully examined the GITT data obtained from coin cells made of pristine EcoPro NMC-811 electrodes (named as E-C cells to stand for EcoPro-coin cells). Independently, the INL team conducted evaluations using cells made of Targray NMC-811 electrodes (named as T-C cells to denote Targray-coin cells). To evaluate cell performance, they typically conduct reference performance tests (RPTs) with a specific protocol to ensure consistency in the assessment using the same condition for analysis. During the initial RPT (RPT 0) using C/20 rate in a charge-discharge process, they obtained a reliable pseudo-open-circuit-voltage (pseudo-OCV) versus SOC curve, where the SOC is the normalized specific capacity. To obtain this pseudo-OCV versus SOC curve, the process usually entails normalization of the voltage profiles using the specific capacity measured in each charge-discharge process to obtain a normalized specific capacity in percentage or capacity ratio and use it as the SOC. Subsequently, a process of averaging the voltage profiles according to the SOC is performed to obtain the pseudo-OCV. At C/20 rate, the polarization effect is assumed small, and averaging the voltage profiles is further assumed capable of annihilating the polarization effect and yielding a dependable pseudo-OCV in correspondence with SOC. The caveat is "if the SOC represents the Li content *x*?"

The conundrum, either the GITT data (for Cell ID: E-C #3_4.4 as an example) or the pseudo-OCV profile (for Cell ID: T-C_4.4) in correspondence with specific capacity, as shown in Figure 167a, is a riddle that has not been answered to date. It is hard to pinpoint the origination of the differences in the experimental measurements. If the team uses the normalized specific capacity as SOC to present the data, as shown in Figure 167b, the similarity and consistency among the three profiles are improved, but the disparities in voltage correspondence with SOC among the three remain difficult to explain, since the polarization potential has been removed in the analysis. It could be suspected that the state of the cell during the measurement had not reached equilibrium, thus a certain degree of inhomogeneity may exist. However, the cell voltage and capacity should represent the volume-averaged results, so such an inhomogeneity should not be revealed on the global scale in this case. To resolve this conundrum, a proper analytic method would be highly desired.

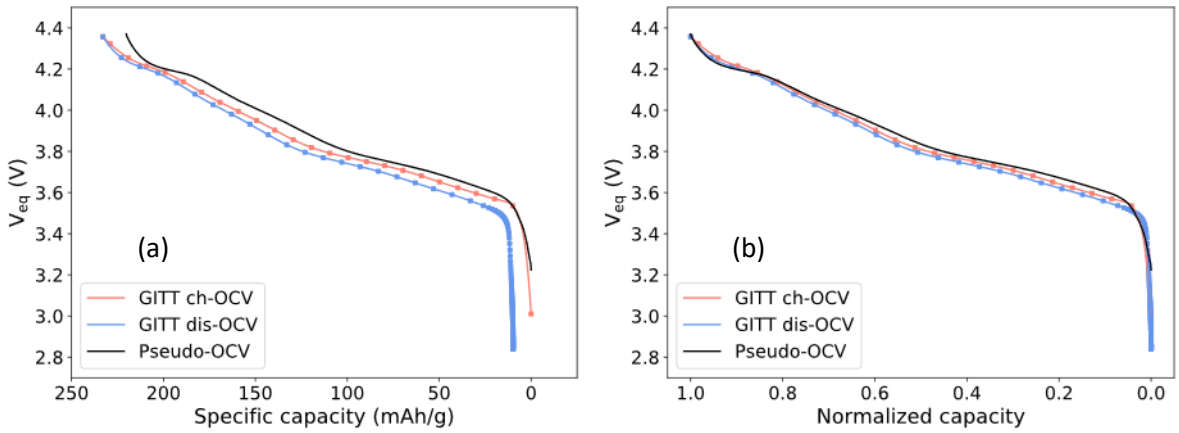

Figure 167. (a) Voltage profiles obtained from a GITT experiment using an EcoPro NMC-811 cathode by the University of Binghamton team (Cell ID: E-C #3_4.4) and the pseudo-OCV profile obtained from RPT 0 test using a Targray NMC-811 cathode by Idaho National Laboratory (Cell ID: T-C_4.4). (b) Voltage profiles presented in normalized capacity as state of charge.

Here, the INL team presented an interesting analytic solution to solve this riddle. Figure 168 shows that such a method is possible if these voltage profiles are presented in a true stoichiometric correspondence with the lithium content in the NMC-811 (or any CAM in general) composition. The data of these voltage profiles, shown in Figure 168a, were analyzed as follows:

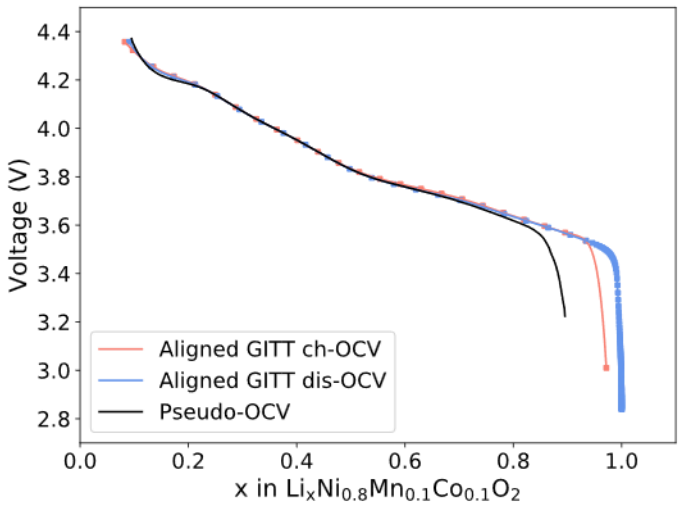

Figure 168. V_{eq} versus *x* profiles derived from the three voltage profiles shown previously in Figure 167 using dQ/dV obtained in each experiment and dQTh/dx derived from the theoretical capacity for NMC-811.

From each profile, the incremental differential capacity (dQ/dV) was calculated in the region between 4.1 V and 3.9 V, a composition range in which the capacity retention is usually quite reversible, in the team's experience. Based on the NMC-811 chemical formula/stoichiometry, they calculated the theoretical capacity of NMC-811 to be Q_{Th} = 275.5 mAh g^{-1}. For one percent of lithium content change in the NMC-811 stoichiometry, a corresponding $dQ_{Th}/dx|_{(Dx=0.01)}$ = 2.755 mAh g^{-1} of capacity should be obtained in principle when NMC-811 is fully utilized. Using the dQ/dV determined in the experiments and dQ_{Th}/dx derived from the chemical formula, the voltage profiles of the charge-discharge process in GITT and the pseudo-OCV profile are transformed consistently into a V_{eq} versus *x* correspondence. Such a transformation of a voltage profile in capacity to a corresponding profile in lithium stoichiometry in the CAM composition resolved the riddle of the differences in the capacities in the measurements associated with heterogeneous cell formulations and test protocols along with the issues about the origination of the capacity measured. More importantly, the cathode utilization efficiency can now be determined without ambiguity, as shown in Table 7.

Table 7. NMC-811 utilization coefficient and differential capacity (dQ/dV) for the three voltage profiles in Figure 166.

Voltage Profile	Capacity Q Measured (mAh g^{-1})	Utilization Coefficient	dQ/dV (mAh g^{-1} V^{-1})	Traversed Stoichiometry	Δx
Pseudo-Open Circuit Voltage	220.27	1.00	225.33	0.10 → 0.90	0.80
GITT charge	232.91	0.95	214.30	0.97 → 0.08	0.89
GITT discharge	223.09	0.89	200.71	0.09 → 1.00	0.91

One last riddle that needs clarification is the true correspondence with the lithium stoichiometry in the NMC-811 composition. The true stoichiometry of the pristine NMC-811 was unknown for all electrode materials used in this work. However, if the team examined the section toward the end-of-discharge in the GITT experiment, the sluggish lithium transport in the lattice created a challenging situation to conclude a stoichiometric point of a fully discharged state in NMC-811. Nonetheless, a very steep voltage drop with a tiny lithium content increment was observed in Figure 167. They thus postulated that it is prudent to hypothesize that the NMC-811 composition might be close to a stoichiometric point where $x = 1.00$ as fully discharged. Once this stoichiometric point was affirmed, all the other data points in the three voltage profiles should fall into place nicely with the lithium stoichiometry in the NMC-811 composition. Table 7 tabulates the results of the analysis and the NMC-811 utilization in the three voltage profiles. This analysis demonstrates that the CAM utilization coefficient can be reliably determined to reflect the true compositional changes in the charge-discharge process, whereas the capacity measured in each experiment was rationalized.

The implications from this analysis and the results suggest that the presumption of a one-to-one "charge-to-composition" correspondence might falsely give a correlation that is not well justified. Via correcting the charge-to-composition correspondence properly by using the CAM utilization efficiency, they obtained a truthful charge-to-composition correspondence to clearly reflect the kinetic impact on the CAM utilization and performance, which was not possible with capacity-based analysis. More reports on analyses of the data from different CAM synthesis methods, CAM compositions, electrode and cell formulations (including the electrolyte composition, electrode engineering, and cell geometry), and test conditions (including test protocols and aging conditions) will follow.

Highlights of Keystone Project 4

The highlights for this quarter are as follows:

- The BNL team employed XRF mapping to characterize TM dissolution on lithium metal. Surprisingly, nickel, rather than manganese, was found to be the main crossover species. This observation is consistent across various electrolytes.
- The SLAC team employed glovebox AFM to map nanoscale Young's modulus of SEI grown on lithium metal, providing fundamental understanding on how the SEI mechanical property regulates the microstructure of the deposited lithium metal.
- Using first-principle calculations, the Texas A&M team simulated the lithium transport mechanism in SEI. In a Li_2O-rich SEI, lithium transport occurs at the domain interfaces in the SEI. On the other hand, in LiOH-rich SEI, lithium migrates through the bulk of the SEI.
- The INL team carefully characterized the open-circuit potential of NMC-811, with the objective to link the lithium content change associated with the capacity in the cathode, which can be used to determine the utilization efficiency of the CAM in an electrode.

Patents/Publications/Presentations

Patent

- U.S. Provisional Patent Application No. 63/267,781. "Titration-Gas Chromatography Method and System for Anode Detection and Quantification in Energy Storage Devices." Y. S. Meng, C. Fang, et al.

Publications

- Zhang, X., P. Gao, Z. Wu, M. H. Engelhard, X. Cao, H. Jia, Y. Xu, H. Liu, C. Wang, J. Liu, J-G. Zhang, P. Liu,* and W. Xu.* "Pinned Electrode/Electrolyte Interphase and Its Formation Origin for Sulfurized Polyacrylonitrile Cathode in Stable Lithium Batteries." *ACS Applied Materials & Interfaces* 14, No. 46 (2022): 52046–52057. https://doi.org/10.1021/acsami.2c16890.
- Boyle, D. T., S. C. Kim, S. T. Oyakhire, R. A. Vilá, Z. Huang, P. Sayavong, J. Qin, Z. Bao, and Y. Cui. "Correlating Kinetics to Cyclability Reveals Thermodynamic Origin of Lithium Anode Morphology in Liquid Electrolytes." *Journal of the American Chemical Society 144, No. 45 (2022):* 20717–20725. https://doi.org/10.1021/jacs.2c08182.
- Gong, H., Y. Chen, S. Chen, C. Xu, Y. Yang, Y. Ye, Z. Huang, R. Ning, Y. Cui, and Z. Bao. "Fast-Charging of Hybrid Lithium-Ion/Lithium-Metal Anodes by Nanostructured Hard Carbon Host." *ACS Energy Letters* 7, No. 12 (2022): 4417–4426. https://doi.org/10.1021/acsenergylett.2c02130.
- Huang, Z., J-C. Lai, X. Kong, I. Rajkovic, X. Xiao, H. Celik, H. Yan, H. Gong, P. E. Rudnicki, Y. Lin, Y. Ye, Y. Li, Y. Chen, X. Gao, Y. Jiang, S. Choudhury, J. Qin, J. B-H. Tok, Y. Cui, and Z. Bao. "A Solvent-Anchored Non-Flammable Electrolyte." *Matter* 6, No. 2 (2022): 445–459. https://doi.org/10.1016/j.matt.2022.11.003.
- Boyle, D. T., Y. Li, A. Pei, R. A. Vilá, Z. Zhang, P. Sayavong, M. S. Kim, W. Huang, H. Wang, Y. Liu, R. Xu, R. Sinclair, J. Qin, Z. Bao, and Y. Cui. "Resolving Current-Dependent Regimes of Electroplating Mechanisms for Fast Charging Lithium Metal Anodes." *Nano Letters* 22, No. 20 (2022): 8224–8232. https://doi.org/10.1021/acs.nanolett.2c02792.
- Ren, Y., and A. Manthiram. "A Dual-Phase Electrolyte for High-Energy Lithium-Sulfur Batteries." *Advanced Energy Materials* 12, No. 46 (2022): 2202566. https://doi.org/10.1002/aenm.202202566.
- Su, L., S. S. Kumar, A. Manthiram, and B. Reeja-Jayan. "A Review on Application of Poly(3,4-Ethylenedioxythiophene) (PEDOT) in Rechargeable Batteries." *Organic Materials* 4 (2022): 292–300. https://doi.org/10.1055/a-1990-3149.
- Pan, R., E. Jo, Z. Cui, and A. Manthiram. "Degradation Pathways of Cobalt-Free $LiNiO_2$ Cathode in Lithium Batteries." *Advanced Functional Materials* 33, No. 10 (2022). https://doi.org/10.1002/adfm.202211461.
- Angarita-Gomez, S., and P. B. Balbuena. "Lithium-Ion Transport through Complex Interphases in Lithium Metal Batteries." *ACS Applied Materials & Interfaces* 14, No. 51 (2022): 56758–56766. https://doi.org/10.1021/acsami.2c16598.
- Beltran, S. P., and P. B. Balbuena. "SEI Formation Mechanisms and Li^+ Dissolution in Lithium Metal Anodes: Impact of the Electrolyte Composition and the Electrolyte-to-Anode Ratio." *Journal of Power Sources* 551 (2022): 232203. https://doi.org/10.1016/j.jpowsour.2022.232203.
- Lu, B., W. Li, D. Cheng, M. Ceja, W. Bao, C. Fang, and Y. S. Meng. "Suppressing Chemical Corrosions of Lithium Metal Anodes." *Advanced Energy Materials* 12, No. 48 (2022): 2202012. https://doi.org/10.1002/aenm.202202012.

- Liaw, B., G. Pawar, Y. S. Meng, C. Fang, and B. Lu. "Perspective—Lithium Metal Nucleation and Growth on Conductive Substrates: A Multi-Scale Understanding from Atomistic, Nano-, Meso-, to Micro-Scales." In Special Issue on Nucleation and Growth: Measurements, Processes, and Materials, *Journal of the Electrochemical Society* 169 (2022): 112505. https://doi.org/10.1149/1945-7111/ac9a08.
- Tan, S., J-M. Kim, A. Corrao, S. Ghose, H. Zhong, N. Rui, X. Wang, S. Senanayake, B. J. Polzin, P. Khalifah, J. Xiao, J. Liu, K. Xu, X-Q. Yang, X. Cao,* and E. Hu.* "Unravelling the Convoluted and Dynamic Interphasial Mechanisms on Li Metal Anodes." *Nature Nanotechnology* 18 (2022): 243–249. https://doi.org/10.1038/s41565-022-01273-3.

Presentations (Invited)

- 242nd Electrochemical Society (ECS) Meeting, Atlanta, Georgia (October 9, 2022): "Development of Li Metal Batteries with Improved Safety"; X. Cao (presenter), W. Xu, J. Kim, and J-G. Zhang.
- American Chemical Society (ACS) Western Regional Meeting, Las Vegas, Nevada (October 20, 2022): "Enabling Lithium Metal Anode by Advancing Electrolytes and Lithium Protection"; W. Xu (presenter), J-G. Zhang, X. Cao, and X. Ren.
- International Battery Association Meeting (IBA22), Bled, Slovenia (October 2–7, 2022): "Pushing the Limits of Layered Oxide Cathodes"; A. Manthiram. Plenary talk.
- IEEE Electrical Energy Storage Applications and Technologies, Austin, Texas (November 7–9, 2022): "Sustainable Battery Chemistries for a Cleaner Planet"; A. Manthiram. Plenary talk.
- 11th Sustainable Nanotechnology Organization Conference, Austin, Texas (November 11–13, 2022): "Sustainable Battery Technologies for a Cleaner Environment"; A. Manthiram. Plenary talk.
- 242nd ECS Fall Meeting, Atlanta, Georgia (October 2022): "Pushing Lithium-Metal Batteries to the Limit: Fast Charging, Low Temperature, and Safety"; P. Liu.
- Korean Institute of Science and Technology, Seoul, Korea (December 2022): "Developing High Performance and Safe Lithium Batteries"; P. Liu.
- 13th International Conference on Advanced Lithium Batteries for Automobile Applications (ABAA-13), Marrakech, Morocco (October 16–19, 2022): "Approaches to Long-Life Li-S Batteries"; P. Liu.
- Korea Brainlink Conference, Incheon, Korea (November 2022): "Approaches to Long-Life Li-S Batteries"; P. Liu.
- Seminar to Polymer Technology Center, Texas A&M University (October 7, 2022): "Role of Polymers at Interfaces in Advanced Batteries"; P. B. Balbuena.
- Department of Chemical Engineering, Georgia Institute of Technology, Atlanta, Georgia (November 9, 2022): "On the Importance of Assessing Interfacial Instabilities in Materials Design"; P. B. Balbuena.
- Department of Electrical Engineering, University of Houston, Houston, Texas (December 2, 2022): "SEI Formation at the Li Metal/Electrolyte Interface: Structure, Morphology, Composition, and Properties"; P. B. Balbuena.
- 242nd ECS Meeting, Research and Development of Primary and Secondary Batteries Symposium, Atlanta, Georgia (October 9–13, 2022): "From Lithiated Transition Metal Oxides to Silicon to Lithium-Sulfur: Evolution of Electrochemically Active Materials"; P. N. Kumta.
- ABAA-13, Marrakech, Morocco (October 19, 2022): "The Key Challenges for Rechargeable Lithium Metal Batteries"; Y. S. Meng.
- ACS Western Regional Meeting, Las Vegas, Nevada (October 20, 2022): "Understanding and Improvement of High-Energy Density Li Metal Batteries"; B. Li.
- 242nd ECS Fall Meeting, Atlanta, Georgia (October 9–13, 2022): "A New Perspective on Layered Transition Metal Oxides as Cathode Active Materials"; B. Liaw and M. Li.

- IBA22, Bled, Slovenia (October 2–7, 2022): "A Unified Perspective and Analytical Approach of Layered Cathode Active Materials"; B. Liaw and M. Li.
- Muhlenberg College, Allentown, Pennsylvania (November 4, 2022): "Clockwork Inside Cathodes – Unparalleled Insights into Defects and Inhomogeneities"; P. Khalifah.

Cathode-Electrolyte Interphase (CEI) Consortium (Jie Xiao, Pacific Northwest National Laboratory)

Project Objective. The goal of the Cathode-Electrolyte Interphase (CEI) Consortium is to develop a platform to quickly identify, understand, and tackle key challenges of CEI relevant to realistic Li-ion batteries by integrating different scientific tools and expertise from various laboratories and universities. The CEI Consortium examines the interfacial reactions between cathode and electrolytes at high voltages, which critically dictate the observed cell performances. The capabilities developed and integrated within the CEI Consortium also directly support the Earth-abundant Cathode Active Materials (EaCAM) Consortium and the Cation Disordered Rocksalt (DRX+) Materials Consortium, which both focus on cathode materials development.

Project Impact. The CEI Consortium will identify and address fundamental challenges in stabilizing CEI to accelerate research and development of cathode materials such as nickel-rich Ni-Mn-Co (polycrystal and/or single crystal in this consortium), disordered rocksalt (DRX+ Consortium) and Mn-rich (EaCAM Consortium) cathode materials. The knowledge gathered from the CEI Consortium will not only be utilized to enhance CEI properties, but it will also provide guidelines for designing compatible electrolytes and stabilizing cathode materials at high voltages.

Approach. All the hypotheses and new discoveries from the CEI Consortium will be cross validated in coin cells assembled and tested at industry relevant conditions to ensure the consortium is tackling real world challenges for battery industry. Each laboratory under this consortium has at least one university partner, most of which are from Minority Serving Institutions or underrepresented groups. Through collaborative research between laboratories and universities, the CEI Consortium will cultivate future scientists and engineers in battery research, development, and demonstration and support the U.S. Department of Energy on workforce retraining in energy storage.

Out-Year Goals. The out-year goal is to establish a database of baseline performances of model cathodes and electrolytes to be used under this consortium to benchmark full research progress. Both half-coin-cell and full-coin-cell assembly and testing protocols will be developed.

Collaborations. Collaboration among consortium team members will be well coordinated by Pacific Northwest National Laboratory. The CEI Consortium has three focused groups: (1) model cathode materials, (2) electrolyte, and (3) characterization & modeling. The lead of each focused group will work with the principal investigators of the corresponding group for periodical information and materials exchange. The three groups will have joint biweekly meetings and quarterly reviews.

Milestones

1. Complete selection and synthesis of model cathode materials and baseline electrolytes to be studied in the consortium. (Q1, FY 2023; Delayed start)
2. Demonstrate consistent performances of cathode and reliable/repeatable CEI properties. (Q2, FY 2023)
3. Probe CEI at different scales aided by modeling. (Q3, FY 2023)
4. Develop full-coin-cell testing protocols (using graphite anode) for future hypothesis/discovery validation. (Q4, FY 2023)

NOTE: **This new project will begin reporting progress next quarter.**

Cation Disordered Rocksalt (DRX+) Materials Consortium (Gerbrand Ceder, University of California, Berkeley)

Project Objective. This project aims to develop high-energy, high-rate Ni- and Co-free cation disordered rocksalt (DRX) cathode materials based on manganese as a cost-effective, earth-abundant, and safe redox-active element. Specifically, Gen1-DRX achieving 650 Wh/kg at 100 mA/g for at least 100 cycles will be optimized and scaled up. Gen2-DRX achieving at least 700 Wh/kg at 100 mA/g for 300 cycles will be developed through the application of functional coatings on Gen1, incorporation of electrolyte improvements, and further compositional and morphological refinements. Gen3-DRX with very high specific energies between 850 Wh/kg and 1100 Wh/kg will be explored by introducing partial disorder in the structure.

Project Impact. DRX and related materials are well positioned to address resource limitations and cost concerns posed by use of nickel and cobalt in traditional Ni-Mn-Co based cathodes. This promising sustainable cathode technology can potentially scale Li-ion batteries to multiple TWh annual production at low cost.

Approach. Technical approaches in this research program span from materials development to electrode fabrication optimization, including:

- Develop high-voltage electrolytes specifically optimized for the DRX materials being pursued in the consortium. Investigate additives as well as solvent and salt modifications to enable more stable cycling of Gen1 and Gen2 cathodes at high voltage.
- Apply inorganic and carbonaceous coatings to DRX surface for protection and creation of electronic pathways in cathode composites with low carbon content. Develop, evaluate, and optimize an effective, scalable process of creating carbonaceous conformal coatings on DRX powder materials.
- Evaluate synthesis approaches and conditions; optimize composition and morphology of Gen1-DRX. Scale up the synthesis to produce larger quantity of materials needed in the consortium.
- Explore partially disordered Mn-based materials as high-energy, high-rate cathodes made with scalable synthesis methods. Investigate in detail the structure and synthesis pathways of these metastable materials, leading to materials with > 1000Wh/kg.
- Improve DRX electrode fabrication by lowering carbon content and optimizing particle size and morphology of components. Establish optimal voltage limits and cycling protocols for DRX cathodes.

Out-Year Goals. DRX cathodes that match or exceed the performance metrics of the current state-of-the-art NMC-based cathode materials will be delivered. Gen1-DRX with 650 Wh/kg at 100 mA/g for 100 cycles will be optimized and scaled up. Gen2-DRX with at least 700 Wh/kg at 100 mA/g for 300 cycles will be developed. Development of Gen3-DRX with very high specific energies between 850 and 1100 Wh/kg will be initiated.

Collaborations. This multiorganizational consortium effort includes the following participants: Lawrence Berkeley National Laboratory; University of California, Santa Barbara; Pacific Northwest National Laboratory; Oak Ridge National Laboratory; Argonne National Laboratory; and SLAC National Accelerator Laboratory.

Milestones

1. Construct models for structural disorder in partially disordered spinels and the relation to lithium mobility. (Q1, FY 2023; In progress)
2. Determine thermal properties of DRX cathodes charged to 4.4 V, 4.6 V, 4.8 V, and 5.0 V. (Q2, FY 2023)
3. Deliver at least three baseline composite DRX/C materials with carbon or nanocrystalline graphite coating. Evaluate their electrochemical performance. (Q3, FY 2023)
4. Complete high-voltage stability tests on ethylene carbonate – lean electrolytes with three additives (FEC, VC, TMSPa). Down-select to the top performing electrolyte. (Q4, FY 2023)

***NOTE:* This new project will begin reporting progress next quarter.**

Earth-Abundant Cathode Active Materials (EaCAM) Consortium (Jason Croy, Argonne National Laboratory)

Project Objective. The long-term objectives of this program are the discovery and development of mechanistic insights, novel materials, new processes, and design strategies as well as dissemination of information that enable cathode compositions based 100% in earth abundant, sustainable chemistries. The ultimate goal will be synthetic control of pre-determined particle designs, local ordering, integrated structures, dopant site-selectivity, and primary and secondary morphologies, including monolithic architectures, of high-energy earth-abundant cathode active materials (EaCAM). Such advancements would contribute greatly to lowering cost and increasing sustainability of next-generation technologies for transportation applications and beyond.

Project Impact. Prioritizing earth-abundant elements in the search for new technologies has direct and positive impacts across the Three Pillars of Sustainable Development and will substantially accelerate progress toward diversifying supply chains, increasing sustainability, and broadening the portfolio of storage technologies. In addition, the space of exploration related to the complex integration of structure types, local- and long-range, as well the correlations to synthesis-structure-property relationships is large. It is expected that detailed investigations in this space will lead to new insights and directions in advanced design and synthesis of cathode active materials. Furthermore, new approaches to oxide surface stabilization, including electrolyte formulations, will be developed.

Approach. The EaCAM team will build on its considerable experience in areas of critical importance to advance project goals. Focused areas of collaboration will be established to gain insight on complex synthesis-structure-property relationships that govern materials properties from the atomic scale to electrode-level performance. Atomistic, electrochemical, and techno-economic modeling will be combined with synthesis/processing, advanced structural/chemical characterization, and electrochemical analysis to establish mechanistic models of performance and degradation across length scales. Manganese, and Mn-based cathodes will serve as the initial platforms to explore the complex and broad space of EaCAM design related thereto.

Out-Year Goals. The out-year goal is for Mn-rich (> ~ 50%) cathode materials that can achieve 250-300 Wh/kg_{cell} for ~ 1000 cycles at C/3.

Collaborations. The EaCAM Consortium is a collaboration between seven national laboratories (that is, Argonne National Laboratory, National Renewable Energy Laboratory, Oak Ridge National Laboratory, Pacific Northwest National Laboratory, SLAC National Accelerator Laboratory, Idaho National Laboratory, and Lawrence Berkeley National Laboratory) and eight universities represented through embedded graduate students.

Milestones

1. Establish targeted test protocols for EaCAM oxides. (Q1, FY 2023; Complete/Ongoing)
2. Identify high figure of merit additives and surface treatments and correlate performance to properties. (Q2, FY 2023; In progress)
3. Publish report on strategic cation doping of EaCAM oxides with electrochemical/physical evaluation. (Q3, FY 2023; On track)
4. Publish report on charge compensation in newly developed, novel EaCAM oxides. (Q4, FY 2023; On track)

***NOTE:* This new project will begin reporting progress next quarter.**

APPENDIX – ACRONYM GUIDE

Acronym	Full Description
1,4-DX	1,4-dioxane
1D	one-dimensional
2D	two-dimensional
3D	three-dimensional
3DOM	three-dimensional ordered microporous
3D-OMSH	three-dimensionally ordered microporous sulfur host
AA	ammonium assisted
AB	acetylene black
ABAA	Advanced Lithium Batteries for Automobile Applications
ABL	active buffer layer
AC	alternating current
ACN	acetonitrile
ACPA	4,4'-azobis(4-cyanopentanoic acid
ACS	American Chemical Society
ADF	annular dark-field
AEI	anode-electrolyte interphase
AFLB	anode-free lithium battery
AFM	atomic force microscopy
AFSB	anode-free sodium battery
AFSE	fluorinated saturated electrolyte with 0.1 wt% additive
AGG	aggregate
AIBN	azobisisobutyronitrile
AIMD	*ab initio* molecular dynamic
AIR	areal interfacial resistance
ALD	atomic layer deposition
ALS	Advanced Light Source
ANL	Argonne National Laboratory
ANN	artificial neural network
AOM	amphipathic organic molecules
APS	Advanced Photon Source
APUP	Alliance Partner University Program
AQC	anthraquinone-2-carboxylic acid
AQT	1,5-bis(2-(2-(2methoxyethoxy)ethoxy)ethoxy) anthra-9,10-quinone
ARC	accelerating rate calorimetry
ARL	U. S. Army Research Laboratory
ASR	area specific resistance
ASSB	all-solid-state battery
ASSLB	all-solid-state lithium battery
ASSLMB	all-solid-state Li-metal battery
ASSLSB	all-solid-state Li-S battery
ATR	attenuated total reflectance
β-LPS	β-phase Li_3PS_4

Acronym	Full Description
BBP	benzyl butyl phthalate
BCC	body-centered cubic
BE	baseline electrolyte
BEV	battery electric vehicle
BL	bottom layer
BMIM	1-butyl-3-methylimidazolium
BMR	Advanced Battery Materials Research Program
BNL	Brookhaven National Laboratory
BPO	benzoyl peroxide
BSC	baseline sulfur cathode
BTFE	bis(2,2,2trifluoroethyl) ether
BV	Butler-Volmer
c-AIMD	constrained – *ab initio* molecular dynamics
CA	chronoamperometry
CAM	cathode active material
CC	constant current
CCCV	constant current / constant voltage
CCD	critical current density
$CCD^{plating}$	plating critical current density
$CCD^{stripping}$	stripping critical current density
CE	Coulombic efficiency
CEI	cathode electrolyte interface
CEI Consortium	Cathode-Electrolyte Interphase Consortium
CFM	carbon-based framework material
CI-NEB	climbing image nudged elastic band
CIP	contact ion pair
CLP	cycle life projection
CM	co-melting
CMC	carboxymethyl cellulose
CMD	classical molecular dynamics
CN	coordination number
CNC	carbon nano-cage
CNM	Center for Nanoscale Materials
CNT	carbon nanotube
COF	covalent organic frameworks
COP	critical overpotential
CP	cold pressed
CPE	composite polymer electrolyte
cryo	cryogenic
cryo-EM	cryogenic electron microscopy
cryo-FIB	cryogenic – focused ion beam
cryo-FIB-SEM	cryogenic – focused ion beam – scanning electron microscopy
cryo-STEM	cryogenic – scanning transmission electron spectroscopy
cryo-TEM	cryogenic – transmission electron microscopy
CS	corner-sharing
CSC	compressed sulfur cathode

Acronym	Full Description
CSF	corner-sharing frameworks
CSM	continuous symmetry measure
Csp	specific discharge capacity
CSSE	cluster-based solid-state electrolyte
CT	computed tomography
CV	cyclic voltammetry
CVT	chemical vapor transport
DAPS	diallyl polysulfide
DBE	dibutyl ether
DB-ML-FF	density-based machine-learning force field
DC	direct current
DCA	dicyanamide
DCT	diffraction contrast tomography (DCT)
DEB	double-end binding
DEC	diethyl carbonate
DEE	1,2-diethoxyethane
DEGDME	diethylene glycol dimethyl ether
DEMS	differential electrochemical mass spectrometry
DFE	defect formation energy
DFOB	difluoro(oxalate) borate
DFT	density functional theory
DiPE	diisopropyl ether
DIW	direct ink writing
DI	dual layer
DLR	Deutsches Zentrum für Luft- und Raumfaurt
DMC	dimethyl carbonate
DME	1,2-dimethoxyethane
DMF	dimethyl formamide
DMSO	dimethylsulfoxide
DOD	depth-of-discharge
DOE	U. S. Department of Energy
DOL	1,3-dioxolane
DOS	density of states
dP/dV	differential pressure
dPEO	dynamic bonds between polymer chains
dQ/dV	differential capacity
DRT	distribution of relaxation times
DRX	disordered rocksalt
DRX+ Consortium	Cation Disordered Rocksalt Materials Consortium
DSC	differential scanning calorimetry
DTL	dimethyl ether – trimethylolpropane – lithium nitrate
EaCAM	earth-abundant cathode active material
EaCAM Consortium	Earth-Abundant Cathode Active Material Consortium
E/C	electrolyte/capacity
EC	ethylene carbonate
eCAD	electrochemical analytic diagnosis

Acronym	Full Description
EC-AFM	electrochemical atomic force microscopy
ECS	The Electrochemical Society
EDB	denotation for electrolyte of 1 M $LiPF_6$ in ethylene carbonate / diethyl carbonate (v/v = 1:1) with 1 wt% % lithium difluoro(oxalate)borate
EDF	denotation for electrolyte of 1 M $LiPF_6$ in ethylene carbonate / diethyl carbonate (v/v = 1:1) with 15 wt% fluoroethylene carbonate
EDFB	denotation for electrolyte of 1 M $LiPF_6$ in ethylene carbonate / diethyl carbonate (v/v = 1:1) with 15 wt% fluoroethylene carbonate and 1 wt% lithium difluoro(oxalate)borate
EDL	electrical double layer
EDLi	electrochemically deposited lithium
EDS	energy-dispersive X-ray spectroscopy (also known as EDX)
EELS	electron energy loss spectroscopy
eGF	exfoliated graphene fluoride
EIS	electrochemical impedance spectroscopy
eLi	engineered lithium
EM	electron microscopy
EMC	ethyl methyl carbonate
EMIM-BF_4	1-ethyl-3-methylimidazolium tetrafluoroborate
eNMR	electrophoretic nuclear magnetic resonance
EO	ethylene oxide
EPR	electron paramagnetic resonance
EQ-SANS	extended Q-range small-angle neutron scattering diffractometer
E/S	electrolyte/sulfur
EtOH	ethylene
EV	electric vehicle
EXAFS	extended X-ray absorption fine structure
EY	electron yield
F_4EO_2	1,1,1,2,2,3,3,4,4-nonafluoro-6-(2-methoxyethoxy)hexane
F4-DFOB	1.2 M LiFSI in F4DEE with difluoro(oxalate) borate additive
F5DEE (F5)	fluorinated-1,2-diethoxyethanes electrolyte
FAM	functional monomer additive molecule
FCC	face-centered cubic
FDEB	fluorinated 1,4-diethoxybutane
FDMB	fluorinated 1,4-dimethoxylbutane
FDMH	fluorinated 1,6-dimethoxyhexane
FDMO	fluorinated 1,8-dimethoxyoctane
FDMP	fluorinated 1,5-dimethoxypentane
FEC	fluoroethylene carbonate
FEM	finite element method
FESEM	field emission scanning electron microscopy
FF	force field
FFT	fast Fourier transform
FIB	focused ion beam
fs	femtosecond
FSE	fluorinated saturated electrolyte

Acronym	Full Description
FSI	bis(fluorosulfonyl)imide
FTIR	Fourier transform infrared
FWHM	full width at half maximum
FY	fluorescence yield
FZJ	Forschungszentrum Jülich
G3	triethylene glycol dimethyl ether
GAUSS	graphdiyne aerogel assisted ultra-fast sparking synthesis
GB	grain boundary
gc	glass/ceramic
GCMA	glycerol carbonate methacrylate
GC-MS	gas chromatography – mass spectrometry
GCPL	galvanostatic cycling with potential limitation
GDL	gas diffusion layer
GE	gel electrolyte
GGA	generalized gradient approximation
GITT	galvanostatic intermittent titration technique
GL	lithium glycerol
GM	General Motors
GOMD	Glass & Optical Materials Division
GP	Gaussian process
GPC	gel permeation chromatography
GPRA	Government Performance and Results Act
Gr	graphene
GRC	Gordon Research Conference
GSE	glassy solid electrolyte
GtO	graphite oxide
HAADF	high-angle annular dark-field
HATN	hexaazatrinaphthylene
HATN/CNT-S	hexaazatrinaphthylene / carbon nanotube polymer – sulfur composite
HATN-S	hexaazatrinaphthylene polymer – sulfur composite
HC	hard carbon
HCE	high-concentrated electrolyte
HCFM-S	sulfur-infiltrated high-surface-area carbon-based complex framework materials
HEV	hybrid electric vehicle
HEXRD	high-energy X-ray diffraction
HFB	hexafluorobenzene
HFE	hydrofluoroether
HFP	hexafluoropropylene
HG	hand grinding
HGDY	hydrogen substituted graphdiyne
H-NMR	hydrogen nuclear magnetic resonance
HOMO	highest occupied molecular orbital
HOPG	highly oriented pyrolytic graphite
HP	hot pressed
HPC	high-performance computing
HpLC	high precision leakage current

Acronym	Full Description
HPLC	high-performance liquid chromatography
HRTEM	high-resolution transmission electron microscopy
HT	high throughput
HV	high voltage
IBA	International Battery Materials Association
IEEE	Institute of Electrical and Electronics Engineers
IL	ionic liquid
INL	Idaho National Laboratory
in-SEM	*in situ* scanning electron microscopy
IOFM	inorganic-organic framework material
IPA	isopropanol
IR	infrared
ISC	internal short circuit
ISEL	Israel Electrochemical Society
ISU	Iowa State University
KAIST	Korea Advanced Institute of Science and Technology
KB	Ketjenblack
KMC	kinetic Monte Carlo
KPFM	Kelvin probe force microscopy
LAGP	Li-Al-Ge-P
LAMMPS	large-scale atomic/molecular massively parallel simulator
LATP	Li-Al-Ti-P, such as $Li_{1+x}Al_xTi_{2-x}(PO_4)_3$ or $Li_{1.3}Al_{0.3}Ti_{1.7}(PO_4)_3$
LBNL	Lawrence Berkeley National Laboratory
LBO	Li-B-O, such as Li_3BO_3
LBS	Li-B-S
LCD	limiting current density
LCE	low-concentration electrolyte
LCO	$LiCoO_2$
LCRC	Laboratory Computing Resource Center
LDBE	1.8 M LiFSI in dibutyl ether
LDEE	1.8 M LiFSI in diethyl ether / BTFE
LDiPE	1.8 M LiFSI in diisopropyl ether
LDME	LiFSI in 1,2-dimethoxyethane / bis(2,2,2-trifluoroethyl) ether
LE	liquid electrolyte
LEDC	lithium ethylene dicarbonate
LFP	lithium iron phosphate
LGPS	Li-Ge-P-S, such as $Li_{10}GeP_2S_{12}$
LHCE	localized high-concentration electrolyte
LHS	left-hand side
Li_2EDC	di-lithium ethylene di-carbonate
LiBOB	lithium bis(oxalate)borate
LIC	Li-ion conductor
LiDFOB	lithium difluoro(oxalate) borate
LiDFP	lithium difluorophosphate
LiEDC	lithium ethylene decarbonate
LiFSI	lithium bis(fluorosulfonyl)imide

Acronym	Full Description
Li-Gr	lithiated graphite
Li-Si	lithiated silicon
Li-MCA	lithium multicomponent alloy
Li-NMC	lithium – nickel manganese cobalt oxide
LiPS	lithium polysulfide
LiPSes	lithium polyselenides
Li-SIA	Li-containing structurally isomorphous alloy
LiTFSI	lithium bis(trifluoromethanesulfonyl)imide
LLNL	Lawrence Livermore National Laboratory
LLTO	Li-La-Ti-O, such as $Li_{3x}La_{2/3-x}TiO_3$
LLZ	Li-La-Z
LLZO	Li-La-Z-O, such as $Li_7La_3Zr_2O_{12}$
LLZTO	Li-La-Zr-Ta-O, such as $Li_{6.75}La_3Zr_{1.75}Ta_{0.25}O_{12}$
LMO	$LiMn_2O_4$
LMR-NMC	Li- and Mn-rich Ni-Mn-Co
LNO	$LiNiO_2$
LNTO	Li-Nb-Ti-O_3
LOB	Li-O battery
LPC	large particle cathode
LPS	Li-P-S, such as Li_3PS_4
LPSB	Li-P-S-Br, such as Li_3PS_4 + ½LiBr
LPSBI	Li-P-S-Br-I, such as $Li_7P_2S_8Br_{0.5}I_{0.5}$
LPSBr	Li-P-S-Br, such as Li_6PS_5Br
LPSCl	Li-P-S-Cl, such as Li_6PS_5Cl
LPSI	Li-P-S-I, such as Li_3PS_4 + ½LiI
LPSIB	Li-P-S-I-Br, such as $Li_7P_2S_8I_{0.5}Br_{0.5}$
LSE	localized saturated electrolyte
LSiPCl	Li-Si-P-Cl, such as $Li_{9.54}Si_{1.74}P_{1.44}S_{11.7}Cl_{0.3}$
LSnS	Li-Sn-S, such as $Li_{3.85}Sn_{0.85}Sb_{0.15}S_4$
LSV	linear sweep voltammetry
LTO	$Li_4Ti_5O_{12}$
LUMO	lowest unoccupied molecular orbital
LV	low voltage
LYC / LYCl	Li-Y-Cl, such as Li_3YCl_6
MC	Monte Carlo; mechanochemical
MCA	multicomponent alloy; mechanochemical annealed
MD	molecular dynamics
METS	multiharmonic electrothermal spectroscopy
MGF	mixed glass former
MIC	molecular ionic composite
MIC-SPE	mixed ion conductor solid polymer electrolyte
ML	machine learning
MLD	molecular layer deposition
MLFF	machine learning force field
MLMD	molecular dynamics simulation with machine-learning potential
MOF	metal-organic framework

Acronym	Full Description
MOS	mixed oxy-sulfide
MOSN	mixed oxy-sulfide nitride
MPI	message-passing interface
MRS	Materials Research Society
MS	mass spectrometry
MSD	mean square displacement
MSE	mean squared error
MTU	Michigan Technological University
MWCNT	multiwalled carbon nanotube
MYEGA	Mauro–Yue–Ellison–Gupta–Allan model
NA	$LiNi_{0.95}Al_{0.05}O_2$
NaFSI	sodium bis(fluorosulfonyl)imide
NaNMC	Na-N-Mn-Co, such as $NaNi_{0.4}Mn_{0.4}Co_{0.2}O_2$ and $NaNi_{0.68}Mn_{0.22}Co_{0.1}O_2$
nano-CT	X-ray nano-computed tomography
nano-FTIR	Fourier transform infrared nano-spectroscopy
NASICON	sodium super ionic conductor
NaTFSI	sodium bis(trifluoromethylsulfonyl)imide
NATM	Ni-Al-Ti-Mg, such as $LiNi_{0.93}Al_{0.05}Ti_{0.01}Mg_{0.01}O_2$
NBO	nonbridging oxygen
NBR	nitrile butadiene rubber
NBS	nonbridging sulfur
NC	Ni-Co, such as $LiNi_{0.94}Co_{0.06}O_2$
NCA	$LiNi_{0.8}Co_{0.15}Al_{0.05}O_2$
NCEM	National Center for Electron Microscopy
NCM	Ni-Co-Mn
NCM-85105	$LiNi_{0.85}Co_{0.10}Mn_{0.05}O_2$
NCSE	non-calendered sulfur electrode
ND	di-coordinated nitrogen
NEB	nudged elastic band
NewEle	New Element
NF	nanoflake
NFM	P2 $Na_{0.67}Fe_{0.3}Mn_{0.5}O_2$ without Mg/Ti co-doping; also, $NaNi_{0.4}Fe_{0.2}Mn_{0.4}O_2$
NMFMT	P2 $Na_{0.67}Fe_{0.3}Mn_{0.5}O_2$ with Mg/Ti co-doping
NKB	nitrogen-doped integrated Ketjen Black
NLNMF	Na-Li-Ni-Mn-Fe, such as $Na_{0.85}Li_{0.1}Ni_{0.175}Mn_{0.525}Fe_{0.2}O_2$
NM	$LiNi_{0.95}Mn_{0.05}O_2$
NM11	$NaNi_{0.5}Mn_{0.5}O_2$
NMA	$LiNi_{0.9}Mn_{0.05}Al_{0.05}O_2$
NMC	Ni-Mn-Co
NMC-111	$LiNi_{1/3}Mn_{1/3}Co_{1/3}$
NMC-622	$LiNi_{0.6}Mn_{0.2}Co_{0.2}$
NMC-811	$LiNi_{0.8}Mn_{0.1}Co_{0.1}$
NMDC	Nanotechnology Materials and Devices Conference
NMF	nonnegative matrix factorization
NMF-111	$NaNi_{1/3}Mn_{1/3}Fe_{1/3}O_2$
NMF-112	$NaNi_{1/4}Mn_{1/4}Fe_{1/2}O_2$

Acronym	Full Description
NMFCN	Na-Mn-Fe-Co-Ni
NMP	N-methyl-pyrrolidone
NMR	nuclear magnetic resonance
NN	neural network
NNP	neural network interatomic potentials
NNT	sodium nonatitanate
N/P ratio	capacity ratio between anode (negative electrode) and cathode (positive electrode)
NP	nanoparticle
NPCE	nonflammable polymer composite electrolyte
n-PDF	neutron diffraction and pair distribution function
NPT	constant number of atoms (N), pressure (P), and temperature (T)
NREL	National Renewable Energy Laboratory
ns	nanosecond
NSLS	National Synchrotron Light Source
NT	tri-coordinated nitrogen
NTO	sodium titanate
NVE	constant number (N), volume (V), and energy (E)
NVP	$Na_3V_2(PO_4)_3$
NVT	constant temperature, constant volume ensemble
OBD	Organic Battery Days Workshop
OCV	open circuit voltage
OER	oxygen evolution reaction
OMSH	ordered microporous sulfur host
ORNL	Oak Ridge National Laboratory
ORR	oxygen reduction reaction
OSU	Ohio State University
PAH	polycyclic aromatic hydrocarbon
PAN	polyacrylonitrile
PAQS	poly(anthraquinonyl sulfide)
PB	Prussian blue
PBDT	poly(2,2'-disulfonyl-4,4'-benzidine terephthalamide)
PC	propylene carbonate; polycrystalline
PCA	principal component analysis
PCC	Pearson correlation coefficient
PC-LCHE	polymeric colloidal localized high-concentration electrolyte
PDF	pair distribution function
PDMS	polydimethylsiloxane
PE	polyelectrolyte, or polymer electrolyte
PEEK	polyether ether ketone
PEG	poly(ethylene glycol)
PEGDA	poly(ethylene glycol) diacrylate
PEGMA	poly(ethylene glycol) methacrylate
PEGMEA	poly(ethylene glycol) methyl ether acrylate
PEI	polyethylenimine
PEM	poly(ethylene malonate)

Acronym	Full Description
PEO	poly(ethylene oxide)
PES	photon emission spectroscopy
PETEA	pentaerythritol tetraacrylate
PFG	pulsed field gradient
PFIB	plasma focused ion beam
PFPE	perfluoropolyether
PFY	partial fluorescence yield
PGE	polymer gel electrolyte
PHEV	plug-in hybrid electric vehicle
PHM	poly(hexylene malonate)
PI	principal investigator
PIB	poly(isobutylene)
PICOFM	porous inorganic covalent-organic framework materials
PI-G	polyimide-graphene
PLiMTFSI	poly((trifluoromethanesulfon)imide lithium methacrylate)
PM	planetary mill
PMF	poly(melamine-co-formaldehyde) methylation
PMMA	polymethyl methacrylate
PMTFSI	poly(lithium bistrifluorosulfonylimide methacrylate)
PMTH	dipentamethylenethiuram hexasulfide
PNNL	Pacific Northwest National Laboratory
POFM	porous organic framework materials
POSS	polyhedral oligomeric silsesquioxane
PP	polypropylene
ppm	parts per million
PPM	poly(pentylene malonate)
PPO	poly(phenylene oxide)
PR	peak region
PSC	patterned sulfur cathode
PS-PES-PS	polystyrene-polyester-polystyrene
PS-SEI	polymer-supported solid electrolyte interphase
PST	partially sintered tape
PSTFSI	poly(4-styrenesulfonyl(trifluoromethanesulfonyl)imide)
PSU	Pennsylvania State University
PTFE	polytetrafluoroethylene
PTFSI	triflimide-based polyion
PTM	poly(trimethylene malonate)
PTO	pyrene-4,5,9,10-tetraone
PVB	polyvinyl butyral
PVDF	polyvinylidene (di)fluoride
PVP	polyvinylpyrrolidone
PXRD	powder X-ray diffraction
Pyr	pyrrolidinium
PyTFSI	pyrrolidinium (trifluoromethanesulfonyl)imide
RAFT	reversible addition−fragmentation chain-transfer
RDF	radial distribution function

Acronym	Full Description
RDS	rate determining step
RE	rare earth
ReaxFF	reactive force field
RF	random forest
rGO	reduced graphene oxide
RHS	right-hand side
RIXS	resonant inelastic X-ray scattering
RM	redox mediator
RMD	reactive molecular dynamics
RMSE	root mean square error
RNGC	Realizing Next Generation Cathodes rate protocol
ROI	regions of interest
RP	red phosphorus
rpm	revolutions per minute
RPT	reference performance test
RR	reduced-repulsion
rSEI	residual solid electrolyte interface
R_{wp}	weighted-profile R-factor
SAED	select area electron diffraction
SAEP	salt affinitive electrolyte phobic
SAM	scanning Auger microscopy
SANS	small angle neutron scattering
SASP	salt affinity solvent phobic
SAXS	small-angle X-ray scattering
SBR	styrene-butadiene rubber
SC	single crystalline
SE	solid electrolyte
SEB	single-end binding
SEI	solid electrolyte interphase
SEM	scanning electron microscopy
SEO	polystyrene-*b*-poly(ethylene oxide) block copolymer
SERS	surface-enhanced Raman spectroscopy
SFSU	San Francisco State University
SHE	standard hydrogen electrode
SIA	structurally isomorphous alloy
SIC	single ion conductor
SIC-SPE	single ion conductor solid polymer electrolyte
SIL	solvate ionic liquid
SIMS	secondary ion mass spectrometry
SLAC	Stanford Linear Accelerator Center
SLD	scattering length density
SLPC	single-layer pouch cell
SN	succinonitrile
SNL	Sandia National Laboratory
SnS	tin sulfide
SOC	state of charge

Acronym	Full Description
SP^2	salt-philic solvent-phobic
SP^2_{perF}	salt-philic solvent-phobic, with addition of a perfluorinated side chain
SPAN	sulfurized polyacrylonitrile
SPC	small particle cathode; sulfur polymerized composite
SPC-1	sulfur polymerized composite – generation 1
SPC-2	sulfur polymerized composite – generation 2
SPE	solid polymer electrolyte
SPM	scanning probe microscopy
SPZ	sulfur polymerized composite
SQUID	superconducting quantum interference device
SRO	short-range order
SS	solid-state
SSB	solid-state battery
SSE	solid-state electrolyte
SSI	solid-state ion
SSLB	solid-state lithium battery
SSLMB	solid-state Li-metal battery
SS-NEB	solid-state nudged elastic band
SSPC	Solid-State Proton Conductors Conference
SSRL	Stanford Synchrotron Radiation Lightsource
S-SSE	sulfide-based solid-state electrolyte
STD	standard deviation
STEM	scanning transmission electron microscopy
STZ	shear transformation zone
SUS	stainless steel
SWCNT	single-walled carbon nanotube
sXAS	soft x-ray absorption spectroscopy
SXRD	synchrotron-based X-ray diffraction
T_c	glass crystallization temperature
TCR	thermal contact resistance
TEGDME	tetraethylene glycol dimethyl ether
TEM	transmission electron microscopy
TEMPO	2,2,6,6-tetramethyl-1-piperidinyloxy
TEP	triethyl phosphate
TES	tender energy X-ray absorption spectroscopy
TEY	total electron yield
TFC	thin-film composite
TFP	tris(2,2,2-trifluoroethyl) phosphate
TFSI	(trifluoromethanesulfonyl)imide
TFTFE	1,1,2,2-tetrafluoroethyl 2,2,2-trifluoroethyl ether
T_g	glass transition temperature
TGA	thermal gravimetric analysis
TGC	titration gas chromatography
THF	tetrahydrofuran
TiMS	titration mass spectrometry
TL	top layer

Acronym	Full Description
TM	transition metal
TMA	trimethylaluminum
TMD	transition metal dichalcogenide
TME	trimethylolethane
TMP	trimethyl phosphate
TMPMA	acetonide-protected trimethylolpropane methacrylate
TMS	tetramethylsilane
TOF-SIMS	time-of-flight secondary ion mass spectrometry
TRL	technology readiness level
TTE	1,1,2,2-tetrafluoroethyl-2,2,3,3-tetrafluoropropyl ether
TXM	transmission X-ray microscopy
UCB	University of California, Berkeley
UCSD	University of California, San Diego
UH	University of Houston
UHV	ultrahigh vacuum
UIC	University of Illinois, Chicago
UK	University of Kentucky
UM	University of Michigan
UMD	University of Maryland
UNC	University of North Carolina
UNLS	ultra-nanocrystalline lithium superoxide
U-Pitt	University of Pittsburgh
UT	University of Texas
UV	ultraviolet
UW	University of Washington
UWM	University of Wisconsin, Madison
VASP	Vienna A*b initio* Simulation Package
VBM	valence band maximum
VC	vinylene carbonate
VE	virtual electrode
VE-SAM	virtual electrode scanning Auger microscopy
VE-XPS	virtual-electrode X-ray photoelectron spectroscopy
VGCF	vapor-grown carbon fibers
VOC	volatile organic compound
VR	valley region
VTF	Vogel-Tammann-Fulcher
VTO	Vehicle Technologies Office
WAXS	wide-angle X-ray scattering
WL	white light
XAFS	X-ray absorption fine structure
XANES	X-ray absorption near-edge structure
XAS	X-ray absorption spectroscopy
x-PDF	synchrotron X-ray diffraction and pair distribution function
xPEO	crosslinked poly(ethylene oxide)
XPS	X-ray photoelectron spectroscopy
XRD	X-ray diffraction

Acronym	Full Description
XRF	X-ray fluorescence
XRT	X-ray tomography
zPU	zwitterionic polyurethane
ZR	Zhang-Rice singlet